International Journal of Photoenergy

Recent Advances in Sustainable Solar Energy Technologies

Lead Guest Editor: Kumarasamy Sudhakar
Guest Editors: Evgeny Solomin, Erdem Cuce, and S. Shanmuga Priya

Recent Advances in Sustainable Solar Energy Technologies

International Journal of Photoenergy

Recent Advances in Sustainable Solar Energy Technologies

Lead Guest Editor: Kumarasamy Sudhakar
Guest Editors: Evgeny Solomin, Erdem Cuce, and S. Shanmuga Priya

Copyright © 2021 Hindawi Limited. All rights reserved.

This is a special issue published in “International Journal of Photoenergy.” All articles are open access articles distributed under the Creative Commons Attribution License, which permits unrestricted use, distribution, and reproduction in any medium, provided the original work is properly cited.

Chief Editor

Giulia Grancini, Italy

Academic Editors

Mohamed S.A. Abdel-Mottaleb, Egypt
Angelo Albini, Italy
Mohammad Alghoul, Malaysia
Alberto Álvarez-Gallegos, Mexico
Vincenzo Augugliaro, Italy
Detlef W. Bahnemann, Germany
Simona Binetti, Italy
Fabio Bisegna, Italy
Thomas M. Brown, Italy
Joaquim Carneiro, Portugal
Yatendra S. Chaudhary, India
Kok-Keong Chong, Malaysia
Věra Cimrová, Czech Republic
Laura Clarizia, Italy
Gianluca Coccia, Italy
Daniel Tudor Cotfas, Romania
P. Davide Cozzoli, Italy
Dionysios D. Dionysiou, USA
Elisa Isabel Garcia-Lopez, Italy
Wing-Kei Ho, Hong Kong
Siamak Hoseinzadeh, Italy
Jürgen Hüpkes, Germany
Fayaz Hussain, Brunei Darussalam
Mohamed Gamal Hussien, Egypt
Adel A. Ismail, Kuwait
Chun-Sheng Jiang, USA
Zaiyong Jiang, China
Yuanzuo Li, China
Manuel Ignacio Maldonado, Spain
Santolo Meo, Italy
Claudio Minero, Italy
Regina De Fátima Peralta Muniz Moreira, Brazil
Maria da Graça P. Neves, Portugal
Tsuyoshi Ochiai, Japan
Kei Ohkubo, Japan
Umapada Pal, Mexico
Dillip K. Panda, USA
Carlo Renno, Italy
Francesco Riganti-Fulginei, Italy
Leonardo Sandrolini, Italy
Jinn Kong Sheu, Taiwan
Kishore Sridharan, India
Elias Stathatos, Greece
Jegadesan Subbiah, Australia
Chaofan Sun, China
K. R. Justin Thomas, India
Koray Ulgen, Turkey
Ahmad Umar, Saudi Arabia
Qiliang Wang, China
Xuxu Wang, China
Huiqing Wen, China
Weijie Yang, China
Jiangbo Yu, USA

Contents

Hindawi
International Journal of Photoenergy
Volume 2021, Article ID 9921940, 19 pages
https://doi.org/10.1155/2021/9921940

Research Article

A Technoeconomic Feasibility Analysis for Affordable Energy System in the East African Community Countries

Samuel Bimenyimana[1], **Chen Wang**[1], **Godwin Norense Osarumwense Asemota**[2,3], **Aphrodis Nduwamungu**[3], **Cicilia Kemunto Mesa**[4], **Jeanne Paula Ihirwe**[5,6], **Jean De Dieu Niyonteze**[7], **Shilpi Bora**[1,8], **Chun-Ling Ho**[1], **Noel Hagumimana**[9], **and Yiyi Mo**[1]

[1]*Huaqiao University, Intelligence and Automation in Construction Provincial Higher-Educational Engineering Research Centre, 361021, Xiamen, China*
[2]*Morayo College, Nairobi, Kenya*
[3]*University of Rwanda, African Centre of Excellence in Energy for Sustainable Development, Kigali 4285, Rwanda*
[4]*Kenya Industrial Research and Development Institute, Nairobi, Kenya*
[5]*Hebei University of Technology, Department of Economics and Management, Tianjin, China*
[6]*Hello Renewables Ltd, Kigali, Rwanda*
[7]*Carnegie Mellon University Africa, Kigali, Rwanda*
[8]*Ajeenkya D Y Patil University, Lohegaon, Pune, Maharashtra, India*
[9]*Fujian Province Key Laboratory of Automotive Electronics and Electric Drive, Fujian University of Technology, Fuzhou 350118, China*

Correspondence should be addressed to Chen Wang; wch@hqu.edu.cn

Received 25 March 2021; Revised 14 July 2021; Accepted 6 August 2021; Published 24 August 2021

Academic Editor: Kumarasamy Sudhakar

Copyright © 2021 Samuel Bimenyimana et al. This is an open access article distributed under the Creative Commons Attribution License, which permits unrestricted use, distribution, and reproduction in any medium, provided the original work is properly cited.

Access to energy is among the key pillars to socioeconomic and improved life style. The East African Community (EAC) countries, also members of sub-Saharan Africa, are among countries with enough energy resources but still struggling with low electricity access, and the lower proportion of citizens with electricity access challenges such as expensive tariff, frequent blackouts, and unreliable service still persists. Diesel technology is among the easy and fast installation technologies for a location with an urgent need of electricity while solar is a clean technology with free fuel. Considering the diversity of electricity tariffs, cost of diesel fuel, and suitability to solar energy exploitation in EAC, this paper intends to provide a technoeconomic analysis for reliable, affordable, and sustainable energy system in the region. A daily load of 94.44 kWh recorded from averaging electricity bills of a luxury house in Kigali, Rwanda, is used as research object, and HOMER simulations are carried on considering the level of such daily load being supplied by either (a) diesel generator, (b) solar + diesel technology, (c) PV + battery storage, or (d) PV + battery storage + grid system in each member country of the EAC. The results show that (a) solar energy is a feasible and applicable technology for energy generation for the whole six EAC countries; (b) for South Sudan, if it is a standalone system, the diesel technology is less costly than solar technology; however, solar energy can still be recommended to be adopted as it has no gas emissions; (c) except South Sudan, PV + battery storage technology is found to be more affordable and cleaner than any technology including diesel; and (d) the option of connecting PV + battery storage to the grid is found more economical for locations where grid interaction is possible because their levelized electricity costs (LCOE) are lower than the real electricity tariffs currently in use within each of the six EAC countries. The solar energy system with battery storage (both off-grid and grid connected) proposed in this research can lead to an efficient increase of national energy resource exploitation in the EAC countries, resulting in reliable, affordable, and sustainable energy access to all the citizenry of the EAC.

1. Introduction

Access to energy is among the key pillars to socioeconomic and improved life style [1]. Key indicators from different research perspectives show that electrification has acquired steady progress worldwide within the past decade. However, there is a huge population around the globe who has not yet acquired access to electricity (estimation of 770 million population globally with energy poverty where around 577.5 million (75%) are located in sub-Saharan Africa) [2, 3]. Living without access to electricity is a major challenge and ultimate economic obstacle as it prevents people from fully participating in the modern economy. The East African Community (EAC) countries, which are also members of sub-Saharan Africa, are among countries with enough energy resources but still struggling with low electricity access, and to the lower proportion of citizens with electricity access, challenges such as expensive tariffs, frequent blackouts, and unreliable service still persist [4, 5]. Figure 1 indicates the actual location of the East African Community countries as both an economic and a linguistic block on the map of Africa [6].

Figure 1: Location of EAC countries on the map of Africa.

In modern era, different technologies (renewables and nonrenewable) are adopted, and others are being developed all for the purpose of taking off energy crisis and shortage worldwide in different countries. Diesel technology is a fast and rapid energy solution for a location with urgent need of electrification due to its straightforward and swift installation; diesel generators are highly useful devices that apply diesel fuel to generate electricity [1, 3, 5]. To produce electricity, these devices combine an electric generator with a diesel engine. However, with the current mitigation policies and regulations, their adoptions must be carefully analysed before their recommended usage to a certain area [3]. Solar energy technologies transform sunlight radiations into usable electrical energy either through PV modules or mirrors that concentrate sunlight radiation. This energy can be utilized to produce electric power or can be kept in energy-storing devices (batteries) or thermal storage battery devices. Africa is considered the "sun mainland" or the landmass with the highest sun's effect. Also, the "World Sunshine Map" indicates that Africa receives abundant sunlight all year than other continents on the Earth. Despite the enormous solar capacity, the penetration of solar power in Africa is presently very low [7–11]. Photovoltaic solar energy is a viable and promising alternative and prospect because it authorizes the rapid deployment of carbon-free, economically accessible energy on a large scale. But, only a limited number of solar technologies have been installed in Africa to date.

Except diesel technology and solar energy, there are other energy technologies like hydropower, coal-fired, biomass, wind, tidal, geothermal, and bioenergy. Hybrid energy technology and systems tie together two or more technologies in order to build more effective systems. They integrate multiple power generation and storage units to meet the needs of the environment [12]. There is some existing research exploring and analysing technoeconomic concepts of applicability and adoption of different renewable energies in some African regions such as sub-Saharan Africa and each country as well; however, (a) there is no existing research analysing solution to affordable energy option for the whole EAC country members; (b) some EAC members such as Burundi and South Sudan still have not enough scientific research works published investigating technoeconomic situation related to renewable energy exploration. Thus, the research in this paper is intended to provide cost comparison of technology approaches which can lead to affordable and reliable energy systems and services in the East African Community countries. Different alternative technologies: (a) diesel technology, (b) solar PV + diesel technology, (c) PV + battery storage, and (d) PV + storage battery + grid, are analysed to find the least cost and affordable technology with respect to different climatic weather conditions and diesel fuel price levels in the six EAC countries. It is hypothesised that high solar energy exploitation in EAC countries can contribute a lot to ameliorate the energy crisis and shortage in EAC with citizens without electricity access and solve the affordability and unreliability issues for grid-connected users in the region. Table 1 describes the analogy of different state-of-the-art analyses with the proposed solution.

2. Experimental Methodology

2.1. Site Location and Visit. Site visits were made to an electricity user with luxury house located in Rwanda, Kigali city (Kimisagara National Road, Kigali, Rwanda) (1° 57.2′ S, 30° 2.8′ E), and its average electric load was calculated based on the electricity bill for the past eight months and the electricity tariff. The average load was estimated at 23.85 kW daily peak load, 182°kWh per day, and 66430°kWh annual load. This load structure was used as a research object in the other five EAC countries with different locations (as shown in Figure 2) such as at 2 Mulago III 2662, Kampala, Uganda (0° 20.8′ N, 32° 34.9′ E), for Uganda; at Unnamed Road, Dodoma, Tanzania (6° 10.3′ S, 35° 45.6′ E), for Tanzania; at Times Tower, Nairobi, Kenya (1° 17.5′ S, 36° 49.4′ E), for Kenya; at Bentiu, South Sudan (9° 13.9′ N, 29° 48.0′ E), for

Table 1: Analogy of different state-of-the-art analyses with the proposed solution.

Reference	Country of application	Resource parameters	Power ratings of model architecture	Expression of initial capital cost	Operating cost ($/year)	NPC(US$)	LCOE (US$/kWh)	Other metric parameters
[27]	Mbuguni, Arumeru district, Tanzania	Global horizontal irradiation for the entire country varies between 5.2 and 6.4 kWh/m^2 Annual average solar irradiation: 5.6 kWh/m^2/day Annual average wind speed: 5.17 m/s	SPV-W-GEN Solar PV: 0.764 kW 1 wind turbine: 1 kW 5 batteries: 12 V, 83.4 Ah Converter system: 0.824 kW Generator: 1.40 kW	Capital cost Solar PV: 1000$/kW Wind turbine: 780$/kW Battery: 150$ Replacement cost Solar PV: 900$/kW Wind turbine: 780$/kW Battery: $150	239.86	6259.86	0.21467	52.42 L of diesel
			SPV Solar PV: 3.36 kW 16 batteries: 12 V, 83.4 Ah Converter system: 1.37 kW		359.30	10638.52	0.32599	Pure renewable
			SPV-wind Solar PV: 1.30 kW 1 wind turbine: 1 kW 10 batteries: 12 V, 83.4 Ah Converter system: 1.15 kW		218.95	7110.53	0.24394	Pure renewable
			SPV-Gen Solar PV: 2.25 kW 9 batteries: 12 V, 83.4 Ah Converter system: 1.1 kW Generator: 1.40 kW		388.90	9505.97	0.32599	69.92 L of diesel
			Wind-Gen 10 batteries: 12 V, 83.4 Ah Converter system: 0.75 kW		413.81	8031.25	0.27541	183.32 L of diesel

Table 1: Continued.

Reference	Country of application	Resource parameters	Power ratings of model architecture	Expression of initial capital cost	Operating cost ($/year)	NPC(US$)	LCOE (US$/kWh)	Other metric parameters
			Generator: 1.40 kW Gen Generator: 1.40 kW		2409.94	31,854.57	1.09238	1654.39 L of diesel
[28]	Djounde, Mora, Cameroon 11° 30′ 00″ north 14° 18′ 00″ east	Average annual wind speed at the site was 4.95 m/s at 50 m anemometer 6.67 kWh/m^2/day maximum solar irradiation and minimum: 4.77 kWh/m^2/day	PV: 81.8 kW Biogas generator: 15 kW Wind turbine: Pumped hydrostorage converter: 40 kW	323,750$	4031	451165.19	0.316	Power production (kWh/year) PV array: 141,046 Wind turbine: 0 Biogas generator: 17,794 Total: 158,840 Consumption (kWh/year) 125,056
[29]	Batocha, Cameroon	5.93 kWh/m^2/day Annual average horizontal irradiation 9 L/s annual average flow rate	Solar PV: 5 kW Hydroturbine: 2.12 kW Diesel: 1 kW 125 batteries Inverter: 6 kW Rectifier: 6 kW	Solar PV: 21,000$ Hydroturbine: 6000$ Diesel: 1000$ Batteries: 3000$ Converter:5143$ Total system replacement: 28,897$	PV: 703 Hydroturbine: 1562 Diesel:1765 Battery: 976 Converter: 1339 Other: 101	70,042	0.278	Power production (kWh/year) PV array: 9831.0 (39.0%) Diesel: 191.0 (1.0%) Hydroturbine: 15,493.0 (61.0%) Unmet load: 172.0 (1.0%) Capacity shortage: 309.0 (2.0%) Excess electricity: 9110.0 (33.0%)
[30]	Rwanda	—	Hydro: 10 kW Wind turbine: 100 kW Solar PV: 1.09 kW Converter: 0.05 kW	Capital cost Wind turbine: 80,000$ Hydro: 20,000$ Solar PV: 16,000$ Batteries (1 kWh each): 2400$ Converter: 30,000$	1895.49	126,324.10	0.1715	Production (kWh/year) Hydro: 122,716 (82.6%) Solar PV: 1620 (1.09%) Wind turbine: 24,203 (16.3%)
			Hydro (1 turbine): 10 kW PV: 1.09 kW Converter: 10 kW		1495.49	41,210.80	0.05601	Production (kWh/year) Hydro: 122,716 (98.7%) Solar PV: 1620 (1.3%)
			Hydro: 10 kW Wind turbine: 100 kW		1873.48	124,175.90	0.1688	Production (kWh/year) Hydro: 122,716 (83.5%) Wind turbine: 24,401.3 (16.5%)
[26]	Golbo II village, Adaa district,	Solar radiation: 3.74 kWh/m^2/day	Scenario 1 Solar PV: 20 kW 3 wind turbines:	Wind turbine: initial cost 2000$/kW	Wind turbine 50$/year/turbine Diesel generator:	82,734	0.207	Power production PV array: 41,957 (80%) Wind turbines: 7306 (14%)

Table 1: Continued.

Reference	Country of application	Resource parameters	Power ratings of model architecture	Expression of initial capital cost	Operating cost ($/year)	NPC(US$)	LCOE (US$/kWh)	Other metric parameters
	Oromia Region, Ethiopia		3 kW Diesel generator: 5 kW 24 batteries: 2 V, 3000 Ah Converter	Replacement 1600$/kW Diesel generators: Capital outlay: USD 250/kW Restoration: USD 200/kW Converter; capital cost: 1300.0 USD/kW Replacement: 1000 USD/kW Batteries: Capital cost: 400 USD/kWh Replacement: 300 USD/kWh	USD 0.3/hour Converter: 5 USD/year Battery: 20 USD/year			
		Solar radiation: 3.74 kWh/m^2/day Diesel consumption: 2233 L	Scenario 2 Solar PV array: 20 kW Diesel generator: 7 kW 24 batteries: 2 V 3000 Ah			85,754	0.214	Generator: 3073 (6%) Total production: 52336 kWh AC primary load served: 37,780 kWh Excess electricity: 5779 kWh (11%) Unmet load: 1676 kWh (4%) Capacity shortage: 2295 kWh (6%) Power production: PV array: 41,957 (87%) Generator: 6014 (13%) Total production: 47,970 kWh AC primary load served: 37,838 kWh Excess electricity: 1686 kWh (4%) Unmet load: 1619 kWh (4%) Capacity shortage: 2303 kWh (6%)
		Diesel consumption: 12,973 L	Scenario 3 3 water turbine: 3 kW each 24 batteries: 2 V, 3000 Ah Diesel generator: 7 kW			141,126	0.352	—
		Diesel consumption: 15,278 L	Scenario 4 Diesel generator: 7 kW 20 batteries: 2 V, 3000 Ah			153,249	0.384	—
[31]	Ethiopia 2 3 sites Site 1: Serwat	Diesel consumption: 17,507 L/year	5 wind turbines: Diesel generator: 110 kW 240 batteries Converter: 100 kW	USD 501,031	—	1,248,119	0.574	Renewable fraction: 0.86
		Diesel consumption: 16,898 L/year	Solar PV: 5 kW 5 wind turbines: Diesel generator: 110 kW 240 batteries Converter: 100 kW	USD 521,031	—	1,253,599	0.576	Renewable fraction: 0.87

Table 1: Continued.

Reference	Country of application	Resource parameters	Power ratings of model architecture	Expression of initial capital cost	Operating cost ($/year)	NPC(US$)	LCOE (US$/kWh)	Other metric parameters
		Diesel consumption: 5767 L/year	Solar PV: 180 kW Diesel generator: 70 kW 400 batteries Converter: 150 kW	USD 1,170,839	—	1,526,634	0.702	Renewable fraction: 0.94
		Diesel consumption: 0 L/year	Solar PV: 180 kW 3 wind turbines 560 batteries Converter: 130 kW	USD 1,404,230	—	1,733,954	0.797	Renewable fraction: 1.00
		Diesel consumption 137,797 L/year	Diesel generator: 150 kW	USD 27,083	—	6,161,842	2.831	Renewable fraction: 0
		Diesel consumption: 11,299 L/year	Solar PV: 30 kW 2 wind turbines: Diesel generator: 50 kW 120 batteries Converter: 50 kW	USD 353,875	—	754,408	0.605	Renewable fraction: 0.85
		Diesel consumption: 13,092 L/year	3 wind turbines: Diesel generator: 50 kW 160 batteries Converter: 70 kW	USD 323,445	—	766,324	0.614	Renewable fraction: 0.85
	Site 2: Feleg Daero	Diesel consumption: 5991 L/year	Solar PV: 100 kW Diesel generator: 30 kW 200 batteries Converter: 70 kW	USD 624,249	—	$886,466	0.711	Renewable fraction: 0.91
			Solar PV: 100 kW 2 wind turbines, 320 batteries	USD 814,060	—	1,030,860	0.827	Renewable fraction: 1.00

Table 1: Continued.

Reference	Country of application	Resource parameters	Power ratings of model architecture	Expression of initial capital cost	Operating cost ($/year)	NPC(US$)	LCOE (US$/kWh)	Other metric parameters
			Converter: 90 kW Diesel generator: 85 kW	USD 24,505	—	3,758,776	3.012	Renewable fraction: 0.00
		Diesel consumption: 2184 L/year	Solar PV: 5 kW 1 wind turbine Diesel generator: 10 kW 32 batteries Converter: 10 kW	USD 101,081	—	191,580	0.410	Renewable fraction: 0.90
	Site 3: Adi Mesanu	Diesel consumption: 3377 L/year	1 wind turbine Diesel generator: 10 kW 32 batteries Converter: 10 kW	USD 81,081	—	$198,261	0.425	Renewable fraction: 0.84
			Solar PV: 15 kW 1 wind turbine 80 batteries Converter: 15 kW	USD 179,390	—	241,049	0.517	Renewable fraction: 1.00
		Diesel consumption: 22,009 L/year	Diesel generator: 15 kW	USD 7762	—	781,317	1.673	Renewable fraction: 0.00
[32]	Khartoum, Sudan	—	Solar PV: 0.15 kW 2 batteries: 6 V, 225 Ah	150.98707$	—	224.1269	0.12	—
			Solar PV: 1 kW 1 wind generator: 3 turbines, 0.5 kW 16 batteries: 6 V, 225 Ah	1902.8909$	—	2052.8777	0.06	—
			Solar PV: 2 kW 1 wind generator: 3 turbines, 0.5 kW 24 batteries: 6 V, 225 Ah	2388.1036$	—	3569.872	0.05	—

Table 1: Continued.

Reference	Country of application	Resource parameters	Power ratings of model architecture	Expression of initial capital cost	Operating cost ($/year)	NPC(US$)	LCOE (US$/kWh)	Other metric parameters
			Solar PV: 2.5 kW 2 wind generators 24 batteries: 6 V, 225 Ah	5338.6579$	—	4878.2071	0.06$/kWh	—
			Solar PV: 3.5 kW 2 wind generators 3 turbines, 0.5 kW 8 batteries 6 V, 225 Ah	3823.3956$	—	4735.2341	0.04	—
[33]	Sokoto, Nigeria Latitude 10.0° N and longitude 8.0° E	Wind speed: between 4.5 m/s and 5.2 m/s at ≥10 m	Solar/wind system Solar PV: 35.21 kW Wind turbine: 25.0 kW and 4.75 kW mean output 24 batteries : 12 V, 83400 Ah Converter: inverter: 17.44 kW Rectifier: 15.66 kW	Capital cost Solar PV: 105,604.91 USD Wind turbine: 58,333.33 Battery: 80,700 USD Converter: 5232 USD Total system cost: 249910.24 USD	Operation & replacement cost for solar PV: 4501.66 Wind turbine: 33,102.53 Battery: 96,930.33 Converter: 2183 Total system replacement cost: 82914.85 Maintenance cost: 53802.80	—	—	Total production/year: 93,300 kWh PV: 57.5% Wind: 42.5%
[34]	NyongYapalsi, Karaga district, Ghana 9° 46.601′ N, 0° 36.944′ W	Solar resource: average annual solar irradiance of 5.57 kWh/m^2/day	Solar PV minigrid with storage batteries Solar PV: 24.4 kW Converter: 11.4 kW 156 batteries: 12 V, 200 Ah	Capital cost: $72,324.00	Operating cost: $4233/yr.	119,479.00	$0.480	Total electricity production: 53,211 kWh Surplus: 46.5%
			Solar PV minigrid with storage batteries Solar PV: 24.4 kW	—	—	82,166.00	$0.330	—

Table 1: Continued.

Reference	Country of application	Resource parameters	Power ratings of model architecture	Expression of initial capital cost	Operating cost ($/year)	NPC(US$)	LCOE (US$/kWh)	Other metric parameters
[35]	Gweru, Zimbabwe	Wind potential: 15.0 W/m^2 in Kariba to 115.0 W/m^2 at 50.0 m hub height in Gweru Monthly wind speed: 4.215 m/s Solar potential: 5.81 kWh/m^2/day annual average	Converter: 11.4 kW 156 batteries: 12 V, 200 Ah This arrangement has free solar PV panels Solar PV-wind hybrid: Battery capacity: 245.0 Ah/24.0 V Power source: 300.0 W Wind turbine and 2 × 125.0 W PV modules LED streetlights 80 W/24 V Charge controller 20 A/24 V Solar-Wind Hybrid (PMW)	—	—	4350.0	0.175	(400 − 245)/400 = 38.75% Energy storage reduced by 38.75%
			PV stand-alone Battery capacity 400 Ah/24 V Power source: 2 × 210.0 W PV modules LED streetlights: 80.0 W/24 V Charge controller 20.0 A/24 V Solar charger Controller (PWM)	—	—	—	—	—

Table 1: Continued.

Reference	Country of application	Resource parameters	Power ratings of model architecture	Expression of initial capital cost	Operating cost ($/year)	NPC(US$)	LCOE (US$/kWh)	Other metric parameters
[36]	South Africa		Solar PV: 5 kW 30 batteries 2 V, 720 Ah: Generator: 5.5 kW, 50 Hz, rpm3000 Converter: 6 kW	Capital cost: Solar PV: $4250 Battery: $269 Generator: $313 Converter: $3731 Fuel: $0.7/L: $32,990 Fuel: $0.9/L: $15,398	—	$62,402.0 at 0.7$/L $65,833.0 at 0.9$/L	—	Least case diesel use (Upington) 1267.0 L/year at $0.7/L and 1275 L/year at $0.9/L 3.336 tons/year CO_2 emissions for diesel priced at 0.7$/L and 3.359 tons/year CO_2 emissions for diesel priced at 0.7$/L

Conversion rate: 1 euro equals 1.2179631$; 1$ equal to 409.903 Sudan Pound; date of conversion: 23rd May 2021; conversion source: https://www.xe.com/. Table 1 indicates the analogy of different state-of-the-art analyses (studies using different energy technologies including renewable and conventional energy resources) and the proposed solution. It can be seen that different parameters such as net present value cost (NPC), levelized electricity expense (LCOE), renewable energy percentage, and electricity production from the system have played a key role in deciding and concluding the energy system which is optimal, reliable, sustainable, and affordable for the study cases.

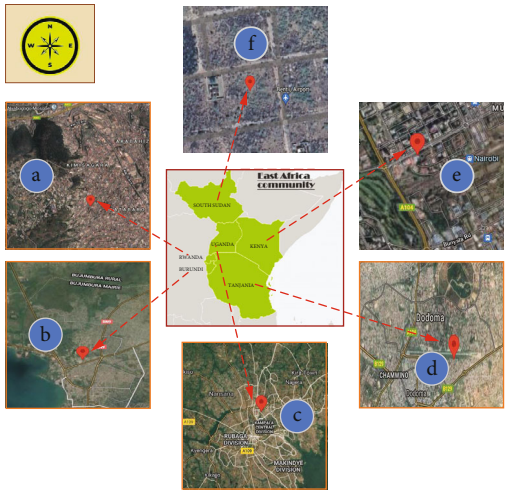

Figure 2: A map that depicts different selected sites in the East African Community countries: (a) is the Kimisagara National Road, Kigali, Rwanda (1° 57.2′ S, 30° 2.8′ E); (b) is the Chaussee de L'Agriculture, Bujumbura, Burundi (3° 21.7′ S, 29° 21.5′ E); (c) is the 2 Mulago III 2662, Kampala, Uganda (0° 20.8′ N, 32° 34.9′ E); (d) is the Unnamed Road, Dodoma, Tanzania (6° 10.3′ S, 35° 45.6′ E); (e) is the Times Tower, Nairobi, Kenya (1° 17.5′ S, 36° 49.4′ E); while the Bentiu, South Sudan (9° 13.9′ N, 29° 48.0′ E) is shown in (f).

South Sudan; and at Chaussee de L'Agriculture, Bujumbura, Burundi (3° 21.7′ S, 29° 21.5′ E), for Burundi. The luxury house electric load data was used in the paper to prove that solar energy can still be an affordable and reliable option regardless of the energy consumption size range.

2.2. Load Profile. Figure 3 depicts the daily load variation of the luxury house used in the research.

The load pattern indicates a fluctuation from 4.00 kW (0.00 hr) to 2.50 kW (04.075 hrs), 5.00 kW (05.00 hrs), 10.00 kW (08.15 hrs), 9.25 kW (9.15 hrs), 12.00 kW (13.225 hrs), 9.00 (15.00 hrs), 10.00 kW (16.375 hrs), 15.00 kW (18.45 hrs), 16.50 kW peak (19.30 hrs), 15.00 kW (20.00 hrs), and 7.00 kW (23.45 hrs).

2.3. HOMER Simulation and Scenario Analysis. The scenarios to be carefully analysed as shown in Figure 4, include (a) use the diesel system to supply the loads during day and night times; (b) solar PV system without battery storage system to supply the loads at daytime and diesel generator as alternative to supply the load during daytime if the irradiance is not enough to generate the level of electricity which can satisfy the load and also at night; because there is no sunshine, the diesel generator will be the supply; (c) use the PV system with storage systems during daytime and night time,;(d) use the PV with storage the whole day to supply the loads and inject extra electricity to the grid or draw electricity from the grid in case the electricity generation capacity from the hybrid system is lower than the load capacity.

2.4. Estimation of LCOE, NPC, and OPEX. The LCOE is also the income estimation needed to develop and run an energy/electricity generation plant during the cost recovery period. The LCOE can be expressed by Equations (1) and (2) [13–15].

$$\text{LCOE} = \frac{\text{Cycle life of the total life}}{\text{Total lifetime power generated}}, \tag{1}$$

$$\text{LCOE} = \frac{\sum_{t=1}^{n}\left((I_t + M_t + F_t)/(1+t)^t\right)}{\sum_{t=1}^{n}\left(E_t/(1+t)^t\right)}, \tag{2}$$

where I_t stands for the spending on investments for the year t; M_t, expenditures on operations and maintenance during the fiscal year t; F_t, fuel expenses for the year t; E_t, amount of electrical energy produced in a given year t; r is the discount rate; and n is the anticipated system or power station lifespan.

Homer software uses the concept shown in Equation (3) to calculate and compute the levelized cost of energy depending on different parameters.

$$\text{LCOE} = \frac{C_{\text{ann},t}}{E_{\text{prim}} + E_{\text{def}} + E_{\text{grid,sales}}}, \tag{3}$$

where $C_{\text{ann},t}$ stands for the total cost for the whole year and E_{prim} and E_{def} stand for the yearly total primary and deferrable load.

$$\text{LCOE}_{\text{PV}} = \frac{\sum_{t=0}^{n}\left((C_{\text{PVextra}} + C_{\text{PVdirect}})_t/(1+r)^t\right)}{\sum_{t=0}^{n}\left((E_{\text{PVextra}} + E_{\text{PVdirect}})_t/(1+r)^t\right)}, \tag{4}$$

$$\text{LCOE}(E_{\text{out}}) = \frac{C_{\text{PVextra}}}{\eta E_{\text{PVdirect}}} + \frac{C_{\text{EES}}}{E_{\text{EES}}}. \tag{5}$$

Then, the overall levelized cost of electricity for the whole hybrid system (stand-alone PV and storage) $\text{LCOE}_{(\text{system})}$ can be expressed in the following equation.

$$\text{LCOE}_{(\text{system})} = \frac{\sum_{t=0}^{n}\left(C_{\text{system}}/(1+r)^t\right)}{\sum_{t=0}^{n}\left(E_{\text{system}}/(1+r)^t\right)} = \frac{C_{\text{PVextra}} + C_{\text{EES}} + C_{\text{PVdirect}}}{E_{\text{EES}} + E_{\text{PVdirect}}}, \tag{6}$$

where r stands for the discount rate factor; n stands for the lifespan; E_{PVdirect} and C_{PVdirect} stand for the direct energy from the PV to the load and its cost, respectively; E_{system} and C_{system} stand for the system's energy and its cost; and E_{EES} and C_{EES} stand for the energy in the energy storage device and its cost.

The term "net present cost" (NPC) refers to the present value of all expenses during the term of interest, including residual values such as negative costs, all added together; it is the present value of all expenses associated with installing and running the Component during the project's lifespan, subtracting the present value of all revenues earned over the project's duration [4, 16, 17]. The operating expenses or expenditure (OPEX) refer to the expenses incurred by a firm in carrying out its day-to-day activities [18].

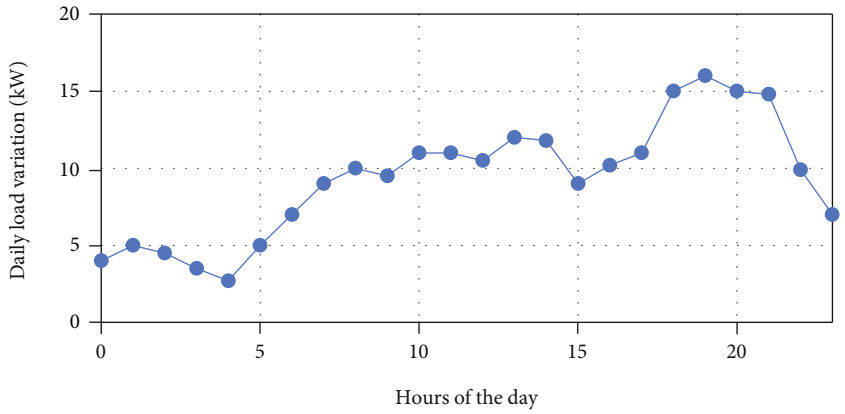

Figure 3: Daily load variation for the luxury house used as a research object.

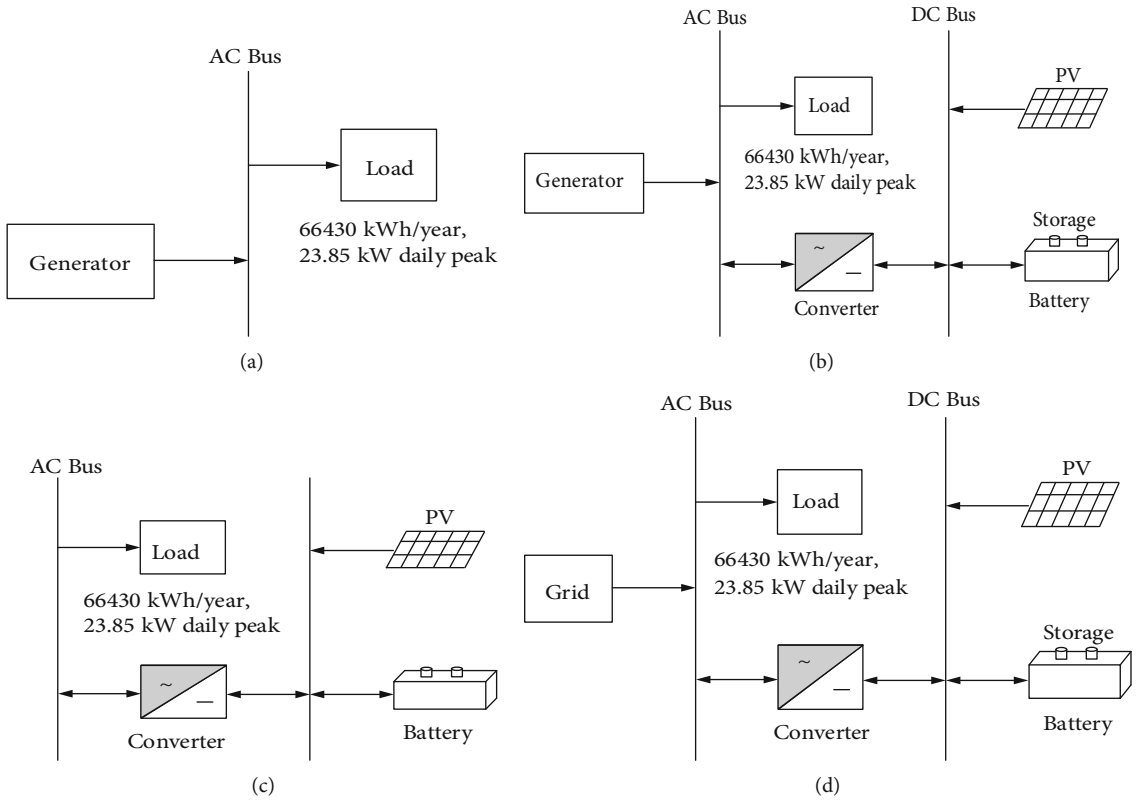

Figure 4: Various configurations of energy technologies: (a) diesel technology, (b) diesel + PV technology, (c) PV + battery storage technology, and (d) PV + battery storage + grid.

The NPC (C_{NPC}) and OPEX (can be expressed through the following equation [13]:

$$C_{NPC} = \frac{C_{ann,tot}}{CRF(i,N)},$$
$$CRF(i,N) = \frac{i(1+i)^N}{(1+i)^N - 1}, \quad (7)$$
$$C_{OPEX} = C_{ann,tot} - C_{ann,cap},$$

where $C_{ann,tot}$ stands for the annualized total cost, i stands for the interest rate (discount rate), N represents the project lifetime, $C_{ann,cap}$ stands for the annualized capital cost, and CRF stands for the capital recovery factor.

From Figure 5 [13], it can be seen that the climatic weather conditions and geographical location of different African countries are attractive to the exploitation of different renewable energy resources. Figure 6 [19–22] depicts the cost of diesel fuels as used in this research.

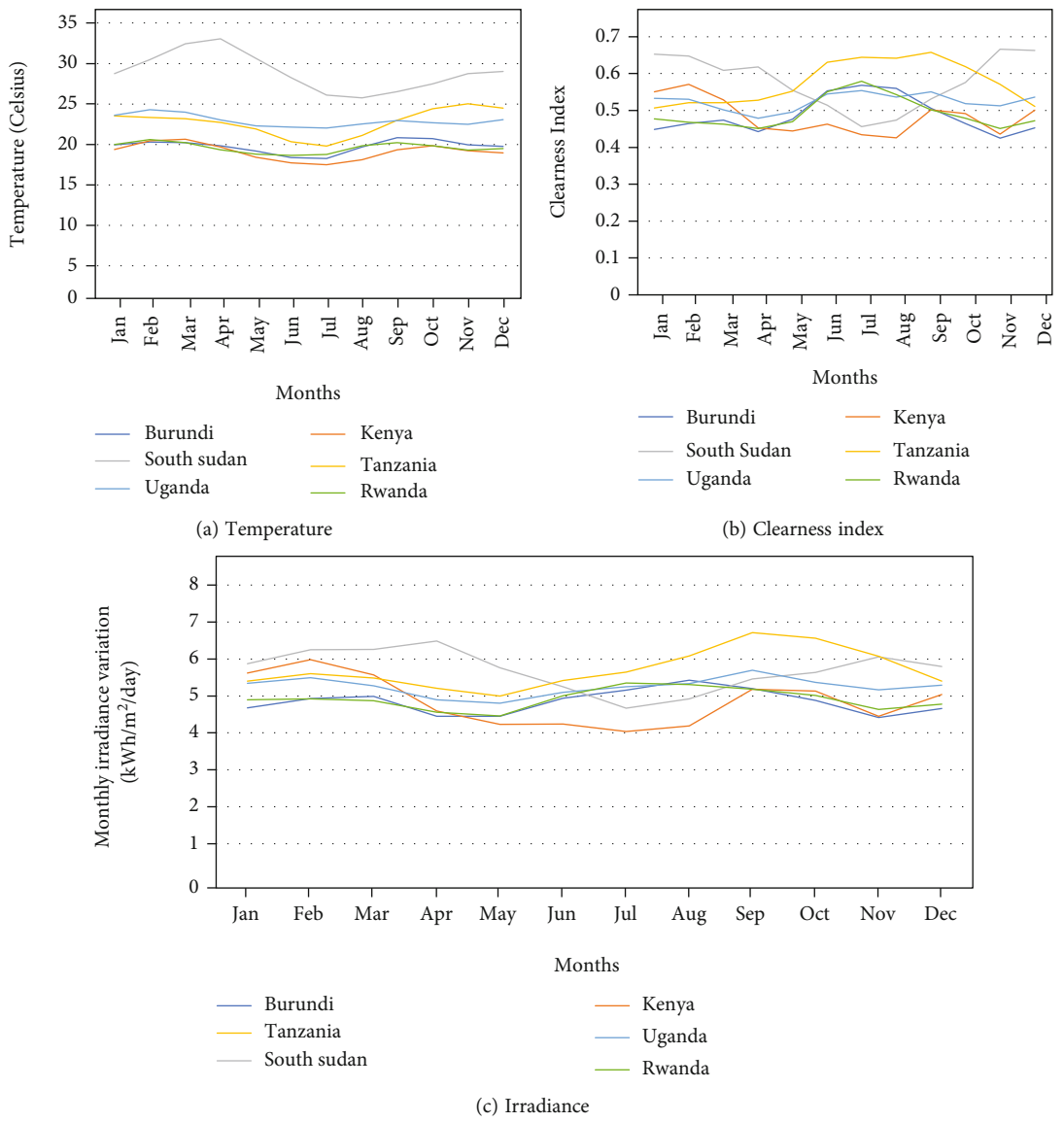

Figure 5: Climatic weather parameters (annual) for the six EAC countries.

3. Results and Discussion

3.1. Levelized Cost of Electricity (LCOE) for Various Scenarios

3.1.1. Scenario 1: Diesel. Figure 7 indicates that the LCOE of diesel generator microgrid technology for each of the six EAC countries was US$ 0.719/kWh for Uganda, US$ 0.813/kWh for Burundi, US$ 0.667/kWh for Kenya, US$ 0.411/kWh for South Sudan, US$ 0.617/kWh for Tanzania, and US$ 0.701/kWh for Rwanda, respectively. The most expensive LCOE for diesel technology was for Burundi (US$ 0.813/kWh). The most optimal and least cost LCOE US$ 0.411/kWh was for South Sudan. The LCOE for South Sudan with diesel microgrid technology is the lowest among the other cases analysed in this study as the price for diesel fuel is lower than in the other EAC member countries. The lowest LCOE US$ 0.411/kWh for South Sudan was twice cheaper and more affordable than the LCOE US$ 0.945/kWh in Tanzania [23]. Also, the US$ 0.617/kWh (LCOE) obtained in this study for Tanzania is lower than that in [23].

3.1.2. Scenario 2: Diesel + PV. The diesel + PV hybrid technology LCOE in Figure 7 indicates that each of the LCOE for the six EAC countries was US$ 0.661/kWh for Uganda, US$ 0.728/kWh for Burundi, US$ 0.626/kWh for Kenya, US$ 0.411/kWh for South Sudan, US$ 0.560/kWh for Tanzania, and US$ 0.625/kWh for Rwanda. Simulation analysis shows that combining PV and diesel is not optimal. Also, HOMER optimization results showed that energy from diesel generator microgrid is more affordable than combining diesel and PV system. This conclusion is due to the low price of diesel in South Sudan. Apart from South Sudan, the US$ 0.560/kWh LCOE for Tanzania was the lowest among the EAC countries analysed. It is also higher than both the calculated LCOE (US$ 0.433/kWh) of the hybrid diesel-generator and storage energy systems for Tanzania in [23]

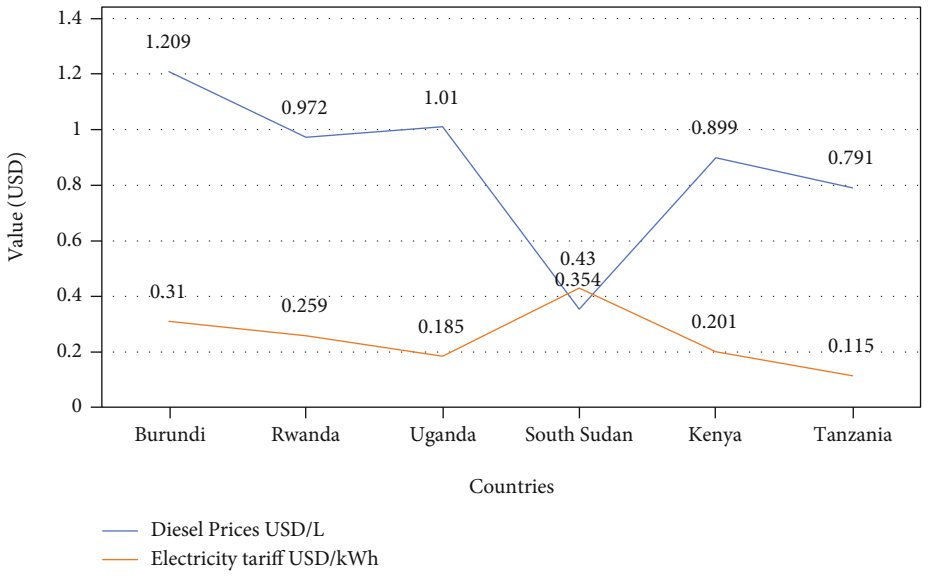

Figure 6: Diesel prices (USD/L) and electricity tariff (USD/kWh) for the six EAC countries.

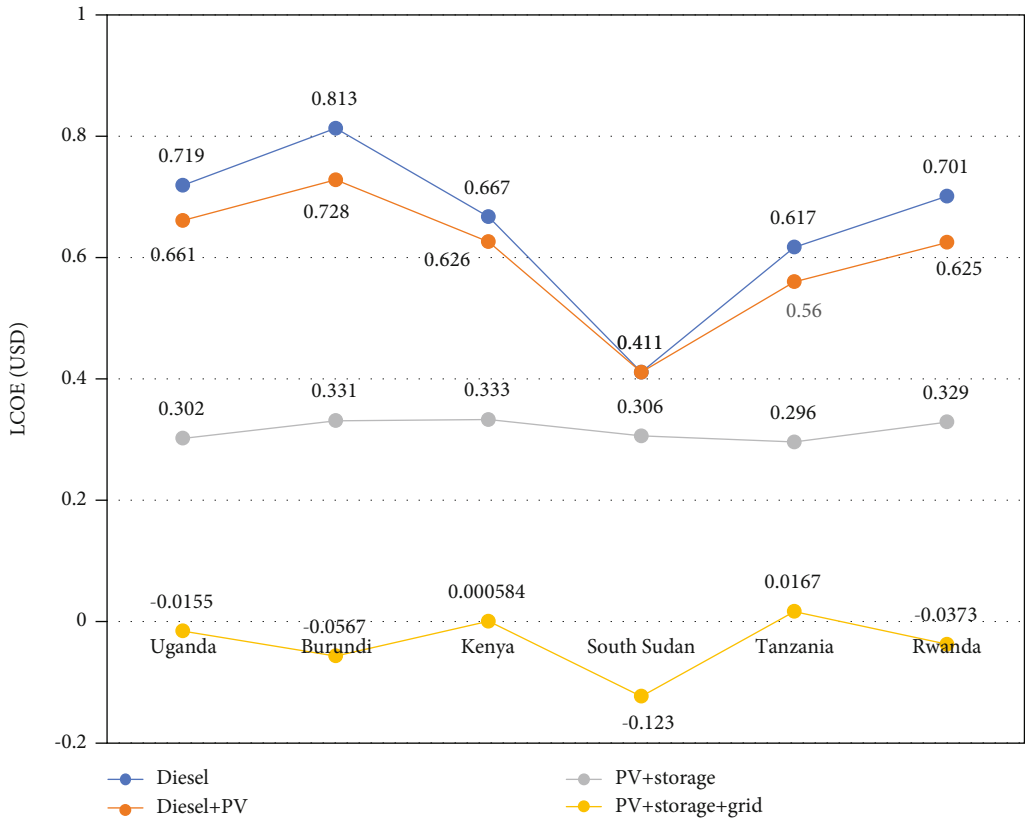

Figure 7: Levelized cost of electricity for all EAC countries with all the analysed energy technologies.

and the LCOE $0.260/kWh for a PV-diesel-battery microgrid system designed for Algeria [24].

3.1.3. Scenario 3: PV + Battery Storage Technology. The LCOE for the PV + battery storage technology is plotted in Figure 7 where each of the six EAC countries' LCOE for the technology was US$ 0.302/kWh (Uganda), US$ 0.331/kWh (Burundi), US$ 0.333/kWh (Kenya), US$ 0.306/kWh (South Sudan), US$ 0.296/kWh (Tanzania), and US$0.329/kWh (Rwanda), respectively. The least LCOE for the system was US$ 0.296/kWh (Tanzania) which was also lower than US$ 1.820/kWh LCOE obtained from the "Comparative Analysis of Reliable, Feasible, and Low-Cost Photovoltaic Microgrid for a Residential Load in Rwanda"

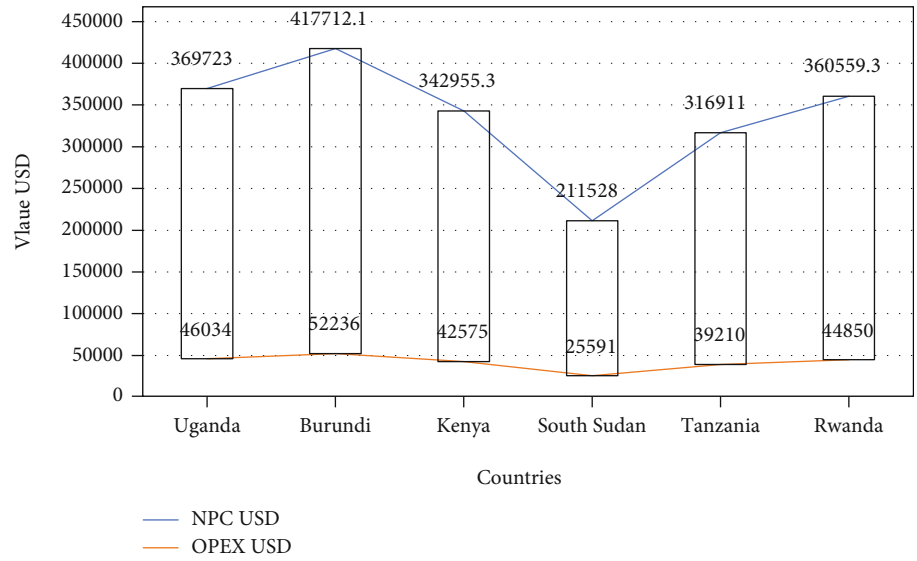

Figure 8: NPC and OPEX with diesel technology.

[16]. The US$ 0.360/kWh LCOE for the "Photovoltaic Solar Technologies: Solution to Affordable, Sustainable, and Reliable Energy Access for All in Rwanda" [4] was more expensive than US$ 0.333/kWh (Kenya); more expensive than 0.2$/kWh for a hybrid made of a microhydropower technology, diesel, and storage [25]; and more expensive than US$0.207/kWh for "Optimization and Cost-Benefit Assessment of Hybrid Power Systems for Off-Grid Rural Electrification in Ethiopia" [26].

3.1.4. Scenario 4: PV + Battery Storage + Grid Hybrid Technology. Figure 7 plots the LCOE for the PV + battery storage + grid hybrid technology of the six EAC countries. The LCOE for each of the six EAC countries was US$ -0.0155/kWh (Uganda), US$ -0.567/kWh (Burundi), US$ 0.000584/kWh (Kenya), US$ -0.123/kWh (South Sudan), US$ 0.0167/kWh (Tanzania), and US$ -0.0373/kWh (Rwanda), respectively. Also, the LCOEs of the grid tied PV systems with storage in the study were lower than both the US$ 0.125/kWh and US$ 0.0645/kWh LCOEs obtained by other researchers in [4, 16]. The implementation of the proposed system indicates that Uganda gains US$ 0.0155 for every kWh generated, Burundi gains US$ 0.0567 per kWh generated, Kenya spends US$ 0.000584 per kWh generated, South Sudan gains US$ 0.123 for every kWh generated, Tanzania spends US$ 0.0167 for every kWh generated, and Rwanda gains US$ 0.0373 for every kWh generated, respectively.

3.2. Analysis of Net Present Cost (NPC) and Operating Expenditure (OPEX). Figure 8 depicts the net present cost and OPEX of using the diesel technology for each of the six EAC countries as focused in this study. The NPC for Uganda was US$ 369,723.00, US$ 417,712.10 for Burundi, US$ 342,955.30 for Kenya, US$ 211,528.00 for South Sudan, US$ 316,911.00 for Tanzania, and US$ 360,559.30 for Rwanda, respectively. The most expensive NPC was Burundi (US$ 417,712.10), and the lowest NPC was South Sudan (US$ 211,528.00). The NPCs hover between US$ 417,712.00 (Burundi) and US$ 211,528.00 (South Sudan), respectively.

The OPEX for each of the six EAC countries was US$ 46,034.00 for Uganda, US$ 52,236.00 for Burundi, US$ 42,575.00 for Kenya, US$ 25,591.00 for South Sudan, US$ 39,210.00 for Tanzania, and US$ 44,850.00 for Rwanda, respectively. The OPEX varied between US$ 25,591.00 (South Sudan) and US$ 52,236.00 (Burundi). The OPEXs lie between US$ 52,236.00 (Burundi) and US$ 25,591.00 (South Sudan), respectively.

Figure 9 shows the NPC and OPEX for the diesel + PV hybrid technology for the EAC cases simulated in this paper. Each NPC of the six EAC countries was US$ 339.718.50 for Uganda, US$ 374,418.10 for Burundi, US$ 321,602.80 for Kenya, US$ 211,528.00 for South Sudan, US$ 287,930.00 for Tanzania, and US$ 321,290.40 for Rwanda. Moreover, the least cost was US$ 211,528.00 (South Sudan), but there was no PV penetration, and US$ 374,418.10 for Burundi was the most expensive for the hybrid technology. The NPCs lie between US$ 374,418.10 (Burundi) and US$ 211,528.00 (South Sudan).

Each of the OPEX values for the six EAC countries was US$ 34,682.00 for Uganda, US$ 39,176.00 for Burundi, US$ 33,128.00 for Kenya, US$ 25,591.00 for South Sudan, US$ 29,108.00 for Tanzania, and US$ 32,644.00 for Rwanda. However, the OPEX for the diesel + PV hybrid varied between US$ 39,176.00 (Burundi) and US$ 25,591.00 (South Sudan). The OPEXs ranged between US$ 39,176.00 (Burundi) and US$ 25,591.00 (South Sudan), respectively.

Figure 10 shows the NPC and OPEX for the PV + storage battery technology for the simulated case studies. Each NPC of the six EAC countries was US$ 155,191.40 (Uganda), US$ 170,139.40 (Burundi), US$ 171,266.50 (Kenya), US$ 157,082.60 (South Sudan), US$ 157,107.30 (Tanzania), and US$ 169,290.10 (Rwanda). Moreover, US$ 171,266.50 was the highest NPC (Kenya) and the lowest (US$ 152,107.30) was for Tanzania. The NPCs hover around

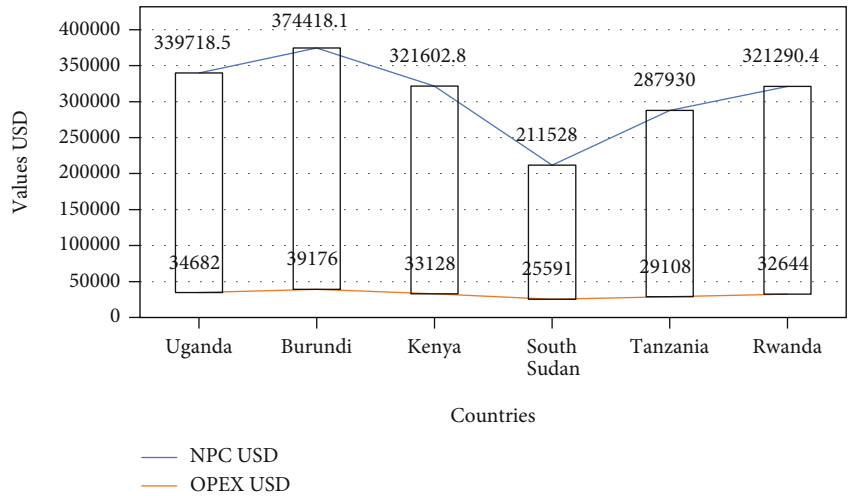

Figure 9: NPC and OPEX with the diesel + PV technology.

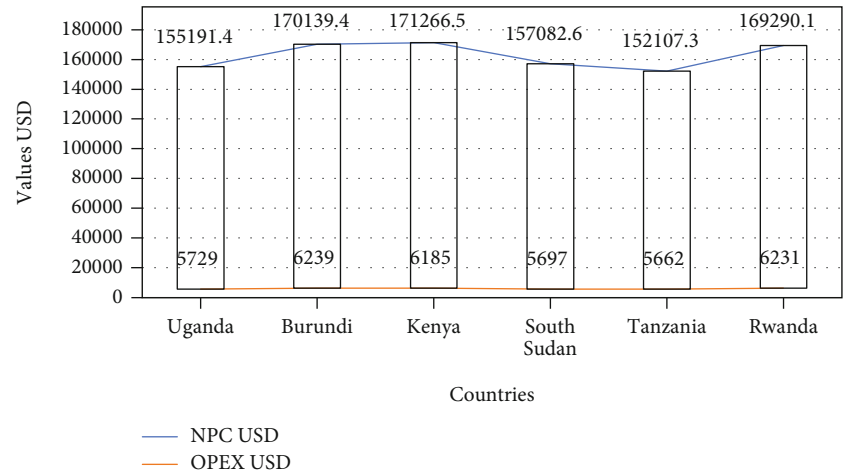

Figure 10: NPC and OPEX with the PV + storage technology.

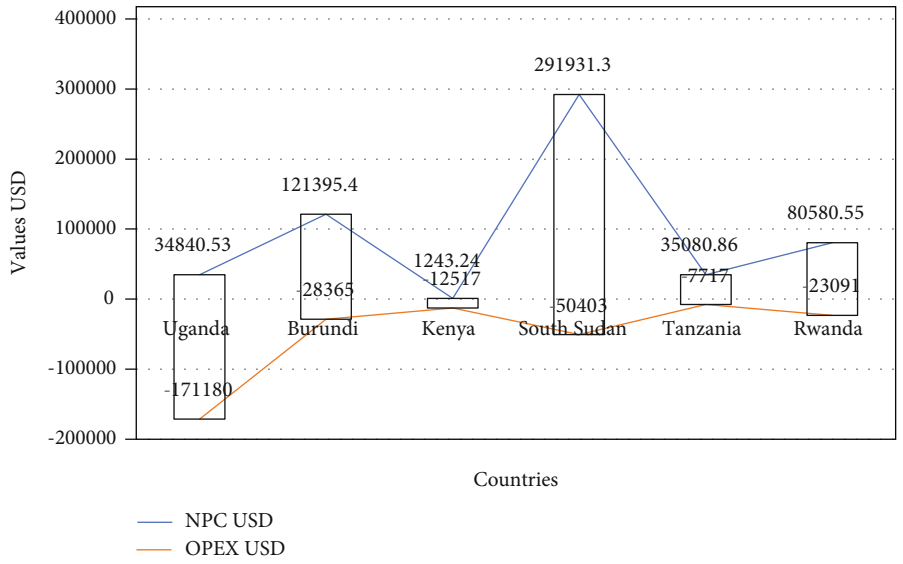

Figure 11: NPC and OPEX with the PV + storage + grid technology.

Table 2: Summary.

Diesel technology					
	NPC ($)	LCOE ($/kWh)	FGC ($/hr)		MGC ($/kWh)
Burundi	417712.1	0.813	3.53		0.285
Kenya	342955.3	0.667	3.07		0.212
Rwanda	360559.3	0.701	3.18		0.229
Tanzania	316911.0	0.617	2.90		0.187
South Sudan	21528.0	0.411	2.24		0.0835
Uganda	369723.0	0.719	3.23		0.238
PV + diesel technology					
	NPC ($)	LCOE ($/kWh)	DFGC($/hr)	MGC ($/kWh)	PV LC($/kWh)
Burundi	374418.1	0.728	3.53	0.285	0.00326
Kenya	321602.8	0.626	3.07	0.212	0.0327
Rwanda	321290.4	0.625	3.18	0.229	0.0322
Tanzania	287930.3	0.560	2.90	0.187	0.0281
South Sudan	211528.0	0.411	2.24	0.0835	—
Uganda	339718.5	0.661	3.23	0.238	0.00327
PV + storage technology					
	NPC ($)		LCOE ($/kWh)		PV LC($/kWh)
Burundi	170139.4		0.331		0.0326
Kenya	169290.1		0.329		0.0327
Rwanda	169290.1		0.329		0.323
Tanzania	152107.3		0.296		00.281
South Sudan	157082.6		0.306		0.0285
Uganda	155191.4		0.302		0.0307
PV + battery + grid technology					
	NPC ($)		LCOE ($/kWh)		PV LC($/kWh)
Burundi	121395.40		-0.0567		0.0326
Kenya	1243.24		0.000584		0.00327
Rwanda	80580.55		-0.0373		0.0322
Tanzania	35080.86		0.0167		0.0322
South Sudan	291931.30		-0.123		0.285
Uganda	34840.53		-0.0155		0.0307

NPC: net present cost; LCOE: levelized cost of electricity; DFGC: diesel fixed generation cost; MGC: marginal generation cost; hr: hour; PVLC: levelized cost for photovoltaic system.

US$ 171,266.50 (Kenya) and US$ 152,107.30 (Tanzania), respectively.

Each of the OPEX values was US$ 5,729.00 (Uganda), US$ 6,239.00 (Burundi), US$ 5,729.00 (Kenya), US$ 5,697.00 (South Sudan), US$ 5,662.00 (Tanzania), and US$ 6,231.00 (Rwanda), respectively. The PV + storage technology ranged between US$ 6,239.00 (Burundi) and US$ 5,662.00 (Tanzania). The OPEXs lie between US$ 6,239.00 (Burundi) and US$ 5,697.00 (South Sudan), respectively.

Figure 11 indicates the NPC and OPEX for the PV + storage + grid hybrid technology as simulated in the cases study. Each of the six EAC countries' NPC was 34,840.53 (Uganda), US$ 121,395.40 (Burundi), US$ 1243.24 (Kenya), US$ 192,931.30 (South Sudan), US$ 35,080.86 (Tanzania), and US$ 80,580.55 (Rwanda), respectively. However, the NPC varied between US$ 1243.24 (Kenya) and US$ 291,931.30 (South Sudan). The NPCs ranged between US$ 291,931.30 (South Sudan) and US$ 12,432.40 (Kenya).

Each of the OPEX prices was US$ -17,180.00 (Uganda), US$ -281,365.00 (Burundi), US$-12,517.00 (Kenya), US$ -50,403.00 (South Sudan), US$ -7,717.00 (Tanzania), and US$ -23,091.00 (Rwanda), respectively. These results indicate that all the six EAC countries will benefit immensely by implementing the PV + storage + grid hybrid technology for electricity generation. The OPEX of the PV + battery storage + grid hybrid technology ranged between US$ -50,403.00 (South Sudan) and US$ -7,717.00 (Tanzania). The OPEXs hover around US$ -171,180.00 (Uganda) and US$ -7,717.00 (Tanzania), respectively.

The implementation of this grid-connected system indicates that Uganda gains US$ 0.0155 for every kWh generated, Burundi gains US$ 0.0567 per kWh generated, Kenya spends US$ 0.000584 per kWh generated, South Sudan gains US$ 0.123 for every kWh generated, Tanzania spends US$ 0.0167 for every kWh generated, and Rwanda gains US$ 0.0373 for every kWh generated, respectively.

4. Discussion and Summary

Table 2 summarizes the details of important parameters from each technology covered in the research of this manuscript. We note that the results were based on the simulation of different energy technologies through HOMER software and with different parameter assumptions such as prices of diesel and electricity tariffs, respectively: (0.899$/L and 0.201$/kWh for Kenya, 0.7911$/L and 0.115$/kWh for Tanzania, 1.209$/L and 0.310$/kWh for Burundi, 0.972$/L and 0.259$/kWh for Rwanda, 1.010$/L and 0.185$/kWh for Uganda, and 0.354$/L and 0.43$/kWh for South Sudan).

5. Conclusion

The research used a daily load of one luxury house as a research object and carried out modelling and optimization of least cost, efficient, and reliable electricity generation technology among four technologies: (a) diesel energy technology, (b) PV + diesel technology, (c) PV + storage battery, and (d) PV + battery storage + grid, for all the EAC countries. The following conclusions were drawn from the study:

(1) For off-grid users, the PV + storage battery technology was found to be the least costly and recommendable than any other technology including diesel technology

(2) However, for South Sudan, the combination of PV + diesel technology, the sensitivity, and optimization analysis showed that the diesel technology would still dominate and be least costly technology than solar energy. This is so because South Sudan has the lowest price for diesel than any other countries in the EAC, but due to greenhouse gas emissions, solar energy would still need to be highly recommended

(3) The proposed technology for the study is PV + battery storage + grid hybrid because the LCOE was each US$ -0.0155/kWh (Uganda), US$ -0.0373/kWh (Rwanda), US$ 0.0167/kWh (Tanzania), US$ 0.000584/kWh (Kenya), US$ -0.123/kWh (South Sudan), and US$ -0.0567/kWh (Burundi), respectively. Furthermore, each of the NPCs of the proposed PV + battery storage + grid hybrid technology was US$ 34840.53 (Uganda), US$ 80580.55 (Rwanda), US$ 35080.86 (Tanzania), US$ 1243.24 (Kenya), US$ 291931.30 (South Sudan), and US$ 121395.40 (Burundi), respectively

(4) The proposed PV + battery storage + grid hybrid technology is recommended for possible adoption in each of the six EAC countries because both the LCOEs and NPCs are lower than the real electricity tariffs currently in use within these six EAC countries. Also, the connection of PV + battery storage to the grid (for locations wherever possible) would lower and provide affordable, reliable, and sustainable electricity prices in these countries. The findings in this paper are limited to a technoeconomic feasibility analysis of affordable energy systems that focuses only on the EAC region

Data Availability

The data used in this research are available upon the request from the corresponding author.

Conflicts of Interest

The authors declare that they have no conflicts of interest.

Acknowledgments

The authors are grateful to Quanzhou Tongjiang Scholar Special Fund for the financial support through grant number 600005-Z17X0234; Quanzhou Science and Technology Bureau for the financial support through grant number 2018Z010; Huaqiao University through grant number 17BS201; and the Fujian Provincial Department of Science and Technology for the financial support through grant 2018J05121.

References

[1] S. Bimenyimana, G. N. O. Asemota, and L. Li, "The state of the power sector in Rwanda: a progressive sector with ambitious targets," *Frontiers in Energy Research*, vol. 6, 2018.

[2] IEA, *Access to electricity*https://www.iea.org/reports/sdg7-data-and-projections/access-to-electricity.

[3] J. Corfee-Morlot, P. Parks, J. Ogunleye, and F. Ayeni, *Achieving clean energy access in sub-Saharan Africa, a case study for the OECD, UN Environment*World Bank projecthttps://www.oecd.org/environment/cc/climate-futures/Achieving-clean-energy-access-Sub-Saharan-Africa.pdf.

[4] S. Bimenyimana, G. N. O. Asemota, J. D. D. Niyonteze, C. Nsengimana, P. J. Ihirwe, and L. Li, "Photovoltaic solar technologies: solution to affordable, sustainable, and reliable energy access for all in Rwanda," *International Journal of Photoenergy*, vol. 2019, 29 pages, 2019.

[5] M. P. Blimpo and M. Cosgrove-Davies, *Electricity access in sub-Saharan Africa: uptake, reliability, and complementary factors for economic impact*https://openknowledge.worldbank.org/bitstream/handle/10986/31333/9781464814884.pdf.

[6] Wikipedia, *Africa-countries-EAC*https://commons.wikimedia.org/wiki/File:Africa-countries-EAC.svg.

[7] Global Solar Atlas, *Welcome to Global Solar Atlas v2.4*, 2020, https://globalsolaratlas.info/map?c=60.844911,94.921875,2.

[8] I. L. Griffiths, *The Atlas of African Affairs*, Routledge, 2013.

[9] D. Bowden, D. Tresemer, W. Bento et al., *Journal for Star Wisdom 2013*, SteinerBooks, 2012.

[10] L. Osborn, *Sunniest places and countries in the world*https://www.currentresults.com/Weather-Extremes/sunniest-places-countries-world.php.

[11] IEA, *A snapshot of global PV*https://iea-pvps.org/publications/.

[12] J. F. Manwell, "Hybrid energy systems," *Encyclopedia of Energy*, vol. 3, pp. 215–229, 2004.

[13] H. Energy, *Homer Pro*https://www.homerenergy.com/products/pro/index.html.

[14] C. S. Lai, G. Locatelli, A. Pimm, Y. Tao, X. Li, and L. L. Lai, "A financial model for lithium-ion storage in a photovoltaic and biogas energy system," *Applied Energy*, vol. 251, p. 113179, 2019.

[15] C. S. Lai, Y. Jia, Z. Xu et al., "Levelized cost of electricity for photovoltaic/biogas power plant hybrid system with electrical energy storage degradation costs," *Energy Conversion and Management*, vol. 153, pp. 34–47, 2017.

[16] C. Nsengimana, X. T. Han, and L.-l. Li, "Comparative analysis of reliable, feasible, and low-cost photovoltaic microgrid for a residential load in Rwanda," *International Journal of Photoenergy*, vol. 2020, 14 pages, 2020.

[17] A. Shtub, "The trade-off between the net present cost of a project and the probability to complete it on schedule," *Journal of Operations Management*, vol. 6, no. 3-4, pp. 461–470, 1986.

[18] L. Uwineza, H.-G. Kim, and C. K. Kim, "Feasibility study of integrating the renewable energy system in Popova Island using the Monte Carlo model and HOMER," *Energy Strategy Reviews*, vol. 33, p. 100607, 2021.

[19] Global Petrol Prices, *Retail energy price data*https://www.globalpetrolprices.com/.

[20] Glocal Petrol Prices, *Electricity prices*https://www.globalpetrolprices.com/electricity_prices/.

[21] Energy Capital & Power, *Lighting up South Sudan's power sector*https://www.africaoilandpower.com/2020/09/23/lighting-up-south-sudans-power-sector/.

[22] S. Tanzania, *Electricity and fuel prices in Tanzania*http://www.smartsolar-tanzania.com/solar-sector-information/electricity-and-fuel-prices-in-tanzania/.

[23] E. J. Kitindi, "Techno-economic and environmental analysis for off-grid mobile base stations electrification with hybrid power system in Tanzania," *International Journal of Advanced Research in Computer and Communication Engineering*, vol. 4, no. 10, 2021.

[24] H. Rezzouk and A. Mellit, "Feasibility study and sensitivity analysis of a stand-alone photovoltaic-diesel-battery hybrid energy system in the north of Algeria," *Renewable and Sustainable Energy Reviews*, vol. 43, pp. 1134–1150, 2015.

[25] O. Ugirimbabazi, *Analysis of power system options for rural electrification in Rwanda [M.S. thesis]*, University of Agder, 2015.

[26] K. Gebrehiwot, M. A. H. Mondal, C. Ringler, and A. G. Gebremeskel, "Optimization and cost-benefit assessment of hybrid power systems for off-grid rural electrification in Ethiopia," *Energy*, vol. 177, pp. 234–246, 2019.

[27] M. A. Khan, K. Zeb, P. Sathishkumar, S. S. Rao, C. V. V. Gopi, and H.-J. Kim, "A novel off-grid optimal hybrid energy system for rural electrification of Tanzania using a closed loop cooled solar system," *Energies*, vol. 11, no. 4, p. 905, 2018.

[28] N. Yimen, O. Hamandjoda, L. Meva'a, B. Ndzana, and J. Nganhou, "Analyzing of a photovoltaic/wind/biogas/-pumped-hydro off-grid hybrid system for rural electrification in Sub-Saharan Africa—case study of Djoundé in Northern Cameroon," *Energies*, vol. 11, no. 10, p. 2644, 2018.

[29] J. Kenfack, F. P. Neirac, T. T. Tatietse, D. Mayer, M. Fogue, and A. Lejeune, "Microhydro-PV-hybrid system: sizing a small hydro-PV-hybrid system for rural electrification in developing countries," *Renewable Energy*, vol. 34, no. 10, pp. 2259–2263, 2009.

[30] J. D. D. Niyonteze, F. Zou, G. N. O. Asemota, S. Bimenyimana, and G. Shyirambere, "Key technology development needs and applicability analysis of renewable energy hybrid technologies in off-grid areas for the Rwanda power sector," *Heliyon*, vol. 6, no. 1, p. e03300, 2020.

[31] A. H. Abraha, M. B. Kahsay, and C. Z. M. Kimambo, "Hybrid solar-wind-diesel systems for rural application in North Ethiopia: case study for three rural villages using HOMER simulation," *Momona Ethiopian Journal of Science*, vol. 5, no. 2, p. 62, 2013.

[32] M. Elhassan, Z. Abdallah, M. F. M. Zain, K. Sopian, and A. Awadalla, "Design of hybrid power system of renewable energy for domestic used in Khartoum," *Journal of Applied Sciences*, vol. 11, no. 12, pp. 2270–2275, 2011.

[33] A. A. Masud, "The application of homer optimization software to investigate the prospects of hybrid renewable energy system in rural communities of sokoto in Nigeria," *International Journal of Electrical and Computer Engineering*, vol. 7, no. 2, 2017.

[34] M. Issahaku, S. A. Sandow, E. K. Addo, and A.-F. SeiniYussif, "Meeting the electricity demand with a decentralized autonomous solar PV system using HOMER PRO. A case study of NyongYapalsi, Karaga district, Northern Region, Ghana," *IOSR Journal of Engineering*, vol. 10, no. 3, pp. 41–50, 2020.

[35] W. R. Nyemba, S. Chinguwa, I. Mushanguri, and C. Mbohwa, "Optimization of the design and manufacture of a solar-wind hybrid street light," *Procedia Manufacturing*, vol. 35, pp. 285–290, 2019.

[36] J. Dekker, S. Chowdhury, and S. P. Chowdhury, "Economic viability of PV/diesel hybrid power systems in different climatic zones in South Africa," in *In IEEE PES General Meeting*, pp. 1–8, IEEE, 2010.

Hindawi
International Journal of Photoenergy
Volume 2021, Article ID 9928551, 17 pages
https://doi.org/10.1155/2021/9928551

Research Article

Integration of Microgrids and Electric Vehicle Technologies in the National Grid as the Key Enabler to the Sustainable Development for Rwanda

Samuel Bimenyimana[1], **Chen Wang**[1], **Aphrodis Nduwamungu**[2], **Godwin Norense Osarumwense Asemota**[2], **Wellars Utetiwabo**[3], **Chun-Ling Ho**[1], **Jean De Dieu Niyonteze**[4], **Noel Hagumimana**[4], **Theobald Habineza**[5], **Waqar Bashir**[6], **Cicilia Kemunto Mesa**[7,8] and **Yiyi Mo**[1]

[1]*Huaqiao University, Intelligence and Automation in Construction Provincial Higher-Educational Engineering Research Centre, 361021 Xiamen, China*
[2]*Africa Centre of Excellence in Energy for Sustainable Development, University of Rwanda, Kigali, Rwanda*
[3]*School of Education, University of Rwanda, Rwanda*
[4]*Fujian Province Key Laboratory of Automotive Electronics and Electric Drive, Fujian University of Technology, Fuzhou 350118, China*
[5]*Department of Climate Change Observatory Secretariat, Ministry of Education, Kigali, Rwanda*
[6]*School of Electrical Engineering and Automation, Tianjin Polytechnic University, China*
[7]*Kenya Industrial Research and Development Institute, Nairobi, Kenya*
[8]*Hello Renewables Ltd., Kigali, Rwanda*

Correspondence should be addressed to Chen Wang; wch@hqu.edu.cn

Received 26 March 2021; Accepted 20 June 2021; Published 13 July 2021

Academic Editor: Kumarasamy Sudhakar

Copyright © 2021 Samuel Bimenyimana et al. This is an open access article distributed under the Creative Commons Attribution License, which permits unrestricted use, distribution, and reproduction in any medium, provided the original work is properly cited.

Rwanda is an East African Community (EAC) nation with rapid and remarkable past development in different sectors and still with the ambitious targets and plans to be achieved in the coming years ahead. The government plans universal electricity access by 2024 with 52% grid connection and 48% off-grid connections. In the transport sector, the concept of electric vehicles has been initiated and started in order to contribute to the UN Paris agreement and decrease the reliance of the transport sector on gaseous fuels which are one source of air pollutants leading to climate change, premature deaths, and morbidity associated with poor air quality. With higher electricity demand than the generation of the Rwandan power grid, different energy strategies are being developed with the overall objective to achieve the targeted universal energy access. In order to overcome the aforementioned issue, this paper proposes an integration of solar PV microgrids for the satisfaction of electric vehicle (EV) technology in Rwanda. Using HOMER Grid software, a managed EV charging station is simulated to a grid connected solar PV microgrid with storage in order to assess the economic impact. The results show that the proposed technology can lower the levelized cost (LCOE) of electricity by 139.7%. This study can contribute to further research developments in either different perspectives related to the integration of distributed energy resources (DERs) with electric vehicles or studies related to affordable and environment-energy systems.

1. Introduction

Current electricity access all over the world is about 89.589% of the population according to the statistics of the World Bank using the database of Sustainable Energy for All (SE4ALL) [1]. Ten years of continuous improvement enabled the global electrification rate to reach 89.6%, with 153 million people gaining electricity access every year. Moreover, the greatest threat lies with over 573 million people remaining in the dark, especially those living in sub-Saharan Africa and in the remotest parts of the globe. Therefore, solar lighting, solar home systems, and more mini grids would be important at reaching the poor and the remotest of households. Universally, about 34 million people accessed basic electricity services using off-grid technologies in 2017 [2].

To date, access to electricity in Rwanda is estimated at 51% and those not grid connected are about 14% [3]. Rwanda has many distributed energy resources (DERs) like solar, biomass, hydro, methane gas in Lake Kivu, geothermal [4], and availability of feasible microgrids with different distributed energy resources like photovoltaics, battery storage, diesel generator, and electric vehicles are possible and implementable [4, 5].

Sustainable development is among key and crucial pillars for Rwanda and challenges for future community. By December 2015, around 195 countries ratified the Paris agreement to reduce greenhouse gas (GHG) emissions as entrenched in the United Nations Framework Convention on Climate Change (UNFCC) [6]. Rwanda's mitigation effort comprises reducing the GHG emissions to 63.0% of the baseline over the period 2015-2030. This translates to 37.0% GHGs emission reduction and 4.6 million tonnes (CO_2) in 2030 [6, 7].

From energy generation viewpoint, the government of Rwanda decided to increase the use of renewables through different technologies such as microgrids and electric vehicle technologies (which is still in its initial stages) in order to meet increasing energy demand and tackle gas emissions [8]. Additionally, electric vehicles and vehicle fuel economy implementation guidelines are significant assumptions over the coming decade for new vehicles entering the fleet, development of charging infrastructure, and electricity grid decarburization rate. The main aim of the paper is to analyze and enhance the contribution of microgrids and electric vehicles as key enablers for sustainable development. A firm EV station is analyzed by simulation considering that it is to be connected to a national power grid or a grid connected microgrid having storage, to assess the system contribution for affordable electricity tariff. The paper is organized into Introduction, Literature Review of Microgrids and Electric Vehicle Technologies, Methodology, Simulation Results, and Conclusion.

2. Literature Review of Microgrids and Electric Vehicle Technologies

Microgrids are small networks composed of different distributed energy resources, frequently linked to an integrated national grid that is able to operate in grid connected or islanded mode, and can be controlled by different control techniques such as traditional droop controller, modified droop controllers, and PQ controllers [9, 10].

2.1. Vehicle-to-Grid (V2G) Technology. Vehicle-to-Grid (V2G) technology discharges energy back to the grid to improve grid utilization, level demand, and improve reliability for utilities of the future. It can be used to support the utility grid services with stability increase and reliability of the network [11, 12]. The control of active power (P), and reactive power (Q) between electric vehicles (EVs), and microgrids through bidirectional energy flows make them to be considered distributed energy storage (DES) units [13]. The owner of electric vehicle is able to control the charging and discharging times and, thus, can be used as sources of income because they can sell excess energy to the utility grid operators. V2G enables energy to be pushed back to the utility grid while Grid-to-Vehicle (G2V) is the process in which electric vehicles are charged via the power grid. Therefore, it is very easy to control and monitor power flow in Vehicle-to-Home (V2H or V2B), and its implementation is not difficult compared to Vehicle-to-Grid because the reverse power interface is not required, but islanding detection capability and other power quality delivery detection interfaces. Different models of charging are considered depending upon the software package. Meanwhile, in energy planning, the four models considered include a dumb battery charger, flexible demand, smart charger, and V2G charging that contains EVs charging control based on different electricity tariff models [14]. Table 1 describes the power levels for the alternating and direct current for charging systems [15].

As the United Nations set guidelines for climate change and greenhouse gas emission limitations, many industries and researchers are still carrying out research on the development of different electric vehicles based on emissions and consumption [16].

2.2. Air Quality Standards in Rwanda. For climate change mitigations, every country should have an air quality standard based on the World Health Organization (WHO) guidelines, and air quality standards, set by Rwanda Environment Management Authority (REMA), are summarized in Table 2:

Table 3 describes the comparison of electric vehicles based on their driving component, energy sources, pros, and cons [16, 20–22]. Rajashekara discovered a new type of electric vehicles, which is slightly different from others and called plug-in fuel cell vehicle (PFCV) with a large battery and small fuel cell storage capacity that makes it a battery dominant car [19].

2.3. Grid-to-Vehicle (G2V) Technology. Grid-to-vehicle technology (G2V) is used in the design of suitable charging algorithm to control charging, battery balance, and condition of charge estimation that enhance the battery life [23]. The vehicle-to-grid (V2G) technology is deployed by the plug-in electric vehicle (PHEV) to release energy to the grid to enhance grid utilization, balance demand, and improve reliability. Furthermore, it is an effective distributed energy resource (DER) [23, 24].

2.4. Smart Charging (V1G) Technology. Different researchers revealed that the utility grid must be innovative and upgraded and with Supervisory Control and Data

Table 1: Alternating current (AC) and direct current (DC) power levels [15].

AC charging levels	DC charging levels
AC level 1: 120.0 volt alternating current (VAC). Single-phase (maximum) 16.0 amps (A); maximum 1.9 kilowatts (kW)	DC level 1: 200.0 to 450.0 volt direct current (VDC), maximum 80.0 A and maximum power is 19.2 kW
AC level 2: 240.0VAC, single phase, maximum 80.0 A, maximum 19.2 kW	DC level 2: 200.0 to 450VDC, maximum 200.0 A, maximum 90.0 kW
AC level 3: to be determined, can include AC three phases	DC level 3: to be determined and may cover from 200.0 up to 600.0 VDC, maximum 400.0 A, and maximum 240.0 kW

Table 2: Rwanda air quality standards versus WHO air quality guidelines [17–19].

Type of pollutant	Averaging period (hours)	Rwanda standards ($\mu g/m^3$)	World Health Organization (WHO) standards ($\mu g/m^3$)
Carbon monoxide (CO)	1.0	30,000.0	30,000.0
	8.0	10,000.0	10,000.0
Sulphur dioxide (SO_2)	10.0 minutes	500.0	500.0
	24.0 hours	125.0	125.0
Ozone (O_3)	1.0 hour	200.0	200.0
	8.0 hours daily maximum	120.0	120.0
Nitrogen dioxide (NO_2)	1.0 hour	200.0	200.0
	Annual	40.0	40.0
Particulate matter ($PM_{2.5}$)	24.0 hours	75.0	75.0
	Annual	35.0	35.0
Particulate matter (PM_{10})	24.0 hours	100.0	100.0
	Annual	50.0	50.0

Table 3: Comparison of electric vehicles (EVs) [20–22].

Type of electric vehicles	Type of driving component	Energy source	Pros	Cons
Solar electric vehicles (SEV)	Electric motor	Battery ultra-capacitor	(i) No expenses (ii) Environment friendly (iii) Zero net emissions (iv) Low maintenance (v) Able to utilize full power at all speeds	(i) Prices depend on the quality (ii) Dependence on the solar radiation
Fuel cell electric vehicles (FCEV)	Electric motor	Fuel cell	(i) Zero net emissions (ii) High efficiency compared to others slightly not expensive (iii) Available in market abundantly for some countries (iv) Energy recovery from regenerative braking	(i)Production of fuel (ii) Fueling facilities and storage security concern (iii) Standard development in process (iv)Scalable for mass manufacturing
Battery electric vehicle (BEV)	Electric motor	(i) Ultra capacitor battery	(i)Zero emissions (ii) Charging and discharging at convenient time and controlled (iii) No dependence on oil (iv) Income generation (v)Prosumer option (vi) Without gas and oil changes (vii) Capacity to conveniently charge at home (viii)Rapid and steady acceleration	(i) Battery life (ii) Battery price and capacity as well (iii) Charging time (iv) Expensive in some country of low and middle income generally (v) Availability of charging stations
Hybrid electric vehicles (HEV)	Internal combustion engines Electric motor	(i) Internal combustion engines (ii) Ultra capacitor (iii) Battery	(i) Composed of electrical and mechanical drive trains (ii) May be powered by both electric supply and other fuels (iii) Long range (iv) Low emissions	(i) Battery and engine capacity optimization (ii) High initial outlay
Plug-in hybrid electric vehicles (PHEV)	Electric motor	(i) Internal combustion engines	(i) Zero net emissions (ii) Little consumption (iii) Optimized performance	(i) Higher initial cost (ii) May be fed by a power from electrical and mechanical sources

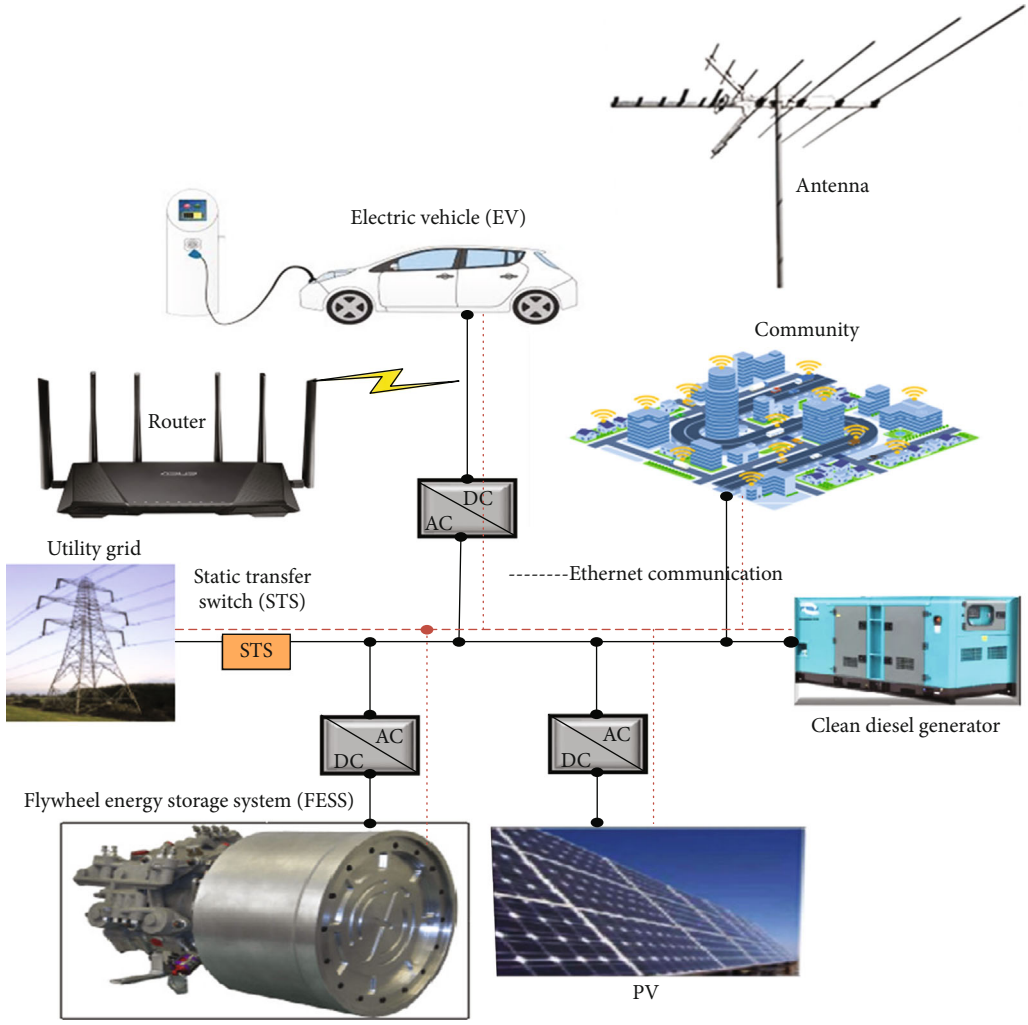

Figure 1: Diagram of microgrid with different distributed energy resources (DERs). Note: the figure is based on the authors' understanding and analysis of different energy technology exploitations and the desire of EV exploitation for Rwandan market; no source or reference is linked to the figure.

Acquisition (SCADA) software package integration in order to shift from traditional grid to the smart grid, so that it will be able to cooperate with future demand [25]. Smart charging (V1G) is a charging process in which electric vehicles, charging stations, and charging operators exchange data connections. Also, the charging stations can supervise, organize, and regulate EVs for enhanced time, charging power size, direction, and utility applications. V1G is applied in traffic congestion management, frequency control, and charging photovoltaic systems (PV) [25]. V2G can also supply electricity to the home (V2H), building (V2B), load (V2L), and grid (V2G). The major threats to V1G and V2G depend on the uniformity requirements and information exchange protocols between the various systems [26, 27].

2.5. Flywheel Energy Storage System (FESS) Technology. The flywheel energy storage system (FESS) is among the best storage technologies and keeps energy in terms of kinetic energy (KE) through electronics converters [28]. Flywheel is composed of converters (rectifiers and inverters), generator, motor bearings, protection cover, and control systems, built by different controllers in charge of controlling and maintaining charging, discharging cycle, and the status of flywheel [29, 30]. Therefore, the speed of flywheel usually varies between 6000.0 and 12000.0 revolutions per minute (r.p.m.). Consequently, energy storages are varying between 2 Mega Joules (MJ) and 500 MJ, and so many types of energy storage devices, namely, batteries, super capacitors, and super conducting magnetic energy storage systems, and every storage device has its own disadvantages and advantages [29, 30].

2.6. Microgrid System with an Electric Vehicle. Contemporary transportation systems using fossil fuels based on conventional vehicles are being capability replaced by electric vehicles which are eco-friendly to the environment [23]. Based on the knowledge that EV technologies are still at their infancy and taking also into consideration that some forms of energy technologies (such as usage of flywheel energy storage systems) have not yet been introduced to the Rwandan energy market, the authors of this paper suggest a new technology which can also be analyzed for energy exploitation and EV technology as it is shown in Figure 1. The concept

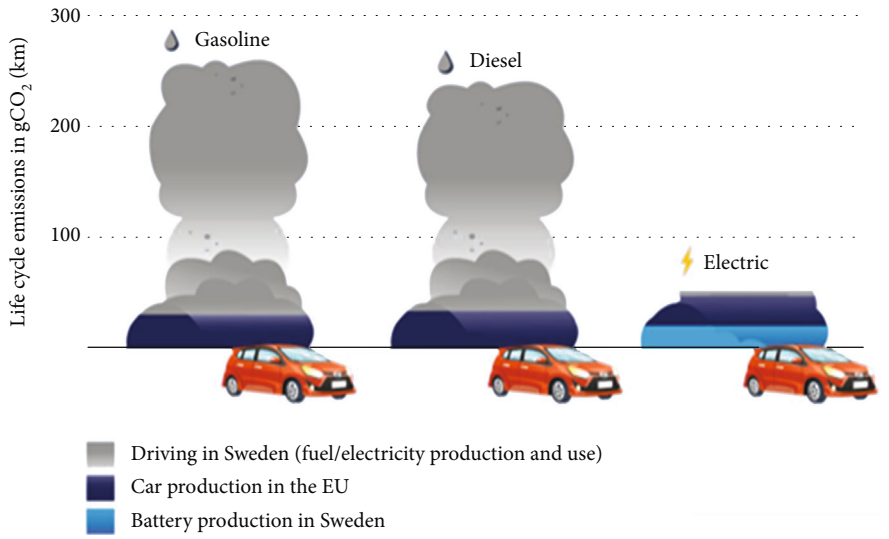

Figure 2: The lifetime carbon dioxide (CO_2) emission savings from electric vehicles (best case scenario) [33].

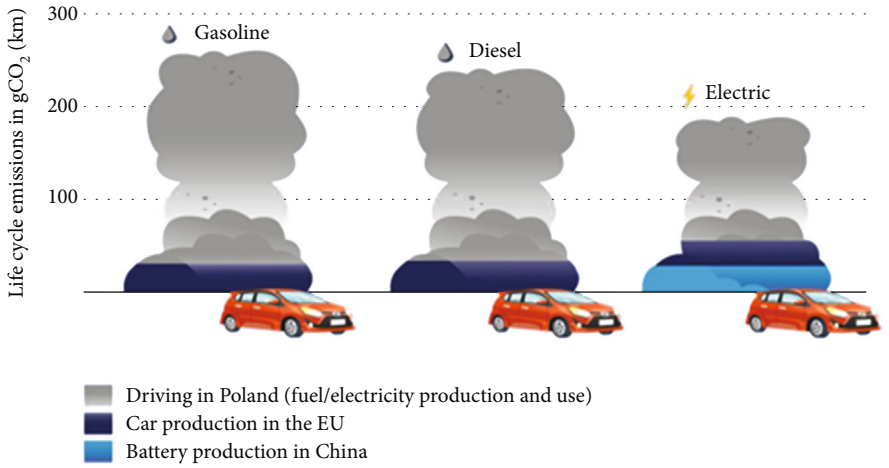

Figure 3: The lifetime carbon dioxide (CO_2) effluent savings from electric vehicles (worst-case) [33].

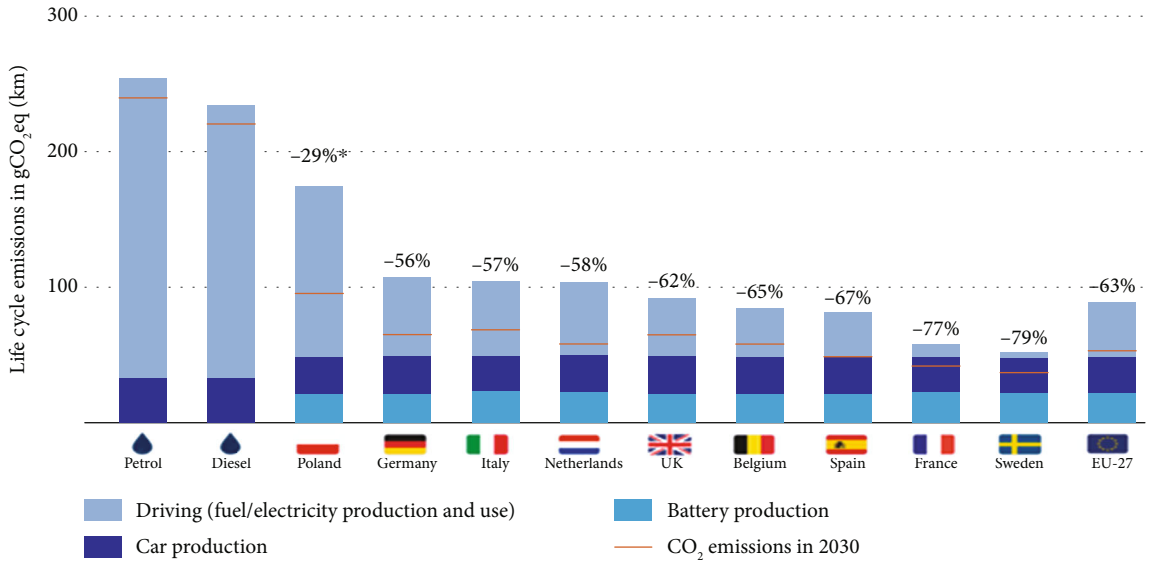

Figure 4: The carbon dioxide (CO_2) savings in EVs compared to typical diesel and petrol car emissions [33, 34].

Table 4: State of the art based on research for electric vehicles and contribution.

Research carried out on	Vehicle to-grid (V2G)	Load shedding scenarios	Multi-objective economic dispatch			Single objective economic dispatch	Algorithms/tools/optimizer	Ref.
			Operating cost (op)	Pollutant treatment cost (PTC)	Carbon dioxide emission (CDE)			
Wind turbine generators (WTG), photovoltaics (PV), cooling heating and power (CHP), battery storage systems (BSS)	Yes	No	Yes	No	No	Yes	CPLEX optimization tool box of MATLAB 2014b	[40]
Wind turbine (WT), photovoltaics (PV), battery storage systems (BSS)	Yes	No	No	No	No	Yes	Hybrid genetic algorithm with interior (pattern search-IP) methods	[39]
Wind turbines, microturbines, photovoltaics, battery storage systems	No	No	No	No	No	Yes	Enhanced bee colony optimization (EBCO), bee colony optimization (BCO), evolutionary programming (EP), genetic algorithms (GA), and Particle Swarm Optimization (PSO)	[40]
Wind turbine, Photovoltaics (PV)	No	No	No	No	Yes	No	Composite imperialist competing and gray wolf algorithms (HIC-GWA)	[41]
Electric vehicles	Yes	No	No	No	No	No	Fuzzy logic controllers, traditional droop control and synchronverter	[42]
Photovoltaics (PV), wind turbine (WT), dispersed generation (DG), fuel cell (FC), battery depository system (BES)	No	No	No	No	No	Yes	Artificial bee colony (ABC), fuzzy logic controller (FLC), genetic algorithm (GA), Particle Swarm Optimization (PSO), seeker optimizations approach (SOA)	[43]
Photovoltaics (PV), battery repository system (BSS)	Yes	No	Yes	No	No	Yes	Dynamic programming (DP)	[44]
Microturbines (MT), fuel cell (FC), battery repository system (BSS), wind turbine (WT), Photovoltaics (PV)	No	No	Yes	Yes	No	No	Model Predictive Control (MPC)	[45]
Battery repository system (BSS), wind turbine, Photovoltaics, energy depositories, distributed energy resources (DERs)	Yes	No	No	No	No	No	Multiobjective Particle Swarm Optimizations (MPSO)	[46]
Wind turbine (WT), Photovoltaics (PV), distributed energy resources (DERs), battery depository system (BSS)	Yes	No	Yes	Yes	No	No	Particle Swarm Optimizations (PSO)	[47]

Table 4: Continued.

Research carried out on	Vehicle to-grid (V2G)	Load shedding scenarios	Multi-objective economic dispatch			Single objective economic dispatch	Algorithms/tools/optimizer	Ref.
			Operating cost (op)	Pollutant treatment cost (PTC)	Carbon dioxide emission (CDE)			
Electric vehicles (EVs)	Yes	No	No	No	No	Yes	Bi-level optimization (BLP)	[48]
Thermal power plant (TPP), wind turbine (WT), electric vehicles (EVs), battery depositories system (BSS)	Yes	No	Yes	No	Yes	No	Multiobjective Particle Swarm Optimizations (MPSO), fuzzy logic controller (FLC), supervisory control and data acquisition (SCADA)	[49]
Wind turbine, Photovoltaics (PV), microturbines (MT), diesel engine, battery depository system (BSS), electric vehicles,	Yes	No	Yes	Yes	No	No	Adjustable robust optimizations (ARO)	[50]
Wind turbine, Photovoltaics, diesel engine, fuel cell, battery repository system (BSS)	Yes	No	Yes	Yes	Yes	Yes	Particle Swarm Optimization	[51]
Wind turbine, Photovoltaics, diesel engine, fuel cell, battery repository system (BSS)	Yes	Yes	Yes	Yes	Yes	Yes	Particle Swarm Optimization (PSO), artificial bee colony,	[52]
Solar-powered electrical autorickshaw for rural transportation	No	No	No	No	No	No	SPEA as an alternative to conventional autorickshaws	[53]

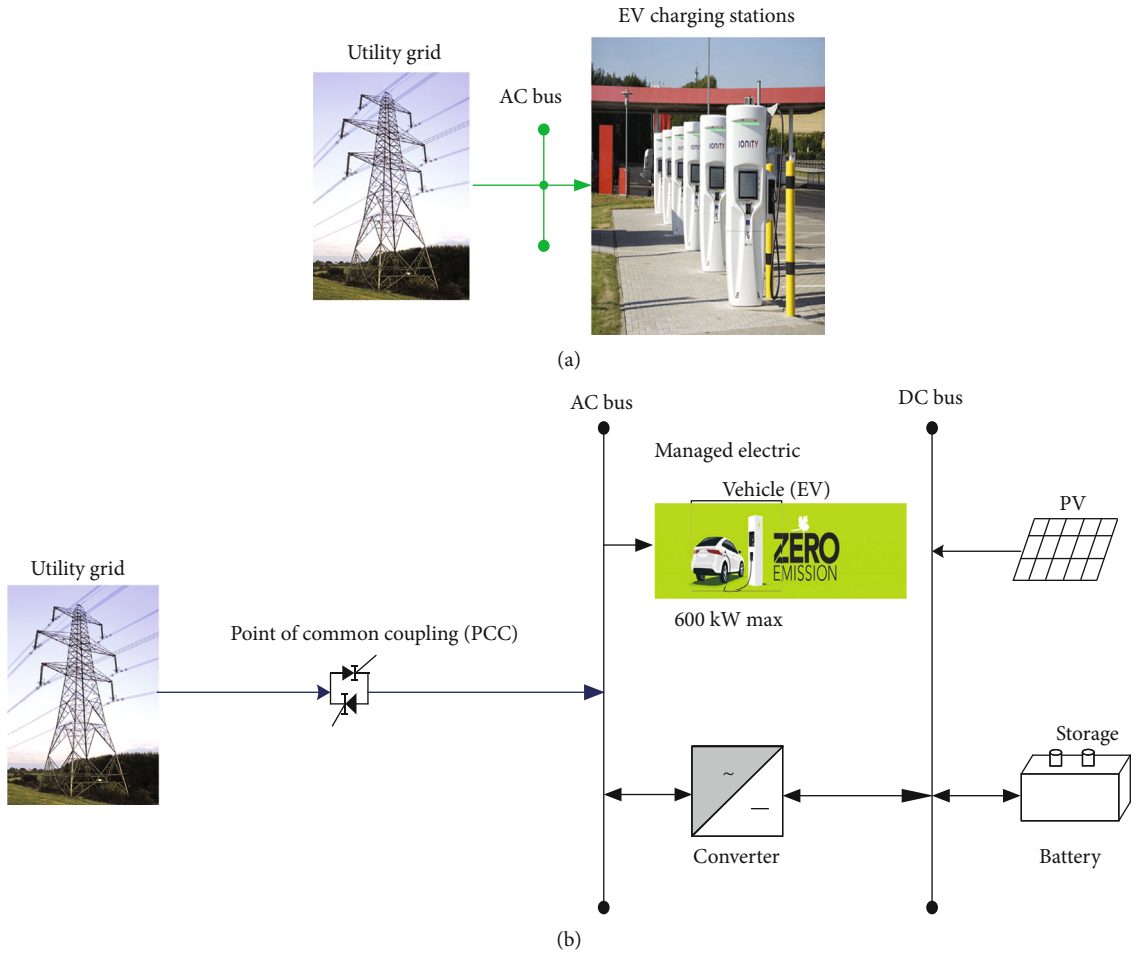

Figure 5: The proposed system (a) and the current system (b).

in Figure 1 can also be mimicked and perfected using the Hybrid Optimization of Multiple Energy Resources (Homer) grid software as it has different distributed energy resources such as PV, flywheel storage, clean diesel generator (CDG), and plug-in hybrid electric vehicles (PHEV). Every microgrid component is connected via a local network communication system based on wired and wireless technologies (WIFI). Figure 1 represents the microgrids composed of different distributed energy resources with electric vehicles. Every component is advantageous to the network, and the different constraints have been analyzed during the design, which is summarized below:

(i) At the beginning, microgrids and EVs are working in an islanded mode, which means that the PV and flywheel supply the community load while EVs are being charged

(ii) Whenever the PV system is incapable of supplying the load, at that time, the clean diesel generator will be able to feed the load

(iii) In case the PV is not able to supply the load and there is no fuel in the diesel generator but the EVs are charged, then the EVs can intervene and supply the community load

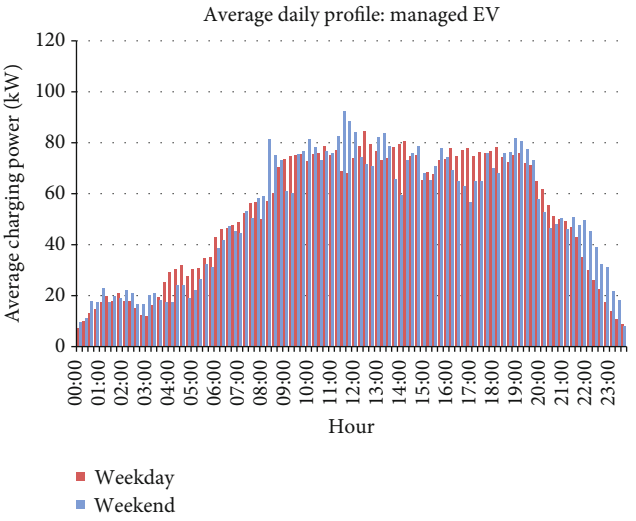

Figure 6: Average daily profile for the managed EV station.

(iv) In case PV, diesel generator, EVs, and flywheel are not able to satisfy the demand, the system will be halted, and priority loads will be supplied

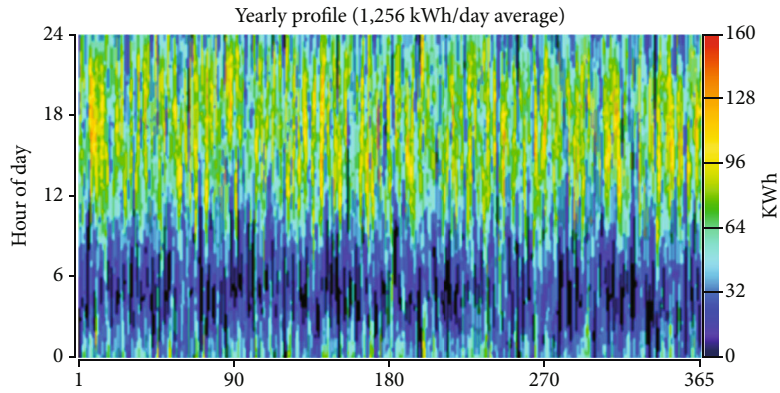

Figure 7: Annual load profile for the managed EV (average of 1258 kWh/day).

(v) Microgrids will be responsible for controlling and managing variations of active power, reactive power, voltage, and frequency, which depend upon the type of controllers like traditional droop control and modified droop control

(vi) During utility grid supply, all parameters will be monitored by the utility grid, especially because the PV, diesel generator, and EVs become incapable of satisfying the demand at that time. The utility grid will intervene depending upon the type of controllers, which are mostly PQ controllers, Virtual Synchronous Machines (VSG) or synchronverter method

2.7. Microgrid Operation. A microgrid operation (MGO) is a distributed class of electricity supply points and loads that typically connect and synchronize with the conventional wide area synchronous grid but could disconnect to an islanded mode through static transfer switch (STS) and function without support. As material or fiscal environments may demand, a ranked order structure could lead to a microgrid main controller (MMC) [31]. The diverse configurations and properties of the electronics in the microturbines, fuel cells, PV panels, wind including twice-fed induction generator technology (DFIG), and wind including permanent magnet synchronous machines (PMSM) technology make microgrids distinct from traditional power systems. Hence, energy repository equipment like flywheels and supercapacitors is interfaced to the grid to provide starting energy balance when the microgrid is islanded. Furthermore, these energy repositories provide active power whenever the microgrid either is islanded or swings in demand and supply occurs [31].

2.8. Technical Problems Based on V2G. The V2G technology, participation, and swift integration of electric vehicles (EVs) in the peak load periods of the network operations [32] provoke instability in the network and generate harmonics with frequencies greater than 50 Hz and 60 Hz, high penetration of EVs in the utility grid which may cause network weakness, electric vehicle smart charging arrangement, and effects of

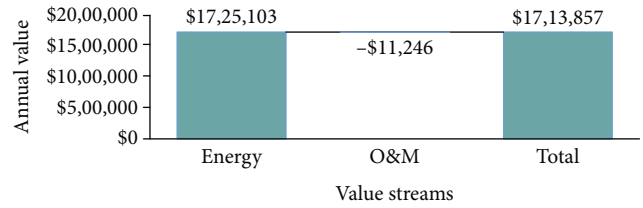

Figure 8: Categorized annual savings.

charging/discharging on EV battery and V2G charger topology.

The bids and purchases of EVs have risen sharply because of the need of carmakers to satisfy the CO_2 emission reduction stipulated by the EU car regulations of 2020 and 2021. Furthermore, within the coming decades, EVs are expected to experience so much mass marketing that the number of EVs on the EU roads would be over thirtyfold by 2030. Based on the statistics, about 3.0% (1.3 million EVs) were sold by the end of 2019 and a total of 44.0 million electric cars are expected to be on the roads by 2030. This translates to over 97.0% EVs which would have been added to the fleet in the coming days and years to 2030. Consequent lifestyle changes would bring with them a collection of lifecycle analyses that measure EV pollutant emissions like carbon dioxide (CO_2), and battery charging/discharging cycles contrasted with traditional fossil fueled cars [33].

Investigators are advised not to use obsolete data in their research because unreliable data can deliberately confuse lifecycle assessments. The obsolete data were used to compare electric vehicles and traditional cars which use either a diesel generator or petrol which needs upgrading [33]. The transport and environment (T&E) company have created detailed and useful analogies of electric, diesel, and petrol engines in distinctive car capacities between 2020 and 2030 as shown in Figure 2. Figure 2 is the lifetime plot of carbon dioxide (CO_2) emission savings from electric vehicles. In the European Union (EU), electric cars emit 80.0% less carbon dioxide (CO_2) than diesel and 81.0% than petrol [33].

Research indicates that the typical EU electric car has about three times superior performance than the traditional equivalence today. It is expected that electric cars will become

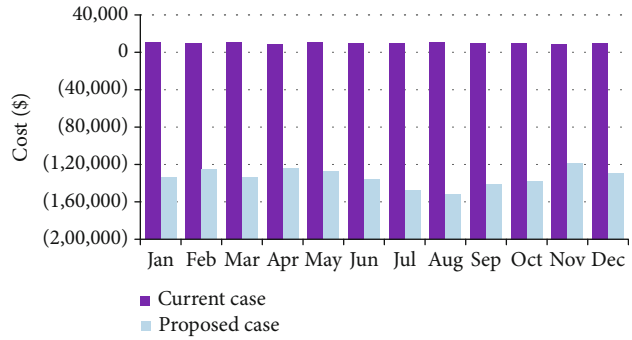

Figure 9: Monthly utility bills.

over four times cleaner than their traditional equivalents in the EU by 2030 [33].

Typical medium-sized EU electric cars sold in 2020 released about 90.0 gCO_2 e/km, diesel car vented 234.0 gCO_2 e/km, and gasoline car emitted 253.0 gCO_2 e/km over their lifetimes, respectively. Typically, in the EU, the EV releases about 2.7 times less CO_2 than the traditional car in 2020 (2.6 times less than diesel and 2.8 times less than gasoline). A storage battery produced with clean electricity reduces the electric car emission to 86.0 gCO_2 e/km or 2.7-3.0 times less. Electric cars were operated on clean renewable electricity (hydro power); then, the GHG emission reduces to 11.0 tons of CO_2 (47.0 g/km), which is between 5.0 and 5.4 times less than diesel and gasoline equivalents, as shown in Figure 2 [33]. For substantial and leadership classes, the typical EU electric cars are between 2.8 and 3.1 times superior to their traditional equivalents [34].

At the worst, the battery storage is manufactured in China and used in electric vehicles operated on Poland's carbon demanding grids. Therefore, the lifespan effect rises to 41.0 tons of CO_2 (182.0 g/km) and EVs are still 22.0% cleaner than their diesel equivalent and 28.0% cleaner than their gasoline equivalent as shown in Figure 3 [33]. A per European Union (EU) member state testing is possible in the device.

Figure 4 [33, 34] describes the carbon dioxide (CO_2) savings correlated with the typical diesel and petrol emissions. Up to date petrol and diesel cars emit almost 3.0 times more carbon dioxide (CO_2) than the typical European Union electric car [33, 34].

2.9. Levelized Cost Components. EV owners have multiple options for recharging their vehicles, for example, different places such as grocery stores, home, public, shopping malls, workplaces, and private parking area where the charging stations are installed. The vehicle purchase cost, on-fuel operations and maintenance cost, fuel cost, and, occasionally, transportation cost are considered in the overall cost of the EV. The levelized cost is the likely vehicle age current value of the consumer cost per kilometer (km) as depicted in equation (1). Therefore, the vehicle's leftover value is removed from consumer cost analysis. This value may be deducted from the total cost if considered. Some assumptions are made such as ignoring the vehicle residual value mainly because some data are not available conventionally for residual value

Table 5: Annual utility bills and savings by category.

	Consumption charge	Total
Base case	$118,946.00	$118,946.00
Proposed case	-$1.61M	-$1.61M
Annual savings	$1.73M	$1.73M

of battery electric vehicles (BEVs) [35–37]. Consequently, the general equation for levelized cost is written as follows:

$$LC_n = \frac{\left(PC + \sum_{i=1}^{n}(\mathrm{FC}_i + \mathrm{OC}_i + \mathrm{AC}_i)/\left((1+\mathrm{DR})^{i-1}\right)\right)}{\sum_{i=1}^{n}\mathrm{DT}_i}. \quad (1)$$

AC is the vehicle age substitute transportation cost (only for BEVs) (Rwandan Francs); DR is the 6.0% deduction rate assumed for the analysis, in which a sensitivity analysis addresses the uncertainty; DT is vehicle age (km) distance traveled, OC is vehicle age nonfuel operation and maintenance (O&M) cost (Rwandan Francs); LC_n is the vehicle's levelized cost for n years (Rwandan Francs/km); PC is vehicle purchase price (Rwandan Francs); and FC is the vehicle age fuel cost (Rwandan Francs) exclusively for battery electric vehicles (BEVs).

2.10. State of the Art Based on Research for Electric Vehicles and Contributions. Table 4 summarizes the state-of-the-art researches carried out and the gaps associated with electric vehicles (EVs) in [38] wherein the authors detailed the performance analysis and optimization of solar-powered E-rickshaw for environmental sustainability in rural transportation and [39] wherein the authors described different types of fuel cell usually used in microgrids.

3. Methodology

The research in this paper used the HOMER Grid software, a powerful tool for detailed simulation concerning the needs (hourly, daily, monthly, and annual scenarios), capable of optimization (able to optimize for cost effectiveness), and able to carry out sensitivity analysis [53]. Given the fact that EV technology is still at its initial phases in Rwanda (configuration shown in Figure 5(a) where the EV is linked to the power grid), the system used the High E-Tech Smart Grid

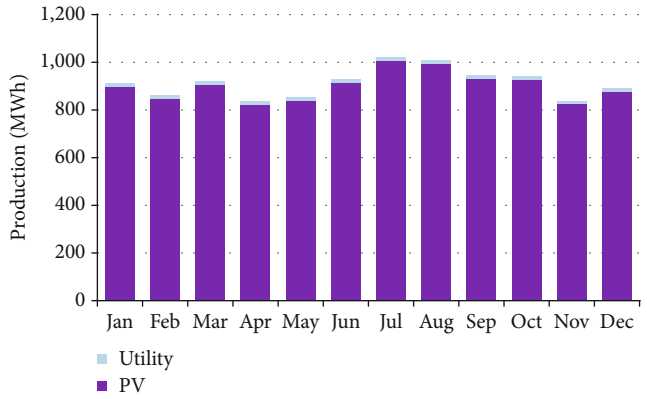

Figure 10: Utility and the solar PV microgrid electricity production.

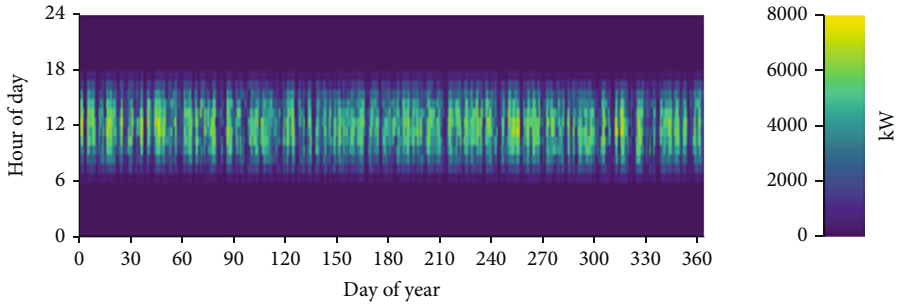

Figure 11: Daily electricity production over the year from the PV microgrid system.

Laboratory location resources of the African Centre of Excellence in Energy for Sustainable Development (ACE-ESD), University of Rwanda, Kigali, Rwanda, to simulate the grid-connected solar PV microgrid with storage and a managed EV station (as shown in Figure 5(a)), precisely located at KN 3 Avenue, Kigali, Rwanda (1°57.6′S, 30°3.8′E). Rwanda electricity and feed-in tariffs data, NASA climatic weather conditions for solar energy generation, and National Renewable energy laboratory database were adopted as the HOMER resource database. A managed EV station with 100.0 as proportion of the EV population, 150.0 kW maximum charging power per EV (charger output power kW), 40.0 chargers, and 7.0 hours connected mean time were obtained from HOMER software and incorporated into the Rwanda case study in order to study and analyze the impact of integrating solar PV microgrid and EV in the Rwandan network. Note that the managed EVs term used in the concept of this paper is well known as deferrable EV as it allows users to optimize their charging stations, lower their monthly utility bills, and have some flexibility for when the EV load is served [54]. Not only these data, there are also several research documents which were consulted by the authors to make the research work content in this paper more concise and communicative. Note that it was clarified for the whole body of this paper that the term "base case" refers to a system where the EV is connected directly to the national power grid for charging as shown in Figure 5(a), while the "proposed case" refers to the technology where the EV can be connected to the grid-connected solar PV microgrid for charging as shown in Figure 5(b).

Table 6: The EV charging load (managed EV).

Annual energy served	459,250.0 MWh
Peak load	300.0 kW
Energy per session	125.0 kWh
Charging sessions per day	10.1
Charging sessions per year	3,674.0
Average missed sessions per day	0
Utilization factor	7.34%
Average session duration	7.00 hr

4. Simulation Results

Electricity generation through solar energy technologies is dependent on climatic weather conditions such as irradiance and clearness index (CI) which is the division output of the sun-oriented radiation that is transmitted through the atmosphere to strike the surface of the Earth; a dimensionless number between 0 and 1 and temperature variation were parameters used for the simulated location in the case study. For the location used in this research paper as the research object location, the average monthly Global Horizontal Irradiance (GHI) (which is the total solar radiation incident on a horizontal surface expressed in kW/m^2/day) shows variation throughout the year and within the range between 4.457 and 5.348 kWh/m^2/day in which the overall annual average was 4.914 kWh/m^2/day for one month. The clearness index falls within the range of between 0.451 and 0.579; and the

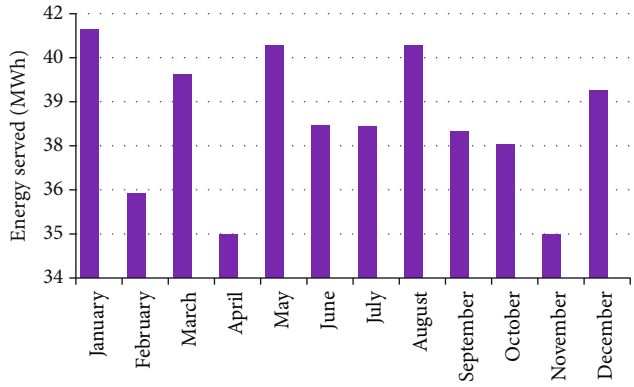

Figure 12: Energy served (MWh), monthly energy served to the managed EV.

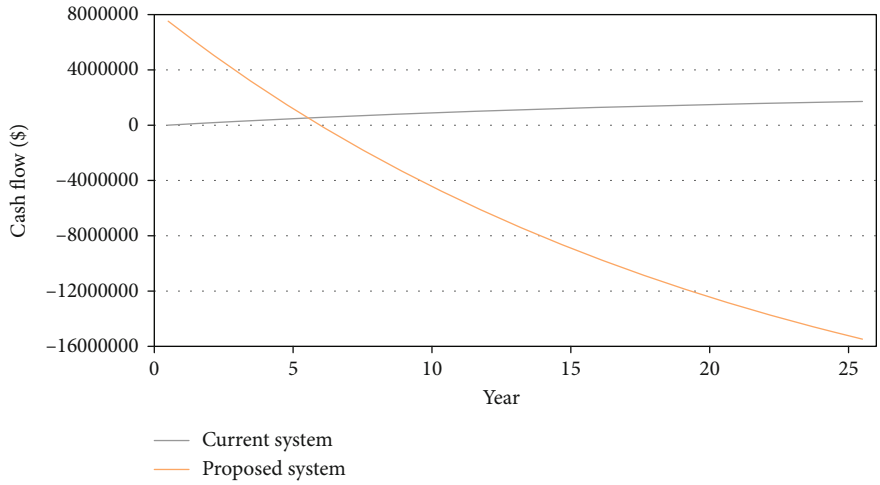

Figure 13: Cumulative cash flow over the project lifetime.

temperature is within the range 18.66 and 20.59°C with overall monthly average temperature of 19.583°C throughout the year. Such subjected climatic weather parameters and conditions are the major incentives for high output energy production from solar technologies once well exploited.

Figure 6 describes the average daily load profile for the managed EV stations as simulated in the case study used as the research object of this paper, and Figure 7 shows its variation throughout the year. The managed EV loads usually also referred as deferrable load by HOMER software permits clients and owners to improve EV charging stations and lower their electricity service bill month by month. The managed EV load as simulated in this research has an average of 1258.0 kWh/day. The load consumption structure varies from hour to hour within a day, and it is shown that the minimum consumption was between 7.279 kWh and 8.173 kWh occurring around 00:00 pm (midnight), respectively, for both weekdays and weekends, the maximum consumption was between 84.82 kWh and 92.307 kWh occurring at 12:30 pm and 11:30 am, and the highest consumption of 9.0 kWh occurs within 09:00 am up to 19:00 pm.

Figures 8 and 9 describe the categorized annual savings per year for the proposed system and the monthly electricity bills for both basic and proposed systems. With the proposed system, there will be annual energy savings with the value equal to US$1,725,103.00, and it will decrease the cost for operation and maintenance (O&M) which is considered the cost associated with operating and maintaining the proposed project to US$-11,248.00 and the total annual overall energy value stream was US$1,173,857.00. As it can be shown in Figure 9, the monthly electricity bill for the proposed system is lower than that for the basic (current) system for the whole year.

Table 5 describes the annual utility bills and savings by category for both the current system and the proposed system, and it can be shown that the consumption charge with the proposed system is around -$1.6M while for the base case system is estimated at $118,946 which results in overall annual saving for the consumption charge equals $1.73M. Note that the base case is the EV connection to the grid, and the proposed case is the EV connection to a grid-connected system with solar PV microgrid with its storage.

Figure 10 describes the monthly electricity production as expressed in MWh for both the utility grid and the PV system, and Figure 11 is the daily electricity production from the PV system over a period of one year with hourly details for one day. The minimum electricity production required from the grid of 10.995 MWh occurred during November, while for the PC system, a minimum production of 823.731

Table 7: Cash flow through the project lifetime (25 years).

(a)

Year	1	2	3	4	5	6	7	8	9	10
PV	($11,246.0)	($11,246.0)	($11,246.0)	($11,246.0)	($11,246.0)	($11,246.0)	($11,246.0)	($11,246.0)	($11,246.0)	($11,246.0)
PV bonus depreciation	$0.00	$0.00	$0.00	$0.00	$0.00	$0.00	$0.00	$0.00	$0.00	$0.00
PV capital incentive	$0.00	$0.00	$0.00	$0.00	$0.00	$0.00	$0.00	$0.00	$0.00	$0.00
Grid tariff	$1.61M	$1.61M	$1.61M	$1.61M	$1.61M	$1.61M	$1.61M	$1.61M	$1.61M	$1.61M

(b)

Year	11	12	13	14	15	16	17	18	19	20
PV	($11,246.0)	($11,246.0)	($11,246.0)	($11,246.0)	($11,246.0)	($11,246.0)	($11,246.0)	($11,246.0)	($11,246.0)	($11,246.0)
PV bonus depreciation	$0.00	$0.00	$0.00	$0.00	$0.00	$0.00	$0.00	$0.00	$0.00	$0.00
PV capital incentive	$0.00	$0.00	$0.00	$0.00	$0.00	$0.00	$0.00	$0.00	$0.00	$0.00
Gird tariff	$1.61M	$1.61M	$1.61M	$1.61M	$1.61M	$1.61M	$1.61M	$1.61M	$1.61M	$1.61M

(c)

Year	21	22	23	24	25
PV	($11,246.0)	($11,246.0)	($11,246.0)	($11,246.0)	($11,246.0)
PV bonus depreciation	$0.00	$0.00	$0.00	$0.00	$0.00
PV capital incentive	$0.00	$0.00	$0.00	$0.00	$0.00
Grid tariff	$1.61M	$1.61M	$1.61M	$1.61M	$1.61M

Table 8: Utility monthly summary for the base case.

Month	Energy purchased (kWh)	Energy sold (kWh)	Net energy purchased (kWh)	Peak load (kW)	Energy charge	Demand charge	Fixed charge	Minimum charge	Taxes	Total
January	41,125.0	0.0	41,125.0	300.0	$10,651.0	$0.0	$0.0	$0.0	$0.0	$10,651.0
February	36,125.0	0.0	36,125.0	300.0	$9,356.0	$0.0	$0.0	$0.0	$0.0	$9,356.0
March	39,750.0	0.0	39,750.0	300.0	$10,295.0	$0.0	$0.0	$0.0	$0.0	$10,295.0
April	34,875.0	0.0	34,875.0	300.0	$9,033.0	$0.0	$0.0	$0.0	$0.0	$9,033.0
May	40,625.0	0.0	40,625.0	300.0	$10,522.0	$0.0	$0.0	$0.0	$0.0	$10,522.0
June	38,200.0	0.0	38,200.0	300.0	$9,894.0	$0.0	$0.0	$0.0	$0.0	$9,894.0
July	38,175.0	0.0	38,175.0	300.0	$9,887.0	$0.0	$0.0	$0.0	$0.0	$9,887.0
August	40,625.0	0.0	40,625.0	300.0	$10,522.0	$0.0	$0.0	$0.0	$0.0	$10,522.0
September	38,000.0	0.0	38,000.0	300.0	$9,842.0	$0.0	$0.0	$0.0	$0.0	$9,842.0
October	37,625.0	0.0	37,625.0	300.0	$9,745.0	$0.0	$0.0	$0.0	$0.0	$9,745.0
November	34,875.0	0.0	34,875.0	300.0	$9,033.0	$0.0	$0.0	$0.0	$0.0	$9,033.0
December	39,250.0	0.0	39,250.0	300.0	$10,166.0	$0.0	$0.0	$0.0	$0.0	$10,166.0

Table 9: Utility monthly summary for the proposed system.

Month	Energy purchased (kWh)	Energy sold (kWh)	Net energy purchased (kWh)	Peak load (kW)	Energy charge	Demand charge	Fixed charge	Minimum charge	Taxes	Total
January	14,700.0	826,677.0	-811,977.0	300.0	-$133,421.0	$0.0	$0.0	$0.0	$0.0	-$133,421.0
February	13,149.0	776,038.0	-762,889.0	300.0	-$125,417.0	$0.0	$0.0	$0.0	$0.0	-$125,417.0
March	13,496.0	825,538.0	-812,042.0	300.0	-$133,544.0	$0.0	$0.0	$0.0	$0.0	-$133,544.0
April	12,666.0	765,615.0	-752,949.0	300.0	-$123,811.0	$0.0	$0.0	$0.0	$0.0	-$123,811.0
May	13,684.0	790,264.0	-776,580.0	300.0	-$127,640.0	$0.0	$0.0	$0.0	$0.0	-$127,640.0
June	13,472.0	835,826.0	-822,354.0	300.0	-$135,258.0	$0.0	$0.0	$0.0	$0.0	-$135,258.0
July	14,305.0	914,351.0	-900,046.0	300.0	-$148,077.0	$0.0	$0.0	$0.0	$0.0	-$148,077.0
August	14,004.0	933,383.0	-919,379.0	300.0	-$151,314.0	$0.0	$0.0	$0.0	$0.0	-$151,314.0
September	13,368.0	871,782.0	-858,414.0	300.0	-$141,253.0	$0.0	$0.0	$0.0	$0.0	-$141,253.0
October	12,789.0	852,903.0	-840,114.0	300.0	-$138,269.0	$0.0	$0.0	$0.0	$0.0	-$138,269.0
November	10,695.0	734,075.0	-723,379.0	300.0	-$119,086.0	$0.0	$0.0	$0.0	$0.0	-$119,086.0
December	13,017.0	797,812.0	-784,794.0	300.0	-$129,065.0	$0.0	$0.0	$0.0	$0.0	-$129,065.0
Annual	159,347.0	9,924,264.0	-9,764,917.0	300.0	-$1.61M	$0.0	$0.0	$0.0	$0.0	-$1.61M

MWh occurred in April and the maximum PV production of 1008.212 MWh occurred in July and 14.699 MWh in January, respectively, for the PV system and the utility grid. The PV system has a nominal capacity of 7,497.0 kW. The annual production was 10,762,281.0 kWh/yr; capital cost, $10.8 million; specific yield, 1436.00 kWh/kW; and maintenance cost, $11,246.00 per year.

As given by the simulation results and as shown in Table 6, the annual energy consumption of this EV depot is 459,250.0 kWh and the peak load is 300.0 kW. The 10.1 charging sessions per day are supplied through 40.0 chargers, each capable of providing 150.0 kW maximum power output. The average session duration is 7.0 hours. The electric vehicles served by this depot have the following charging characteristics: 100.0% percentage of EV population, 150.0 kW maximum charging power per EV, and the 125.0 kWh as average required energy.

Figure 12 describes the energy served in Megawatts hour for every month to the managed EV load where it kept fluctuating within the year. The highest 41.125 MWh was achieved during January, and the lowest 34.875 MWh occurred during April and November, respectively. Figure 13 represents the cumulative cash flow over the project lifetime, and Table 7 describes in detail the cash flow through the project lifetime over 25 years. It can be seen from Figure 13 that the cost (cash flow) for the base system slightly increases as time goes on while the cost with the proposed system greatly decreases with the project time frame period. Tables 8 and 9 describe the utility monthly summary for both the base system and the proposed system, respectively. It can be shown in Table 9, through peak load shaving of the PV system on the 300.0 kW peak load each month which led to a good system profit through energy sold, energy purchased, net energy purchased (kWh), energy charge, and the overall system total.

5. Conclusion

The geographical location of Rwanda promises a good and fruitful output of solar energy once well and highly exploited. The study in this research proves it through an integrated solar PV microgrid connected to the national power grid with a managed EV charging station. The proposed technology once implemented promises the reduction of NPC from $1,715,610 to -$15,480,080 and the LCOE from $0.259/kWh to -$0.103/kWh all contributing to affordable and reliable energy system (the negative value of levelized cost of electricity and net total net present cost means that the income obtained from selling electricity to grid is more than the money spent to purchase electricity from the grid; and this indicates that the revenues exceed the costs). The solar energy system (integrating a solar PV system to a grid for the EV charging) as proposed in this research can lead to an efficient increase of national energy resource exploitation in the Rwanda, resulting in reliable, affordable, and sustainable energy access to all the citizens, and is known to be reliable and affordable and to have pillar sustainable development.

Data Availability

The data used in this research are available upon the request from the corresponding author.

Conflicts of Interest

The authors declare that they have no conflicts of interest.

Acknowledgments

The authors are grateful to Quanzhou Tongjiang Scholar Special Fund for the financial support through grant number 600005-Z17X0234; Quanzhou Science and Technology Bureau for the financial support through grant number 2018Z010; Huaqiao University through grant numbers 17BS201 and 605-50Y14007; and the Fujian Provincial Department of Science and Technology for the financial support through grant 2018J05121.

References

[1] The World Bank, "Access to electricity (% of population)," https://data.worldbank.org/indicator/EG.ELC.ACCS.ZS?end=2018&start=1990&view=chart.

[2] World Health Organization, "More people have access to electricity than ever before, but world is falling short of sustainable energy goals," https://www.who.int/news-room/detail/21-05-2019-more-people-have-access-to-electricity-than-ever-before-but-world-is-falling-short-of-sustainable-energy-goals.

[3] J. Mugisha, M. A. Ratemo, B. C. Keza, and H. Kahveci, "Assessing the opportunities and challenges facing the development of off-grid solar systems in Eastern Africa: the cases of Kenya, Ethiopia, and Rwanda," *Energy Policy*, vol. 150, p. 112131, 2021.

[4] S. Bimenyimana, G. N. Asemota, and L. Li, "The state of the power sector in Rwanda: a progressive sector with ambitious targets," *Frontiers in Energy Research*, vol. 6, p. 68, 2018.

[5] S. Bimenyimana, G. N. O. Asemota, J. D. D. Niyonteze, C. Nsengimana, P. J. Ihirwe, and L. Li, "Photovoltaic solar technologies: solution to affordable, sustainable, and reliable energy access for all in Rwanda," *International Journal of Photoenergy*, vol. 2019, Article ID 5984206, 29 pages, 2019.

[6] FCCC, U, "FCCC. CP/2015/L. 9/Rev. 1: Adaptation of the Paris Agreement," 2015, February 2014, http://unfccc.int/resource/docs/2015/cop21/eng/l09r01.pdf.

[7] S. G. Yoon and S. G. Kang, "Economic microgrid planning algorithm with electric vehicle charging demands," *Energies*, vol. 10, no. 10, p. 1487, 2017.

[8] Volkswagen, "First for Africa: Volkswagen and Siemens launch joint electric mobility pilot project in Rwanda," https://www.volkswagen-newsroom.com/en/press-releases/first-for-africa-volkswagen-and-siemens-launch-joint-electric-mobility-pilot-project-in-rwanda-5510.

[9] A. Nduwamungu, "Review on the coordination and energy management of microgrids broad based on PQ controller and droop control. Some useful information is given in this paper," *Open Access Library Journal*, vol. 4, no. 7, p. 1, 2017.

[10] N. Aphrodis, E. Ntagwirumugara, B. J. M. Vianney, and F. Mulolani, "Design, control and validation of a PV system based on supervisory control and data acquisition (SCADA) viewer in smartgrids," in *2019 5th International Conference on Control, Automation and Robotics (ICCAR)*, pp. 23–28, Beijing, China, 2019, April.

[11] M. Jun and A. J. Markel, "Simulation and analysis of vehicle-to-grid operations in microgrid," in *2012 IEEE Power and Energy Society General Meeting*, pp. 1–5, San Diego, CA, USA, 2012, July.

[12] M. H. Sarparandeh and M. Ehsan, "Pricing of vehicle-to-grid services in a microgrid by Nash bargaining theory," *Mathematical Problems in Engineering*, vol. 2017, Article ID 1840140, 11 pages, 2017.

[13] M. Bayati, M. Abedi, G. B. Gharehpetian, and M. Farahmandrad, "Short-term interaction between electric vehicles and microgrid in decentralized vehicle-to-grid control methods," *Protection and Control of Modern Power Systems*, vol. 4, no. 1, pp. 1–11, 2019.

[14] A. Šare, G. Krajačić, T. Pukšec, and N. Duić, "The integration of renewable energy sources and electric vehicles into the power system of the Dubrovnik region," *Energy, Sustainability and Society*, vol. 5, no. 1, p. 27, 2015.

[15] SAE, "SAE International Releases Updated Visual Chart for Its "Levels of Driving Automation" Standard for Self-Driving Vehicles," https://www.sae.org/news/press-room/2018/12/sae-international-releases-updated-visual-chart-for-its-%E2%80%9Clevels-of-driving-automation%E2%80%9D-standard-for-self-driving-vehicles.

[16] S. A. A. S. Bukhari, W. P. Cao, T. A. Soomro, and D. Guanhao, "Future of microgrids with distributed generation and electric vehicles," *Development and integration of microgrids*, vol. 55, 2017.

[17] IFC, "Environmental, Health, and Safety Guidelines," http://ifc.org/.

[18] World Health Organization, *Evolution of WHO Air Quality Guidelines: Past, Present and Future*, WHO Regional Office for Europe, Copenhagen, 2017.

[19] REMA, "Inventory of Sources of Air Pollution in Rwanda Determination of Future Trends and Development of a National Air Quality Control Strategy," https://rema.gov.rw/fileadmin/templates/Documents/rema_doc/Air%20Quality/Inventory%20of%20Sources%20of%20Air%20Pollution%20in%20Rwanda%20Final%20Report..pdf.

[20] F. Un-Noor, S. Padmanaban, L. Mihet-Popa, M. N. Mollah, and E. Hossain, "A comprehensive study of key electric vehicle (EV) components, technologies, challenges, impacts, and future direction of development," *Energies*, vol. 10, no. 8, p. 1217, 2017.

[21] C. Mahmoudi, A. Flah, and L. Sbita, "An overview of electric vehicle concept and power management strategies," in *2014 International Conference on Electrical Sciences and Technologies in Maghreb (CISTEM)*, pp. 1–8, Tunis, Tunisia, 2014, November.

[22] K. Rajashekara, "Present status and future trends in electric vehicle propulsion technologies," *IEEE Journal of Emerging and Selected Topics in Power Electronics*, vol. 1, no. 1, pp. 3–10, 2013.

[23] L. Barote and C. Marinescu, "Li-Ion energy storage capacity estimation in residential applications with EV," in *2019 8th International Conference on Renewable Energy Research and Applications (ICRERA)*, pp. 326–330, Brasov, Romania, 2019, November.

[24] V. Shrivastava, "Research on structure for flywheel energy storage system in long lifetime UPS," *International Journal of Engineering Research and Application*, vol. 7, no. 11, (Part -3), pp. 16–21, 2017.

[25] Gautham Ram, "Roadmap Electric Vehicles and Grid Integration (V1G versus V2G)," http://www.pr-electronics.nl/en/news/85/roadmap-electric-vehicles-and-grid-integration-v1g-versus-v2g/.

[26] P. Paulraj, "SMART CHARGING 102: What are V1G, V2G and V2H/V2B/V2X smart charging? Integrating electric vehicles into power grid," https://www.emobilitysimplified.com/2019/12/what-is-vehicle-to-grid-v1g-v2g-v2x-v2h.html.

[27] NewMotion, "The future of EV charging with V2X technology," https://newmotion.com/en/the-future-of-ev-charging-with-v2x-technology/.

[28] K. Wei, X. Dai, and P. Liu, "Model and balance of flywheel energy storage system with composite flywheel and rolling bearings," in *2017 IEEE Conference on Energy Internet and Energy System Integration (EI2)*, pp. 1–6, Beijing, China, 2017, November.

[29] C. Jin, X. Jiang, G. Zhong, and X. Li, "Research on coordinated control strategy of flywheel energy storage array for island microgrid," in *2017 IEEE Conference on Energy Internet and Energy System Integration (EI2)*, pp. 1–6, Beijing, China, 2017, November.

[30] A. A. El-Naga, M. I. Marei, and H. S. K. El-Goharey, "Second order adaptive notch filter-based wind power smoothing using flywheel energy storage system," in *2017 Nineteenth International Middle East Power Systems Conference (MEPCON)*, pp. 314–319, Cairo, Egypt, 2017, December.

[31] M. J. Chaudhry, "Enhancements in micro-grid operation through electric vehicle charging and discharging," in *2020 9th International Conference on Industrial Technology and Management (ICITM)*, pp. 245–250, Oxford, UK, 2020, February.

[32] S. Iqbal, A. Xin, M. U. Jan et al., "Role of power electronics in primary frequency control and power quality in an industrial micro-grid considering V2G technology," in *2019 IEEE 3rd Conference on Energy Internet and Energy System Integration (EI2)*, pp. 1188–1193, Changsha, China, 2019, November.

[33] Transport & Environment, "How clean are electric cars?," https://www.transportenvironment.org/what-we-do/electric-cars/how-clean-are-electric-cars.

[34] World Bank, "Electric power transmission and distribution losses (% of output)," https://datacatalog.worldbank.org/electric-power-transmission-and-distribution-losses-output-1.

[35] H. Hao, M. Wang, Y. Zhou, H. Wang, and M. Ouyang, "Levelized costs of conventional and battery electric vehicles in China: Beijing experiences," *Mitigation and Adaptation Strategies for Global Change*, vol. 20, no. 7, pp. 1229–1246, 2015.

[36] B. Borlaug, S. Salisbury, M. Gerdes, and M. Muratori, "Levelized cost of charging electric vehicles in the United States," *Joule*, vol. 4, no. 7, pp. 1470–1485, 2020.

[37] The World Bank, *Rwanda has achieved impressive development gains since the 1994 genocide and civil war*, The World Bank supports the energy, agriculture and transport sectors, 2021, https://www.worldbank.org/en/country/rwanda/overview.

[38] L. P. Nadimuthu and K. Victor, "Performance analysis and optimization of solar-powered E-rickshaw for environmental sustainability in rural transportation," *Environmental Science and Pollution Research*, pp. 1-2, 2021.

[39] N. Kamalimeera and V. Kirubakaran, "Prospects and restraints in biogas fed SOFC for rural energization: a critical review in Indian perspective," *Renewable and Sustainable Energy Reviews*, vol. 143, p. 110914, 2021.

[40] Z. Wang, Y. Tang, X. Chen, X. Men, J. Cao, and H. Wang, "Optimized daily dispatching strategy of building-integrated energy systems considering vehicle to grid technology and room temperature control," *Energies*, vol. 11, no. 5, article 1287, 2018.

[41] J. Ben Hmida, M. Javad Morshed, J. Lee, and T. Chambers, "Hybrid imperialist competitive and grey wolf algorithm to solve multiobjective optimal power flow with wind and solar units," *Energies*, vol. 11, no. 11, p. 2891, 2018.

[42] D. Liu, Q. Zhong, Y. Wang, and G. Liu, "Modeling and control of a V2G charging station based on synchronverter technology," *CSEE Journal of Power and Energy Systems*, vol. 4, no. 3, pp. 326–338, 2018.

[43] S. Al-Sakkaf, M. Kassas, M. Khalid, and M. A. Abido, "An energy management system for residential autonomous DC microgrid using optimized fuzzy logic controller considering economic dispatch," *Energies*, vol. 12, no. 8, p. 1457, 2019.

[44] U. Abronzini, C. Attaianese, M. D'Arpino, M. Di Monaco, and G. Tomasso, "Cost minimization energy control including battery aging for multi-source EV charging station," *Electronics*, vol. 8, no. 1, p. 31, 2019.

[45] Z. Zhao, J. Guo, C. S. Lai, H. Xiao, K. Zhou, and L. L. Lai, "Distributed model predictive control strategy for islands multi-microgrids based on non-cooperative game," *IEEE Transactions on Industrial Informatics*, vol. 17, pp. 3803–3814, 2020.

[46] H. Hou, M. Xue, Y. Xu et al., "Multiobjective joint economic dispatching of a microgrid with multiple distributed generation," *Energies*, vol. 11, no. 12, p. 3264, 2018.

[47] G. Saldaña, J. I. San Martin, I. Zamora, F. J. Asensio, and O. Oñederra, "Electric vehicle into the grid: charging methodologies aimed at providing ancillary services considering battery degradation," *Energies*, vol. 12, no. 12, p. 2443, 2019.

[48] L. Yu, T. Zhao, Q. Chen, and J. Zhang, "Centralized bi-level spatial-temporal coordination charging strategy for area electric vehicles," *CSEE Journal of Power and Energy Systems*, vol. 1, no. 4, pp. 74–83, 2015.

[49] D. Liu, Y. Wang, and Y. Shen, "Electric vehicle charging and discharging coordination on distribution network using multi-objective particle swarm optimization and fuzzy decision making," *Energies*, vol. 9, no. 3, p. 186, 2016.

[50] R. Shi, S. Li, C. Sun, and K. Y. Lee, "Adjustable robust optimization algorithm for residential microgrid multi-dispatch strategy with consideration of wind power and electric vehicles," *Energies*, vol. 11, no. 8, p. 2050, 2018.

[51] H. Liu, Y. Ji, H. Zhuang, and H. Wu, "Multi-objective dynamic economic dispatch of microgrid systems including vehicle-to-grid," *Energies*, vol. 8, no. 5, pp. 4476–4495, 2015.

[52] Y. Zhou, A. Vyas, and D. Santini, "Tracking national household vehicle usage by type, age, and area in support of market assessments for plug-in hybrid electric vehicles," *Journal of Transportation Technologies*, vol. 3, no. 2, pp. 174–183, 2013.

[53] K. S. Reddy, S. Aravindhan, and T. K. Mallick, "Techno-economic investigation of solar powered electric auto-rickshaw for a sustainable transport system," *Energies*, vol. 10, no. 6, p. 754, 2017.

[54] Homer energy, "HOMER Grid," https://www.homerenergy.com/products/grid/index.html#:~:text=HOMER%20Grid%20lets%20you%20accurately,tiered%20rates%2C%20and%20much%20more.&text=Our%20experts%20are%20also%20available,you%20need%20for%20accurate%20modeling.

Hindawi
International Journal of Photoenergy
Volume 2021, Article ID 5551014, 10 pages
https://doi.org/10.1155/2021/5551014

Research Article

Performance Modeling of the Weather Impact on a Utility-Scale PV Power Plant in a Tropical Region

Ajith Gopi,[1,2,3] K. Sudhakar,[3,4,5] Ngui Wai Keng,[1] Ananthu R. Krishnan,[6] and S. Shanmuga Priya[7]

[1]*College of Engineering, Universiti Malaysia Pahang, 26300, Gambang, Kuantan, Pahang, Malaysia*
[2]*Agency for New and Renewable Energy Research and Technology (ANERT), Thiruvananthapuram, Kerala, India*
[3]*Centre for Automotive Engineering, Universiti Malaysia Pahang, 26600 Pekan, Pahang, Malaysia*
[4]*Faculty of Mechanical and Automotive Engineering Technology, Universiti Malaysia Pahang, 26600 Pekan, Pahang, Malaysia*
[5]*Energy Centre, Maulana Azad National Institute of Technology, Bhopal, India*
[6]*IEEE, Kerala Section, Thiruvananthapuram, 695001 Kerala, India*
[7]*Department of Chemical Engineering, Manipal Institute of Technology, Manipal Academy of Higher Education, Manipal, Karnataka, India*

Correspondence should be addressed to K. Sudhakar; sudhakar@ump.edu.my and S. Shanmuga Priya; shan.priya@manipal.edu

Received 25 January 2021; Revised 31 May 2021; Accepted 15 June 2021; Published 28 June 2021

Academic Editor: Umapada Pal

Copyright © 2021 Ajith Gopi et al. This is an open access article distributed under the Creative Commons Attribution License, which permits unrestricted use, distribution, and reproduction in any medium, provided the original work is properly cited.

Solar photovoltaics and the associated applications are now considered the most promising technologies for a sustainable future. The performance of the PV power plants is not studied in detail with respect to the influence of various weather parameters like rain, relative humidity, and atmospheric pressure on energy generation. The objective of this research work is to analyze and model the weather impact of a utility-scale PV power plant in a tropical region. The methodology involves the detailed analysis of the PV plant performance for various weather seasons and modeling the energy generation based on important weather parameters obtained from a Solar Radiation Resource Assessment (SRRA) station installed at the PV power plant location itself. Solar generation and its performance are affected during the rainy seasons, and it turns out to be a typical phenomenon in the humid tropical region. A regression model of solar generation for all the weather seasons is generated based on different weather parameters.

1. Introduction

Solar PV has a greater role in the global energy transition for meeting the challenges of climate change. The Paris Agreement demands the global nations to limit the global temperature rise to 1.5°C. Energy-related carbon emission has to be reduced by around 3.5% per year to 2050 to address this challenge. The demand for solar PV is increasing across the world, and it becomes the most competitive option for electricity generation in many numbers of countries. Solar PV is expected to become the cheapest source of energy by 2050 in the regions where solar radiation is abundant [1]. A total cumulative solar PV capacity of 627 GW was installed up to 2019. The interest in solar PV capacity addition resulted in the addition of at least 1 GW capacity in more than 29 countries up to 2019. The major share in grid-connected renewables is from utility-scale solar power plants and also from the rooftop sector. The cost of solar PV continued to decline mainly due to the reduction in the price of PV modules [2]. According to the International Renewable Energy Agency, solar generation is increased by 28% from the previous year based on the data available from the sources [3]. Ground-mounted utility-scale solar PV projects had a major share of 70-72% in the global installed capacity. Utility-scale PV plants continue to be the major contributor to PV capacity addition in the world [4]. The performance of the solar PV power plant is influenced by various weather parameters like solar irradiation, temperature, wind speed,

Table 1: Summary of the relevant performance studies conducted in a different climate region.

Reference	Country/site	Capacity	Climate	Performance ratio (PR)	Method of data collection	Module technology
[14]	Sivaganga, India	5 MW	Tropical and hot climate	80%	SCADA	Thin amorphous
[15]	Ramagundam, India	10 MW	Tropical and hot climate	86.12%	SCADA	Poly C-Si
[16]	Tiruchirappalli, India	20 kWp	Tropical and hot climate	82%	—	Poly C-Si
[17]	Agra (city), Uttar Pradesh, India	40 kWp	Semiarid climate	63%	—	Mono C-Si
[18]	Visakhapatnam, India	1 MWp	Tropical and hot climate	88%	—	Poly C-Si
[19]	Dhaka, Bangladesh	80 kWp		66%	—	Mono C-Si
[20]	Cochin International Airport, Kochi, India	12 MWp	Tropical and hot climate	86.56%	SCADA	Poly C-Si
[21]	Raja Bhoj International Airport, Bhopal, India	2 MWp	Tropical and hot climate	85.54%	—	Poly C-Si
[22]	Roorkee, India	1816 kWp	N/A	63.68%	—	Poly C-Si
[23]	Morocco	5 kWp	N/A	79%	—	Poly C-Si
[24]	Ghana, 2013	2.5 MW	Tropical country	70.4%	Data logging system	Poly C-Si
[25]	Algeria	2.5 kWp	Hot dry climate	73.85%	—	Mono C-Si
[26]	Djibouti	302.4 kWp	Tropical desert maritime climate	84%	—	Poly C-Si
[27]	Nouakchott, Mauritania	15 MWp	Arid climate	63.59 to 73.56%	Data logger	Thin film
[28]	Nouakchott, Mauritania	954,809 kWp	Arid climate	61% to 71%	Data monitoring system	Thin film

rain, humidity, and atmospheric pressure. The output of the PV modules depends on the solar radiation falling on the surface. The operation and maintenance of solar PV plants play a vital role in improving the performance of PV power plants. The operation and maintenance of a PV plant are extremely important for its sustainability [5].

2. Literature Review: Weather-Related Studies Conducted in Solar Power Plants

The performance of the solar PV power plant is influenced by various weather parameters like solar irradiation, temperature, wind speed, rain, humidity, and atmospheric pressure. The output of the PV modules depends on the solar radiation falling on the surface [6]. Parretta et al. evaluated the performance of various PV technologies in the tropical region. Wijeratne et al. described the various software tools which deal with feasibility, operation, and maintenance cost, the performance of the PV plant, and the irradiation calculation [7]. Killinger et al. described the power generation between differently oriented PV systems based on a measurement from a reference system [8]. Martín-Martínez et al. studied the influence of ambient temperature and wind speed on the performance of six large-scale PV power plants in Spain [9]. Mussard and Amara discussed the performance analysis of various PV module technologies in an arid climatic condition [10]. Dabou et al. evaluated the power output on various climatic conditions in South Algeria [11]. Pina et al. analyzed the solar PV plant installed in Latvia utilizing a regression model [12]. Vasel and Iakovidis discussed the effect of wind direction on the performance of a utility-scale PV plant [13]. The relevant performance studies conducted in different climate regions are summarized in Table 1.

Based on Table 1, the performance ratio of the PV plant was found to vary between 61% and 88%. There is a large variation in the performance of the plant among different climates.

Most of the utility-scale power plants are installed with an embedded data monitoring system which includes a cell-based or thermopile-based pyranometer for solar radiation measurement. Most of the studies were conducted by utilizing the data from conventional data monitoring systems embedded with the solar power plant project when it is constructed by the developer. Sensors for measuring the ambient temperature, wind speed, and module temperature are also incorporated in most of the embedded data monitoring systems. All these studies have limitations since the data is completely dependent upon the measuring instruments of various qualities. Also, there is a chance that the instruments may not be calibrated as per the standards. However, these measuring instruments if not calibrated regularly may end up with erroneous measurement which will lead to wrong performance conclusions of the solar power plants. All the above studies were conducted based on the average monthly

Figure 1: Site view of ANERT 2 MWp Kuzhalmannam solar PV power plant.

data and not based upon an hourly average or daily average. Hence, the results and the conclusion in the referred studies have the limitation of detailed hourly/daily analysis.

A comprehensive analysis of the performance modeling of PV plant generation and the influence of weather parameters like the effect of humidity, atmospheric pressure, and rain are not reported by researchers in detail. Considering the gaps in studies as found in the literature, this research work is carried out with the most accurate and reliable data from a Solar Radiation Resource Assessment (SRRA) station installed as part of the National Solar Resource Assessment Programme conducted in India.

In this paper, the influence of weather parameters like solar irradiation, air temperature, rain, wind speed, atmospheric pressure, and dew point on the performance of PV plants is studied in detail using a very sophisticated Solar Radiation Research Assessment (SRRA) station.

The objectives of this research work are as follows:

(1) To analyze the weather impact of a utility-scale PV power plant in a humid tropical region utilizing SRRA data

(2) To develop a mathematical regression model for the solar generation in different weather seasons utilizing all weather parameters

(3) To establish a probability distribution model to predict the solar generation on varying irradiance

3. Methodology

3.1. Site Details and Conditions. The PV plant is situated in the southern state of Kerala in South India. This research is conducted based on the recent SRRA data of 2019. The 2 MW solar power plant selected for the study is located in a humid tropical region where the rain has got a more considerable influence on the weather pattern of the area [29]. The 2 MW solar power plant is situated at Kuzhalmannam in the Palakkad District of Kerala, South India. A site view of the 2 MWp PV power plant is given in Figure 1. The site is situated 17 km away from Palakkad Town. The plant was commissioned in December 2016. The geographical coordinates of the PV plant are 10.717 latitude and 76.613 longitude. The PV plant is solely owned by the Agency for New and Renewable Energy Research and Technology (ANERT), which is the State Nodal Agency of Renewable Energy under the Power Department of the Kerala Government.

Thomas and Prasannakumar described that the state of Kerala is experiencing tropical humid climatic conditions with two monsoon periods with more than three months of heavy rainy seasons [29]. Ananthakrishnan and Soman had described a comprehensive estimation of the rain in Kerala [30]. According to Hunt and Menon, the monsoon is spread over 6 months in Kerala with an average of 300 mm rain [31].

3.2. Data Collection. A typical SRRA station installation is shown in Figure 2. This SRRA station is installed as part of a separate Solar Radiation Resource Assessment Programme in different parts of the country and installed on the same premises of the 2 MW solar PV plant which turned out to be a novel arrangement for the measurement of different weather parameters utilizing state-of-the-art measuring instruments. The methodology involves accurate weather data collection from a Solar Radiation Resource Assessment (SRRA) station. This SRRA station is used as a primary data collection source for the study. The SRRA station is operational since November 2018, and the big data is streaming since then from the SRRA station and is being stored in the central server. This data is continuously monitored in the central server. This data at a one-minute interval is collected through the above measuring sensors and transferred in real-time from the SRRA station. The most recent year of 2019 is taken for analyzing the influence of weather along with the generation data of the PV power plant which is available from the traditional embedded data monitoring system.

Table 2 gives the summary of the measuring instruments in the SRRA station which are used for measuring the weather parameters at the site of the PV power plant.

The following data is available from the SRRA station:

(i) Direct normal irradiation (DNI)

(ii) Global horizontal irradiation (GHI)

(iii) Diffused horizontal irradiation (DHI)

(iv) Wind speed and direction

(v) Relative humidity

(vi) Rain

(vii) Atmospheric pressure

(viii) Solar elevation

(ix) Solar azimuth

(x) Dew point

The SRRA station provides the data of global horizontal irradiation through a pyranometer. Global tilted irradiation is calculated for determining various performance parameters like performance ratio and module temperature. The data logger and modem at the SRRA station combined with GPRS will accomplish the task of data collection and monitoring.

Figure 2: Dedicated SRRA station at the site and central data server for the real-time collection of the data.

Table 2: Summary of measuring instruments in an SRRA station.

Sl no.	Instrument	Manufacturer	Parameter
A. Solar measuring instruments			
1	Pyranometer	Phase I: Eppley, USA Phase II: Hukseflux, NL	Global radiation (W/m^2)—instantaneous, average
2	Shaded pyranometer	-do-	Diffuse radiation (W/m^2)—instantaneous, average
3	Pyrheliometer	-do-	Direct irradiance (W/m^2)—instantaneous, average
4	Solar tracker	Geonica, Spain	Mounted with shaded pyranometers and pyrheliometer
B. Meteorological measuring instruments			
5	Ultrasonic wind sensor	R. M. Young, USA	Wind speed and wind direction—standard deviation, maximum, and average
6	Rain gauge	-do-	Rain accumulation
7	Pressure sensor	-do-	Atmospheric pressure
8	Temperature & relative humidity sensor	-do-	Temperature and humidity—average, maximum, and minimum
C. General instruments			
9	GPS	Garmin, USA	To synchronize sun tracker with sun movement
10	Data logger & modem	Geonica, Spain	Collecting data from sensors
11	GPRS	Garmin, USA	To transfer data through mobile SIM cards
12	Solar PV panel	Moser Baer, India	For charging battery for powering the station
13	External battery	Exide, India	For electrical storage

3.3. Determination of Global Tilted Irradiation and Module Temperature from SRRA Data. The methodology of this research work includes the following:

(i) Primary data collection from the SRRA station

(ii) Determination of global tilted radiation and module temperature from SRRA data

(iii) Modeling the PV generation utilizing Minitab software

(iv) Analysis of the variation of PV plant performance

(v) Comparison of the seasonal performance of the plant

Kalogirou has consolidated various mathematical equations used for the determination of global tilted irradiation and module temperature [32]. The equations are given below.

3.3.1. Estimation of Global Tilted Irradiation. Global tilted irradiation (G_{Bt}) or the beam radiation on a tilted surface is calculated by multiplying global horizontal irradiation (GB) and beam radiation tilt factor (RB). Global horizontal irradiation is the sum of the beam (direct) and diffuse radiation and is also known as "global radiation."

$$G_{Bt} = G_B \times R_B. \quad (1)$$

The beam radiation tilt factor (RB) is given by

$$R_B = \frac{\sin(L-\beta)\sin(\delta) + \cos(L-\beta)\cos(\delta)\cos(h)}{\sin(L)\sin(\delta) + \cos(L)\cos(\delta)\cos(h)}. \quad (2)$$

The declination angle (δ) is defined as the angle between the lines joining the centers of the sun and the earth, which also determines the direction of the direct rays coming from the sun and their projection on the equatorial plane and is given by

$$\delta = 23.45 \sin\left[\frac{360}{365}(284+N)\right]. \quad (3)$$

The value of N is the date number which ranges from 1 to 365.

The zenith angle is the angle between the sun's rays and the line perpendicular to a horizontal plane, and the hour angle is the angular displacement of the sun from the local meridian because of the earth's rotation around its own axis [33].

The hour angle (h) is given by

$$\cos(\omega s) = -\tan(L)\tan(\delta). \quad (4)$$

The latitude (N) is also an important factor determining the hour angle as given above.

Estimation of module temperature is given by

$$T_c = 30 + 0.0175(G_t - 300) + 1.14(T_a - 25),$$
$$\text{Plant efficiency} = \frac{E_{grid} * 100}{G_{Bt} * A_{mod}}. \quad (5)$$

3.4. Data Analysis and Modeling. Weather in the state is broadly divided into four seasons including two monsoons and summer and winter seasons. The performance of the solar PV power plant is assessed for the above four seasons by utilizing the SRRA data collected for the entire year of 2019. Northeast monsoon, southwest monsoon, and summer and winter seasons are separately taken for analyzing the PV plant behavior based on the variation of different weather parameters. The following analysis is done for the 2019 data collected from the SRRA station:

(1) Detailed analysis for a selected month in a season

(2) Yearly data analysis

The various months that represent the typical characteristics of the season are selected for the regression modeling and arrive at the energy generation model equations.

3.5. Modeling the PV Generation with Weather Parameters. Minitab is the statistical tool used for this analysis and for arriving at regression model equations from big data. Minitab is a statistical package developed at Pennsylvania State University, USA. It offers various computations in the field of big data analytics. Here, the weather parameters are selected as variables, and the generation is made as a response to various seasons. The outcome of this methodology is the development of a mathematical model for the 2 MWp PV power plant based on various weather parameters. Once the model is created, the generation can be theoretically calculated from the mathematical model. The important weather parameters selected for regression modeling are given in Table 3.

Minitab is also used for fitting the probability distribution plot for a typical generation (kWh) in a day against the representative average daily solar generation (G_{POA}) of the year.

Table 3: Weather parameters for regression modeling.

Parameter	Notations	Remarks
Global tilted irradiation	G_{POA}	kWh/m^2
Wind speed	WS	m/s
Air temperature	T	°C
Relative humidity	RH	%
Atmospheric pressure	P_{ATM}	Mb
Rain	R	mm

4. Results and Discussion

The energy generation profile for different seasons is discussed in the following section. The plant performance results are summarized in Table 4 for arriving at conclusions.

4.1. Seasonal Plant Performance. The classification of seasons is as follows:

(i) Southwest monsoon (June to September)

(ii) Northeast monsoon (October to November)

(iii) Summer (February to May)

(iv) Winter (December to January)

The year 2019 was faced with heavy rain in Kerala, particularly in Palakkad District where the PV plant is located. Tropical humid regions are characterised by rainy seasons, and there will be impact on the PR in these regions due to rain. Month-wise generation, global tilted generation, peak sun hours, PR, wind speed, air temperature, relative humidity, atmospheric pressure, and rain are summarized in Table 4.

It is observed that the performance ratio (PR) of the plant was reasonable during the summer season (Feb—71.67, March—71.72, April—69.75, and May—72.69), obviously due to higher energy generation. The advantage of colder temperature improves the PR of the plant further during the rainy months of June (75.95) and July (74.09) as compared to the summer season though the overall generation was lower. The highest PR of the plant was observed during September (79.50) owing to the lesser solar radiation. The lowest sun peak hours have been observed as 4.41, 4.04, 3.48, and 4.18 during June, July, August, and September of 2019, respectively, which indicate the reduction in solar insolation during the rainy season. This directly influences the performance of the plant as well.

4.2. Effect of Temperature on Generation. Eight representative days were chosen for different seasons to study the effect of temperature on generation and are presented in Table 5. Among the eight days, selected for the study, the lowest average ambient temperature was recorded during January obviously due to the winter season. The daily energy generation for the winter days is higher than that for other days chosen for the analysis. The combined effect of optimum temperature and sunshine duration contributed to the higher

Table 4: Summary of monthly average weather parameters.

Month	Generation (MWh)	Monthly tilted irradiation (kWh/m^2)	Peak sun hours per day during the month	PR	Wind speed (m/s)	Air temp (°C)	Rel. humidity	Atm. pressure (mb)	Rain (mm)
Jan	267.262	190.80	6.15	69.93	3.01	26.88	68.89	1010.96	7.8
Feb	260.593	181.53	5.86	71.67	2.35	28.53	59.52	1013.18	0.0
Mar	295.842	205.95	6.64	71.72	2.14	29.90	63.69	1010.61	2.0
Apr	258.129	184.77	5.96	69.75	2.25	30.42	68.15	1006.45	70.7
May	252.834	173.65	5.60	72.69	2.98	30.16	70.28	1006.09	37.5
Jun	207.927	136.68	4.41	75.95	2.76	27.87	81.51	1003.14	208.0
Jul	186.007	125.34	4.04	74.09	2.56	26.25	86.37	1004.85	270.9
Aug	142.496	107.98	3.48	65.88	2.63	25.51	89.24	1005.71	571.6
Sept	206.299	129.55	4.18	79.50	2.25	26.57	86.34	1008.90	154.8
Oct	211.321	168.87	5.45	62.47	1.76	26.66	83.30	1006.89	337.3
Nov	209.165	185.72	5.99	56.23	2.17	27.53	76.21	1010.44	80.2
Dec	211.726	169.06	5.45	62.53	3.01	26.88	68.89	1010.96	7.8

Table 5: PR and generation variation for various selected days with an average temperature.

Date	Average ambient temperature (°C)	Average module temperature (°C)	Daily generation (kWh)	PR (%)	Days
22-01-19	24.33	36.14	9865	73.36	Winter
21-08-19	25.97	30.05	6718	77.67	Southwest monsoon
26-10-19	27.67	38.41	8772	60.84	Northeast monsoon
14-04-19	31.99	44.26	8960	70.55	Summer
20-03-19	30.08	40.64	8277	73.82	Spring equinox
23-09-19	26.84	35.66	7259	65.98	Fall equinox
21-06-19	26.08	31.77	5840	84.97	Summer solstice
22-12-19	26.90	36.83	8247	66.14	Winter solstice

generation which clearly shows that the winter seasons are also favorable for energy generation in tropical humid regions. The summer solstice in the tropical region falls in the southwest monsoon season, and hence, lesser generation was observed due to the cloudy and rainy conditions prevailing in the regions. This emphasizes the influence of rain in keeping the ambient temperature lower when compared to the winter months. The air temperature and module temperature show a continuous correlation throughout the seasons. On a typical summer day, the module temperature can reach above 44°C and the module temperature shows a comparatively lower level in rainy months as a general tendency in tropical regions. The module temperature follows the air temperature almost constantly throughout the summer seasons which is a common trend in tropical regions.

4.3. Effect of Irradiance on Generation. The eight representative days were chosen for different seasons to study the effect of irradiance on energy generation as illustrated in Table 6. The highest global tilted irradiance has been observed on winter days, and correspondingly higher energy generation happened. Out of 8 days, 4 days achieved more than 8000 kWh generation which shows the correlation between higher global tilted irradiance and generation. It has been observed that the highest average global tilted irradiations happened during both summer and winter seasons. It is found that both summer and winter days provide the best solar generation among the selected days. The highest global tilted irradiance was observed mostly in summer days except for three days in monsoon. This indicates the importance of summer in tropical regions in achieving higher performance as it is evident from the higher generation values during the summer season.

Hence, it can be concluded that the typical Kerala humid climate supports good generation in the first six months of a year and dips into the lesser generation in monsoon months until it regains the status in the final months of the year.

4.4. Modeling of Solar Generation in Different Weather Seasons. The data from the SRRA weather monitoring station is analyzed for the year 2019, and that has been used to develop a regression model for the entire four weather seasons for a 2 MWp PV power plant installed in a tropical region. The modeling output is calculated for the typical one day of the selected season as per the model equation below, and then, that value has to be multiplied by the number of days in that season to get the total generation. The weather parameters considered for the study are global tilted irradiation, wind speed, air temperature, relative humidity, atmospheric pressure, and the rain of the site. Here, the solar generation is derived from the selected weather parameters

Table 6: Generation and PR for the days with the average irradiance.

Date	Global horizontal irradiation (kW/m^2/day)	Global titled irradiance (kWh/m^2/day)	Generation (kWh)	Performance ratio (%)	Days
22-01-19	6.08	6.70	9865	73.36	Winter
21-08-19	4.43	4.31	6718	77.67	Southwest monsoon
26-10-19	6.04	7.19	8772	60.84	Northeast monsoon
14-04-19	6.44	6.33	8960	70.55	Summer
20-03-19	5.48	5.59	8277	73.82	Spring equinox
23-09-19	5.37	5.49	7259	65.98	Fall equinox
21-06-19	3.68	3.43	5840	84.97	Summer solstice
22-12-19	5.56	6.22	8247	66.14	Winter solstice

Table 7: Model testing and validation using 2020 measured data.

Year	Global tilted irradiance (kWh/m^2)	Wind speed (m/s)	Air temp (°C)	Rel. hum.	Atm. pressure (mb)	Rain (mm)	Actual generation (kWh)	Predicted with the AGS model	Variation (%)
2020 (SW)	4.5	2.46	26.76	83.58	1003.354	154	6010	6492.33	7.29
2020 (S)	7.21	2.53	28.25	57.04	1011.88	0	9455.8	10478.92	9.76
2020 (W)	5.8	2.44	27.34	62.90	1011.92	0.40	8697.96	9947.81	12.56
2020 (NE)	Not tested due to lack of SRRA data for NE monsoon								

above. The mathematical model equations (developed by Ajith Gopi, Sudhakar, and Co hereafter named as the AGS model) for typical days of different weather seasons, arriving at utilizing the regression modeling, are listed below:

Southwest monsoon:

$$E = 2422 + 1402.9G_{\mathrm{POA}} + 157\,\mathrm{WS} - 89T_{\mathrm{a}} - 7.2\,\mathrm{RH} + 0.8P_{\mathrm{ATM}} - 2.91R. \quad (6)$$

Northeast monsoon:

$$E = -58186 + 1480G_{\mathrm{POA}} + 709\,\mathrm{WS} + 248T_{\mathrm{a}} + 56.0\,\mathrm{RH} + 42.9P_{\mathrm{ATM}} - 3.6R. \quad (7)$$

Summer:

$$E = -22790 + 1259G_{\mathrm{POA}} + 57\,\mathrm{WS} + 9T_{\mathrm{a}} - 24.8\,\mathrm{RH} + 24.9P_{\mathrm{ATM}} - 579R. \quad (8)$$

Winter:

$$E = 147222 + 1759G_{\mathrm{POA}} - 1567\,\mathrm{WS} + 202T_{\mathrm{a}} - 64.6\,\mathrm{RH} - 145P_{\mathrm{ATM}} + 4069R. \quad (9)$$

The above models are tested utilizing the 2020 SRRA data, and the results are checked and compared with the actual generation data as given in Table 7.

The above AGS model can be used to predict energy generation of a 2 MWp PV plant for a typical day in each season based on the important weather parameters in a tropical region as discussed above. The model has been tested and validated utilizing the 2020 year's measured data. The percentage average variation in the prediction of energy generation using the model is within the acceptable limits (9.87%). The novelty of this work is that this model brings important weather parameters like wind speed, air temperature, relative humidity, atmospheric pressure, and rain into this model which was not previously taken up in any research work along with seasonal solar power PV plant generation.

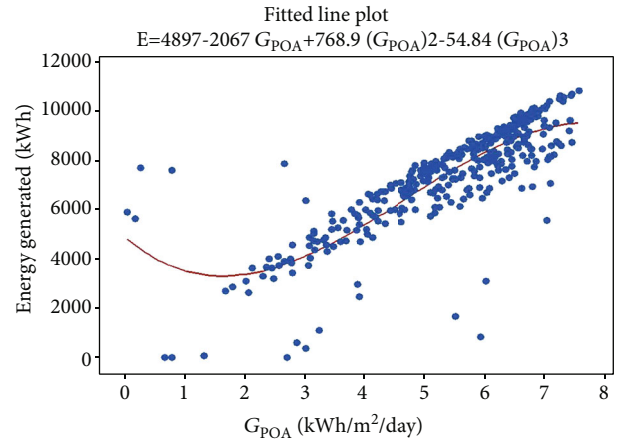

Figure 3: Probability distribution model fitted for the 2 MW PV plant.

4.5. Probability Distribution Model. The data set for the average daily generation (kWh) is plotted against global tilted irradiance as a scatter plot, and a line curve is fitted for the best value as given in Figure 3. The cubic model is arrived at by utilizing the Minitab statistical tool. The scatter plot is

Table 8: Validation of the probability distribution model using 2020 measured data.

Description	Annual G_{POA} (kWh/m^2)	Annual average G_{POA} per day	Actual generation (kWh)	Prediction by model (MWh)	Percentage of variation (%)
2018	2011.60	5.51	2701.46	2803.05	-3.76
2020	1916.25	5.25	2704.18	2668.56	1.31
PVsyst	2011.70	5.51	3034.30 (simulated)	2803.19	7.61

accomplished as a probability distribution as per the cubic model equation given below.

$$E = 4897 - 2067G_{POA} + 768.9\,(G_{POA})^2 - 54.84(G_{POA})^3. \quad (10)$$

This probability distribution predicts the values for generation in a day on varying irradiance which when multiplied by 365 days will predict the annual generation.

The validation of the probability distribution model is tested using the measured data of 2018 and 2020, and the model is also compared with the PVsyst simulated generation, and the details are summarized in Table 8. The percentage variation of predicted generation by the probability model in the years of 2018 and 2020 is within the acceptable limits with the actual generation.

This simple model predicts the average daily generation of a 2 MWp PV power plant installed in a tropical region for a complete year with a single parameter of global tilted irradiation in the equation. This model helps for a quick prediction of solar generation PV power plant sites in a tropical region. Predictive maintenance, remote sensing, and solar forecasting will help in monitoring the solar power plant performance.

5. Conclusion

This research work studied the influence of important weather parameters on the performance of a utility-scale power plant installed in a humid tropical region in the state of Kerala, a southern state of India. Unlike conventional data collection, big data collected from the Solar Radiation Resource Assessment (SRRA) station is used in this research work for accurate estimation. In addition to the usual weather parameters like ambient temperature, global tilted irradiance, and wind speed, other influential parameters like rain, atmospheric pressure, and humidity are also analyzed and modeled for the major weather seasons of the region. The following are the major outcomes of the study.

(i) Solar generation and its performance are affected during the rainy seasons, and it turns out to be a typical phenomenon in humid tropical regions. It is also understood that the prevailing wind during the monsoon periods does not make much influence on the performance of the PV power plant

(ii) The generation of the PV plant in a tropical region strictly follows the irradiance pattern. Global horizontal irradiation and global tilted irradiation are in analogy providing comparatively higher values compared to monsoon months

(iii) It is observed that higher generation happens during the period of lower atmospheric pressure in tropical regions

(iv) Higher generation and reasonable PR are the highlights of summer seasons. The solar generation and performance characteristics of the winter season are almost the same as those of the summer season in tropical regions since all the performance parameters are observed to be similar. The plant performed well during the summer and winter seasons when compared with the monsoon seasons

(v) The monsoon rain has an influence on the ambient temperature of the region which lowers the module temperature. As a general trend, module temperature follows the ambient temperature throughout the seasons

(vi) The 2 MWp solar PV plant has got comparatively higher PR during rainy seasons due to the advantage of colder temperature during rainy seasons

(vii) The lowest sun peak hours of 4.41, 4.04, 3.48, and 4.18 were observed during June, July, August, and September of 2019, respectively, which hints the lower values of solar insolation during the monsoon months

(viii) The PV power plant has an annual generation of 2709.601 MWh for the year 2019 with an annual irradiance of 1959.9 kWh/m^2

(ix) A solar generation model, hereafter named as the AGS model, which predicts the generation for the weather seasons has been developed for a 2 MWp PV plant in a tropical region utilizing regression modeling in Minitab software utilizing important weather parameters like global tilted irradiation, wind speed, air temperature, relative humidity, atmospheric pressure, and the rain of the site

(x) The optimum generation in a typical day for a 2 MWp PV plant in a tropical region utilizing generation and global tilted irradiation is obtained based on the probability distribution model: $E = 4897 - 2067\,G_{POA} + 768.9\,(G_{POA})^2 - 54.84\,(G_{POA})^3$

This research work will aid future studies on performance analysis of PV plants in other geographical regions with different climatic conditions.

Nomenclature

G_{Bt}: Beam radiation on a tilted surface (global tilted irradiation) (W/m^2)
G_B: Beam radiation on a horizontal plane (global horizontal irradiation) (W/m^2)
R_B: Beam radiation tilt factor
L: Latitude (°)
β: Tilt angle for PV module (°)
δ: Declination angle (°)
h: Hour angle (°)
N: Date number in a year, value ranges from 1 to 365
G_t: Global tilted irradiance (kWh/m^2)
T_a: Ambient air temperature (°C)
G_{POA}: Tilted irradiance (kWh/m^2)
WS: Wind speed (m/s)
T: Air temperature (°C)
RH: Relative humidity (%)
P_{ATM}: Atmospheric pressure (mb)
R: Rain (mm)
E_{Grid}: AC energy injected to the grid (kWh)
A_{mod}: Area of the PV module (m^2)
PR: Performance ratio.

Data Availability

All the performance data used to support the findings of this study are included within the article.

Disclosure

The authors acknowledge that the data involved in this study, information, and uncertainties in results may contain assumptions, inaccuracies, or errors. So the authors of this manuscript expressly exclude the liability for any such inaccuracies or errors to the fullest extent permitted by law. The opinions or facts or insights and discussions in this document are solely of the authors. It does not necessarily reflect the policy and standpoint of any organization directly or indirectly. Hence, the authors are not responsible for any consequences thereof with the use of information presented in this work.

Conflicts of Interest

The authors declare that they have no conflicts of interest.

Acknowledgments

The authors acknowledge the Agency for New and Renewable Energy Research and Technology (ANERT), which is the Kerala State Renewable Nodal Agency under the Department of Power in Government of Kerala, in India, for providing the data for this research work. The authors also acknowledge the National Institute of Wind Energy (NIWE), Chennai, India, for the information provided regarding the SRRA station. The support provided by Universiti Malaysia Pahang (http://www.ump.edu.my) through PGRS210349 and Mr. Sreenath Sukumaran, Ph.D. scholar, UMP, and former master student of MANIT-Bhopal, India, is greatly acknowledged. The second author is greatly indebted to the Board of Management, Maulana Azad National Institute of Technology (MANIT), Bhopal, India, for providing long-term unpaid leave to carry out teaching and research activities at Universiti Malaysia Pahang.

References

[1] I. International and R. Energy, *Future of Deployment, investment technology, grid integration and socio-economic aspects*, International Renewable Energy Agency, Abu Dhabi, 2018.

[2] R. E. N. Members, *Renewables 2020 global status report 2020, REN21.2020*, REN21 Secretariat, Paris, 2020.

[3] I. Renewable and E. Agency, *Renewable Energy Statistics 2020*, International Renewable Energy Agency, Abu Dhabi, 2020.

[4] F. S. Power, *Mobilising Investments in Emerging Markets*, International Renewable Energy Agency, Abu Dhabi, 2019.

[5] L. Hernández-callejo, S. Gallardo-saavedra, and V. Alonso-gómez, "A review of photovoltaic systems: design, operation and maintenance," *Solar Energy*, vol. 188, pp. 426–440, 2019.

[6] A. Parretta, A. Sarno, and L. R. M. Vicari, "Effects of solar irradiation conditions on the outdoor performance of photovoltaic modules," *Optics Communications*, vol. 153, no. 1-3, pp. 153–163, 1998.

[7] W. M. P. U. Wijeratne, R. J. Yang, E. Too, and R. Wakefield, "Design and development of distributed solar PV systems: do the current tools work?," *Sustainable Cities and Society*, vol. 45, pp. 553–578, 2019.

[8] S. Killinger, F. Braam, B. Müller, B. Wille-Haussmann, and R. McKenna, "Projection of power generation between differently-oriented PV systems," *Solar Energy*, vol. 136, pp. 153–165, 2016.

[9] S. Martín-Martínez, M. Cañas-Carretón, A. Honrubia-Escribano, and E. Gómez-Lázaro, "Performance evaluation of large solar photovoltaic power plants in Spain," *Energy Conversion and Management*, vol. 183, pp. 515–528, 2019.

[10] M. Mussard and M. Amara, "Performance of solar photovoltaic modules under arid climatic conditions: a review," *Solar Energy*, vol. 174, pp. 409–421, 2018.

[11] R. Dabou, F. Bouchafaa, A. H. Arab et al., "Monitoring and performance analysis of grid connected photovoltaic under different climatic conditions in south Algeria," *Energy Conversion and Management*, vol. 130, pp. 200–206, 2016.

[12] A. Pina, P. Ferrão, J. Fournier, B. Lacarrière, O. Le Corre, and A. I. Andri, "First solar power plant in Latvia. Analysis of operational data," *Energy Procedia*, vol. 147, pp. 162–165, 2018.

[13] A. Vasel and F. Iakovidis, "The effect of wind direction on the performance of solar PV plants," *Energy Conversion and Management*, vol. 153, pp. 455–461, 2017.

[14] S. Sundaram and J. S. C. Babu, "Performance evaluation and validation of 5 MW$_p$ grid connected solar photovoltaic plant in South India," *Energy Conversion and Management*, vol. 100, no. 2015, pp. 429–439, 2015.

[15] B. Shiva Kumar and K. Sudhakar, "Performance evaluation of 10 MW grid connected solar photovoltaic power plant in India," *Energy Reports*, vol. 1, pp. 184–192, 2015.

[16] K. A. Kumar, K. Sundareswaran, and P. R. Venkateswaran, "Performance study on a grid connected 20 kW$_p$ solar photovoltaic installation in an industry in Tiruchirappalli (India),"

Energy for Sustainable Development, vol. 23, pp. 294–304, 2014.

[17] K. P. Satsangi, D. B. Das, G. S. S. Babu, and A. K. Saxena, "Energy for sustainable development performance analysis of grid interactive solar photovoltaic plant in India," *Energy for Sustainable Development*, vol. 47, pp. 9–16, 2018.

[18] S. Thotakura, S. Chandan Kondamudi, J. F. Xavier et al., "Operational performance of megawatt-scale grid integrated rooftop solar PV system in tropical wet and dry climates of India," *Case Studies in Thermal Engineering*, vol. 18, article 100602, 2020.

[19] F. Touati, N. A. Chowdhury, K. Benhmed et al., "Long-term performance analysis and power prediction of PV technology in the State of Qatar," *Renewable Energy*, vol. 113, pp. 952–965, 2017.

[20] S. Sukumaran and K. Sudhakar, "Fully solar powered airport: a case study of Cochin International Airport," *Journal of Air Transport Management*, vol. 62, pp. 176–188, 2017.

[21] S. Sukumaran and K. Sudhakar, "Fully solar powered Raja Bhoj International Airport: a feasibility study," *Resource-Efficient Technologies*, vol. 3, no. 3, pp. 309–316, 2017.

[22] K. Sangram, S. Pundir, N. Varshney, and G. K. Singh, "Comparative study of performance of grid connected solar photovoltaic power system in IIT Roorkee campus," *International Jounal of Innoative Research in Science and Engineering*, vol. 2, pp. 319–328, 2016.

[23] K. Attari, A. Elyaakoubi, and A. Asselman, "Performance analysis and investigation of a grid-connected photovoltaic installation in Morocco," *Energy Reports*, vol. 2, pp. 261–266, 2016.

[24] L. D. Mensah, J. O. Yamoah, and M. S. Adaramola, "Performance evaluation of a utility-scale grid-tied solar photovoltaic (PV) installation in Ghana," *Energy for Sustainable Development*, vol. 48, pp. 82–87, 2019.

[25] A. Necaibia, A. Bouraiou, A. Ziane et al., "Analytical assessment of the outdoor performance and efficiency of grid-tied photovoltaic system under hot dry climate in the south of Algeria," *Energy Conversion and Management*, vol. 171, pp. 778–786, 2018.

[26] D. H. Daher, L. Gaillard, M. Amara, and C. Ménézo, "Impact of tropical desert maritime climate on the performance of a PV grid-connected power plant," *Renewable Energy*, vol. 125, pp. 729–737, 2018.

[27] C. E. B. Elhadj Sidi, M. L. Ndiaye, M. El Bah, A. Mbodji, A. Ndiaye, and P. A. Ndiaye, "Performance analysis of the first large-scale (15 MW_p) grid-connected photovoltaic plant in Mauritania," *Energy Conversion and Management*, vol. 119, pp. 411–421, 2016.

[28] M. el Hacen Jed, R. Ihaddadene, N. Ihaddadene, C. E. L. B. Elhadji Sidi, and M. el Bah, "Performance analysis of 954,809 kWp PV array of Sheikh Zayed solar power plant (Nouakchott, Mauritania)," *Reinforced Plastics*, vol. 32, pp. 45–54, 2020.

[29] J. Thomas and V. Prasannakumar, "Temporal analysis of rainfall (1871-2012) and drought characteristics over a tropical monsoon-dominated State (Kerala) of India," *Journal of Hydrology*, vol. 534, pp. 266–280, 2016.

[30] R. Ananthakrishnan, "The onset of the south west monsoon over Kerala: 1901–1980," *J. Climate*, vol. 8, pp. 283–296, 1988.

[31] K. M. R. Hunt and A. Menon, "The 2018 Kerala floods: a climate change perspective," *Climate Dynamics*, vol. 54, no. 3-4, pp. 2433–2446, 2020.

[32] S. Kalogirou, *Solar Energy Engineering*, Academic Press, Amsterdam, 2014.

[33] T. Arvind and T. Shyam, *Handbook of Solar Energy, 2016th ed*, Springer, Singapore, 2016.

Hindawi
International Journal of Photoenergy
Volume 2021, Article ID 5515513, 32 pages
https://doi.org/10.1155/2021/5515513

Research Article

Concentrated Solar Power and Photovoltaic Systems: A New Approach to Boost Sustainable Energy for All (Se4all) in Rwanda

Noel Hagumimana,[1] **Jishi Zheng**,[1] **Godwin Norense Osarumwense Asemota**,[2,3] **Jean De Dieu Niyonteze**,[1] **Walter Nsengiyumva**,[4] **Aphrodis Nduwamungu**,[2] **and Samuel Bimenyimana**[5,6]

[1]*Fujian Province Key Laboratory of Automotive Electronics and Electric Drive, Fujian University of Technology, Fuzhou 350118, China*
[2]*University of Rwanda, African Centre of Excellence in Energy for Sustainable Development, Kigali 4285, Rwanda*
[3]*Morayo College, Nairobi, Kenya*
[4]*Laboratory of Optics, Terahertz and Non-destructive Testing, School of Mechanical Engineering and Automation, Fuzhou University, Fuzhou 350116, China*
[5]*Huaqiao University, Intelligence and Automation in Construction Provincial Higher-Educational Engineering Research Centre, 361021 Xiamen, China*
[6]*Hello Renewables Ltd., Kigali, Rwanda*

Correspondence should be addressed to Noel Hagumimana; hagumanoel@gmail.com, Jishi Zheng; zhengjiishi@fjut.edu.cn, and Jean De Dieu Niyonteze; niyontezejado@gmail.com

Received 26 January 2021; Revised 5 April 2021; Accepted 11 May 2021; Published 16 June 2021

Academic Editor: Kumarasamy Sudhakar

Copyright © 2021 Noel Hagumimana et al. This is an open access article distributed under the Creative Commons Attribution License, which permits unrestricted use, distribution, and reproduction in any medium, provided the original work is properly cited.

The energy sector of today's Rwanda has made a remarkable growth to some extent in recent years. Although Rwanda has natural energy resources (e.g., hydro, solar, and methane gas, etc.), the country currently has an installed electricity generation capacity of only 226.7 MW from its 45 power plants for a population of about 13 million in 2021. The current national rate of electrification in Rwanda is estimated to 54.5% (i.e.; 39.7% grid-connected and 14.8% off-grid connected systems). This clearly demonstrates that having access to electricity is still a challenge to numerous people not to mention some blackout-related problems. With the ambition of having electricity for all, concentrated solar power (CSP) and photovoltaic (PV) systems are regarded as solutions to the lack of electricity. The production of CSP has still not been seriously considered in Rwanda, even though the technology has attracted significant global attention. Heavy usage of conventional power has led to the depletion of fossil fuels. At the same time, it has highlighted its unfriendly relationship with the environment because of carbon dioxide (CO_2) emission, which is a major cause of global warming. Solar power is another source of electricity that has the potential to generate electricity in Rwanda. Firstly, this paper summarizes the present status of CSP and PV systems in Rwanda. Secondly, we conducted a technoeconomic analysis for CSP and PV systems by considering their strengths, weaknesses, opportunities, and threats (SWOT). The input data of the SWOT analysis were obtained from relevant shareholders from the government, power producers, minigrid, off-grid, and private companies in Rwanda. Lastly, the technical and economical feasibilities of CSP and PV microgrid systems in off-grid areas of Rwanda were conducted using the system advisor model (SAM). The simulation results indicate that the off-grid PV microgrid system for the rural community is the most cost-effective because of its low net present cost (NPC). According to the past literature, the outcomes of this paper through the SWOT analyses and the results obtained from the SAM model, both the CSP and PV systems could undoubtedly play a vital role in Rwanda's rural electrification. In fact, PV systems are strongly recommended in Rwanda because they are rapid and cost-effective ways to provide utility-scale electricity for off-grid modern energy services to the millions of people who lack electricity access.

1. Introduction

Until recently, electrical energy is seen as a basic need in human life everywhere in the world. However, Rwanda along with many other countries is struggling from a severe lack of access to electricity. Frequent outage due to unbalance between supply and consumer demand continues to rise because of the rise in the Rwanda population as well as the world, the growth of industrial activities, and the improvement of living standards; the electricity demand for the population is growing day by day and has become a major concern, and it will also be much more needed in the years to come. The little dependency on solar energy and a small amount of hydropower in Rwanda is behind the lack of electricity access. Traditional fossil fuels such as oil and coal are continually depleted, causing emissions of carbon dioxide and global warming [1].

Solar energy is seen as one of the most promising sources of energy for producing electricity. On the surface of the earth, the energy obtained from the sun is around 885 million TWh, and this energy is projected to be 6200 times the commercial power needs of the world's population [2]. Each hour, 430 quintillion Joules of energy from the sun reaches the earth [3]. Solar energy production has traditionally been expensive and fairly inefficient, although there has been an improvement over the previous two decades. This is so because the worldwide amount of energy obtained from solar energy increased 300-fold from 2000 to 2019 [4]. The solar radiation beam is a key to CSP to generate electricity by using mirrors that focus onto a small area and concentrates the solar energy to energize the heat transfer fluid (HTF). The solid or gas is heated up to higher temperatures for generating steam required to move a heat engine for the generation of electricity, instead of using fossil fuels or nuclear reactions [5].

Unlike conventional power plants, concentrated solar power or solar thermal systems have an environmentally suitable electricity source, with no carbon dioxide emissions and no need for fuel consumption but sunlight [6]. The only concern on the environment of concentrating solar power plants (CSPs) is land use. Even though the land usage of concentrating solar power plants seems to be larger than that of a fossil fuel plant, it was found that the extra land for load building and mining exploration has led to approximately equal usage of the amount of land [7]. Other benefits of concentrating solar power plants include low operating costs and the ability to produce power during high-energy demand periods and to help increase the country's energy security and independence from foreign oil imports. Because CSPs store energy, they can operate in cloudy weather and after sunset. When combined with fossil fuels as a hybrid system, they can operate around the clock regardless of the weather [8].

Solid and liquid storage media are a sensible heat storage media used for thermal energy storage for CSP systems, and reversible chemical reactions like latent heat storage using phase change materials (PCMs) and thermochemical storage. The following variables are considered when implementing a thermal energy system (TES) for a CSP farm: (1) maximum load and specific enthalpy drop in load, (2) operational strategy, (3) nominal temperature, and (4) integration into the power plant [9]. Several studies have studied the cost of TES, taking into account the different elements involved, including storage media, tanks, and other expenses.

Since Rwanda lies within the tropical and subtropical regions, it obtains large amounts of solar irradiation that is ideal for power generation. In recent years, Rwanda's peer influence on solar energy has increased and the production of electricity using solar energy is relatively inexpensive and suitable for rural and urban centers [10].

As Rwanda's weather condition is relatively stable, we can turn on emphasizing the availability of CSP generation during the dry and hot season, with CSP's ability to just provide firm capacity for eight hours a day, as data were reported daily throughout the year [5].

The fast integration of TES allows CSP to be dispatchable and unique out of all the other alternative options for generating renewable energy. As an intermediate phase for electricity generation, a TES system provides a highly efficient heat storage process [11]. It may minimize short load fluctuations and shifts or expand the energy supply, based on the size of the TES device. The economic benefit of CSP with TES is that it provides energy at times of strongest need with typically the maximum electricity costs [9].

The PV system is another way to produce electric power because they absorb sunlight and transforms part of it into electricity. There are no practical parts in motion that wear out, no fluids or gases (except in hybrid systems) can escape, there is no need for fuel to function, it has a rapid response, it can immediately attain full output, and it is able to operate at moderate temperatures [12]. The growth of Rwanda's solar energy infrastructure may boost energy security levels because it is an independent energy supply for imports.

The purpose of this research is twofold as follows: (a) to summarize the present status of CSP and PV systems in the Rwanda power sector, to see how the implementation of some new energy technologies can be the best strategies for rural electrification, and (b) to examine a technoeconomic analysis for CSP and PV systems using the system advisor model based on the data from the selected area and downloaded from NSRDB and SWOT analysis based on data collected from the top power producers in Rwanda. Also, the best option based on the past successful regional projects will be recommended after a comprehensive analysis.

2. Concept of CSP Technologies

CSP is an in-depth business methodology for electricity generation exploitation alternative from solar energy. CSP is suitable for areas with a lot of solar radiation and a lot of daylight hours. In CSP technologies, incoming sunlight is focused on a small target area through mirrors or lenses, resulting in medium- or high-temperature heat, depending on the technology [13, 14].

A CSP plant typically consists of a solar field, TES system, and power block as mentioned in Figure 1. The solar field is referred to as thermal energy production, and solar multiple (SM) determines the size of a solar field [15]. The solar field

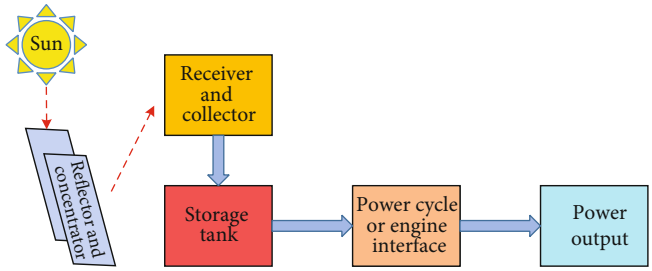

Figure 1: Concept of the CSP technology.

focuses solar radiation into a specific point (point focus) or line (line focus) where the heat transfer fluid is located in order to heat it. This HTF that has been heated can be used either directly or indirectly [16]. Directly, water is employed as HTF for direct steam generations; whereas within the indirect case, totally different HTFs like artificial oil, liquid salt, and Therminol VP-1 are accustomed to heat water for a steam generation [16]. While direct HTF is less expensive, commercial steam storage is insufficient. Indirect HTFs, on the other side, are more costly but can be stored. As a result, indirect HTFs are commonly used in CSP plants around the world [17].

The solar-heated HTF passes into the TES system, which stores extra energy for unceasing activity. As a result, the HTF is used to generate steam throughout the steam generator, which then drives the power unit to generate electricity. There are different kinds of CSP technologies depending on the structure and the way radiation is focused, with the same purpose of generating electricity but resulting in different temperature levels. According to the concentration technique, CSP is classified into 4 main types as listed [18, 19]. CSP static receivers stay put, unaffected by the focusing system, while mobile receivers follow it around. Furthermore, line focusing receivers focus solar radiation onto a single spot of line, while point focusing receivers project solar radiation onto a specific point of a receiver.

There are various CSP technologies as shown in Figure 2, but their operating system is the same. The structure and the focus of each of these systems are different, so they result in different temperature ranges that are generated [19].

2.1. Parabolic Trough Systems. The parabolic trough (PT) CSP is a very well-tested and mature solar power plant designed for CSP [16, 17, 20] as shown in Figure 3. This is why in comparison to other CSP configurations, PT plants are more commonly commercialized [17]. A series of parabolically curved mirrors/collectors and receivers make up the PT system. Solar radiation is focused on the receivers, which are loaded with HTF, by the collectors. Thermal storage is used to direct heat HTF to the power unit for power generation. Material demand and land use considerations are reduced due to a single-axis tracking system that follows solar radiation. This is why the PT plant's initial cost is less than that of double-tracking systems [17]. In most CSP plants, the power block uses a steam turbine to generate electricity, which consists of a boiler/steam generator. As a result,

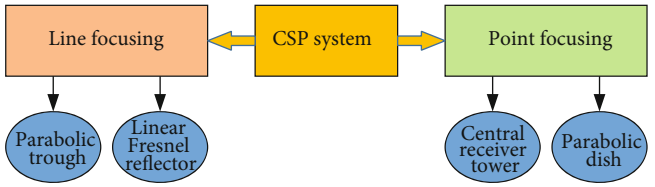

Figure 2: Flow diagram shows different CSP systems.

CSP plants can be easily integrated with traditional power plants [17].

2.2. Linear Fresnel Reflector Systems. The linear focusing CSP concentrates solar radiation on a linear absorber tube to keep the reflectors focused on a single axis fixed on the top (see Figure 4). The HTF inside the linear absorber tube can be oil or steam, which transfers the absorbed heat onto a steam turbine for the power cycle. The arrangements allow reflective glass strips to concentrate on an elevated linear receiver rotating around an independent parallel axis, which then in fact transfers the heat to the HTF. Unlike PT systems, linear fresnel reflector (LFR) systems detach the receiver from the reflectors, eliminating needed resources and the need for high-pressure rotating components. The cost of the LFR system is reduced due to the simplicity of the mirror's usage and small land usage [16].

2.3. Solar Tower System (STS). Solar tower technology concentrates solar radiation on a receiver at the upper point of the tower that generates higher temperatures. As noted in Figure 5, the mirrors in a solar power tower receive sunlight with the use of two axes for tracking the sun. Different heliostats of the solar tower are responsible for concentrating solar radiation on the receiver, which in turn are used to transfer the heat from absorbed radiation to the HTF, and later, HTF transfers the energy to the start power cycle fluid [22]. STS has a concentration ratio of 300–1000, resulting in higher working temperatures [16, 23]. This is why, as compared to other CSP configurations, the STS plant has a greater efficiency (20%–35%) [16, 23]. The initial/capital cost of the STS plants is high due to dual tracking and relatively large land needs. It is worth noting that STS systems continued to dominate the CSP market after PT systems were phased out [24].

2.4. Parabolic Dish Concentrator. Parabolic dish concentrators with a point focus device are composed of two main

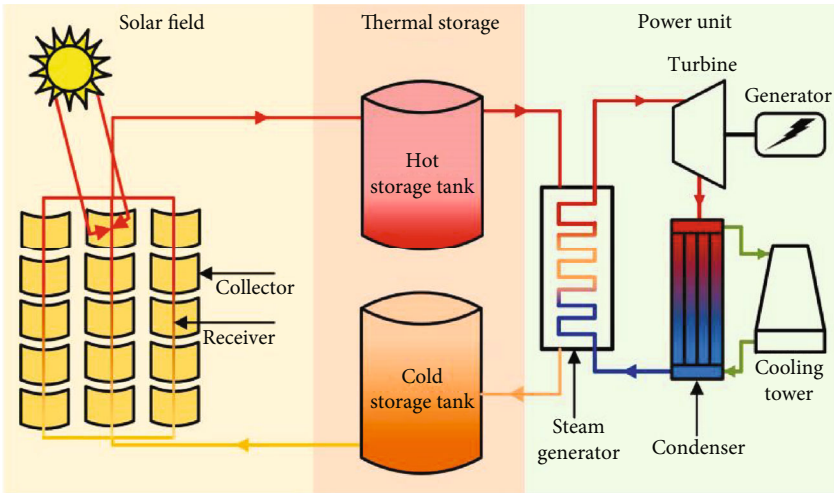

Figure 3: Schematic of the parabolic trough [21].

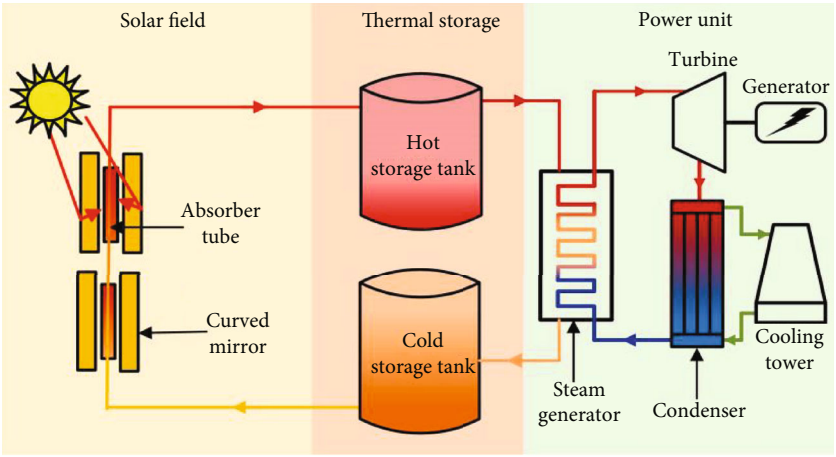

Figure 4: Illustration of a linear Fresnel reflector (LFR) system [21].

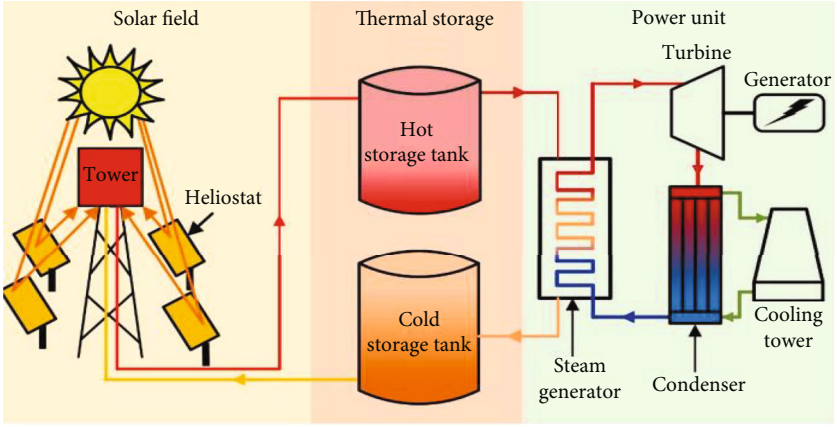

Figure 5: Schematic diagram of the solar tower system [21].

parts (in Figure 6), namely, parabolic reflectors and solar thermal receivers, which are located at the focal point [25].

The Stirling engine technology also uses a parabolic dish concentrator to generate electricity. In the shape of a sheet of reflective material, the parabolic mirrors are constructed into a parabolic shape that concentrates incoming sunlight on a central receptor tube at the focal line of the collector. Parabolic dish technology can reduce the load on centralized

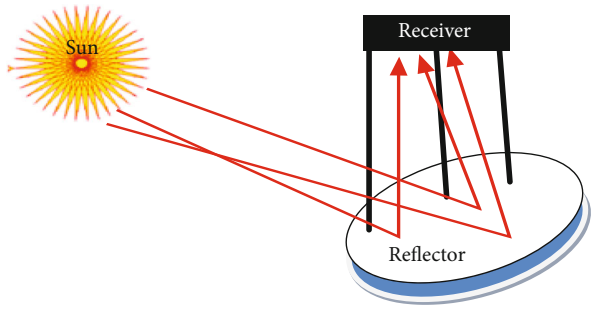

Figure 6: A diagram of the parabolic dish concentrator.

power plants [26]. The dish Stirling engine of the parabolic dish concentrator has comparatively good efficiency at approximately 30% and consists of an advanced Stirling converter, which is a linear alternator that directly generates electricity from the countering motion [27].

Stirling engines that are popular and do not require big water cooling systems like steam engines because as it is heated and cooled; they are powered by hydrogen gas expansion-contraction [28].

Direct normal irradiation (DNI) is the sum of solar radiation that is perpendicular (normal) to the unit area received from the incoming sun rays, depending on the time of the day. DNI should be at least 2000 kWh/m^2 per year to sustain a feasible energy production plant [29]. To estimate the expected energy production from future projects, the accuracy of the DNI data is very critical. Depending on each country's location as illustrated in Table 1, DNI values are different for various countries.

3. Concept of Photovoltaic Cell Based on Power Generation

A solar cell, also known as a photovoltaic cell (PV), is a device that uses the photoelectric effect to transform light into an electric current without interfering with any heat engine. When presented to light, a solar cell which is a solid-state device made up of thin layers of semiconductor materials generates an electric current.

The following modules are the commonly examined in the study: (1) crystalline silicon (c-Si), (2) laser grooved buried contact (LGBC) c-Si, (3) polycrystalline silicon (p-Si), (4) triple-junction amorphous silicon (3j a-Si), (5) copper indium diselenide (CIS), and (6) cadmium telluride [34]. The PV industry, on the other hand, has been able to dramatically reduce production costs and sale prices [35] by mass producing a large number of identical cells and modules in order to achieve a maximum economy scale. The PV industry as a whole has shown that this is possible, thanks in part to business incentives in Germany and other countries for their large contribution. Based on the end-user, there are two categories of solar PV systems: (a) grid-connected systems produce direct current (DC) power and are connected to the grid, which are first to convert DC into the compatible grid alternating current (AC) power and (b) autonomous systems (off-grid systems or stand-alone systems) produce electricity and operate on an independent basis and are usually installed at isolated sites in remote areas where the power grid is far away [36]. Figure 7 demonstrates various components for solar power production.

The PV cell technology is categorized into two main types and another special one (see Figure 8); they are all made of light-sensitive semiconductor materials that dislodge electrons using photons to transfer electrical current.

4. Potential of Solar Energy in Rwanda

Rwanda is a small Sub-Saharan African country situated just under two degrees below the equator in East Africa with a 12,089,721 (March 2018) [38] population on the land surface of 26,338 km^2. 94.7% of the overall surface is land and the remaining 5.3% is water occupied [39].

Geographically, it is enclosed with latitudes of 1.050 and 2.840°S and longitudes 28.860 and 30.900°E [40]. Rwanda usually experiences two annual rainy seasons a year, supplying water to the country's various river systems. The US National Air and Space Agency (NASA) and the University of Rwanda have measured solar radiation and solar resources in Rwanda. The report found that the Eastern Province of Rwanda has the strongest potential to generate electricity from solar resources.

In cooperation with the MININFRA Department of Meteorology, the approximate mean monthly solar irradiance ranges from 4.3 to 5.2 kWh per square meter per day across all regions of Rwanda though remains mostly unexploited [41, 42]. The data collected showed that the minimum value of global solar radiation for the Kigali station (R_G = 4942 Wh/m^2/day, R_G = 4960 Wh/m^2/day) arises in May, while the maximum value (R_G = 5721/m^2/day, R_G = 5738 Wh/m^2/day) occurs in May, based on research carried out in the global solar radiation estimation in Rwanda [42]. In recent decades, Rwanda has achieved rapid economic growth and is gifted with ample energy resources like hydro, solar, peat, gas, and biomass, but not fully exploited. Figure 9 shows that it presently has only around 226.7 MW of electricity installed used to supply the entire country [43].

Therefore, petroleum-based fuels, hydro, solar, methane gas, peat, geothermal, biomass, waste, and wind [44] are considered to contribute to electricity generation in Rwanda. Although Rwanda is in the proper direction to increasing access to electricity, reports indicate that the cost of supplying electricity is among the uppermost in the region and continues to restrict the economic and industrial growth of the country [45]. It is by 2024 that the National Transformation Plan intends to provide universal access to affordable electricity [10].

As shown in Figure 10, the basic energy resource utilization in Rwanda indicates that biomass covers 85% of the main energy consumed, where wood comprises 57%, charcoal 23%, crop residues, and peat 5% [46]. Nonbiomass sources contribute 15%, where petroleum products have 11% and electricity contribute approximately 4%.

4.1. Current Status of CSP and PV Technologies in Rwanda. Renewable energy is naturally available with no limited supply; this means that it can be used endlessly. However, only

Table 1: Threshold values of DNI in some countries.

Researchers	The threshold value of annual DNI (kWh/m^2/year)	References
Dawson and Schlyter, Australia, 2012	1,800	[30]
Breyer and Knies, Germany, 2009	2,000	[31]
South Africa, 2009	2,100	[32]
Purohit and Purohit, 2010	1,800	[33]
Qatar 2013	2,200	[32]
Australia 2013	2,564	[32]

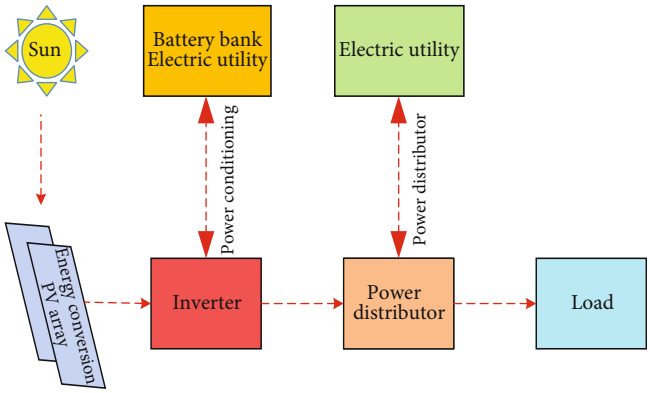

Figure 7: PV systems convert solar energy into electrical power with various components.

three renewable energy sources (biomass, geothermal, and solar) can be used to generate ample heat energy in Rwanda to generate electricity. Since geothermal sources are restricted to a few areas, solar energy has the greatest global potential and the supply of biomass does not exist everywhere in nature [18]. In parallel with the Global Solar Atlas, solar resource maps were published for Rwanda by the World Bank Group, funded by ESMAP, and prepared by Solargis in 2017 [48]. With a possible 4.5 kWh per m^2 per day and approximately 5 peak hours of sunlight, solar energy in Rwanda has enormous potential. Rwanda's total on-grid installed solar energy is 12.08 MW but CSP here remains untouched [49]. Figure 11 shows the global horizontal irradiation for Rwanda, which indicates that the country can benefit from solar energy in different locations and weather conditions, in particular the eastern province which is known for its high irradiance values [50].

PV and CSP penetration levels in the country are not very high, and it is known that solar panels contribute a lot to the mitigation of climate change since they promote a green economy. Rwanda's energy mix shows that solar energy has not reached a high level of production compared to the potential of solar radiation, where thermal is 27%, methane 14%, peat 7%, solar 6%, import 3%, and hydro 57% [52]. Solar PV is not sufficiently popular in Rwanda, although it is heavily connected to transnational actors like outside donors, nongovernmental organizations (NGOs), and other private sector operatives, which have helped in developing and executing Rwanda's response to its rising energy requirements.

The total on-grid installed solar energy in Rwanda is 12,230 MW from 5 solar power plants, i.e., Jali power plant 0.25 MW, Rwamagana Gigawatt 8.5 MW, Nasho Solar 3.3 MW, Nyamata solar 0.03 MW, and Ndera solar 0.15 MW (see Table 2) [53, 54].

A major restriction to the implementation of such systems is the high initial cost of PV systems. Luckily, the government of Rwanda is committed to supporting renewable energy options, such as imported solar equipment is exempted from all taxes [46]. Also, people are encouraged to use energy-efficient equipment. This can be seen in the continuous substitution of incandescent bulbs with compact fluorescent lamps (CFLs), which save electricity [55]. Energy-efficient appliances enable individuals to reduce their monthly electricity bills, in terms of making cost-effective solar systems. Besides, the use of energy-saving equipment enables the utility to reach more clients, one of the goals of the Economic Development and Poverty Reduction Strategy (EDPRS) [56].

The Rwandan government is targeting to raise solar power plants. To minimize the cost of electricity access, individuals are encouraged to use stand-alone solar PVs. Taking advantage of available renewable sources in Rwanda and lessening the production cost are the cornerstone as the government is targeting 100% electricity access by 2024 [10].

The purpose of the government of Rwanda (GoR) is to increase the number of solar power plants. Figure 12 below shows a 17-hectare solar field located near the Agahozo Shalom Youth Village in Rwamagana with 28,000 panels, which was built by private power companies. It is the first large-scale commercial solar field in East Africa, producing 8.5 megawatts of energy at its height, and generates 4% of the country's total power capacity [57]. This has provided power to more than 15,000 homes and is the largest solar plant in Africa. This ensures Rwanda's commitment to solar energy. Regardless of the amount of solar power capacity available, Rwanda still has many people without access to electricity [49].

In Rwanda, the daily solar insolation varies between 4 kWh/m^2/day and 5 kWh/m^2/day from the Photovoltaic Geographical Information System [47]. The highest solar radiation for the selected site is seen in July where the value is 5.87 kWh/m^2/day. The yearly average solar radiation was 5.415 kWh/m^2/day and the corresponding average clearness index was 0.541 as shown below. Clearness is characterized as a measure of the fraction of solar radiation transmitted to the earth's surface through the atmosphere [58].

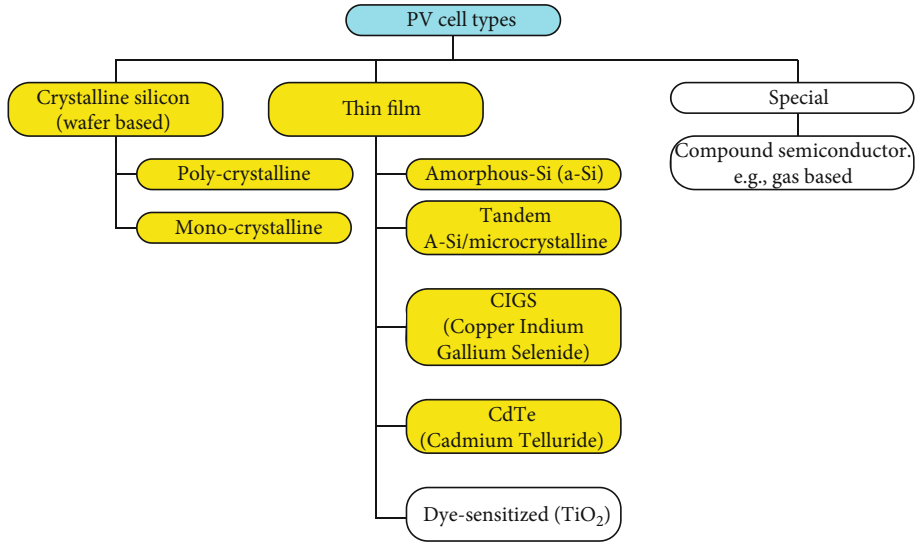

Figure 8: Common PV module technology [37].

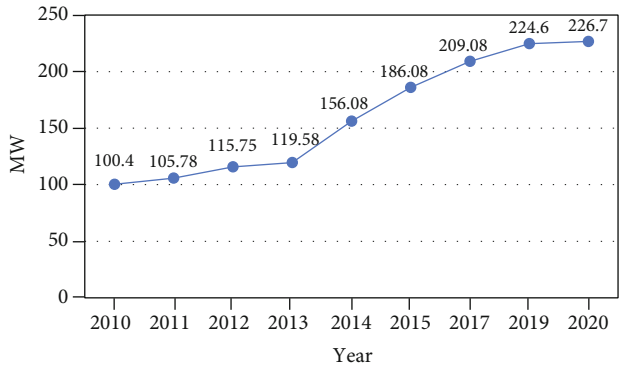

Figure 9: Assessment of installed generation capacity in MW on the national grid [43].

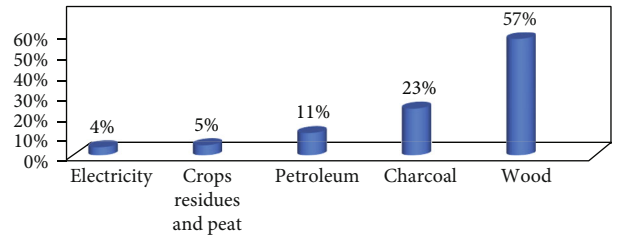

Figure 10: Main energy sources in Rwanda 2016 [47].

4.1.1. Impact of Hydropower on the Environment. Rwanda is gifted with two seasons: (a) dry season and (b) wet season. During the wet season, the rain provides water to numerous rivers that can be utilized for electricity generation. The growth of hydroelectric power resources is critical from a macroperspective in order to replace fossil fuels, diminish environmental pollution, and improve the energy structure for sustainable economic growth [59]. However, since the hydropower project is so massive and widespread, it will unavoidably damage the regional environment. The hydropower station building is destined to take up a large amount of land and kill vegetation, resulting in the depletion of agricultural land, water, and soil resources. Big reservoirs, extensive building, and a wide range of equipment, loads, and machinery [60] in use during construction and operation require big land and large investment as well.

The amount of land needed to generate hydroelectric power varies greatly depending on the location. Water reservoirs in a flat terrain are likely to be long and wide, while dams in mountains are likely to be higher and shorter, requiring less ground. Furthermore, reservoir-type hydroelectric power plants necessitate a large amount of land for the water reservoir. Table 3 gives an example of estimation of land utilization from Pacca and Horvath's data [61] during the construction of the Glen Canyon Hydroelectric Plant. After land transformation factors, the result demonstrates an occupation area of 13.6 m^2/GWh [61, 62].

Energy improvement can affect land use from various perspectives, going from peak evacuations and surface mining to the resteering of waterways and flooding for hydroelectric dams [60].

Despite the occurrence of two rainy seasons, as shown below, Figure 13 indicates how suitable solar PV and CSP can be applied in Rwanda on the latitude of −3° and longitude of 29° for a ten-year average.

As the temperature increases, the PV system's output voltage decreases, while the output current is directly proportional to solar radiation [64].

In Rwanda, the average solar insolation is around 5.15 kWh/m^2/day [66]. Although this value is a good indication for PV system deployment in Rwanda, it is important to know the average PV generation given by the insolation for different locations in Rwanda as shown in Figure 13.

In summary, the PV technology for off-grid Rwandan rural electrification has been tremendously grown. There are not only the PV solar power plants that are previously mentioned in Table 4, but there are also PV solar home systems that help 11% of Rwandan households to access electricity through solar off-grid solutions [67].

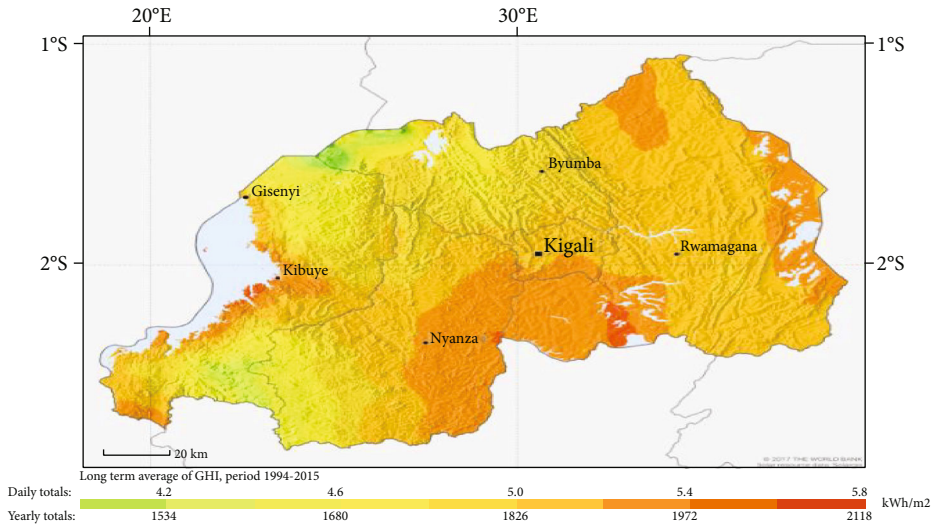

Figure 11: Global horizontal irradiation for Rwanda [49, 51].

Table 2: Solar energy existing projects in Rwanda.

Plant name	Power plant capacity	Established time	Connection
Mont Jali solar power plant	0.25 MW	2007	Grid connected
Rwamagana solar power plant	8.5 MW	2014	Grid connected
Nasho solar power plant	3.3 MW	2015	Off grid
Nyamata solar power plant	0.03 MW	2016	Off grid
Ndera solar power plant	0.15 MW	2016	Off grid

Figure 12: The Rwamagana solar power station [53].

On the other hand, during the first drafting of this paper, there is no evidence or data from government energy agencies or private power producers that show that CSP technology has been deployed in Rwanda yet. However, as a country with sufficient solar radiation intensity, CSP can also be implemented. Until recently, researchers have widely considered PV technology for millions of people who still lack electricity. Table 4 summarizes the recent publications on solar energy in Rwanda in the last ten years.

4.1.2. Rwanda's Off-Grid Situation. Until December 2020, 59.7% of Rwandan households are wired, with 43.8 percent being connected to the national grid and 15.9% using off-grid systems (mainly solar) [68]. Rwanda's government (GoR) is collaborating more closely with businesses that operate off grid and wants to electrify the whole nation by 2024 [10, 69]. Rwanda currently has five small stand-alone minigrid plants in service, three of which use solar power as a source of energy, and the other two use water as a generation source [70]. However, attempting to hit last-mile households, difficult landscape, rural households' remoteness, low demand, and minimal availability will require higher capital investment to extending the grid engendering slow electrification. Solar minigrid and solar off-grid systems offer investment opportunities in the country [71], though the sector's growth is hampered by high initial costs and restrictions on high load use. Despite the fact that minigrids and stand-alone systems are playing an important role in increasing the rate of electrification, the rate is not quite as fast as it could be because their prices are prohibitively high, particularly for low-income households scattered, which predominate in rural communities [72].

Rwanda's modern and green energy supply is typically subpar. The off-grid focus is to electrify more from locally accessible photovoltaic panels, lowering upfront costs as well as overall device costs, allowing low-income families to access power, and promoting local tenure [72]. Minigrids, in general, have made it easier for rural areas to evolve socio-economically. Furthermore, electricity will provide opportunities for rural residents to start new businesses as well as grow and prosper in existing ones [73].

Generally, many of the world's smallest developed economies are found in Sub-Saharan Africa where Rwanda is among them. Furthermore, many people in this area do not have elementary electricity access. In a wider context, an increase in per capita energy intake is likely to be related to the social and economic growth of Sub-Saharan Africa [74].

In Table 5, the report in 2018, regarding Sub-Saharan countries where Rwanda takes part, shows the trajectory of Rwanda in terms of renewable energy accessibility. It

Table 3: Direct land transformation of the hydroelectric power plant [61, 63, 64].

Location/type	Capacity (MW)	Area (10^4 m^2)	Lifetime electricity generation (GWh)	Lifetime (years)	Land transformation (m^2/GWh)	Reference
Colorado, Lake Powel Reservoir	1296	65,313	277,500	50	2,350	[61]
U.S., generic reservoir	114	75,000	30,000	30	25,000	[63]
Canada, reservoir	N/A	N/A	N/A	30	3,700	[65]
Canada, run-of-river	N/A	N/A	N/A	30	3	[65]

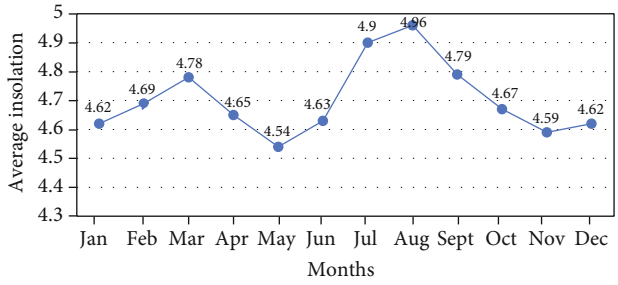

Figure 13: Rwanda monthly average solar insolation incident on a horizontal surface (kWh/m^2/day). The data was collected from the National Administration of Aeronautics and Space (NASA), 2017.

suggests that 30.8% of the Sub-Saharan countries in the rural area have less than 20.6% of electricity access. Just nine countries had accessibility to over 60% of their rural populations, whereas access to electricity in rural areas ranged from 20% to 60% in the rest of the countries [75].

Table 6 demonstrates the final share of renewable energy in Rwanda compared to the rest where there is progress but is lower with respect to others [76].

5. SWOT Analysis of the Concentrated Solar Power and Photovoltaic Systems in Rwanda

5.1. Introduction to SWOT Analysis. Analysis of strengths, weaknesses, opportunities, and threats (SWOT) is an apparatus used to gauge the "strengths," "weaknesses," "opportunities," and "threats" from accepted levels in an organization, a plan, a project, a person, or a business activity for the benefit of assisting planners to classify and prioritize the business goals and identify the procedures for accomplishing them [116].

SWOT analysis is introduced to help decision makers share and compare notes, arrive at clearer common goals, and understand factors for success or failure in business. It involves as demonstrated in Figure 14 internal and external environmental scanning for positive tangible and intangible assets, internal or external to the organization like constraints, financial resources, products, services, and decisions and activities to create and nurture competitive advantages. SWOT analysis is also helpful energy [117].

SWOT analysis was seen as a good tool for energy planning wherein we made a detailed study of the characteristic of energy in Rwanda. This study is aimed at mentioning through a literature review the existence of solar power in Rwanda, its potential, availability, and associated barriers. We focused on the availability and barriers to the fulfillment of solar energy production that affects the private sector or government to invest more. Besides, SWOT analysis was performed based on a comprehensive literature review and stakeholder interviews.

5.2. Data Collection and Analysis. This paper uses a literature review to gather data from government energy agencies, power producers, and minigrid off-grid private companies in Rwanda and a SWOT approach to investigate the internal and external factors for PV and CSP development in Rwanda. In brief, all the secondary data used in this research analysis were collected through documents of projects and existing literature, and finally, we conducted the face-to-face interview which was done using a designed questionnaire to assess each factor from literature and other documents in detail. However, during the interviews, we obtained very many different factors and divergent views. Therefore, only those factors relevant and important to our research were included in the final SWOT analysis.

This study suggests that it is a critical time for Rwanda together with Sub-Saharan African countries to consider exploring their locally available and abundant solar resources. Africa requires more effort to meet Se4all's target of universal access to sustainable energy. Climate change is also an existential challenge to the world's poorest and most vulnerable on this occasion. That is why Africa needs an urgent and unprecedented effort to enjoy universal access to electricity. In Rwanda, especially for the World Bank cooperation, Rwanda can strive to seize the development opportunities brought by the World Bank through credit agreement of electricity access for all. Although the GoR is working to increase incentives for private sector participation in solar energy projects, consistent policies and the support from government are required to facilitate the sustainable and long-term developments of different solar technology deployments in Rwanda, especially in remote areas.

5.3. SWOT Analysis Results of CSP and PV Systems in Rwanda. The research process led to the identification of internal and external factors for SWOT analysis. This study was conducted for CSP and PV system deployment in Rwanda by applying SWOT analysis. Table 7 summarizes the SWOT analysis of solar technologies in Rwanda.

5.3.1. Strengths

(1) Increase Experience in Solar Technologies through Off-Grid Projects. Solar is already among Rwanda's fastest-

Table 4: Recent publications on solar energy in Rwanda in the last five years.

S. no.	Years	Authors & references	Technology application	Case studies	A summary description of the main objective of the study
1.	2016	Abrams [77]	Solar energy investment	Rwanda	From the perspective of a licensed professional, this research examined the creation of East Africa's first utility-scale solar sector. The study used a plant in Rwanda as a case study to examine the elements needed for the effective implementation of financially successful utility-scale solar energy projects with the potential to help Africa bridge its severe power supply deficit.
2.	2021	Kizilcec and Parikh [78]	Pay-as-you-go solar home system	Rwanda (Bugesera and Kayonza districts)	This study examined the journey of a Pay-as-you-go solar home system customer using the case of Rwanda. This study clearly revealed that the journey of the customer is nonlinear and cyclical, recognizing that a household operates in a social network within which others may affect or be influenced. Moreover, it highlighted the increasing importance of solar home system recommendations in raising awareness of solar home systems, pointing to the shifts in the environment of the off-grid energy market where customer awareness no longer appears to be a key barrier to adoption.
3.	2021	Alonso-Montesinos et al. [79]	Solar-diesel hybrid minigrids	Rwanda (Nyabiheke camp)	The environmental and economic benefits of the fully renewable and diesel-hybrid minigrid were studied in this study. This research showed how environmental goals, operational timeframes, financial resources, and will influence the most appropriate system designed for humanitarian actors on a case-by-case basis.
4.	2021	Asemota [80]	Off-grid solar	Rwanda	A preview of off-grid solar performance targets in Rwanda.
5.	2020	Bisaga et al. [81]	Off-grid solar energy	Rwanda	This paper is aimed at mapping the synergies and trade-offs between energy and sustainable development goals by using the case of Rwanda.
6.	2020	Grimm et al. [82]	Off-grid solar energy	Rwanda	The study showed a willingness to pay for various solar technologies in rural Rwanda.
7.	2020	Brunet et al. [83]	Photovoltaic solar power plant	Rwanda	A large-scale solar PV solar power plant through a multilevel and multiscalar perspective in Rwanda was assessed.
8.	2020	Nsengimana et al. [84]	Photovoltaic microgrid	Rwanda (Kigali)	A comparative study of the on-grid PV microgrid system and the off-grid PV microgrid system was designed and compared in this study.
9.	2020	Grimm et al. [85]	Off-grid solar electricity	Rwanda	The study was focused on the ability of households to pay significant sections of their electricity budget for various off-grid solar technologies in rural areas.
10.	2019	Bamundekere [86]	Solar energy in Rwanda	Rwanda	The study is aimed at disclosing the contributions of renewable energy to sustainable development.
11.	2019	Niyonteze et al. [87]	Solar-powered minigrids	Rwanda	The strategy and semiprivate operator model for solar-powered minigrids and smart metering systems have been suggested to provide a sustainable solution to the energy crisis and power to various energy users in Rwanda.
12.	2019	Kennedy et al. [88]	Off-grid solar energy	Rwanda and Kenya	A comparison of the nonparametric customer segmentation clustering approach with linear customer behavior models, classifying customers and exploring customer behavior-related demographic and recruitment variables.
13.	2019	Bisaga [71]	Off-grid solar energy access	Rwanda	The study is aimed at resolving a knowledge gap concerning the actions, needs, and expectations of energy usage, focusing on users of the solar home system.

Table 4: Continued.

S. no.	Years	Authors & references	Technology application	Case studies	A summary description of the main objective of the study
14.	2019	Bimenyimana et al. [51]		Rwanda	HOMER software has been used to model optimal, sustainable, effective, and accessible solar photovoltaic technologies as energy solutions for all (off-grid and on-grid users) to provide all people with affordable and reliable access to electricity.
15.	2019	Gloria et al. [89]	Solar energy	Rwanda (Agahozo Shalom)	A researcher reviews solar energy for sustainable urban development in rural areas.
16.	2019	Felix et al. [90]	Potential of solar and wind energies	Rwanda	In their report, an evaluation of the capacity of wind and solar energies in the eastern region of Rwanda was carried out. The potential for wind energy and the potential for solar energy were calculated and compared. The analysis indicated that wind energy potential is greater than solar energy potential in the area considered.
17.	2019	Mushimiyimana [91]	Solar energy	Rwanda (Kamonyi)	The research is concentrating and looking on a design of a photovoltaic of 0.8 kWh/day for a single household. The aimed target of the design was to increase the number of households connected to an off-grid photovoltaic system in Kamonyi District.
18.	2019	Soltowski et al. [92]	Off-grid systems	Rwanda	The main focuses were on the role of smart energy management (SEM) platform in the interconnection of off-grid systems and making bottom-up electrification scalable and how it can improve the overall sustainability, efficiency, and flexibility of off-grid technology.
19.	2019	Muvunyi [93]	Viability of micro-hydro-solar PV	Rwanda (Mwogo)	The study was based on the feasibility of a microhydro/PV pump hybrid electric supply system to one pilot village in Rwanda using PVSYST software as an optimization and sensitivity analysis tool. They came up saying that the integration of a solar PV pump and microhydro proved to be a viable operational system.
19.	2019	Munyaneza et al. [94]	Solar photovoltaic minigrid	Rwanda (Rwumba)	Solar photovoltaic minigrid that can provide the required power for the village was designed and optimized using HOMER software. The results that indicated the best results corresponding to the optimum PV minigrid were obtained at a capacity shortage of 3%.
20.	2018	Rodríguez-Manotas et al. [95]	Utility-scale solar PV	Rwanda	The multi-level perspective (MLP) has been used to model the study and interaction of the different sociotechnical levels to fully understand the conditions that allow this transformation. The study revealed the critical importance of bureaucratic and regulatory support for investment in low-carbon energy technology in a neoliberalization process-influenced political economy, thus creating substantial space for negotiating private contracts.
21.	2018	Bimenyimana et al. [96]	Stand-alone and grid-tied solar PV systems	Rwanda (Rwamagana)	Site visits and energy conservation estimates for a standard residential house were used to compare stand-alone and grid-linked PV systems capable of supplying 7.2 kWh/day, loading efficiently. The result was an increase in the production of electricity by domestic energy producers in Rwanda, due to lower initial investment costs and reduced payback periods.
22.	2018	Williams et al. [97]	Microgrid utilities for rural electrification	Rwanda	The outcome is the implementation of the Stochastic Techno-Economic Microgrid Model (STEMM), which allows it possible to determine, from an investment perspective, the influence of technological design decisions as well as the financial conditions on the financial feasibility of microgrid projects.

Table 4: Continued.

S. no.	Years	Authors & references	Technology application	Case studies	A summary description of the main objective of the study
23.	2018	Rutibabara [98]	Solar PV, diesel, and hybrid PV-diesel water pumping systems	Rwanda (Bugesera)	The project was conducted to examine the cost of solar PV, diesel, and hybrid PV-diesel water pumping systems for agricultural irrigation in Rwanda, both environmentally and economically. To determine both the environmental and economic feasibility of the proposed pumping systems, the HOMER optimization program was used to take account of the fluctuations in both solar radiation and fuel prices.
24.	2018	Nshimiyimana [99]	Solar PV on a grid system	Rwanda (Masaka)	The research discussed in this study explores the feasibility of using a grid-connected solar PV system in the village to supply electricity. To assess whether the investment will be financially worthwhile, a cost-benefit analysis was conducted. The findings show that solar energy is feasible at a moderate cost in this selected village.
25.	2018	Lameck [100]	PV-biogas hybrid system	Rwanda (Gakenke)	The analysis proposes a hybrid system consisting of PV and biogas with battery storage from renewable energy sources. The hybrid system is modeled and optimized utilizing HOMER software for technological and economic feasibility.
26.	2018	Emmanuel [101]	Solar-wind hybrid system	Rwanda (Kayonza)	During this work, they presented the development of an effective approach of design, simulation, and analysis of a wind-solar hybrid system for a typical rural village in one of the villages of our country. The optimal dispatch strategy of the diesel generator is load following and the total net present cost of each system configuration has been calculated for 20 years of the lifetime of the system to examine the lowest energy cost option.
27.	2017	Uwibambe [102]	Design of photovoltaic	Rwanda	The key focus of the project was on the design of off-grid photovoltaic systems, which included an economic assessment of the usage of a 200 W person solar home system and a 10 kW village PV system.
28.	2017	Ituze [103]	Hybrid solar photovoltaic-bioenergy system	Rwanda (Gicumbi)	The project evaluated the hybrid solar photovoltaic-bioenergy system for powering remote dwellings in the country.
29.	2017	Cyulinyana and Winkler [104]	Surface solar spectrum characteristics	Rwanda	The study represented a model adopted for tropical regions that shows the reliance on atmospheric constituents of surface solar radiation reaching ground level.
30.	2017	Rwema [105]	Energy policy implementation	Rwanda	The research describes hydro, solar, and wind: the effect of energy policy on the deployment of renewable energy in Rwanda.
31.	2017	Ma and Ma [106]	Off-grid photovoltaic system	Rwanda	There was a simple implementation of the development and design of a portable off-grid photovoltaic device with contingency functions for rural areas.
32.	2017	Bisaga et al. [107]	Scalable off-grid energy services	Rwanda and Kenya	This research project is aimed at demonstrating how BBOXX, a solar home system company operating in South-Western Kenya and across Rwanda, can also use Internet of Things (IoT) technology to solve development problems.
33.	2017	Kuppa and Zimmerle [108]	Sizing off-grid electrical systems	Rwanda	Estimation of statistical failure method to scale off-grid electrical systems for developing world villages.
34.	2017	Bimenyimana et al. [109]	Photovoltaic power system	Rwanda	The research centered on the comparison of maximum power point output monitoring between incremental performance with disruption and observation of architectures in photovoltaic power generation.

Table 4: Continued.

S. no.	Years	Authors & references	Technology application	Case studies	A summary description of the main objective of the study
35.	2016	Collings and Munyehirwe [110]	Pay-as-you-go solar PV	Rwanda	The study claimed that different delivery problems were faced during the implementation of the project and valuable lessons were learned. The effect of considerably more hours of light and the opportunity to charge telephones at home on households using Azuri systems.
36.	2016	Grimm al. [111]	Solar kits	Rwanda	The research paper examined the adoption and impact of a fundamental pico-photovoltaic kit that barely meets the modern energy standard of the United Nations.
37.	2016	Collings and Munyehirwe [110]	Pay-as-you-go solar PV	Rwanda	The research found that small solar lantern adoption substantially decreased household spending on dry cell batteries and kerosene and improved air quality in the home.
38.	2016	Beyer and Habyarimana [112]	Increased application of solar energy	Rwanda	Detailed information from a dedicated network of ground stations on irradiance characteristics in Central Africa (Rwanda) for the characterization of irradiance field statistics and validation of satellite data derived from satellite data.
39.	2016	Nshimiyimana [113]	Hybrid solar PV-wind-fuel cell	Rwanda (Mukondo)	The work focused on sizing of a hybrid solar PV-wind-fuel cell power system for an isolated location.
40.	2016	Karugarama [114]	Microgrid	Rwanda (Kigali)	The analysis was carried out in Kigali on blackout prevention using a microgrid with advanced energy storage and solar photovoltaics.
41.	2015	Crossland et al. [115]	Off-grid photovoltaic system	Rwanda	The sociotechnical approach to increasing the battery life of off-grid photovoltaic systems used in a case study in Rwanda was the key focus.

growing renewable energy technologies. Accordingly, experts suggest that 100% electricity access for the country can be envisaged to come from off-grid technologies by using Rwanda's energy resources like hydro, solar, and methane gas. Presently, the off-grid electricity access rate is 15% of Rwandan households according to the Rwanda Energy Group (REG) [119]. Communities far from the proposed national grid coverage have been advised to use cheaper connections as an option like minigrids and PVs to access the electricity they can afford. Rwanda solar irradiance ranges from 4.3 to 5.2 kWh per square meter per day across all regions [42]. The country experiences a tropical climate, but there is a piercing difference between the northern and eastern sectors in climate conditions. This location places Rwanda in a proper location to establish a large-scale PV and CSP strategy.

(2) Very High Interest among Investors. Rwanda is considered to be one of the most politically stable countries in Sub-Saharan Africa, providing investors with a peaceful and predictable working environment. Rwanda, like the whole world, has the ambition of electricity for all. After the national demarcation electrification plan (NEP), there is an increase of registered solar companies, to make PV energy contributions more visible in the energy mix [120]. The solar market is rather very small, and it is mainly limited to the project market driven by donor funding. The main issue is the budget that is needed but talks are being held with all stakeholders, Ministry of Infrastructure (MININFRA), Ministry of Finance and Economic Planning (MINECOFIN), and others to see how the exploitation of different energy resources can help to ensure energy for all. The government aims to promote the green economic growth of the country by opening the gates to investors in the country's numerous renewable energy projects. The monitoring of project implementation has to be followed under REG, stakeholder coordination, research, and knowledge management as a key to achieving this goal. The government has also begun a risk reduction facility that decreases the risk of supplying solar products to the private sector and lowers the price charged by the consumer to an acceptable level.

(3) Areas with Higher Solar Potential Near to an Existing National Grid. PV and CSP have tremendous potential to contribute to a large degree and to fill the energy deficit in Rwanda. The NEP report demarcates the areas where solar energies should be applied. Geographically, Rwanda is on a horizontal surface near the equator, with plentiful sunlight and global solar radiation, which lies between 4.8 kWh/m^2 day and 5.5 kWh/m^2/day. The yearly total global solar radiation per day is around 5.2 kWh/m^2/day, and solar energy is a decent choice. Compared to the rest of the country, Rwanda's eastern province has the highest solar radiation potential [41]. Table 8 shows the potential of solar energy and daily sunshine duration.

(4) Public Support for Solar (in Contrast to Other Energy Resources). The fact that Rwanda is gifted with abundant

Table 5: Access to electricity in SSA [75].

Country	Access to electricity (% of population) (2018)	Access to electricity, rural (% of rural population) (2018)	Access to electricity, urban (% of urban population) (2018)	Electric power consumption kWh per capita) (2014)
Angola	43.3	3.8(2015)	73.7	312
Benin	41.5	18.3	67.4	100
Botswana	64.9	27.9	81.1	1816
Burkina Faso	14.4	4.7	62.3	—
Burundi	11.0	3.4	61.7	—
Cabo Verde	93.6	96.9	91.9	—
Cameroun	62.7	23.0	93.3	275
Central African Republic	32.4	16.3	55.2	—
Chad	11.8	2.7	41.8	—
Comoros	81.9	77.0	94.0	—
Congo, Demo. Republic	19.0	1.8	50.7	109
Congo, Rep.	68.5	20.2	92.4	203
Cote d'Ivoire	67.9	32.9	100.0	275
Equatorial Guinea	67.0	6.6	90.4	—
Eritrea	49.6	34.6	77.1	97
Ethiopia	45.0	32.7	92.0	69
Gabon	93.0	62.5	96.7	1168
Gambia, The	60.3	35.5	76.0	—
Ghana	82.4	67.3	94.2	351
Guinea	44.0	19.7	87.0	—
Guinea-Bissau	28.7	10.0	53.1	—
Kenya	75.0	71.7	84.0	164
Lesotho	47.0	37.7	70.7	—
Liberia	25.9	7.4	43.6	—
Madagascar	25.9	0.0	69.6	—
Malawi	18.0	10.4	55.2	—
Mali	50.9	25.4	85.6	—
Mauritania	44.5	0.6	82.4	—
Mauritius	97.5	100.0	88.5	2183
Mozambique	31.1	8.0	72.2	479
Namibia	53.9	35.5	72.2	1653
Niger	17.6	11.7	47.6	51
Nigeria	56.5	31.0	81.7	145
Rwanda	34.7	23.4	89.1	—
Sao Tome and Principe	71.0	55.7	76.7	—
Senegal	67.0	44.2	92.4	229
Seychelles	100	100.0	99.6	—
Sierra Leone	26.1	6.4	53.2	—
Somalia	35.3	14.6	60.5	—
South Africa	91.2	89.6	92.1	4198
South Soudan	28.2	23.7	46.8	44
Sudan	59.8	47.1	83.8	257
Switzerland	100	100.0	100.0	7520
Tanzania	35.6	18.8	68.3	104

Table 5: Continued.

Country	Access to electricity (% of population) (2018)	Access to electricity, rural (% of rural population) (2018)	Access to electricity, urban (% of urban population) (2018)	Electric power consumption kWh per capita) (2014)
Togo	51.3	22.4	91.9	155
Uganda	42.6	38.0	57.5	—
Zambia	39.8	11.0	77.2	717
Zimbabwe	41.0	20.0	85.3	609

Table 6: Renewable energy targets for share of primary or final energy of SSA, 2018, and progress, end-2016 [76].

Country	Primary energy Share	Target	Final energy Share	Target
Angola	—	7.5% by 2025	4.4%	
Benin	59.6%	—	8.8%	25% by 2025
Burundi			2.6%	2.1% by 2020
Cote d'Ivoire	3%	15% by 2020 20% by 2030	7.6%	—
Gabon	76.7%	—	60.1%	—
Ghana	42.5%	—	13.5%	10% by 2030
Guinea	—	—	2.4%	30% by 2030
Guinea Bissau	—	—	7.8%	—
Liberia	5%	30% by 2030	73.8%	10% by 2030
Madagascar	—	—	38.6%	54% by 2020
Malawi	—	7% by 2020	47.3%	—
Mali	—	50% by 2020	4.3%	—
Mauritania	—	20% by 2020	1.1%	—
Niger	74.7%	10% by 2020	—	—
Rwanda	—	—	8.2%	—
Sudan	—	20% by 2020	24.7%	—
Switzerland	—	24% by 2020	—	—
Tanzania	22.3%	24% by 2020	19.8%	—
Togo	78.9%	—	12.7%	4% (no date given)

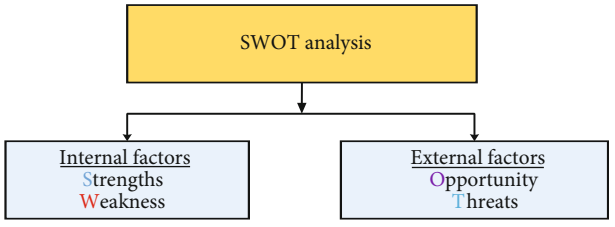

Figure 14: Basic elements of the SWOT analysis [118].

natural energy resources like solar has to be fully exploited. The identification and suggestion of an effective solar photovoltaic (PV) and the introduction of CSP technology depend on its annual capacity to generate electricity, electricity load, percentage of penetration of renewable energy, economic viability, feasibility, availability, carbon footprint, and degree of greenhouse gas emissions for climate change implications towards a green and clean future. The GoR has firmly defined the policy and regulatory structure for implementing the NEP, involving guidelines and technical requirements for minigrids and off-grid solar items, among the energy indicators for all, and REG has endorsed an incentive scheme to make these electrification options viable (2019) [121]. In the power sector, the Nationally Determined Contribution (NDC) highlights (a) increasing the share of new grid-connected renewable capacity compared to fossil fuels, (b) installing solar photovoltaic (PV) minigrids in rural communities, and (c) increasing energy efficiency through demand-side measures and supply-side loss reduction measures [121]. Rwanda's ambition of 48% of the universal electrification target through off-grid solar systems by 2024 shows a big initiative in expanding electricity access to low-income households which is affordable for consumers and the government's capacity to fulfil its mandate [122].

(5) A Possibility of Using Micropower Plants. The NEP report demarcates the microgrid zone for solar, hydro, or hybrid systems all over the country. The GoR has stated that having access to electricity in Rwanda will require the supply of DC solar kits for low-demand residential customers below 50 Wp (watt peak). It will also determine a favorable place where

Table 7: Internal and external factors identified for SWOT analysis.

(a)

Strengths	Weaknesses
(1) Increase experience in solar technologies through off-grid projects	(1) High initial investment costs
(2) Very high interest among investors	(2) Lack of community engagement
(3) Areas with higher solar potential near to an existing national grid	(3) Highly subsidized electricity tariffs to final consumers
(4) Public support for solar (in contrast to other energy resources)	
(5) A possibility of using micropower plants	
(6) Shorter lead time for the construction of solar power plants	

(b)

Opportunities	Threats
1. Seasonal complementarity between solar and hydro resources	Lack of project financing
2. Establishment of new plans to privatize the solar energy market	Lack of international development partners
3. Development of industry connected to the solar power sector	Low participation of the private sector
4. Reduced emission of greenhouse gases	Insecure revenues
5. Decreasing global prices for solar energy	
6. Growing investment in solar energy in Rwanda	

Table 8: The minima and maxima values of monthly averaged global solar radiation over the period of 1974–1993 [41].

Year	G_{min} (kWh/m^2/day)	Month	G_{max} (kWh/m^2/day)	Month
1974	4.1	Jul	5.2	Aug
1975	4.1	May	5.1	Jan
1976	4	May	4.9	Jan
1977	4	Apr	5	Jul
1978	4.2	Jan	4.9	Jan
1979	3.8	May	5.1	Jul
1980	4.1	May	5.3	Aug
1981	—	—	—	—
1982	4.1	May	4.9	Jul
1983	4.2	Apr	4.9	Sep
1984	4.1	Nov	5.1	Jun
1985	4	Apr	5.4	Aug
1986	4.4	Apr	5.1	Jul
1987	4.1	May	5.3	Jan
1988	4.3	Apr	4.9	Jun
1989	4.3	May	5.1	Aug
1990	4.3	Feb	5.4	Jul
1991	4.1	May	5.2	Aug
1992	4.4	Dec	5.5	Aug
1993	4.4	Jun	5.7	Aug
Average	**4.3**		**5.2**	

stand-alone AC solar systems should be provided to larger customers who are too isolated from the network to justify an individual connection to the central grid or an off-grid microgrid [123]. Rwanda has shown improvement towards energy access, from 6% on-grid access in 2000 to 37% on-grid access in 2019. Though there is a change, the off-grid access still has to gain more potential, as it accounts for about 14% of the population which is small compared to other countries. The potential for renewable energy minigrids is high [124]. Research conducted by the Energy Development Corporation Ltd. and funded by the Sustainable Energy Fund for Africa (SEFA) acknowledged over 200 potential minigrid sites. The recently approved NEP by REG Ltd. foresees 10% of off-grid targets to be met by minigrids connecting over 300,000 households [125]. This highlights that the PV and CSP can provide more assurance for energy generation in Rwanda.

(6) Shorter Lead Time for the Construction of Solar Power Plants. Electricity has been indispensable for improving economic activity and improving the quality of life of humans. Solar energy projects have a shorter time for project implementation compared to other energies. But it all depends on the suppliers we have and how much we want to invest in the construction. Generally, solar power plant technology construction is shorter and quicker than other forms of energy [125]. Despite the fact that CSP necessitates land preparation and water availability, the overall implementation time is also short.

5.3.2. Weaknesses

(1) High Investment Cost. Renewable energy power plants have high initial construction costs, with virtually no fuel costs and comparatively lower operating and maintenance costs, unlike traditional fossil fuel power plants [126]. Nevertheless, the large starting cost of capital associated with renewable energy technologies (RETs) makes it hard to attract investors to the sector, particularly in countries that are considered to be at risk [127]. The high initial cost

associated with PV and CSP technologies makes it difficult for Rwanda to develop. These expenses include the cost of solar panels, inverters, hardware for installation, wiring, installation, approvals, repairs, surveillance, maintenance, and other operations and overhead expenses. Such prices do not provide a storage system for batteries, which is an additional expense. Many power utilities in Sub-Saharan Africa (SSA) where Rwanda is located have inadequate electricity generation capacity, unreliable services, and high costs. They also face capital limitations that prevent them from making the required investments for expansion projects. Shortages of capacity have pushed power companies to use leased power-generating emergency units, at great socioeconomic and environmental costs [128].

(2) Lack of Community Engagement. While off-grid systems are the safest way to supply electricity to remote and island communities far from the national electricity grid, as a result of the lack of a clear policy structure for its growth, the development of this sector has not seen the necessary investment. Access to electricity, reliability, and costs remain problems across most Sub-Saharan Africa countries. The PV market in Rwanda is growing and largely dominated by an institutional market guided by the needs of providers of rural health and education services. Many of the installations have been fully funded by donors with little national government cooperation. People have explored various ways to get power to their new neighborhoods, and some have realized that the grid will never supply them who currently lack electricity because they live in neighborhoods that are spread around large areas and are too poor to afford such comprehensive infrastructure. Due to the high initial cost of solar energy projects, most people cannot afford it and makes it difficult for community engagement [129].

(3) Highly Subsidized Electricity Tariffs to Final Consumers. The production capacity of electricity and access to electricity is limited, and the size of the infrastructure is inadequate to meet requirements. Although Rwanda is on a high growth trajectory access to electricity, the cost of supplying electricity has been seen to be among the highest in the region and continues to hamper the economic and industrial growth of the country [45]. Most of the solar energy projects in Rwanda need high financial grants to be bankable or viable. It was suggested that for Rwanda to be able to reap and deepen the benefits of this reform program of electricity for all over the coming decade, The Rwandan Energy Group (REG), the country's publicly owned electricity corporation, is to place new public-private partnership investments defined in the lowest-cost plan in the driver's seat, rather than depending on unsolicited private sector suggestions [45]. The cost of electricity production employing solar PV and CSP which are yet-to-be-implemented technologies has declined significantly in recent years, and this trend is expected to continue. Thus, it is reasonable to consider this potential as an option and incentive for utilizing solar energy for future electricity demand. Solar electricity generation using PV and CSP is more favorable cost competitively against fossil fuels even in large interconnected systems in developed countries [130]. Under the extremely costly conditions of generating electricity in Rwanda (because of its geopolitical situation), the solar output could be even more competitive and results in lower electricity costs. Rwanda has set out motivations for investors interested in this sector, like "(a) provision of transmission access to all power projects on government's cost, (b) authorized road access, water service, and all infrastructure needed during energy project development, (c) free tax on power equipment during energy project development, and (d) provision of land on power projects by the government or compensation to private developers on the cost of land" [40].

5.3.3. Opportunities

(1) Seasonal Complementarity between Solar and Hydro Resources. A major opportunity for rural power supply is microhydropower with rainfall that generates streams in various areas. Rwanda has restricted electricity generation, especially during the dry season, when many hydropower plants experience problems with water shortages. Rental diesel generation is then used to provide the power demands during this time, and this generation comes with a high cost. Therefore, solar energy generation would provide the highest output in the months when it is most needed. The GoR advises to combine both solar and hydroenergies which were applicable due to the small run-off rivers and also reduce the cost of solar energy storage [131].

(2) Establishment of New Plans to Privatize the Solar Energy Market. In Rwanda, solar power is predominantly a procurement sector for institutional government and NGO systems, while demand for solar homes is growing. The national policy is based on attracting investors and showing them the energy development opportunities including solar energy [132].

At the heart of Rwanda's National Strategy for Transformation is access to electricity for all Rwandans (NST) (2017/18–2023/24), with a view of achieving upper–middle-income country status by 2035 and high-income status by 2050. Off-grid solutions where on-grid solution is not reachable are expected to be driven by the private sector [133]. As specified by NEP, about US$370 million of private finance is expected to be mobilized up to 2024 to support the implementation of off-grid solutions. Therefore, the NEP demarcates on-grid and off-grid energy expansion regions in order to mobilize private funding for off-grid solutions, providing a clear path to the private sector regarding their operations in off-grid areas [122].

Energy subsidies in the use of energy resources present an inefficient distortion in related technologies and a very big burden on the government budget that could undermine fiscal sustainability [134]. The poor participation of the private sector remains the biggest challenge to the growth outlook of Rwanda, as reforms to promote the business situation have not yet led to significant private sector investment in all sectors [40]. Therefore, appropriate energy pricing is important to make sure the consumers are encouraged to make efficient

and productive uses of energy and to ensure that energy suppliers can operate on a sustainable basis. Lack of investment and proper maintenance expertise have contributed to several technical issues, including malfunctioning batteries, defective wiring, and broken down DC appliances [135]. According to a participation commission organized by donors to improve the performance of institutional PV systems, the following measures were undertaken to (1) specify energy systems suitable for Rwandan health facilities, (2) enable partners in the creation of consistent design, installation, and after-service operations,(3) help grow the quality chain, by offering capacity-building exercises and implementing standards and good practices, and (4) organize periodic meetings among key stakeholders [135].

(3) Development of an Industry Connected to the Solar Power Sector. Rwanda is well favored with solar energy; even during the months of the rainy seasons, there is daily sufficient sunshine. The seasonal conditions change, with the average daily irradiation in the cloud hitting around 4.5 kWh/m^2, and the total annual capacity in 2015 was estimated at 66.8 TWh [136]. Two solar PV plants, namely, GIGAWATT Global Solar Power (8.5 MW) and Jali Solar Power (0.25 MW), are connected to the national grid in the districts of Rwamagana and Gasabo, respectively [43]. Energy generation could be boosted through solar energy by increasing the development in other sectors such as industries. This is because electricity is the lifeblood of manufacturing, where raw materials are processed into finished goods. Furthermore, electrical energy is also one of the most convenient, safe, and clean forms of energy used in the home and job creation.

(4) Reduced Emission of Greenhouse Gases. Climate change is a major global issue for the world. It affects the society and biodiversity. It can jeopardize the world economy and generate international conflicts and political crises. Seasonal mean temperature anomaly distribution has changed to higher temperatures. The range of anomalies has since increased; therefore, researchers have turned to the benefits of clean energy where it decreases our dependency on fossil fuels and can combat climate change [137]. Therefore, adopting renewable energy use including solar energy technology reduces atmospheric pollution. This change is pushing down greenhouse gas emissions from power generation, heating and cooling of homes, and transport [138].

(5) Decrease in Global Prices of Solar Energy. RE prices are now dropping across the world, so it has been shown to be a cheaper source of electricity production compared to traditional sources that rely on fossil fuels—a 70% decrease since 2010 [139]. This rapid price decline has nothing to do with any other energy technology [140]. Accordingly, the Rwanda national electrification plan recommends the use of a solar home or solar stand-alone system to reduce energy costs. The government will assist people in different ways, like (a) setting up facilities that allow low-income households to gain access to modern, clean, and sustainable energy services using basic solar power systems, (b) establishing a strategy that makes it easier for the private sector and consumers to make solar power products more affordable, and (c) enabling the private sector to build and establish minigrids, and the government will provide the assistance of site identification and adequate structure for site identification [141].

(6) Growing Investment in Solar Energy in Rwanda. Much of present installations have been financed by donors with low governmental coordination. The major constraints of the Rwanda power sector include (a) electricity demands almost equal with the generation, and with little reserves, (b) high petroleum product expenditures, (c) lack of investment financing, (d) lack of government subsidies, which cushion electricity retail prices, and (e) inability to participate in a large number of energy exports and trade due to relatively uncompetitive pricing structures [40]. It is vital to the private sector that minigrid projects are allowed in minigrid areas and subsidies for solar home systems (SHS) only are available in SHS areas, although the systems can be sold anywhere [134].

5.3.4. Threat

(1) Lack of Project Financing. High-capital investment ventures need reasonably easy access to capital in order to be viable. However, capital markets are not as developed in almost all Sub-Saharan African countries where Rwanda is located as in many other countries, making it difficult to access external investment. Sub-Saharan African countries' power generation has been facing some challenges like illiquidity, lack of depth, and small size. Special local support systems are needed to meet energy-poor rural communities through a market system targeted at supporters. Investors need to consider and limit the risks of investing in renewable energy ventures, as well as in the industry itself. To ensure fair returns over the life of the project, the private sector needs long-term assurances, since some projects last for decades. Also, long-term contracts and identifying components with a clear comparative advantage over imports will attract investors [142].

(2) Lack of International Development Partners. Rwanda needs the electricity sector to ensure an adequate, secure, sustainable, and more affordable electricity supply by 2024. It is important to learn how to mobilize global awareness and resources to boost access to solar energy (PV) and to reinforce the knowledge base of national governments on the ties between poverty, renewable energy, and climate change to guarantee secure operations [143]. Rwanda's private sector participation in solar power technology for rural development projects has established an enabling policy framework to encourage private sector investments through standardized power purchase agreements and feed-in tariff schemes [40]. The challenges of high electricity cost and frequent power outages (blackouts) in a small country with a relatively low average income and extremely low average consumption volumes lead to generation capacity and demand misalignment. These challenges are making it impossible to maintain an efficient tariff structure because if demand fails to keep pace with the increased generation capacity, then, the tariff will increase [144]. Commercial enterprises are hardly

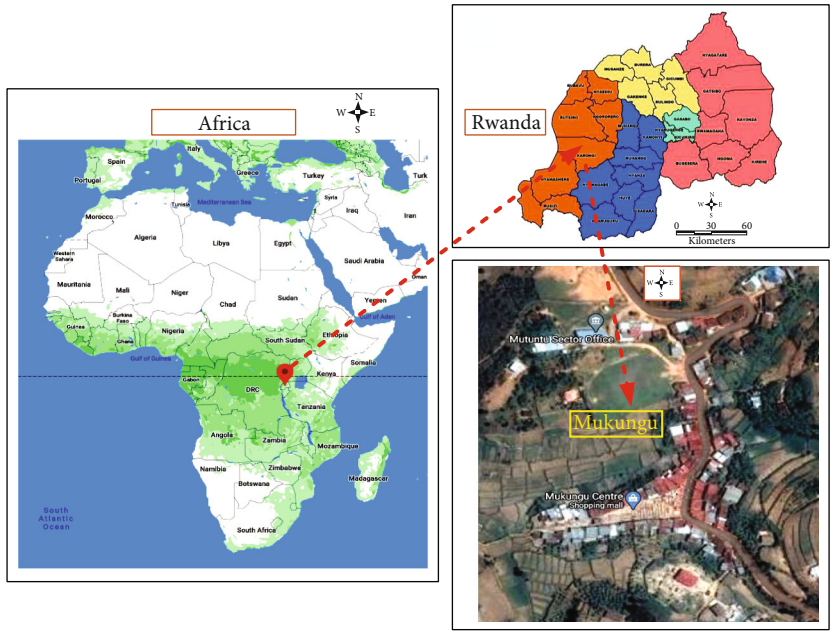

Figure 15: Map of the selected location study area.

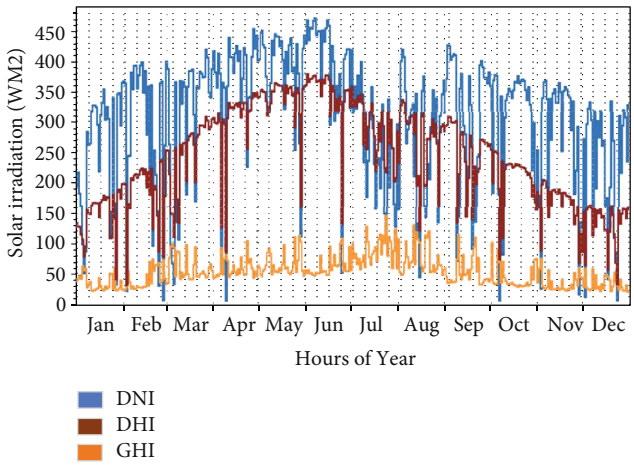

Figure 16: Hourly GHI, DNI, and DHI during a year.

interested in investing in energy generation since feed-in tariffs are kept low by the import parity price for electricity from neighboring countries. Enterprises are now focusing on the market through public tenders for broader programs for public institutions, such as hospitals and schools. In urban areas, the demand for solar water heating systems is booming [143]. Thus, all these constraints are sometimes due to a lack of international development partners.

(3) Low Participation of the Private Sector. The contribution of the private sector in enabling solutions to renewable energy to be integrated into the grid is also becoming economically viable. Compared to the fossil fuel cost spectrum, solar PV, CSP, and all other renewable energy generation technologies currently in commercial use are projected to decline, with most fossil fuel prices at the lower end or decreasing. Therefore, the International Renewable Energy Agency (IRENA) thus aims to address obstacles to high upfront costs, investment risks, regulatory instability, the lack of trained practitioners, and environmental issues [145]. Energy sector financing should be accessible, which has been a big barrier in project implementation. IRENA addresses challenges that seem to halt or limit the African development in renewable energy, especially solar energy that includes [145] (a) high costs being inherent to the energy sector, (b) limited access to funding, (c) creditworthy utilities/insufficient cost recovery, (d) elastic demand/affordability, (e) foreign exchange risk, (f) lack of competition for networks, (g) inefficient tendering processes, (h) breach of contracts, and (i) inability to raise tariffs to cover costs [145].

(4) Insecure Revenues. The contribution of the private sector in enabling solutions to the renewable energy sector is profitability since it is the basis for establishing solar energy investment. The financial returns will be based on the underlying technology, and at which level of competitiveness it operates with other forms of technology is critical. Nevertheless, renewable energy production costs drop significantly and certain technologies are already productive in many parts of the world, or at "grid parity" with conventional sources of electricity [145]. Underpricing of power in Africa leads to poor revenues from public utilities in line with the low purchasing power of the population, poor revenue collection mechanisms, and high transmission and distribution losses. To inject capital for infrastructure maintenance and expansion, many countries have opened their markets to the private sector. The absence of laws and regulations promoting the creation of renewable energy technologies will delay their deployment [146]. This helps policies to build stable and predictable investment environments that address obstacles and ensure that project revenue sources are predictable [146].

6. Feasibility, Optimization, and Technoeconomic Assessment of Concentrated Solar and Photovoltaic Systems in Rwanda

6.1. Methodology

6.1.1. Introduction. As a result of increased industrial activities, growing populations, and significant changes in people's total energy consumption in recent times, global energy demand has exploded. This chapter traces the effectiveness of the PV and CSP system's technoeconomic model for a real residential aggregated load. The world's energy demand is expected to increase by 30% by the year 2040 [147]. So, many countries are taking advantage of their economic potential in order to meet their energy needs [148]. Rwanda, like many other developing countries, faces difficulties in meeting its energy demands. Rwanda's latest national electrification pace is at 59.7% (43.8% grid-connected and 15.9% off-grid-connected systems) [68]. An economic study is typically carried out to justify the use of PV and CSP systems in buildings and to illustrate the idea so that homeowners are willing to invest. PV and CSP system economic output is determined by a variety of factors, namely, capital cost, installation cost, operating and maintenance costs, and electricity tariff as well as payback period (PB), which is the time it takes to recoup the initial investment. Throughout the project, the technoeconomic study estimates the cost savings gained by implementing green technology against the cost of installed systems [149]. CSP and PV technologies are part of feasible and promising renewable energy technologies that can be built to produce electricity in order to further enhance renewable energy use across the world.

6.1.2. System Advisor Model. The system advisor model (SAM) is a computer model that measures renewable energy project technoeconomic efficiency and financial metrics. SAM was developed by the U.S. Department of Energy's National Renewable Energy Laboratory (NREL) [150]. SAM simulates photovoltaic, concentrated solar power, solar water heating, wind, geothermal, and biomass power system efficiency, as well as a simple standardized model for comparisons with traditional or other types of systems [151]. This is an electricity-generating model that assumes the RE system delivers its power to a grid- and off-grid-connected house, the electric grid, or a facility to satisfy an electric demand [150]. It is used to model real-world scenarios using local weather data and manufacturer-supplied equipment data. A system's produced output may also be used as an input into that system or other systems [152].

6.1.3. The Selected Site and Data Collection. In this study, to achieve the study's goal of evaluating the technical and economic performance of CSP and PV systems at the chosen location, the selected site as shown in Figure 15 was chosen to collect data based on the size of the system and load demand. The location was selected to analyze their ability to support large-scale PV and CSP power plants by evaluating their technoeconomic potentials. The provision of quality solar resources (i.e., DNI) is of the greatest priority when selecting the best sites for CSP implementation in a country [153]. CSP technologies absorb and concentrate DNI incident on the surface of the earth to heat a working fluid and then generate energy through a thermodynamic cycle. The selected site Mukungu is located in the western province at 50.29°N latitude and 2.42°E longitude. This site according to data from the National Solar Radiation Database (NSRDB) records has an annual average of solar global horizontal of 3.06 kWh/m^2/day. Solar radiation availability has a major impact on the economic feasibility of large-scale PV power plants. The amount of solar radiation available at a given location has a major effect on the levelized cost of energy (LCOE) [154]. The hourly weather data features of the study sites collected from NSRDB are shown in the graph of Figure 16 below.

Table 9: Selected site geographical data.

Parameters	Values
Latitude (°N)	50.29
Longitude (°E)	2.42
Altitude (m)	121
Annual DNI (kWh/m^2/day)	3.22
Average ambient temperature (°C)	19.98
Average wind speed (m/s)	3.0

Table 10: Monthly energy consumption in 2019.

Month	Consumption (kWh)
January	193
February	200
March	200
April	250
May	250
June	250
July	300
August	300
September	200
October	200
November	250
December	193

6.1.4. Selected System Details and Components

(1) PV System. This technoeconomic feasibility study's key contribution is to provide fundamental information for the viability of residential PV system use in the off-grid area in Rwanda. The proposed residential system design has a 5 kWp capacity and is made up of 20 monocrystalline silicon modules with a nominal power rating of 250 Wp each and a total module surface of 35 m^2. Furthermore, two inverters with a combined AC power of 4.2 kW have been employed in this analysis. The system configuration is 10 modules per string with a DC-to-AC ratio of 1.2. PV modules have a 25-

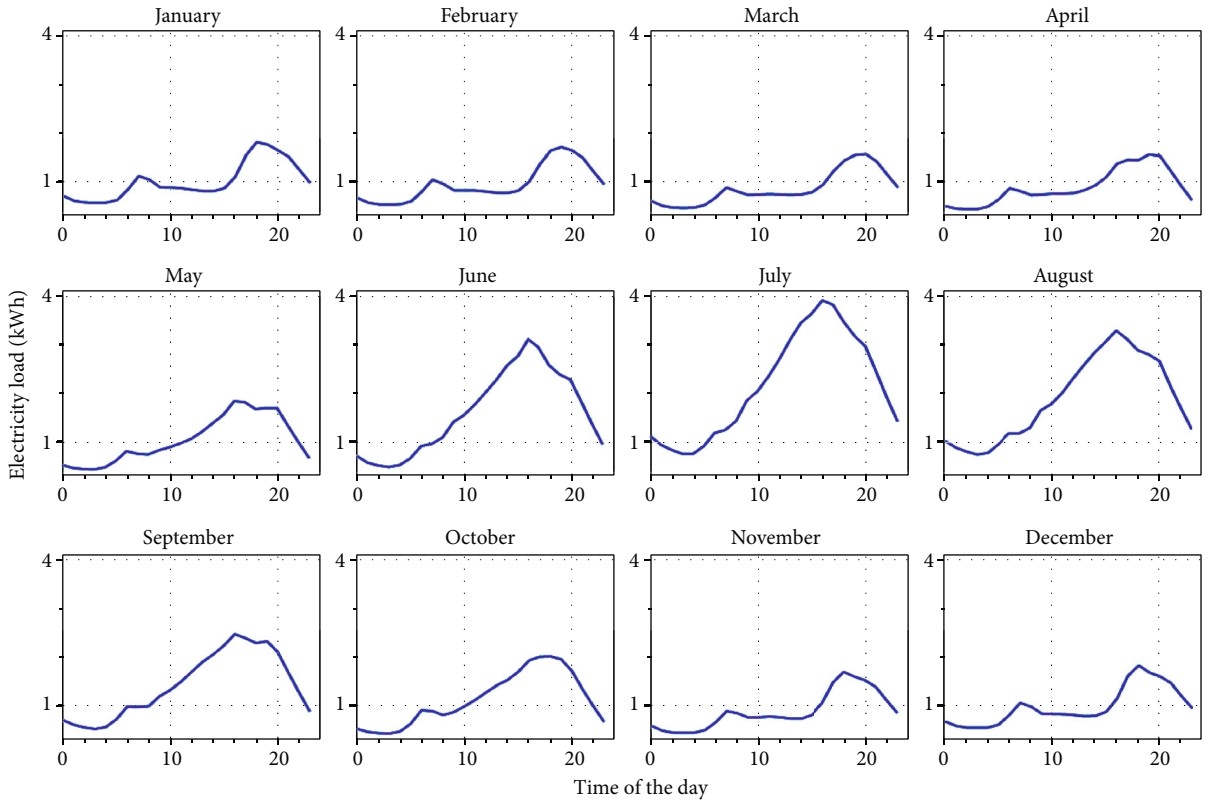

Figure 17: Load profile.

year life expectancy, with a 0.5 percent annual deterioration factor, while the inverter's life expectancy is set at 15 years.

(2) CSP System. CSP technologies absorb and concentrate DNI incident on the earth's surface to heat a working fluid and then generate energy via a thermodynamic cycle. The solar resource assessment is crucial for solar project site selection, annual power generation forecasting, and temporal output forecasting. Many factors go into determining the best locations for CSP installations in a country, but the availability of good solar resources (i.e., DNI) is critical [155]. For modeling CSP plants in the specified locations, reliable hourly DNI predictions are needed. The study introduces a methodology that can be used to investigate the technoeconomic feasibility of CSP technology in other developing countries, especially those in Sub-Saharan Africa since the methodology addresses the effects of such economies' high financial uncertainties. A solar tower plant was chosen to be implemented in our study because it has the highest annual electrical energy generation, higher capacity factor, and lowest levelized cost of electricity.

In this report, Mukungu village, which is located in the Karongi district of Rwanda's western province and has GPS coordinates of S 02o13 9310′ and E 29o24.590′, was chosen to be used. Table 9 shows the survey site's essential topography and ambient weather conditions (as determined by the NSRDB). Different parameters like direct normal irradiation (DNI), global horizontal irradiance (GHI), and direct horizontal irradiance (DHI) are presented as shown in Figure 16.

6.1.5. Load Demand. The selected site as illustrated in Table 10 shows the monthly energy usage of the area based on real electricity bills. There is no significant change in load consumption since there is no summer or winter as a result of moderate temperature. The average annual average load consumption is 232 kWh/m^2. The monthly cumulative electricity consumption is used by the system advisor model to approximate the monthly and annual load demands as shown in Figure 17.

6.1.6. System Costs and Economic Parameters. The capital cost, operating maintenance cost, and running cost of residential PV systems all play a role in the project's economic viability. The technology and installation costs were calculated using the cost database of the International Renewable Energy Agency (IRENA) [156]. The overall cost of capital investment is estimated to be $11,529.46. Dissimilar to rotary power conversion technologies, a PV system has no tangible operating costs, though dust accumulation on the PV module's surface necessitates minimal cost of maintenance. The annual cost of operation and maintenance (O&M) is calculated to be $9 per kW. Furthermore, financial variables such as Rwanda's interest and inflation rates were also taken into account. The deposit fraction (percentage of total capital cost to be borrowed) is set at 100% in this report, with a five-year loan term and a 2.5 percent interest rate.

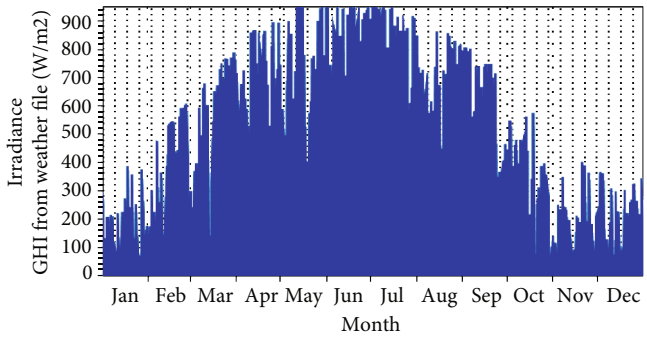

Figure 18: Time series data of GHI.

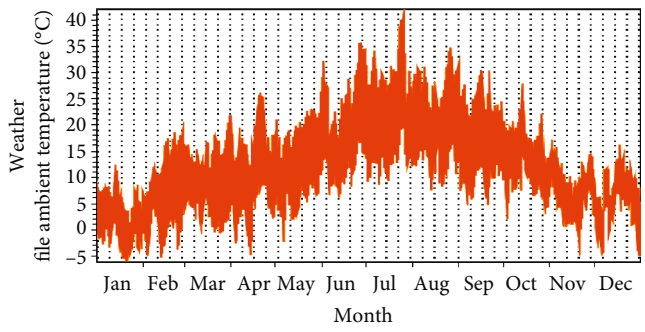

Figure 19: Time series data of ambient temperature.

6.1.7. Solar Resource. Solar irradiance and ambient temperature are two important factors that affect the performance of a PV system. As a result, the main inputs for estimating the system's size and performance are daily average solar radiation and daily average ambient temperature. Rwanda is located on a horizontal surface near the equator, with plenty of sunshine and global solar radiation ranging from 4.8 to 5.5 kWh/m^2/day [41]. The PV module output as shown in equation (1) can be calculated by [157]

$$P_{PV} = Y_{PV} f_{PV} \left(\frac{G_T}{G_{T,STC}} \right) [1 - \alpha P (T_C - T_{C,STC})], \quad (1)$$

where Y_{PV} is the PV power output under standard test conditions (kW), f_{PV} is the PV module derating factor (%), G_T refers to the solar radiation incident on the PV module (kW/m^2), $G_{T,STC}$ represents the incident radiations at STC (1 kW/m^2), αP indicates the temperature coefficient of power (%/°C), T_C refers to PV cell temperature in the current time step (°C), and $T_{C,STC}$ is PV cell temperature at STC (°C).

A system advisor model allows the user to download data files from the National Solar Radiation Database (NSRDB) or upload any available climatic data in a comma-separated values (CSV) format for solar resource data for sites not included in the software library for the selected location.

In this study, we used data derived from the weather data of 2019 downloaded from NSRDB. The global horizontal irradiance (GHI) and ambient temperature time series data are presented in Figures 18 and 19 based on the data obtained.

6.2. Economic Metrics Modeling for CSP and PV. In order to determine energy management policies for any country, feasibility analyses and assessments of different energy system projects are essential. A viability study helps capital owners make the best decisions by contributing to the optimal allocation of energy resources at the state level. The LCOE and NPV metrics were used to calculate the viability of the power plants to perform the economic analysis. The software's financial model determines the project's inflows and outflows of cash over the course of its operating period. The value of electricity produced, incentives, project capital costs, operating and maintenance costs, dividends, and debt are all included in cash flow. The model also determines the after-tax cash flow's net present value and the payback period, which is the time it takes for the total after-tax cash flow to cover the project's initial capital cost.

6.2.1. Levelized Cost of Energy (LCOE). Over the project's lifetime, the levelized cost of energy (LCOE) estimates the price of per unit energy ($/kWh). The LCOE is a metric that is used to compare the kWh costs of various power system technologies. As expressed in equation (2), the LCOE is calculated by dividing the project's lifespan cost by the predicted energy output [158].

$$\text{LCOE} = \frac{\text{LCC}}{E_{grid}}, \quad (2)$$

where LCC is shown in equation (3) which is the lifecycle cost and E_{grid} is the system energy yield. The lifecycle cost covers the initial capital cost, operation, and maintenance costs, as well as the substitution cost minus the salvage value, which is the project value at the end of the system's lifecycle.

$$\text{LCC} = C_{capital} + \sum C_{O\&M} + \sum C_{replacement} - C_{salvage}, \quad (3)$$

where $C_{capital}$ is the capital cost, $C_{O\&M}$ is the operation and maintenance cost, $C_{replacement}$ is the replacement cost, and $C_{salvage}$ is the salvage value or the project value at end of life.

The modeled CSP plants' main goal is to reduce the levelized cost of electricity (LCOE) provided by the CSP installations over their lifetime. To optimize a CSP plant, evaluate the TES capability and solar field size (i.e., SM) that maximize the economic benefits (i.e., reduce the LCOE). The ideal solar field area should optimize the amount of time the solar field produces enough thermal energy to drive the power block (at its rated capacity), reduce installation and operating costs, and take into account the TES system's efficiency and cost-effectiveness. The whole project lifespan costs and the total amount of electricity provided by the system are accounted for in the LCOE.

The model calculates both the real and the nominal LCOE for CSP as illustrated in equation (4). The nominal LCOE is a current dollar value, while the real LCOE is a fixed dollar (inflation-adjusted) value. The real (current) dollar LCOE was used in our analysis because it is more suitable for long-term analyses (to account for many years of inflation over the project life), while the nominal (constant) dollar

LCOE is more appropriate for short-term analyses (to account for many years of inflation over the project period). The following equation shows the real LCOE [159]:

$$\text{LCOE(real)} = \frac{-C_0 - \left(\sum_{n=1}^{n} c_n/(1+d_{\text{nominal}})^n\right)}{\left(\sum_{n=1}^{n} Q_n/(1+d_{\text{real}})^n\right)}, \quad (4)$$

where Q_n (kWh) is electricity generated by the system in year n (calculated by the performance model), N is the analysis period in years, C_0 is the project's equity investment amount, C_n is the annual project costs in year n (incl. installation, operation and maintenance, financial costs and fees—account for developer's margin defined by the project's internal rate of return, and tax benefit or liability and also account for incentives and salvage value), d_{real} is the real discount rate (the discount rate without inflation), and d_{nominal} is the nominal discount rate (the discount rate with inflation).

6.2.2. Net Present Value (NPV). The distinction between today's cash inflow and cash outflow over the lifetime of a project or company is referred to as the net present value. NPV in equation (5) is calculated during the planning phase of a project to determine its profitability, as shown in the following [160]:

$$\text{NPV} = \sum_{t=0}^{N} \frac{\text{revenue}_t - \text{cost}_t}{(1+d)^t}, \quad (5)$$

where N is the number of years of the economic analysis, t is the year variable in each summation, d refers to the discount rate, revenue_t is the PV system revenue in year t, and cost_t represents the system cost in year t.

6.2.3. Internal Rate of Return (IRR). The internal rate of return is the discount rate at which the net present value of a specific investment's cash flow is zero. This rate is used to determine whether or not a potential investment would be profitable [160]. It can be calculated in equation (6) as follows:

$$\text{IRR} : \text{NPV} = \sum_{t=0}^{N} \frac{\text{revenue}_t - \text{cost}_t}{(1+d)^t} = 0. \quad (6)$$

6.2.4. Payback Period (PbP). The time it takes for an investment to pay for itself in terms of earnings or net cash flow is known as the payback period. A simple payback period and a discounted payback period are the two types of payback periods. A simple payback period is one where the income equals the investment cost, whereas a discounted payback period takes the time value of money into the account. For residential PV systems, a simple payback period is provided as shown in equation (7) as follows [160]:

$$\text{Simple payback period} = \frac{\text{PV price} - \text{federal ITC}}{\text{annual PV revenue} - \text{O\&M}}. \quad (7)$$

6.3. Results and Analyses

6.3.1. Technical Analysis. The technoeconomic results for the modeled 5 kW solar PV power plant and 50 MW concentrated solar tower for the chosen Rwandan site are presented in this section. According to simulation results, the Mukungu solar power plant (PPP) produced good annual energy, owing to the area's high solar radiation. PV power plants differ from other renewable energy sources in that they go offline at sunset and stay that way until sunrise, which contributes to their low-capacity factor (CF) values when compared to other power plants. From the results obtained, the selected site has a CF of 15.5% and the recorded CF for the studied area is within the permissible CF range for PV power plants all over the world. According to [161], the CF for fixed mounted PVs around the world, as in the case of the modeled PV power plants in this research, ranges from 15% to 21%, putting this work on the right track in terms of performance, similar to what is currently available in other operating power plants around the world.

On the other hand, for CSP systems, the parameters representing energy quantities and the total energy production, the performance ratio, and the capacity factor are among their components. These variables aid in the evaluation of similar projects in order to decide which is the most efficient. To evaluate the effectiveness of the CSP technologies examined, the total energy yield (annual electrical energy generation (AEG)), the capacity factor (CF), the land (area) requirement, and the annual water usage/consumption (AWU) have been used.

6.3.2. Energy Production. The simulation result indicates that the total monthly energy production over the first year varies between 195 kW in January and 300 kW in July. The total electric energy generated by the system in the first year is estimated to be 839 kWh, with the monthly energy produced as shown in Figure 20 with an average of 416 kWh.

The annual energy production over the lifetime period is depicted in Figure 21. CSP systems focus the sun's energy using reflective devices to generate heat, which is then used to generate electricity. The upfront and the overall cost is high though the output power is also high.

6.3.3. Economic Analysis. The levelized cost of energy, payback period, and net present value are all part of the economic feasibility analysis for the PV system. The economic indicators for the PV system are summarized in Table 11 after determining the system's lifetime expenses and revenues using IRENA's renewable energy cost estimate. The nominal and real LCOEs are 0.96 \$/kWh and 0.76 \$/kWh, respectively. The nominal and real LCOE are both competitive with Rwanda's electrical company tariff.

The LCOE is a useful tool for comparing the cost of PV energy production in different sites or with alternative power generation, but it is insufficient for determining financial profitability. That is why the net present value and payback time

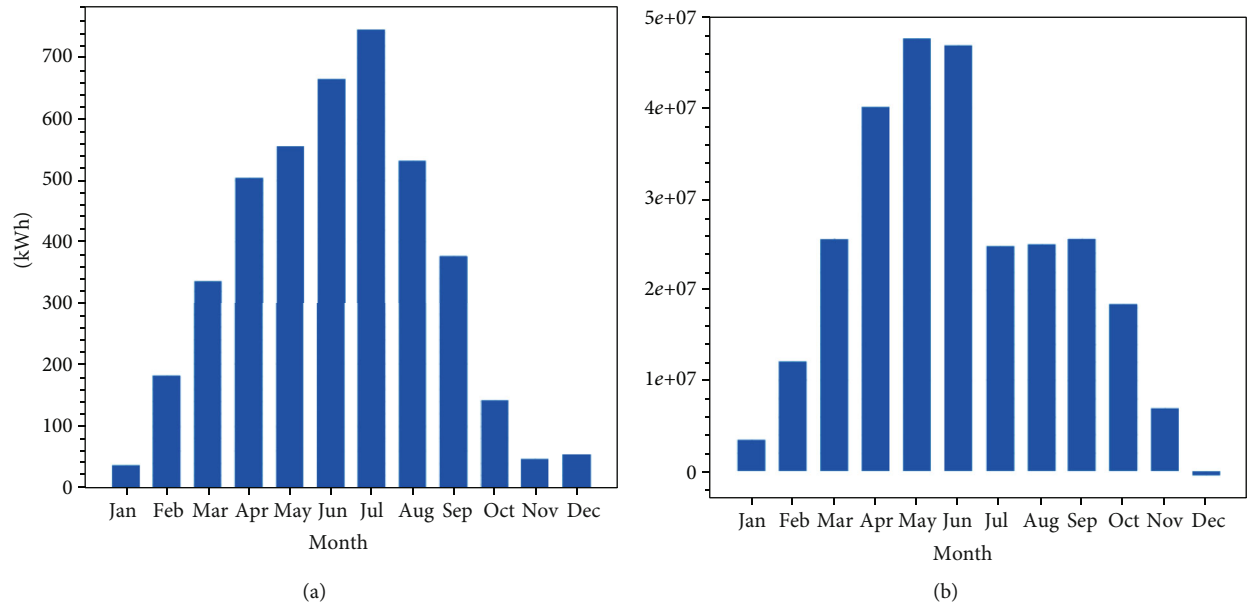

Figure 20: Monthly energy production (a) by the PV system and (b) by the CSP system.

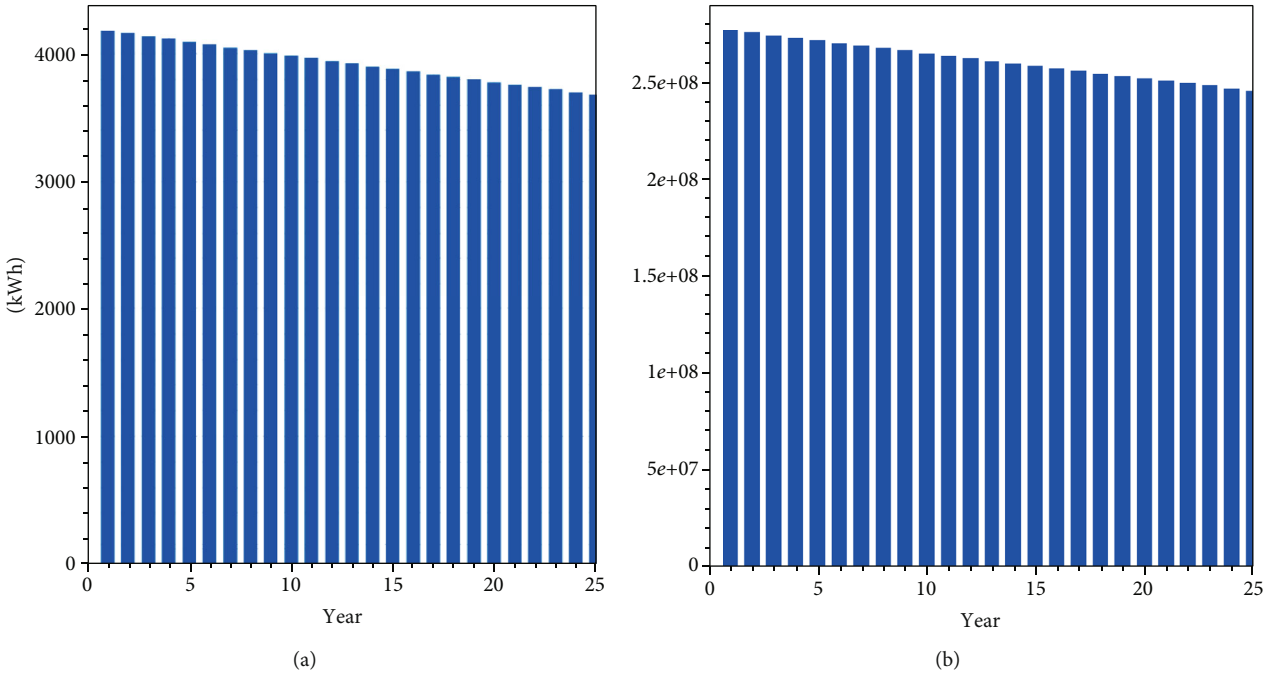

Figure 21: Total yearly lifetime energy yield (a) by the PV system and (b) by the CSP system.

are calculated. The net present value is one of the key principles that cannot be overlooked when evaluating grid-connected PV system feasibility. The net present value depicts the current worth of future net income over the task's lifetime. The estimated net present value of the system over its lifetime is \$131,239 for our PV system while it is \$451.091million for our CSP system which is big compared to that for the PV system. CSP provides a lot of electricity to the user but investment cost is very high compared to the PV system. A positive NPV means that the investor is making money and vice versa as shown in Table 11. This PV system discounted payback period, or the amount of time it will take to recoup its investment cost is 11.1 years. LCOE and NPV indicators highlight residential PV systems' competitiveness as electric utilities in terms of energy costs. The long-term discounted payback period, on the other hand, decreases the investment appeal and desirability of PV system installation for investors.

Eventually, we compared the optimized cost metrics of a 50 MW solar CSP power plant under the same condition with PV. To evaluate the performance of the CSP technologies under consideration, the total energy yield (annual electrical energy production (AEP)), the capacity factor (CF), the land

Table 11: Economic evaluation between PV and CSP systems.

Indicator	PV	CSP
LCOE (nominal)	0.82 $/kWh	16.89 ¢/kWh
LCOE (real)	0.24 $/kWh	14.08 ¢/kWh
Electricity bill without the system (year 1)	$474	—
Electricity bill with the system (year 1)	$175	—
Net saving with the system (year 1)	$298	—
NPV	$131,239	—
Simple payback period	6 years	—
Discounted payback period	11.1 years	25 years
Net capital cost	$13,400	$899,820,288
Loan	$13,400	—
Equity	$0	$1,247,413,248
Capacity factor	—	21.0%
Annual water usage	—	79,921 m^3
Year IRR is achieved	—	25 years
Annual net electrical energy production	—	505,789,536 kWh

(area) requirement, and the annual water consumption (AWC) were used. The levelized cost of electricity (LCOE), an economic estimate of the cost of energy from a generating project, is the value at which electricity from a given source must be produced in order for the project to break through over its lifespan. Because the study is based on a long-term scenario, the real LCOE, instead of the nominal one, is more fitting. The modeled solar tower CSP that was chosen due to its potential to work in hotter conditions (high temperature) has an LCOE of 14.08 ¢/kWh (¢/kWh, cent per kilowatt hour) which is high with respect to that of the PV system. Having a positive net present value of $451.091 million means that the project is viable. They do, however, have the highest overall installation cost (OIC), which is approximately $643.90 million compared to the PV system. Some parameters as shown in Table 11 determine our CSP solar tower output characteristics and PV system.

7. Discussion

Geographical position, political stability, and the availability of the RE Act were established as the key strengths for the sector as the results of the weighted analysis. The key opportunities are regional integration and growing electricity demand, while inadequate research and development (R&D) and changing environmental conditions are the main challenges to the successful development of RE in the country.

A strong desire for growth in the industrial, commercial, and domestic sectors in Rwanda will increase electricity demand. The erratic and unpredictable existence of solar energy can be replaced by CSP thermal energy storage technology, and its advancement is of great importance for the welfare of human communities.

To ensure solar energy access to the people of developing countries requires understanding their everyday life. Finance conditions dictate whether or not the implementation of the project will be successful or not. SAM as a computer techno-economic model that helps financial metrics of renewable energy projects has made easy the decision making on the project feasibility. Technologies represented in SAM include photovoltaics (flat plate and concentrating), concentrating solar power (parabolic troughs, towers, linear Fresnel, dish Stirling), solar water heating, wind, geothermal, and biomass [162]. Project developers, equipment manufacturers, and researchers use SAM results in the process of evaluating financial, technological, and incentive options for the renewable energy project. SAM calculates the levelized cost of energy (LCOE) and other metrics for renewable energy projects by integrating annual time series power output models with financial models [163]. The final results of SAM allowed researchers to look at patterns for various system designs and compare them to other technologies.

Thermal storage involves transferring usable energy from the collector to the storage medium, which is converted into a rise in internal energy. Solar energy can be captured and stored by thermal, electrical, chemical, and mechanical methods [164]. This can happen with or without a phase change. Storage medium, tube, insulation, heat exchangers, heat-transfer fluid, pumps or blowers, and controls are commonly found in the recognizable subsystem. The storage temperature(s) and the storage period are two factors to consider when selecting a thermal storage device. Some storage technologies are currently being demonstrated to add value to solar, but a cost reduction is needed to achieve broader profitability [165]. The storage shall possess the following properties to be very useful to the users: (a) storage properties—high storage capacity, long charge/discharge times, good partial-load feature, and acceptable round-trip efficiency and (b) financial performance—low price per kWh heat energy stored, easy to maintain, and environment friendly [166]. The storage systems are projected to have a combined power rating of 1–20 MW (charging and discharging) and a storage capacity of 2–6 hours for on-demand transmission to the electric grid [167].

Stand-alone PV solar home systems (SHSs) and solar lamps (which are collectively referred to as off-grid solar devices, as well as solar PV minigrids) are some of the modern solutions that have rapidly increased in popularity throughout the developing countries [168]. Rwanda declared goals to improve access to electricity to even more than 70 percent by 2018, out of which 22 percent will be by off-grid connections [169]. At least 9% of the citizens in at least ten territories—Benin, Burkina Faso, Fiji, Jordan, Kenya, Papua New Guinea, Rwanda, Samoa, Tanzania, and Vanuatu—has gained from off-grid solar lighting systems [169]. In Table 5, the report in 2018 compares Rwanda's success in terms of renewable energy access to that of other countries with comparable levels of growth. The Rwandan government has shown transparent and massive support for the off-grid solar sector and included it in its budget of Economic Development and Poverty Reduction Strategy II [170]. In Sub-Saharan countries, e.g., Rwanda like other countries, grid connections are typically only located in the urban centers and their neighborhoods. Electricity companies do not have enough generating capacity or facilities to increase access to electricity [171–173]. Due to the human landscape of the country, where a significant majority of the population reside in rural areas and smaller communities, widespread access to electricity by grid extension is extremely expensive [171, 174, 175].

Given high energy savings and high energy efficiency, CSP plants are expected to generate a global electricity supply of 7% by 2030 and 25% by 2050 and could reach up to 6% of the world's energy demand by 2030 and 12% by 2050, as per the European Solar Thermal Power Association's forecasts [7]. Many variables demand the need to broaden or diversify the energy generation mix of a nation. For its electricity production, Rwanda relies mainly on hydro and fossil fuels. This puts a lot of pressure on the country's budget as fossil fuel prices rise, particularly as the country imports more fuel to run its thermal power plants.

Research on the SWOT study of the RE sector in Rwanda suggests the following suggestions for policy makers and decision makers in the country to assist with the growth of the RE sector.

(i) Strengthen political regime: the country's stable politics of sustainability and development needs to be strengthened to further open up the country to domestic and foreign investments. The continuity of foreign direct investment (FDI) projects, in particular projects that are severely affected by current policies, is maintained by a stable political regime [176]. This is because FDI ventures are generally long-term investments, so investors prevent such investments in nations with risks that could adversely affect their potential return. In certain situations, political uncertainty leads to changes in policies, economic support, and legislation that pose a major challenge to FDI projects in the RE sector [177].

(ii) Foreign cooperation: because of the high initial investments necessary for RES growth, it is difficult for the country to fund large-scale power plants alone, hence the need for foreign participation. By offering consistent policy support that can survive any regime change, the government can encourage international cooperation

(iii) Enhance research and development: this sector is efficient with strong R&D, the higher the sector's production, the more energy generated, and therefore, it will be necessary for the government to take a serious look at R&D. A research fund for the sector needs to be set up where research centers can access funds to embark on their research. By setting up technology centers where such research can be sent for further study and commercialization if bankable, the situation where research performed by scientists is not commercialized can also be reduced

With broad consensus among various stakeholders, the SWOT analysis revealed several supporting and limiting factors. Due to solar energy abundance, Rwanda will be positively and significantly impacted if it is well exploited. Therefore, minigrids and PVs are mostly encouraged to get affordable electricity to the people. This is so because the solar power plant construction period is shorter and quicker than other forms of energy. This may positively impact the Rwandan economy as the price of energy may fall and people may access it more readily.

Nonetheless, the SWOT study found some risks that could prevent this from happening. A typical burden for the government to invest in new generation capacity has been the heavily subsidized electricity costs. Since most solar energy, especially CSP, requires a large financial investment to be bankable or feasible, a national policy based on recruiting investors might demonstrate the energy development potential in solar energy by generating new plans to privatize the solar energy market.

8. Conclusion

In general, Rwanda has already accepted the critical role of electricity in enhancing the health and living conditions of its citizens. To this end, the country has been working vigorously to increase the rate of electrification especially in rural and remote areas where the distribution of electricity is generally difficult. For example, the Sustainable Energy for All (SE4All) Initiative launched in 2011 was mainly to boost the contribution of energy from renewables in the overall energy mix. It was also initiated to serve as a direct response to the problems of electricity shortage that was observed in the country, especially in the regions far away from the grid connection. High energy cost has been a heavy burden for the low- and middle-income people and it has greatly affected both their economic growth and basic infrastructure development. In this study, we summarized the status quo of CSP and PV systems in Rwanda by considering their strengths, weaknesses, opportunities, and threats (SWOT). Also, we conducted the techno-economic assessment on the practicability of PV and CSP systems and implementation using the System Advisor Model (SAM). The results of the

study provide an overview of the features of the solar technologies available.

The input data used in the implementation of the SWOT analysis were obtained from relevant shareholders from the government, power producers, and operators of mini-grid off-grid private companies in Rwanda. The study examined the likelihood of finding a reliable and affordable power generation system by considering the accessibility of people in the low- and middle-income groups. This is because the electric grid is not widely available to the masses, especially to those living beyond urban areas where regular power outages lead to significant losses. When the grid is down, customers must absorb the loss of production or resort to the relatively high cost of diesel backup power. The techno-economic performance and financial metrics result from modeled PV and CSP systems using SAM are shown in Table 11. The net present value has proved that the viability of both PV and CSP is possible where the net capital investment for PV is low compared to that for CSP. Also, both the Levelized and the project internal rate of return showed that the investment can be returned after a short period for the PV system than for the CSP system. Therefore, the viability of CSP can be greatly influenced by the government budget as it requires lots of money; PV system design and implementation are preferred due to its low investment cost and payback period.

Recently, the implementation of huge hydropower projects in Rwanda has destroyed large areas of the country. Through the SWOT analysis and using the data from government, power producers, and mini-grid off-grid private companies, the scenarios for deploying the CSP and PV systems are recommended as the first choice to boost sustainable energy for all in Rwanda (achieving universal energy access). As Rwanda receives some of the highest levels of annual radiation globally, people have to understand the contribution that solar energy could make in enhancing access to energy for all using PV and CSP plants. Undoubtedly, renewable energy such as solar PV is one of the best technologies to tackle the issues of the rising of carbon emissions, as the former does not pose any threat to key conservation areas in the country. Accordingly, the proposed solar technologies could be applied to other rural areas in Sub-Saharan African countries and elsewhere in the world, particularly the regions with similar climate conditions and SWOT analysis factors.

From the very recent literature of the Rwanda power sector and elsewhere, the comparison summary describing the analysis of the SWOT methodology is provided in Table 7. In light of this, we believe that both the PV and CSP technologies can significantly boost the continued implementation of Sustainable Energy for All (Se4all) in Rwanda today, tomorrow, and beyond. Although our findings have shown that CSP systems have the potential of producing a large amount of electricity which can serve a big number of citizens and help to avoid frequent power outages in the country, the initial/upfront investment and material use pose a big barrier to the investor wherein a country like Rwanda, people can be exposed to the high cost of electricity. However, the CSP system is more advantageous for industrial use and other big projects and this study recommends the implementation of PV solar technology for general use (i.e.; to provide utility-scale electricity for the people who do not have access to electricity) to accelerate the universal electrification in Rwanda due to its availability, reliability, and affordability.

Data Availability

The data used to support the findings of this study are available from the corresponding author upon request.

Conflicts of Interest

The authors declare no conflict of interest.

Acknowledgments

This research was supported by the Natural Science Foundation of Fujian Province (Grant no. 2017J01728) and the Fujian University of Technology (Grant no. GY-H-20154).

References

[1] V. Quaschning, *Understanding Renewable Energy Systems - (Malestrom)*, Earthscan, 2005.

[2] International Energy Agency, *Solar energy perspectives*2020, http://www.eng.uc.edu/~beaucag/Classes/SolarPowerForAfrica/SolarEnergyPerspectives6111251e.pdf.

[3] B. Online, "Nuclear fusion energy 8.1," *Online*8–112011, http://www.pitt.edu/~tjs120/writing_assignment_3.pdf.

[4] "The future of solar is bright - science in the news," 2020, http://sitn.hms.harvard.edu/flash/2019/future-solar-bright/.

[5] A. Kumar, O. Prakash, and A. Dube, "A review on progress of concentrated solar power in India," *Renewable and Sustainable Energy Reviews*, vol. 79, pp. 304–307, 2017.

[6] M. S. Răboacă, G. Badea, A. Enache et al., "Concentrating solar power technologies," *Energies*, vol. 12, no. 6, pp. 1–17, 2019.

[7] Estela, Greenpeace, and SolarPACES, *Solar thermal electricity - global outlook 2016*, 2016.

[8] ASES, SolarPACES, SEIA, and EREN, "Concentrating solar power : energy from mirrors," *Energy Effic. Renew. energy*2001, http://www.nrel.gov/docs/fy01osti/28751.pdf.

[9] J. Jorgenson, M. Mehos, and P. Denholm, "Comparing the net cost of CSP-TES to PV deployed with battery storage," in *AIP Conference Proceedings*, vol. 1734, p. 080003, AIP Publishing LLC, 2016.

[10] J. D. D. Niyonteze, F. Zou, G. Norense Osarumwense Asemota, S. Bimenyimana, and G. Shyirambere, "Key technology development needs and applicability analysis of renewable energy hybrid technologies in off-grid areas for the Rwanda power sector," *Heliyon*, vol. 6, no. 1, article e03300, 2020.

[11] S. J. Wagner and E. S. Rubin, "Economic implications of thermal energy storage for concentrated solar thermal power," *Renewable Energy*, vol. 61, pp. 81–95, 2014.

[12] P. Hersch and K. Zweibel, "Basic photovoltaic principles and methods," *Antimicrobial Agents and Chemotherapy*, vol. 58, no. 12, pp. 7250–7257, 1982.

[13] W. Fuqiang, G. Zhennan, T. Jianyu, M. Lanxin, Y. Zhenyu, and T. Heping, "Transient thermal performance response characteristics of porous-medium receiver heated by multi-dish concentrator," *International Communications in Heat and Mass Transfer*, vol. 75, pp. 36–41, 2016.

[14] X. Chen, X. L. Xia, X. L. Meng, and X. H. Dong, "Thermal performance analysis on a volumetric solar receiver with double-layer ceramic foam," *Energy Conversion and Management*, vol. 97, pp. 282–289, 2015.

[15] T. Stoffel, D. Renné, D. Myers, and S. Wilcox, *Concentrating Solar Power Best Practices Handbook for the Collection and Use of Solar Resource Data*, National Renewable Energy Lab.(NREL), Golden, CO (United States), 2010.

[16] B. Belgasim, Y. Aldali, M. J. R. Abdunnabi, G. Hashem, and K. Hossin, "The potential of concentrating solar power (CSP) for electricity generation in Libya," *Renewable and Sustainable Energy Reviews*, vol. 90, pp. 1–15, 2018.

[17] A. Kassem, K. Al-Haddad, and D. Komljenovic, "Concentrated solar thermal power in Saudi Arabia: definition and simulation of alternative scenarios," *Renewable and Sustainable Energy Reviews*, vol. 80, pp. 75–91, 2017.

[18] Concentrating Solar Power, "Technology Roadmap Concentrating Solar Power," *Current*, vol. 5, pp. 1–52, 2010.

[19] J. J. C. S. Santos, J. C. E. Palacio, A. M. M. Reyes, M. Carvalho, A. J. R. Freire, and M. A. Barone, "Concentrating solar power," *Advances in Renewable Energies and Power Technologies*, vol. 1, pp. 373–402, 2018.

[20] M. I. Soomro, A. Mengal, Q. N. Shafiq, S. A. Ur Rehman, S. A. Soomro, and K. Harijan, "Performance improvement and energy cost reduction under Different scenarios for a parabolic Trough Solar Power Plant in the Middle-East Region," *Processes*, vol. 7, no. 7, p. 429, 2019.

[21] M. I. Soomro, A. Mengal, Y. A. Memon, M. W. A. Khan, Q. N. Shafiq, and N. H. Mirjat, "Performance and economic analysis of concentrated solar power generation for Pakistan," *Processes*, vol. 7, no. 9, p. 575, 2019.

[22] J. Liu, D. Lei, and Q. Li, "Vacuum lifetime and residual gas analysis of parabolic trough receiver," *Renewable Energy*, vol. 86, pp. 949–954, 2016.

[23] H. L. Zhang, J. Baeyens, J. Degrève, and G. Cacères, "Concentrated solar power plants: Review and design methodology," *Renewable and Sustainable Energy Reviews*, vol. 22, pp. 466–481, 2013.

[24] "Renewables global status report - REN21," 2021, https://www.ren21.net/reports/global-status-report/.

[25] A. Ummadisingu and M. S. Soni, "Concentrating solar power - technology, potential and policy in India," *Renewable and Sustainable Energy Reviews*, vol. 15, no. 9, pp. 5169–5175, 2011.

[26] S. Skouri, S. Bouadila, M. Ben Salah, and S. Ben Nasrallah, "Comparative study of different means of concentrated solar flux measurement of solar parabolic dish," *Energy Conversion and Management*, vol. 76, pp. 1043–1052, 2013.

[27] T. Mancini, P. Heller, B. Butler et al., "Dish-Stirling systems: an overview of development and status," *Journal of Solar Energy Engineering, Transactions of the ASME*, vol. 125, no. 2, pp. 135–151, 2003.

[28] T. Jennings and L. Parsons, "Concentrated Solar Power-Focusing the sun's energy for large-scale power generation," *Environmental and Energy Study Institute*, pp. 1–4, 2009.

[29] L. Martín and M. Martín, "Optimal year-round operation of a concentrated solar energy plant in the south of Europe," *Applied Thermal Engineering*, vol. 59, no. 1–2, pp. 627–633, 2013.

[30] L. Dawson and P. Schlyter, "Less is more: strategic scale site suitability for concentrated solar thermal power in Western Australia," *Energy Policy*, vol. 47, pp. 91–101, 2012.

[31] C. Breyer and G. Knies, "Global energy supply potential of concentrating solar power," 2009, 2020, http://www.desertec-uk.org.uk/reports/Breyer_paper_SolarPACES_GlobalEnergySupplyPotentialCSP_final_090630_proc.pdf.

[32] M. Krarti, "Integrated design of communities," in *Optimal design and retrofit of energy efficient buildings, communities, and urban centers*, pp. 385–470, Elsevier, 2018.

[33] I. Purohit and P. Purohit, "Techno-economic evaluation of concentrating solar power generation in India," *Energy Policy*, vol. 38, no. 6, pp. 3015–3029, 2010.

[34] O. M. Abubakar and B. I. Adamu, "Comparative study of monocrystalline and polycrystalline silicon solar modules in Kebbi state environment," vol. 10, no. 9, 2019, https://www.ijser.org/researchpaper/Comparative-Study-of-Monocrystalline-and-Polycrystalline-Silicon-Solar-Modules-in-Kebbi-State-Environment.pdf.

[35] ITRPV, "International technology roadmap for photovoltaics (ITRPV): Crystalline silicon technology-current status and outlook," in *Proceedings of the PV Manufacturing in Europe Conference*, pp. 18–40, Brussels, Belgium, 2017.

[36] A. K. S. David Tan, *Handbook for Solar Photovoltaic Systems*, Energy Mark. Authority, Singapore Publ., 2011.

[37] *Handbook for Solar Photovoltaic (PV) Systems Contents*2020, https://www.bca.gov.sg/publications/others/handbook_for_solar_pv_systems.pdf.

[38] "Rwanda | The Commonwealth," 2020, https://thecommonwealth.org/our-member-countries/rwanda.

[39] "Environmental and social management and framework for RSSP 3," *Rural Sector Support Project (RSSP 3)*2020, http://documents1.worldbank.org/curated/en/285631468336663680/text/E28960v10P126400Box369243B00PUBLIC0.txt.

[40] S. Bimenyimana, G. N. O. Asemota, and L. Li, "The state of the power sector in Rwanda: a progressive sector with ambitious targets," *Frontiers in Energy Research*, vol. 6, 2018.

[41] C. Museruka and A. Mutabazi, "Assessment of global solar radiation over Rwanda," in *2007 International Conference on Clean Electrical Power*, pp. 670–676, Capri, Italy, 2007.

[42] B. K. Safari and J. Gasore, "Estimation of global solar radiation in Rwanda using empirical models," *Asian Journal of Scientific Research*, vol. 2, no. 2, pp. 68–75, 2009.

[43] Rwanda Energy Group (REG), *Evaluation of the installed generation capacity*2020, https://www.reg.rw/index.php?id=2.

[44] C. Turchi, "Solar power and the electric grid grid 101: how does the electric grid work?," 2020, https://www.nrel.gov/docs/fy10osti/45653.pdf.

[45] "Rwanda economic update: making electricity accessible and affordable," 2020, https://www.worldbank.org/en/news/feature/2019/07/01/rwanda-economic-update-making-electricity-accessible-and-affordable.

[46] J. Polo, L. Martín, and J. M. Vindel, "Correcting satellite derived DNI with systematic and seasonal deviations: application to India," *Renewable Energy*, vol. 80, pp. 238–243, 2015.

[47] J. D. D. Uwisengeyimana, A. Teke, and T. Ibrikci, "Current overview of renewable energy resources in Rwanda," *Journal of Energy and Natural Resources*, vol. 5, no. 6, pp. 92–97, 2016.

[48] E. Kabir, P. Kumar, S. Kumar, A. A. Adelodun, and K. H. Kim, "Solar energy: potential and future prospects," *Renewable and Sustainable Energy Reviews*, vol. 82, pp. 894–900, 2018.

[49] "Solar resource maps and GIS data for 180+ countries | Solargis," 2020, https://solargis.com/maps-and-gis-data/download/rwanda.

[50] J. Uwibambe, *Design of photovoltaic system for rural electrification in Rwanda, [M. S. thesis]*, Universitetet i Agder; University of Agder, 2017, http://dr.ur.ac.rw/bitstream/handle/123456789/201/JeannineUwibambe.pdf?sequence=1&isAllowed=y.

[51] S. Bimenyimana, G. N. O. Asemota, J. D. D. Niyonteze, C. Nsengimana, P. J. Ihirwe, and L. Li, "Photovoltaic solar technologies: solution to affordable, sustainable, and reliable energy access for all in Rwanda," *International Journal of Photoenergy*, vol. 2019, Article ID 5984206, 29 pages, 2019.

[52] H. Eustache, D. Sandoval, U. G. Wali, and K. Venant, "Current status of renewable energy technologies for electricity generation in Rwanda and their estimated potentials," *Energy and Environmental Engineering*, vol. 6, no. 1, pp. 8–15, 2019.

[53] Rwanda Energy Group (REG), *Solar*2020, https://www.reg.rw/what-we-do/generation/solar/.

[54] G. Geoffrey, D. Zimmerle, and E. Ntagwirumugara, "Small hydropower development in Rwanda: trends, opportunities and challenges," *IOP Conference Series: Earth and Environmental Science*, vol. 133, no. 1, p. 012013, 2018.

[55] L. G. Rosa, J. Cruz Fernandes, and B. Li, "Structural integrity assessment of glass components in concentrated solar power (CSP) systems," *Theoretical and Applied Fracture Mechanics*, vol. 80, pp. 14–21, 2015.

[56] E. M. Framework, "Environmental and social management framework," May 2018, http://documents1.worldbank.org/curated/en/231671528451531272/pdf/SAIP-Environmental-and-Social-Management-Framework.pdf.

[57] "Rwanda's largest solar field also empowers orphans | Voice of America - English," 2020, https://www.voanews.com/silicon-valley-technology/rwandas-largest-solar-field-also-empowers-orphans.

[58] "Rwanda energy sector review and action plan," 2020, https://www.afdb.org/fileadmin/uploads/afdb/Documents/Project-and-Operations/Rwanda_-_Energy_Sector_Review_and_Action_Plan.pdf.

[59] X.-z. Li, Z.-j. Chen, X.-c. Fan, and Z.-j. Cheng, "Hydropower development situation and prospects in China," *Renewable and Sustainable Energy Reviews*, vol. 82, pp. 232–239, 2018.

[60] M. Dorber, R. May, and F. Verones, "Modeling net land occupation of hydropower reservoirs in Norway for use in life cycle assessment," *Environmental Science & Technology*, vol. 52, no. 4, pp. 2375–2384, 2018.

[61] S. Pacca and A. Horvath, "Greenhouse gas emissions from building and operating electric power plants in the upper Colorado river basin," *Environmental Science & Technology*, vol. 36, no. 14, pp. 3194–3200, 2002.

[62] D. V. Spitzley and G. A. Keoleian, "Life cycle environmental and economic assessment of willow biomass electricity: a comparison with other renewable and non-renewable sources | Center for Sustainable Systems," 2011, http://css.umich.edu/publication/life-cycle-environmental-and-economic-assessment-willow-biomass-electricity-comparison.

[63] D. Pimentel and M. H. Pimentel, "Renewable energy: current and potential issues," in *Food, Energy, and Society*, vol. 52-no. 12pp. 259–276, CRC Press, 2007.

[64] F. Brihmat and F. B. S. Mekhtoub, "PV cell temperature / PV power output relationships Homer methodology calculation," *Conférence Internationale des Energies Renouvelables" CIER'13"/International Journal of Scientific Research & Engineering Technology*, vol. 2, no. 1, pp. 1–12, 2014.

[65] V. Fthenakis and H. C. Kim, "Land use and electricity generation: a life-cycle analysis," *Renewable and Sustainable Energy Reviews*, vol. 13, no. 6–7, pp. 1465–1474, 2009.

[66] D. Dusabe, J. L. Munda, and A. A. Jimoh, "Small scale solar energy systems in Rwanda: status and sustainability," *International Conference Domestic Use Energy*, vol. 2009, pp. 1–6, 2009.

[67] "Solar home systems," 2021, https://www.reg.rw/what-we-do/offgrid-solutions/solar-home-systems/.

[68] Rwanda Energy Group, "Electricity access," 2021, https://www.reg.rw/what-we-do/access/.

[69] Rwanda Energy Group (REG), "Mini-grids," 2021, http://www.reg.rw/what-we-do/offgrid-solutions/mini-grids/.

[70] "Rwanda off-grid sector status report PDF free download," 2021, https://docplayer.net/amp/151460710-Rwanda-off-grid-sector-status-report-2018.html.

[71] I. Bisaga, "Scaling up off-grid solar energy access through improved understanding of customers ' needs, aspirations and energy use of decentralised (SMART) solar home systems – a case study of BBOXX customers in Rwanda," p. 401, 2018, https://discovery.ucl.ac.uk/id/eprint/10069395/13/Bisaga_10069395_thesis_redacted_id_removed.pdf.

[72] G. I. Rashed, G. Shyirambere, and G. Gasore, "Applicability study of battery charging stations in off-grid for rural electrification – the case of Rwanda," in *Advances in Natural Computation, Fuzzy Systems and Knowledge Discovery*, vol. 1075, pp. 272–283, Springer, 2020.

[73] A. Yadoo and H. Cruickshank, "The role for low carbon electrification technologies in poverty reduction and climate change strategies: a focus on renewable energy mini-grids with case studies in Nepal, Peru and Kenya," *Energy Policy*, vol. 42, pp. 591–602, 2012.

[74] K. J. Warner and G. A. Jones, "Energy and population in Sub-Saharan Africa: energy for four billion?," *Environments*, vol. 5, no. 10, pp. 107–119, 2018.

[75] "Indicators. Washington: The World Bank; c2021 – [cited 2021]," 2021, https://data.worldbank.org/indicator.

[76] H. E. Murdock, D. Gibb, and T. André, *Renewables 2019 Global Status Report*, vol. 8, Tech. Rep. 3, REN21, 2019.

[77] "Rwanda–A Case Study in Solar Energy Investment on JSTOR," 2021, https://www.jstor.org/stable/26256477?seq=1.

[78] V. Kizilcec, P. Parikh, and I. Bisaga, "Examining the Journey of a Pay-as-You-Go Solar Home System Customer : A Case Study of Rwanda," *Energies*, vol. 14, no. 2, p. 330, 2021.

[79] J. B. Alonso, P. Sandwell, and J. Nelson, "The Potential for Solar-Diesel Hybrid Mini-Grids in Refugee Camps: A Case Study of Nyabiheke Camp, Rwanda," *Sustainable Energy Technologies and Assessments*, vol. 44, article 101095, 2019.

[80] G. N. O. Asemota, "Rwanda's Off-Grid Solar Performance Targets," *Joule*, vol. 5, no. 1, pp. 22-23, 2021.

[81] I. Bisaga, P. Parikh, J. Tomei, and L. S. To, "Mapping synergies and trade-offs between energy and the sustainable development goals: a case study of off-grid solar energy in Rwanda," *Energy Policy*, vol. 149, article 112028, 2020.

[82] M. Grimm, L. Lenz, J. Peters, and M. Sievert, "Demand for off-grid solar electricity: experimental evidence from Rwanda," *Journal of the Association of Environmental and Resource Economists*, vol. 7, no. 3, pp. 417–454, 2020.

[83] C. Brunet, O. Savadogo, P. Baptiste et al., "The three paradoxes of the energy transition - assessing sustainability of large-scale solar photovoltaic through multi-level and multi-scalar perspective in Rwanda," *Journal of Cleaner Production*, vol. 288, article 125519, 2021.

[84] C. Nsengimana, X. T. Han, and L. L. Li, "Comparative analysis of reliable, feasible, and low-cost photovoltaic microgrid for a residential load in Rwanda," *International Journal of Photoenergy*, vol. 2020, Article ID 8855477, 14 pages, 2020.

[85] W. Paper, R. E. Papers, and R. Economic, 2018, https://www.econstor.eu.

[86] G. Bamundekere, *Contributions of renewable energy to sustainable development in Africa: case study of solar energy in Rwanda*, PAUWES, 2019.

[87] J. D. D. Niyonteze, F. Zou, G. N. O. Asemota, and S. Bimenyimana, "solar-powered mini-grids and smart metering systems, the solution to Rwanda energy crisis," *Journal of Physics: Conference Series*, vol. 1311, article 012002, 2019.

[88] R. Kennedy, S. Numminen, J. Sutherland, and J. Urpelainen, "Multilevel customer segmentation for off-grid solar in developing countries: evidence from solar home systems in Rwanda and Kenya," *Energy*, vol. 186, 2019.

[89] H. Gloria, H. Olivier, and I. M. Angella, "Contribution of solar energy for sustainable urban development in Rwanda," *Civil Engineering and Architecture*, vol. 7, no. 6, pp. 271–277, 2019.

[90] M. J. Felix, O. C. Uche, and O. P. Anthony, "Potential of solar and wind energy for large scale power generation in eastern region of Rwanda," vol. 1, no. 2, pp. 135–140, 2019.

[91] A. Mushimiyimana, *Domestic Solar Energy as Solution for Non-Connected Rural Areas [Ph.D. thesis]*, University of Rwanda, 2019.

[92] B. Soltowski, D. Campos-Gaona, S. Strachan, and O. Anaya-Lara, "Bottom-up electrification introducing new smart grids architecture-concept based on feasibility studies conducted in Rwanda," *Energies*, vol. 12, no. 12, p. 2439, 2019.

[93] R. Muvunyi, *Viability of Micro Hydro–Solar PV Hybrid in Rural Electrification in Rwanda [Ph.D. thesis]*, University of Rwanda, 2019.

[94] A. Munyaneza, K. Kaberere, and M. K. W. Mangoli, "Optimal design of a solar photovoltaic mini-grid for electrifying Rwumba village of Rwanda," *International Journal of Engineering Technology and Scientific Innovation*, vol. 4, no. 5, pp. 272–284, 2019.

[95] J. Rodríguez-Manotas, P. L. Bhamidipati, and J. Haselip, "Getting on the ground: exploring the determinants of utility-scale solar PV in Rwanda," *Energy Research & Social Science*, vol. 42, pp. 70–79, 2018.

[96] S. Bimenyimana, G. N. O. Asemota, and P. J. Ihirwe, "Optimization comparison of stand-alone and grid-tied solar PV systems in Rwanda," *OALib*, vol. 5, no. 5, pp. 1–18, 2018.

[97] N. J. Williams, P. Jaramillo, and J. Taneja, "An investment risk assessment of microgrid utilities for rural electrification using the stochastic techno-economic microgrid model: a case study in Rwanda," *Energy for Sustainable Development*, vol. 42, pp. 87–96, 2018.

[98] J. B. Rutibabara, *Environmental and Economic Cost Analysis of a Solar PV, Diesel and hybrid PV-Diesel water Pumping Systems for Agricultural Irrigation in Rwanda: Case study of Bugesera district [M. S. thesis]*, PAUWES, 2018.

[99] E. Nshimiyimana, *Design of Home Electricity Supply System Using Solar PV and Its Integration to the National Grid: A Case Study of Masaka Village [M. S. thesis]*, PAUWES, 2018.

[100] N. Lameck, "Design and Optimisation of PV-Biogas Hybrid system for rural electrification in Rwanda," 2018.

[101] N. Emmanuel, C. W. Wabuge, and M. K. Mang'oli, *Design of Solar–Wind Hybrid System for Rural Electrification in Rwanda*, 2017.

[102] J. Uwibambe and A. Prior, *Design of photovoltaic system for rural electrification in rwanda [M. S. thesis]*, Universitetet i Agder; University of Agder, 2017.

[103] G. Ituze, *Evaluation Of A Hybrid Solar Photovoltaic-Bioenergy System For Powering Remote Dwelling In Rwanda [M. S. thesis]*, PAUWES, 2017.

[104] M. Cyulinyana and H. Winkler, "Surface solar spectrum characteristics in tropical regions with specific reference to Rwanda," *Energy Procedia*, vol. 142, pp. 545–551, 2017.

[105] M. Rwema, *Hydro, solar and wind: energy policy implication in renewable energy deployment in Rwanda*, Pan African University, 2017.

[106] H. Ma and H. Ma, *Development and Design of a Portable Off-Grid Photovoltaic System with Contingency Functions for Rural Areas (Case Study Rwanda) Shaida Faiqi*, DiVA, 2017.

[107] I. Bisaga, N. Puźniak-Holford, A. Grealish, C. Baker-Brian, and P. Parikh, "Scalable off-grid energy services enabled by IoT: a case study of BBOXX SMART Solar," *Energy Policy*, vol. 109, pp. 199–207, 2017.

[108] S. H. Kuppa and D. J. Zimmerle, "Statistical failure estimation method to size off-grid electrical systems for villages in developing countries," in *2017 IEEE Global Humanitarian Technology Conference (GHTC)*, pp. 1–6, San Jose, CA, USA, 2017.

[109] S. Bimenyimana, G. N. O. Asemota, and L. Li, "Maximum power point performance tracking comparison between incremental conductance with perturb and observe algorithms in photovoltaic power systems," in *2017 2nd Int. Conf. Power Renew. Energy, ICPRE 2017*, pp. 919–924, Chengdu, September 2017.

[110] S. Collings and A. Munyehirwe, "Pay-as-you-go solar pv in rwanda: evidence of benefits to users and issues of affordability," *Field Actions Science Reports*, vol. 2016, no. Special Issue 15, pp. 94–103, 2016.

[111] M. Grimm, A. Munyehirwe, J. Peters, and M. Sievert, "A first step up the energy ladder? Low cost solar kits and household's welfare in rural Rwanda," *World Bank Economic Review*, vol. 31, no. 3, pp. lhw052–lhw649, 2016.

[112] H. G. Beyer and F. Habyrarimana, "Detailed information on irradiance characteristics in Central Africa (Rwanda) from a dedicated network of ground stations and satellite derived data," vol. 2013, pp. 1–7, 2017.

[113] D. Nshimiyimana, *Sizing of a hybrid solar PV-wind-fuel cell power system for isolated location*, PAUWES, 2016.

[114] M. Karugarama, *Masters thesis: mitigation of blackout in Kigali using a microgrid with advanced energy storage and solar photovoltaics*, Virginia Polytech. Inst. State Univ., 2015.

[115] A. F. Crossland, O. H. Anuta, and N. S. Wade, "A socio-technical approach to increasing the battery lifetime of off-grid photovoltaic systems applied to a case study in Rwanda," *Renewable Energy*, vol. 83, pp. 30–40, 2015.

[116] Z. Srdjevic, R. Bajcetic, and B. Srdjevic, "Identifying the criteria set for multicriteria decision making based on SWOT / PESTLE analysis : a case study of reconstructing a water

intake structure," *Water Resources Management*, vol. 26, no. 12, pp. 3379–3393, 2012.

[117] J. Terrados, G. Almonacid, and L. Hontoria, "Regional energy planning through SWOT analysis and strategic planning tools.: Impact on renewables development," *Renewable and Sustainable Energy Reviews*, vol. 11, no. 6, pp. 1275–1287, 2007.

[118] K. C. Wang, "A process view of SWOT analysis," in *Int. Soc. Syst. Sci. -51st Annu. Meet. Int. Soc. Syst. Sci. ISSS 2007*, pp. 484–495, Tokyo, Japan, 2007.

[119] Rwanda Energy Group (REG), "Offgrid , 2020," 2020, https://www.reg.rw/what-we-do/access/offgrid/.

[120] *Solar energy distributions and manufactures in Rwanda*, Rwanda | Sun-Connect-News, 2020, https://www.sun-connect-news.org/de/databases/distributorsmanufacturers/rwanda/.

[121] "Third Rwanda energy sector development policy financing," 2020, http://documents1.worldbank.org/curated/en/139261567389640856/pdf/Rwanda-Third-Rwanda-Energy-Sector-Development-Policy-Financing-Project.pdf.

[122] "The World Bank, Rwanda energy sector development policy financing," 2019, 2020, http://documents1.worldbank.org/curated/en/139261567389640856/pdf/Rwanda-Third-Rwanda-Energy-Sector-Development-Policy-Financing-Project.pdf.

[123] Mininstry of Infrastructures, Rwanda Energy Group, "Review Assessment of current electrification programs," 2020, http://www.reg.rw/fileadmin/user_upload/Task_Design_of_the_National_Electrification_Plan_in%20Rwanda_Report.pdf.

[124] "Off-Grid Solar Market Assessment Rwanda Power Africa Off-grid Project," 2019, 2020, https://sun-connect-news.org/fileadmin/DATEIEN/Dateien/New/PAOP-Rwanda-MarketAssessment-Final_508.pdf.

[125] B. K. Sovacool, A. Gilbert, and D. Nugent, "An international comparative assessment of construction cost overruns for electricity infrastructure," *Energy Research and Social Science*, vol. 3, no. C, pp. 152–160, 2014.

[126] I. Renewable and E. Agency, *Concentrating Solar Power*, International Renewable Energy Agency (IRENA), 2013.

[127] E. B. Agyekum, V. I. Velkin, and I. Hossain, "Sustainable energy : is it nuclear or solar for African countries? Case study on Ghana," *Sustainable Energy Technologies and Assessments*, vol. 37, p. 100630, 2020.

[128] A. Scott, "Building electricity supplies in Africa for growth and universal access," 2020, https://newclimateeconomy.report/workingpapers/wp-content/uploads/sites/5/2016/04/Building-Electricity-Supplies-in-Africa_NCE_final.pdf.

[129] M. Grimm, L. Lenz, J. Peters, and M. Sievert, "Demand for off-grid solar electricity: experimental evidence from Rwanda," 2016, 2020, http://ftp.iza.org/dp10427.pdf.

[130] G. R. Timilsina, L. Kurdgelashvili, P. A. N. The, and W. Bank, "A review of solar energy markets, economics and policies," 2011, 2020, http://documents1.worldbank.org/curated/en/546091468178728029/pdf/WPS5845.pdf.

[131] "Catalyzing global markets for off-grid energy access," 2016, 2020, https://clasp.ngo/en/Resources/Resources/Headlines/2015/EA-EE-Using-Energy-Efficiency-to-Enhance-Energy-.

[132] "Rwanda Energy Group, investment /Opportunities," 2020, https://www.reg.rw/what-we-do/investments/opportunities/.

[133] "2019 Rwanda voluntary national review (VNR) report," 2019, 2020, https://sustainabledevelopment.un.org/content/documents/23432Rwanda_VNR_Document__Final.pdf.

[134] "Rwanda: off-grid sector status report 2017," 2020, https://endev.info/images/6/69/EnDev_Rwanda_-_Off-Grid_Sector_Status_Report_2017.pdf.

[135] "Rwanda energy situation - energypedia.info," 2020, https://energypedia.info/wiki/Rwanda_Energy_Situation.

[136] R. Shabaneh and F. Tomas, *Identifying the roadblocks for energy access: a case study for Eastern Africa ' s gas*, King Abdullah Petroleum Studies and Research Center, 2018.

[137] M. A. Lima, L. F. R. Mendes, G. A. Mothé et al., "Renewable energy in reducing greenhouse gas emissions: reaching the goals of the Paris agreement in Brazil," *Environmental Development*, vol. 33, article 100504, 2020.

[138] O. Edenhofer, *IPCC, 2011: Summary for Policymakers*, IPCC Special Report on Renewable Energy Sources and Climate Change Mitigation, 2011.

[139] "World Energy outlook 2017 – analysis - IEA," 2020, https://www.iea.org/reports/world-energy-outlook-2017.

[140] G. F. Nemet, "Beyond the learning curve: factors influencing cost reductions in photovoltaics," *Energy Policy*, vol. 34, no. 17, pp. 3218–3232, 2006.

[141] "Rural electrification strategy," 2016, 2020, https://www.mininfra.gov.rw/fileadmin/user_upload/aircraft/Rural_Electrification_Strategy.pdf.

[142] I Renewable Energy Agency, "Africa's renewable future: the path to sustainable growth," 2020, https://www.irena.org/documentdownloads/publications/africa_renewable_future.pdf.

[143] "IOB evaluation access to energy in Rwanda impact evaluation of activities supported by the Dutch Promoting Renewable Energy Programme," 2020, https://www.oecd.org/derec/netherlands/Access-to-Energy-in-Rwanda.pdf.

[144] W Bank Group, "Growing affordable grid and off grid access while slimming subsidies," 2019, 2020, https://olc.worldbank.org/system/files/133963-BRI-PUBLIC-23-1-2019-12-26-0-CountryBriefRwanda.pdf.

[145] IRENA, "Scaling up renewable energy deployment in Africa detailed overview of IRENA'S engagement and impact," 2020, 2020, https://www.irena.org/-/media/Files/IRENA/Agency/Publication/2020/Feb/IRENA_Africa_Impact_Report_2020.pdf?la=en&hash=B1AD828DFD77D6430B93185EC90A0D1B72D452CC.

[146] "Barriers to renewable energy technologies development," 2020, https://www.energytoday.net/economics-policy/barriers-renewable-energy-technologies-development/.

[147] M. T. Islam, N. Huda, and R. Saidur, "Current energy mix and techno-economic analysis of concentrating solar power (CSP) technologies in Malaysia," *Renewable Energy*, vol. 140, pp. 789–806, 2019.

[148] H. Zou, H. Du, M. A. Brown, and G. Mao, "Large-scale PV power generation in China: a grid parity and techno-economic analysis," *Energy*, vol. 134, pp. 256–268, 2017.

[149] K. Say, M. John, R. Dargaville, and R. T. Wills, "The coming disruption: the movement towards the customer renewable energy transition," *Energy Policy*, vol. 123, pp. 737–748, 2018.

[150] N. Blair et al., "System advisor model (SAM) general description," no. NREL/TP-6A20-70414, 2018, https://www.nrel.gov/docs/fy18osti/70414.pdf.

[151] A. Jain, R. Mehta, and S. K. Mittal, "Modeling impact of solar radiation on site selection for solar PV power plants in India," *International Journal of Green Energy*, vol. 8, no. 4, pp. 486–498, 2011.

[152] S. E. Trabelsi, R. Chargui, L. Qoaider, A. Liqreina, and A. A. Guizani, "Techno-economic performance of concentrating solar power plants under the climatic conditions of the southern region of Tunisia," *Energy Conversion and Management*, vol. 119, pp. 203–214, 2016.

[153] A. Aly, S. S. Jensen, and A. B. Pedersen, "Solar power potential of Tanzania: identifying CSP and PV hot spots through a GIS multicriteria decision making analysis," *Renewable Energy*, vol. 113, pp. 159–175, 2017.

[154] E. B. Agyekum, "Techno-economic comparative analysis of solar photovoltaic power systems with and without storage systems in three different climatic regions, Ghana," *Sustainable Energy Technologies and Assessments*, vol. 43, article 100906, 2021.

[155] J. Alonso-Montesinos, J. Polo, J. Ballestrín, F. J. Batlles, and C. Portillo, "Impact of DNI forecasting on CSP tower plant power production," *Renewable Energy*, vol. 138, pp. 368–377, 2019.

[156] IRENA, *Renewable Power Generations Costs*, International Renewable Energy Agency (IRENA), 2018.

[157] J. O. Oladigbolu, M. A. M. Ramli, and Y. A. Al-Turki, "Techno-economic and sensitivity analyses for an optimal hybrid power system which is adaptable and effective for rural electrification: a case study of Nigeria," *Sustainability*, vol. 11, no. 18, p. 4959, 2019.

[158] A. K. Abu-Rumman, "JARIE_Volume 4_Issue 4_Pages 252-258," *Journal of Applied Research on Industrial Engineering*, vol. 4, pp. 1–7, 2017.

[159] W. Short, D. Packey, and T. Holt, "A manual for the economic evaluation of energy efficiency and renewable energy technologies," *Renawable Energy*, vol. 95, pp. 73–81, 1995.

[160] E. Drury, P. Denholm, and R. Margolis, *The impact of different economic performance metrics on the perceived value of solar photovoltaics*, Tech. Rep., 2011.

[161] S. Martín-Martínez, M. Cañas-Carretón, A. Honrubia-Escribano, and E. Gómez-Lázaro, "Performance evaluation of large solar photovoltaic power plants in Spain," *Energy Conversion and Management*, vol. 183, pp. 515–528, 2019.

[162] N. Blair, C. Christensen, M. Mehos, and C. Cameron, "Modeling photovoltaic and concentrating solar power trough performance, cost, and financing with solar advisor model," in *Am. Sol. Energy Soc. - Sol. 2008, Incl. Proc. 37th ASES Annu. Conf., 33rd Natl. Passiv. Sol. Conf., 3rd Renew. Energy Policy Mark. Conf. Catch Clean Energy Wave*, vol. 2, pp. 1051–1076, USA, 2008.

[163] A. Dobos, T. Neises, and M. Wagner, "Advances in CSP simulation technology in the system advisor model," *Energy Procedia*, vol. 49, pp. 2482–2489, 2014.

[164] G. Alva, L. Liu, X. Huang, and G. Fang, "Thermal energy storage materials and systems for solar energy applications," *Renewable and Sustainable Energy Reviews*, vol. 68, pp. 693–706, 2017.

[165] W. A. Braff, J. M. Mueller, and J. E. Trancik, "Value of storage technologies for wind and solar energy," *Nature Climate Change*, vol. 6, no. 10, pp. 964–969, 2016.

[166] Y. Ding, Y. Li, C. Liu, and Z. Sun, *Solar Electrical Energy Storage*, Elsevier Ltd., 2015.

[167] A. Thesis, *Optimal implementation of energy storage systems in power distribution networks*, Convers. Congr., 2012, http://conservancy.umn.edu/handle/11299/132215.

[168] "The 2018 global off-grid solar market trends report / Lighting Global," 2021, https://www.lightingglobal.org/2018-global-off-grid-solar-market-trends-report/.

[169] D. Henner and REN21, *Renewables 2020 Global Status Report*, REN21, 2017, https://www.ren21.net/wp-content/uploads/2019/05/GSR2017_Full-Report_English.pdf'13.

[170] F. I. Monetary, *Rwanda: poverty reduction strategy paper; IMF Country Report; 2013-2018*, Tech. Rep. 13, International Monetary Fund, 2013.

[171] M. T. S. C. Alleyne and M. M. Hussain, *Energy subsidy reform in Sub-Saharan Africa: Experiences and lessons*, International Monetary Fund, 2013.

[172] A. Eberhard, O. Rosnes, M. Shkaratan, and H. Vennemo, *Africa's power infrastructure: investment, integration, efficiency*, The World Bank, 2011.

[173] A. Eberhard, V. Foster, C. Briceño, F. Ouedraogo, and M. Shkaratan, *Africa infrastructure underpowered : the state of the power sector in Sub-Saharan Africa*, World Bank, 2008.

[174] A. Eberhard and M. Shkaratan, "Powering Africa: meeting the financing and reform challenges," *Energy Policy*, vol. 42, pp. 9–18, 2012.

[175] A. W. Bank and B. Practice, *Rural energy and development: improving energy supplies for 2 billion people – a World Bank best practice paper*, World Bank, 1996.

[176] E. Asiedu, "On the determinants of foreign direct investment to developing countries : is Africa different?," *World Development*, vol. 30, no. 1, 2002.

[177] A. R. Ikeeley and Y. Ikeda, "Determinants of foreign direct investment in wind energy in developing countries," *Journal of Cleaner Production*, vol. 161, pp. 1451–1458, 2017.

Hindawi
International Journal of Photoenergy
Volume 2021, Article ID 6690128, 10 pages
https://doi.org/10.1155/2021/6690128

Research Article

Thermal Performance Study on a Sensible Cool Thermal Energy Storage System for Building Air-Conditioning Applications

Kesavan Muthaiyan,[1] **Chidambaram Lakshmanan**,[1] **Kaiwalya Raj**,[2] **Mangat Ram Sharma**,[2] **Rajamani Narayanasamy**,[2] **Pandiyarajan Vellaichamy**,[3] **and Velraj Ramalingam**[2]

[1]*Mechanical Engineering, Annamalai University, Annamalainagar, 608002, India*
[2]*Institute for Energy Studies, CEG, Anna University, Chennai 600 025, India*
[3]*Department of Chemical Engineering, Anna University, Chennai 600 025, India*

Correspondence should be addressed to Kesavan Muthaiyan; kesavanapme@gmail.com

Received 11 December 2020; Revised 29 January 2021; Accepted 26 May 2021; Published 8 June 2021

Academic Editor: Kumarasamy Sudhakar

Copyright © 2021 Kesavan Muthaiyan et al. This is an open access article distributed under the Creative Commons Attribution License, which permits unrestricted use, distribution, and reproduction in any medium, provided the original work is properly cited.

In most developed and developing nations, nearly 40% of the energy generated is utilized in the building sector, in which nearly 50% of the energy is consumed by building cooling/heating systems. However, the energy requirement for building cooling/heating varies continuously with respect to time. Hence, in hot countries, if the cooling system is integrated with a storage system, the cooling system need not be designed for the peak load requirement. Further, this kind of storage system is very useful and economically beneficial in the scenario of dynamic electricity tariff, being introduced in many countries in the emerging renewable energy scenario to solve the grid stability issues. Further, it is very useful to promote microgrid with distributed renewable power generation. Considering the above, the major objective of the present research is to demonstrate the integration of the air-conditioning system with a sensible heat storage unit for residential applications. An experimental setup is constructed, and experiments were conducted to evaluate the heat exchange behavior during the charging and discharging process by varying the inlet temperature and the mass flow rate of the heat exchange fluid through the circuit. It is observed that the set temperature of the cool storage tank is to be maintained above +5°C to achieve better efficiency during the charging process. During the discharging process, the room could be maintained at the required comfort condition for a duration of 285 min with 29 cycles of operations between the set point temperature limits of 25°C to 28°C. When the inlet brine temperature of the cooling unit reached 20°C, in the next cycle, bringing down the room temperature again to 25°C could not be achieved. The results shown in this work are beneficial for efficiently operating the cooling system and useful in promoting renewable energy in the near future in the building sector. Also, the low-temperature sensible heat storage system is capable of maintaining the storage temperature at approximately +4°C, instead of -4°C normally employed in the case of latent heat-based storage system that allows higher performance in the sensible heat storage system.

1. Introduction

The development of a nation mostly depends on the production of power, effective utilization of energy, and environmental condition. In most developed and developing nations, the energy consumption by the building sector is nearly 40% of the total energy produced [1]. In hot climatic countries like India, the major share of energy is utilized in buildings by large capacity AC units that consume approximately 50% of the energy spent on building [2]. Hence, these countries near the equator spend nearly 20% (50% of 40%) of the total power generated for air-conditioning. Hence, scientists are targeting the energy-intensive air-conditioning sector, for energy efficiency, building demand-side management, and the introduction of renewable energy. In the recent years, there are different control strategies established in the air-conditioning for energy-efficient operation of the chiller system. Further, the load requirement in the central air-conditioning system is very high during the afternoon hours, particularly in the commercial buildings. Accordingly, the

chiller systems are designed to meet the peak load demand, and hence, the capacity of the chiller is usually more than twice the average load requirement. Considering the above, the cool thermal storage systems are introduced in some of the building air-conditioning systems between the chiller and the air-handling units, thereby the chiller capacity requirement could be reduced to 50% of the peak load requirement. The various research work available in the literature about this kind of storage system in the present energy scenario is detailed in this section.

Sebzali et al. [3] demonstrated the employment of the chilled water energy storage (CWES) system, which for any design day condition, reduced the peak electricity demand and annual energy consumption for AC systems in the range of 36.7%-87.5% and 4.5%-6.9%, respectively, compared with conventional cooling systems, where pumps and chillers extensively contributed to reduction in energy consumption. They showed that a load-leveling strategy applied to the CWES system resulted in the lowest life cycle cost (LCC) compared to full storage and 50% demand limiting strategies and was the most cost-effective choice for both the electric utilities and the consumers. Lin et al. [4] studied the impact of energy-saving by incorporating LTSHS along with the air-conditioning system. Two systems were studied: one system used chilled storage technology, and the other system utilized some parts of chilled water back from the user. They concluded that both systems could save energy and power cost compared with traditional chilled storage systems. Velraj et al. [5] studied the integration of the cool thermal energy storage (CTES) system, along with a large building AC system. The authors mentioned various advantages of the coupled system and also demonstrated a saving of INR 2.26 million per annum with the storage integrated system for the building considered in their work.

Kim et al. [6] examined the thermal performance of the thermal energy storage (TES) integrated outdoor air system used in a daycare center located in Jincheon. The results indicated an increase in total cooling load by 48% and a saving of up to 38% in the energy consumption than existing systems. Yan et al. [7] described an optimization method for the combined cool storage (CCS) system where the cool energy for the building cooling in summer was provided by the CWES system, which utilized the cool energy from the heat pipe-based seasonal ice storage wherein the low ambient temperature was used to freeze the ice. The optimization methodology was also implemented in a real building situated in Beijing. Their results showed that compared to the conventional cooling system, the proposed CCS system in the building could reduce the operational cost, annual electricity consumption, and life-cycle cost by 76%, 22%, and 40%, respectively.

Boonnasa and Namprakai [8] reported an approach to find the optimal chilled water energy storage (CWES) capacity and operating strategies for the AC loads at various electricity tariffs. They concluded that the continuous operation of the CWES system comprising two chiller units of cooling capacity 450 TR each, a cool storage of 9413 ton-hr, and volume of 5175 m^3 was found to be suitable. Further, 35.7% of energy consumption was shifted from the on-peak to the off-peak periods. They also concluded that the nighttime operation of the mechanical chiller could increase the COP of the cooling chiller. Sebzali and Rubini [9] studied the effect of integrating the CWES system with air-cooled chillers and its impact on the energy performance for the Kuwaiti climate. They showed that the results for the peak design day, chillers operating with demand limiting, and load-leveling partial storage strategies resulted in 4% higher energy consumption than a conventional system. The full storage strategy resulted in a 4% lower energy consumption compared to the conventional system. Therefore, it was concluded that the full storage strategy operated CWES system was the optimal choice for the Kuwaiti climate.

Song et al. [10] studied the economic viability of the implementation of ice storage and chilled water storage combined LTSHS system for building cooling applications. They concluded that the addition of an ice thermal storage system into an existing CWES system significantly reduced the design day operating cost. Lin et al. [11] presented a methodology to evaluate the thermoeconomic performance of a CWES system in which the return cool water (i.e., from the load side) was mixed with the supplied chilled water (i.e., from the chiller side). Operation cost and exergy consumption were cut down by 15% for the above system compared with the CWES system, which directly utilized chilled water at 5°C. Henze et al. [12] developed a program to optimize the chiller operation and the storing/extracting (i.e., cool energy) strategies of the CWES system. Due to more cooling demand in a pharmaceutical building that already had ten chillers installed, an investigation was done to find the viable option between adding an extra chiller and integrating the CWES system. The program developed was also utilized to find the economic and operational benefits of installing a CWES system over the addition of an extra chiller. It was concluded that the integration of a CWES system was expected to provide energy cost savings. The incorporation of the CWES system in the existing cooling system improved the availability and the reliability.

Rosiek and Garrido [13] studied the performance of a solar-thermal operated vapour absorption chiller system with chilled water storage tanks for building cooling application. It was noticed that the efficiency of the solar-assisted cooling system got improved owing to the reduction in chiller on/off cycles due to the incorporation of chilled water storage tanks. Also, a maximum saving in water resource consumption, total electrical energy consumption, and CO_2 emission was found to be about 30%, 20%, and 1.7 tons, respectively, for the summer. Rosiek and Batlles [14] demonstrated a new operation strategy in monitoring real-time occupancy for a solar-assisted VARS-based air-conditioning system incorporated with chilled-water storage tanks to improve the system efficiency. It was found that the reduction in CO_2 emission and total electrical energy usage was nearly 1.3 tons and 42%, respectively. Mohammadi et al. [15] had introduced a methodology of enhancement for the day ahead planning of a multichiller framework consolidated with chilled-water storage. The modeling is done in GAMS software, and CONOPT was used as a solver. Four units of 2900 ton capacity multichiller system were used for simulation. The results

show that the storage unit increased the robustness of the total cost against the variation in the cooling load. It was concluded that the storage unit was more efficient for the unit having a high cooling load during peak hours.

Alva et al. [16] reviewed different aspects of the thermal energy storage, which are as follows: (1) broad scope of storage field; (2) material for storage with their cost, physical properties, operational performance, and suitability for different applications; and (3) different kinds of TES systems. Different active TES systems were analyzed, such as packed bed, moving bed, thermocline, and fluidized bed, and various passive TES systems were also analyzed with their implementation in buildings, automobiles, textiles, etc. Design parameters, cost models, and operational issues of TES systems were also discussed. She et al. [17] reviewed various cooling techniques. The importance of cold storage is explained in terms of storing the cool energy at night (i.e., off-peak period) and utilizing the cool energy stored at day time (i.e., on-peak period). Based on types of cold storage utilization, it was classified into ice storage, chilled water storage, and phase change material-based cool energy storage. Li [18] has done a detailed review of the available technologies for sensible heat storage under various operating conditions and storage tank geometries in the aspects of sensible storage material, water stratification phenomenon, heat storage, heat transfer modes, and various influencing factors. The energy and exergy performance were investigated and summarized from the fluid mass flow rate, storage tank geometrical structure, fluid properties, fluid inlet temperature, etc. Li and Zheng [19] have explained and summarized performance enhancement of the various TES systems, including sensible, latent, and sorption. They systematically introduced various integration forms of TES for different applications, such as hot water supply, air conditioners, and heat pumps, with building construction systems and with power production cycles, cogeneration, food transport, solar cookers, and vehicle systems for thermal comfort. Rajamani et al. [20] have performed an experimental investigation on a packed bed cool storage system integrated with a chiller system which has major advantages in the central air-conditioning system for demand management strategies. They have initially performed an experiment for evaluating the subcooling behavior of the PCM with various pseudomonas concentrations. Further, they have performed experiments to determine the heat transfer behavior during the charging process in a cool thermal storage tank of capacity 50,000 kJ. They have presented the essential parameters such as reduction in subcooling, instantaneous and cumulative heat transfer during the charging process for the efficient operation.

It is observed from the literature that the cool thermal storage systems are normally employed for the demand-side management in large building air-conditioning systems. There are no studies reported towards the supply side-management like the integration of solar energy with the chiller operation. Further, it is not seen from the literature about the feasibility of integrating cool thermal energy storage in residential air-conditioning applications. Hence, the objective of the present study is to introduce a small capacity low temperature sensible cool thermal energy storage system with a residential cooling unit which could be integrated with a solar power generation unit. Further, the main problem associated with cool water storage tank is the limitation in bringing down the temperature below 0°C due to freezing which demands increased size of the storage tank. Considering the above, the present work is also focused on mixing an appropriate percentage of monoethylene glycol with water to develop a sensible cool thermal energy storage system to bring down the storage temperature even below 0°C and to study the charging/discharging performance of a low-temperature sensible heat storage (LTSHS) system for room air-conditioning applications.

2. Experimental Investigation

In the present work, an experimental unit is constructed to charge the cool energy produced by a chiller in the LTSHS tank and discharge the cool brine in the LTSHS tank through a cooling coil unit kept inside the room for space cooling. An experimental investigation is done to study the feasibility of using an LTSHS tank integrated with a chiller system for residential space cooling applications. The experimental setup details and the charging/discharging experiments are presented in this section.

2.1. Experimental Setup. The experimental setup consists of a VCR system, LTSHS tank, a room, and a cooling coil unit as the major components, and the line diagram for the experimental unit is shown in Figure 1. The photographic view of the experimental unit is shown in Figure 2. The vapour compression refrigeration (VCR) system of 1 TR capacity produced chilled brine at a required temperature of -5°C. The LTSHS tank made up of stainless steel with a capacity of 0.212 m^3 was filled with brine solution prepared from a mixture of distilled water and monoethylene glycol in a ratio of 6 : 4, which acted as a HEF. The specific heat (C_p), freezing temperature, density (ρ), and thermal conductivity (k) of the heat exchanging fluid were 3.69 $kJkg^{-1}$ K^{-1}, -25°C, 995 kgm^{-3}, and 0.3 Wm^{-1} K^{-1}, respectively. The storage tank was connected to the buffer tank of the VCR system, and the chilled brine produced in the chiller was circulated through this storage tank while performing the charging experimentation.

The VCR system has a buffer tank of capacity 0.009 m^3 filled with brine to accommodate the evaporator coil, heating coil of 2000 W capacity, and a stirrer. A proportionate differential temperature controller (PDTC) was used to maintain a desired constant temperature in the buffer tank. This enabled the supply of a constant temperature HEF from the buffer tank to the LTSHS tank. Valves were provided to control the flow rate of HEF in the charging/-discharging circuits. The brine flow from the chiller to the LTSHS tank and from the LTSHS tank to the cooling coil unit was measured using rotometers with the measuring range of 0-1000 LPH and 0-3 LPM, respectively. The cooling coil unit was kept in a room of size 2 m × 2.7 m × 2.72 m, and it was maintained at a controlled temperature of 25°C to 28°C during the discharging experiment. This cooling coil unit was connected to the LTSHS tank by a

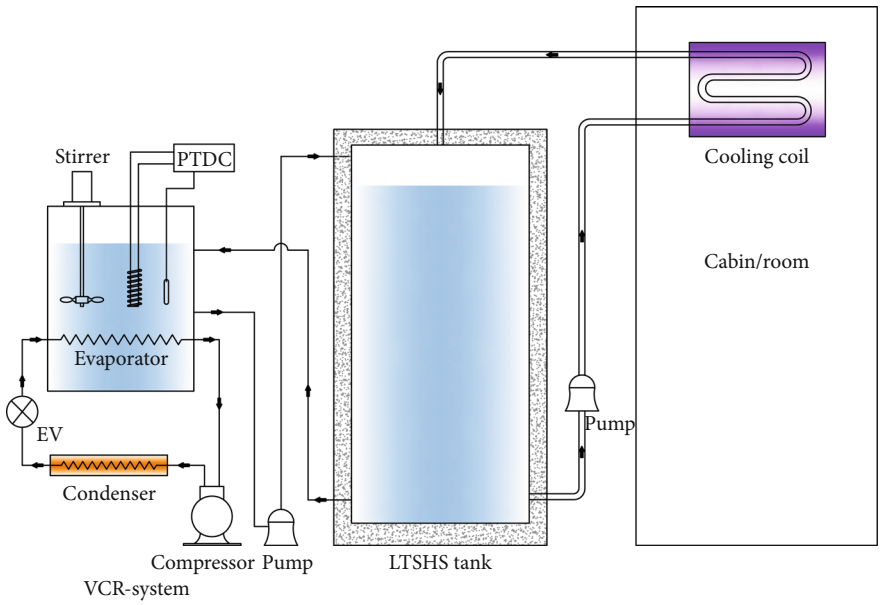

Figure 1: Schematic view of the experimental setup.

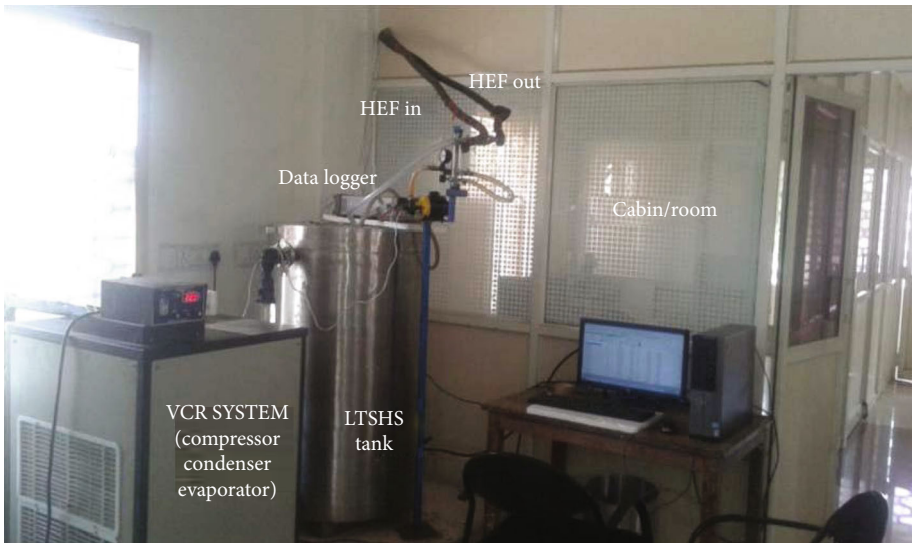

Figure 2: Photographic view of the experimental setup.

6 mm diameter pipe, properly insulated with foam material. T-type thermocouples were utilized to measure the inlet, outlet, and inside temperatures of the LTSHS tank during the charging process. Two thermocouples of PT 100–RTD with an accuracy of ±0.1°C were kept at inlet and outlet locations of the cooling coil unit for the brine temperature measurement. Further, 3 RTDs were kept at various locations in the room to measure the room air temperature during the discharging process. Agilent makes the 34972A data acquisition system with an accuracy of 0.004% to connect the temperature sensors. In both the charging and discharging circuits, 100 W capacity pumps were used for the circulation of the brine.

2.2. Experiments. The experiments were performed to study the charging and discharging performance of the developed system. During the charging experiment, brine was circulated from the buffer tank of the chiller unit to the LTSHS tank through a pump, and a flow rate of 400 LPH was maintained by adjusting the valves. The chiller unit was operated at a constant load. HEF temperature of -5°C was maintained in the buffer tank by the PDTC and for varying the heating coil output based on the temperature sensor located in the HEF bath of the buffer tank. The brine temperature was measured at an interval of 10 seconds during the entire experiment using a data logger and stored in the desktop PC connected to the experimental setup, and also, energy meter readings

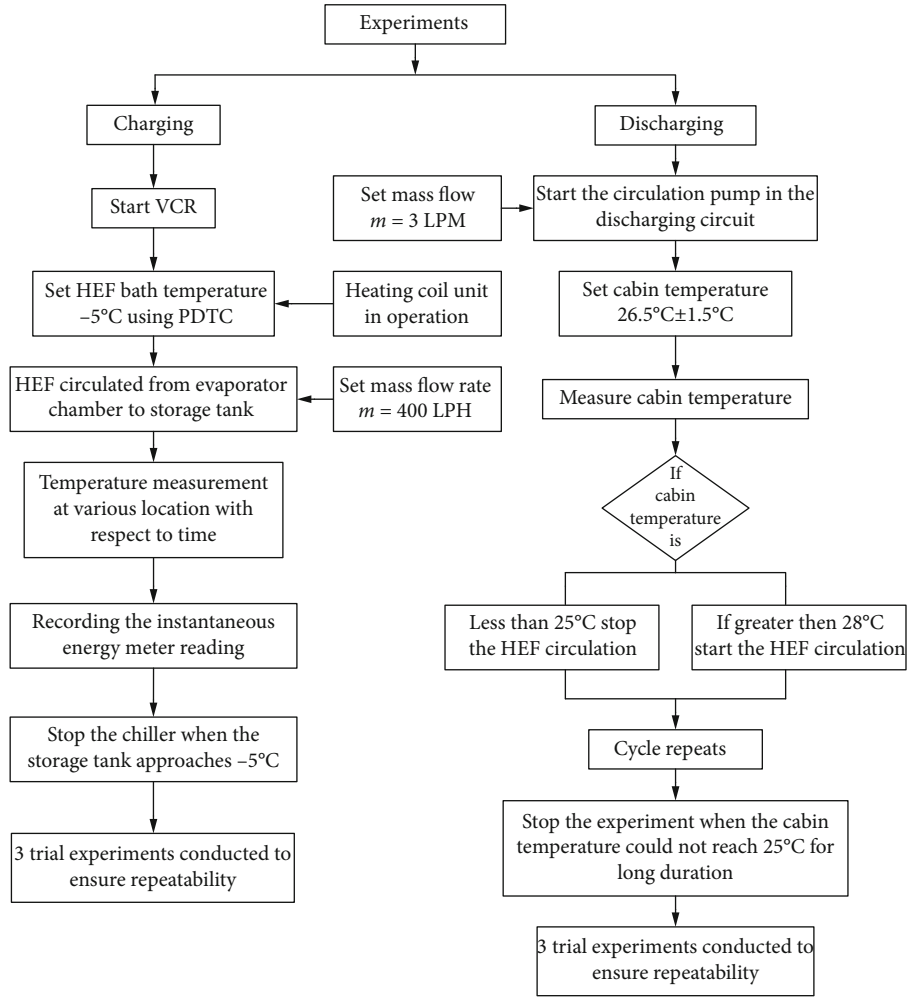

Figure 3: Methodology adopted for the experimental investigation.

were noted once in every half an hour. The VCR system was operated continuously, and experiments were continued until the brine in the LTSHS tank approached a temperature of -5°C. Figure 3 explains the detailed methodology adopted in the experimental investigation.

Discharging experiments were carried out with brine flow by operating the circulation pump between the LTSHS tank and the cooling coil unit. The brine's uniform mass flow rate was maintained at 3 LPM using the valve arrangement and measured by the flow meter. Average room air temperature at three different locations, one in front of the cooling coil unit and the other two at suitable locations in the room, was considered for the analysis. The brine's inlet and outlet temperature flowing through the cooling coil unit kept in the room was also measured continuously during the experiment. The pump's operation controlled the brine flow from the LTSHS tank to the cooling coil unit for maintaining the room temperature within 26.5 ± 1.5°C. The discharging experiments were started when the brine was initially at a temperature of -5°C in the storage tank. The discharging experiment was discontinued when the available brine from the storage tank could not attain the room temperature of nearly 25°C. Many experiments were conducted to ensure its repeatability. The heat transfer (i.e., instantaneous and cumulative), the heat loss while charging, and the cooling load while discharging were evaluated using the mass flow rate and measured temperatures of the HEF. The technical specification of components involved in the present system is shown in Table 1.

An estimation of the uncertainties in the measured/derived data was made, and the values are shown in Table 2.

3. Data Analysis

The instantaneous heat transfer, cumulative energy stored, and heat removed from the room were evaluated using the measured temperature values, and the equations used for the estimation of these parameters are presented.

The instantaneous heat transfer (the rate at which the thermal energy is stored in the storage tank) during the charging process is estimated using

$$Q_{\text{ins}} = mC_p\,(\text{Tout} - T_{\text{in}}), \text{kW}, \tag{1}$$

where m is the mass flow rate of the HTF through the storage tank (kg s^{-1}), C_p is the specific heat capacity of HTF

Table 1: Technical specifications of system components.

Components	Rated capacity/range/make
VCR system	1 TR (3.5 kW)
Evaporator tank capacity	11 litres
Refrigerant	R 134a
HEF circulation pump (chiller unit to LTSHS tank)	0.25 horsepower (hp)
HEF circulation pump (LTSHS tank to cooling unit)	100 Watts
CTES tank capacity	212 litres
Flow meters:	VA-make
(i) Charging circuit	0–1000 LPH
(ii) Discharging circuit	0–180 LPH
Thermocouple	T-type
HEF	HDPE-ethylene

Table 2: Uncertainty in various measured/derived quantities.

Measured quantities	Accuracy/error (%)
Temperature	±0.1°C
Volume (100 ml)	±0.015 ml
Mass flow rate	±2.7%
Derived quantities	Error (%)
Instantaneous heat transfer	±1.85%

(kJ kg^{-1} K^{-1}), T_{in} is the inlet temperature of the HTF in the storage tank at any instant (K), and T_{out} is the outlet temperature of the HTF in the storage tank at any instant (K).

The cumulative heat transfer (Q_{cum}) is estimated by integrating the instantaneous heat transfer Q_{ins} using

$$Q_{cum} = \sum_{k=1}^{n} Q_{ins}^{k} \bullet \Delta t, \text{ kJ}, \quad (2)$$

where "n" is the number of time steps and Δt is the size of each time step (10 seconds considered in the present evaluation).

The heat removed (Q_R) from the room during the discharging process in each cycle of operation is evaluated using

$$Q_R = mC_p(T_{out,ave} - T_{in,ave}) \times \tau, \text{ kW}, \quad (3)$$

where m is the mass flow rate of the HTF through the cooling coil unit (kg s^{-1}), $T_{in,ave}$ is the average inlet temperature of the HTF to the cooling coil unit in each cycle (K), $T_{out,ave}$ is the average outlet temperature of the HTF from the cooling coil unit in each cycle (K), and τ is the time taken for the completion of cycle (sec).

4. Results and Discussion

The results of the experiments performed during the charging/discharging of the storage tank and cooling of the room by discharging the cool thermal energy are presented and discussed in this section.

4.1. Temperature-Time History of Brine during Charging Process. Figure 4 shows the temperature-time history of the brine at the inlet, outlet, and inside of the storage tank when the brine from the buffer tank set point temperature was maintained at -5°C and the mass flow rate was maintained at 400 LPH. It is seen from the figure that the variations in HEF temperature from the initial state (i.e., at 35°C) to 5°C is approximately linear, and the water temperature at the outlet and the water inside the tank coincide. The figure shows that the time taken for the sensible cooling of the brine from 35°C to 0°C is approximately 550 min and the time taken for the sensible cooling of the brine from 0°C to -5°C is approximately 150 min. It is construed from the figure that the time taken for the same reduction of ΔT of brine has increased when the VCR system is operated to reduce the brine temperature below 0°C compared to above 0°C. The process ended when the brine reached at -5°C, owing to appreciable incremental time required to reduce the temperature further. It is construed from the results that it is efficient to operate the chiller set point temperature around +5°C. However, this demand may increase the size of the storage tank, to store the same quantity of cool energy. It should be noted that for every 1°C increase in set point temperature, there is an increase of 2.5% COP (Velraj et al. [5]). Hence, increasing the set point temperature from -5°C to 5°C may yield an increased COP of 25%.

4.2. Instantaneous Heat Transfer and Cumulative Energy Storage. Figure 5 shows the instantaneous heat transfer and the cumulative energy stored in the storage tank, which was evaluated continuously from the measured temperature difference between the inlet and outlet brine (i.e., brine entry/exit of the storage tank). The figure shows that the instantaneous heat transfer initially started to decrease from 1.2 kW and extended for 250 min, and instantaneous heat transfer of 0.8 ± 0.1 kW is maintained for 250 min to 600 min. Further, when operating below 0°C, an appreciable decrease in instantaneous heat transfer is noticed due to the reduction in the VCR system's performance. The figure also shows that the cumulative energy stored is increasing linearly until the end of charging. During the complete charging, the approximate energy stored was 38,000 kJ. The time taken for

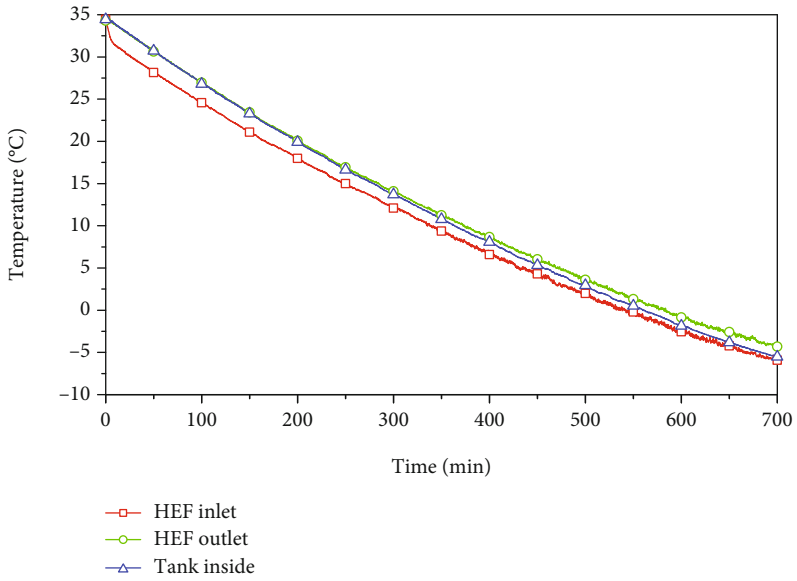

Figure 4: Temperature-time history of brine at inlet, outlet, and inside of the tank for a mass flow rate of 400 LPH.

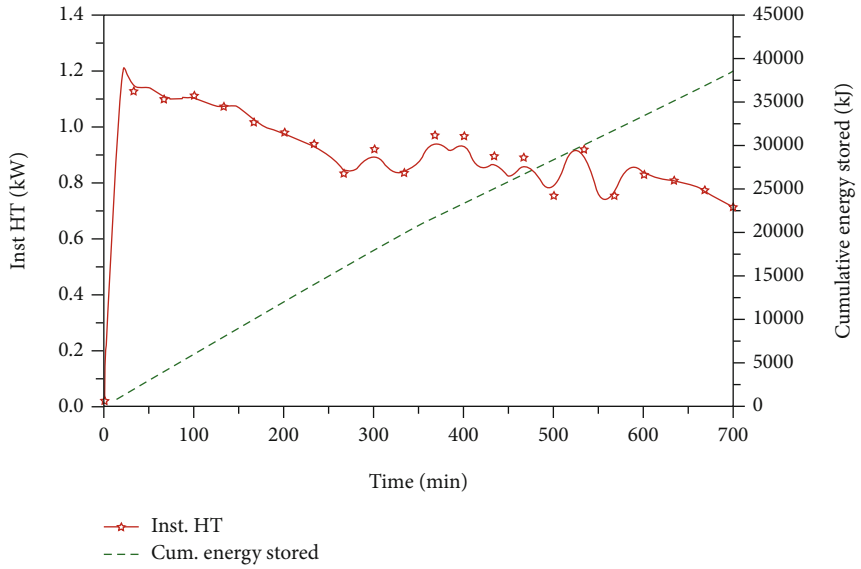

Figure 5: Instantaneous heat transfer and cumulative energy stored in the storage tank for a mass flow rate of 400 LPH.

the entire charging was 700 min. During the chiller's operation, the energy meter was seen consuming one kW-hr as the power consumption for every one-hour operation. It is construed from the above results that nearly 80% of the cool energy available in the storage tank could be charged at a near-uniform rate.

4.3. Variation of COP of VCR with Brine Temperature Reduction for Every 5°C Drop. Figure 6 shows the variation in COP of the VCR system for cooling of 200 litres of brine from its initial temperature of 34.5°C to the final temperature of -5°C and the time taken for every reduction in brine temperature of 5°C. The figure shows that the COP varies with marginal difference from 2.4 to 1.5 for every 5°C of brine temperature reduction until reaching the brine temperature to +5°C. Further, as brine temperature reduces from +5°C to -5°C, the COP of the VCR system reduces appreciably. Hence, it is construed that the VCR system should be operated to bring the brine solution only up to +5°C for better performance and economical way of using the storage tank integrated with the VCR system.

4.4. Discharging Process. The brine temperature at the inlet and outlet of the cooling coil units is an important parameter based on which the heat transfer to the room and thereby the cabin temperature will be maintained. These parameters are studied and reported in this section.

4.4.1. Temperature-Time History of Brine in the Cooling Coil Unit and Cabin Temperature. Figure 7 shows the temperature-time history of the room and the brine inlet/outlet of the cooling coil unit when the set point

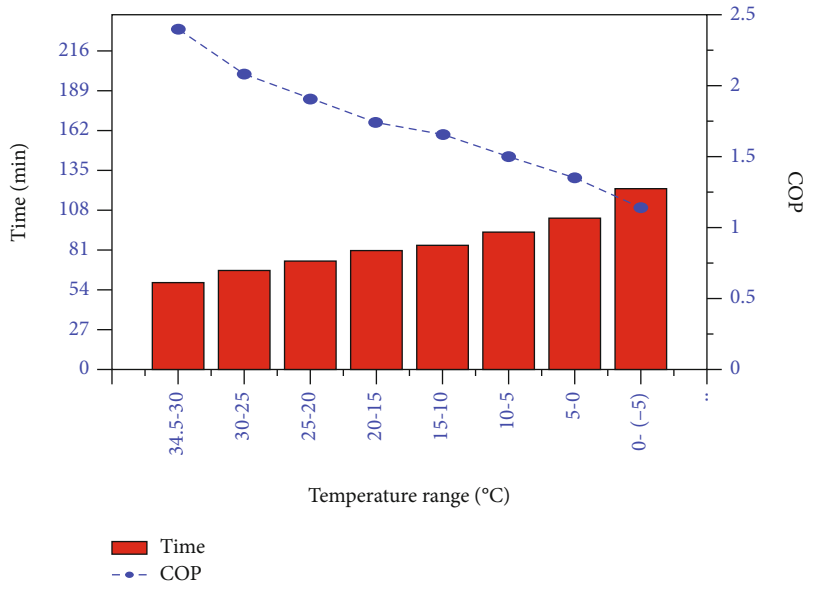

Figure 6: Time duration of HEF temperature reduction for every 5°C drop and corresponding COP of VCR.

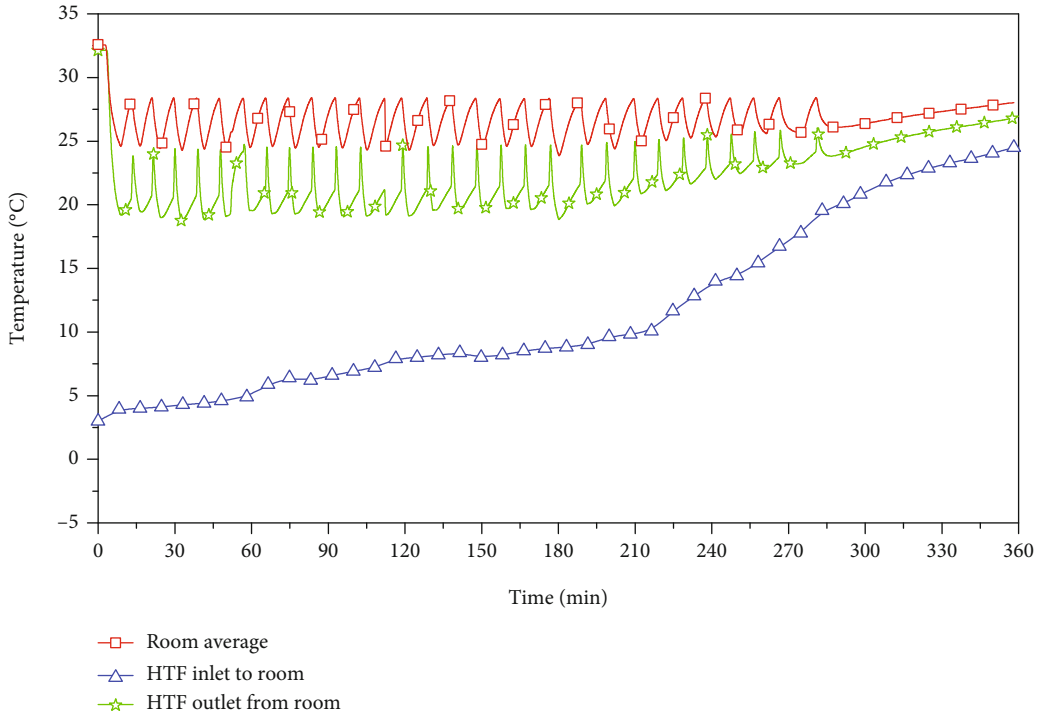

Figure 7: Temperature-time history of the room and the brine inlet/outlet of the cooling coil unit.

temperature in the room was maintained between 25°C and 28°C, and the mass flow rate of the brine was maintained at 3 LPM. During each cyclic operation (time taken from 25°C to 28°C and back to 25°C is one cycle), when the brine circulation was stopped, inlet and outlet brine temperatures of the cooling coil unit were increased until the room temperature reached 28°C. When the circulation was started, the inlet temperature of brine in the room decreased, and the flow was continued till the room temperature reached 25°C. It is seen from the figure a sharp increase in the room temperature when the brine circulation is stopped and decreases when the brine circulation is started through the cooling coil unit. In addition to that, the idle condition's duration is more than the duration of the circulation of brine in one cycle. It was observed that the room could be maintained at the required comfort condition for a duration of 285 min with 29 cycles of operation. When the inlet brine temperature of the cooling coil unit reached 20°C, bringing down the room temperature to 25°C could not be achieved and hence the experiment was stopped at that stage and hence it is

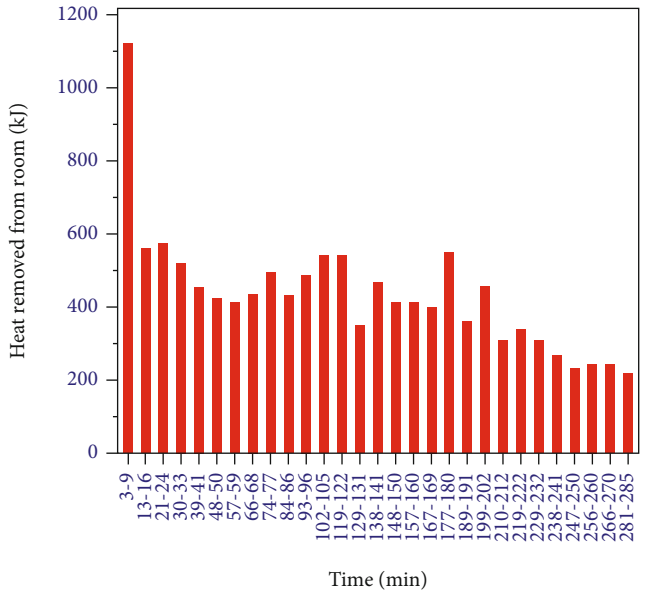

FIGURE 8: Heat removed from the cabin by HEF during each cycle of operation.

construed that further cool energy is not available in the storage tank to produce the required cooling effect in the room.

4.4.2. Heat Removed from the Room. The heat transferred from the room by the brine during each cycle of operation is shown in Figure 8, which indicates that the heat removed from the room is in the range of 300 kJ to 600 kJ during all cycles of operation. The variation could be due to the changes in the cooling load required as there was a variation in the heat leak to the room during the experiment. It was observed that the first cycle of operation completes during 3-9 min and the heat removal is more since the temperature is reduced from 32°C to 25°C.

The heat removal required decreased in the last few cycles of operations because of lesser ΔT between room and brine temperatures. Further, the total heat removed from the room during the entire discharging cycle was evaluated as 12,560.5 kJ, which was only 60% of the cool energy initially available in the storage tank. This is due to the higher heat loss from the storage tank and the loss through the piping and other valve joints between the storage tank and room.

5. Conclusions

In the present work, experimentations were done to find the heat transfer behavior while charging/discharging process in a cool thermal storage tank of capacity 38,000 kJ. The major conclusions arrived from the charging/discharging experiments are summarized in this section.

(i) During the charging process, when the HEF temperature decreases from 35°C to -5°C, the time taken to achieve a temperature drop of 5°C increases appreciably below +5°C

(ii) The COP of the chiller system also reduces appreciably when the HEF temperature decreases below 5° C

(iii) Hence, it is recommended to operate the storage system with a temperature not less than +5°C to achieve higher efficiency

(iv) When the inlet brine temperature of the cooling coil unit reached 20°C, in the subsequent cycle, bringing back the room temperature to 25°C could not be achieved

(v) The heat removed from the room is in the range of 300 kJ to 600 kJ during all the cycles of operation

The cool energy released during the discharging process was only 60% of energy charged. This is due to the considerable heat loss incurred through various modes which should be avoided. This ensures the requirement of the distance between the storage tank and cooling coil unit to be very close and the storage tank/piping to be insulated very well to prevent heat loss during the storage period and during the passage of flow.

The major scope and the limitations are as follows.

In the near future, when the renewable energy share increases, the demand for cool thermal storage will increase and this kind of LTSHS system is used to smoothen the fluctuations in the solar operated VCR system and to keep the electricity grid smart as large share of electricity is being deployed in building air-conditioning applications. The economic benefits of this cool thermal storage system will be very high if the dynamic tariff is introduced, as in practise in some of the countries in order to keep the grid smart. However, when the capacity of the cooling unit increases, the requirement of the storage tank size also increases appreciably. Hence, in the thickly populated cities, due to space constraints, implementation becomes difficult.

Nomenclature

CCS: Combined cool storage
AC: Air conditioning
HEF: Heat exchanging fluid
COP: Coefficient of performance
CTES: Cool thermal energy storage
TR: Tonnage refrigeration
LTES: Low-temperature energy storage
VCR: Vapour compression refrigeration
CWES: Chilled water energy storage
LTSHS: Low-temperature sensible heat storage
TES: Thermal energy storage
LPM: Litres per minute
VARS: Vapour absorption refrigeration system
CO_2: Carbon dioxide
PDTC: Potential differential temperature controller
LCC: Life cycle cost
RTD: Resistance temperature detector
LPH: Litres per hour.

Data Availability

All data used to support the findings of this study are included within the article.

Conflicts of Interest

The authors declare that there is no conflict of interest regarding the publication of this article.

References

[1] X. Cao, X. Dai, and J. Liu, "Building energy-consumption status worldwide and the state-of-the-art technologies for zero-energy buildings during the past decade," *Energy and Buildings*, vol. 128, pp. 198–213, 2016.

[2] K. Panchabikesan, K. Vellaisamy, and V. Ramalingam, "Passive cooling potential in buildings under various climatic conditions in India," *Renewable and. Sustainable Energy Reviews*, vol. 78, pp. 1236–1252, 2017.

[3] M. J. Sebzali, B. Ameer, and H. J. Hussain, "Comparison of energy performance and economics of chilled water thermal storage and conventional air-conditioning systems," *Energy and Buildings*, vol. 69, pp. 237–250, 2014.

[4] H. Lin, X. H. Li, P. S. Cheng, and B. G. Xu, "Study on chilled energy storage of air-conditioning system with energy saving," *Energy and Buildings*, vol. 79, pp. 41–46, 2014.

[5] R. Velraj, M. Cheralathanand, and S. Renganarayanan, "Energy management through encapsulated PCM based storage system for large building air conditioning application," *International Energy Journal*, vol. 7, pp. 253–259, 2006.

[6] M. H. Kim, J. E. Son, J. Heo, D. Kim, and D. W. Lee, "Energy saving potential of an independent dedicated outdoor air system integrated with thermal energy storage for a childcare center," *Applied Thermal. Engineering*, vol. 152, pp. 377–390, 2019.

[7] C. Yan, W. Shi, X. Li, and Y. Zhao, "Optimal design and application of a compound cold storage system combining seasonal ice storage and chilled water storage," *Applied Energy*, vol. 171, pp. 1–11, 2016.

[8] S. Boonnasa and P. Namprakai, "The chilled water storage analysis for a university building cooling system," *Applied Thermal Engineering*, vol. 30, no. 11-12, pp. 1396–1408, 2010.

[9] M. J. Sebzali and P. A. Rubini, "The impact of using chilled water storage systems on the performance of air cooled chillers in Kuwait," *Energy and Buildings*, vol. 39, no. 8, pp. 975–984, 2007.

[10] X. Song, L. Liu, T. Zhu, S. Chen, and Z. Cao, "Study of economic feasibility of a compound cool thermal storage system combining chilled water storage and ice storage," *Applied Thermal Engineering*, vol. 133, pp. 613–621, 2018.

[11] H. Lin, X. H. Li, P. S. Cheng, and B. G. Xu, "Thermoeconomic evaluation of air conditioning system with chilled water storage," *Energy Conversion Management*, vol. 85, pp. 328–332, 2014.

[12] G. P. Henze, B. Biffar, D. Kohn, and M. P. Becker, "Optimal design and operation of a thermal storage system for a chilled water plant serving pharmaceutical buildings," *Energy and Buildings*, vol. 40, no. 6, pp. 1004–1019, 2008.

[13] S. Rosiek and F. J. Batlles Garrido, "Performance evaluation of solar-assisted air-conditioning system with chilled water storage (CIESOL building)," *Energy Conversion Management*, vol. 55, pp. 81–92, 2012.

[14] S. Rosiek and F. J. Batlles, "Reducing a solar-assisted air-conditioning system's energy consumption by applying real-time occupancy sensors and chilled water storage tanks throughout the summer: A case study," *Energy Conversion Management*, vol. 76, pp. 1029–1042, 2013.

[15] M. Sadat-Mohammadi, S. Asadi, M. Habibnezhad, and H. Jebelli, "Robust scheduling of multi-chiller system with chilled-water storage under hourly electricity pricing," *Energy and Buildings*, vol. 218, article 110058, 2020.

[16] G. Alva, Y. Lin, and G. Fang, "An overview of thermal energy storage systems," *Energy*, vol. 144, pp. 341–378, 2018.

[17] X. She, L. Cong, B. Nie et al., "Energy-efficient and -economic technologies for air conditioning with vapor compression refrigeration: a comprehensive review," *Applied Energy*, vol. 232, pp. 157–186, 2018.

[18] G. Li, "Sensible heat thermal storage energy and exergy performance evaluations," *Renewable and Sustainable Energy Reviews*, vol. 53, pp. 897–923, 2016.

[19] G. Li and X. Zheng, "Thermal energy storage system integration forms for a sustainable future," *Renewable and. Sustainable Energy Reviews*, vol. 62, pp. 736–757, 2016.

[20] R. Narayanasamy, P. Vellaichamy, M. R. Sharma, and V. Ramalingam, "Experimental investigation on packed bed cool storage system for supply-demand management in building air-conditioning system suitable for micro thermal grid," *Thermal Science*, vol. 25, no. 1 Part A, pp. 95–106, 2021.

Hindawi
International Journal of Photoenergy
Volume 2021, Article ID 9940862, 15 pages
https://doi.org/10.1155/2021/9940862

Research Article

Active Power Management for PV Systems under High Penetration Scenario

Fernando Medina,[1] **Nimrod Vazquez**,[1] **Joaquín Vaquero**,[2] **Jaime Arau**,[3] **Leonel Estrada**,[4] **and Elso Rodriguez**[1]

[1]*Electronics Engineering Department, TecNM-Instituto Tecnológico de Celaya, 38010 Celaya, Mexico*
[2]*Electronics Technology Area, Rey Juan Carlos University, 28933 Mostoles, Madrid, Spain*
[3]*Electronics Department, Tecnológico Nacional de México-Cenidet, 63490 Cuernavaca, Mexico*
[4]*Electronics Department, Instituto Tecnológico Superior del Sur de Guanajuato, 38980 Uriangato, Mexico*

Correspondence should be addressed to Nimrod Vazquez; n.vazquez@ieee.org

Received 25 March 2021; Accepted 23 May 2021; Published 4 June 2021

Academic Editor: Kumarasamy Sudhakar

Copyright © 2021 Fernando Medina et al. This is an open access article distributed under the Creative Commons Attribution License, which permits unrestricted use, distribution, and reproduction in any medium, provided the original work is properly cited.

Although PV systems are one of the most widely used alternatives as a renewable energy source due to their well-known advantages, there are significant challenges to address related to voltage fluctuations and reverse power flow caused by high PV penetration scenarios. As a potential solution to this problem, an active power management strategy is proposed in this work using a residential cluster as a benchmark. The proposed strategy is analyzed and experimentally verified, offering a simple way to reduce the voltage fluctuations by regulating the active power delivered by the PV system, achieving also relevant functionalities for the system, such as the regulation of the DC bus voltage, maximum power point tracking (MPPT), synchronization with the grid voltage, detection of high penetration conditions, and a simple strategy for the main controller with an effective performance. The proposal system shows satisfactory results being able to maintain grid voltage fluctuations within the voltage standard specifications.

1. Introduction

The number of photovoltaic (PV) systems connected to the electric grid has grown considerably in recent decades. It is estimated that the demand for PV systems will maintain its growth for the coming years. According to the International Energy Agency, by 2050, solar PV power generation will be around 16% of the world's electricity [1]. The fastest-growing areas of electricity production from PV systems are in the low-voltage (LV) grid that corresponds to the private and residential sectors.

The ease of connecting PV systems to the grid is an important factor for their growth, but also the availability of the technology, which allows users to install them quickly and easily. The distributed generation (DG) based on PV systems is currently high and increases every day; e.g., the installed capacity in Australia and Germany in recent years has increased by 80% and 99%, respectively [2–5], while in Europe, it was estimated at 49% [6]. Some of the benefits of using PV systems to improve the quality of the power grid are the reduction of losses and maintenance cost, as well as, of course, significant savings in the electricity billing for the end-user.

However, the massive use of grid-connected PV systems may affect the power quality; this is known as high PV penetration [7–9]. Some first cases of problems due to high penetration scenarios were reported in European countries such as Germany [10], the Netherlands [11], and the United Kingdom [12]. The electrical grid under a high PV penetration scenario should have variations in frequency and voltage levels [13, 14]. Different studies deal with the effects of high PV penetration into the electric grid [15–20]. The most

important effect is the variation in the voltage level [15–21]. The relevance of this problem is that the safe operating area of sensitive electronic equipment such as computers or medical devices may be lost [22].

In recent years, different techniques associated with voltage regulation and control methods to mitigate the effect of high PV penetration have been proposed. These solutions include studies to determine the maximum loads connected to the grid [23], grid layout and loads residential design [24], variable tap transformers [25] and smart transformers applications [26], battery bank systems [27–29], inverters with reactive power capability [30–33], and the interconnectivity of external devices with the grid as smart electrical vehicles [34]. Additionally, the theoretical use of a communication network that allows making decisions based on grid variations has been suggested [35].

Since the deviation in voltage level is the main objective to control [36], the use of smart inverters is being the best option. They will have a direct impact on users and consumers in the LV distribution network and be used with great flexibility under high PV penetration scenarios [37].

Inverters with reactive power capability are an interesting option [30–33]; however, the main disadvantages are not only the increase in the inverter nominal power to offer good performance but also an increment in the grid power losses and in the semiconductor stress, which entails a reduction in the useful life of the inverter.

In [31, 32], a static reactive power compensator is suggested and an analysis to select the best connection point is detailed. The main drawback of this work is that the proposal is no longer valid if the grid parameters change, like new loads and distribution transformer replacements.

In [38], coordinated hierarchal control of PV modules is discussed, which mitigates the voltage fluctuations using a smart control system; this system requires inverters with reactive power compensation capability, storage elements, and static synchronous compensators. The proposal is good to regulate the voltage; however, the disadvantages are the use of extra elements, increasing the complexity and cost.

Other works with extra elements are [39–41]; in [39], a multienergy storage system set is controlled through a complex communication network; in [40], a tapped transformer is considered, which should be a better solution than reactive power control because no extra current is handled, although the cost and complexity increase; in [41], a combination of tapped transformers and an energy storage system is proposed, and a particle swarm optimization is performed, resulting in a complex and expensive system; in [42], the use of electric vehicles by all consumers to ensure an efficient operation is considered, which is not practical in many regions and therefore a disadvantage.

In [43], a coordinated operation of a hybrid energy storage system (HESS) that can improve the utilization rate of PV systems is considered. A supercapacitor and a lithium battery are employed, coordinated with a complex particle swarm controller. Besides, the infrastructure involved in energy storage systems is large, which implies a high initial economic investment.

In this paper, a strategy to control a PV inverter is proposed, which allows reducing the voltage variations in an LV distribution network under a high PV penetration scenario through active power management. The proposal is simple because no extra elements are required, like tapped transformers, complex communication systems, electric vehicles, or energy storage systems. However, the use of an energy storage system is suggested, but optional to offer better characteristics.

The proposal does not consider either injecting/absorbing reactive power towards/from the grid. Only active power is managed; therefore, the power losses in the grid are not incremented and it is not required to oversize the inverter rated power. The proposal manages the active power delivered by the PV system depending on the grid conditions and the PV panel employing an algorithm that controls the PV inverter; therefore, there is no additional cost compared to the traditional PV system.

The proposed control strategy detects when a voltage variation is due to a high PV penetration scenario. This is an advantage compared to other methods that require the characterization of the complete grid to operate. The proposed strategy effectively mitigates voltage variations in the grid caused by high PV penetration and in addition achieves relevant functionalities for the system, such as the regulation of the DC bus voltage, maximum power point tracking (MPPT), grid voltage synchronization, the detection of high penetration conditions, and the active power strategy for the main controller.

The paper is organized as follows: Section 2 presents a simplified model of the LV distribution network considered. In Section 3, the effects of high PV penetration are shown, and the most critical configurations are illustrated. In Section 4, the proposed control strategy is detailed. The experimental results are shown in Section 5. Finally, the main conclusions are considered to resume the advantages and disadvantages of the proposed solution.

2. LV Distribution Network under High PV Penetration Scenario

For a better understanding of the high PV penetration phenomena, an LV distribution network is modeled. This illustrates the troubles associated with it in a simple way. It is assumed an axial grid connection since it is the most typical configuration in an LV distribution network in a resident area [44]. There are different grid configurations described in other works [14, 21, 45].

A typical residential cluster is considered, which is illustrated in Figure 1(a). The distribution network consists of the power transformer (v_g), residences (L_n), grid wiring (Z_n), and photovoltaic system (PV_n).

To simplify the analysis, some considerations and assumptions are made. The power injected by PV systems (PV_n) and residence load (L_n) are represented by a current source (i_n); both are considered sinusoidal. The transformer output (v_g) is replaced by a sinusoidal voltage source, and the grid impedances are equal (Z). The simplified circuit is shown in Figure 1(b).

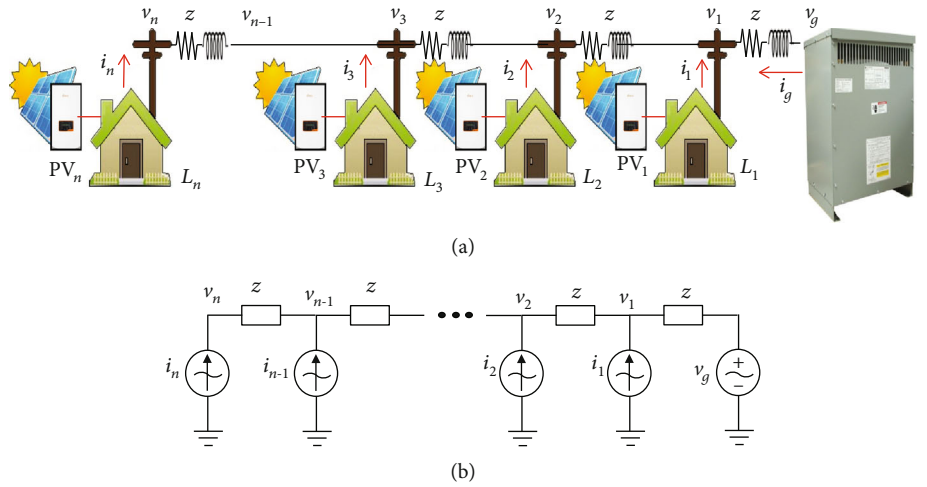

Figure 1: Analyzed system: (a) residential area with axial connection; (b) simplified circuit.

Analyzing the simplified circuit, it is obtained that

$$\begin{aligned} v_n &= v_{n-1} + Zi_n, \\ v_{n-1} &= v_{n-2} + Z(i_n + i_{n-1}), \\ &\vdots \\ v_1 &= v_g + Z(i_n + i_{n-1} + \cdots + i_1), \end{aligned} \tag{1}$$

where v_g is the transformer voltage, Z is the wiring impedance, n is the number of residences in the cluster, and i_n is the current that is injected into the grid from the residence point (n) according to its position.

The voltage in the n_{th} residence can be determined solving the equation system (1), as a function of current sources, giving

$$v_n = v_g + Z \sum_{m=1}^{n-1} (m \cdot i_m) + Zn \sum_{m=n}^{r} (i_m), \tag{2}$$

where n is the n_{th} residence in the cluster, and r is the number of residences.

Based on (2), a set of voltage equations that determine the voltage of each residence may be obtained. As an example, a distribution network consisting of 11 residences gives the following equations, for residences 1, 2, 5, 6, 10, and 11 which are, respectively,

$$v_1 = v_g + Z(i_1 + i_2 + \cdots + i_{10} + i_{11}), \tag{3}$$

$$v_2 = v_g + Z(i_1 + 2(i_2 + \cdots + i_{10} + i_{11})), \tag{4}$$

$$v_5 = v_g + Z(i_1 + 2i_2 + 3i_3 + 4i_4 + 5(i_5 + \cdots + i_{10} + i_{11})), \tag{5}$$

$$v_6 = v_g + Z(i_1 + 2i_2 + \cdots + 5i_5 + 6(i_6 + \cdots + i_{10} + i_{11})), \tag{6}$$

$$v_{10} = v_g + Z(i_1 + 2i_2 + \cdots + 9i_9 + 10(i_{10} + i_{11})), \tag{7}$$

$$v_{11} = v_g + Z(i_1 + 2i_2 + \cdots + 10i_{10} + 11i_{11}). \tag{8}$$

3. Grid Voltage Deviations under High PV Penetration Scenario

According to the mathematical model (2), the voltage variation in each residence depends on the actual injected/absorbed current towards/from the grid. Understanding the phenomenon will make it possible to establish a strategy to mitigate the harmful effects of high PV penetration.

A distribution network composed of 11 residences is used as an example. The parasitic elements of the grid are calculated considering the wiring impedance and the distance between residences, which is 11 m ($R_{\text{cable}} \approx 1.61\,\Omega$/km, $X_{L_{\text{cable}}} \approx 0.21\,\Omega$/km). The value of the current source i_n is calculated as the difference between the current delivered by each renewable source (I_{PV_n}) and the current demanded by each residence (I_{L_n}). The grid voltage is 120 V.

In Figure 2, the normalized voltages in six different residences (1, 2, 5, 6, 10, and 11) are shown. The sign of the current source (i_n) has been defined as positive if the renewable source generates more power than the one demanded by the residence; on the other hand, the current is negative if the residence demands more power than the one delivered by the renewable source. The vertical axis represents voltage while the horizontal axis represents time.

In Figure 2(a), the normalized voltage levels of the transformer and the residences are shown, and the current demanded by each residence is minus 4.4 A (residence plus PV system); then, the residences demand more energy than the PV systems deliver. The voltage in each residence is lower than the voltage of the transformer (v_g), and therefore, there is not an increment of the voltage grid.

In Figure 2(b), the voltage levels of the transformer and the residences are shown again, but now, the current delivered to the grid by each residence is 4.4 A (residence plus PV system); then, the residences demand less power than the PV system delivers. The voltage in each residence is now higher than the voltage of the transformer (v_g).

Figure 2(c) shows the same case as Figure 2(b), but the current is incremented to 8.8 A (residence plus PV system).

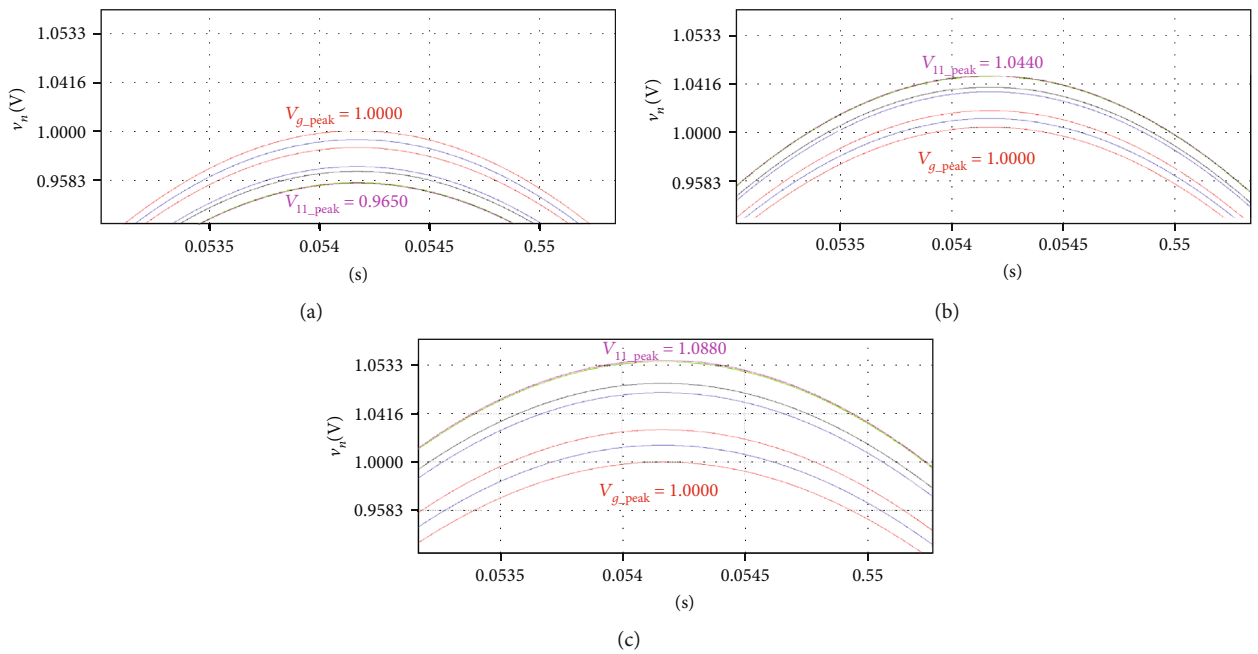

Figure 2: Voltage levels on the transformer and residences: (a) residences demanding power (-4.4 A), (b) residences injecting power (4.4 A), and (c) residences injecting power (8.8 A).

As it can be observed, the voltage in each residence is higher compared to the previous case, which may represent a load malfunction or damage due to the overvoltage. Moreover, it can be noticed that the umpteenth residence, which is the one farthest from the transformer, is the most affected since the voltage deviation is greater. Therefore, the umpteenth residence is the most critical in the distribution network.

Based on these observations, a control strategy for mitigating the harmful effects of high PV penetration is proposed. The active power delivered by the PV system may be appropriately managed once a voltage increment is detected due to a high PV penetration scenario, and then reduce the voltage increment to safe values.

4. Proposed System

Since the voltage fluctuation due to high PV penetration is caused by the grid parasitic elements and the inverse power injected by the PV system, in this paper, a power management strategy to alleviate the voltage variation is proposed. The reactive power compensation is not used to avoid oversizing the inverter rated power and to avoid wiring power losses. The proposed system is shown in Figure 3.

The power stage selected is the HERIC converter, suitable for PV applications [46]. This topology was selected because it offers good characteristics like lightweight (without transformer), low leakage current that satisfies the regulations, and high efficiency, and its operation and construction are similar with a traditional inverter, simplifying the implementation. The power stage is shown in Figure 3(a). However, any other topology with similar characteristics may be also used.

The proposed controller (Figure 3(b)), which manages the PV system power flow, consists of a proportional resonant (PR) current controller, a DC voltage regulator including an MPPT, a grid voltage synchronization stage, a high PV penetration detector (PD), the active power controller (APC), and finally an energy storage system (ESS). The latter, although optional, certainly improves the performance of the entire system.

For evaluating purposes, the proposed system is placed on the umpteenth residence since it is the most critical point, but it can be placed in another point. The other residences are considered as independent current sources, the wiring impedance is the same between the different residences, and the transformer voltage is considered as an independent voltage source. The power delivered by the residence PV system is managed to alleviate the local voltage fluctuation through the local grid injected current; the system changes the amplitude of the set point of the injected current.

4.1. Proportional Resonant Controller (PR). A proportional-integral (PI) control is commonly used for stationary or time-invariant references. However, when the reference has a sinusoidal shape, the PI control is not the best option, since a control that minimizes the steady-state error in sinusoidal variations and external disturbances is desirable. A PR control features an infinite gain, which eliminates the sinusoidal steady-state error at the operating frequency [47, 48].

The control law used is

$$G_c(s) = K_p\left(1 + K_r\frac{s}{s^2 + \omega_o^2}\right), \tag{9}$$

where K_p is the proportional constant, K_r is a controller constant, and ω_o is the resonance frequency.

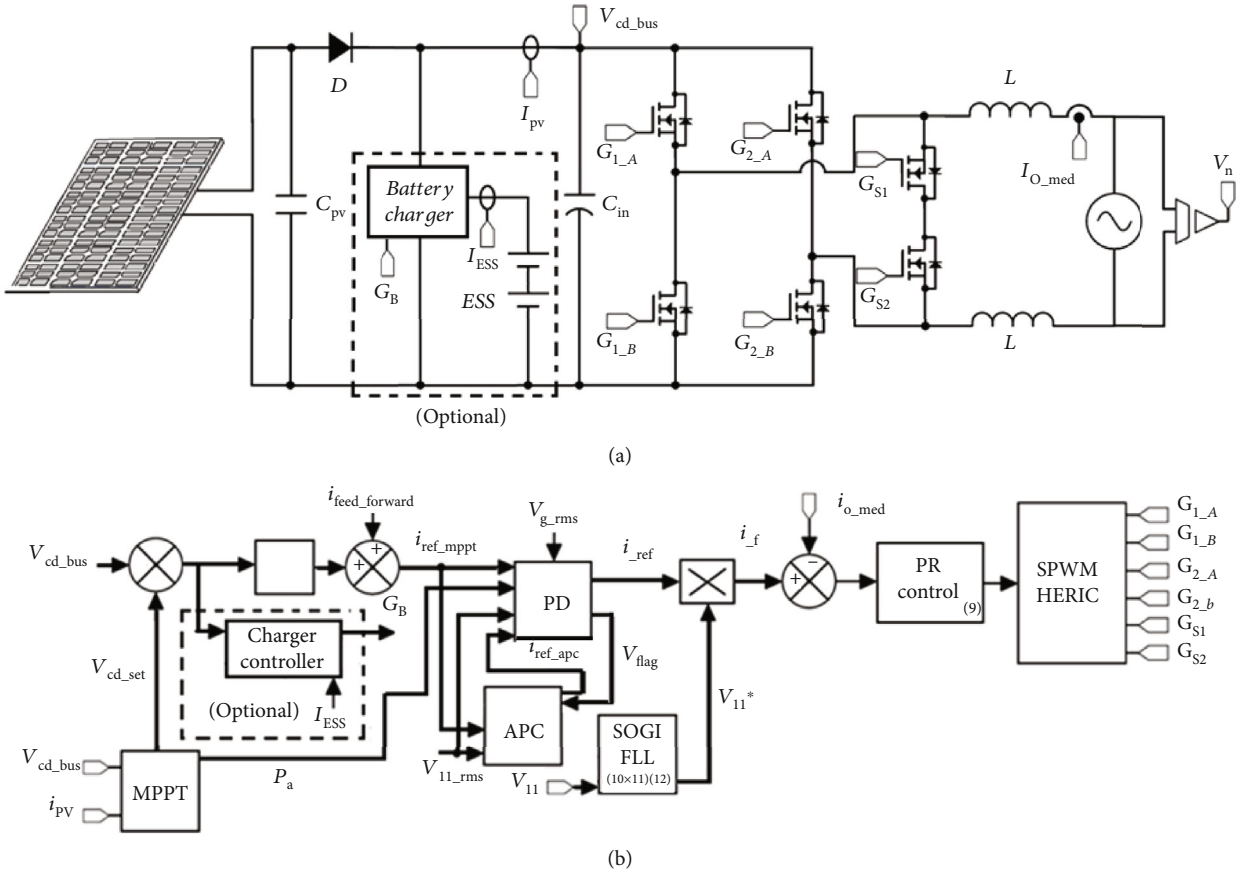

Figure 3: Proposed system: (a) power stage; (b) proposed controller.

Gain K_p is tuned to get the best dynamics of the system in terms of bandwidth but assuring stability with the proper phase and gain margins. Gain K_r is tuned to eliminate the steady-state error [48].

This controller allows obtaining the injected current as required by the APC or MPPT section. The K_p and K_r values are shown in Table 1. This type of controller employs averaged models, which assumes that the switching frequency may be neglected.

4.2. Voltage Synchronization. To synchronize the injected current with the local voltage, a second-order generalized integrator (SOGI) and a frequency locked loop (FLL) were used [49]. The equations used are

$$v_{11}^*(s) = \frac{k\omega_o s}{s^2 + \omega_o s + \omega_o^2} v_{11}(s), \tag{10}$$

$$v_{q11}^*(s) = \frac{k{\omega_o}^2}{s^2 + \omega_o s + \omega_o^2} v_{11}(s), \tag{11}$$

$$\omega_o = -\frac{\gamma}{s}(v_{11} - v_{11}^*)v_{q11}^*, \tag{12}$$

where k is a tuning constant, γ is a tuning constant, v_{11} is the input voltage (n_{th} residence), and v_{11}^* is the orthogonal synchronized output.

Table 1: Controller parameters.

Parameters	Units
K_p	2
K_r	10
k_i	1
k	1/170
Y	1

This section allows injecting the current synchronized with the voltage grid. For its implementation (Table 1), a value of k was selected to assure a normalized reference at nominal voltage to determine the current amplitude directly by the PD and γ is tuned to offer a good steady-state operation [49].

4.3. DC Bus Voltage Regulation and MPPT. When no voltage fluctuation occurs due to the high PV penetration, the PV system works traditionally; that is, the MPPT of the PV panel is tracked through the perturb and observe (P&O) algorithm [50]. The MPPT determines the voltage set point at the maximum power point, measuring the voltage and current of the PV panel.

To assure a low distortion in the injected current, the bandwidth of the voltage loop must be small; therefore, the

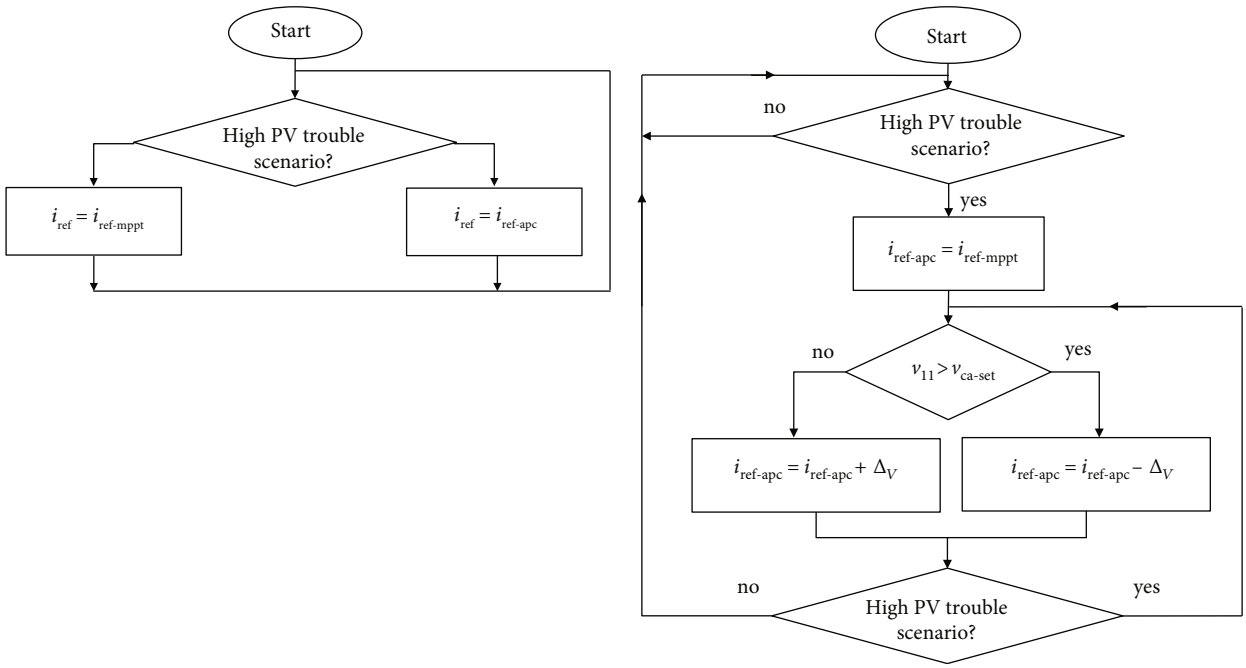

Figure 4: Flowchart: (a) penetration detector; (b) active power controller.

use of an integrator is enough to assure a good operation. Nevertheless, a feed-forward compensator is used to increase the fastness of the system under grid voltage variations, by using the actual power (P_a) of the PV panel to determine the current reference in a steady state. The equation used for the voltage controller is

$$i_{ref-mppt} = k_i \frac{v_{cd-bus} - V_{cd-set}}{s} + i_{feed-forward}. \quad (13)$$

The value of k_i was tuned to have a slow response, and then, to avoid distortion in the injected current, the bandwidth is selected ten times lower than 60 Hz.

4.4. High PV Penetration Detector (PD). To avoid the voltage fluctuations in a high PV penetration scenario, a PD is employed. This PD switches the operation between the MPPT voltage regulator and the APC (Figure 4(a)). The setpoint for the PR controller (i_{ref}) is set by the MPPT algorithm, in normal operation, or by the APC when a voltage increment is detected due to high PV penetration; additionally, it provides a flag that indicates the operating mode (V_{flag}).

To determine if there is voltage fluctuation due to high PV penetration, the voltage conditions are used. That is, if the local voltage is higher than the transformer voltage and above 5% of the nominal value, APC operations begin. If the local voltage is higher than the transformer voltage and below 4% of the nominal voltage, the MPPT voltage regulator is operating. This operating way allows extracting more power from the PV system when possible until the voltage is reasonably fulfilling the standard. According to the ANSI c84.1 standard, the maximum overvoltage allowed is 5.8%

Table 2: Experimental setup data.

Parameters/elements	Value
V_g	120 V @ 60 Hz
P_o	1 kW
L	4 mH
C_{in}	$2 \times 470\ \mu$F
MPPT algorithm	P&O
Proposed algorithm	APC
MOSFETs	C2M0160120D
Voltage sensor	LV25-P
Current sensor	LA25-NP
Digital platform	NI MyRIO 1900
Switching frequency of G_{1A}, G_{1B}, G_{2A}, G_{2B}	35 kHz
Switching frequency of G_{s1}, G_{s2}	60 Hz
DC bus voltage	250 V

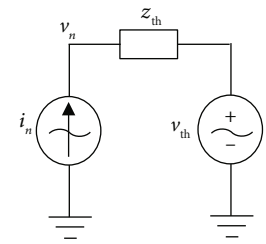

Figure 5: Simplified circuit.

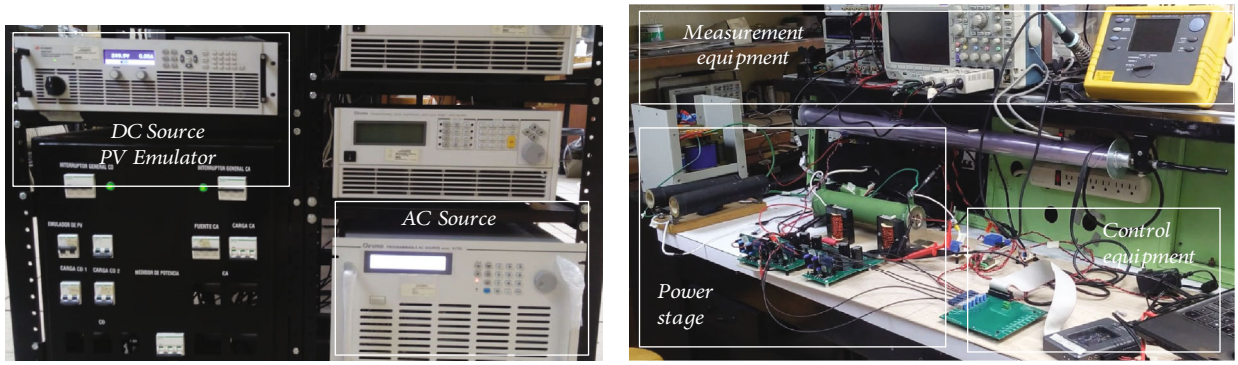

(a) (b)

Figure 6: Photography of the system: (a) power supplies; (b) power stage and controller.

above the nominal grid voltage, so it is assumed that the proposed voltage increment is acceptable for any residence. These two limits (5% and 4%) establish a hysteresis band, which determines the operation of the PD. Certainly; each limit may be adjusted according to other applicable standards in different regions.

The actual power of the PV panel (P_a) is considered to switch the operating mode from APC to MPPT since the APC delivers power regardless of the PV panel power availability. In case the PV panel cannot provide the power set by the APC, the MPPT voltage regulator must be selected instead of the APC.

4.5. Active Power Controller (APC). The APC goes into operation when it is detected that there are voltage fluctuations due to the high PV penetration. Then, the local voltage is regulated by changing the active power through the injected current.

Figure 4(b) shows the flowchart used to determine the APC current setpoint (i_{ref_apc}), which establishes the power injected into the grid during this mode. When a voltage increment due to a high PV penetration scenario occurs, the PD gives control to the APC. The initial current setpoint is the last current set point given by the MPPT algorithm ($i_{ref\_apc} = i_{ref\_mppt}$), and it is incremented or decremented according to the local voltage conditions to keep it regulated. If the local voltage at the residence is greater than the setpoint established ($V_{11} > V_{ca\_set}$), a decrease in the current reference is made, otherwise it is increased. Finally, the operating conditions are checked again to determine if whether the APC mode should be maintained or not.

The increment is given by an adaptive step, which is proportional to the absolute value of the voltage error. The ac voltage setpoint is selected as the center of the hysteresis band. Then, the equation used is

$$\Delta_V = K_{pe}|v_{11} - V_{ca\text{-}set}|, \tag{14}$$

where Δ_v is the increment, K_{pe} is the controller parameter, V_{11} is the local residence voltage, and V_{ca-set} is the reference for the regulated voltage.

This equation allows avoiding fluctuations in a steady state when the APC is operating.

4.6. Energy Storage System (ESS). The use of an ESS is suggested for a better performance of the system, but it is certainly optional, as it does not affect the voltage regulation on the ac side. If an ESS is not employed in a scenario where the APC is active, part of the energy available in the PV system is not injected into the grid and then dissipated by the PV system itself, which may affect the lifespan. Therefore, to improve the performance of the PV system, the energy that is not injected into the grid should be stored and when possible delivered to the grid or used for other types of applications.

In the case of using an ESS, a battery charger should be employed, which is enabled only in APC mode, the energy is taken from the DC bus voltage. The proposal of the charger controller is beyond the purpose of this work.

5. Experimental Validation

To verify that the proposed system operates properly and mitigate the voltage deviations in the ac grid, a laboratory prototype was built. Different tests were conducted to evaluate the performance of the proposed system: steady-state operation, startup, power variation in the renewable sources, distribution transformer voltage variations, and test under grid voltage distortion.

5.1. Workbench. For the tests, it is considered that the nominal grid voltage is 120 V (transformer voltage); the wiring impedances between residences are equal and have a value of $Z \approx 0.018\,\Omega$; the number of residences considered is 11, and the first 10 residences inject current to the grid but selectable to emulate the voltage fluctuations due to the high PV penetration. It is considered 100% of penetration, which means that all residences deliver power to the grid; to simplify the implementation, the same current is considered at each residence, but certainly, different power should be considered. The ANSI c84.1 standard is considered; then, the maximum allowed overvoltage is 5.8%, which is 126.96 V.

The proposed system is connected to the last residence, its PV system is working during the tests, but the last residence is not demanding energy to have the worst case. It is

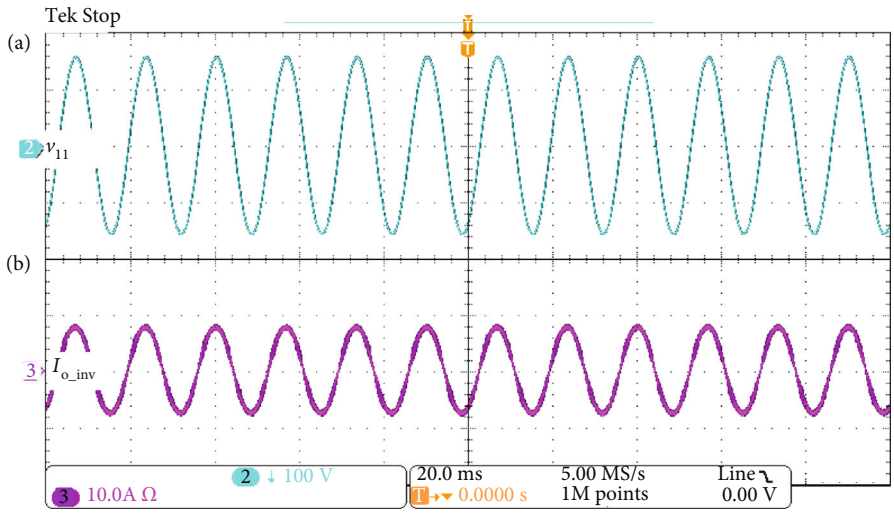

Figure 7: System operating at MPPT mode: (a) local voltage in residence 11 (V_{11}, 100 V/div); (b) current in residence 11 (I_{11}, 10 A/div). Time 20 ms/div.

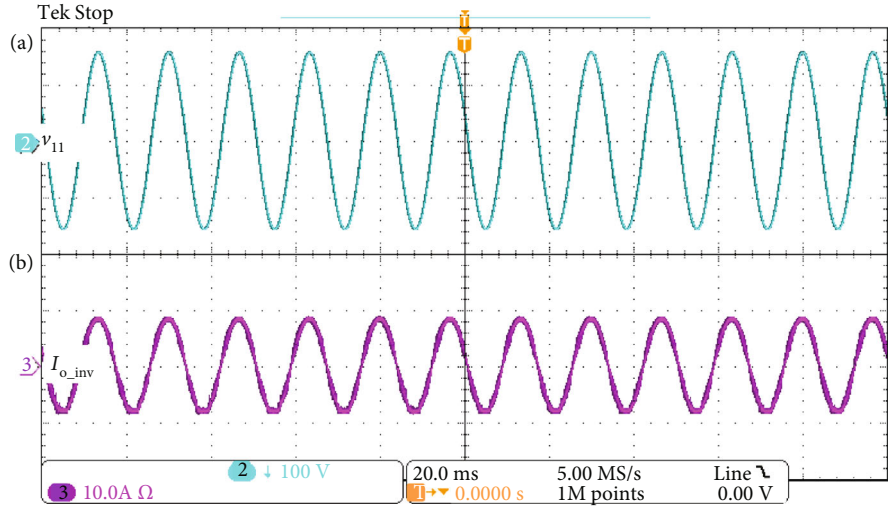

Figure 8: System operating at APC mode: (a) local voltage in residence 11 (V_{11}, 100 V/div); (b) current in residence 11 (I_{11}, 10 A/div). Time 20 ms/div.

considered that each PV system generates till 1 kW_p. The parameters of the implemented system are shown in Table 2.

To simplify the implementation, the Thévenin equivalent circuit of the first 10 residences is considered, resulting in the simplified circuit shown in Figure 5. Therefore, for the tests, only a single voltage source and impedance are used to emulate the first 10 residences.

The Thévenin voltage is

$$v_{\text{th}} = v_g + Z \sum_{m=1}^{r-1} (mi_m), \tag{15}$$

where r is the number of residences.

The Thévenin impedance is

$$Z_{\text{th}} = nZ. \tag{16}$$

To simplify the calculation of the Thévenin voltage, it is assumed that the injected current by each of the first 10 residences is equal, resulting in

$$v_{\text{th}} = v_g + Zi_{pv} \sum_{m=1}^{n-1} (m) = v_g + Zi_{pv} \frac{n(n-1)}{2}, \tag{17}$$

where i_{pv} is the injected current by the $n-1$ residences.

However, the experimental setup would be valid for any other configuration using (15) for the Thévenin voltage calculation.

A photograph of the implemented system is shown in Figure 6, where the ac power supply (Chroma 61703), the photovoltaic emulator (Keysight N8937APV), the power converter, the measurement equipment (oscilloscope Tek MSO3014 and power quality logger Fluke 1735), and the

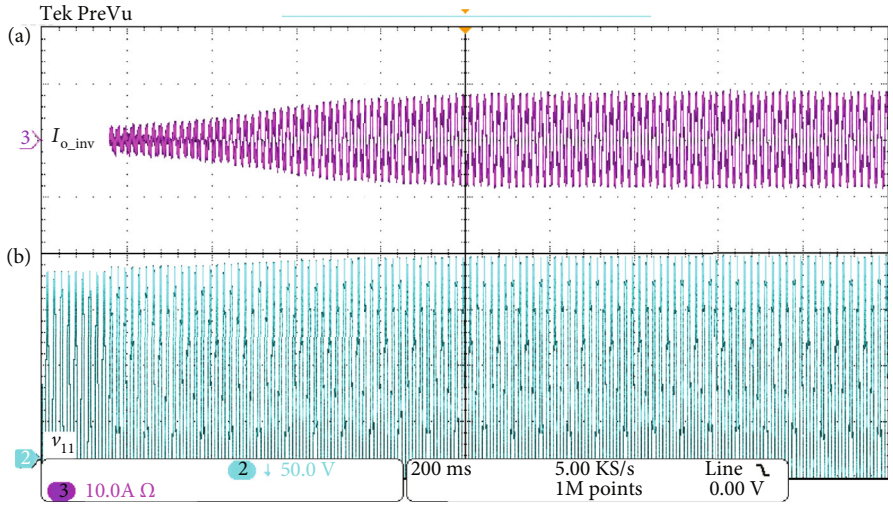

Figure 9: Startup: (a) current in residence 11 (I_{11}, 10 A/div); (b) local voltage in residence 11 (V_{11}, 50 V/div). Time 200 ms/div.

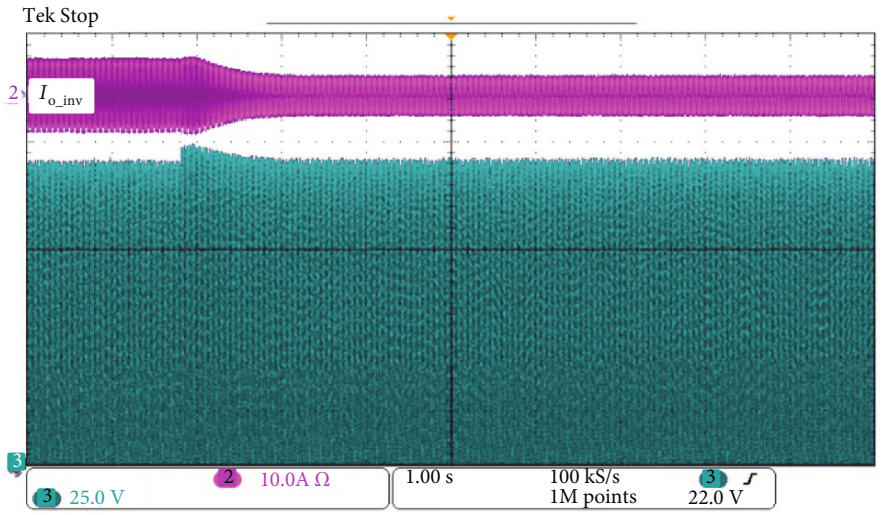

(a)

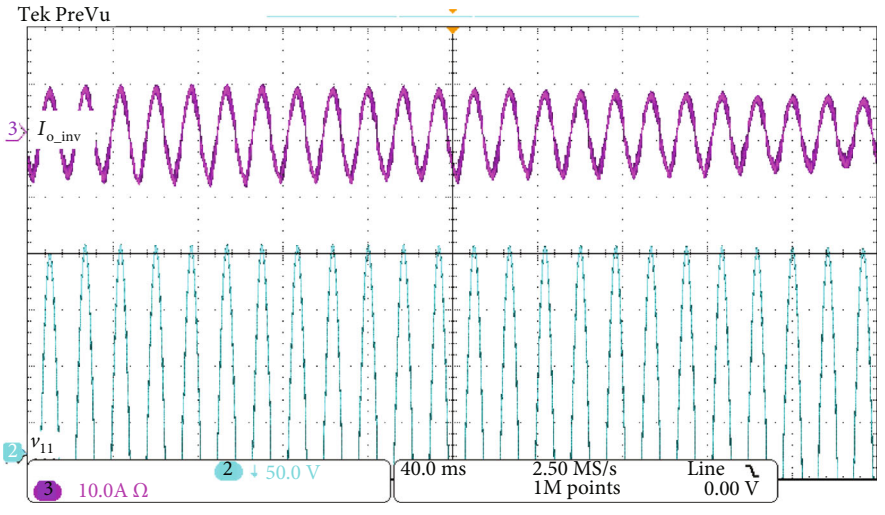

(b)

Figure 10: Power variation, for positive deviation. From top to bottom: current in residence 11 (I_{11}, 10 A/div), local voltage in residence 11 (V_{11}, 25 V/div). (a) Full transition, time 1 s/div; (b) zoom, time 40 ms/div.

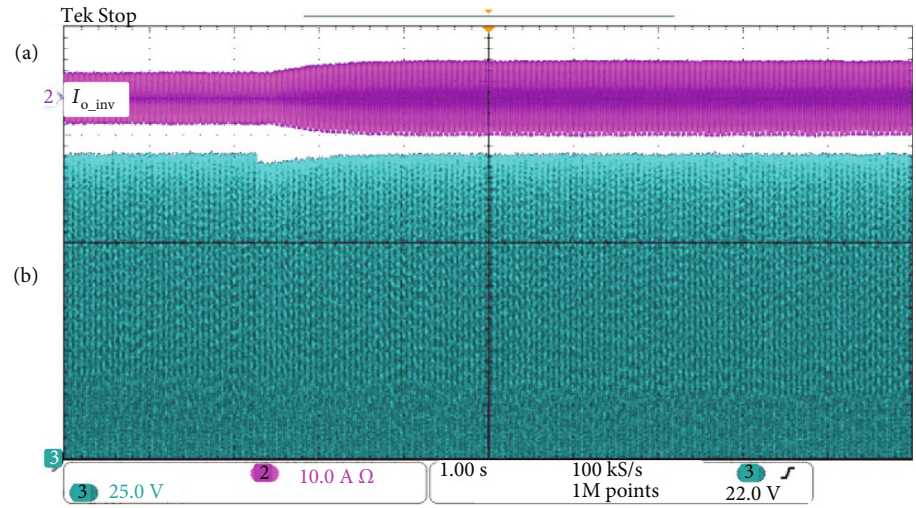

FIGURE 11: Power variation, for negative deviation: (a) current in residence 11 (I_{11}, 10 A/div); (b) local voltage in residence 11 (V_{11}, 25 V/div). Time 1 s/div.

control system employed (National Instruments myRIO 1900) can be observed.

Since the ac power supply cannot receive energy, otherwise it will be damaged, a dummy load is employed to emulate the electric grid. The energy that is injected is consumed by the dummy load; then, a safe test is made; this load is connected in parallel to the ac power supply.

5.2. Steady-State Operation. The proposed system offers a good steady-state operation due to the PR controller employed. In Figure 7, the voltage and current in residence 11 are shown, operating in MPPT mode. The current THD is 1.1%, and the PF is 0.99. Figure 8 shows the steady-state waveforms of voltage and current in residence 11, when the proposed system operates in the APC mode, thus regulating the voltage. The current THD is 1.2%, and the PF is 0.99. The leakage current is lower than 300 mAp in all cases, which complies with the VDE-0126-1-1 standard.

5.3. Startup. Figure 9 shows the injected current and the voltage in residence 11 during system startup. A smooth transition is performed when the system starts. The voltage of the evaluated residence is slightly affected by the grid impedance, so the voltage rises. For this test, the initial condition of the MPPT was set to have a fast transition.

5.4. Power Variation of PV Panels. To evaluate the dynamic performance of the proposal, power variations in the PV panels were performed. First, the current injected by the first 10 residences is increased. Second, the injected current by the first 10 residences is decreased. Finally, a third test is conducted with the PV system operating in a high PV penetration scenario without the APC and then enabling it. For all tests, the maximum voltage limit is set at 126 V, which is 0.8% below the value established by the ANSI c84.1 standard.

For the first two tests, the conditions given imply that there is a high PV penetration in the residential electrical grid, so that the APC algorithm comes into operation, maintaining the voltage in the last residence fulfilling the standard, according to the proposed operation. A sudden change in the injected current of the first 10 residences results in a fast voltage variation at the evaluated residence, which allows testing the dynamic response of the proposed system.

First, a positive deviation is performed (Figure 10). The injected current for the first 10 residences is incremented from 4 A to 6.7 A causing a voltage increment to 128 V at the residence under test, which is out of the standard limit. The proposed system begins to reduce the injected current to the point where the voltage is within standard limits. The injected current changes from an initial value of 7.1 A to approximately 3.5 A, in less than 1 s. Figure 10(a) shows the injected current and the voltage of residence under test; the time scale allows illustrating the voltage and current evolution. In Figure 10(b), a zoom is performed to illustrate the waveforms during the transition.

Second, a negative deviation is performed (Figure 11). The injected current by the first 10 residences is decremented from 4.2 A to 3.3 A, causing a voltage decrement to 124 V at the residence under test, which indicates that the PV system may inject more energy into the grid. The proposed system begins to increase the injected current to the point where the voltage is still within standard limits. The injected current changes from an initial value of 4.8 A to approximately 7 A, in less than 1 s. The figure shows the injected current and the voltage of the residence under test.

For the third test (Figure 12), a transition between operating modes is made. In the beginning, the prototype is working as a traditional PV system, regulating the injected current according to the MPPT, but in a high PV penetration scenario. This causes the voltage level at the residence under test to exceed the maximum limit allowed by the standard. Then, at a certain time, the proposed APC algorithm is enabled, which starts the modulation of the active power and reduces the local voltage within standard limits and according to the proposed operation.

5.5. Transformer Voltage Variation. To evaluate the performance of the proposal, distribution transformer voltage

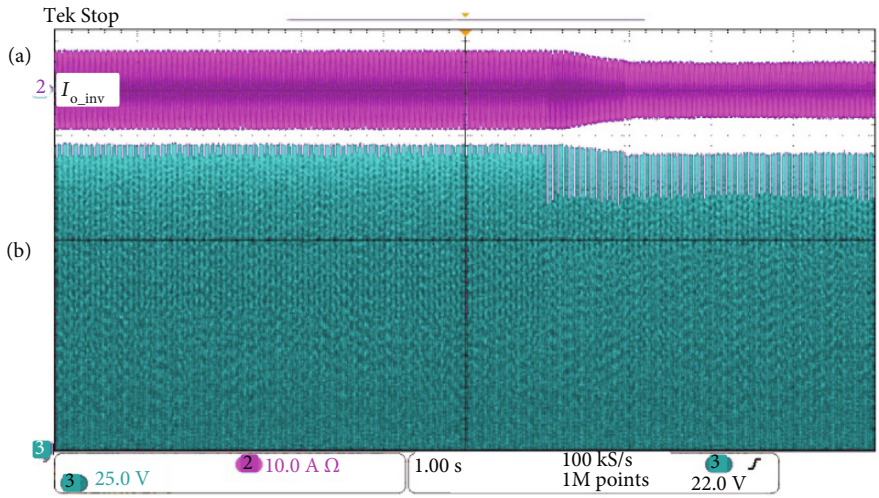

Figure 12: Transition from traditional MPPT and the proposed APC: (a) current in residence 11 (I_{11}, 10 A/div); (b) local voltage in residence 11 (V_{11}, 25 V/div). Time 1 s/div.

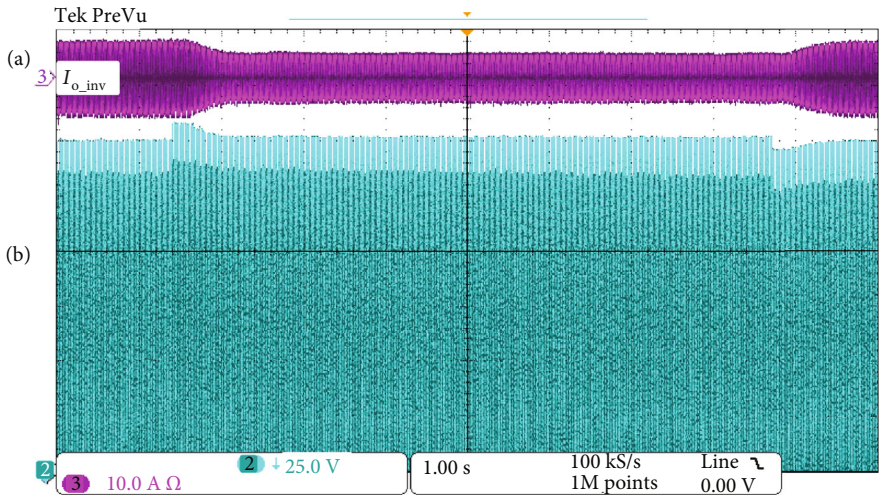

Figure 13: System response under transformer voltage variation (increment): (a) current in residence 11 (I_{11}, 10 A/div); (b) local voltage in residence 11 (V_{11}, 25 V/div). Time 1 s/div.

variation tests have been carried out. For these tests, the first 10 residences inject a constant current.

For the first test, it is considered that the last residence is operating in the APC mode. The initial transformer voltage is 120 V, suddenly increases to 125 V, and after 7 seconds approximately returns to 120 V. This is illustrated in Figure 13, where the local voltage and current at the 11th residence are shown. As it can be observed, during the first transition, the local voltage increases and the system reacts by injecting less power to regulate the voltage; in the second transition, the opposite behavior is observed while maintaining the voltage regulation.

The second test again considers that the last residence is operating in the APC mode, but now the transformer voltage drops suddenly from 120 V to 115 V and after 7 seconds returns to 120 V. This is illustrated in Figure 14, where the local voltage and current of the 11th residence are shown. As it can be observed, in the first transition, the local voltage decreases and the system reacts by injecting more power to regulate the voltage; in the second transition, the opposite behavior is shown while maintaining the voltage regulation.

5.6. Grid Voltage Distortion. Finally, a voltage distortion at the transformer voltage was imposed; since a synchronization circuit is employed, the injected current offers good performance. In Figure 15, the voltage and current at the last residence can be observed. The current THD is 1.4%, and the voltage THD is 5%. The transformer voltage distortion is also reflected in the evaluated residence. The proposal does not control the voltage waveform, and so the distortion remains at the voltage of residence under test.

5.7. Comparison Analysis. The proposed system is compared with other techniques; this is illustrated in Table 3. A methodology to design the grid under high PV penetration scenario is given in [24], which is a good alternative when the distribution system is a new design. However, for existing residential areas, the method is complex and expensive, and

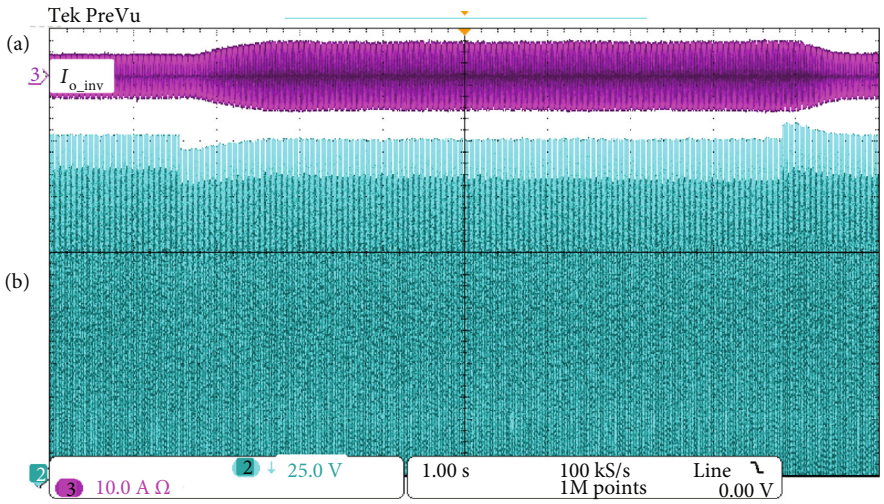

FIGURE 14: System response under transformer voltage variation (decrement): (a) current in residence 11 (I_{11}, 10 A/div); (b) local voltage in residence 11 (V_{11}, 25 V/div). Time 1 s/div.

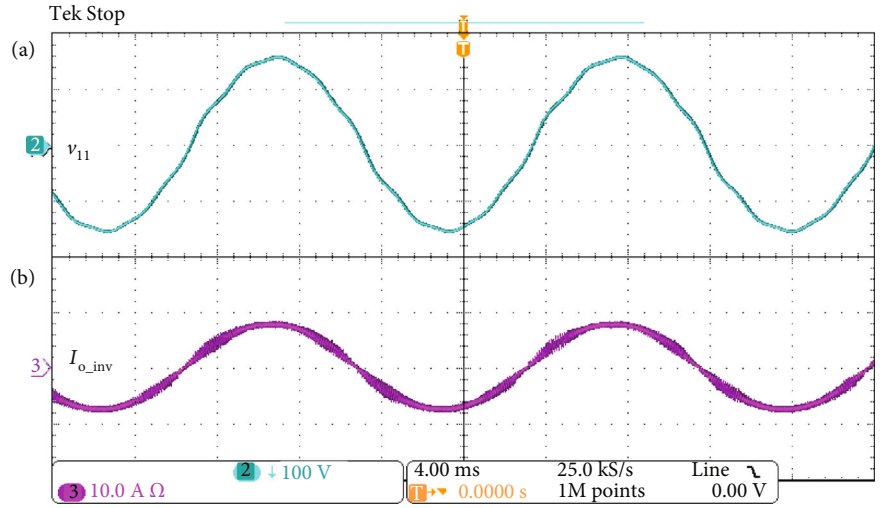

FIGURE 15: Grid voltage distortion test: (a) local voltage in residence 11 (V_{11}, 100 V/div); (b) current in residence 11 (I_{11}, 10 A/div). Time 4 ms/div.

in most cases, it would not be feasible due to the time and costs of the infrastructure modification. Then, it is not comparable with the proposed solution.

The use of variable tap transformers is proposed in [25]. The main advantage is that it is not invasive to the users; only a communication network may be added. The effectiveness of the proposal depends on the communication network and the number of taps in the transformer. There is still a possibility that depending on the grid conditions, the voltage variation may not keep within standard limits, resulting in a method that should be combined with other methods like the proposed in this work.

The use of ESS or electric vehicles may be a good alternative [27–29, 34]. This allows storing the PV energy; however, the ability to regulate the voltage variations depends on the storage capacity. That is, if the ESS is fully charged, the system may no longer compensate for the voltage variations, and therefore, the trouble may continue. This solution may be combined with other schemes to assure good operation.

In terms of cost (including power devices and controllers), it can be observed in Table 3 that the two best alternatives use a smart inverter with reactive power compensation [30–33] and the proposed strategy in this work. This is because no extra elements or devices or modifications on the infrastructure are required, just software modifications. However, if losses in the distribution grid are considered, our proposal becomes the better solution, since the injected current is not incremented for the reactive power compensation. Moreover, it is not necessary to increase the inverter power rate.

According to the experimental results (Figures 13 and 14), the settling time of the proposed system is less than 1 s, which is comparable with other techniques reported in the literature, but certainly, this time depends on the penetration detector not only on the proposed active power compensation.

Table 3: Strategy comparison to alleviate the high PV penetration troubles.

Reference/method	Advantages	Disadvantages	Complexity	Cost/economics	Setting time
[24]/grid design	Structured system and efficient No need for extra equipment and devices to mitigate high penetration	Only applicable for new residential areas under construction The phenomenon of high penetration may continue depending on grid conditions	High: although the method is desirable for residential areas under construction, its implementation can also be carried out in existing residential areas, which would involve complexity and cost	High: if the infrastructure already exists, it will imply high costs to make changes. On the other hand, if it is a new design, the solution would be cheaper.	Not applied
[25]/tapped transformer	Good for centralized and decentralized techniques It is not invasive for the users of the electrical network	The phenomenon of high penetration may continue, especially at critical points of connection Requires a bidirectional communication network	Low: exchange the transformer for one with variable tap	Medium: tapped transformer implies costs and also requires external communication components.	<0.3 s
[27–29]/energy storage	Store the energy not used in the moments of maximum PV generation. No losses at the PV system and then increase its lifespan	Not so ecological, due to the use of batteries Depending on the ESS capacity, the voltage variation may continue	Medium: extra stages and controllers are required	Medium: the batteries are expensive, and also a program for its maintenance is required.	≈0.3 s
[30–33]/reactive power	Good performance No extra infrastructure	Extra losses in wiring and inverter due to injection of reactive power The power inverter rated should be incremented In some cases, the grid must be characterized	Medium: in some cases, prior knowledge of critical points in the distribution system	Low: only software modifications are required, no extra infrastructure.	≈10 s
[33]/electric vehicles	Good performance Taking advantage of electric vehicles	For future implementation Extra infrastructure Synchronize users' times with cogeneration by PV systems	High: high logistics process to carry out the best use of the system	High: the cost of electrical or hybrid vehicles is high.	Not available
Proposed APC	No extra infrastructure No extra losses in the wiring network No increment on power inverter rated When batteries are employed, there are no losses at the PV system and then it increases its lifespan	If no batteries are employed, the PV MPPT is not reached when APC operates	Low: the implementation uses the same infrastructure of a traditional PV system	Low: only software modifications are required, no extra infrastructure. The use of batteries is suggested which may imply extra costs.	<1 s

The proposed method certainly is a good alternative that may reduce the voltage variations; however, the energy of the PV panel may be wasted or lost in the PV panel, which becomes its disadvantage. Therefore, the proposal may be combined with energy storage systems or tapped transformers to inject the most energy possible into the grid.

6. Conclusion

This paper presents a different solution to reduce voltage fluctuations in the power grid, caused by high PV penetration when a residential cluster is the load. The proposal uses the PV inverter to perform the voltage compensation, without

the need of extra devices or infrastructure. The active power is controlled instead of the reactive one, which permits the reduction of wiring and power converter losses but also avoids the increment of inverter nominal power.

The experimental results show that the proposed system is capable of reducing the voltage deviations in the power grid caused by high PV penetration. Tests were carried out under different conditions such as transformer voltage variations, PV panel variations, and voltage distortions, obtaining satisfactory results and keeping the voltage within the standard specifications. The proposal offers good characteristics compared to other schemes reported in the literature, which makes it competitive.

Certainly, the proposal has the drawback of not being able to harvest and inject all the energy available in the PV panels under all operating conditions, so it is suggested to combine the solution with energy storage systems or other methods.

Data Availability

The data used to support the findings of this study are included within the article.

Conflicts of Interest

The authors declare that there is no conflict of interest regarding the publication of this paper.

Acknowledgments

This work was supported in part by Tecnológico Nacional de México under project No. 10166.21-P.

References

[1] The Internal Energy Agency, 2021, http://www.iea.org.

[2] B. Ernst and B. Engel, "Grid integration of distributed PV-generation," in *2012 IEEE Power and Energy Society General Meeting*, pp. 1–7, San Diego, USA, 2012.

[3] V. Sharma, S. Mahfuzul, M. H. Haque, and T. Kauschke, "Effects of high solar photovoltaic penetration on distribution feeders and the economic impact," *Renewable and Sustainable Energy Reviews*, vol. 131, p. 110021, 2020.

[4] B. Matthiss, A. Momenifarahani, and J. Binder, "Storage placement and sizing in a distribution grid with high PV generation," *Energies*, vol. 142, 2021.

[5] B. Noone, *PV Integration on Australian Distribution Networks: Literature Review*, The Australian PV Association, UNSW, Australia, 2013, http://www.ceem.unsw.edu.au/sites/default/files/documents/APVA%20%20PV%20and%20DNSP%20Literature%20review%20September%202013.pdf.

[6] T. Aziz and N. Ketjoy, "PV penetration limits in low voltage networks and voltage variations," *IEEE Access*, vol. 5, pp. 16784–16792, 2017.

[7] N. Samaan, M. A. Elizondo, B. Vyakaranam et al., "Combined transmission and distribution test system to study high penetration of distributed solar generation," in *2018 IEEE/PES Transmission and Distribution Conference and Exposition (T&D)*, pp. 1–9, Denver, USA, 2018.

[8] K. A. Alboaouh and S. Mohagheghi, "Impact of rooftop photovoltaics on the distribution system," *Journal of Renewable Energy*, vol. 2020, 23 pages, 2020.

[9] T. Matsumura, M. Tsukamoto, A. Tsusaka et al., "Line-end voltage and voltage profile along power distribution line with large- power photovoltaic generation system," *International Journal of Photoenergy*, vol. 2019, 8 pages, 2019.

[10] K. Burges and J. Twele, "Power systems operation with high penetration of renewable energy - the German case," in *2005 International Conference on Future Power Systems*, pp. 1–5, Amsterdam, Netherlands, 2005.

[11] B. C. Ummels, M. Gibescu, E. Pelgrum, and W. L. Kling, "System integration of large-scale wind power in the Netherlands," in *2006 IEEE Power Engineering Society General Meeting*, pp. 1–8, Montreal, Canada, 2006.

[12] D. Infield and W. Lei, "The challenges of high wind energy penetration in the UK power system," in *2014 International Conference on Power System Technology*, pp. 2999–3003, Chengdu, China, 2014.

[13] I. Kouveliotis-Lysikatos, P. Kotsampopoulos, and N. Hatziargyriou, "Harmonic study in LV networks with high penetration of PV systems," in *2015 IEEE Eindhoven PowerTech*, pp. 1–6, Eindhoven, Netherlands, 2015.

[14] J. Hu, Z. Li, J. Zhu, and J. M. Guerrero, "Voltage stabilization: a critical step toward high photovoltaic penetration," *IEEE Industrial Electronics Magazine*, vol. 13, no. 2, pp. 17–30, 2019.

[15] O. Gandhi, D. S. Kumar, C. D. Rodríguez-Gallegos, and D. Srinivasan, "Review of power system impacts at high PV penetration Part I: factors limiting PV penetration," *Solar Energy*, vol. 210, pp. 181–201, 2020.

[16] S. Homan, N. Mac Dowell, and S. Brown, "Grid frequency volatility in future low inertia scenarios: challenges and mitigation options," *Applied Energy*, vol. 290, p. 116723, 2021.

[17] M. Karimi, H. Mokhlis, K. Naidu, S. Uddin, and A. H. A. Bakar, "Photovoltaic penetration issues and impacts in distribution network–A review," *Renewable and Sustainable Energy Reviews*, vol. 53, pp. 594–605, 2016.

[18] S. F. Kagadi and M. J. Prasad, "Impacts of high rooftop PV penetration in distribution network and its mitigation using DSTATCOM," in *7th International Conference on Electrical Energy Systems (ICEES)*, pp. 1–4, IEEE, Chennai India, 2021.

[19] C. Essayeh, M. R. El-Fenni, H. Dahmouni, and M. A. Ahajjam, "Energy management strategies for smart green microgrid systems: a systematic literature review," *Journal of Electrical and Computer Engineering*, vol. 2021, 21 pages, 2021.

[20] M. Thomson and D. G. Infield, "Network power-flow analysis for a high penetration of distributed generation," *IEEE Transactions on Power Apparatus and Systems*, vol. 22, no. 3, pp. 1157–1162, 2007.

[21] A. Lucas, "Single-phase PV power injection limit due to voltage unbalances applied to an urban reference network using real-time simulation," *Applied Sciences*, vol. 8, no. 8, p. 1333, 2018.

[22] G. Lv, Q. Wu, C. Wu, and C. XZG, "Dynamic parameters tracking and voltage sag source location in the distribution system with DG," in *2018 2nd IEEE Conference on Energy Internet and Energy System Integration (EI2)*, pp. 1–6, Beijing, China, 2018.

[23] S. Afonaa-Mensah, Q. W. Stephen, and B. B. Uzoejinwa, "Investigation of daytime peak loads to improve the power generation costs of solar-integrated power systems," *International Journal of Photoenergy*, vol. 2019, 2019.

[24] R. A. Shayani and M. Oliveira, "Photovoltaic generation penetration limits in radial distribution systems," *IEEE Transactions on Power Systems*, vol. 26, no. 3, pp. 1625–1631, 2011.

[25] Y. Liu, J. Bebic, B. Kroposki, J. de Bedout, and W. Ren, "Distribution system voltage performance analysis for high-penetration PV," in *2008 IEEE Energy 2030 Conference*, pp. 1–8, Atlanta, USA, 2008.

[26] D. Das, V. M. Hrishikesan, C. Kumar, and M. Liserre, "Smart transformer-enabled meshed hybrid distribution grid," *IEEE Transactions on Industrial Electronics*, vol. 68, no. 1, pp. 282–292, 2021.

[27] A. Alzahrani, H. Alharthi, and M. Khalid, "Minimization of power losses through optimal battery placement in a distributed network with high penetrations of photovoltaics," *Energies*, vol. 13, no. 1, pp. 1–16, 2020.

[28] N. Mahmud, A. Zahedi, and A. Mahmud, "A cooperative operation of novel PV inverter control scheme and storage energy management system based on ANFIS for voltage regulation of grid-tied PV system," *IEEE Transactions on Industrial Informatics*, vol. 13, no. 5, pp. 2657–2668, 2017.

[29] Y. Xing, H. Zhao, Z. Shen et al., "Optimal coordinated energy management in active distribution system with battery energy storage and price-responsive demand," *Mathematical Problems in Engineering*, vol. 2021, 12 pages, 2021.

[30] A. Singhal, V. Ajjarapu, J. Fuller, and J. Hansen, "Real-time local volt/var control under external disturbances with high PV penetration," *IEEE Transactions on Smart Grid*, vol. 10, no. 4, pp. 3849–3859, 2019.

[31] M. Hasheminamin, V. G. Agelidis, A. Ahmadi, P. Siano, and R. Teodorescu, "Single-point reactive power control method on voltage rise mitigation in residential networks with high PV penetration," *Renewable Energy*, vol. 119, pp. 504–512, 2018.

[32] S. Ouali and C. Abdeljabbar, "Elimination of the impact produced by DG units on the voltage profile of distribution networks," *Journal of Applied Mathematics*, vol. 2020, 8 pages, 2020.

[33] S. Singh, V. B. Pamshetti, A. K. Thaur, and S. P. Singh, "Multistage multiobjective volt/var control for smart grid-enabled CVR with solar PV penetration," *IEEE Systems Journal*, pp. 1–12, 2021.

[34] A. Ali, D. Raisz, and K. Mahmoud, "Mitigation of voltage fluctuation in distribution system connected with PV and PHEVs using artificial bee colony algorithm," in *2018 6th International Istanbul Smart Grids and Cities Congress and Fair (ICSG)*, pp. 144–148, Istanbul, Turkey, 2018.

[35] M. Chamana, B. Chowdhury, and F. Jahanbakhsh, "Distributed control of voltage regulating devices in the presence of high PV penetration to mitigate ramp-rate issues," *IEEE Transactions on Smart Grid*, vol. 9, no. 2, pp. 1086–1095, 2018.

[36] J. A. P. Lopes, N. Hatziargyriou, J. Mutale, P. Djapic, and N. Jenkins, "Integrating distributed generation into electric power systems: a review of drivers, challenges and opportunities," *Electric Power Systems Research*, vol. 77, no. 9, pp. 1189–1203, 2007.

[37] J. Matevosyan, B. Badrzadeh, and T. Prevost, "Grid-forming inverters: are they the key for high renewable penetration?," *IEEE Power and Energy Magazine*, vol. 17, no. 6, pp. 89–98, 2019.

[38] F. Rafi, H. M. Hossain, and J. Lu, "Hierarchical controls selection based on PV penetrations for voltage rise mitigation in a LV distribution network," *International Journal of Electrical Power & Energy Systems*, vol. 81, pp. 123–139, 2016.

[39] P. Yu, C. Wan, Y. Song, and Y. Jiang, "Distributed control of multi-energy storage systems for voltage regulation in distribution networks: a back-and-forth communication framework," *IEEE Transactions on Smart Grid*, vol. 12, no. 3, 2021.

[40] T. Aziz and N. Ketjoy, "Enhancing PV penetration in LV networks using reactive power control and on load tap changer with existing transformers," *IEEE Access*, vol. 6, pp. 2683–2691, 2018.

[41] R. Zafar, J. Ravishankar, and H. R. Pota, "Centralized control of step voltage regulators and energy storage system under high photovoltaic penetration," in *2016 IEEE Innovative Smart Grid Technologies - Asia (ISGT-Asia)*, pp. 511–516, Melbourne, Australia, 2016.

[42] E. Vega-Fuentes and M. Denai, "Enhanced electric vehicle integration in the UK low-voltage networks with distributed phase shifting control," *IEEE Access*, vol. 7, pp. 46796–46807, 2019.

[43] D. L. Zhang, J. B. Guo, and J. L. Li, "Coordinated control strategy of hybrid energy storage to improve accommodating ability of PV," *The Journal of Engineering*, vol. 2017, no. 13, pp. 1555–1559, 2017.

[44] E. Mandefro Getie, G. Belachew Bantyirga, and T. Gera Workneh, "Photovoltaic generation integration with radial feeders using GA and GIS," *International Journal of Photoenergy*, vol. 2020, 7 pages, 2020.

[45] M. G. Kashani, S. Bhattacharya, J. Matamoros, D. Kaiser, and M. Cespedes, "Autonomous inverter voltage regulation in a low-voltage distribution network," *IEEE Transactions on Smart Grid*, vol. 9, no. 6, pp. 6909–6917, 2018.

[46] P. Somani and D. Vaghela, "Design of HERIC configuration based grid-connected single-phase transformerless photovoltaic inverter," in *2016 International Conference on Electrical, Electronics, and Optimization Techniques (ICEEOT)*, pp. 892–896, Chennai, India, 2016.

[47] G. Shen, X. Zhu, J. Zhang, and D. Xu, "A new feedback method for PR current control of LCL-filter-based grid-connected inverter," *IEEE Transactions on Industrial Electronics*, vol. 57, no. 6, 2010.

[48] R. Teodorescu, F. Blaabjerg, U. Borup, and M. Liserre, "A new control structure for grid-connected LCL PV inverters with zero steady-state error and selective harmonic compensation," in *Nineteenth Annual IEEE Applied Power Electronics Conference and Exposition, 2004. APEC 04*, pp. 580–586, Anaheim, USA, 2004.

[49] H. Yi, X. Wang, F. Blaabjerg, and F. Zhuo, "Impedance analysis of SOGI-FLL-based grid synchronization," *IEEE Transactions on Power Electronics*, vol. 32, no. 10, pp. 7409–7413, 2017.

[50] N. Khaehintung, T. Wiangtong, and P. Sirisuk, "FPGA implementation of MPPT using variable step-size P&O algorithm for PV applications," in *2006 International Symposium on Communications and Information Technologies*, pp. 212–215, Bangkok, Thailand, 2006.

Hindawi
International Journal of Photoenergy
Volume 2021, Article ID 5580264, 40 pages
https://doi.org/10.1155/2021/5580264

Research Article

Solar PV Minigrid Technology: Peak Shaving Analysis in the East African Community Countries

Jeanne Paula Ihirwe,[1] **Zibiao Li**,[1] **Keyuan Sun**,[1] **Samuel Bimenyimana**,[2,3] **Chen Wang**,[2] **Godwin Norense Osarumwense Asemota**,[4,5] **Aphrodis Nduwamungu**,[4] **and Cicilia Kemunto Mesa**[6]

[1]*Department of Economics and Management, Hebei University of Technology, Tianjin, China*
[2]*Huaqiao University, Intelligence and Automation in Construction Provincial Higher–Educational Engineering Research Centre, 361021 Xiamen, China*
[3]*Hello Renewables Ltd., Kigali, Rwanda*
[4]*University of Rwanda, African Centre of Excellence in Energy for Sustainable Development, Kigali 4285, Rwanda*
[5]*Morayo College, Nairobi, Kenya*
[6]*Kenya Industrial Research and Development Institute, Nairobi, Kenya*

Correspondence should be addressed to Zibiao Li; lizibiao2008@126.com

Received 27 January 2021; Revised 14 April 2021; Accepted 13 May 2021; Published 4 June 2021

Academic Editor: Evgeny Solomin

Copyright © 2021 Jeanne Paula Ihirwe et al. This is an open access article distributed under the Creative Commons Attribution License, which permits unrestricted use, distribution, and reproduction in any medium, provided the original work is properly cited.

Solar PV research in East Africa has concentrated on solar home systems (SHS) in each country. However, several other fundamental advances in the solar photovoltaic (PV) industry have emerged, and the developments have seen the sector experienced significant growth and diversification of models, regulation, and financing. This paper begins with an extensive narrative on the solar PV outlook of each of the six countries studied. A solar PV minigrid was also simulated using HOMER software with a critical load of 2800.0 kWh/day in order to analyze the peak shaving capability and assess the affordability of the solar PV microgrid having commercial and industrial loads. The regional overview of the efforts was identified, followed by a description of the models, payment methods, and barriers encountered collectively. The lessons from this research suggest that there is a vast potential for solar PV micro and minigrid deployment in the region with a population of over 100 million people lacking access to electricity by the end of 2019. It shows that solar PV minigrid deployment in East Africa is still at a nascent phase. Also, minigrid developers face several challenges operating in rural areas. While solar PV minigrids remain fairly nascent in the East Africa region, the technology is gaining traction, a development that indicates budding confidence in the solar PV minigrid technology. This study identifies that (1) with large critical loads (industrial and commercial), solar PV minigrid can still contribute to affordable electricity through peak shaving, except Tanzania; (2) solar PV minigrid projects are largely dependent on donor financing, require vast financial diversity to get off the ground, and offer consistent service; (3) Governments support in the form of National electrification strategies, policies, and regulation are key ingredients for realizing the electrification of rural populations through minigrids; (4) hybrid minigrids and power demand creation have emerged as an approach that ensures sustainability or profitability for the operating solar minigrid firms. Overall, government policy and regulation, funding, and financial sustainability remain the major hurdles to minigrid uptake in the region.

1. Introduction

The African continent basks on exceptional solar radiations globally, receiving a minimum of 4 kWh/m^2/day as the continent lies within the Sunbelt region. The dissemination of modern energy technologies (MET) in African countries remains quite low with the penetration rate of solar technology rising from 1% in 2010 to 4% in 2013 [1]. Sub-Sahara Africa remains prevalent in electricity access deficit where 625 million people live without access [2, 3]. Eighty percent

of the affected communities stay in the countryside where the cost of grid connection is deemed exorbitant by national utilities. Burundi, one of the 20 countries with the lowest electrification rates according to the IEA electrification rates in 2017 [4], is lodged in the region. Advancements in the electrification of rural areas have been limited most informal households are still connected through flimsy distribution networks with urban access rates significantly higher than rural rates. Given the situation, off-grid solutions are indispensable; these include solar home systems for lighting and heating and increasingly now, micro and minigrids [4].

With the aforementioned concept, there is a huge quantity of solar energy potential which has not yet been well exploited, and research is among the key pillars to the development of productive technologies once their results are feasible and implementable. The research in this paper is intended to give an extensive narrative review on solar PV outlook of each of the six countries of the East African Community (EAC) which are also members of Sub-Saharan Africa; study analysis on how a grid-connected solar PV minigrid with its storage contribute to peak shaving of a critical load (commercial or industrial) with an average of 2800.0 kWh/day and 200.0 kW daily peak load. Not only these, but the paper also intends to give a regional overview of the efforts identified followed by a description of models, payment methods, and barriers encountered collectively and provide concluding remarks upon the case already built.

2. Literature Search

The International Energy Agency (IEA) indicates that the population with access to electricity in 2015 was 1.0% in South Sudan, 9.1% in Burundi, 18.5% in Uganda, 26.4% in Rwanda, 30.0% in Tanzania, and 41.2% in Kenya against 84.5% in the world. By the end of 2019, South Sudan was at 1.1%, 10.9% in Burundi, 28.9% in Uganda, 39.5% in Tanzania, 52.6% in Rwanda, and 84.5% in Kenya against 90.0% in the world [5]. The transformation has partly been achieved through the deployment of solar PV projects both off and grid-connected. The projects are being funded by major international financiers, governments, donors, and a few coming to being through private firms in the energy business [6, 7].

Tanzania and Uganda are leading with the highest population without access to electricity at 36 and 25 million, respectively. Rwanda, South Sudan, and Burundi are the countries with the least populations without access in that order at populations of 10 million and below.

Kenya has an access deficit of 13 million people [5]. As it can be seen from Figure 1[4], Kenya is leading in electrification efforts at 84.5% followed by Rwanda at 52.6%, the rest are below 50.0%.

Minigrids have become a significant solution in rural electrification, being considered next to large-scale grid extension and solar home systems (SHS). The International Energy Agency (IEA) submits that globally about 70.0% of rural areas are unsuitable for central grid electricity. Micro and minigrids utilizing renewable energy are pertinent in achieving universal electrification [4, 8]. A minigrid is also

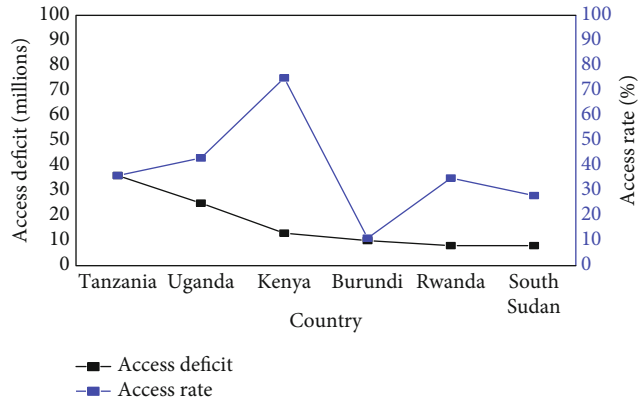

Figure 1: Access deficit population in millions and access rate percentage.

known as a nano or microgrid depending on the size of the population served is a power plant with generation, transmission, and distribution capacity but operating within a specific geographical location, serving specific customers. They can be connected to the central grid or operate independently [9]. Currently, there are three minigrid generations. First-generation minigrids that normally utilize diesel as an energy resource, second-generation minigrids that utilize hydro as an energy resource, and third-generation utilize renewable energy resources like solar and biomass. The third generation is also described as renewable-hybrid minigrids, and the term renewable-hybrid could be used to refer to two different systems. It could mean a minigrid setup that utilizes multiple energy resources with at least one being renewable or it could also mean a minigrid that combines power generation from a renewable energy resource and has storage batteries for back up when generation is not viable [10]. In this research, the term will also mean either of the two meanings. This research is focused primarily on renewable hybrid minigrids in the six East African nations as they are shown in Figure 2.

Solar hybrid minigrids are the fastest-growing segment globally. While 32.0% of installed minigrids are either powered by fossil fuels or hydro, PV technology is dominantly being used in minigrid installations currently. Modern minigrids installations presently combine energy storage with PV while hybridizing old fossil fuel minigrids by adding PV resources. In recent years, with the evolution of the solar hybrid minigrid market, international corporates have also joined their ranks offering electrochemical storage systems like batteries, uninterrupted power supply (UPS), and remote-control technologies [11].

Renewable energy is maturing as a global resource, and the sector had its most significant growth in the year 2015. A combination of wind power and solar PV constituted more than 75.0% of new global energy installations in 2015, trailed by hydropower. Renewable power installations are leading compared to combined new fossil fuel installations by capacity annually. As of 2015, renewable energy installations could supply a quarter of the world's universal electricity [12]. Advances in all components of renewable energy resources are important; however, this study is most concerned with the evolution of the solar PV minigrid segment. Solar PV is

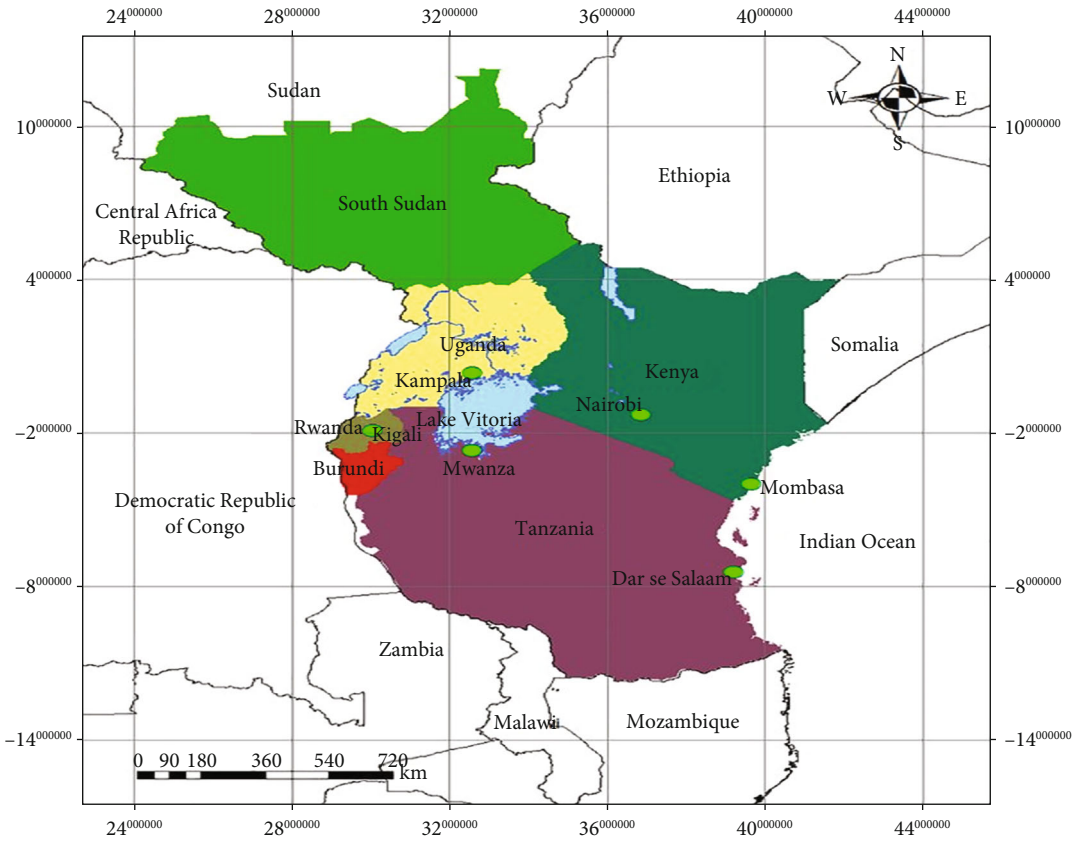

Figure 2: The six East Africa Community countries (Source: Telesphore Kabera).

remarkable for its ease of installation and operation at diverse scales. Recently, solar PV prices have reduced significantly, and this is attributed to the confluence of increase in global production, research and development, and a positive deployment environment [13].

3. Methodology

This paper is based on HOMER (Hybrid Optimization Model for Multiple Energy Resources) software simulations and a desk study encompassing multiple literature sources complemented by data collected from relevant minigrid developers and market players. The review of existing literature includes 31 existing reports from major sector players, 16 peer-reviewed research publications, 26 web pages including government websites, 14 government, legal documents, and legitimate online databases. The gathered information and data were used to examine the progress of the minigrids utilizing solar PV in the six East African countries, policy and regulations, institutional framework, payment methods, market potential, and existing challenges. Not only this, a model of peak shaving was adopted from HOMER software (model with critical load), and simulations were carried out specifically for each country member of the EAC to analyze and assess the capability of a grid-connected solar PV minigrid and its storage in contributing to the load peak shaving condition as shown in Figure 3. Electricity tariff prices were from different databases (references), and others were collected through voice-to-voice interview with local citizens in those countries. This critical load structure (adopted from HOMER software) was used as research object in six EAC countries with different locations such as at this load structure was as research object in other five EAC countries with different locations such as at Jinja Road, Kampala, Uganda (0°20.2′N, 32°37.5′E) for Uganda (location for Uganda Industrial Research Institute), at Kimweri Ave, Dar es Salaam, Tanzania (6°45.9′S, 39°16.2′E) for Tanzania (location for Tanzania Industrial Research and Development Organization), at South C Nairobi KE, Nairobi, Kenya

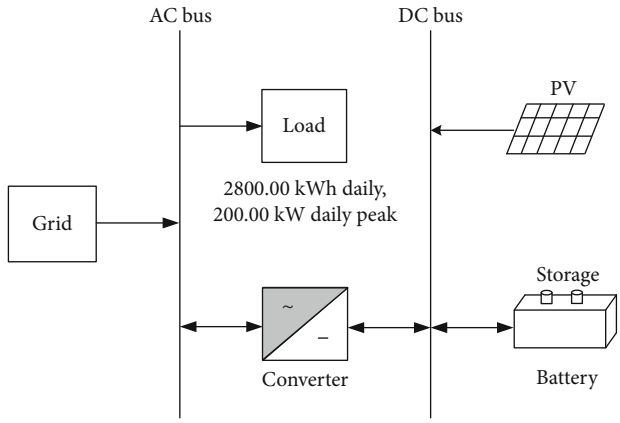

Figure 3: Schematic diagram of the HOMER model.

(1°19.4′S, 36°49.9′E) for Kenya (location for Kenya industrial research and development institute), at Ayod, South Sudan (8°22.8′N, 30°42.7′E) for South Sudan (location for the SUDD Institute), at Boulevard de l'Indépendance, Bujumbura, Burundi (3°23.1′S, 29°22.4′E) for Burundi (location for Institute Statistics and Studies Economic Du Burundi), and at 2 KG 2 Ave, Kigali, Rwanda (1°57.1′S, 30°5.1′E) for Rwanda (location for Institute of Policy Analysis and Research).

4. Solar Minigrid Developments in the East Africa Region

4.1. Narrative Review and Simulation Results Analysis

4.1.1. Uganda. Uganda's yearly sunshine hours range from 1753 to 2264 with global horizontal radiation of 4.8–6.2k Wh/m^2 per day. The northeast experiences the highest insolation. Annually, the solar irradiation ranges from 1,825.0 kWh/m^2 to 2,500.0 kWh/m^2 [14]. However, the use of solar energy is still relatively low in Uganda and projects barely get off the ground without significant donor and government support. Uganda is reported to have a capacity of 56.8 MW from 34 installed minigrids [11], 34.0% of them being hydro minigrid power plants as shown in Figure 4. Forty percent of these are either solar PV (27%) or solar PV hybrid (13%) minigrids as of the end of 2019.

The component of solar minigrid plants tripled in 2015 and has not changed significantly since then. There are two-megawatt scale solar PV plants in Uganda with each having a capacity of 10.0MW inaugurated in 2016 and 2017, respectively [15, 16]. Few other solar PV minigrids with a capacity totaling 30.0MW are either on proposal or development stage [16–18]. The trend on general solar PV technology deployment is unlike the minigrid component trend as shown in Figure 4. Since 2017, there has been a tremendous increase in installations, the deployment of solar PV almost doubled in both 2017 and 2019 suggesting an aggressive growth due to the acquisition of stand-alone solar home systems compared to solar minigrids.

Uganda is the second highest with solar PV installation of 82.16 MW after Kenya in the countries considered in this study (Figure 5). Uganda has installed a significant number of megawatt-scale solar PV plants and has several plans to continue with this trend. The situation can be attributed to several favorable regulations. Presently, projects in Uganda are regulated based on their capacity. Minigrids producing 2.0 MW or more are under the same regulations as independent power producers (IPPs) in the acquisition of the license, approval of tariffs, and technical standards. Minigrids producing less than 2.0MW of power are exempt from licensing but undergo a process of developing a Memorandum of Understanding (MoU) with the Electricity Regulatory Authority (ERA) [11]. After approving the license-exempted minigrids, the Rural Electrification Agency (REA) provides distribution infrastructure, connecting households without charge. Developers are therefore left to provide generation capacity and meet the cost of operations

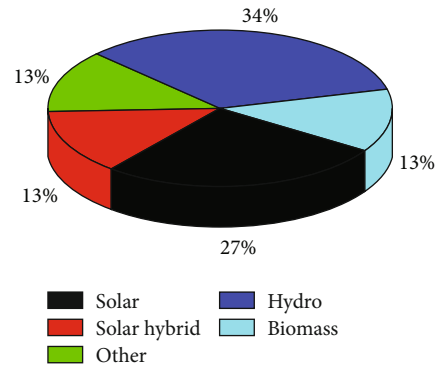

Figure 4: Minigrids in Uganda by resource utilized. (Source: Bloomberg NEF, GIZ, Carbontrust, CLUB-ER, Surveyed developers).

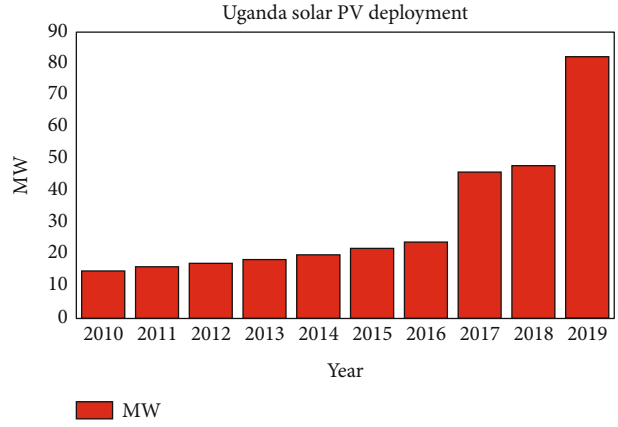

Figure 5: Solar PV deployment trends in Uganda by IRENA.

and maintenance for the plant. REA installs grid-compliant distribution infrastructure to avoid the risk of grid arrival going forward, and this effectively represents nearly 30.0% of each minigrid project [11, 19]. Table 1 describes the institutions involved in the energy sector in Uganda.

As shown in Figure 6, sixty-seven percent of minigrids in Uganda are owned privately, twenty-seven percent are community-owned, and six percent are developed under the public-private partnership.

Uganda's electricity connection policy approved in January 2018 works towards 30.0% electrification by 2020 60.0% by 2027 and 80.0% by 2040 [20]. Currently, Uganda's electrification stands at 28.9% [22]. Going forward, immense minigrid development opportunities arise over the several habitable islands on Lake Victoria under Uganda's jurisdiction where the main grid extension is not practical. In 2018, Uganda's regulatory authority (REA) embarked on a planning exercise and identified 320 locations seemly for minigrid deployment. When developed the minigrids will supply electricity to 70,000 households. Several bundled tender schemes for minigrid development are also underway since 2018 [11, 23]. Figure 7 depicts the monthly solar global horizontal irradiation index (GHI) for Uganda. The GHI slightly rose from 4.894 kWh/m^2/day in January to 4.923 kWh/m^2/day in February, declined unevenly to the

Table 1: Institutions involved in the energy sector in Uganda.

Institution	Mandate	Ref
Uganda Electricity Board (UEB)	Consists of three entities: (1) Uganda Electricity Generation Company Limited (UEGCL). (2) Uganda Electricity Transmission Company Limited (UETCL). (3) Uganda Electricity Distribution Company Limited (UEDCL)	[11]
Rural Electrification Agency (REA)	Develops and owns the distribution infrastructure of minigrids through the Rural Electrification Fund. It also leases assets to private minigrid developers.	[20]
UMEME	Awarded a 20-year concession for distribution and retail of power in 2005 by UEDCL. UMEME was formed in 2004 and is presently doing distribution of 98.0% of central grid electricity.	[19]
Eskom	Oversees the operation and maintenance of generation assets since 2003 when UEGCL subleased its generation mandate to ESKOM, a South African utility owned by the state.	
Electricity Regulatory Authority (ERA)	Main regulatory authority of Uganda's minigrids. It manages approval of licenses, tariff setting, and maintains technical standards.	[21]

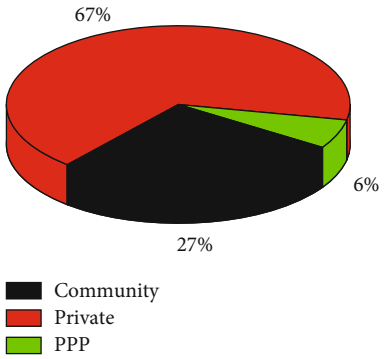

Figure 6: Minigrid ownership options in Uganda. Source: Bloomberg NEF, GIZ, Carbontrust, CLUB-ER, Surveyed developers.

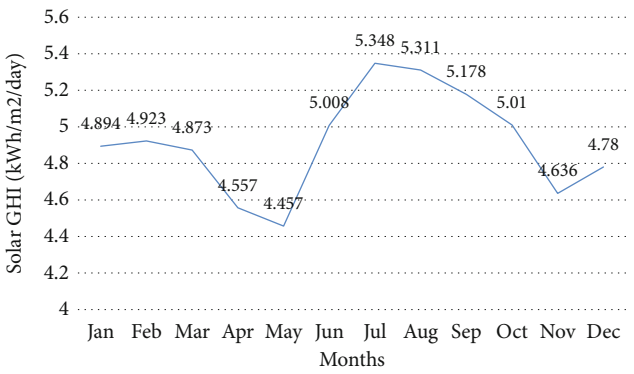

Figure 7: Monthly solar Global Horizontal Irradiation (GHI kWh/m^2/day) for Uganda.

lowest point of 4.457 kWh/m^2/day in May, and rose sharply to 5.348 kWh/m^2/day peak in July. The GHI for Uganda decreased to 4.636 kWh/m^2/day in November and rose slightly to 4.78 kWh/m^2/day in December.

Figure 8 indicates the monthly clearness index (CI) for Uganda. The CI slightly decreased from 0.488 in January to 0.446 in April and rose to 0.46 in May, respectively. The CI gently rose to 0.565 in July (peak) and gradually declined to 0.461 in November and rose to 0.484 in December.

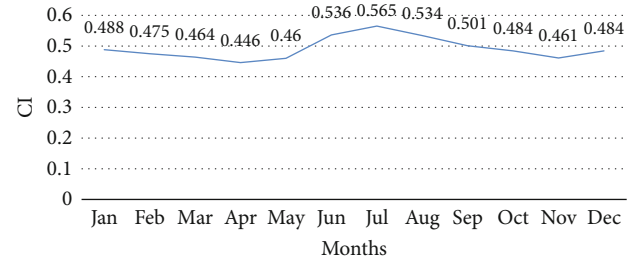

Figure 8: Monthly clearness index (CI) for Uganda.

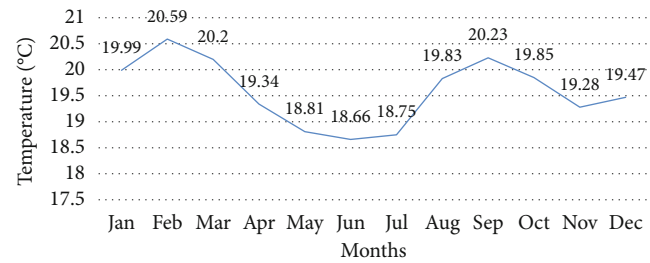

Figure 9: Monthly temperature variation (°C) for Uganda.

Figure 9 shows the monthly temperature variation for Uganda. The temperature rose from 19.99°C in January to 20.59°C in February (peak). It gradually declined to the least 18.66°C in June and rose to 18.75°C in July. The temperature rose to 20.23°C in September and gradually decline to 19.28°C in November and rose to 19.47°C in December.

Figure 10 reflects the cumulative cash flows for the current and proposed power systems over the life of the projects for Uganda. The cash flow for the current power system at the inception was around US$-184,931.51, and the cash flow rose steadily to US$1,800,000.00 in 15 years, where it had the same cash flow as the proposed power system. The cash flow for the current power system rose to about US$2,459,589.04 at the 25th life span. Furthermore, the cash flow for the proposed power system rose gradually from US$900,000.00 at inception to US$2,145,205.48 in year 25, which was the end of the economic life of the proposed power system. Comparing the cumulative cash flows of the two power systems, using

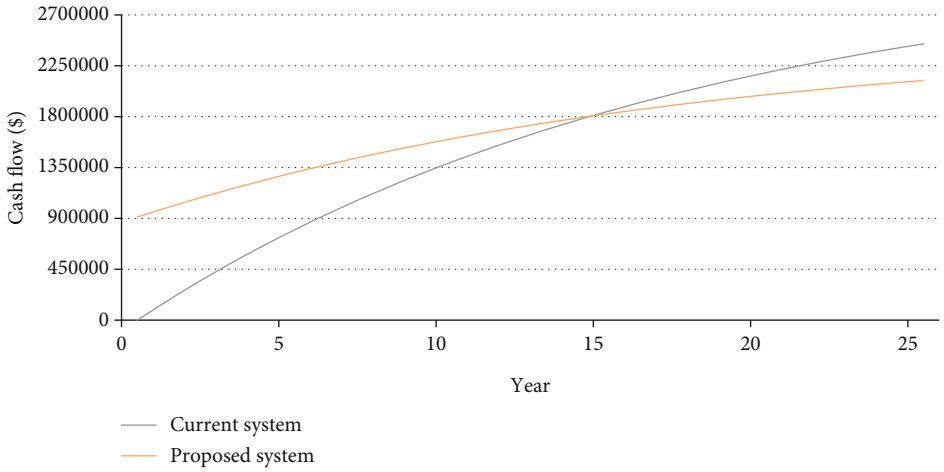

Figure 10: Cumulative cash flows over project lifetime for the current and proposed systems for Uganda.

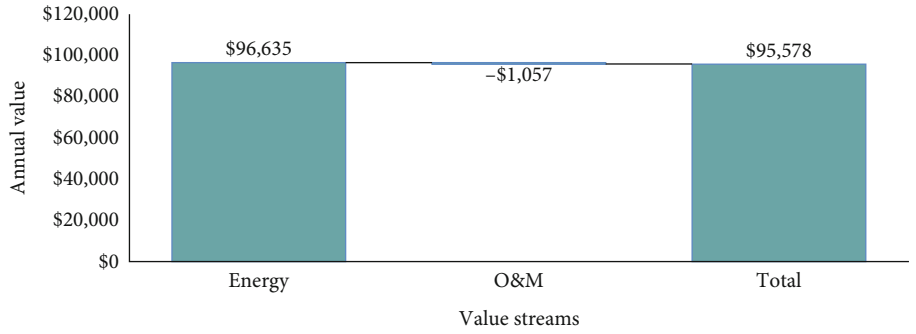

Figure 11: Categorized annual savings for the proposed system for Uganda.

the approximate area under their respective cash-flow curves, US$30,748,238.00 was for the current power system while US$38,065,068.50 was for the proposed power system. Therefore, the proposed power would generate about US$7,316,830.50 cash flows than the current power system in Uganda.

Figure 11 indicates the categorized annual savings for the proposed power system in Uganda. The annual energy amount was US$96,635.00, and US$-1,057.00 was the operations and maintenance expense, while the annual energy savings was US$96,578.00, respectively.

Figure 12 depicts the monthly utility bills for the current and proposed power systems in Uganda. The January bills for both the current and proposed power systems were US$15,965.41 and US$8,056.93, respectively. The February bills for both the current and proposed power systems were US$14,571.67 and US$7,414.05, respectively. The March bills for both the current and proposed power systems were US$15,965.41 and US$7,885.40, respectively. The April bills for both the Current and proposed power systems were US$15,600.04 and US$8,056.80, respectively. The May bills for both the current and proposed power systems were US$16,114.60 and US$8,571.00, respectively. The June bills for both the current and proposed power systems were US$15,600.40 and US$7,370.20, respectively. The July bills for both the current and proposed power systems were US$16,114.60 and US$7,114.10, respectively. The August bills for both the current and proposed power systems were US$16,114.60 and US$7,199.80, respectively. The September bills for both the current and proposed power systems were US$15,600.40 and US$7,371.20, respectively. The October bills for both the current and proposed power systems were US$16,028.90 and US$7,714.00, respectively. The November bills for both the current and proposed power systems were US$15,600.40 and US$8,142.50, respectively. The December bills for both the current and proposed power systems were US$16,114.60 and US$8,056.80, respectively.

Table 2 shows the annual utility bills and savings by category for Uganda. The US$189,070.00 base case consumption charge and US$92,435.00 proposed power system consumption charge, respectively. The annual savings which is the difference between the current and proposed power systems consumption charges was US$96,635.00.

Figure 13 reflects the electrical production capacities for both the current (grid) and proposed solar PV microgrid power systems technology in Uganda. The January power generation for both the grid and solar PV microgrid was 100.98 MWh and 48.29 MWh, respectively. The February power production for both the grid and solar PV microgrid was 89.27 MWh and 43.90 MWh, respectively. The March power production for both the grid and solar PV microgrid was 100.0 MWh and 48.29 MWh, respectively.

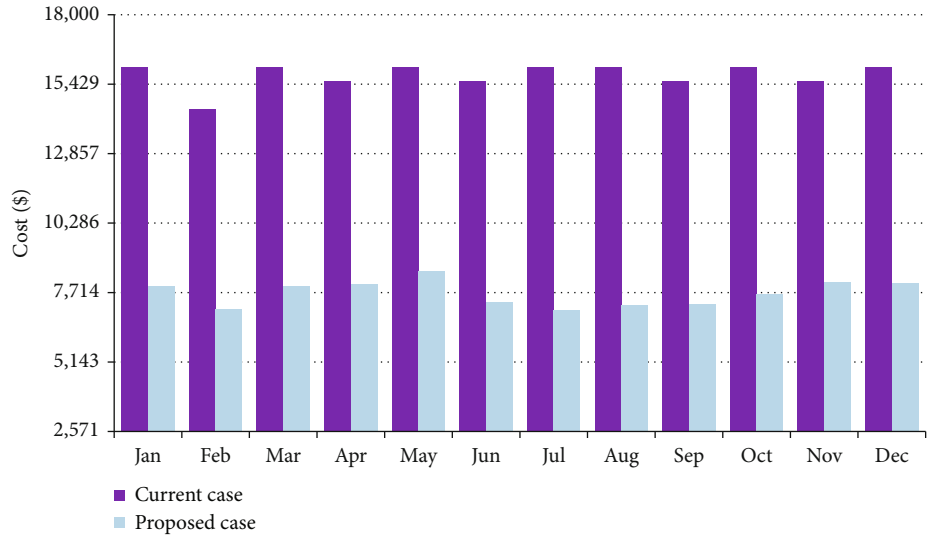

Figure 12: Monthly utility bills for the current and proposed systems for Uganda.

Table 2: Annual utility bills and savings by category.

	Consumption charge	Total
Base case	$189,070.00	$189,070.00
Proposed case	$92,435.00	$92,435.00
Annual savings	$96,635.00	$96,635.00

Note: the base case is considered as the current system (grid connection) and the proposed case is the grid-connected solar PV microgrid with storage.

The April power production capacities for both the grid and solar PV microgrid were 92.20 MWh and 42.44 MWh, respectively. The May power production capacities for both the grid and solar PV microgrid were 96.59 MWh and 43.90 MWh, respectively. The June power production capacities for both the grid and solar PV microgrid were 93.66 MWh and 46.93 MWh, respectively. The July power production capacities for both the grid and solar PV microgrid were 98.78 MWh and 52.58 MWh, respectively. The August power production capacities for both the grid and solar PV microgrid were 100.24 MWh and 52.68 MWh, respectively. The September power production capacities for both the grid and solar PV microgrid were 98.05 MWh and 49.76 MWh, respectively. The October power production capacities for both the grid and solar PV microgrid were 98.05 MWh and 49.76 MWh, respectively. The November power production capacities for both the grid and solar PV microgrid were 75.40 MWh and 43.79 MWh, respectively. The December power generation capacities for both the grid and solar PV microgrid were 98.78 MWh and 46.83 MWh, respectively.

The solar PV system has a nominal capacity of 400.0 kW, its annual production is 573619.0 kWh/year, and the specific yield is 1434.05 h/year.

Table 3 depicts the project cost details for both the grid and solar PV systems for the lifetime of the projects in Uganda. The yearly project cost throughout the 25-year economic lives of both the solar PV and grid power systems was US$1,057.00 and US$92,435.00, respectively.

Table 4 is the utility monthly summary for the current grid system for the whole project's economic life for Uganda. The energy purchased varied between 86,800.0 kWh and 84,000.0 kWh in alternate months except 78,400.0 kWh for February. Specifically, the energy purchased was 86,800.0 kWh for January, March, May, July, August, October, and December, respectively. The energy purchase was 84,000.0 kWh each for April, June, September, and November, respectively, and the annual energy purchase was 1,022,000.0 kWh. There was no energy sold, and the peak load was 200.0 kW. The energy charge was each US$16,058.00 for January, March, May, July, August, October, and December, respectively. The energy charge was each US$15,540.00 for April, June, September, and November, respectively, while the energy charge for February was US$14,504.00. The demand charge, fixed charge, minimum charge, and taxes were each zero, respectively. Also, the annual total energy charge was US$189,070.00.

Table 5 indicates the utility monthly summary of the proposed power system for Uganda. The energy purchased (kWh), energy sold (kWh), and net energy purchased (kWh) were each different for every month from January to December. The peak load was 200.0 kW every month and throughout the year. The energy charge (US$) was equally variable every month, while each of the demand charge, fixed charge, minimum charge, and taxes was zero, respectively. The total annual energy purchase was 594,299.0 kWh, the annual energy sold was 145,918.0 kWh, and the annual net energy purchase was 448,382.0 kWh, respectively. Also, the total annual energy charge was US$92,435.00.

4.1.2. Kenya. The electrification level in Kenya stands at 84.5% [22]. While Kenya is one of the countries with a very extensive grid network, most of the marginalized counties have not benefited from this government initiative [24]. Given this situation, several minigrid solar projects have been initiated. These minigrids are both off-grid and some are grid-connected. Despite the potential of minigrids to electrify

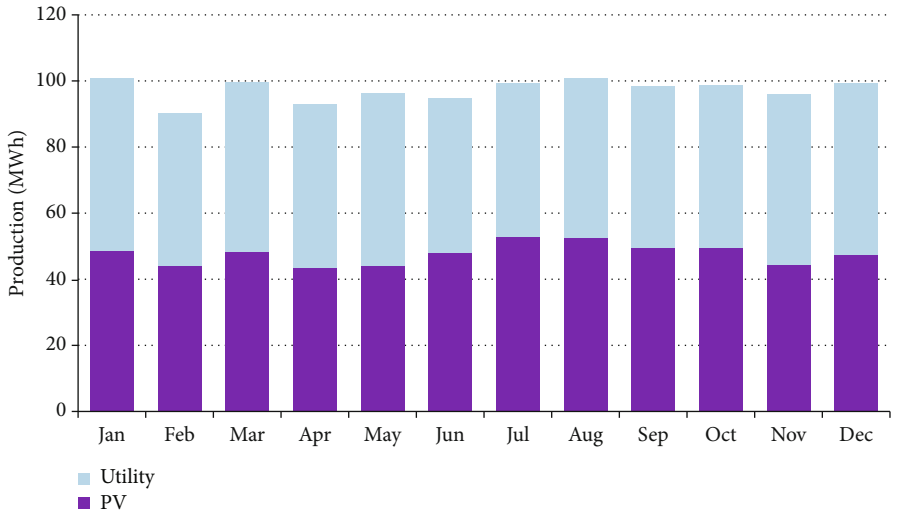

Figure 13: The electrical production for both utility and solar PV microgrid for the proposed technology in Uganda.

Table 3: Project cost details (both grid and PV systems) for the whole project lifetime in Uganda.

Year	1	2	3	4	5	6	7	8	9	10
PV system	($1,057.0)	($1,057.0)	($1,057.0)	($1,057.0)	($1,057.0)	($1,057.0)	($1,057.0)	($1,057.0)	($1,057.0)	($1,057.0)
Uganda grid	($92,435.0)	($92,435.0)	($92,435.0)	($92,435.0)	($92,435.0)	($92,435.0)	($92,435.0)	($92,435.0)	($92,435.0)	($92,435.0)
Year	11	12	13	14	15	16	17	18	19	20
PV system	($1,057.0)	($1,057.0)	($1,057.0)	($1,057.0)	($1,057.0)	($1,057.0)	($1,057.0)	($1,057.0)	($1,057.0)	($1,057.0)
Uganda grid	($92,435.0)	($92,435.0)	($92,435.0)	($92,435.0)	($92,435.0)	($92,435.0)	($92,435.0)	($92,435.0)	($92,435.0)	($92,435.0)
Year	21	22	23	24	25					
PV system	($1,057.0)	($1,057.0)	($1,057.0)	($1,057.0)	($1,057.0)					
Uganda gird	($92,435.0)	($92,435.0)	($92,435.0)	($92,435.0)	($92,435.0)					

Table 4: Utility monthly summary—current system.

Month	Energy purchased (kWh)	Energy sold (kWh)	Net energy purchased (kWh)	Peak load (kW)	Energy charge	Demand charge	Fixed charge	Minimum charge	Taxes	Total
January	86,800.0	0.0	86,800.0	200.0	$16,058.0	$0.0	$0.0	$0.0	$0.0	$16,058.0
February	78,400.0	0.0	78,400.0	200.0	$14,504.0	$0.0	$0.0	$0.0	$0.0	$14,504.0
March	86,800.0	0.0	86,800.0	200.0	$16,058.0	$0.0	$0.0	$0.0	$0.0	$16,058.0
April	84,000.0	0.0	84,000.0	200.0	$15,540.0	$0.0	$0.0	$0.0	$0.0	$15,540.0
May	86,800.0	0.0	86,800.0	200.0	$16,058.0	$0.0	$0.0	$0.0	$0.0	$16,058.0
June	84,000.0	0.0	84,000.0	200.0	$15,540.0	$0.0	$0.0	$0.0	$0.0	$15,540.0
July	86,800.0	0.0	86,800.0	200.0	$16,058.0	$0.0	$0.0	$0.0	$0.0	$16,058.0
August	86,800.0	0.0	86,800.0	200.0	$16,058.0	$0.0	$0.0	$0.0	$0.0	$16,058.0
September	84,000.0	0.0	84,000.0	200.0	$15,540.0	$0.0	$0.0	$0.0	$0.0	$15,540.0
October	86,800.0	0.0	86,800.0	200.0	$16,058.0	$0.0	$0.0	$0.0	$0.0	$16,058.0
November	84,000.0	0.0	84,000.0	200.0	$15,540.0	$0.0	$0.0	$0.0	$0.0	$15,540.0
December	86,800.0	0.0	86,800.0	200.0	$16,058.0	$0.0	$0.0	$0.0	$0.0	$16,058.0
Annual	1,022,000.0	0.0	1,022,000.0	200.0	$189,070.0	$0.0	$0.0	$0.0	$0.0	$189,070.0

Table 5: Utility monthly summary—proposed system.

Month	Energy purchased (kWh)	Energy sold (kWh)	Net energy purchased (kWh)	Peak load (kW)	Energy charge	Demand charge	Fixed charge	Minimum charge	Taxes	Total
January	52,212.0.	14,065.0	38,147.0.0	200.0	$7,971.0	$0.0	$0.0	$0.0	$0.0	$7,971.0
February	46,023.0	11,782.0	34,241.0	200.0.0	$7,100.0	$0.0	$0.0	$0.0	$0.0	$7,100.0
March	51,411.0	12,956.0	38,455.0	200.0	$7,956.0	$0.0	$0.0	$0.0	$0.0	$7,956.0
April	49,352.0	9,040.0	40,312.0	200.0	$8,045.0	$0.0	$0.0	$0.0	$0.0	$8,045.0
May	52,337.0	9,631.0	42,706.0	200.0	$8,527.0	$0.0	$0.0	$0.0	$0.0	$8,527.0
June	46,764.0	10,692.0	36,071.0	200.0	$7,368.0	$0.0	$0.0	$0.0	$0.0	$7,368.0
July	46,397.0	12,516.0	33,881.0	200.0	$7,082.0	$0.0	$0.0	$0.0	$0.0	$7,082.0
August	48,330.0	14,123.0	34,207.0	200.0	$7,246.0	$0.0	$0.0	$0.0	$0.0	$7,246.0
September	48,923.0	14,567.0	34,356.0	200.0	$7,303.0	$0.0	$0.0	$0.0	$0.0	$7,303.0
October	49,226.0	12,061.0	37,165.0	200.0	$7,659.0	$0.0	$0.0	$0.0	$0.0	$7,659.0
November	51,545.0	12,024.0	39,521.0	200.0	$8,093.0	$0.0	$0.0	$0.0	$0.0	$8,093.0
December	51,780.0	12,461.0	39,319.0	200.0	$8,084.0	$0.0	$0.0	$0.0	$0.0	$8,084.0
Annual	594,299.0	145,918.0	448,381.0	200.0	$92,435.0	$0.0	$0.0	$0.0	$0.0	$92,435.0

off-grid communities, roughly 63 minigrids were operating in Kenya by the end of 2017 [25]. Twenty-nine are operated by either the national utility Kenya Power (KP) or the Rural Electrification and Renewable Energy Corporation (REREC), and 23 of them are run by private developers and 11 by communal organizations.

Kenya is leading the East African community nations in solar PV deployment with a total of 94.54 MW already installed [26]. Although the number of minigrids is less than that of Tanzania (as can be shown in Figure 14), the country has installed several megawatt-scale minigrids in several institutions, private agricultural farms, and for local populations among others. The solar PV minigrid technology is well understood in the country, and there is also motivation from the substandard service offered by the national utility where power cuts are very common and the billing exorbitant [25]. Most private institutions have also been encouraged to get a minigrid as there is provision for a power purchase agreement (PPA) with the national utility at a somewhat reasonable price of USD 0.12 [27, 28] besides avoiding the power cuts and overpriced bills. Private minigrids on agricultural estates are a common phenomenon as they do not require a permit or license to generate electricity equal to or less than 1.0 MW for their use [25].

According to Kenya national electrification strategy, the country has an ambitious plan to achieve 100.0% electrification by 2022 [29]. Currently, it also has the leading electricity access rate in East Africa at 84.5% [22] both from on-grid and off-grid solutions and is home to the largest (50.0 MW) grid-connected solar PV minigrid in East and Central Africa, located in Garissa county as shown in Figure 15. The country experienced extensive growth in the year 2018 with an additional 55.0 MW being installed, before that, the growth was rather gentle. In 2019, only 2.0 MW was installed, signaling a return to a slow rise as experienced before.

Going forward, additional minigrids are under development or planned for construction, typically funded by donors but cofinanced and implemented by the private sector. These

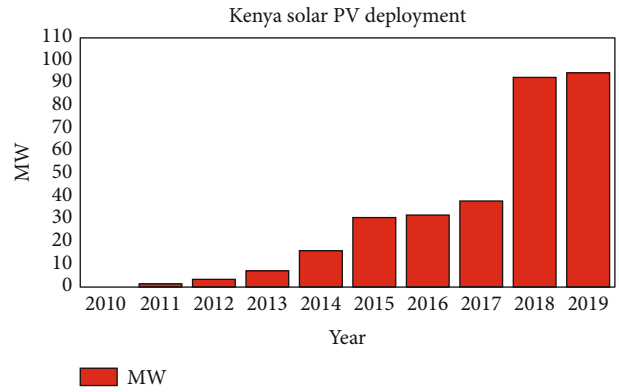

Figure 14: Solar PV trends in Kenya by IRENA.

include the 120 minigrids under an off-grid solar access project to be implemented under a public-private partnership (PPP) model jointly by REREC and Kenya Power [30]. Each specific minigrid will combine solar PV, storage batteries, and thermal units running on fossil fuels. REREC is developing another 53 sites with financing from donors and the exchequer, all while the private sector is currently at various development stages on at least 133 minigrids [31]. Table 6 describes the institutions involved in Kenya's energy sector.

Presently, projects in Kenya are regulated by the Energy and Petroleum Regulatory Authority (EPRA) based on their capacity, with minigrids of up to 3.0 MW a capacity requiring a permit, tariff approval, technical standards, and general oversight. Minigrids exceeding 3 MW require a license while those under 1.0 MW generating for private use require neither a permit nor a license [37]. Figure 16 indicates the monthly solar GHI for Kenya. It rises from 5.614 kWh/m^2/day in January to 5.977 kWh/m^2/day in February and decreases irregularly to 4.231 kWh/m^2/day in May. The GHI rose slightly to 4.241 in June and declines slightly to the lowest point in July at 4.038 kWh/m^2/day. It rises again slightly to 4.191 kWh/m^2/day in August and then 5.179 kWh/m^2/day

Figure 15: Mbalambala Garissa solar PV minigrid with 200,200 solar panels and 50.0 MW capacity (photo on-site at Mbalambala Garissa).

Table 6: Description of institutions involved in Kenya's energy sector.

Institution	Mandate	Ref
Ministry of Energy	Makes policies on energy and does strategic planning for the energy sector	[32]
Energy and Petroleum Regulatory Authority (EPRA)	Formulates and enforces regulations on grid codes, tariffs, and other relevant tools necessary.	[21]
Kenya Electricity Generating Company (KenGen)	Oversees electricity generation,70.0% owned by the government, 30.0% by private investors	[33]
Kenya Power	Manages the grid, purchases power from KENGEN and other IPPs after which it does transmission and distribution to customers. 50.1% is owned by the Government of Kenya and the National Social Security Fund (NSSF) and the rest by private investors.	[34]
Rural Electrification and Renewable Energy Corporation (REREC)	Accelerates the pace of RE in Kenya by implementing the Rural Electrification Program.	[35]
Energy Tribunal	Settles disputes between parties in the energy industry.	
IPP's (Independent Power Producers)	Private investors involved in the generation of power selling it to the off-taker under an agreed feed-in tariff.	[36]

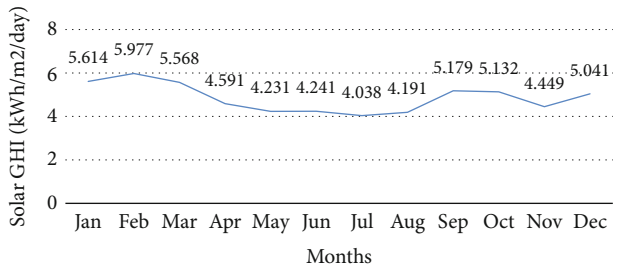

Figure 16: Monthly solar Global Horizontal Irradiation (GHI kWh/m^2/day) for Kenya.

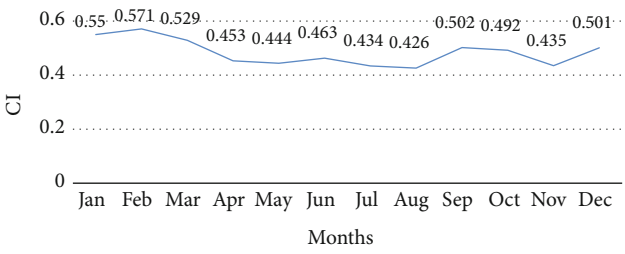

Figure 17: Monthly clearness index (CI) for Kenya.

peak in September. It decreases slightly to 5.132 kWh/m^2/day in October and falls to 4.449 kWh/m^2/day in November, before rising to 5.041 kWh/m^2/day in December, respectively.

Figure 17 depicts the clearness index (CI) for Kenya. The CI rises from 0.55 in January to 0.571 in February and falls to 0.529 in March. It gradually declines to 0.453 in April, 0.444 in May, and 0.463 in June. It further declines to 0.434 in July and 0.426 in August. It rises to 0.502 in September, declines to 0.492 in October and 0.435 in November, and rose to 0.501 in December.

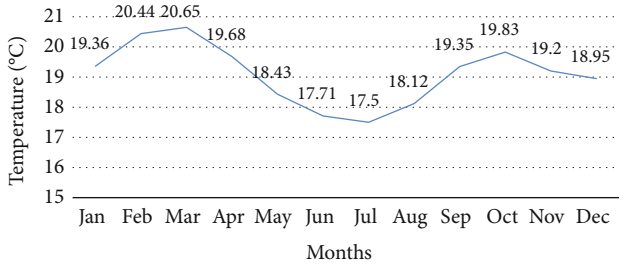

Figure 18: Monthly temperature variation (°C) for Kenya.

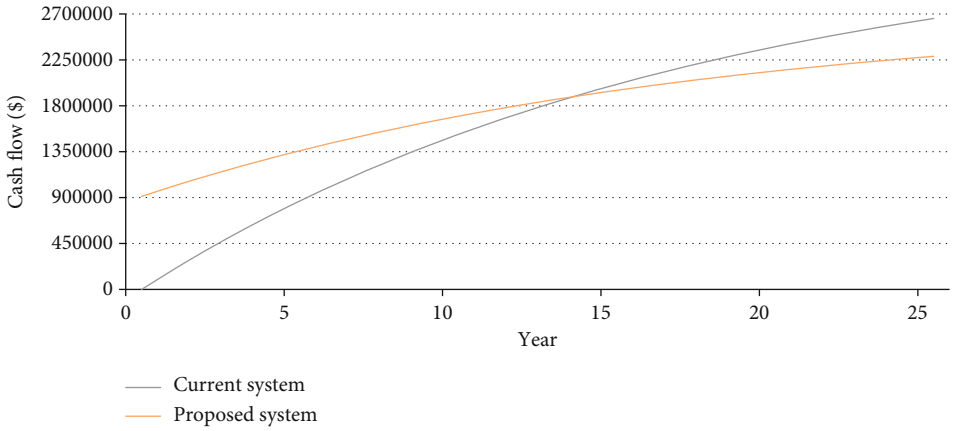

Figure 19: Cumulative cash flows over project lifetime for the current and proposed systems for Kenya.

Figure 18 shows the monthly temperature variation for Kenya. The temperature rose from 19.36°C in January to 20.44°C in February and 20.65°C (peak) in March. The temperature declines to the lowest 17.50°C in July, rose to 19.83°C in October, and declined to 18.93°C in December. Figure 19 indicates the cumulative cash flow over the project life for both the current and proposed power systems for Kenya. The current and proposed power systems curves were graphed. At inception, the current system cash flow was around US$-217,741.94 while the proposed power system cash flow was US$900,000.00. Both the proposed and current power systems cash flows were US$1,872,580.65 and US$1,872,580.65 respectively, and at the same 14.17 years. At the end of their economic lives, both the current and proposed power systems cash flows were around US$2,656,451.16 and US$2,250.00, respectively. Assuming a triangle for the current power system and a trapezium for the proposed power system, both the current and proposed power systems cash flows will be about US$33,205,645.20 and US$39,375,000.00, respectively. Therefore, US$6,139,354.80 is the cash flow advantage of the proposed power system over the current power system.

Figure 20 reflects the categorized annual savings for the proposed power system in Kenya. The annual energy value was US$100,246.00, and US$-1,057.00 was the operations and maintenance costs, while US$99,190.00 was the annual energy savings using the proposed power system for electrification.

Figure 21 indicates the monthly utility bills for both the current and proposed power systems in Kenya. The January bills for both the current and proposed power systems were US$17,437.50 and US$7,875.00, respectively. The February bills for both the current and proposed power systems were US$15,750.00 and US$6,562.50, respectively. The March bills for both the current and proposed power systems were US$16,901.37 and US$7,875.00, respectively. The April bills for both the current and proposed power systems were US$16,875.00 and US$8,812.50, respectively. The May bills for both the current and proposed power systems were US$16,901.37 and US$9,843.75, respectively. The June bills for both the current and proposed power systems were US$16,875.00 and US$9,375.00, respectively. The July bills for both the current and proposed power systems were US$17,437.50 and US$10,125.00, respectively. The August bills for both the current and proposed power systems were US$16,901.37 and US$9,937.50, respectively. The September bills for both the current and proposed power systems were US$16,875.00 and US$9,937.50, respectively. The October bills for both the current and proposed power systems were US$17,437.50 and US$8,437.50, respectively. The November bills for both the current and proposed power systems were US$16,875.00 and US$9,375.00, respectively. The December bills for both the current and proposed power systems were US$17,437.50 and US$8,812.50, respectively.

Table 7 depicts annual utility bills and savings by category in Kenya. The current consumption charge was US$205,422.00 while the proposed power system consumption charge was US$105,176.00 and US$100,246.00 was the annual energy savings.

Figure 22 indicates the electrical production capacities for both the current and proposed power systems in Kenya. The January electricity production capacities for both the grid and solar PV microgrid were 104.07 MWh and 55.22 MWh, respectively. The February production capacities for both the grid and solar PV microgrid were 95.56 MWh and 53.10 MWh, respectively. The March production capacities for both the grid and solar PV microgrid were 104.07 MWh and 55.22 MWh, respectively. The April production capacities for both the grid and solar PV microgrid were 93.45 MWh and 44.60 MWh, respectively. The May production capacities for both the grid and solar PV microgrid were 95.56 MWh and 42.48 MWh, respectively. The June production capacities for both the grid and solar PV microgrid were 91.33 MWh and 40.35 MWh, respectively. The July production capacities for both the grid and solar PV microgrid were 95.56 MWh and 40.35 MWh, respectively. The August production capacities for both the grid and solar PV microgrid were 95.56 MWh and 41.42 MWh, respectively. The September production capacities for both the grid and solar PV microgrid were 98.76 MWh and 49.91 MWh, respectively. The October production capacities for both the grid and solar PV microgrid were 99.18 MWh and 50.97 MWh, respectively. The November production capacities for both the grid and solar PV microgrid were 95.58 MWh and 42.48 MWh,

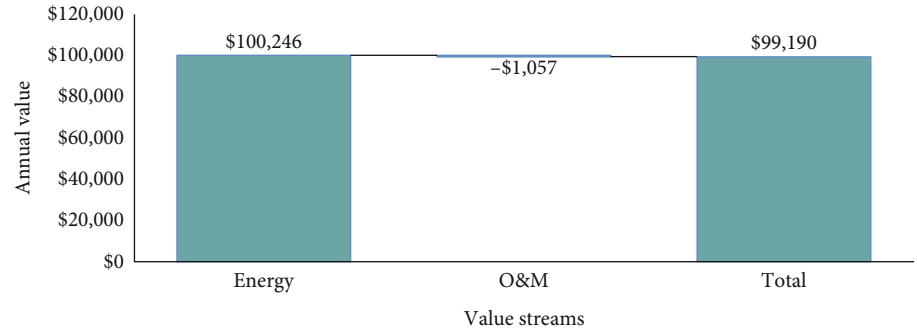

Figure 20: Categorized annual savings for a proposed system for Kenya.

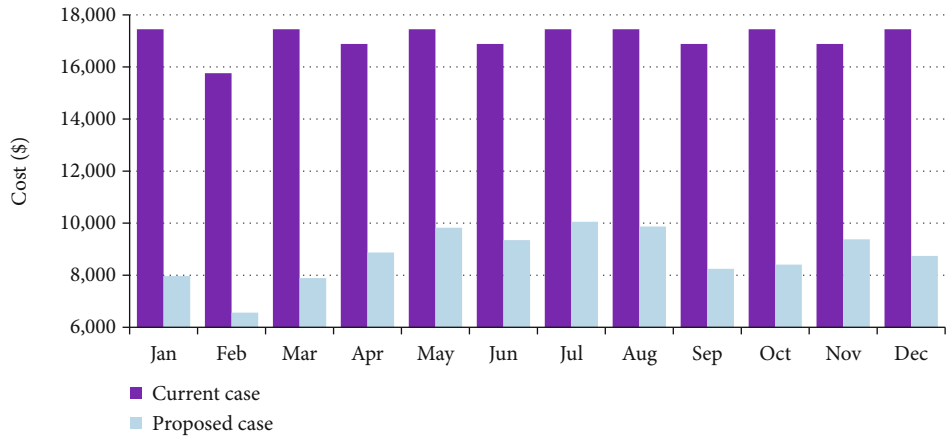

Figure 21: Monthly utility bills for the current and proposed systems for Kenya.

Table 7: Annual utility bills and savings by category (Kenya).

	Consumption charge	Total
Base case	$205,422.0	$205,422.0
Proposed case	$105,176.0	$105,176.0
Annual savings	$100,246.0	$100,246.0

Note: the base case is considered as the current system (grid connection) and the proposed case is the grid-connected solar PV microgrid with storage.

respectively. The December production capacities for both the grid and solar PV microgrid were 100.0 MWh and 48.85 MWh, respectively.

The solar PV system has a nominal capacity of 400.0 kW, and its annual production is 565217.0 kWh/year, and a specific yield of 1413.0 kWh/kW.

Table 8 depicts the project cost details for grid and solar PV systems in Kenya. The economic life span for each power system was 25 years, and the grid project cost was US$105,176.00 per year while US$1,057.00 was the yearly cost for the solar PV system.

Table 9 indicates the monthly utility summary for the current power system in Kenya. The energy purchase (kWh) for January, March, May, July, August, October, and December was each 86,800.0 kWh while 78,400.0 kWh was for February, the months of April, June, September, and November was each 84,000.0kWh, respectively. The annual energy purchase was 1,022,000.0 kWh. The peak load was 200.0 kWp, and the total energy charge was US$205,422.00.

Table 10 depicts the monthly utility summary for the proposed power system in Kenya. The energy purchase, energy sold, and net energy purchase for each month of the year were variable. The annual energy purchased and sold were 603,622 kWh and 146,889.0 kWh, respectively. The peak load was 200.0 kWp but the energy charge was as variable as each month of the year. The demand charge, minimum charge, fixed charge, and taxes were each zero, respectively. Also, the total annual energy charge was US$105,176.0

4.1.3. United Republic of Tanzania. Tanzania has between 2,800.0 and 3,500.0 sunshine hours per year with a maximum global horizontal radiation of 7.0 kWh per m^2 per day [14]. Currently, 25.56 MW of solar PV energy has been installed in Tanzania [26]. Tanzania has 209 identified minigrids installed with a collective capacity of 231.7 MW [9]. These projects are roughly 15.0 percent of the country's entire capacity of 1,461.0 MW. Nearly one-third of these projects are either solar-hybrid or solar minigrids. According to the World Resources Institute (WRI) and Tanzania Traditional Energy Development Organization (TATEDO), there were 109 minigrids in Tanzania by the end of 2017, 46.0% of the minigrids are hydro, 18.0% are fossil fuels, 24.0% are biomass, and 12.0% are solar minigrids and no wind minigrids

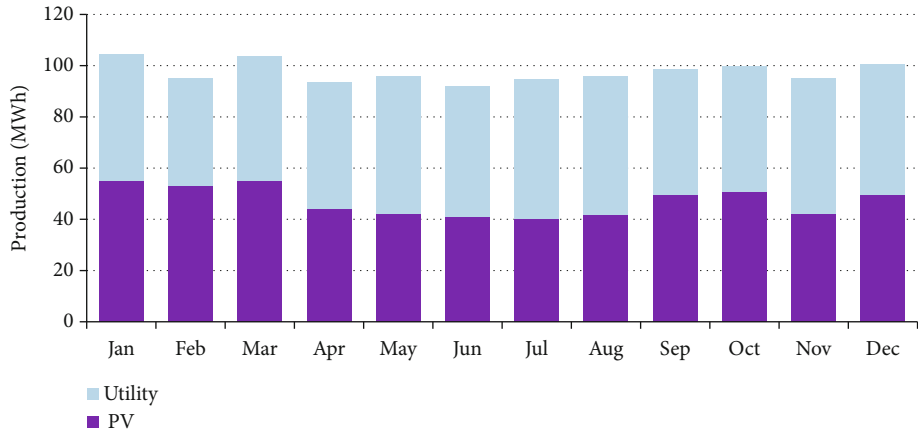

Figure 22: The electrical production for both utility and the solar PV microgrid for the proposed technology in Kenya.

in Tanzania [38]. Sixteen of these plants were tied to the central grid with the other 93 operating in isolation. While a majority of the capacity is distributed to the customers, some are sold to Tanzania Electric Supply Company (TANESCO) for distribution through the central grid. Figure 23 shows the minigrids location and numbers in Tanzania [38]. Figure 23 is a map indicating the locations of minigrids in Tanzania. The minigrids comprise biomass, fossil fuels, hybrid, solar, and hydropower.

The electricity access rate in Tanzania was 36% by the end of 2019 [22], and the country is home to the largest population without electricity at slightly above 35 million compared to the other East African nations [5, 22]. This makes Tanzania the largest market in East Africa for electrification technologies. Minigrid technologies in Tanzania are a fairly mature concept, and the growth of solar PV deployment in Tanzania has been steady [39] as it can be shown by Figure 24. There was a big leap in installations in the years 2014 and 2016 when 7 MW and 6 MW of solar power were injected into the market respectively (Figure 9). There was no increase experienced in 2019 an indication of slowing growth, and the total solar PV electricity capacity stood at 25.56 MW by the end of 2019 [26]. Figure 24 reflects the solar PV trends in Tanzania between 2010 and 2019 (inclusive) in MW. The solar PV deployment was around 0.17 MW in 2010, 0.52 MW in 2011, 1.03 MW in 2012, 3.62 MW in 2013, 11.12 MW in 2014, 12.93 MW in 2015, 18.36 MW in 2016, 21.88 MW in 2017, 25.34 MW in 2018, and 25.50 MW in 2019.

A government initiative by the name of small power producers (SPP) framework seems to have a positive impact on minigrid installations [40]. The SPP policy structure terms a small power producer (SPP) as any minigrid less than 10.0 MW a capacity. The policy allows the direct sale of electricity from minigrids to consumers. It provides that if the national grid extends to minigrid territory then power can be sold to TANESCO, the national utility. Nine registered SPPs were serving off-grid populations as of the year 2018. The policy has had a significant impact by nearly doubling both the capacity and number of minigrids in Tanzania since 2008 when the SPP framework was introduced. A total of 67.0 MW of new capacity were installed through fifty-two additional minigrids commissioned between 2008 and 2016 [2, 11]. The SPP structure requires all minigrids to have a license and tariff approval; however, any mini-grid with a capacity above 100.0 kW does not enjoy tariff structure flexibility and therefore operates under a fixed tariff [11]. Further support from the government includes removing value-added tax (VAT) and other importation duties on most solar components. Additionally, the government through the Rural Energy Agency (REA) which manages the Rural Energy Fund (REF) offers the following incentives to rural energy projects; (a) grants of up to USD 100,000.0 for feasibility studies or 80 percent of the cost of study, (b) grants for each home connection to the national utility grid or minigrids of up to 500.0 USD, or a maximum of 80.0 percent of the project's distribution and transmission costs, and (c) infrastructure credits up to 85.0 percent for power generation investments of less than 3.0 MW (70.0 percent for projects greater than 3.0 MW).

Onwards, Tanzania is planning to develop an extra 60 solar minigrids in rural areas following a business deal between a local developer and several international funding agencies as of July 2019 [41]. Innovative project financing remains key for the construction of the minigrids intended to connect a majority of the 36 million people still inaccessible to electricity in Tanzania. Currently, there are several megawatt-scale solar PV developments being installed or planned. Once built, the projects will improve the service offered by the local grid, which has habitual power cuts fluctuations. Table 11 describes the institutions involved in the Tanzanian energy sector.

Figure 25 indicates the monthly solar GHI (kWh/m^2/day) for Tanzania. The GHI rose from 5.614 kWh/m^2/day in January to 5.977 kWh/m^2/day in February kWh/m^2/day (peak) and decreases to 5.568 kWh/m^2/day in March to 4.591 kWh/m^2/day in April to 4.231 kWh/m^2/day in May. The GHI rose slightly to 4.241 kWh/m^2/day in June, decreases to 4.038 kWh/m^2/day in July, and rose to 4.191 kWh/m^2/day in August. From 5.197 kWh/m^2/day in September, it decreases slightly to

Table 8: Project cost details (both grid and PV systems) for the whole project lifetime in Kenya.

Year	1	2	3	4	5	6	7	8	9	10
PV system	($1,057.0)	($1,057.0)	($1,057.0)	($1,057.0)	($1,057.0)	($1,057.0)	($1,057.0)	($1,057.0)	($1,057.0)	($1,057.0)
Kenya grid	($105,176.0)	($105,176.0)	($105,176.0)	($105,176.0)	($105,176.0)	($105,176.0)	($105,176.0)	($105,176.0)	($105,176.0)	($105,176.0)
Year	11	12	13	14	15	16	17	18	19	20
PV system	($1,057.0)	($1,057.0)	($1,057.0)	($1,057.0)	($1,057.0)	($1,057.0)	($1,057.0)	($1,057.0)	($1,057.0)	($1,057.0)
Kenya grid	($105,176.0)	($105,176.0)	($105,176.0)	($105,176.0)	($105,176.0)	($105,176.0)	($105,176.0)	($105,176.0)	($105,176.0)	($105,176.0)
Year	21	22	23	24	25					
PV grid	($1,057.0)	($1,057.0)	($1,057.0)	($1,057.0)	($1,057.0)					
Kenya grid	($105,176.0)	($105,176.0)	($105,176.0)	($105,176.0)	($105,176.0)					

Table 9: Utility monthly summary—current system (Kenya).

Month	Energy purchased (kWh)	Energy sold (kWh)	Net energy purchased (kWh)	Peak load (kW)	Energy charge	Demand charge	Fixed charge	Minimum charge	Taxes	Total
January	86,800.0	0.0	86,800.0	200.0	$17,447.0	$0.0	$0.0	$0.0	$0.0	$17,447.0
February	78,400.0	0.0	78,400.0	200.0	$15,758.0	$0.0	$0.0	$0.0	$0.0	$15,758.0
March	86,800.0	0.0	86,800.0	200.0	$17,447.0	$0.0	$0.0	$0.0	$0.0	$17,447.0
April	84,000.0	0.0	84,000.0	200.0	$16,884.0	$0.0	$0.0	$0.0	$0.0	$16,884.0
May	86,800.0	0.0	86,800.0	200.0	$17,447.0	$0.0	$0.0	$0.0	$0.0	$17,447.0
June	84,000.0	0.0	84,000.0	200.0	$16,884.0	$0.0	$0.0	$0.0	$0.0	$16,884.0
July	86,800.0	0.0	86,800.0	200.0	$17,447.0	$0.0	$0.0	$0.0	$0.0	$17,447.0
August	86,800.0	0.0	86,800.0	200.0	$17,447.0	$0.0	$0.0	$0.0	$0.0	$17,447.0
September	84,000.0	0.0	84,000.0	200.0	$16,884.0	$0.0	$0.0	$0.0	$0.0	$16,884.0
October	86,800.0	0.0	86,800.0	200.0	$17,447.0	$0.0	$0.0	$0.0	$0.0	$17,447.0
November	84,000.0	0.0	84,000.0	200.0	$16,884.0	$0.0	$0.0	$0.0	$0.0	$16,884.0
December	86,800.0	0.0	86,800.0	200.0	$17,447.0	$0.0	$0.0	$0.0	$0.0	$17,447.0
Annual	1,022,000.0	0.0	1,022,000.0	200.0	$205,422.0	$0.0	$0.0	$0.0	$0.0	$205,422.0

Table 10: Utility monthly summary—proposed system (Kenya).

Month	Energy purchased (kWh)	Energy sold (kWh)	Net energy purchased (kWh)	Peak load (kW)	Energy charge	Demand charge	Fixed charge	Minimum charge	Taxes	Total
January	49,312.0	17,658.0	31,653.0	200.0	$7,969.0	$0.0	$0.0	$0.0	$0.0	$7,969.0
February	41,806.0	16,698.0	25,108.0	200.0	$6,566.0	$0.0	$0.0	$0.0	$0.0	$6,566.0
March	48,471.0	16,855.0	31,616.0	200.0	$7,889.0	$0.0	$0.0	$0.0	$0.0	$7,889.0
April	49,341.0	9,481.0	39,860.0	200.0	$8,875.0	$0.0	$0.0	$0.0	$0.0	$8,875.0
May	53,773.0	8,967.0	44,806.0	200.0	$9,822.0	$0.0	$0.0	$0.0	$0.0	$9,822.0
June	50,797.0	7,832.0	42,965.0	200.0	$9,349.0	$0.0	$0.0	$0.0	$0.0	$9,349.0
July	54,367.0	7,952.0	46,415.0	200.0	$10,053.0	$0.0	$0.0	$0.0	$0.0	$10,053.0
August	54,031.0	9,011.0	45,020.0	200.0	$9,869.0	$0.0	$0.0	$0.0	$0.0	$9,869.0
September	49,175.0	14,876.0	34,299.0	200.0	$8,248.0	$0.0	$0.0	$0.0	$0.0	$8,248.0
October	48,819.0	12,750.0	36,068.0	200.0	$8,410.0	$0.0	$0.0	$0.0	$0.0	$8,410.0
November	52,791.0	11,173.0	41,618.0	200.0	$9,382.0	$0.0	$0.0	$0.0	$0.0	$9,382.0
December	50,940.0	13,586.0	37,354.0	200.0	$8,744.0	$0.0	$0.0	$0.0	$0.0	$8,744.0
Annual	603,622.0	146,839.0	456,783.0	200.0	$105,176.0	$0.0	$0.0	$0.0	$0.0	$105,176.0

5.132 kWh/m^2/day in October, to 4.459 kWh/m^2/day in November, and rises to 5.041 kWh/m^2/day.

Figure 26 shows the monthly clearness index (CI) for Tanzania. The CI increased from 0.550 in January to 0.571 (peak) in February and declines to 0.529 in March, 0.453 in April, 0.444 in May, rose slightly to 0.463 in June, and declines to 0.434 in July. The lowest 0.426 CI occurred in August, it rose to 0.502 in September and decreases to 0.492 in October, and 0.435 in November, and finally rose to 0.501 in December.

Figure 27 depicts the monthly temperature variation for Tanzania. The temperature rose from 19.36°C in January to 20.44°C in February and peaked at 20.65°C in March. It declines to 19.68°C in April, 18.43°C in May, 17.71°C in June, and 17.5°C in July. The temperature gently rose to 18.12°C in August, 19.35°C in September, and 19.83°C in October. The temperature decreases to 19.2°C in November and 18.95°C in December, respectively.

Figure 28 indicates the cumulative cash flows over the lifetime of the proposed power system in Tanzania. The cumulative cash flows at inception were zero while it was US$1,500,000.00 at the 25-year economic life span. The cash flow at 2.83 years was US$300,000.00, US$600,000.00 at 6.5 years, US$900,000.00 at 10.83 years, US$1,200,000.00 by 16.5 years, and US$1,500,000.00 by the 25th year, respectively.

Table 12 shows the projected grid cost details for the 25-year economic lifespan for Tanzania. The cost detail was US$117,530.00 for each of the 25 years, respectively.

4.1.4. Republic of Burundi. Burundi's sunshine hours range between 1680 and 2045 per year with global horizontal

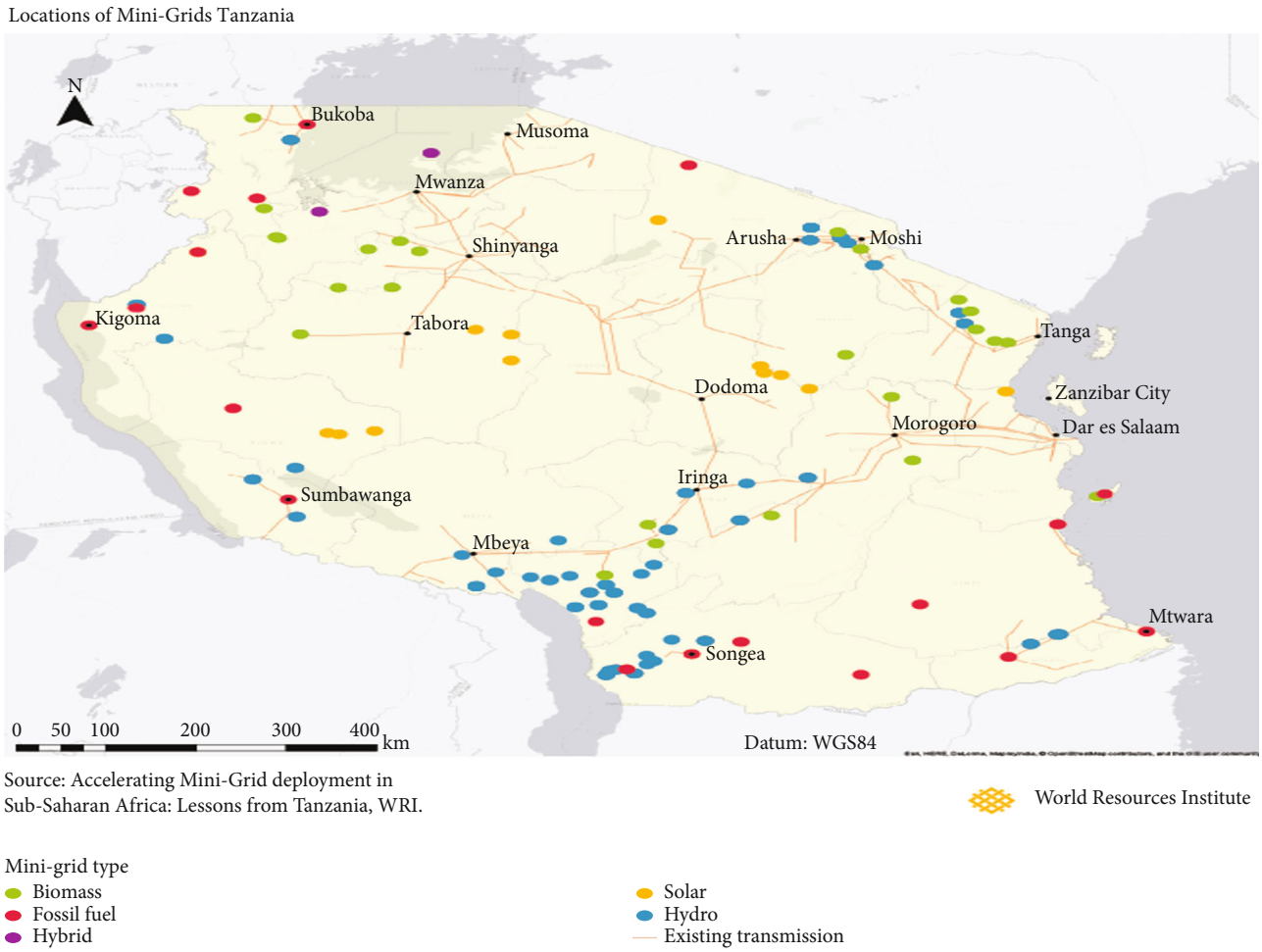

Figure 23: Minigrid locations and numbers in Tanzania.

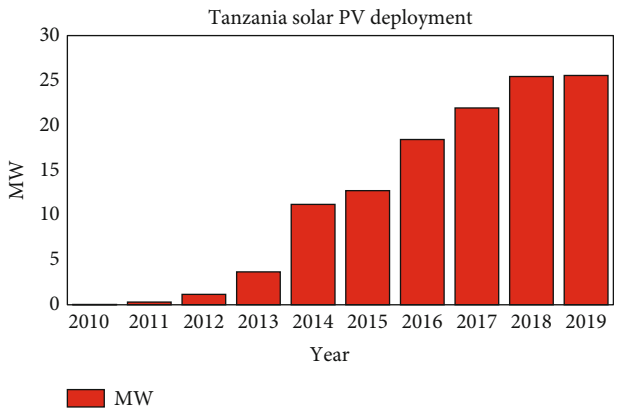

Figure 24: Solar PV trends in Tanzania by IRENA.

radiation of 4.6 to 5.6 kWh per m^2 per day [14]. Burundi has an electricity access rate of 9.3% and is one of the seven countries with the least electricity access globally [9, 26]. The energy institutional structure in Burundi is greatly constrained. It is composed of "Regideso" which is the national utility. The national utility has a mandate for power generation, transmission, and distribution with a 25-year legal monopoly renewed in 2015 [9]. Regideso owns and operates the generation assets made up of 8 hydroelectric and 2 thermal plants producing a total of 45.0 MW for nearly 10 million people. Most of the grid infrastructure is very old and incapable to handle any additional grid power [47].

There are a few Independent Power Producers (IPPs), providing electricity mainly for their own needs [47]. On policy and institutional efforts, the Decentralized Rural Electrification Strategy (2015–2017) outlines approaches of decentralizing renewable energy by establishing institutional, community, commercial level structures, and building capacity. Under the electrification strategy, there are intentions to create a National Agency for Renewable Energy and Energy Efficiency. Under Burundi's vision 2025 approved in 2011, the government is aimed at achieving an electrification rate of 25.0% by 2025 by developing renewable micro and mini plants. The government introduced tax exemptions for PV modules and generators. "Solar Electricity service with Mini-Grids in Africa-Burundi" (SESMA-Burundi) is working on the construction of about 7 initial minigrids [48]. Table 13 describes the institutions involved in the Burundi energy sector.

According to the IRENA, solar PV deployment in Burundi produced a total of 5.103 MW as can be shown by

Table 11: Institutions involved in the energy sector in Tanzania.

Institution	Mandate	Ref
Tanzania Electricity Supply Company (TANESCO)	Manages electricity generation, transmission, and distribution. It also owns most of the assets.	[42]
Rural Energy Agency (REA)	A government organization that manages the Rural Energy Fund (REF). It executes the rural electrification strategy through the central grid and off-grid solutions.	[43, 44]
Ministry of Energy formerly Ministry of Energy and Minerals	Develops policies affecting energy in Tanzania	[39]
Energy and Water Utilities Regulation Authority (EWURA)	Regulates the generation, transmission, and distribution of electricity. Sets and approves tariffs and other management tools.	[45]
Small Power Producers (SPP)	Independent power producers of capacity less than 10 MW. They provide 2.0% of the total power to TANESCO.	
Independent Power Producers (IPP)	Provide 26.0% of total TANESCO capacity	[46]
Emergency Power Producers	Provide 13.0% of total TANESCO capacity	

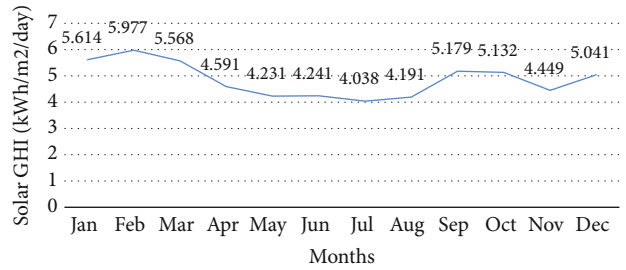

Figure 25: Monthly solar Global Horizontal Irradiation (GHI kWh/m^2/day) for Tanzania.

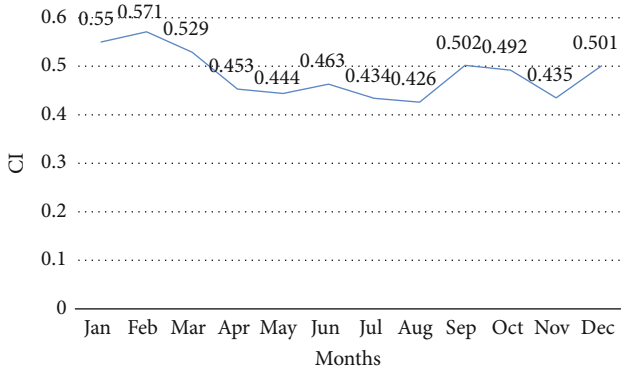

Figure 26: Monthly clearness index (CI) for Tanzania.

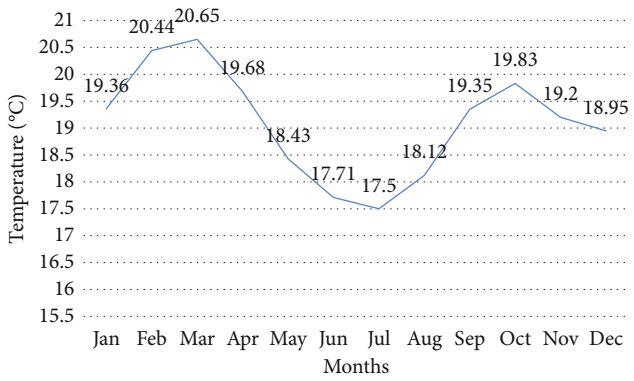

Figure 27: Monthly temperature variation (°C) for Tanzania.

Figure 29, by the end of 2019 [26]. While minigrids are not a novel concept, solar PV minigrids are fairly new to the Burundi market and are very few. Figure 29 indicates solar PV trends in Burundi. The solar PV deployment was about 0.66 MW in 2010, 0.79 MW in 2011, 1.58 MW in 2012, 2.64 MW in 2013, 2.81 MW in 2014, 3.10 MW in 2015, 4.09 in 2016, 5.07 MW in 2017, 5.07 in 2018, and 5.07 in 2019, respectively.

Solar PV technologies experienced steady growth between 2010 and 2017(Figure 10). There was no significant growth between 2017 and 2019; however, plans are underway for an inaugural, megawatt-scale (8.67 MW) solar PV minigrid set to commence construction in 2020 [52]. This solar PV power plant is anticipated to increase the country's generation capacity by more than 10.0%. The development will also be the first grid-connected solar project by an independent power producer (IPP) in Burundi. The project is a public-private partnership between the Government of Burundi and a private corporation. This project has a great demonstration impact to build capacity and give impetus to the minigrid market. Ongoing donor-financed infrastructure operations are assisting the Government of Burundi in funding the electrification of households, small businesses, schools, and health centers in rural areas using minisolar grids which will generate a total capacity of 17.0 MW [53]. The Government of Burundi will install solar minihybrid grids in rural areas. These solar minigrids will be equipped with battery storage systems and generators. Host sites totaling 150 have already been identified across the country. Figure 30 indicates the monthly solar global horizontal irradiation (GHI) for Burundi. The GHI rose from 4.674 kWh/m^2/day in January to 4.928 kWh/m^2/day in February and 4.988 kWh/m^2/day in March. The GHI then decreased to 4.446 kWh/m^2/day in April, 4.447 kWh/m2/day in May, and rose to 4.936 kWh/m^2/day in June, 5.159 kWh/m^2/day in July to peak at 5.425 kWh/m^2/day in August. It declined to 5.198 kWh/m^2/day in September, 4.881 kWh/m^2/day in

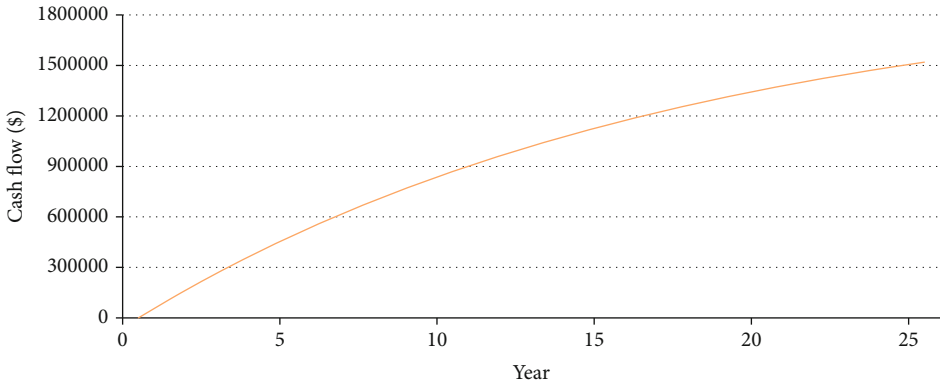

Figure 28: Cumulative cash flows over project lifetime Tanzania.

October, and 4.442 kWh/m^2/day in November (lowest) before rising to 4.659 kWh/m^2/day in December.

Figure 31 depicts the monthly clearness index (CI) for Burundi. The CI increased from 0.449 in January to 0.465 in February, 0.474 in March, and declines to 0.443 in April. It rose again to 0.476 in May, 0.553 in June, 0.568 in July, and 0.560 in August, down to 0.506 in September, 0.464 in October, and to the least at 0.425 in November before rising to 0.453 in December.

Figure 32 indicates the monthly temperature variation for Burundi. The temperature rose from 19.95^{0}C in January to 20.30°C in February, down to 20.23°C in March, 19.85°C in April, 19.85°C in May, 18.36°C in June, and to the least at 18.27°C in July. The temperature rose again to 19.60 in August to peak at 20.84°C in September, down to 20.73°C in October, and 19.93°C in November.

Figure 33 denotes the cumulative cash flows over project lifetimes for both the current and proposed power systems for Burundi. The current power system cumulative cash flows seem to be preferable to the proposed power system for Burundi because the area under the curve is larger than that of the proposed power system. The cash flow was zero at inception for the current power system but around US$898,265.90 for the proposed power system. But at 7.33 years, both the current and proposed power systems cash flows were the same at US$1,845,086.71. At their 25-year economic lives, the cumulative cash flows for both the current and proposed power systems were US$4,078,612.72 and US$2,937,572.25, respectively. If we use the areas under each curve, US$50,982,659.00 and US$47,947,976.88 were the cumulative cash flows for both the current and proposed power systems, respectively. Therefore, the current power system cumulative cash flows were US$3,034,682.12 greater and better than those of the proposed power system.

Figure 34 indicates the categorized annual savings of the proposed power system for Burundi. The energy value amount was US$159,888.00, operations and maintenance costs were US$-1,057.00, and annual savings were US$158,831.00.

Figure 35 depicts the monthly utility bills for both the current and proposed power systems for Burundi. The January utility bills for both the current and proposed power systems were US$26,894.74 and US$14,184.21, respectively. The February utility bills for both the current and proposed power systems were US$24,131.58 and US$11,973.68, respectively. The March utility bills for both the current and proposed power systems were US$26,897.74 and US$12,894.74, respectively. The April utility bills for both the current and proposed power systems were US$ 25,973.68 and US$13,631.58, respectively. The May utility bills for both the current and proposed power systems were US$26,894.74 and US$14,000.00, respectively. The June utility bills for both the current and proposed power systems were US$25,789.47 and US$12,157.90, respectively. The July utility bills for both the current and proposed power systems were US$26,894.74 and US$11,973.68, respectively. The August utility bills for both the current and proposed power systems were US$26,894.74 and US$11,605.26, respectively. The September utility bills for both the current and proposed power systems were US$25,900.00 and US$12,157.90, respectively. The October utility bills for both the current and proposed power systems were US$26,894.74 and US$11,421.05, respectively. The November utility bills for both the current and proposed power systems were US$25,789.47 and US$14,368.42, respectively. The December utility bills for both the current and proposed power systems were US$26,894.74 and US$14,110.53, respectively.

Table 14 depicts the utility annual bills and savings by category for Burundi. The base case consumption was US$316,820.00 and that for the proposed power system was US$156,932.00, while the annual savings were US$159,888.00.

Figure 36 indicates the electrical production capacities for both the grid and proposed solar PV microgrid with storage for Burundi. The January electrical production capacities for both the current grid and proposed solar PV microgrid were 98.36 MWh and 45.25 MWh, respectively. The February electrical production capacities for both the current grid and proposed solar PV micro-grid were 90.49 MWh and 43.28 MWh, respectively. The March electrical production capacities for both the current grid and proposed solar PV microgrid were 100.33 MWh and 49.18 MWh, respectively. The April electrical production capacities for both the current grid and proposed solar PV microgrid were 92.46 MWh and 43.28 MWh, respectively. The May electrical production capacities for both the current grid and proposed

Table 12: Project cost details (grid) for the whole project lifetime in Tanzania.

Year	1	2	3	4	5	6	7	8	9	10
Tanzania grid	($117,530.0)	($117,530.0)	($117,530.0)	($117,530.0)	($117,530.0)	($117,530.0)	($117,530.0)	($117,530.0)	($117,530.0)	($117,530.0)
Year	11	12	13	14	15	16	17	18	19	20
Tanzania gird	($117,530.0)	($117,530.0)	($117,530.0)	($117,530.0)	($117,530.0)	($117,530.0)	($117,530.0)	($117,530.0)	($117,530.0)	($117,530.0)
Year	21	22	23	24	25					
Tanzania grid	($117,530.0)	($117,530.0)	($117,530.0)	($117,530.0)	($117,530.0)					

Table 13: Institutions involved in the energy sector in Burundi.

Institution	Mandate	Ref
Regideso	National utility that owns and manages Burundi's thermal and hydropower plants	[49]
Burundian Agency for Rural Electrification (ABER)	Planning, carrying out studies, and carrying out projects for electrification of rural centers, villages. Regulates the electricity generation, transmission, and distribution.	[50]
Ministry of Energy and Mines	Oversees the development of policy and regulations of the energy sector. It coordinates sector planning as well as for the management of the energy sector	[51]

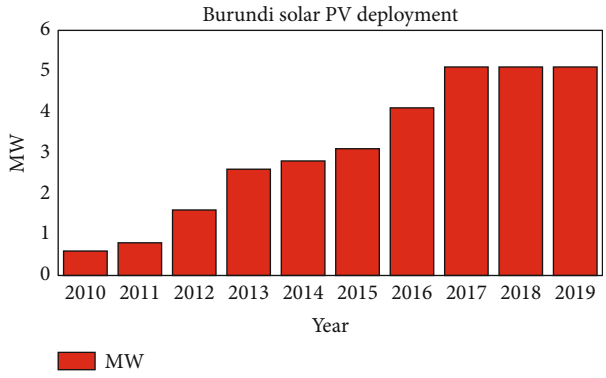

Figure 29: Solar PV trends in Burundi by IRENA.

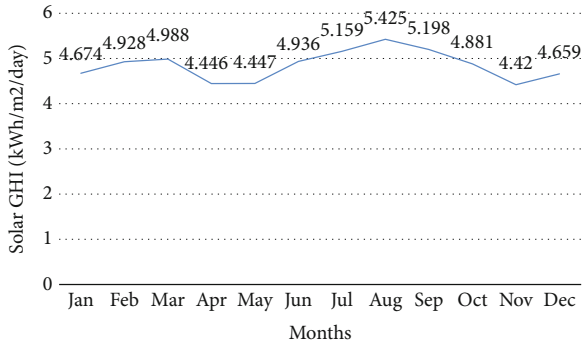

Figure 30: Monthly solar Global Horizontal Irradiation (GHI kWh/m^2/day) for Burundi.

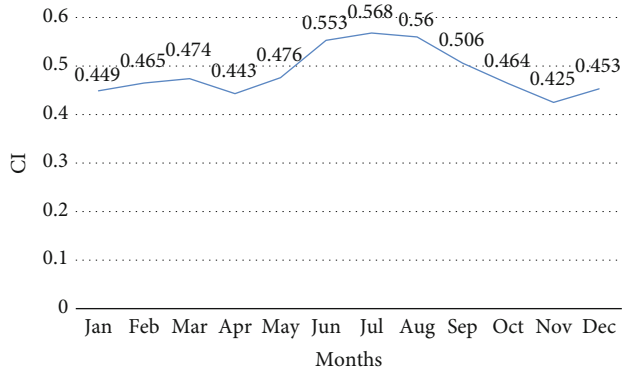

Figure 31: Monthly clearness index (CI) for Burundi.

solar PV micro-grid were 96.39 MWh and 45.25 MWh, respectively. The June electrical production capacities for both the current grid and proposed solar PV microgrid were

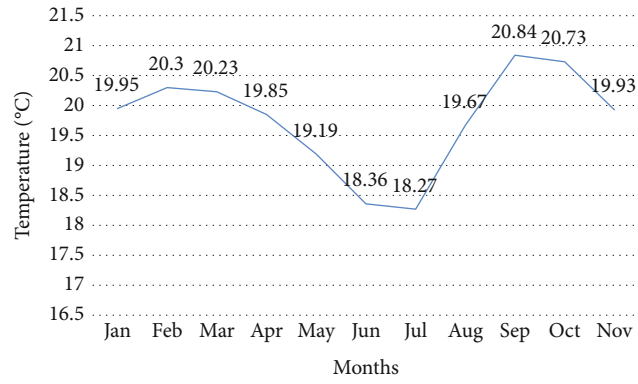

Figure 32: Monthly temperature variation (°C) for Burundi.

95.41 MWh and 48.59 MWh, respectively. The July electrical production capacities for both the current grid and proposed solar PV microgrid were 100.00 MWh and 52.52 MWh, respectively. The August electrical production capacities for both the current grid and proposed solar PV microgrid were 102.30 MWh and 55.08 MWh, respectively. The September electrical production capacities for both the current grid and proposed solar PV microgrid were 99.34 MWh and 50.16 MWh, respectively. The October electrical production capacities for both the current grid and proposed solar PV microgrid were 98.36 MWh and 47.21 MWh, respectively. The November electrical production capacities for both the current grid and proposed solar PV micro-grid were 94.43 MWh and 41.31 MWh, respectively. The December electrical production capacities for both the current grid and proposed solar PV microgrid were 98.36 MWh and 45.25 MWh, respectively.

Furthermore, the solar PV system has a nominal capacity of 400.0 kW, and its annual production was 567100.0 kWh/year, and a specific yield of 1418.0 kWh/kW.

Table 15 denotes the project cost details (both grid and solar PV systems) for the lifespan of the project in Burundi. The project cost for each year of the solar PV system was US$1,057.00 while the yearly grid cost was US$156,932.00, respectively.

Table 16 depicts the monthly utility summary for the current grid system for Burundi. The energy purchase was each US$86,800.00 for January, March, May, July, August, October, and December, respectively. Only the February energy purchase was 78,400.00 kWh while those for April, June, September, and November were 84,000.0 kWh each, respectively. The annual energy purchase was 1,022,000.0 kWh, and the total energy charge was US$316,820.00.

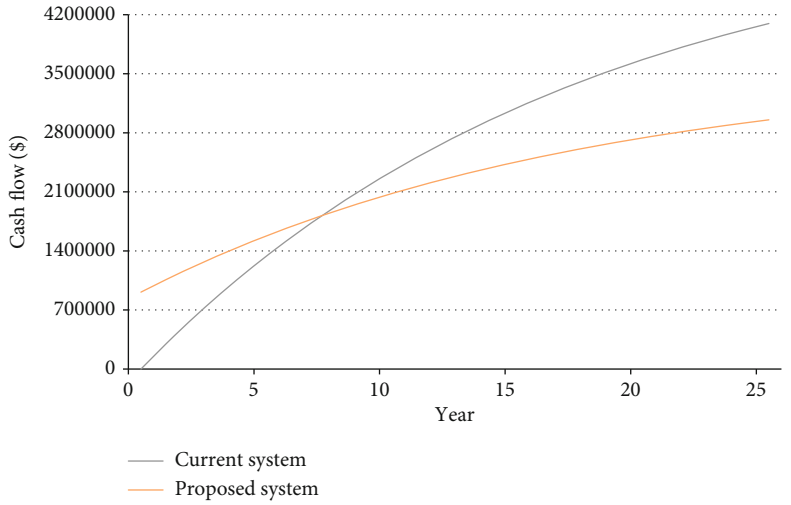

Figure 33: Cumulative cash flows over the project lifetime for the current and proposed systems for Burundi.

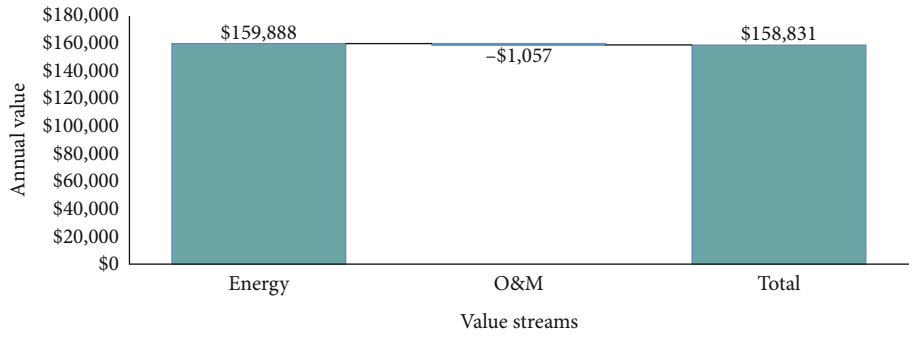

Figure 34: Categorized annual savings for the proposed system for Burundi.

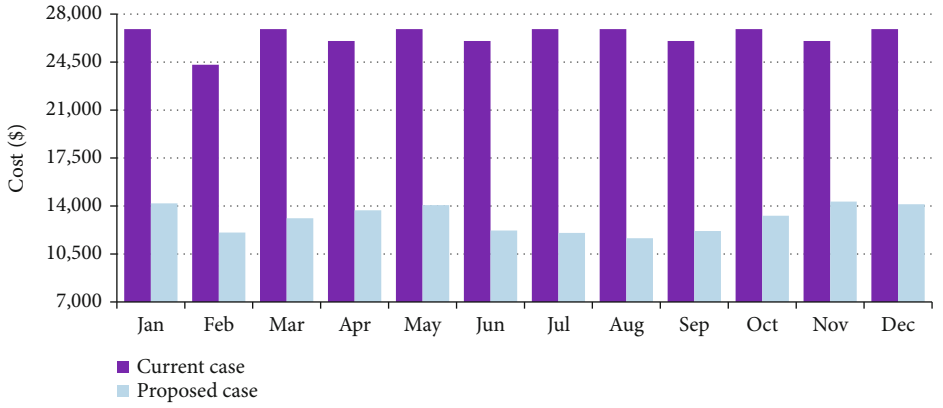

Figure 35: Monthly utility bills for the current and proposed systems for Burundi.

Table 14: Annual utility bills and savings by category (Burundi).

	Consumption charge	Total
Base case	$316,820.0	$316,820.0
Proposed case	$156,932.0	$156,932.0
Annual savings	$159,888.0	$159,888.0

Note: the base case is considered as the current system (grid connection) and the proposed case is the grid-connected solar PV microgrid with storage.

Table 17 indicates the monthly utility summary for the proposed power system from January to December for Burundi. The energy purchase, energy sold, and net energy for each of the months from January to December varied with the month. The annual energy purchase, annual energy sold, and net energy purchase were US$600,892.00, US$145,992.00, and US$454,000.00, respectively. The peak load was 200.0 kW for each month, and the energy charge

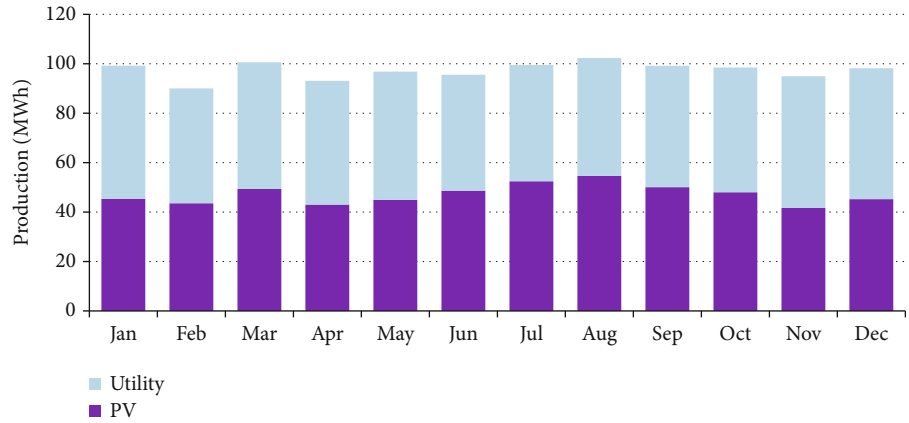

Figure 36: The electrical production for both utility and the solar PV microgrid for the proposed technology on Burundi.

varied with every month of the year. Furthermore, the fixed charge, minimum charge, demand charge, and taxes were each zero, respectively.

4.1.5. South Sudan. South Sudan enjoys between 1899 and 2264 quality sunshine hours annually with global horizontal radiation of 5.2 to 6.2 kWh per m^2 per day [14]. This is a valuable resource that can be utilized to bring electricity to the countryside. South Sudan has an electricity access rate of around 1.1 % [22]. The energy sector in South Sudan is very limited constituting the national utility South Sudan Electricity Corporation (SSEC), the regulatory authority, and the ministry of electricity and dams. There was no transmission infrastructure or any interconnected grid network in South Sudan [54]. South Sudan's installed power capacity was approximately 130 megawatts by 2013, a large portion of which is used to supply electricity for extracting and processing petroleum oil. However, the country's power demand was about 300 megawatts in 2013 [54]. Currently, most of the solar energy deployed is stand-alone PV systems used to supply approximately 40,000 households to power a variety of electrical devices. The country's high insolation could be exploited to generate more electricity but this is still in the planning phase. Table 18 describes the institutions involved in the energy sector in South Sudan.

Solar minigrid deployment in South Sudan is still at the initial level. South Sudan's national utility completed technical evaluations for a 20-megawatt minigrid solar farm in Nesitu County and 35 megawatt-hour battery storage system planned outside of Juba [58]. The project is funded by a commercial bank. It will be the first grid-connected, megawatt-scale solar power plant in the country. According to the International Renewable Energy Agency (IRENA), South Sudan had installed a paltry 0.649 MW of solar by the end of 2019 as shown in Figure 37, most of it off-grid capacity [26]. The sector was stagnant up to 2015 but experienced major growth in 2016 when solar PV installations doubled. Since then, there has been a gradual increase in the installation of solar PV technologies in South Sudan. Figure 37 depicts the South Sudan solar PV deployment from 2010 to 2019 (inclusive). The solar power was 0.16 MW in 2012 up to and including 2015, 0.43 MW in 2016, 0.44 MW in 2017, 0.55 MW in 2018, and 0.64 MW in 2019, respectively.

There are efforts to disseminate about 6800 solar irrigation pumps to rural households in a period stretching between 2012 and 2025. On completion, access of rural households to solar electricity will be at 10.0% [55]. Solar PV installations by several private companies are being used to provide electricity in smaller configurations through minigrids for personal use or clustered population. Some companies are using containerized off-grid solar battery hybrid power systems successfully installed in the southern part of South Sudan. These containerized solar PV minigrids (as can be shown in Figure 38) provide electricity to surrounding populations and institutions [13].

With the absence of a transmission backbone, all electricity in South Sudan is essentially self-generated, largely by diesel generators. Currently, solar minigrids among other solar technologies are being actively initiated and funded by donors for demonstrational purposes of solar PV technology. The country has the least capacity of solar PV installed in the East Africa region compared to the other five member states. The country is yet to adopt a national electrification strategy that can give a road map into the future and attract significant investments. Figure 39 indicates the monthly solar global horizontal irradiation (GHI) in South Sudan. The GHI increased from 5.827 kWh/m^2/day in January to 6.112 kWh/m^2/day in February, 6.137 kWh/m^2/day in March, and 6.349 kWk/m^2/day (peak) in April. It increased to 5.497 kWh/m^2/day in May, 5.024 kWh/m^2/day in June, and 4.663 kWh/m^2/day in July (lowest). It rose gradually to 4.909 kWh/m^2/day in August, 5.277 kWh/m^2/day in September, 5.405 kWh/m^2/day in October, 5.900 kWh/m^2/day in November, and 5.766 kWh/m^2/day.

Figure 40 is the monthly clearness index (CI) for South Sudan. The CI decreased from 0.64 in January to 0.63 in February, 0.59 in March, 0.60 in April, 0.53 in May, 0.50 in June, 0.46 in July (lowest), 0.47 in August, 0.50 in September, 0.55 in October, 0.64 in November, and 0.65 in December.

Figure 41 shows the monthly temperature variation for South Sudan. The temperature increased from 29.11°C in January to 30.85°C in February, 32.53°C in March, 32.37°C

Table 15: Project cost details (both grid and PV system) for the whole project lifetime in Burundi.

Year	1	2	3	4	5	6	7	8	9	10
Burundi grid	($156,932.0)	($156,932.0)	($156,932.0)	($156,932.0)	($156,932.0)	($156,932.0)	($156,932.0)	($156,932.0)	($156,932.0)	($156,932.0)
PV	($1,057.0)	($1,057.0)	($1,057.0)	($1,057.0)	($1,057.0)	($1,057.0)	($1,057.0)	($1,057.0)	($1,057.0)	($1,057.0)
Year	11	12	13	14	15	16	17	18	19	20
Burundi grid	($156,932.0)	($156,932.0)	($156,932.0)	($156,932.0)	($156,932.0)	($156,932.0)	($156,932.0)	($156,932.0)	($156,932.0)	($156,932.0)
PV	($1,057.0)	($1,057.0)	($1,057.0)	($1,057.0)	($1,057.0)	($1,057.0)	($1,057.0)	($1,057.0)	($1,057.0)	($1,057.0)
Year	21	22	23	24	25					
Burundi grid	($156,932.0)	($156,932.0)	($156,932.0)	($156,932.0)	($156,932.0)					
PV	($1,057.0)	($1,057.0)	($1,057.0)	($1,057.0)	($1,057.0)					

Table 16: Utility monthly summary—current system (Burundi).

Month	Energy purchased (kWh)	Energy sold (kWh)	Net energy purchased (kWh)	Peak load (kW)	Energy charge	Demand charge	Fixed charge	Minimum charge	Taxes	Total
January	86,800.0	0.0	86,800.0	200.0	$26,908.0	$0.0	$0.0	$0.0	$0.0	$26,908.0
February	78,400.0	0.0	78,400.0	200.0	$24,304.0	$0.0	$0.0	$0.0	$0.0	$24,304.0
March	86,800.0	0.0	86,800.0	200.0	$26,908.0	$0.0	$0.0	$0.0	$0.0	$26,908.0
April	84,000.0	0.0	84,000.0	200.0	$26,040.0	$0.0	$0.0	$0.0	$0.0	$26,040.0
May	86,800.0	0.0	86,800.0	200.0	$26,908.0	$0.0	$0.0	$0.0	$0.0	$26,908.0
June	84,000.0	0.0	84,000.0	200.0	$26,040.0	$0.0	$0.0	$0.0	$0.0	$26,040.0
July	86,800.0	0.0	86,800.0	200.0	$26,908.0	$0.0	$0.0	$0.0	$0.0	$26,908.0
August	86,800.0	0.0	86,800.0	200.0	$26,908.0	$0.0	$0.0	$0.0	$0.0	$26,908.0
September	84,000.0	0.0	84,000.0	200.0	$26,040.0	$0.0	$0.0	$0.0	$0.0	$26,040.0
October	86,800.0	0.0	86,800.0	200.0	$26,908.0	$0.0	$0.0	$0.0	$0.0	$26,908.0
November	84,000.0	0.0	84,000.0	200.0	$26,040.0	$0.0	$0.0	$0.0	$0.0	$26,040.0
December	86,800.0	0.0	86,800.0	200.0	$26,908.0	$0.0	$0.0	$0.0	$0.0	$26,908.0
Annual	1,022,000.0	0.0	1,022,000.0	200.0	$316,820.0	$0.0	$0.0	$0.0	$0.0	$316,820.0

Table 17: Utility monthly summary—proposed system (Burundi).

Month	Energy purchased (kWh)	Energy sold (kWh)	Net energy purchased (kWh)	Peak load (kW)	Energy charge	Demand charge	Fixed charge	Minimum charge	Taxes	Total
January	53,862.0	12,446.0	41,416.0	200.0	$14,195.0	$0.0	$0.0	$0.0	$0.0	$14,195.0
February	46,446.0	11,618.0	34,828.0	200.0	$12,063.0	$0.0	$0.0	$0.0	$0.0	$12,063.0
March	51,219.0	13,778.0	37,441.0	200.0	$13,108.0	$0.0	$0.0	$0.0	$0.0	$13,108.0
April	50,051.0	9,091.0	40,960.0	200.0	$13,689.0	$0.0	$0.0	$0.0	$0.0	$13,689.0
May	51,852.0	10,005.0	41,847.0	200.0	$14,063.0	$0.0	$0.0	$0.0	$0.0	$14,063.0
June	46,861.0	11,534.0	35,326.0	200.0	$12,208.0	$0.0	$0.0	$0.0	$0.0	$12,208.0
July	47,071.0	12,718.0	34,353.0	200.0	$12,036.0	$0.0	$0.0	$0.0	$0.0	$12,036.0
August	47,662.0	15,557.0	32,105.0	200.0	$11,648.0	$0.0	$0.0	$0.0	$0.0	$11,648.0
September	49,127.0	15,184.0	33,943.0	200.0	$12,177.0	$0.0	$0.0	$0.0	$0.0	$12,177.0
October	50,465.0	11,700.0	38,765.0	200.0	$13,292.0	$0.0	$0.0	$0.0	$0.0	$13,292.0
November	53,316.0	10,977.0	42,339.0	200.0	$14,322.0	$0.0	$0.0	$0.0	$0.0	$14,322.0
December	52,960.0	11,383.0	41,577.0	200.0	$14,130.0	$0.0	$0.0	$0.0	$0.0	$14,130.0
Annual	600,892.0	145,992.0	454,900.0	200.0	$156,932.0	$0.0	$0.0	$0.0	$0.0	$156,932.0

Table 18: Descriptions of institutions involved in the energy sector in South Sudan.

Institution	Mandate	Ref
South Sudan Electricity Corporation (SSEC)	The national electric utility that oversees the generation, transmission, and supply of electricity.	[55]
South Sudan Electricity Regulation Authority (SSERA)	Functional energy regulator of South Sudan's minigrids. It administers license approval, sets tariffs, and maintains technical standards.	[56, 57]
Ministry of Electricity and Dams (MoED)	MoED is responsible for the development of hydro dams for multipurpose use including hydropower generation. It is also responsible for the development of renewable energies. Develop policies, oversee compliance, and set tariffs.	

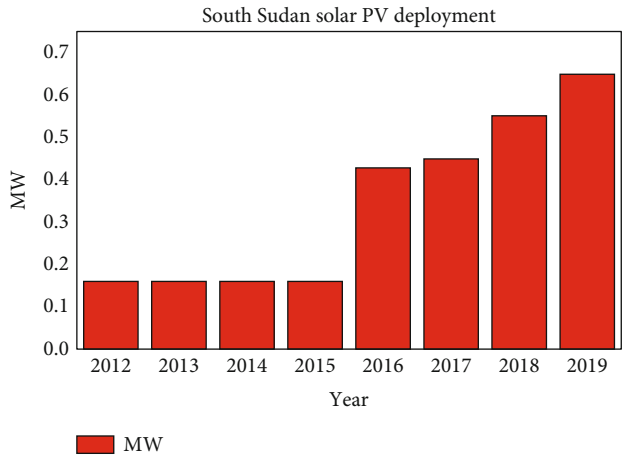

Figure 37: Solar PV trends in South Sudan by IRENA.

in April, 29.95°C in May, 27.81°C in June, 26.09°C in July, 25.95°C in August, 26.71°C in September, 27.48°C in October, 28.71°C in November, and 28.89°C in December.

Figure 42 depicts the cumulative cash flows of the project lifespan for the current and proposed power systems for South Sudan. The areas under the cash flow curves show that the current grid power system was more profitable than the proposed power system because it had a smaller area. At inception, the current power system had zero cash flow while the proposed power system has US$95,000.00 cash flow at the inception of the project. At the end of the project lifespan, the current grid system cash flow was US$5,700,000.00, and the proposed power system cash flow was US$3,300,000.00, respectively. The areas under both the current grid and proposed power systems were US$71,250,000.00 and US$53,125,000.00, respectively. That means that the current grid power system cash flow was US$18,125,000.00 better than that of the proposed power system.

Figure 43 indicates the categorized annual savings of the proposed power system for South Sudan. The energy value was US$254,973.00, US$1,057.00 the operations and maintenance expense, and US$253,917.00 energy savings for South Sudan, respectively.

Figure 44 depicts the monthly utility bills for the current and proposed power systems for South Sudan. The January bills for both the current and proposed power systems were US$37,285.71 and US$13,714.29, respectively. The February bills for both the current and proposed power systems were US$33,857.14 and US$12,000.00, respectively. The March bills for both the current and proposed power systems were US$37,285.71 and US$13,214.29, respectively. The April bills for both the current and proposed power systems were US$36,428.57 and US$13,285.71, respectively. The May bills for both the current and proposed power systems were US$37,285.71 and US$17,142.86, respectively. The June bills for both the current and proposed power systems were US$36,428.57 and US$18,000.00, respectively. The July bills for both the current and proposed power systems were US$37,714.29 and US$19,714.29, respectively. The August bills for both the current and proposed power systems were US$37,714.29 and US$18,857.14, respectively. The September bills for both the current and proposed power systems were US$36,000.00 and US$16,714.29, respectively. The October bills for both the current and proposed power systems were US$37,714.29 and US$15,857.14, respectively. The November bills for both the current and proposed power systems were US$36,428.57 and US$12,857.14, respectively. The December bills for both the current and proposed power systems were US$37,285.71 and US$13,714.29, respectively.

Table 19 indicates the annual utility bills and savings by category for South Sudan. The base case electricity consumption was US$439,460.00, US$184,487.00 the proposed power system consumption charge, and US$254,973.00 the annual savings, respectively.

Figure 45 denotes the electrical production capacities of both the current utility and the solar PV microgrid in South Sudan. The January electrical production capacities for both the current grid and proposed solar PV microgrid were 107.76 MWh and 62.45 MWh, respectively. The February electrical production capacities for both the current grid and proposed solar PV microgrid were 97.96 MWh and 56.33 MWh, respectively. The March electrical production capacities for both the current grid and proposed solar PV microgrid were 107.76 MWh and 62.45 MWh, respectively. The April electrical production capacities for both the current grid and proposed solar PV microgrid were 102.86 MWh and 60.00 MWh, respectively. The May electrical production capacities for both the current grid and proposed solar PV microgrid were 100.00 MWh and 51.43 MWh, respectively. The June electrical production capacities for both the current grid and proposed solar PV microgrid were 93.06 MWh and 46.53 MWh, respectively. The July electrical production capacities for both the current grid and proposed solar PV microgrid were 95.50 MWh and 44.08 MWh, respectively. The August electrical production capacities for both the current grid and proposed solar PV microgrid were 97.96 MWh and 46.53 MWh, respectively. The September electrical production capacities for both the current grid and proposed solar PV microgrid were 99.18 MWh and 51.43 MWh, respectively. The October electrical production capacities for both the current grid and proposed solar PV microgrid were 102.86 MWh and 55.10 MWh, respectively. The November electrical production capacities for both the current grid and proposed solar PV microgrid were 105.31 MWh and 61.22 MWh, respectively. The December electrical production capacities for both the current grid and proposed solar PV microgrid were 107.76 MWh and 62.45 MWh, respectively.

Further, the solar PV system has a nominal capacity of 400.0 kW, and its annual production was 661886.0 kWh/year, and a specific yield of 1655.0 kWh/kW.

Table 20 reflects the project lifespan cost details for both the grid and solar PV microgrid systems for South Sudan. The solar PV system cost annually was US$1,057.00 for 25 years, while grid cost per pear was US$184,487.00 for the 25-year economic lifespan, respectively.

Table 21 depicts the utility monthly summary for the current grid power system for South Sudan.

The energy purchase for January, March, May, July, August, October, and December was each 86,800.0 kWh,

Figure 38: Image of a containerized minigrid system in South Sudan (Source: Aptech Africa).

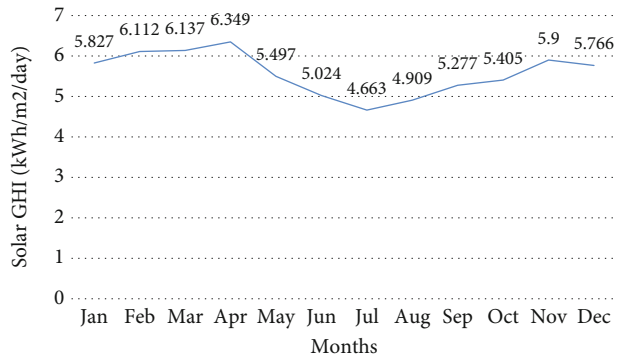

Figure 39: Monthly solar Global Horizontal Irradiation (GHI kWh/m^2/day) for South Sudan.

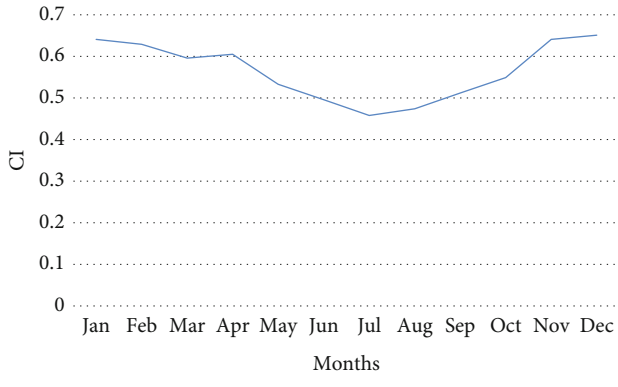

Figure 40: Monthly clearness index (CI) for South Sudan.

respectively. While only February was 78,400.0 kWh, the other months of April, June, September, and November were 84,000.0 kWh, respectively. The total energy purchase was 1,022,000.0 kWh, and the annual energy charge was US$439,460.00, respectively.

Table 22 indicates the proposed power utility monthly summary for South Sudan. The energy purchased, energy sold, net energy purchase, and energy charge were each different for every month of the year. The total annual energy purchase was 555,099.0 kWh, 194,985.0 kWh annual energy sold, 360,114 kWh annual net energy purchase, and US$184,487.00 energy charge, respectively. While 200.0 kWp was the peak load, the demand charge, fixed charge, minimum charge, and taxes were zero each, respectively.

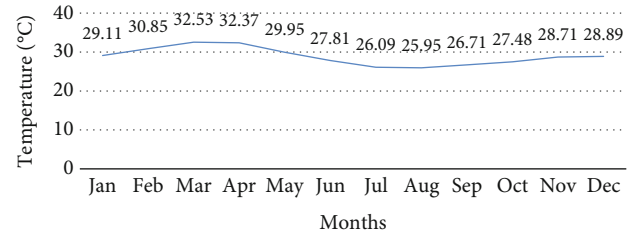

Figure 41: Monthly temperature variation (°C) for South Sudan.

4.1.6. Rwanda. The minigrid sector in Rwanda has made some significant steps since 2017 but is still fairly young. Despite recent substantial financial support for privately owned and operated minigrids, the development of privately operated minigrids in Rwanda remains low. Harmonized efforts including the provision of funds through grants, access to credit, technical assistance, and an enabling regulatory framework are required to realize sector development [59].

The governments' rural electrification strategy has a target of 100.0% electrification by [60]. This includes 48.0% off-grid connections up from a current 14.0% [61, 62]. Currently, there are 84 minigrids in Rwanda with a total capacity of 250.0 kW (Rwanda Energy Group, 2019), slightly more than half of this capacity is supplied by solar PV minigrids (Table 6). Seventy-eight are in direct current (DC) while six are in alternating current (AC), 71 of these are solar PV minigrids. Rwanda has recently realized the commissioning of two solar AC minigrids and the addition of more DC minigrids operated by local developers. Table 23 describes the solar PV minigrids in Rwanda.

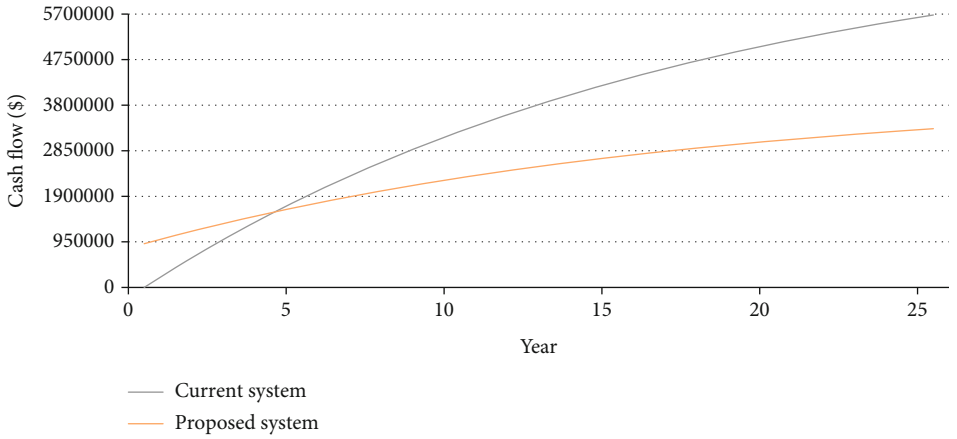

Figure 42: Cumulative cash flows over the project lifetime for the current and proposed systems for South Sudan.

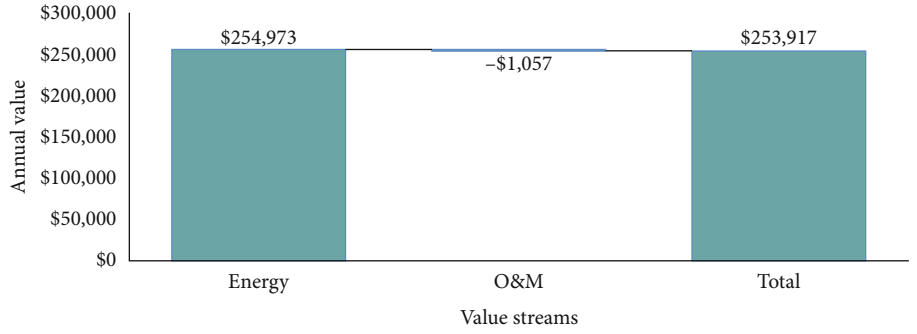

Figure 43: Categorized annual savings for a proposed system for South Sudan.

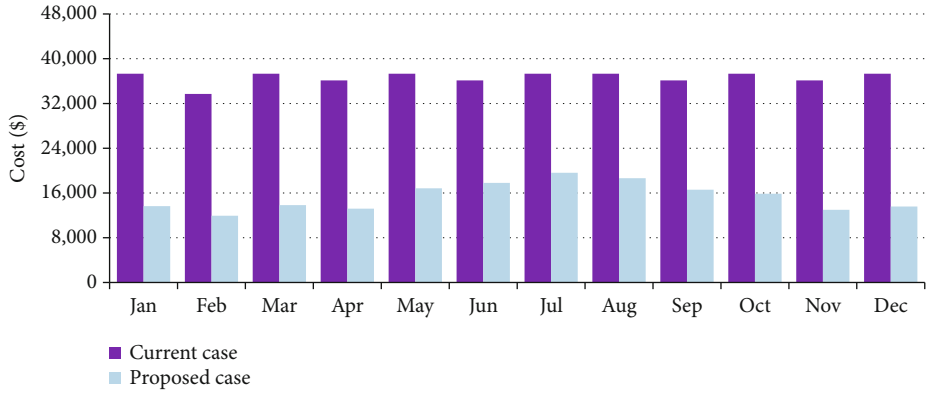

Figure 44: Monthly utility bills for the current and proposed systems for South Sudan.

Table 19: Annual utility bills and savings by category (South Sudan).

	Consumption charge	Total
Base case	$439,460.00	$439,460.00
Proposed case	$184,487.00	$184,487.00
Annual savings	$254,973.00	$254,973.00

Note: the base case is considered as the current system (grid connection) and the proposed case is the grid-connected solar PV microgrid with storage.

In the face of a very low number of minigrids, there is a rising interest by private developers. At least two AC minigrids are in the planning phase while technical support has been offered to support another 37 isolated minigrid, both projects are funded by international agencies [59]. Furthermore, through a combination of financiers, 200 locations have been identified as feasible sites for minigrid development. The funds will also be used to provide advanced feasibility studies for up to 20 sites.

Existing privately-owned minigrids in Rwanda employ both AC and DC solar PV. The power is mainly supplied to

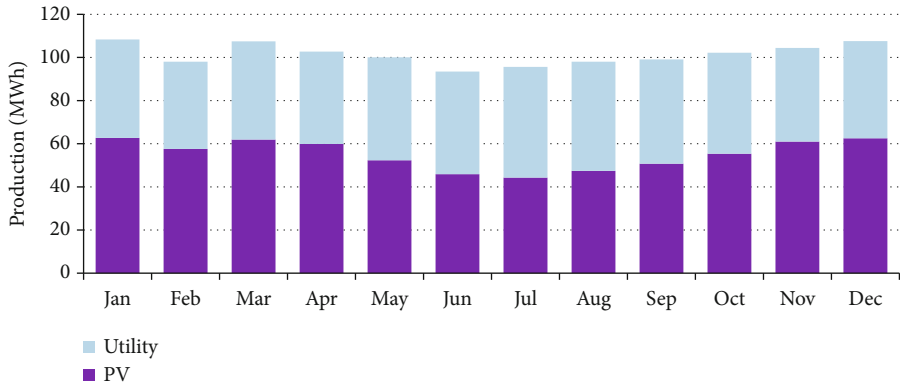

Figure 45: The electrical production for both utility and the solar PV microgrid for the proposed technology in South Sudan.

households, supplemented by few businesses and social institutions. The viability gap in Rwanda is wide with purchase power remaining very low, and the average household demand is between 2.0 kWh and 7.0 kWh per month [31, 60]. Consumption does not increase organically without additional support on the demand side. Some developers using DC grids face relatively low upfront costs as well as operation and maintenance compared to AC developers where the upfront costs are significantly higher, therefore, demanding a specific level of demand to ensure viability. High capital cost, coupled with minimal consumption, means most business models are not able to get commensurate returns without using a tariff that would appear exorbitant for the rural customers. Therefore, the creation of income-generating activities for end users is critical for the success of minigrid [63]. Minigrid construction in Rwanda requires support ranging between 40.0% and 70.0% of capital funding [60, 64, 65], with most operating and upcoming projects either focusing on individual sites or testing business models to be up-scaled later. Minigrid financing in Rwanda is still heavily dependent on grants.

Figure 46 denotes the solar PV deployment in Rwanda between 2010 and 2019 (inclusive). The PV deployment in Rwanda was about 0.20 MW for both 2010 and 2011, respectively; 0.33 MW in 2012; 1.00 MW in 2013; 9.67 MWin 2014; 13.67 MW in 2015; 18.67 MW in 2016; 26.33 in 2017; and 36.67 MW both in 2018 and 2019, respectively.

According to the International Renewable Energy Agency (IRENA) and as shown in Figure 46 [26], Rwanda is the third most vibrant market for solar PV technologies in the East African community. It had installed 37.50 MW by the end of 2019 despite having no significant growth from the previous year [26]. Before 2013, solar PV technology deployment was stagnant but since 2014 there have been installations of at least 4.0 MW per year until 2018.

Rwanda Utility Regulation Authority (RURA) utilizes a simplified licensing structure for isolated renewable power stations which provides an affirmative legal framework to the sector. Developers are required to secure a "simplified electricity license" for small off-grids that, at the time of commissioning or subsequent expansion, have collective power production of between 50.0 kW and 1000.0 kW. Similarly, power distribution networks that, during commissioning or after expansion, have a capacity of at least 1.0 MW require a license [66]. The tariff is set by the developer at a level allowing capital recovery and a satisfactory return with necessary review from RURA. Minigrids of less than 50.0 kW are exempt from the licensing procedure but must notify the authorities. The Regulatory Authority (RURA) requires a separate license for each small isolated minigrid or small power distributor facility and does not consider the total of net generation capacity as the basis for determining whether the minigrid is classified as a small isolated minigrid. Table 24 indicates the institutions involved in the energy sector in Rwanda.

Figure 47 reflects the monthly solar Global Horizontal Irradiation (GHI) for Rwanda. The Rwanda GHI rose from 4.894 kWh/m^2/day in January to 4.923 kWh/m^2/day in February and down to 4.873 kWh/m^2/day in March 4.557 kWh/m^2/day in April, 4.457 kWh/m^2/day (lowest) in May, and rose again to 5.008 kWh/m^2/day in June, 5.348 kWh/m^2/day in July (peak). It declined to 5.311 kWh/m^2/day in August, 5.178 kWh/m^2/day in September, 5.010 kWh/m^2/day in October, 4.636 kWh/m^2/day in November, and rose to 4.780 kWh/m^2/day in December.

Figure 48 indicates the monthly clearness index (CI) for Rwanda. The CI decreased from 0.477 in January to 0.468 in February in March, 0.451 in April, 0.470 in May, and rose to 0.551 in June, 0.579 (peak) in July, and drops to 0.543 in August, 0.502 in September, 0.479 in October, 0.451 in November, and rose to 0.472 in December.

Figure 49 depicts the monthly temperature variation for Rwanda. The temperature rose from 19.99°C in January to 20.59°C in February (peak) and declines to 20.20°C in March, 19.34°C in April, 18.81°C in May, 18.66°C in June, 18.75°C in July, 19.83°C in August, and 20.23°C in September. It declines to 19.85°C in October, 19.28°C in November, and rose to 19.47°C in December.

Figure 50 shows the cumulative cash flows of the current and proposed power systems for Rwanda over the economic lifespan of the power plants. The cash flows at the inception of both the current and proposed power systems were about US$-116,129.03 and US$870,967.42, respectively. Both the current and proposed power systems generated US$1,800,000.00 cash flows each during 8.33 years of their economic lifespan, respectively. At the end of their economic

Table 20: Project cost details (both grid and PV system) for the whole project lifetime in South Sudan.

Year	1	2	3	4	5	6	7	8	9	10
PV	($1,057.0)	($1,057.0)	($1,057.0)	($1,057.0)	($1,057.0)	($1,057.0)	($1,057.0)	($1,057.0)	($1,057.0)	($1,057.0)
South Sudan grid	($184,487.0)	($184,487.0)	($184,487.0)	($184,487.0)	($184,487.0)	($184,487.0)	($184,487.0)	($184,487.0)	($184,487.0)	($184,487.0)
Year	11	12	13	14	15	16	17	18	19	20
PV	($1,057.0)	($1,057.0)	($1,057.0)	($1,057.0)	($1,057.0)	($1,057.0)	($1,057.0)	($1,057.0)	($1,057.0)	($1,057.0)
South Sudan grid	($184,487.0)	($184,487.0)	($184,487.0)	($184,487.0)	($184,487.0)	($184,487.0)	($184,487.0)	($184,487.0)	($184,487.0)	($184,487.0)
Year	21	22	23	24	25					
PV	($1,057.0)	($1,057.0)	($1,057.0)	($1,057.0)	($1,057.0)					
South Sudan	($184,487.0)	($184,487.0)	($184,487.0)	($184,487.0)	($184,487.0)					

Table 21: Utility monthly summary—current system (South Sudan).

Month	Energy purchased (kWh)	Energy sold (kWh)	Net energy purchased (kWh)	Peak load (kW)	Energy charge	Demand charge	Fixed charge	Minimum charge	Taxes	Total
January	86,800.0	0.0	86,800.0	200.0	$37,324.0	$0.0	$0.0	$0.0	$0.0	$37,324.0
February	78,400.0	0.0	78,400.0	200.0	$33,712.0	$0.0	$0.0	$0.0	$0.0	$33,712.0
March	86,800.0	0.0	86,800.0	200.0	$37,324.0	$0.0	$0.0	$0.0	$0.0	$37,324.0
April	84,000.0	0.0	84,000.0	200.0	$36,120.0	$0.0	$0.0	$0.0	$0.0	$36,120.0
May	86,800.0	0.0	86,800.0	200.0	$37,324.0	$0.0	$0.0	$0.0	$0.0	$37,324.0
June	84,000.0	0.0	84,000.0	200.0	$36,120.0	$0.0	$0.0	$0.0	$0.0	$36,120.0
July	86,800.0	0.0	86,800.0	200.0	$37,324.0	$0.0	$0.0	$0.0	$0.0	$37,324.0
August	86,800.0	0.0	86,800.0	200.0	$37,324.0	$0.0	$0.0	$0.0	$0.0	$37,324.0
September	84,000.0	0.0	84,000.0	200.0	$36,120.0	$0.0	$0.0	$0.0	$0.0	$36,120.0
October	86,800.0	0.0	86,800.0	200.0	$37,324.0	$0.0	$0.0	$0.0	$0.0	$37,324.0
November	84,000.0	0.0	84,000.0	200.0	$36,120.0	$0.0	$0.0	$0.0	$0.0	$36,120.0
December	86,800.0	0.0	86,800.0	200.0	$37,324.0	$0.0	$0.0	$0.0	$0.0	$37,324.0
Annual	1,022,000.0	0.0	1,022,000.0	200.0	$439,460.0	$0.0	$0.0	$0.0	$0.0	$439,460.0

Table 22: Utility monthly summary—proposed system (South Sudan).

Month	Energy purchased (kWh)	Energy sold (kWh)	Net energy purchased (kWh)	Peak load (kW)	Energy charge	Demand charge	Fixed charge	Minimum charge	Taxes	Total
January	45,684.0	21,567.0	24,117.0	200.0	$13,649.0	$0.0	$0.0	$0.0	$0.0	$13,649.0
February	40,410.0	19,621.0	20,789.0	200.0	$11,922.0	$0.0	$0.0	$0.0	$0.0	$11,922.0
March	45,537.0	20,662.0	24,874.0	200.0	$13,837.0	$0.0	$0.0	$0.0	$0.0	$13,837.0
April	42,784.0	18,699.0	24,085.0	200.0	$13,199.0	$0.0	$0.0	$0.0	$0.0	$13,199.0
May	47,697.0	13,265.0	34,432.0	200.0	$16,822.0	$0.0	$0.0	$0.0	$0.0	$16,822.0
June	47,516.0	9,442.0	38,074.0	200.0	$17,807.0	$0.0	$0.0	$0.0	$0.0	$17,807.0
July	51,307.0	8,827.0	42,480.0	200.0	$19,608.0	$0.0	$0.0	$0.0	$0.0	$19,608.0
August	50,585.0	11,225.0	39,360.0	200.0	$18,631.0	$0.0	$0.0	$0.0	$0.0	$18,631.0
September	48,309.0	15,079.0	33,229.0	200.0	$16,581.0	$0.0	$0.0	$0.0	$0.0	$16,581.0
October	46,807.0	15,384.0	31,423.0	200.0	$15,850.0	$0.0	$0.0	$0.0	$0.0	$15,850.0
November	43,428.0	20,432.0	22,995.0	200.0	$12,994.0	$0.0	$0.0	$0.0	$0.0	$12,994.0
December	45,037.0	20,781.0	24,255.0	200.0	$13,589.0	$0.0	$0.0	$0.0	$0.0	$13,589.0
Annual	555,099.0	194,985.0	360,114.0	200.0	$184,487.0	$0.0	$0.0	$0.0	$0.0	$184,487.0

Table 23: Solar PV minigrids in Rwanda.

Minigrid	Capacity	Sites
RENERG	30.0 kW	1
Neseltec	30.0 kW	1
Meshpower	1.0 kW	69

life, the cash flows for both the current and proposed power systems were US$3,367,741.94 and US$2,525,806.45. Taking the areas under each cash flow curve, the total cumulative cash flows for both the current and proposed power systems were US$42,096,774.20 and US$42,459,673.40, respectively. The gross cumulative cash flows of the proposed power system were US$362,899.12 greater than those of the current grid system. That means the proposed power is preferable to the current power system in Rwanda.

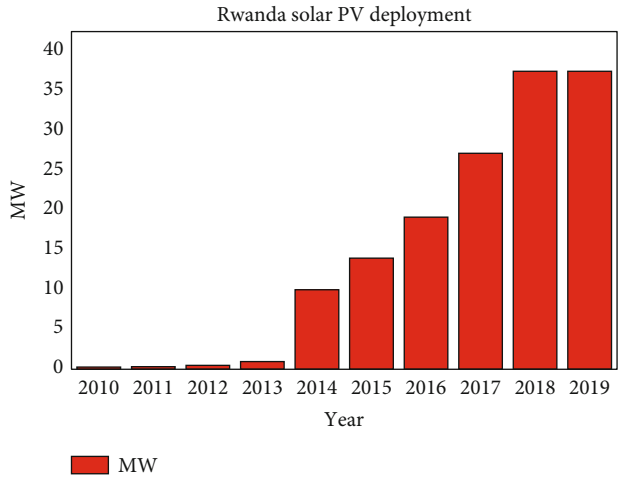

Figure 46: Solar PV trends in Rwanda by IRENA.

Table 24: Institutions involved in the energy sector in Rwanda.

Institution	Mandate	Ref
Rwanda Energy Group	National electric utility overseeing generation, transmission, and supply of electricity to consumers.	[67]
Ministry of Infrastructure (MINIFRA)	Responsible for the construction of national generation, transmission, and distribution infrastructure. Rural energy is part of this portfolio.	[68]
Rwanda's Utility Regulation Authority (RURA)	(i) Ensures set tools of regulation are in place and enforces them.	[66, 69]

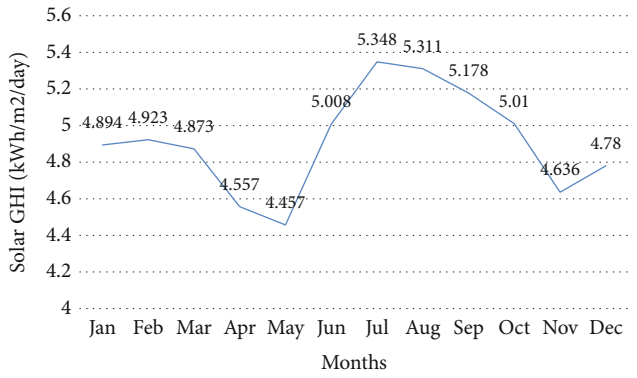

Figure 47: Monthly solar Global Horizontal Irradiation (GHI kWh/m^2/day) for Rwanda.

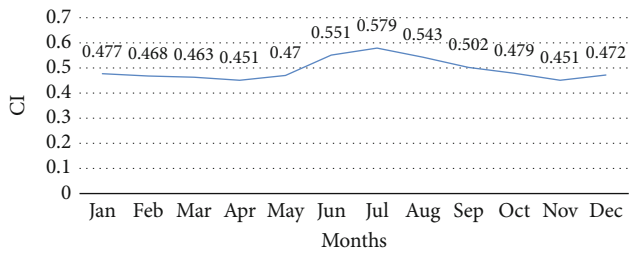

Figure 48: Monthly clearness index (CI) for Rwanda.

Figure 51 depicts the categorized annual savings for the proposed power system for Rwanda. The annual energy was about US$134,816.00, US$1,057.00 the operations and maintenance, while the annual energy cost savings were US$133,760.00, respectively.

Figure 52 shows the monthly utility bills for the current and proposed power systems for Rwanda. The January bills for both the current and proposed power systems were US$22,518.26 and US$11,259.26, respectively. The February bills for both the current and proposed power systems were US$20,296.30 and US$10,074.07, respectively. The March bills for both the current and proposed power systems were US$22,518.52 and US$11,259.26, respectively. The April bills for both the current and proposed power systems were US$21,777.78 and US$11,259.26, respectively. The May bills

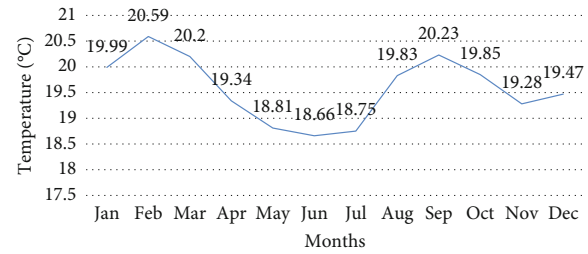

Figure 49: Monthly temperature variation (°C) for Rwanda.

for both the current and proposed power systems were US$22,518.52 and US$11,851.85, respectively. The June bills for both the current and proposed power systems were US$21,777.78 and US$10,222.22, respectively. The July bills for both the current and proposed power systems were US$22,518.52 and US$9,777.78, respectively. The August bills for both the current and proposed power systems were US$22,518.52 and US$10,074.07, respectively. The September bills for both the current and proposed power systems were US$21,777.78 and US$10,370.37, respectively. The October bills for both the current and proposed power systems were US$22,518.52 and US$10,814.82, respectively. The November bills for both the current and proposed power systems were US$21,777.78 and US$11,555.56, respectively. The December bills for both the current and proposed power systems were US$22,518.52 and US$11,555.56, respectively.

Table 25 depicts the annual utility bills and savings by category for Rwanda. The base case consumption charge was US$264,698.00, US$129,882.00 the proposed power system consumption charge, and US$134,816.00 the annual savings.

Figure 53 reflects the electrical production capacities for both the utility grid and the proposed solar PV microgrid power technology in Rwanda. The January electrical production capacities for both the current grid and proposed solar PV microgrid were 101.16 MWh and 47.60 MWh, respectively. The February electrical production capacities for both the current grid and proposed solar PV microgrid were 89.26 MWh and 43.64 MWh, respectively. The March electrical production capacities for both the current grid and proposed solar PV microgrid were 100.00 MWh and 48.00 MWh, respectively. The April electrical production capacities for both the current grid and proposed solar PV microgrid were 94.00 MWh and 44.00 MWh, respectively. The May electrical production capacities for both the current grid and proposed solar PV microgrid were 97.00 MWh and 44.60 MWh, respectively. The June electrical production capacities for both the current grid and proposed solar PV microgrid were 96.00 MWh and 49.00 MWh, respectively. The July electrical production capacities for both the current grid and proposed solar PV microgrid were 100.00 MWh and 54.00 MWh, respectively. The August electrical production capacities for both the current grid and proposed solar PV microgrid were 102.00 MWh and 54.00 MWh, respectively. The September electrical production capacities for both the current grid and proposed solar PV microgrid were 99.00 MWh and 50.00 MWh, respectively. The October

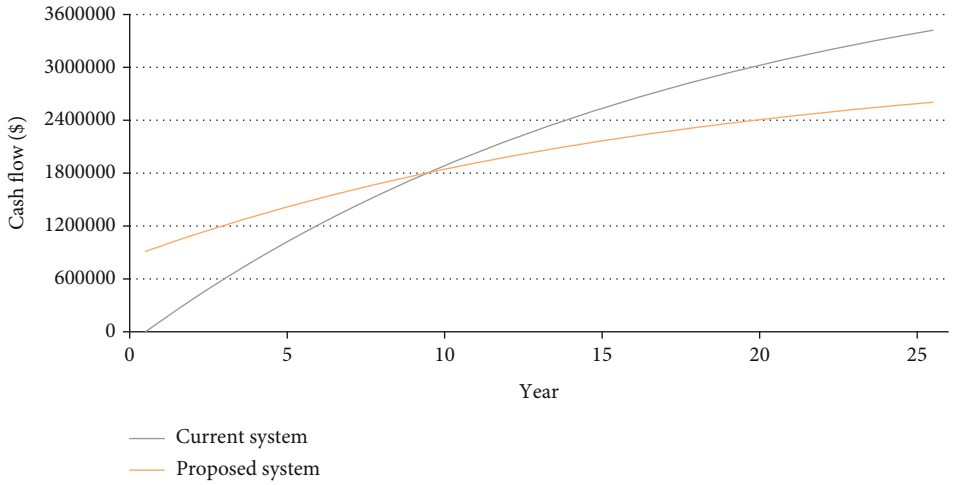

Figure 50: Cumulative cash flows over project lifetime for the current and proposed systems for Rwanda.

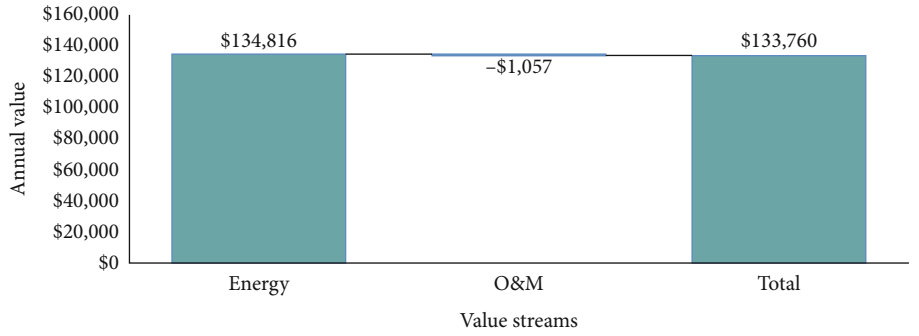

Figure 51: Categorized annual savings for the proposed system for Rwanda.

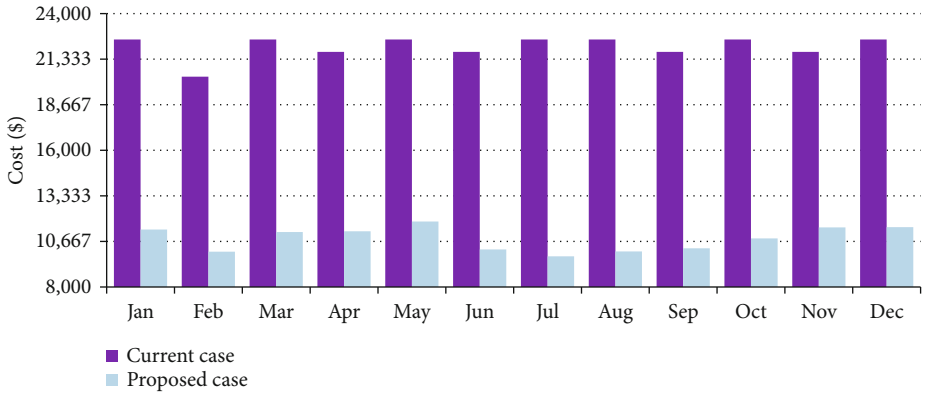

Figure 52: Monthly utility bills for the current and proposed systems for Rwanda.

Table 25: Annual utility bills and savings by category (Rwanda).

	Consumption charge	Total
Base case	$264,698.0	$264,698.0
Proposed case	$129,882.0	$129,882.0
Annual savings	$134,816.0	$134,816.0

Note: the base case is considered as the current system (grid connection) and the proposed power system is the grid-connected solar PV microgrid with storage.

electrical production capacities for both the current grid and proposed solar PV microgrid were 99.00 MWh and 50.00 MWh, respectively. The November electrical production capacities for both the current grid and proposed solar PV microgrid were 96.00 MWh and 44.00 MWh, respectively. The December electrical production capacities for both the current grid and proposed solar PV microgrid were 99.00 MWh and 47.00 MWh, respectively.

Additionally, the solar PV system has a nominal capacity of 400.0 kW, and its annual production is

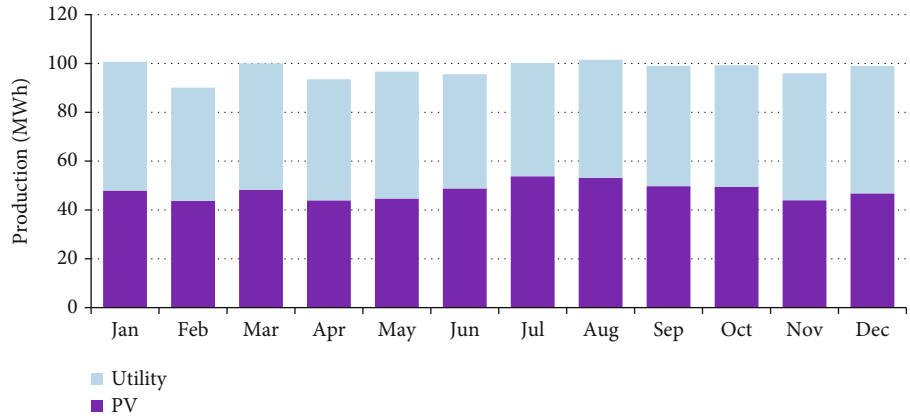

Figure 53: The electrical production for both utility and the solar PV microgrid for the proposed technology in Rwanda.

574217.0 kWh/year, and a specific yield of 1436.0 kWh/kW. Table 26 depicts the project cost details for every year over the 25 years project lifespan for Rwanda. The proposed solar PV power generation costs US$1,057.00 per annum while the current grid power system costs US$129,882.00 every year.

Table 27 is the monthly utility summary for the current grid power system in Rwanda. The energy purchase for January, March, May, July, August, October, and December was each 86,400.0 kWh, respectively. Although the 78,400.0 kWh was the energy purchase for February, 84,000.0 kWh was each of the energy purchases for April, June, September, and November, respectively. The annual energy purchase was 1,022,000.0 kWh, and the peak load was 200.0 kW throughout the year. There was no energy sold, and the annual energy charge was US$264,698.00. Also, each demand charge, fixed charge, minimum charge, and taxes were all zero, respectively.

Table 28 indicates the utility monthly summary for the proposed power system in Rwanda. The energy purchase for every month of the year was variable, and the total annual energy purchase was 597,309 kWh. While the energy sold also varied from one month to another, the annual energy sold was 149,526.0 kWh, and the annual net energy purchase was 444,783.0 kWh. The peak load was 200.0 kWp, and the annual energy charge was US$129,882.0. Also, the demand charge, fixed charge, minimum charge, and taxes were zero, respectively.

4.2. Overview of the Region. Hybrid renewable energy minigrid investment costs greatly fluctuate per kWp, depending on several key factors [27]. The diversity in investment costs and tariffs is due to several economic realities within the countries. Government subsidies, location of minigrids, competing for alternative energy sources, and purchasing power are among the factors that affect the cost of investment and cost of power. While a blended tariff structure is more realistic for most minigrid investments, the East Africa region mostly employs fixed tariffs. Kenya is leading with some of the highest investment costs per kWp ranging from US$ 5,100.0 to US$ 13,575.0 which translates into the most expensive tariffs for off-grid power. Uganda has the highest tariff at US$0.21 for grid-connected customers. Table 29 indicates minigrid investment costs in Uganda.

According to the IRENA, 245.5 MW of power is collectively being generated using the solar PV technology either by grids or stand-alone systems in the six East Africa countries. Kenya is currently treading its last-mile towards achieving complete electricity access initially intended for 2030. It is also considered exemplary in Sub-Saharan Africa in terms of electrification strategies [71]. Kenya is leading in installations and has the highest electrification rates at 84.5% in the region. However, 13 million people, the third-largest population in the region, are yet to be provided with electricity. High-profile government initiatives like the last-mile connectivity project, several PPP solar PV projects, international support, and successful innovations like the pay-as-you-go platform have yielded pronounced growth in electrification. Moreover, previous diesel minigrids are being transformed into diesel-solar minigrids, and the hybrid is also being replicated in rural areas [71].

Tanzania has the largest population without electricity at 36 million despite having a robust and established framework for minigrid regulation using the small power producer policy. It is third in the region with installations totaling 25.56 MW which is an estimated 0.02% of the total country's capacity. The quantity increases to 0.05% with the inclusion of solar hybrid systems. Tanzania's electrification rate is at 39.5 %, which could benefit more from solar electrification as it has a grid-tied solar PV potential of 800 MW which can cover approximately 20% of peak demand during daytime [48].

The policy framework in Rwanda is fairly developed, using their 2018 electrification strategy the country is working to provide electricity to its entire rural and urban population within six years unfolding the most ambitious plan in the region. The country has the second-highest electrification rates at 52.6%. Since 2007, a combination of utility reforms, voluntary suggestions, tenders, donor support, and favorable tax regimes has attracted private investors to Rwanda producing a total of 47 PPAs being signed by the year 2019. All IPPs currently participate through a competitive tendering process supervised by the Rwanda Utility Regulatory Authority (RURA) [49].

Table 26: Project cost details (both grid and PV system) for the whole project lifetime in Rwanda.

Year	1	2	3	4	5	6	7	8	9	10
PV	($1,057.0)	($1,057.0)	($1,057.0)	($1,057.0)	($1,057.0)	($1,057.0)	($1,057.0)	($1,057.0)	($1,057.0)	($1,057.0)
Rwanda grid	($129,882.0)	($129,882.0)	($129,882.0)	($129,882.0)	($129,882.0)	($129,882.0)	($129,882.0)	($129,882.0)	($129,882.0)	($129,882.0)
Year	11	12	13	14	15	16	17	18	19	20
PV	($1,057.0)	($1,057.0)	($1,057.0)	($1,057.0)	($1,057.0)	($1,057.0)	($1,057.0)	($1,057.0)	($1,057.0)	($1,057.0)
Rwanda grid	($129,882.0)	($129,882.0)	($129,882.0)	($129,882.0)	($129,882.0)	($129,882.0)	($129,882.0)	($129,882.0)	($129,882.0)	($129,882.0)
Year	21	22	23	24	25					
PV	($1,057.0)	($1,057.0)	($1,057.0)	($1,057.0)	($1,057.0)					
Rwanda grid	($129,882.0)	($129,882.0)	($129,882.0)	($129,882.0)	($129,882.0)					

Table 27: Utility monthly summary—current system (Rwanda).

Month	Energy purchased (kWh)	Energy sold (kWh)	Net energy purchased (kWh)	Peak load (kW)	Energy charge	Demand charge	Fixed charge	Minimum charge	Taxes	Total
January	86,800.0	0.0	86,800.0	200.0	$22,481.0	$0.0	$0.0	$0.0	$0.0	$22,481.0
February	78,400.0	0.0	78,400.0	200.0	$20,306.0	$0.0	$0.0	$0.0	$0.0	$20,306.0
March	86,800.0	0.0	86,800.0	200.0	$22,481.0	$0.0	$0.0	$0.0	$0.0	$22,481.0
April	84,000.0	0.0	84,000.0	200.0	$21,756.0	$0.0	$0.0	$0.0	$0.0	$21,756.0
May	86,800.0	0.0	86,800.0	200.0	$22,481.0	$0.0	$0.0	$0.0	$0.0	$22,481.0
June	84,000.0	0.0	84,000.0	200.0	$21,756.0	$0.0	$0.0	$0.0	$0.0	$21,756.0
July	86,800.0	0.0	86,800.0	200.0	$22,481.0	$0.0	$0.0	$0.0	$0.0	$22,481.0
August	86,800.0	0.0	86,800.0	200.0	$22,481.0	$0.0	$0.0	$0.0	$0.0	$22,481.0
September	84,000.0	0.0	84,000.0	200.0	$21,756.0	$0.0	$0.0	$0.0	$0.0	$21,756.0
October	86,800.0	0.0	86,800.0	200.0	$22,481.0	$0.0	$0.0	$0.0	$0.0	$22,481.0
November	84,000.0	0.0	84,000.0	200.0	$21,756.0	$0.0	$0.0	$0.0	$0.0	$21,756.0
December	86,800.0	0.0	86,800.0	200.0	$22,481.0	$0.0	$0.0	$0.0	$0.0	$22,481.0
Annual	1,022,000.0	0.0	1,022,000.0	200.0	$264,698.0	$0.0	$0.0	$0.0	$0.0	$264,698.0

Table 28: Utility monthly summary—proposed system (Rwanda).

Month	Energy purchased (kWh)	Energy sold (kWh)	Net energy purchased (kWh)	Peak load (kW)	Energy charge	Demand charge	Fixed charge	Minimum charge	Taxes	Total
January	52,735.0	13,851.0	38,884.0	200.0	$11,359.0	$0.0	$0.0	$0.0	$0.0	$11,359.0
February	46,366.0	11,719.0	34,646.0	200.0	$10,063.0	$0.0	$0.0	$0.0	$0.0	$10,063.0
March	51,789.0	13,245.0	38,544.0	200.0	$11,215.0	$0.0	$0.0	$0.0	$0.0	$11,215.0
April	49,548.0	9,497.0	40,051.0	200.0	$11,256.0	$0.0	$0.0	$0.0	$0.0	$11,256.0
May	52,010.0	9,883.0	42,128.0	200.0	$11,830.0	$0.0	$0.0	$0.0	$0.0	$11,830.0
June	46,791.0	11,587.0	35,204.0	200.0	$10,195.0	$0.0	$0.0	$0.0	$0.0	$10,195.0
July	46,363.0	13,353.0	33,010.0	200.0	$9,791.0	$0.0	$0.0	$0.0	$0.0	$9,791.0
August	48,355.0	14,699.0	33,657.0	200.0	$10,084.0	$0.0	$0.0	$0.0	$0.0	$10,084.0
September	49,253.0	15,026.0	34,227.0	200.0	$10,262.0	$0.0	$0.0	$0.0	$0.0	$10,262.0
October	49,836.0	12,459.0	37,377.0	200.0	$10,839.0	$0.0	$0.0	$0.0	$0.0	$10,839.0
November	52,030.0	11,997.0	40,033.0	200.0	$11,484.0	$0.0	$0.0	$0.0	$0.0	$11,484.0
December	52,232.0	12,210.0	40,022.0	200.0	$11,501.0	$0.0	$0.0	$0.0	$0.0	$11,501.0
Annual	597,309.0	149,526.0	447,783.0	200.0	$129,882.0	$0.0	$0.0	$0.0	$0.0	$129,882.0

Table 29: Minigrid investment costs.

Country	Cost per kWp in US$	Off-grid minigrid Tariff is US$/kWh	Grid-connected Tariff US$/kWh	Ref
Kenya	5,100.0-13,575.0	0.67-0.80	0.20	[27]
Uganda	-	0.30-0.50	0.085-0.21	[11, 19]
Tanzania	-	0.30-0.65	0.20	[70]
Rwanda	4,000.0-7,000.0	0.35-0.70		[59, 65]
Burundi	2,200.0			
South Sudan	-	0.41-1.00		

Notes: the use of the hyphen (-) does not mean a lack of cost but rather the information was unavailable.

Uganda has a policy with the aim of developing grid-compliant distribution infrastructure for minigrid projects, which effect has a value of approximately 30.0% of the total project cost. This feature while showing the robustness of the government's support, it has a risk of dragging the technology uptake if the government does not have the finances. It also has a measure of over complexity and inefficiency in some projects making it counterproductive. The country's electrification rate is at 28.9% with a population of 25 million people without access to electricity. While the minigrids are considered an opportunity for rural electrification, the country remains focused on grid extension. As of 2018, there were no PPA-eligible minigrids in Uganda [19].

Currently, Burundi and South Sudan are the lowest on electrification rates at 10.9% and 1.1% in that order. Solar PV minigrids are essentially donor-funded and are being

Table 30: Minigrid operation models in East Africa.

Model type	Description	Ref.
Independent Power Producer (IPP)	Minigrids manage the generation and sale of power to a national utility, the payment is made under a PPA. These minigrids are constructed using a PPP whereby he Government provides the land, electricity distribution assets, and other support structures through rural electrification authorities.	[29]
Distribution concession	This model gives allows the minigrid operators to do electricity distribution and supply. However, the minigrid can do generation or buy the electricity from elsewhere, i.e., from the national grid and retail to end-users. This arrangement has a definite period and specific location. The private company is therefore responsible for the distribution, supply, and revenue collection. However, in some cases, they also choose to do generation and transmission.	[25]
Electricity supply	The minigrid operator is in charge of distribution, supply, and revenue collection of power within a 50.0 kW capacity. These minigrids are usually movable and therefore can be relocated.	[31, 67, 72]
Multirevenue stream	This is based on the creation of power utilization density by supporting additional services that increase power consumption and increase revenues.	Field interview
Public model	Using this model, a national institution constructs and manages the generation, transmission, and distribution assets. Other national institutions, i.e., the national utility operates and maintains the assets while another institution develops regulation tools like tariffs and approves them.	[30]

Notes: PPP stands for public-private partnership. PPA stands for the power purchase agreement.

developed for demonstrational reasons and capacity building. Burundi is using the decentralized rural electrification strategy as a blueprint for electrification, although not comprehensive enough to attract significant investments for minigrid development. The strategy does not include specific objectives and does not have supportive policies to guide achievements. South Sudan is also yet to develop an inclusive electrification strategy. The two countries also struggle with old and frail transmission and distribution infrastructure, while in the case of South Sudan, there is no significant infrastructural backbone for either transmission or distribution. South Sudan's efforts are also undermined by the ramifications of a protracted period of civil war in the recent past. Therefore, it is at preparatory phases of generation, transmission, and distribution infrastructure as well as policy development. Overall, the region had a population of 100 million without access to electricity as of the end of 2019. This shows immense opportunity for solar PV minigrid deployment.

4.3. East African Minigrid Models. The operation models are currently not well defined yet in the African continent. Many models are at play but still, none has shown pronounced success. Models can be based on ownership, power output size, or even customer target. Some of the established owner-operator models include public utility, community or non-governmental organization (NGO), private, and hybrid such as a public-private partnership (PPP). The PPP has become outstanding in its potential for scale-up and currently has the most projects either planned [30] or in the development phase in the six East African Nations. Table 30 indicates minigrid operation models in East Africa.

4.4. Payment Methods. Solar PV energy in East Africa is evolving rapidly due to its ability to serve an assortment of consumers [73]. Minigrids are currently employing customized systems to monitor, control power supply, and collect revenues. Simple as well as sophisticated smart technologies are already being deployed to the convenience of minigrid operators. Smart technologies with features like remote monitoring, cloud control, and mobile payment functions [74]. The Pay-As-You-Go (PAYGO) model that originated in Kenya is being utilized by several companies in the East Africa region [75]. It solves the challenges of exchanging monies, collecting payments from remote customers, who often have irregular cash flow [76] with the inability to do one-off payments, therefore, employing piecemeal payments. Alternatively, public minigrids deploy prepayment meters, especially for grid connections. With the prevalence of cellular networks, mobile money transfer platforms like M-Pesa are popular in the region. Cloud-based remote systems have also been deployed for both metering and as payment platforms for some minigrid operators which monitor energy use and receive revenues due through mobile transfer. Postpaid metering is also employed by some utilities; this is common for public minigrids. As observed in Rwanda, newer minigrids are increasingly adopting smart technologies for operation, among the minigrids which were operational in Rwanda in early 2016, and none was known to make use of smart technologies in monitoring, control, or payment [77] while Kenya has been utilizing smart technologies through mobile platforms since 2009.

4.5. Barriers to the Minigrid Uptake and Opportunities

4.5.1. Policy and Regulations. The policy and regulations for minigrids are quite nomadic as governments are always incorporating new measures from the lessons gained internationally and locally. In East Africa, the policy and regulatory

framework are largely at experimental phases, in some countries, it is very unspecific or lacking in some countries like South Sudan and Burundi. While the other four countries have policies originally developed for traditional minigrids (generally run by IPPs, communities, and national utilities), third-generation minigrids are steadily increasing and therefore a need for the development of comprehensive policies and regulations covering tariffs, electrification plans, permits, and licenses among other relevant details.

4.5.2. Legal and Licensing Provisions. Securing the required permits and licenses can be a protracted, uncertain and costly process, at times exceeding 10.0% of the capital cost of a minigrid [78]. Clarity on regulatory requirements is necessary to ease entry into the minigrid market. Simplified and efficient regulatory requirements can significantly lessen development costs. Information on regulatory requirements should be easily accessible and in a single-window if possible (e.g., Tanzania's online information portal, minigrids.go.tz). Although all East African countries have some form of regulatory requirements to be fulfilled, the processes are not well streamlined with investors often being required to visit several organizations that mostly give contradictory or overlapping services. These loopholes create room for ambiguity in services to be offered and sometimes corruption.

4.5.3. Investment and Cost Recovery. Tariff as a tool has a critical impact on the viability and longevity of minigrids. Tariffs are set by the minigrid developers and approved by a relevant body or they could be set by an approved body. Tariffs affect project cash flows, operation, maintenance, and investment cost recovery. Prospects of cost recovery are diverse while private operators strive to recover full capital, operational, management, maintenance costs, and a commensurate margin of profitability, grant-financed minigrids do not need to cover fundamental capital costs. Some minigrids that are managed under the public-private partnership may not need to cover infrastructural costs like is the case of many planned and operational minigrids in Kenya and Uganda, respectively. A custom approach to tariff development is critical for catalyzing the growth of the minigrid sector. In Tanzania, developers of small-scale systems of up to 100.0 kW are allowed by the government to set tariffs in consultation with the communities being served and therefore exempted from tariff approvals. This allows project developers to try different tariff structures in a flexible regulatory space. However, the tariff structure in most East African countries is not as comprehensive as it should be to cover all the factors that are faced by minigrids operating in remote areas. The tariff structure is mostly based on the scale of power output and the type of energy resource supplying the minigrid. Several other critical parameters like the purchasing power of the locals, the cost of the investment, and the risk associated with the location are not fully covered.

4.5.4. Arrival of the Main Grid. The arrival of the central grid is a possibility that is ever-present. This can draw off power clients and strain the revenue flows. The risk is higher in the years before the full amortization of the investment. In East Africa, there is an absence of grid-extension plans in countries like South Sudan and Burundi. While the rest of the countries have some plans or drafts yet to be approved, the plans do not address the risk paused exhaustively, sometimes the plans are not adhered to or they are revised frequently. This makes it challenging to project the risk in the planning and development phase of minigrids which heightens the risk even further. In the event of the minigrid arrival, due to a lacking regulatory framework, the government may impound minigrid assets with insignificant reparation, or in the worst case, the investments can be left without recourse.

4.5.5. Facilitation and Access to Finance. Accessing affordable financing is not easy; it is one of the major barriers to the development of minigrids. An assortment of financing mechanisms and creative operation models are necessary for increasing investments. Nearly all minigrids are financed through a mix of finances from subsidies and donations, commercial equity, and rarely loans [79]. Although most minigrids get funding from grants, this kind of funding has high transaction costs and experience significant delays in disbursement, which in turn strain cash flow for developers, most of whom require equity investment to build pilot projects and establish their operation models. Many commercial investors and potential funding partners are discouraged by the lack of a proven, successful model in the sector and the disproportionate returns commonly experienced. Currently, Uganda, Kenya, Rwanda, and Tanzania governments are offering support through conducting feasibility studies for identifying potential minigrid sites. Uganda has a policy with a supportive feature of developing grid-compliant distribution infrastructure for minigrid projects, which effect has a value of approximately 30.0% of the total project cost. Most of the monies being used for these services are sourced from international donors and development financial institutions. South Sudan has no functional transmission grid, Burundi has an old grid that needs to be upgraded, and these auxiliary assets need substantial financing for development as they are critical in minigrid development.

5. Concluding Remarks

The solar PV minigrid uptake in East Africa is still in the formative stages. The most advanced countries have laid down electrification blueprints apportioning the intended use of available natural energy resources and developed supportive measures on how to achieve the plans. Government support in terms of policy and initiatives in Kenya, Rwanda, and Tanzania has been critical in attracting significant funding for rural electrification as well as private investments. For further growth, adherence to policy and regulation, clearing ambiguities in regulations, and adoption of blended tariffs will ease market entry and secure more gains for the sector. In Uganda, while the government is willing to support minigrid deployment, it also has strong indicators focusing on central grid extension. This is a major hurdle for the growth of minigrids. Burundi and South Sudan are yet to define their strategies and develop a functional transmission and distribution

network to attract significant solar PV investors. Generally, government initiatives are fundamental for spurring minigrid uptake, refining operation models to enhance sustainability and adequate margins is also critical before scaling up. Funding from international and national organizations will still be required in the future. Innovative measures like hybridizing old fossil fuel IPPs and power demand creation by minigrids as well as the PPP modeling of minigrids are critical for the sustainability of the minigrids.

The grid-connected solar PV minigrid and its storage applied to critical loads such as industrial and commercial loads used simulations from HOMER software to reveal that it can still contribute to affordable electricity through peak shaving, except for Tanzania because Tanzania electricity tariff is low and serving a big critical load (commercial and industrial) would have no affordability impact on the electricity tariff. For the other five member countries of the EAC, the peak shaving strategy through a solar PV minigrid and its storage reveals that it would decrease the electricity tariff (LCOE) to US$0.196/kWh for Burundi, US$0.151/kWh for Kenya, US$0.172/kWh for Rwanda, US$0.210/kWh for South Sudan, and US$0.140/kWh for Uganda, which are much lower than the real electricity tariffs currently in use in these countries. Future studies can be considered for the feasibility of solar PV minigrids with residential loads which are not critical like industrial and commercial loads; and feasibility studies of solar PV minigrids with off-grid large scale loads (locations where the grid option is not possible). The concepts and results in this paper would be useful to power systems designers, scholars, and policy-makers in East Africa and other parts of the world with similar energy crises.

Data Availability

The data used to support the findings of this study are available from the submitting author upon request.

Conflicts of Interest

The authors declare no conflicts of interest.

Acknowledgments

The authors are grateful to Hebei Social Science Foundation major project "Hebei Province Regional Innovation-Driven Development Mechanism Construction in the New Era" (HB19ZD03), Hebei Province Innovation Capacity Enhancement Project: Research on Hebei Province Regional Innovation System Construction under the Background of Beijing-Tianjin-Hebei Coordinated Development (19457678D), Innovation Strategy Funded project by The Department of Science and Technology of Hebei Province: Research on the Innovative Development Mode of Characteristic Industry in Handan City (20180403), and Hebei Provincial Department of Education Humanities and Social Science Research Major Project "Research on Hebei Province's High-quality Development Mechanism Leaded by Innovative Ecosystem Development" (ZD202004).

References

[1] I. P. Da Silva, G. Ronoh, and J. Ndegwa, "Energy performance of off-grid connected solar PV systems in Kenya-case study," 2013.

[2] Bloomberg, "Lighting global,Bloomberg new energy finance, global off-grid solar market trends," 2016.

[3] World Bank, *Bringing home solar systems to off-grid communities*, World Bank (WB), 2017, http://www.innovationpolicyplatform.org/.

[4] IEA, I, UNSD, World Bank, and World Health Organization, *Tracking SDG 7*, The Energy Progress Report 2019, Washington DC, 2019.

[5] IEA, I, UN, WB, and WHO, "TRACKING SDG 7," *The Energy Progress Report*, The World Bank (WB),World Health Organisation(WHO), Washington DC, IEA, IRENA,United Nations Statistics Division (UN), 2020.

[6] A. K. Aschalew Tigabu, F. H. Wandera, R. Hanlin, M. H. Andersen, and R. Lema, *Capability development and collaboration for Kenya's solar and wind technologies: analysis of major energy policy frameworks*, Innovation and Renewable Electrification in Kenya (IREK), Copenhagen/Nairobi/Eldoret, 2017.

[7] UN, "Transforming our world: rhe 2030 agenda for sustainable development," in *Resolution adopted by the general assembly on 25th December 2015*, United Nations, New York, USA, 2015.

[8] M. B. Pedersen, "Deconstructing the concept of renewable energy -based mini-grids for rural electrification in East Africa," *Energy and Environment*, vol. 5, no. 5, pp. 570–587, 2016.

[9] V. C. K. Kennedy Fohoue-Tchendjou, D. Tieudjo, and L. Bitjoka, "Management of hybrid renewable energy systems using differential hybrid Petri nets," *TECHNIUM*, vol. 2, no. 7, pp. 64–76, 2009.

[10] SEforALL, "State of the global mini-grids market 2020," in *Trends of renewable energy hybrids mini-grids in Sub-saharan Africa, Asia and island nations*, Sustainable Energy for All, 2020.

[11] N. Bloomberg, "State of the minigrid market report 2020," in *trends of renewable energy hybrid mini-grids in Sub-Saharan Africa, Asia and island nations*, Sustainable Energy for All, Mini-Grids Partnership (MGP), Bloomberg NEF, 2020.

[12] H. E. M. Rana Adib, F. Appavou, A. Brown, B. Epp, and C. Lins, *Renewable energy policy network for the 21st century (REN21)*, Renewables 2016 Global Status Report, 2016.

[13] D. M. K. David Mozersky, *South Sudan's renewable energy potential:a building block for peace*, United States Institute of Peace, Washington DC, 2018.

[14] SOLARGIS, "Download solar resource maps and GIS data for 200+ countries," 2020, https://solargis.com/maps-and-gis-data/download/south-sudan/.

[15] RESP, *Market Information*, Africa–EU Renewable Energy Cooperation Programme, Uganda, 2018.

[16] European Union, "10 MW EU funded Tororo Solar Power Plant Opens; Delegation of the European Union to Uganda," 2017, https://eeas.europa.eu/delegations/uganda/34013/10-mw-eu-funded-tororo-solar-power-plant-opens_en/.

[17] Government of Uganda, "Kabulasoke Solar Power Station to be ready in November," 2018, http://vicepresident.go.ug/index.php/vp-news/291-kabulasoke-solar-power-station-tobe-ready-in-november/.

[18] Tryba Energy, "The construction of a 10MWP solar power plant in Uganda is moving ahead rapidly," 2018, http://vicepresident.go.ug/index.php/vp-newswww.tryba-energy.com/en/2018/03/30/construction-of-a-10-mwpsolar-power-plant-in-uganda-is-moving-ahead-rapidly-it-will-be-connected-to-the-grid-and-operational-at-the-endof-the-year//291-kabulasoke-solar-power-station-tobe-ready-in-november/.

[19] W. H. Jon Lane, A. Gous, and R. Kuteesa, "Mini-grid market opportunity assessment:Uganda," 2018.

[20] REA, "Rural electrification agency," 2020, http://www.rea.or.ug/.

[21] EPRA, 2020, https://www.epra.go.ke/.

[22] IEA, *SDG7: data and projections,access to affordable, reliable, sustainable and modern energy for all*, International Energy Agency (IEA), 2020.

[23] REA, "Rural Electrification Strategy and Plan (RESP)," 2013, http://www.rea.or.ug/resources/strategy%20and%20plan%202013-2022.pdf.

[24] K. Lee, E. Brewer, C. Christiano et al., "Electrification for "Under Grid" households in Rural Kenya," *Development Engineering*, vol. 1, pp. 26–35, 2016.

[25] ESMAP, *Mini Grids in Kenya. A Case Study of a Market at a Turning Point*, Energy Sector Management Assistance Program, 2017.

[26] International Renewable Energy Agency: IRENA, 2020, https://www.irena.org/solar/.

[27] I. P. Da Silva, G. Batte, J. Ondraczek, G. Ronoh, and C. A. Ouma, *Diffusion of solar energy technologies in rural Africa*, Durban, South Africa, 2014.

[28] Strathmore University, "Strathmore University and Kenya power sign solar energy purchase deal," 2015, https://www.strathmore.edu/news/strathmore-university-and-kenya-power-sign-solar-energy-purchase-deal/.

[29] GoK, "Kenya National Electrification Strategy," p. 38, 2018.

[30] Rea KP, "Kenya Off-Grid Solar Access Project (K-OSAP)," in *Rural Electrification Authority (REA)*, Kenya Power, 2017.

[31] USAID, *Off-Grid Solar Market Assessment Kenya*, USAID, 2019.

[32] MoE, 2020, http://energy.go.ke/.

[33] KenGen, 2020, http://www.kengen.co.ke/.

[34] Kenya Power, 2020, http://www.kengen.co.ke//https://www.kplc.co.ke/.

[35] REREC, 2020, http://www.rerec.co.ke/.

[36] GoK, "The energy bill, 2015," in *Kenya Gazette Supplement No. 134 (National Assembly Bills No. 50)*, Government of Kenya, 2015.

[37] GoK, "The energy (electricity licensing) regulations, 2012," 2012, https://www.epra.go.ke/download/the-energy-energy-management-regulations-2012/.

[38] E. S. Lily Odarno, M. Swai, M. J. J. Katyega, and A. Lee, *Accelerating minigrid deployment in sub-Saharan Africa lessons from Tanzania, TATEDO*, World Resources Institute, 2017.

[39] Government of Tanzania, "Ministry of energy," 2020, https://www.nishati.go.tz/en/.

[40] Government of Tanzania, "Report: Tanzania mini-grid sector doubles with bold policy approach," 2017.

[41] J. M. Takouleu, *Tanzania: CBEA finances PowerGen to provide 60 solar mini-grids*, Afrik21, 2019.

[42] TANESCO, "TANESCO," 2020, http://www.tanesco.co.tz/.

[43] REA, "Rural Energy Agency (REA)," 2020, http://www.rea.go.tz/.

[44] Government of Tanzania, "The Rural Energy Act," p. 2005, 2005.

[45] IRENA, *Renewables Readiness Assessment*, International Renewable Energy Agency (IRENA), United Republic of Tanzania, 2017.

[46] Government of Tanzania, "The electricity (development of small power projects) rules, 2016. Electricity ACT (CAP 131)," 2016.

[47] J. Barba, *The electricity sector in Burundi: a place for renewable energy in the great lakes region?*, T. E. Platform, 2018.

[48] S. T. Manfred Hafner, G. Falchetta, and G. Occhiali, *Country-level analysis: power sector, energy resources, and policy context*, Springer, 2019.

[49] UNEP, "Energy profile: Burundi," 2017, https://wedocs.unep.org/handle/20.500.11822/20486/.

[50] R. Burundi, "Agence Burundaise De D'electrification Rurale (ABER)," 2020, http://www.aber.bi/indexE.php/.

[51] REEEP, "Burundi (2012)," 2012, https://www.reeep.org/burundi-2012/.

[52] REPP, "MUBUGA; 8.67MWp solar PV power plant," 2020, https://repp.energy/project/mubuga-burundi/.

[53] World Bank, "Solar energy in local communities," 2020, https://projects.worldbank.org/en/projects-operations/project-detail/P164435/.

[54] SEforALL, *The Republic of South Sudan*, Rapid Situation Assessment and Gap Analysis Report, 2013.

[55] African Development Bank, A, "Provision for electricity and rural energy," 2013.

[56] D. Ghandour, "Struggles for electric power supply in Sudan and South Sudan," in *Fifth International Conference On Advances in Economics, Management and Social Study - EMS 2016*, Kuala Lumpur, Malaysia, March 2016.

[57] UNEP, "Energy profile: South Sudan," 2017, https://wedocs.unep.org/handle/20.500.11822/20597/.

[58] E. Bellini, "South Sudan to get 20 MW/35 MWh solar-plus-storage plant. pv magazine," 2019.

[59] S. L. Selen Kesrelioglu, Y. Ingabire, W. Rubasharaza, and I. Troconis, *Rwanda Off-Grid Status Report 2018*, Energising Development Rwanda, 2018.

[60] RWANDA RO, *Rural Electrification Strategy*, M. o. Infrastructure, 2016.

[61] Rwanda Energy Group, R, "Off Grid Electricity Access Expansion Programs in Rwanda," 2019.

[62] S. Bimenyimana, G. N. O. Asemota, and L. Li, "The state of the power sector in Rwanda:a progressive sector with ambitious targets," *Frontiers in Energy Research*, vol. 6, no. 68, 2018.

[63] G. Adwek, S. Boxiong, P. O. Ndolo et al., "The solar energy access in Kenya: a review focusing on Pay-As-You-Go solar home system," *Environment, Development and Sustainability*, vol. 22, no. 5, pp. 3897–3938, 2020.

[64] C. N. Dominic Samoita, P. A. Østergaard, and A. Remmen, "Barriers and solutions for increasing the integration of solar photovoltaic in Kenya's electricity mix," *energies*, vol. 13, no. 5502, 2020.

[65] S. Kesrelioglu, *Rwanda Off-Grid Sector Status Report 2017*, Energising Development Rwanda, 2018.

[66] Republic of Rwanda, "Regulation no. 03/R/EL-EWS/-RURA/2019 governing the simplified electricity licensing framework for rural electrification in Rwanda," 2019.

[67] USAID, *Off-Grid Solar Market Assessment Rwanda*, USAID, Power Africa, 2019.

[68] A. S. Paul Kirai and M. Hankins, *Target Market Analysis*, The Solar Energy Market in Rwanda. D. G. f. technisque, 2009.

[69] RURA, "Rwanda Utilities Regulatory Authority (RURA)," 2020, https://rura.rw/index.php?id=45/.

[70] D. C. Mary Willcox, "NAE Case Study: Tanzania, Mini-Grids Regulatory Framework," 2018, https://energypedia.info/wiki/NAE_Case_Study:_Tanzania,_Mini-Grids_Regulatory_Framework/.

[71] E. Gordon, "The Politics of Renewable Energy in East Africa," 2018.

[72] USAID, *Off-Grid Solar Market Assessment Tanzania*, USAID, Power Africa, 2019.

[73] EnDev, *Rwanda: Off-Grid Sector Status 2016. Achievements in 2016 and trends for 2017*, Energising Develpment (EnDev)Rwanda, 2017.

[74] ECA, *Project Design Study on the Renewable Energy Development for Off-Grid Power Supply in Rural Regions of Kenya*, Economic Consulting Associates', 2014.

[75] EEP, *Solar PV Business Models in East Africa:Lessons Learnt from EEP Supported Projects*, Energy and Environment Partnership/Southern and East Africa, 2016.

[76] A. George, S. Boxiong, M. Arowo, P. Ndolo, Chepsaigutt-Chebet, and J. Shimmon, "Review of solar energy development in Kenya: opportunities and challenges," *Renewable Energy Focus*, vol. 29, pp. 123–140, 2019.

[77] Practical Action, *Real-time monitoring, control and payment technology for mini-grids*, Rwanda field test evaluation report, 2017.

[78] IRENA, "Policies and Regulations for Private Sector Renewable Energy Mini-Grids," 2016.

[79] S. AfDB, "Green Mini-Grids Market Development Programme," 2016.

Hindawi
International Journal of Photoenergy
Volume 2021, Article ID 6612222, 11 pages
https://doi.org/10.1155/2021/6612222

Research Article

Impacts of Ground Slope on Main Performance Figures of Solar Chimney Power Plants: A Comprehensive CFD Research with Experimental Validation

Erdem Cuce,[1,2] **Pinar Mert Cuce**,[2,3] **Harun Sen**,[1,2] **K. Sudhakar**,[4,5,6] **Umberto Berardi**,[7] **and Ugur Serencam**[8]

[1]*Department of Mechanical Engineering, Faculty of Engineering and Architecture, Recep Tayyip Erdogan University, Zihni Derin Campus, 53100 Rize, Turkey*
[2]*Low/Zero Carbon Energy Technologies Laboratory, Faculty of Engineering and Architecture, Recep Tayyip Erdogan University, Zihni Derin Campus, 53100 Rize, Turkey*
[3]*Department of Energy Systems Engineering, Faculty of Engineering and Architecture, Recep Tayyip Erdogan University, Zihni Derin Campus, 53100 Rize, Turkey*
[4]*Faculty of Mechanical and Automobile Engineering Technology, Universiti Malaysia Pahang, 26600, Malaysia*
[5]*Energy Centre, Maulana Azad National Institute of Technology Bhopal, India*
[6]*Department of Electric stations, Grids and Power Supply Systems, South Ural State University, Chelyabinsk, Russian Federation, India*
[7]*Department of Architectural Science, Ryerson University, Toronto, ON, Canada M5B 2K*
[8]*Department of Civil Engineering, Faculty of Engineering Marmara University, 34722 Istanbul, Turkey*

Correspondence should be addressed to Erdem Cuce; erdemcuce@gmail.com

Received 8 November 2020; Revised 8 May 2021; Accepted 14 May 2021; Published 24 May 2021

Academic Editor: Alberto Álvarez-Gallegos

Copyright © 2021 Erdem Cuce et al. This is an open access article distributed under the Creative Commons Attribution License, which permits unrestricted use, distribution, and reproduction in any medium, provided the original work is properly cited.

Geometric parameters in solar chimney power plants are numerically optimised for the purpose of better power output figures. Several parameters have been investigated in the pilot plant such as chimney height and diameter, collector diameter and slope, and slenderness. However, ground slope has not been studied to date despite its perspicuous impact on turbulent flow. In this study, the impacts of the different slope angles of the ground, where the solar radiation is absorbed through the collector, on the main performance parameters of the system are numerically analysed through a reliable CFD software ANSYS FLUENT. By considering the actual geometric figures of the pilot plant, a 3D model is constructed through DO (discrete ordinates) solar ray tracing algorithm and RNG k-ε turbulence model. For the solar intensity of 1000 W/m^2, the maximum velocity inside the system is found to be 14.2 m/s, which is in good accordance with the experimental data of 15.0 m/s. Starting from 5 m inside the collector, the chimney inlet heights are reconfigured 0.209, 0.419, 0.625, 0.838, and 1.04 m, respectively, and when the ground slope is 0.1, 0.2, 0.3, 0.4, and 0.5°, the changes in the performance output of the system are investigated. For the reference case which refers to the horizontal ground, the maximum air velocity is determined to be 14.2 m/s and the power output is 54.3 kW. However, when the ground slope is made 0.5°, it is observed that the maximum velocity increases by 37% to 19.51 m/s, and the power output is enhanced to 63.95 kW with a rise of 17.7%. Sloping ground is found a key solution to improve the turbulent effects inside the plant, thus to enhance the electrical power output.

1. Introduction

The dramatic rise in energy consumption figures is inevitable in today's world with outstanding technological developments and notably increasing human population. The increase in energy use has led to more discussion of CO_2 emissions and environmental pollution than ever before, especially because of the higher consumption of primary

energy resources. Increasing tendency to renewable energy sources for energy production has become a joint work of researchers in recent years. Considering the diversity of renewable energy sources as well as their efficiency and accessibility, it can be easily asserted that the sun is in the most popular position. Although the use of solar energy goes back to ancient times, its use for electricity generation has become widespread in recent years. Solar chimney power plants attracted the attention of researchers with the first prototype, Manzanares, in the late 1900s. Although not physically complex, the system consists of three main structural elements such as collector, chimney, and turbine [1]. The collector directly exposed to the solar radiation creates a dynamic system air at the bottom and provides the transmission of the solar radiation it receives to the ground. The temperature of the air in the dynamic system increases with the solar radiation passing through the collector. Solar radiation reaching the ground causes an increase in temperature here and thus heat transfer takes place from the ground to the system air. This heat transfer yields to an increase in the temperature of the system air as a consequence of the developed upward movement. The system air starting to move upwards is pulled up from the chimney by the vacuum effect at the chimney inlet. The chimney creates a pressure difference due to its height [2]. In the meantime, the kinetic energy of the system air is converted into electrical energy with the turbine at a certain height. In the experiments with the first prototype, 55 kW power output and 15 m/s maximum air velocity are determined [3]. With the experimental data obtained from the first prototype, numerous theoretical and mathematical models on solar chimney power plants are produced. When the studies are examined, it is seen that the researchers analyse the performance parameters of the system in different climatic, environmental, and operational conditions. Dhahri et al. [4] report that the change in radiation intensity affects the airflow rate and temperature increase in the system, and the air velocity, which is 8.8 m/s at 300 W/m^2, increases by 50% at 900 W/m^2 and rises to 13.8 m/s. Similarly, Esfinadi et al. [5] verify that the solar intensity increases the airflow rate in the system. Abdelmohimen and Algarni [6] state that any increase in radiation intensity yields to an increase in the airflow rate and the power output of the system. They claim that the system with 400 W/m^2 radiation intensity gives a maximum air velocity of 6 m/s and a power output of 25 kW. When the radiation intensity is 800 W/m^2, the airflow rate is enhanced by about 30% and the power output rises by 88% to 47 kW.

Solar chimney power plants are significantly affected by environmental factors. Initial temperature and solar radiation intensity are the most important environmental parameters affecting the power output of the system. Other parameters that affect the system performance are geometric and design parameters. Environmental effects cannot be predicted precisely, but the effect of geometric parameters can be analysed in advance with theoretical and numerical studies. It is clear that increasing the collector radius will increase the performance of solar chimney power plants as it will allow the solar radiation to penetrate a greater area. Referring to the Manzanares pilot plant, researchers argue that changing the collector radius affects the power output and efficiency of the system. Li et al. [7] claim that the Manzanares pilot plant will give 53.5 kW power output at 122 m collector radius, and when the collector radius is made 244 m, the power output will increase by 120% to approximately 118 kW, but the power output of the system will not increase after 500 m collector radius. Esfinadi et al. [5] argue that increasing the collector radius of the Manzanares pilot plant will increase the power output of the system while reducing its efficiency. Increasing the height of the chimney in solar chimney power plants has a positive effect on the power output by increasing the flow rate of the system air at the chimney inlet [8]. Researchers state that increasing the chimney height of the Manzanares pilot plant will increase its power output and efficiency [9]. The effect of geometric parameters is analysed not only with the geometric dimensions of the Manzanares pilot plant but also with SCPP systems created by some researchers in different dimensional characteristics. Toghraie et al. [10] develop a SCPP system with 100 m chimney height, 100 m collector radius, 4 m chimney radius, and 2 m collector height. They use the standard k-ε turbulence model, suggesting that the flow within the system is turbulent so viscous effects can be neglected. They claim through the CFD solutions which they repeat at 600 and 800 W/m^2 solar intensities that increasing the chimney height will increase the power output and efficiency of the system while increasing the collector radius will increase the power output and decrease the efficiency. Similarly, by designing large-scale systems, researchers predict the performance of systems with different chimney heights and collector radius [11, 12]. In SCPP systems, the floor plays an important role in energy storage and directing the heated air. Attig-Bahar et al. [13] compare the performance of the SCPP system to be installed in the south of Tunisia with the data obtained without energy storage by analysing the effect of using different energy storage materials on the ground. In the study, which takes the pilot plant in Manzanares as a reference, it is proved that when sand, soil, and gravel materials are used for energy storage on the ground, 35% more power output can be obtained compared to the reference case. Sedighi et al. [14] analyse the effect of the porosity of the soil to be used as an energy storage unit on the performance of the system. He stated that soil porosity is inversely proportional to the yield and output power of the SCPP. They claim that by decreasing the porosity of the soil from 0.4 to 0.1, the system efficiency and the power output of the turbine increase by 3.04%. Fadaei et al. [15] conduct an experimental study to examine the effect of the use of phase change material (PCM) on the performance of SCPPs. In the experimental setup with 3 m chimney height and 3 m collector diameter, while the air velocity with the traditional solar chimney is 1.9 m/s, when the PCM is used on the ground, the airflow rate increases by 8.33% and reaches 2 m/s. Larbi et al. [16] evaluate the impacts of several parameters on the system performance through a mathematical model by referencing the geometric dimensions of the Manzanares pilot plant. They consider different thicknesses of the water layer on the ground for the purpose of energy storage. They claim that 5 cm of water thickness is ideal for energy storage performance, and in July, the power output reaches

120 kW in this case. Yaswanthkumar and Chandramohan [17] analyse the effect of energy storage unit (TES) on the performance of SCPPs with the 3D CFD model. They study a system with a collector diameter of 3.5 m and a chimney height of 6 m which has a collector entrance height of 0.15 m. They evaluate the performance changes in the system by integrating a 0.15 m thick energy storage unit with 3.5 m diameter into this design. It is reported that the air velocity in the system 6.17 m/s to 3.9 m/s according to the reference situation since TES absorbs some of the energy during the daytime hours. Senbeto [18] examines the effect of TES on the performance of SCPP systems with the CFD model. The standard RNG k-ε turbulence model and Boussinesq approximation consider the lifting effects in the model. In his work, which takes the Manzanares prototype as a reference, he claims that the air velocity of the system without a turbine will be 16.5 m/s at the chimney inlet for the solar radiation of 1000 W/m^2. It is stated that the power output of the system decreases by approximately 50% during the sunshine hours due to the energy storage by the water layer. However, the stored energy becomes active after sunset, and the daily power productivity is found to be higher than the reference case. Kalash et al. [19] experimentally investigate the performance of the system with the solar chimney they set up on a sloping ground at Damascus University in Syria. They place the 9 m high chimney about 3 m above the ground. They place a 6.04 m long collector with 3.68 m inlet width and 0.65 m outlet width on the sloping ground and connect it with the chimney. They claim that the system yields a temperature increase of 19°C in the collector even in winter months and 2.9 m/s upward air velocity is measured in the chimney. Bilgen and Rheault [20] make geometric dimensioning for a fixed 950000 m^2 collector area and 54 m chimney diameter for 3 different locations to generate 5 MW power at high latitudes. They state through the annual simulations that the increase in ground inclination angle in different locations will reflect positively on the system. They claim that the chimney height, which is 123 m for 5 MW power output in the Ottawa location with a ground slope of 38.40°, can be achieved in Edmonton with a ground slope of 48.40° and a chimney height of 35 m. Cao et al. [21] evaluate the performance of a SCPP system likely to be used on the sloping mountain in Lanzhou climate conditions. Geometric characteristics of the Manzanares pilot plant are adopted in the numerical model. In the simulations carried out for 12 months, they state that the power output for the horizontal ground reaches its highest value in June and will be approximately 60 kW. They claim that the year-round power output will not fall below 80 kW on sloping ground and will exceed 100 kW in March. Sivalakshmi et al. [22] carry out an experimental study for solar chimneys. Their research compares the performance of the absorber plate for the cases of being dimpled or flat. Thermal performance comparisons are done according to air temperature, air velocity at the chimney outlet, and heat transfer coefficient. When the experimental results are compared, it is observed that the heat transfer coefficient of the system with dimpled absorber plate in the sunny midday is 13.55% higher than the system with a flat absorber plate. It is claimed that a similar situation is observed in the air temperature at the chimney outlet. Similar to the ground, the collector slope also affects the performance of the system. Cuce [23] analyses the effect of the collector slope on the system performance, which takes the geometry of the Manzanares pilot plant as a reference. It emphasises that the power output of 54.5 kW without slope will increase by 4.5% (to approximately 57 kW) when the angle of inclination of the collector is 2°. Different nanoparticles are also utilised in SCPP systems to enhance energy storage performance on the ground. Some researchers claim that the nanoparticle density improves heat transfer in certain situations. It is reported that an increase in Reynolds number in closed loop systems improves heat transfer by increasing the Nusselt number [24, 25].

Although different designs of SCPP systems are available in literature, the impacts of the ground slope on the main performance parameters have not been evaluated to date by researchers. Therefore, the goal of this research is to conduct an elaborative numerical analysis with experimental validation in order to study the aforesaid impact in detail. By considering the slope of the collector constant, the influence of the linear rise of the ground from 5 m inside the collector inlet to the chimney entrance on mass flow rate, power output, dynamic pressure difference, and efficiency is comprehensively examined. DO solar ray tracing algorithm and RNG k-ε turbulence model are applied simultaneously to the 3D symmetric CFD model. Simulations are repeated for different ground angles, following the mesh-independent solution, based on the solar radiation intensity of 1000 W/m^2 and the ambient temperature of 293.15 K as climatic conditions. Climatic parameters are selected according to the literature data. For instance, when the test results obtained by Haaf [3] from the Manzanares pilot plant are examined, it is seen that the maximum solar radiation during the day is 1000 W/m^2 and the air temperature is around 20°.

2. Governing Equations

Based on the geometric dimensions of the pilot plant, the first application of solar chimney power plants, the effects of ground entrance and ground slope on the system are examined in SCPP systems, provided that the chimney entrance height is constant. By keeping the environmental conditions constant in all CFD solutions, by solving the continuity, momentum, energy, and turbulence equations in parallel, the graphs of mass flow rate, dynamic pressure difference around the turbine, and power output are obtained separately in different designs. The following assumptions are made for simplicity and time-saving in the analyses:

(1) System air is considered incompressible

(2) Flow regime is constant, 3D, and turbulent

(3) Environmental conditions are considered constant in all simulations

(4) Boussinesq model is accepted for density

The conservation equations solved by ANSYS FLUENT are as follows [26]:

(a) Continuity equation

$$\nabla.\left(\rho.\vec{v}\right) = 0. \tag{1}$$

(b) Momentum equation

$$\nabla\left(\rho.\vec{v}.\vec{v}\right) = -\nabla p + .\left(\mu\left[\left(\nabla\vec{v}+\nabla\vec{v}^{T}\right) - \frac{2}{3}\nabla.\vec{v}I\right]\right) + \rho\left\{\vec{g}\right\}. \tag{2}$$

(c) Energy equation

$$\nabla.\left(\vec{v}(\rho E + p)\right) = \nabla.\left(k_{\text{eff}}\nabla T - h\vec{j} + \left(\mu\left[\left(\nabla\vec{v}+\nabla\vec{v}^{T}\right) - \frac{2}{3}\nabla.\vec{vI}\right].\vec{v}\right)\right). \tag{3}$$

Since there is no forced flow source in SCPP systems, there is heat transfer by natural convection. Rayleigh's equation for natural convection is as follows:

$$\text{Ra} = \frac{g\beta\Delta T H_c^{\,3}}{\alpha\upsilon}, \tag{4}$$

where H_c refers to the collector height, υ is the kinematic viscosity, and α expresses the thermal diffusion coefficient. The preliminary findings reveal that Ra number takes a notably greater value than 10^9, which is a critical value, and hence, the flow inside the system is accepted as turbulent [23]. There are 3 different k-ε turbulence models in ANSYS FLUENT software. In the current research, the RNG k-ε turbulence model is used, which gives better results in vortex flows [27]. The equations of the model are as follows:

$$\frac{\partial}{\partial x_i}(\rho k u_i) = \frac{\partial}{\partial x_j}\left[\alpha_k \mu_{eff}\frac{\partial k}{\partial x_j}\right] + G_k + G_b + \rho\varepsilon - Y_M + S_k, \tag{5}$$

$$\frac{\partial}{\partial x_i}(\rho\varepsilon u_i) = \frac{\partial}{\partial x_j}\left[\alpha_\varepsilon \mu_{eff}\frac{\partial \varepsilon}{\partial x_j}\right] + C_{1_\varepsilon}\frac{\varepsilon}{k}(G_k + C_{3\varepsilon}G_b) - C_{2\varepsilon}\rho\frac{\varepsilon^2}{k} - R_e + S_\varepsilon. \tag{6}$$

When the experimental studies on SCPP systems are examined, it is seen that the temperature of the air in the system does not change much [3]. In this case, the Boussinesq model can be used for density [6, 22]. Its equation is as follows:

$$(\rho - \rho_a)g \approx -\rho_a\beta(T - T_a)g. \tag{7}$$

In Equation (7), β is the thermal expansion coefficient, and ρ_a and T_a are the density and temperature of the system air at the collector inlet. The collector supplies thermal energy to the system which can be expressed by

$$\dot{Q} = \dot{m}C_p\Delta T. \tag{8}$$

In Equation (8), the temperature increase along the collector is represented by ΔT. When the total collector surface area is A_{coll} and incoming solar radiation is G, collector efficiency can be defined as follows:

$$\eta_{\text{coll}} = \frac{\dot{Q}}{A_{\text{coll}}G}. \tag{9}$$

Different calculations of the power output in SCPPs are available in the literature. Usually, the power output calculation is done through the pressure drop (ΔP_t) in the turbine [28]. In this study, the following equation is used for the power output of the system:

$$P_o = \eta_t\Delta P_t Q_v. \tag{10}$$

In Equation (10), η_t is the turbine-generator efficiency and taken as 0.8 [28]. Although there are different parameters that affect the performance of SCPPs, the two main factors that determine the power output are the pressure drop (ΔP_t) in the turbine and the volumetric flow rate (Q_v) [28]. In this study, the turbine pressure drop is obtained from the average pressure (ΔP_t) where the turbine is placed in the CFD simulation results and is calculated as follows:

$$\Delta P_t = r_t P_t. \tag{11}$$

Here, r_t is considered as the turbine pressure drop rate [29]. Moreover, the efficiency of the system can be calculated as follows:

$$\eta = \frac{P_o}{A_{\text{coll}}G}. \tag{12}$$

3. CFD Model and System Properties

The geometric and climatic parameters that affect the performance of SCPP systems are studied by different researchers in the literature. However, in this study, the performance of the pilot plant at different values of the ground slope is examined for the first time in literature. The study is based on the main dimensions of the Manzanares prototype, Spain, and simulations are carried out for constant environmental conditions. The geometric dimensions and configuration details of the system are given in Table 1 [30]. In the analyses, the

Table 1: Structural details of the pilot plant in Manzanares [28].

Parameter	Value
Average collector height	1.85 m
Average collector radius	122.0 m
Chimney radius	5.08 m
Chimney height	194.6 m
Ground thickness	0.5 m

outlet height is changed provided that the entrance height of the horizontally placed collector is kept constant.

Simulations are repeated at different angle values. In this study, the influence of ground slope on the system performance of SCPPs is investigated by a reliable commercial software ANSYS FLUENT. In the CFD study, a successful 3D model is initially created, and its accuracy and reliability are justified through in situ measurements. In the model developed with reference to the Manzanares prototype, one-quarter of the whole solution domain is taken into consideration to minimise the iteration period. The model has two plane symmetries (XZ and YZ planes). Since it is seen that the temperature does not change from a certain point in the experimental measurements conducted on the prototype before, the ground thickness is taken as 0.5 m [3]. While designing the model, the ground slope is started within 5 m of the collector input. The slope that starts at this point ends at the collector exit. This is the case for the whole system. In simulations, after the results are obtained for the uneven ground condition, the ground slope is changed between 0.1 and 0.5 degrees. While changing the ground slope, the starting point of the slope is kept constant and the end point is the collector outlet. Since the pressure difference created by the collector inlet and the pressure difference at the chimney outlet is very small, 0 is ignored. The temperature at the collector inlet is taken equal to the ambient temperature. The schematic of the sloping ground SCPP design is illustrated in Figure 1.

Based on the adiabatic boundary condition at the ground and the chimney wall, the heat transfer coefficient is taken as 0 W/m^2K, while the heat transfer coefficient between the collector and the system air is assumed to be 10 W/m^2K. Physical properties of chimney, collector, and ground materials are very important in numerical modelling of solar chimney power plants and directly affect the simulation results. Model parameters of the relevant parts are given in Table 2. In addition, environmental parameters and thermophysical properties of the system air used in modelling are given in detail in Table 3. Due to the dimensional characteristics of the study, numerical modelling is carried out in a very dense cell number, which can extend the iteration time up to 6 hours for each parametric study. In order to shorten the iteration period, instead of the whole geometry, a quarterly axial symmetric model is preferred in the research.

Simulations are carried out with ANSYS FLUENT software, which uses the finite volume method in discretization of governing equations. The RNG k-ε turbulence model is preferred in the solution of the momentum equation. The SIMPLE algorithm is used to specify the relationship between

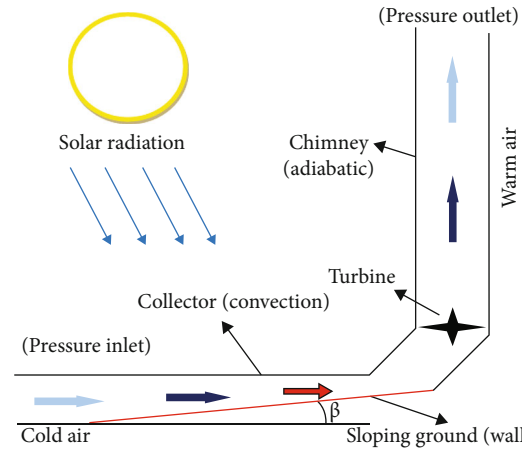

Figure 1: SCPP with sloping ground and corresponding boundary conditions.

Table 2: Physical properties of the materials used in the CFD research [8].

Physical property (unit)	Glass	Ground	Chimney
Density ($kg.m^{-3}$)	2500	2160	2719
Thermal conductivity ($W.m^{-1}K^{-1}$)	1.15	1.83	202.4
Specific heat capacity ($J.kg^{-1}K^{-1}$)	750	710	871
Transmissivity	0.9	Opaque	Opaque
Absorption coefficient	0.03	0.9	0
Refractive index	1.526	1	1
Emissivity	0.1	0.9	1
Thickness (m)	0.004	0.5	0.00125

Table 3: CFD parameters and climatic characteristics [8].

Solar radiation ($W.m^{-2}$)	1000
Atmospheric pressure (Pa)	101325
Ambient temperature (K)	293.15
Ambient air density ($kg.m^{-3}$)	1.2046
Gravitational acceleration ($m.s^{-2}$)	9.81
Air conductivity ($W.m^{-1}K^{-1}$)	0.0259
Ideal gas constant ($J.kg^{-1}K^{-1}$)	287
Kinematic viscosity of air ($m.s^{-2}$)	1.48×10^{-5}
Air heat capacity ($J.kg^{-1}K^{-1}$)	1006.43
Turbine pressure drop ratio	2/3
Stefan-Boltzmann constant ($W.m^{-2}K^{-4}$)	5.667×10^{-8}

pressure and air velocity. The PRESTO approach is preferred for pressure interpolation. Governing equations are discretized by the second-order UPWIND method. The DO radiation model is applied with solar ray tracing technique. The Boussinesq method is adopted to calculate the change in density of the air in the system. In the analyses, 10^{-6} is considered appropriate as the criteria for convergence. For the numerical procedure, first of all, the horizontal ground is modelled with the geometric dimensions of the Manzanares pilot plant. Then, a CFD simulation is performed with the proposed

climatic parameters. The simulation results are compared with the experimental data in the reference situation. If the numerical results are not consistent with the experimental data, the simulation is repeated. In case of the sufficient justification between numerical and experimental results, the model geometry is changed and the new simulation results are produced. The flow chart of the calculation procedure followed in the study is given in Figure 2.

4. Results and Discussion

Before the simulations are repeated for different slope angle values, the mesh-independent solution is examined. For this purpose, the mesh quality and mesh-independent solution are confirmed for three different cell numbers by considering the maximum air velocity (V_{max}) in the system. Table 4 shows the changes in the value of V_{max} for different cell numbers. For the cell number of 386041, the change in V_{max} is determined to be 1.4% only compared to the cell number case of 305619. From this point, the rest of the calculations are done over the cell number of 386041. Model and mesh visuals are given in Figure 3. After the justification of the mesh-free solution, the reliability of the numerical results is evaluated by comparing the CFD findings with the in situ measurements and other well-documented numerical models over the power output (P_o) figures of the system. It is perspicuous from Figure 4 that the numerical methodology adopted in this research is in good agreement with both experimental [31] and numerical results [6] when P_o values are taken into consideration for different solar intensities. Afterwards, simulations of the pilot plant with different ground slopes are carried out with the CFD model, whose mesh-independent solution is obtained and reliability is verified. Type, quality, and intensity of meshing are of vital importance in CFD analyses. Convergence, coherency, and reliability are notably affected by the aforesaid effects as well as discretization techniques. If the previous numerical findings of other researchers given in Figure 4 are examined, it is observed that the numerical approach adopted in the present study is more adaptive to the experimental data due to the abovementioned factors [32].

The most important variables in calculating the power output of solar chimney power plants are volumetric flow rate and turbine pressure drop. The air velocity and the pressure distribution, on which the volumetric flow rate depends, are therefore extremely important. With this approach, while examining the effect of ground slope on the performance parameters of the Manzanares pilot plant, pressure and airflow velocity distributions are especially investigated. The pressure distributions in the Manzanares prototype of horizontal and sloping (0.5°) ground are shown in Figure 5. When the pressure gradients in the existing system are examined, it is seen that it becomes more apparent in general towards the chimney inlet. It is clearly seen that the pressure jumps are more in the area between the collector outlet called the throat and the chimney inlet. This can be attributed to the intensive turbulence effects around the throat and chimney inlet. Considering that the turbine is located at a height of 9 m from the ground in the Manzanares pilot plant, the chimney entrance and its upper part where the pressure difference is maximum coincide here. This allows more power output with greater pressure difference. As the system is open to the atmosphere towards the chimney outlet, it is seen that the pressure value is equal to zero. On sloping ground compared to nonsloping case, the lifting effects are enhanced by the design in an upward direction. This yields to higher air velocities at the throat compared to the horizontal ground. In this case, the mass flow rate is expected to increase, but narrowing the airflow area at the throat with the increase of the ground slope causes a decrease in the mass flow rate. Considering the power output calculation, this is expected to have a negative effect on the system, but sloping ground yields to notable increase in the pressure difference in the throat. In this way, it is seen that higher power is delivered from the system. In the reference state, it is seen that the place where the pressure difference is the highest is the entrance of the chimney. When the ground slope is configured as 0.5°, it is observed that the pressure difference gets the highest value at the collector outlet.

The distribution of the air velocity in the system is given in Figure 6. In the reference state, the maximum air velocity is 14.20 m/s on the ground without slope, and when the ground slope angle is 0.5°, it increases by 37.4% to 19.51 m/s. This can be ascribed to the enhanced turbulence effects and improved

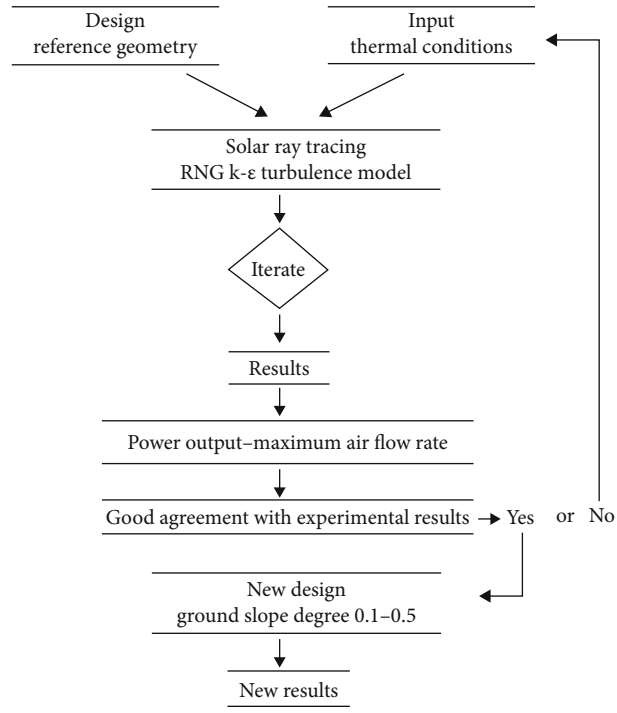

Figure 2: Experimental procedure.

Table 4: Mesh-independent solution over maximum air velocity.

Cell count	Maximum air velocity (m/s)	% change
259800	14.42	—
305619	13.996	2.9
386041	14.202	1.4

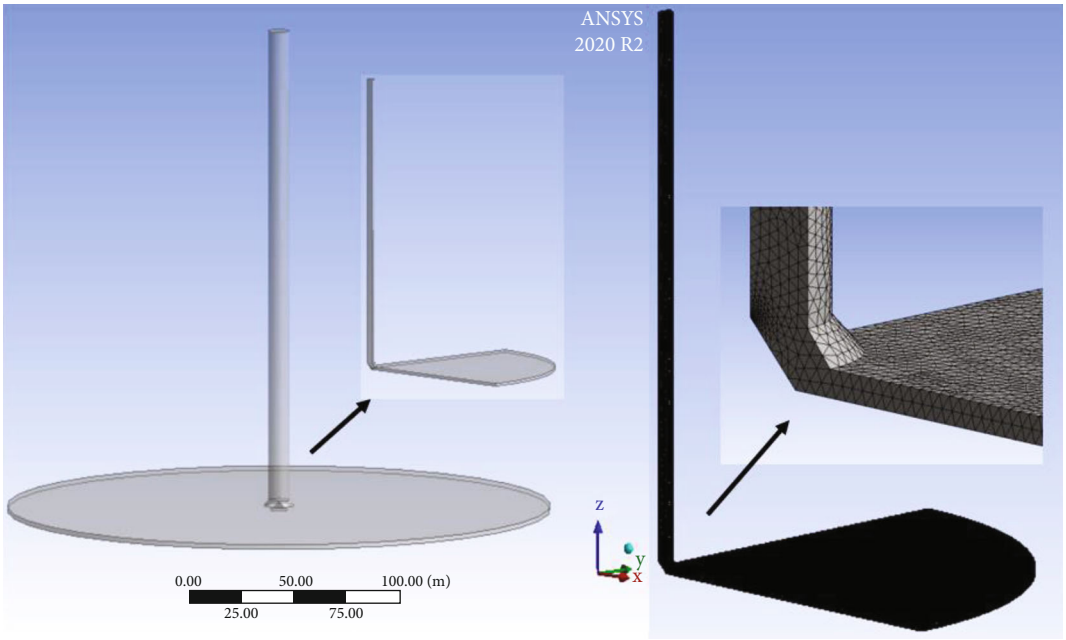

Figure 3: Model and mesh visuals.

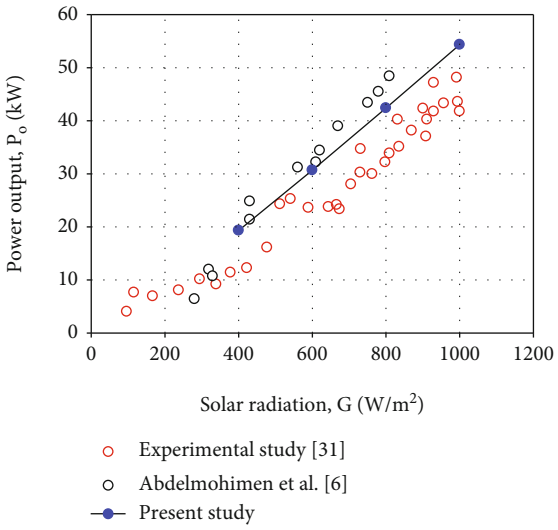

Figure 4: Accuracy justification of the CFD results over P_o values under different solar intensities.

lifting forces near the throat. While the air velocity in the system increases with the slope angle, it is the opposite of the mass flow rate figures. This is because of the narrowed cross-sectional area with the sloping design. The mass flow rate, which is 1117.9 kg/s for the nonsloping system, decreases exponentially with angle. For the slope ranges of 0-0.5°, the mass flow rate of the system can be obtained from the following equation:

$$\dot{m} = 1118 - 106.6\,\beta - 264.5\,\beta^2 - 1129\,\beta^3. \quad (13)$$

The variation of $\dot{m}$ with ground slope (β) is illustrated in Figure 7. Due to the narrowing volume beneath the collector with the increasing ground slope, a considerable decrease in mass flow rate figures is observed. In Equation (13), β is the ground inclination angle. When the ground inclination angle is 0.5°, it is seen that the mass flow rate decreases 32.29% compared to the reference situation and equals to 857.452 kg/s. The mass flow rate of the system decreases exponentially as the ground inclination angle increases. This causes the power output to decrease, but the increase in the turbine pressure drop will tolerate this situation. For this reason, for the optimum power output assessment, the 0-0.5 range of the ground slope is analysed by considering the mass flow rate and pressure difference. Another important parameter in the performance of SCPPs is the pressure drop. Increasing the pressure drop across the turbine directly increases the power output of the system. In the reference state, the pressure drop across the turbine is 109.777 Pa. Increasing the ground slope angle exponentially improves the pressure drop across the turbine. The pressure drop can be interacted with the ground inclination angle by the following equation:

$$\Delta P_{\text{dyn}} = \frac{-109.8 + 366.1\,\beta}{1 - 4.029\,\beta + 2.319\,\beta^2}. \quad (14)$$

When the ground inclination angle is 0.5°, it is seen that the pressure drop across the turbine increases by 53.45% compared to the reference situation and becomes -168.456 Pa. This impact can be clearly seen in Figure 8. The element that causes pressure difference in solar chimney power plants is the chimney. With the ground slope, it is seen that there is a pressure difference in the system due to both the ground geometry and the chimney. There is a clear increase in the pressure difference within the system due to the ground slope. Increasing the ground slope increases the pressure difference and therefore the power output. The parameters that affect the power output of SCPPs are analysed many times in the literature by

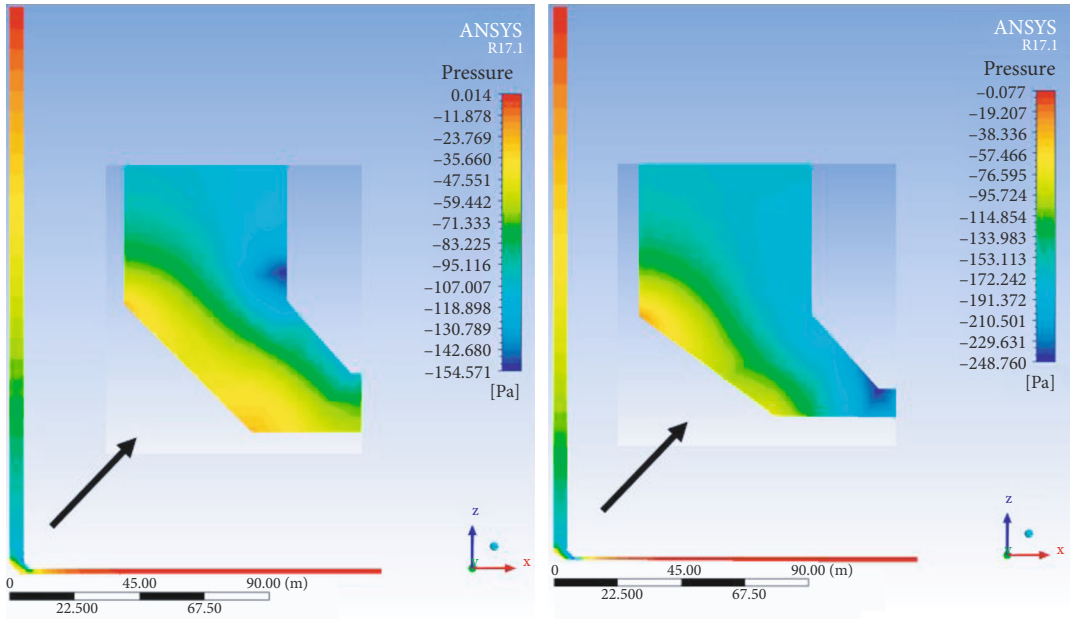

Figure 5: Pressure distributions in the pilot plant for horizontal (left) and sloping (0.5°) ground (right).

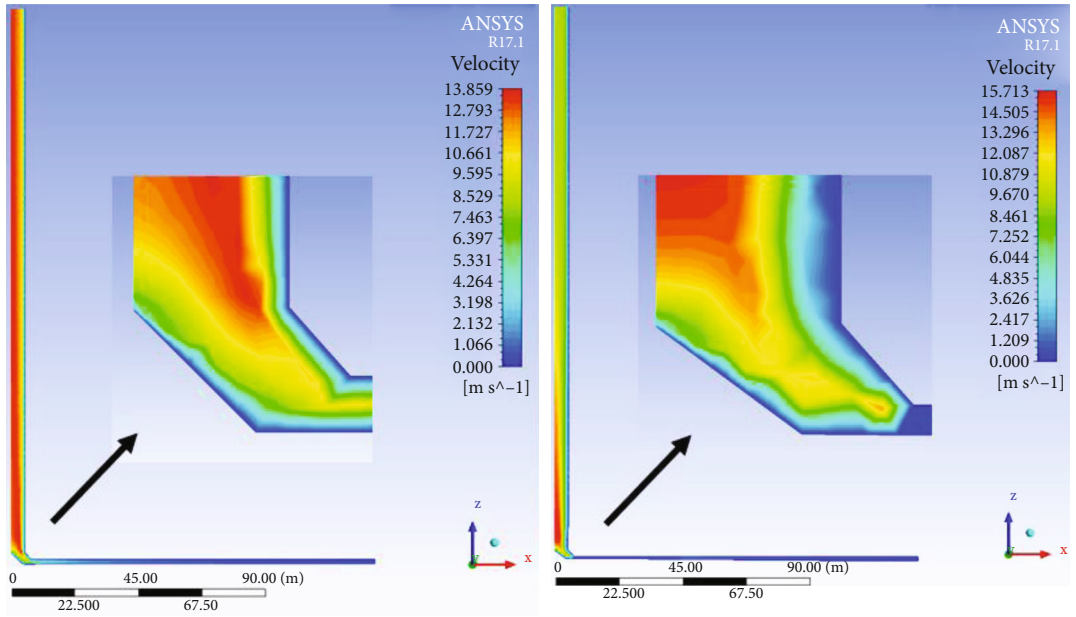

Figure 6: Velocity distributions in the pilot plant for horizontal (left) and sloping (0.5°) ground (right).

different researchers. In this study, the effect of ground inclination angle, which is not studied in the literature, on the performance of the system is analysed. It is seen that the system, which gives a power output of 54.3 kW in the reference state, increases exponentially with the increase in the ground inclination angle, so this effect has a positive effect on the system as shown in Figure 9. The power output of the system in the range of 0-0.5° ground slope angle can be calculated from the following equation:

$$P_o = 54.48 + 37.42\,\beta - 37.02\,\beta^2. \quad (15)$$

When the ground slope angle is made 0.5°, it is seen that the power output is 63.95 kW, increasing by 17.7% compared to the reference situation. The increase in power output with ground slope is very apparent between the reference state and a 0.1° slope. There is a 7.15% increase in power output at 0.1° ground slope compared to the reference situation. This percentage gradually decreases in the same degree intervals and falls below 1% after 0.4°. For this reason, the effect of ground slope on power output has been examined in the range of 0-0.5°, which is seen as the critical range. Apart from the analysed part in the study, examining the parameters affecting the system together for a more detailed optimisation will give

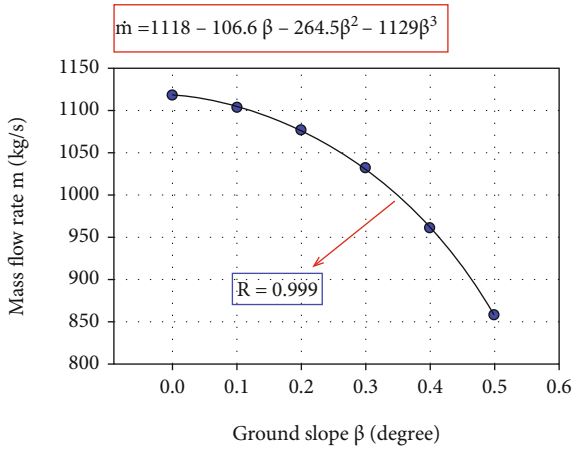

Figure 7: Mass flow rates in the pilot plant for different ground slope angles.

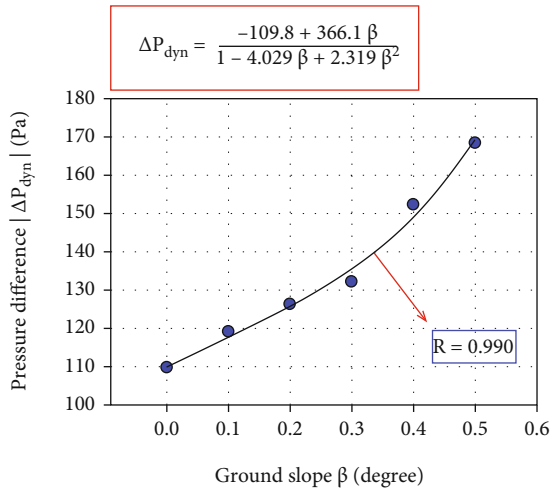

Figure 8: Dynamic pressure difference across the turbine for different ground slope angles.

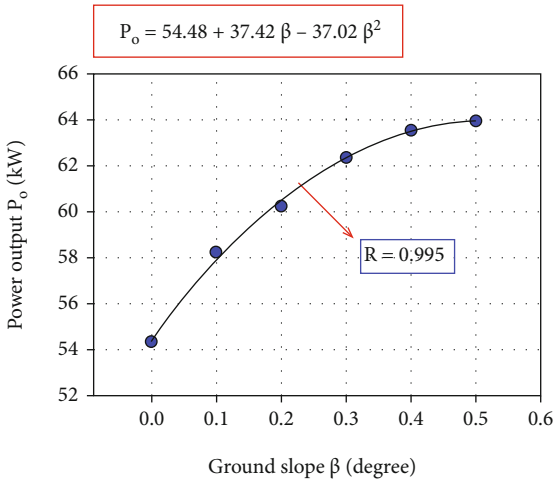

Figure 9: Power output of the pilot plant for different ground slope angles.

Table 5: Rayleigh number for 0 and 0.2° ground slope.

Ground slope (degree)	Rayleigh number	% change
0	8.517×10^9	—
0.2	8.769×10^9	2.95

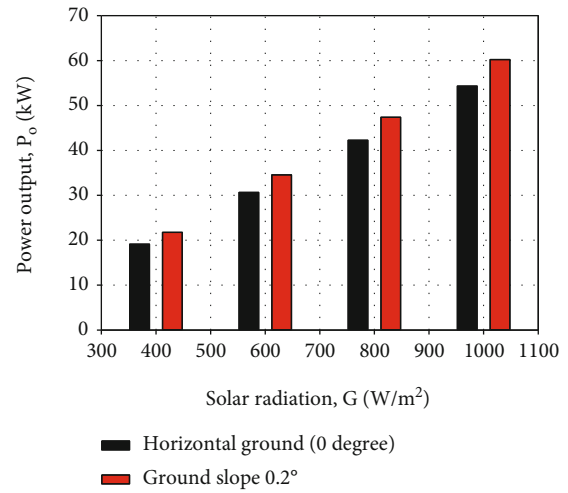

Figure 10: Comparison of power outputs for horizontal and 0.2° sloping ground under different solar radiation conditions.

more reliable results. For this reason, the effect of more than one parameter on the system can be examined with a more detailed study in future works.

For readers' interest, it is useful to clarify the reason of making a range selection for ground slope up to 0.5°. When the plot for power output versus slope of the ground is examined, it is easily understood that there are insignificant changes in power output after the slope value of 0.2°. This output is achieved through a preliminary analysis. Then, the analysis is extended to further slope values and observed that 0.5° is a critical value for the power output. After achieving this output, parametric research is conducted, and increment in ground slope is taken to be 0.1° to clearly illustrate the tendency of the interaction between power output and ground slope. R value is calculated to be 0.995 in the regression analysis, which proves the appropriateness of the increment in slope value.

In the study, it is clearly seen that the power output increases with the ground slope. Rayleigh (Ra) number increasing with the slope of the ground improves the heat transfer under the collector. The comparison of the Ra number for the reference case and the ground slope of 0.2° is given in Table 5. It is seen that the power outputs for the horizontal and sloping ground increase with the solar intensity. The aforesaid comparison is given in Figure 10. When the graph is examined, it can be easily asserted that taking the solar radiation of 1000 W/m^2 aims to show the maximum situation. The results unequivocally indicate that sloping ground gives better performance figures than horizontal ground for each solar intensity level.

5. Conclusions

The impact of ground slope on the main performance parameters of SCPPs is analysed for the first time in literature. The numerical methodology is structured on the material and geometric properties of the pilot SCPP system, and accuracy verification is done over the in situ measurements. A 3D axisymmetric CFD approach is proposed based on a DO solar ray tracing algorithm with the RNG k-ε turbulence technique. Following remarks might be achieved from the study:

(1) DO solar ray tracing algorithm supported by the RNG k-ε turbulence model is found to be an ideal numerical methodology in vortex flows which take place in SCPPs

(2) When the incoming solar radiation is equal to 1000 W/m^2, $V_{\max}$ is determined to be 14.2 m/s, which shows a well-accordance with the in situ tests of 15.0 m/s

(3) Ground slope angle (ω) is an effective parameter on main performance characteristics of SCPPs

(4) Mass flow rate of air shows an experimental decrease with increasing ground slope. $\dot{m}$ is 1117.9 kg/s for the nonsloping system. When ω is 0.5°, it is seen that $\dot{m}$ decreases 32.29% compared to the horizontal ground and equals to 857.452 kg/s

(5) On the contrary to $\dot{m}$, dynamic pressure difference across the turbine is remarkably improved with increasing ω. In the horizontal ground, ΔP_{dyn} across the turbine is found to be -109.777 Pa. When ω is 0.5°, it is observed that ΔP_{dyn} across the turbine increases by 53.45% compared to the reference case and equals to -168.456 Pa

(6) Power output (P_o) in SCPPs can be noticeably enhanced with the design of sloping ground. P_o is determined to be 54.3 kW in the case of horizontal ground. However, when ω is 0.5°, it is improved to 63.95 kW, increasing by 17.7% compared to the reference case

(7) The ideal power output (P_o) of the system can be achieved by optimising the mass flow rate and pressure difference across the turbine. When the ground slope is 0.1°, the power output increases by 7.15% compared to the reference situation, and this is the highest value compared to the other slope increases. A similar situation is valid for the pressure difference across the turbine. When the ground slope is 0.1°, the pressure difference across the turbine increases by 8.52% compared to the reference case

(8) The increase in power output continues to decrease after 0.1°. The increase in power output falls below 1% after the ground inclination angle of 0.4°

(9) In further works, sloping ground design in SCPPs will be studied along with the divergent chimney geometry [33] for extra improvement in performance figures

Nomenclature

A_{coll}: Collector area (m^2)
C_p: The specific heat capacity (J/kg.K)
g: Gravitational acceleration (m/s^2)
G: Solar radiation (W/m^2)
P_o: Power output (W)
T: Temperature (K)
P_t: Average pressure at the turbine location (Pa)
$\dot{Q}$: Heat transfer rate (W)
Q_v: Volumetric flow rate (m^3/s)
r_t: Turbine pressure drop rate

Greek Letters

α: Ambient
β: Ground slope degree (^{0})
η_{coll}: Collector efficiency
ρ: Density (kg/m^3)
ω: Thermal expansion coefficient (1/K)

Data Availability

The numerical data used to support the findings of this study are included within the article.

Conflicts of Interest

The authors have no conflicts of interest to declare.

References

[1] H. Sen and E. Cuce, "Dynamic pressure distributions in solar chimney power plants: a numerical research for the pilot plant in Manzanares, Spain," *WSSET Newsletter*, vol. 12, no. 1, pp. 2–2, 2020.

[2] E. Cuce and H. Sen, "Dünden bugüne güneş bacası güç santralleri: Sistem güç çıkışına etki eden performans parametreleri," *Avrasya*, vol. 7, pp. 256–262, 2020.

[3] W. Haaf, "Solar chimneys: part II: preliminary test results from the Manzanares pilot plant," *International Journal of Sustainable Energy*, vol. 2, no. 2, pp. 141–161, 1984.

[4] A. Dhahri, A. Omri, and J. Orfi, "Numerical study of a solar chimney power plant," *Research Journal of Applied Sciences, Engineering and Technology*, vol. 8, no. 18, pp. 1953–1965, 2014.

[5] M. T. Esfidani, S. Raveshi, M. Shahsavari, and A. Sedaghat, "Computational study on design parameters of a solar chimney," in *International Conference on Sustainable Mobility Applications, Renewables and Technology (SMART),*, pp. 23–25, Kuwait, November 2015.

[6] M. A. H. Abdelmohimen and S. A. Algarni, "Numerical investigation of solar chimney power plants performance for Saudi Arabia weather conditions," *Sustainable Cities and Society*, vol. 38, pp. 1–8, 2018.

[7] J. Li, P. Guo, and Y. Wang, "Effects of collector radius and chimney height on power output of a solar chimney power plant with turbines," *Renewable Energy*, vol. 47, pp. 21–28, 2012.

[8] E. Cuce, H. Sen, and P. M. Cuce, "Numerical performance modelling of solar chimney power plants: influence of

chimney height for a pilot plant in Manzanares, Spain," *Sustainable Energy Technologies and Assessments*, vol. 39, article 100704, 2020.

[9] P. Karimipour Fard and H. Beheshti, "Performance enhancement and environmental impact analysis of a solar chimney power plant: twenty-four-hour simulation in climate condition of Isfahan province, Iran," *International Journal of Engineering*, vol. 30, no. 8, pp. 1260–1269, 2017.

[10] D. Toghraie, A. Karami, M. Afrand, and A. Karimipour, "Effects of geometric parameters on the performance of solar chimney power plants," *Energy*, vol. 162, pp. 1052–1061, 2018.

[11] Y. J. Choi, D. H. Kam, Y. W. Park, and Y. H. Jeong, "Development of analytical model for solar chimney power plant with and without water storage system," *Energy*, vol. 112, pp. 200–207, 2016.

[12] X. Zhou, F. Wang, J. Fan, and R. M. Ochieng, "Performance of solar chimney power plant in Qinghai-Tibet Plateau," *Renewable and Sustainable Energy Reviews*, vol. 14, no. 8, pp. 2249–2255, 2010.

[13] F. Attig-Bahar, M. Sahraoui, M. S. Guellouz, and S. Kaddeche, "Effect of the ground heat storage on solar chimney power plant performance in the South of Tunisia: case of Tozeur," *Solar Energy*, vol. 193, pp. 545–555, 2019.

[14] A. A. Sedighi, Z. Deldoost, and B. M. Karambasti, "Effect of thermal energy storage layer porosity on performance of solar chimney power plant considering turbine pressure drop," *Energy*, vol. 194, p. 116859, 2020.

[15] N. Fadaei, A. Kasaeian, A. Akbarzadeh, and S. H. Hashemabadi, "Experimental investigation of solar chimney with phase change material (PCM)," *Renewable Energy*, vol. 123, pp. 26–35, 2018.

[16] S. Larbi, A. Bouhdjar, K. Meliani, A. Taghourt, and H. Semai, "Solar chimney power plant with heat storage system performance analysis in South Region of Algeria," in *2015 3rd International Renewable and Sustainable Energy Conference (IRSEC)*, pp. 1–6, Marrakech, Morocco, December 2015.

[17] A. Yaswanthkumar and V. P. Chandramohan, "Numerical analysis of flow parameters on solar updraft tower (SUT) with and without thermal energy storage (TES) system," *Journal of Thermal Analysis and Calorimetry*, vol. 136, no. 1, pp. 331–343, 2019.

[18] M. Senbeto, "Numerical simulations of solar chimney power plant with thermal storage," *International Journal of Engineering Research & Technology (IJERT)*, vol. 9, no. 10, pp. 103–106, 2020.

[19] S. Kalash, W. Naimeh, and S. Ajib, "Experimental investigation of the solar collector temperature field of a sloped solar updraft power plant prototype," *Solar Energy*, vol. 98, pp. 70–77, 2013.

[20] E. Bilgen and J. Rheault, "Solar chimney power plants for high latitudes," *Solar Energy*, vol. 79, no. 5, pp. 449–458, 2005.

[21] F. Cao, H. Li, Y. Zhang, and L. Zhao, "Numerical simulation and comparison of conventional and sloped solar chimney power plants: the case for Lanzhou," *The Scientific World Journal*, vol. 2013, Article ID 852864, 8 pages, 2013.

[22] S. Sivalakshmi, V. Sethupathi, and M. Pachiyannan, "A Comparative Analysis on the Thermal Performance of Solar Chimney with Smooth and Dimpled Absorber Plate," *Materials Today: Proceedings*, vol. 43, pp. 1124–1127, 2020.

[23] E. Cuce, "Güneş bacası güç santrallerinde toplayıcı eğiminin çıkış gücüne ve sistem verimine etkisi," *Uludağ Üniversitesi Mühendislik Fakültesi Dergisi*, vol. 25, no. 2, pp. 1025–1038, 2020.

[24] R. Hosseinnezhad, O. A. Akbari, H. H. Afrouzi, M. Biglarian, A. Koveiti, and D. Toghraie, "Numerical study of turbulent nanofluid heat transfer in a tubular heat exchanger with twin twisted-tape inserts," *Journal of Thermal Analysis and Calorimetry*, vol. 132, no. 1, pp. 741–759, 2018.

[25] O. Rezaei, O. A. Akbari, A. Marzban, D. Toghraie, F. Pourfattah, and R. Mashayekhi, "The numerical investigation of heat transfer and pressure drop of turbulent flow in a triangular microchannel," *Physica E: Low-dimensional Systems and Nanostructures*, vol. 93, pp. 179–189, 2017.

[26] ANSYS FLUENT, *Users Theory Guide*, ANSYS, Inc., USA, 2013.

[27] A. Hassan, M. Ali, and A. Waqas, "Numerical investigation on performance of solar chimney power plant by varying collector slope and chimney diverging angle," *Energy*, vol. 142, pp. 411–425, 2018.

[28] T. Ming, R. K. Richter, F. Meng, T. Pan, and W. Liu, "Chimney shape numerical study for solar chimney power generating systems," *International Journal of Energy Research*, vol. 37, no. 4, pp. 310–322, 2013.

[29] J. Li, H. Guo, and S. Huang, "Power generation quality analysis and geometric optimization for solar chimney power plants," *Solar Energy*, vol. 139, pp. 228–237, 2016.

[30] W. Haaf, K. Friedrich, G. Mayr, and J. Schlaich, "Solar chimneys part I: principle and construction of the pilot plant in Manzanares," *International Journal of Solar Energy*, vol. 2, no. 1, pp. 3–20, 1983.

[31] J. R. Schlaich, R. Bergermann, W. Schiel, and G. Weinrebe, "Design of commercial solar updraft tower systems—utilization of solar induced convective flows for power generation," *Journal of Solar Energy Engineering*, vol. 127, no. 1, pp. 117–124, 2005.

[32] P. M. Cuce, E. Cuce, and H. Sen, "Improving electricity production in solar chimney power plants with sloping ground design: an extensive CFD research," *Journal of Solar Energy Research Updates*, vol. 7, no. 1, pp. 122–131, 2020.

[33] E. Cuce, A. Saxena, P. M. Cuce, H. Sen, S. Guo, and K. Sudhakar, *Performance Assessment of Solar Chimney Power Plants with the Impacts of Divergent and Convergent Chimney Geometry*, International Journal of Low-Carbon Technologies, 2021.

Hindawi
International Journal of Photoenergy
Volume 2021, Article ID 5552637, 8 pages
https://doi.org/10.1155/2021/5552637

Research Article

Determining Optimum Tilt Angle for 1 MW Photovoltaic System at Sukkur, Pakistan

Qasir Ali Memon,[1] Abdul Qadir Rahimoon,[1] Khurshed Ali,[2] Muhammad Fawad Shaikh,[1] and Shoaib Ahmed Shaikh[1]

[1]*Department of Electrical Engineering, Sukkur IBA University, Pakistan*
[2]*Department of Computer Science, Sukkur IBA University, Pakistan*

Correspondence should be addressed to Abdul Qadir Rahimoon; aqadir@iba-suk.edu.pk

Received 2 March 2021; Revised 24 April 2021; Accepted 4 May 2021; Published 21 May 2021

Academic Editor: Erdem Cuce

Copyright © 2021 Qasir Ali Memon et al. This is an open access article distributed under the Creative Commons Attribution License, which permits unrestricted use, distribution, and reproduction in any medium, provided the original work is properly cited.

Solar energy is directly converted into electrical energy by using photovoltaic (PV) panels. The efficiency of PV panel varies with its orientation and tilt angle with the horizontal plane. In this paper, we investigate the optimum tilt angle of solar panels installed at Sukkur IBA University. The optimum angle for tilted surfaces varying from 0° to 90° in steps of 1° was calculated for the values of which the daily total solar radiation was maximum for a specific period. It was found that the optimum tilt angle changed between 0° and 61.1° throughout the year in Sukkur IBA University, Sindh Pakistan (latitude = 27.7268° N, longitude = 68.8191° E). For calculating irradiance, optimal fixed (15 and 29.5 degrees) and variable tilt angles are used for every month of year 2019. The irradiance calculated at 15 degrees tilt angle is compared with the fixed angle of 29.5 and variable angles. It was found that optimal tilt angle for the region of Sukkur located in northern Pakistan is to be 29.5 degrees.

1. Introduction

There are two main resources of power, namely, conventional and nonconventional. Nonconventional resources have become popular due to various advantages such as being nonpollutant, fuel free, and nonexhausted [1]. From renewable or nonconventional resources power from solar energy keeps vital role in power sector due to several pros like reliable, economic, environment friendly, and wide availability [2]. Power from solar can be generated from PV modules and thermal process; however, in Pakistan, more focus is on PV modules. It is imperative to check the performance of solar modules which sturdily depends on the solar radiation, tilt angle, and uncontrolled factors such as atmospheric conditions, latitude, season, capacity factor, orientation, and time-of-day [3–9].

A key requirement to achieve maximum power from solar is to avoid the shading effects on solar modules and usage of solar tracking systems. Solar tracking system is the best solution for tracking sunrays to approach the tilt angle continuously, but these trackers are expensive and are not always applicable [10, 11]. Another option is to set the panel with a fixed optimum tilt angle (the angle can be changed in each month or each season manually or have a one tilt angle for the whole year).

Selection of tilt angle has become a hot area research to improve system efficiency. Numerous studies have been carried out to check the performance of PV systems by using different observations, proper diagrams, design, and relationships between different parameters and characteristics related to choosing proper installation site [12–14].

Optimum tilt angle for solar PV system is different due to geographical locations and seasonal variations. The geographical factors include declination angle and data related to solar resources which are important to decide the optimal tilt angle for solar PV system [15].

For determining the optimal tilt angle of solar PV module, it is important to calculate declination angle of the sun

and estimation of solar radiation on the tilted surface [16]. Conversely, solar radiation attenuates after entering the atmosphere of the earth due to absorption, scattering by small particles and reflection of objects [17].

Moreover, researchers have also suggested different theoretical models for calculating the optimum tilt angles of several solar collectors and consider a collector with given structural parameters that the latitude of installation site, climate conditions, tilt, and azimuth angles are related to collectible radiations in a year [18, 19].

Sukkur region, located in northern Pakistan, has great solar radiation potential since the number of sunshine is large. Its rural areas face acute power cut off usually 14 to 16 hours per day. So the farmers are resorting to PV systems to cultivate small areas by using drip irrigation method and for other purposes. But due to unavailability of proper data, PV systems are installed in random orientations so they do not get optimal power. Therefore, by employing the analytical and numerical methods, we have found out the optimal angle for PV systems for the given region. This research work will provide local community a way to achieve maximum power output which is bound to give numerous economic benefits.

2. Theory and Work Flow

In this paper, we have calculated and compared irradiance on fixed and variable optimal tilt angle by using MATLAB/Simulink. The fixed angles are 15 degrees and 29.5 degrees. A 15-degree tilt angle is currently used at Sukkur IBA University for PV solar system.

Initially, constant values G_{SC}, φ, ρ_g, and H have been used, and n is set to one which means first day of the year after that surface is tilted from 0 to 90 degrees for given day and obtain the optimum tilt angle at maximum irradiance. Next, n is increased by one and continue to find the optimum tilt angle at given day results and is continued till the value of 365.

Tilt angle is varying from 0 to 90 degrees with one degree step size for accurate results. For finding irradiances, we have gone through the steps to first calculate the δ, ω_s, and ω_{ss}, then Ho, K_T, H_d, H_b, R_d, R_b, and H_T. These factors can be premeditated by the equations given below.

The equation used to calculate the total solar radiation on the tilted surface is given as [20, 21]:

$$H_T = H_b * R_b + H_d * R_d + H * \rho_g * \left(\frac{1 - cos\beta}{2}\right). \quad (1)$$

R_b and R_d in equation (1) are the tilt coefficients to calculate the beam solar radiation and the diffused solar radiation on the tilted surface, respectively. The coefficient can be determined by [20–23] as given in equations (2) and (6):

$$R_b = \frac{(\cos(\varnothing - \beta) * \cos(\delta) * \sin(\omega_{ss})) + (\omega_{ss}(\pi/180)\sin(\varnothing - \beta)\sin(\delta))}{(\cos(\varnothing) * \cos(\delta) * \sin(\omega_s)) + (\omega_s(\pi/180)\sin(\varnothing)\sin(\delta))}, \quad (2)$$

where P_g is the ground reflectance/albedo (reflectance of ground = 0.2), β is the optimum tilt angle and it is the angle on which PV panel received maximum amount of solar radiations, $\varnothing$ is the latitude of Sukkur IBA University (27.7268° N, 68.8191° E), and δ is the declination angle of the earth and can be calculated by:

$$\delta = 23.45 \sin\left[\frac{360(n + 284)}{365}\right], \quad (3)$$

where ω_s is the sunset hour angle, which is equal to:

$$\omega_s = \cos^{-1}[-\tan\delta \ \tan\varphi]. \quad (4)$$

ω_{ss} is the sunrise hour angle of inclined plane and can be calculated as:

$$\omega_{ss} = \min\left[\cos^{-1}(-\tan\delta \tan\varnothing), \cos^{-1}(-\tan(\varnothing - \beta)\tan\varnothing)\right]. \quad (5)$$

Now, the tilt coefficient diffuse solar radiation on the tilted surface can be calculated as:

$$R_d = \frac{H_b}{H_\circ} * R_b + \left(1 - \frac{H_b}{H_\circ}\right) * \left(1 + \frac{\cos\beta}{2}\right) * \left[1 + \sqrt{\frac{H_b}{H}} * \sin\left(\frac{\beta}{2}\right)^3\right], \quad (6)$$

where H_b is the beam direct radiation incident angle equals to:

$$H_b = H - H_d. \quad (7)$$

Here, H is the global solar radiations at horizontal surface.

The data related to global solar radiations on horizontal surface is taken from NASA database.

H_d is the solar diffused radiations at horizontal surface which is applicable for any location within latitude 40° N and 40° S and calculated by [24, 25]:

$$H_d = 1.00 - 1.13K_T, \quad (8)$$

where K_T is the clearness index.

The clearness index is a measure of the clearness of the atmosphere. It is the fraction of the solar radiation that is transmitted through the atmosphere to strike the surface of the earth. And it can be calculated from equation (9):

$$K_T = \frac{H}{H_o}. \quad (9)$$

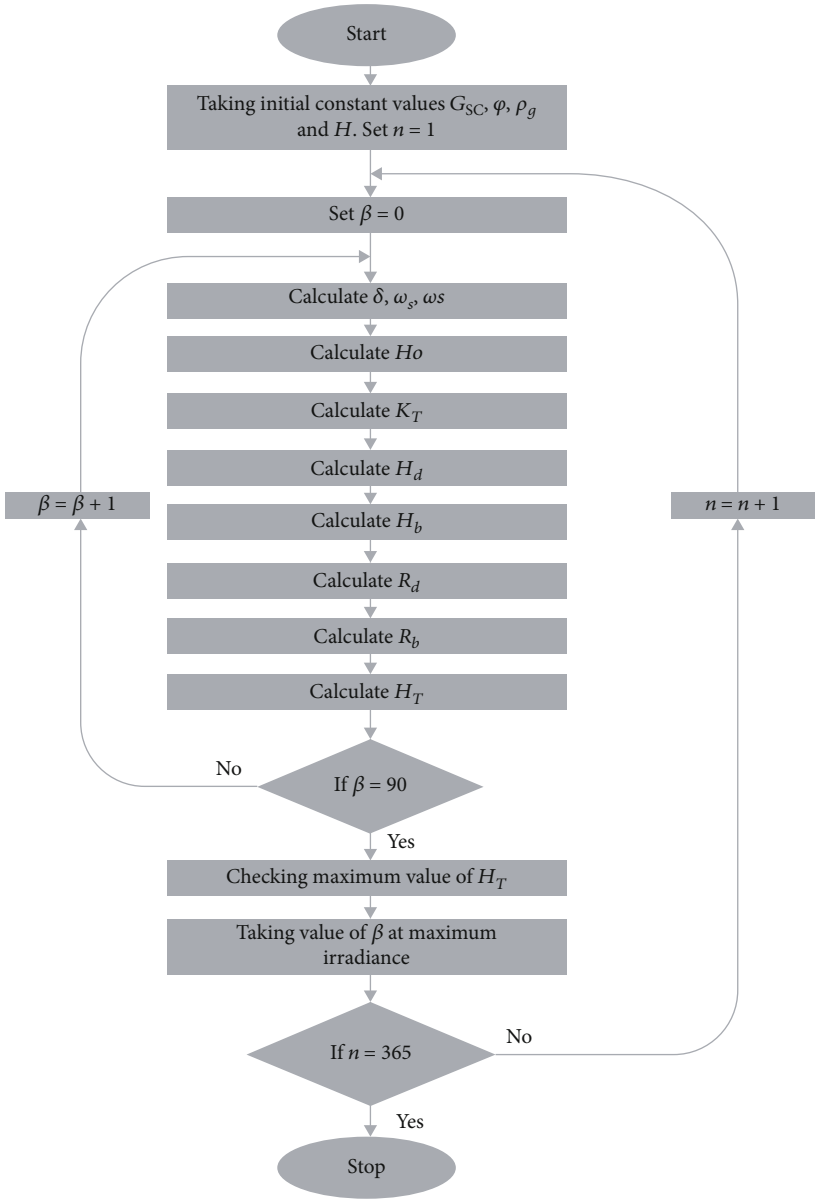

Figure 1: Flowchart for finding optimal tilt angle.

H and H_o in equation (9) are global solar radiations on horizontal surface and monthly average daily extraterrestrial radiation (kwh/m^2/day) and can be calculated by:

$$H_o = \frac{24}{\pi} G_{sc} \left(1 + 0.33 \cos \frac{360\, n}{365}\right) \cdot \left(\cos\varnothing \cos\delta \sin\omega_s + \frac{\pi \omega_s}{180} \sin\varphi \sin\delta\right). \quad (10)$$

G_{sc} in equation (10) is the solar constant referred as 1353 W/m^2 [24]. Other parameters are taken as constant values.

Using equations from (1) to (10), we can now easily calculate the irradiance at different supposed tilted angles. The procedure for finding optimum tilt angle is shown in flow chart in Figure 1.

3. Results and Discussion

Through mathematical modeling as discussed in Section 3, irradiance level on solar panel is calculated at 15° tilt angle, 29.5 degree, and variable tilt angles on every 21st of the every month of 2019. A 15-degree angle is used at Sukkur IBA University. We are going to check the declination angle and irradiance at different angles to compare the results.

3.1. Surface Tilted at 15 Degrees. The input data for finding maximum irradiance on solar panel are global solar radiations on horizontal surface (H) in Wh/m^2/day and W/m^2/day carried from NASA database as shown in Table 1.

Table 1: Monthly specific daily global irradiance (H), year days, days of the month, tilt angle (deg), irradiance level after tilt, and declination angle of the earth.

H-Wh/m^2/day	H-W/m^2/day	Year day	Month day	Tilt angle (deg)	Irradiance level after tilt	Declination angle of earth
7490	913	21	21 Jan	15	1222	-20.14
7560	921	52	21 Feb	15	1125	-11.23
8770	1069	80	21 Mar	15	1186	-0.403
9420	1148	111	21 Apr	15	1161	11.58
10610	1293	141	21 May	15	1227.6	20.14
11210	1367	172	21 Jun	15	1265.5	23.45
11420	1392	202	21 Jul	15	1319	20.44
10250	1250	233	21 Aug	15	1261.5	11.75
10390	1267	264	21 Sep	15	1403	-0.2
8830	1076	294	21 Oct	15	1320	-11.75
9000	1097	325	21 Nov	15	1474	-20.44
6990	852	355	21 Dec	15	1187.5	-23.45

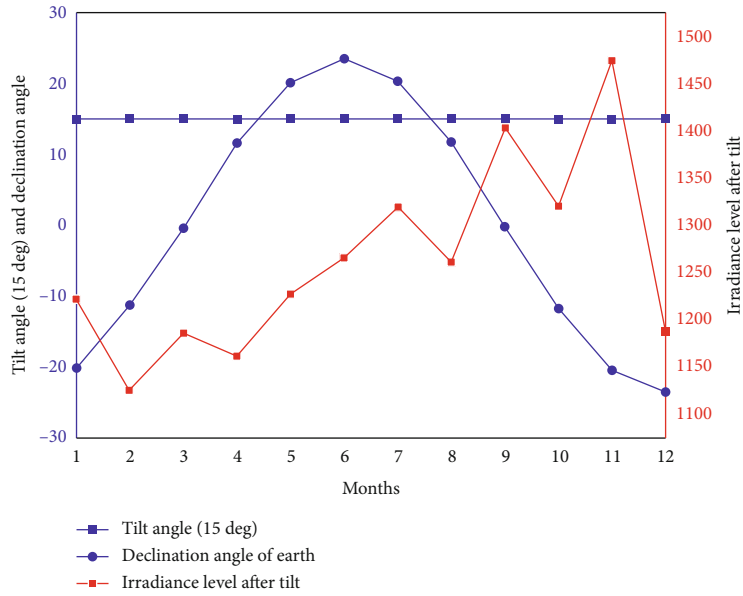

Figure 2: Specific monthly irradiance on fixed tilt angle (15 deg) and declination angle vs. months.

After putting this input data in equations, we have calculated declination angle and irradiance at fixed optimal tilt angle using MATLAB/Simulink model. The value of irradiance is maximum 1474 W/m^2/day in November and minimum 1125 W/m^2/day in February. The average value of irradiance throughout the year will be 1262.675 W/m^2/day. The irradiance is not constant in every month throughout the year, but it is varying as shown in Figure 2.

The graph shows that solar PV module is fixed at tilt angle of 15° where it has received irradiance between 1300 w/m^2/day and 1474 w/m^2/day in 4 months, between 1200 w/m^2/day and 1300 w/m^2/day for 3 months, and 1100 w/m^2/day and 1200 w/m^2/day for 5 months in year 2019. 15° tilt angle is optimal for months (Oct–Feb) referring to Table 1. For input irradiance in these months, the output of tiled surface is high, but in Sukkur region, the maximum irradiance received in months from Apr to Sep. So 15° tilt angle is not optimal for Sukkur region. As shown in Figure 2, the irradiance level is varied because of change in declination angle.

3.2. Surface Tilted at Variable Angles. The input data is used to find the irradiance and declination angle at different variable angles. The results achieved from calculations are shown in Table 2.

Table 2 shows the simulated results of solar irradiance and optimal tilt angles of every 21st of the every month of 2019. Monthly optimal tilt angle of solar photovoltaic of Sukkur IBA University was calculated. In the program, the total solar radiation for tilt angles between 0° and 90° with an interval of 1° is calculated, and the angle with maximum radiations is determined to find optimum tilt angle. The data in Table 2 is plotted in Figure 3, which shows the variable tilt angles of solar panel over the year.

Table 2: Monthly specific daily global irradiance (H), year days, days of the month, tilt angle (deg), irradiance level after tilt, and declination angle of the earth.

H-Wh/m^2/day	H-W/m^2/day	Year day	Month day	Optimum tilt angle (deg)	Irradiance level after tilt	Declination angle of earth
7490	913	21	21 Jan	57.73	1630	-20.14
7560	921	52	21 Feb	47	1310	-11.23
8770	1069	80	21 Mar	30.95	1229	-0.403
9420	1148	111	21 Apr	10.16	1164	11.58
10610	1293	141	21 May	0	1294	20.14
11210	1367	172	21 Jun	0	1367	23.45
11420	1392	202	21 Jul	0	1392.7	20.44
10250	1250	233	21 Aug	9.834	1265.8	11.75
10390	1267	264	21 Sep	30.62	1452	-0.2
8830	1076	294	21 Oct	47.74	1549	-11.75
9000	1097	325	21 Nov	58.06	1977	-20.44
6990	852	355	21 Dec	61.19	1677.6	-23.45

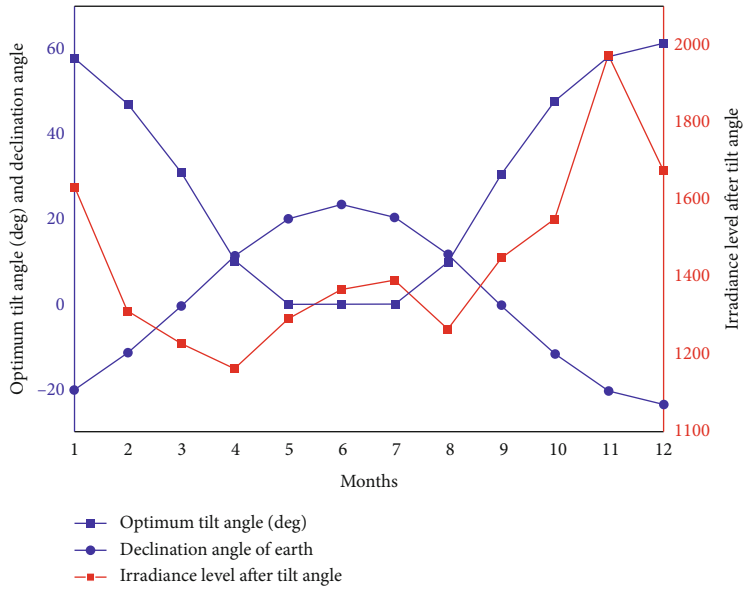

Figure 3: Specific monthly irradiance on variable optimal tilt angle and declination angle versus months.

Table 3: Monthly specific daily global irradiance (H), year days, days of the month, tilt angle (deg), irradiance level after tilt, and declination angle of the earth.

H-Wh/m^2/day	H-W/m^2/day	Year day	Month day	Tilt angle (deg)	Irradiance level after tilt	Declination angle of earth
7490	913	21	21 Jan	29.5	1447.27	-20.14
7560	921	52	21 Feb	29.5	1253.4	-11.23
8770	1069	80	21 Mar	29.5	1229	-0.403
9420	1148	111	21 Apr	29.5	1108	11.58
10610	1293	141	21 May	29.5	1102.8	20.14
11210	1367	172	21 Jun	29.5	1109.5	23.45
11420	1392	202	21 Jul	29.5	1182	20.44
10250	1250	233	21 Aug	29.5	1202.5	11.75
10390	1267	264	21 Sep	29.5	1451.6	-0.2
8830	1076	294	21 Oct	29.5	1476.6	-11.75
9000	1097	325	21 Nov	29.5	1749.5	-20.44
6990	852	355	21 Dec	29.5	1440.2	-23.45

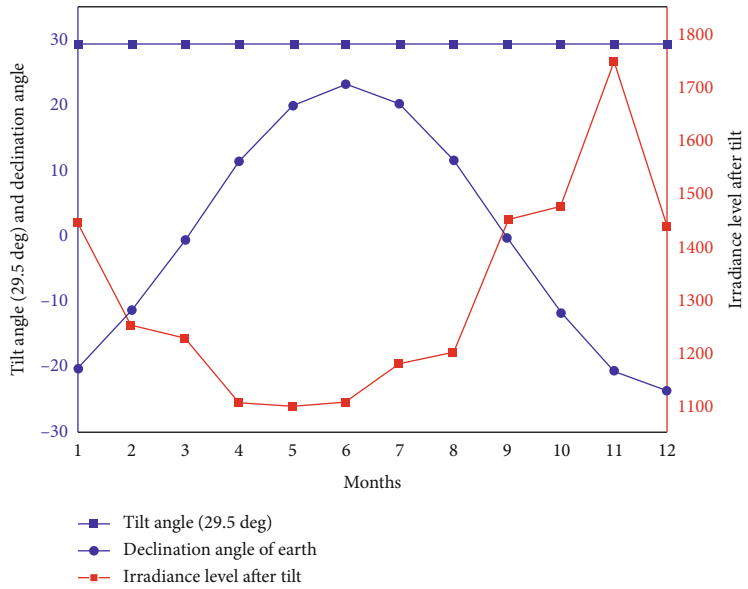

Figure 4: Specific monthly irradiance on optimal fixed tilt angle (29.5 deg) and declination angle versus months.

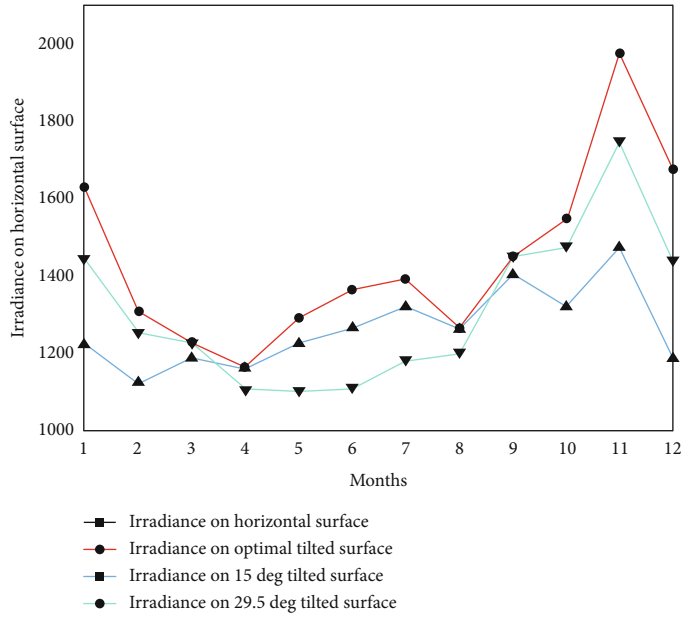

Figure 5: Comparison of irradiance on different tilt angles.

Solar panel with small input global solar irradiance on horizontal surface between 7000 and 9000 Wh/m^2/day received maximum amount of irradiance between 1200 w/m^2/day and 1977 W/m^2/day on tilt angle of 30° or above in the month from September to March. It is actually getting maximum irradiance for seven months at an angle 30° or above. The value of irradiance is found to decrease from April to August at an angle of 0 to 11 degrees, and the average value of irradiance is 1442.342 W/m^2/day. This value of irradiance is greater than the value at 15 degrees optimal tilt angle.

3.3. Surface Tilted at 29.5 Degrees. We have taken a fixed optimal tilt angle of 29.5 degrees to check the irradiance. The value is actually taken as the average value of all variable angles to see the irradiance level. The results of irradiance and declination angle are shown in Table 3.

From Table 3, it is shown that the maximum value of irradiance is 1749.5 in the month of November. The minimum value is 1102.08 in the month of May. The average value of irradiance throughout the year is 1312.698 W/m^2/day. The data of Table 3 is plotted in Figure 4.

Figure 4 shows that solar PV module is fixed at tilt angle of 29.5° that is the suggested angle to Sukkur IBA University, at 29.5° tilt angle solar panel with small input global solar irradiance on horizontal surface between 7000 and 9000 Wh/m^2/day received maximum amount of irradiance

between 1250 w/m^2/day and 1451 w/m^2/day which are greater than irradiance received on solar panel at 15° tilt angle. This value is receiving from September to March. Means solar panel received 7 months out of 12 months maximum irradiance at an angle 29.5°.

3.4. Comparison of Irradiance on Different Tilt Angles. After receiving irradiance at fixed and variable angles, we have get our results. The results at all conditions are compared as shown in Figure 5. At 15 degrees tilted angle, the irradiance is approximately same as in the first four months, then slightly increases for three months and finally reaches at maximum value in the month of November. If we compare irradiance level of 29.5 degrees with 15 degrees, then in first four months, the irradiance value is greater, and then, from 5th to 8th month, it is decreased. However, average value of irradiance will be greater than 15 degrees value. On variable tilted angle case, we have received maximum value of 1977 w/m^2/day in the month of November. Although this value is greater than 15 degree and 29.5 degree values, yet it is impossible to practically use variable optimal tilt angle.

After comparison from all results, we are suggesting to use optimal tilt angle of 29.5 degrees to get the maximum irradiance value.

4. Conclusion

In this paper, an analytical and numerical analysis has been carried out on different tilt angles to check the irradiance by using MATLAB/Simulink. A 15-degree tilt angle is used at Sukkur IBA University for solar system of 1 MW. For finding optimum tilt angle, the PV module is tilted from 0 to 90 degrees, where the value of H is obtained from NASA database, and for simplification, the data is taken at 21st of every month of year 2019. The optimal tilt angle of each month is decided on the maximum value of irradiance taken from calculations at different tilt angles.

The results are taken at both fixed and variable tilt angles which shows that maximum irradiance can be achieved at 29.5 degrees as compared to 15 degrees used at Sukkur IBA University.

The method employed in this paper can also be used for installing the PV systems in other locations so as to obtain maximum power from system.

Nomenclature

H_T: Total solar radiations received on tilted surface
H_b: Solar beam radiations on horizontal surface
R_b: Tilt coefficient to calculate direct solar direct radiations
H_d: Solar diffused radiations on horizontal surface
R_d: Tilt coefficient to calculate solar diffused radiations
H: Global solar radiations on horizontal surface
ρ_g: Ground reflectivity coefficient
β: Tilt angle of surface
ω_{ss}: Sunrise hour angle on tilted surface
ω_s: Sunrise hour angle on horizontal surface
$\emptyset$: Latitude of the place
δ: Declination angle of the earth
n: Counted number of days
K_T: Clearness index
H_o: Monthly average daily extraterrestrial radiation.

Data Availability

Data is available on request.

Conflicts of Interest

The authors declare that they have no conflicts of interest.

References

[1] I. Vidanalage and K. Raahemifar, "Tilt angle optimization for maximum solar power generation of a solar power plant with mirrors," in *2016 IEEE Electrical Power and Energy Conference (EPEC)*, pp. 1–5, Ottawa, ON, Canada, 2016.

[2] M. Z. Jacobson and M. A. Delucchi, "A path to sustainable energy by 2030," *Scientific American*, vol. 301, no. 5, pp. 58–65, 2009.

[3] D. Jain and M. Lalwani, "A review on optimal inclination angles for solar arrays," *International Journal of Renewable Energy Research*, vol. 7, pp. 1053–1061, 2017.

[4] Q. Zhao, P. Wang, and L. Goel, "Optimal PV panel tilt angle based on solar radiation prediction," in *2010 IEEE 11th International Conference on Probabilistic Methods Applied to Power Systems*, pp. 425–430, Singapore, 2010.

[5] F. Cruz-Peragón, P. J. Casanova-Peláez, F. A. Díaz, R. López-García, and J. M. Palomar, "An approach to evaluate the energy advantage of two axes solar tracking systems in Spain," *Applied Energy*, vol. 88, no. 12, pp. 5131–5142, 2011.

[6] A. K. Yadav and S. S. Chandel, "Tilt angle optimization to maximize incident solar radiation: a review," *Renewable and Sustainable Energy Reviews*, vol. 23, pp. 503–513, 2013.

[7] A. G. Siraki and P. Pillay, "Study of optimum tilt angles for solar panels in different latitudes for urban applications," *Solar Energy*, vol. 86, no. 6, pp. 1920–1928, 2012.

[8] P. Maddalena, A. Parretta, P. Tortora, P. Altermatt, and J. Zhao, "Simultaneous optical losses and current measurements in photovoltaic devices at variable angle of the incident light," *Solar Energy Materials and Solar Cells*, vol. 75, no. 3-4, pp. 397–404, 2003.

[9] A. Shariah, M.-A. Al-Akhras, and I. A. Al-Omari, "Optimizing the tilt angle of solar collectors," *Renewable Energy*, vol. 26, no. 4, pp. 587–598, 2002.

[10] C. Sungur, "Multi-axes sun-tracking system with PLC control for photovoltaic panels in Turkey," *Renewable Energy*, vol. 34, no. 4, pp. 1119–1125, 2009.

[11] S. Nann, "Potentials for Tracking Photovoltaic Systems and V-Troughs in Moderate Climates," *Solar Energy*, vol. 45, no. 6, pp. 385–393, 1990.

[12] K. Murat, S. Mehmet, B. Yunus, and D. Sedat, "Determining optimum tilt angles and orientations of photovoltaic panels in Sanliurfa, Turkey," *Renewable Energy*, vol. 29, pp. 1265–1275, 2004.

[13] S. Naihong, K. Nobuhiro, K. Yasumitsu, and S. Hirotora, "Experimental and theoretical study on the optimal tilt angle of photovoltaic panels," *Journal of Asian Architecture and Building Engineering*, vol. 5, no. 2, pp. 399–405, 2006.

[14] T. RunSheng and E. Lu, "The optimal angle of collectors," *Acta Energiae Solaris Sinica*, vol. 9, no. 4, pp. 369–376, 1988.

[15] P. Pangnaada and S. Chaitusaney, "Estimation of solar radiation on the tilted surfaces in Songkhla, Thailand," in *2016 13th International Conference on Electrical Engineering/Electronics, Computer, Telecommunications and Information Technology (ECTI-CON)*, pp. 1–6, Chiang Mai, Thailand, 2016.

[16] D. Vasarevičius and M. Pikutis, "Solar radiation model for development and CONTROL of solar energy sources," *Mokslas – Lietuvos ateitis*, vol. 8, no. 3, pp. 289–295, 2016.

[17] S. R. Madeti and Z. Ahmad, "Development of a MATLAB/LabVIEW model for optimal tilt angle and maximum power generation of a PV module," in *2015 International Conference on Computational Intelligence and Communication Networks (CICN)*, pp. 1493–1498, Jabalpur, India, 2016.

[18] G. Lewis, "Optimum tilt of a solar collector," *Solar and Wind Technology*, vol. 4, no. 3, pp. 407–410, 1987.

[19] A. Balouktsis, D. Tsanakas, and G. Vachtsevanos, "On the optimum tilt angle of a photovoltaic array," *International Journal of Sustainable Energy*, vol. 5, no. 3, pp. 153–169, 1987.

[20] C. A. Tirmikci and C. Yavuz, "The effect of tilt angle in solar energy applications," in *2018 2nd International Symposium on Multidisciplinary Studies and Innovative Technologies (ISMSIT)*, pp. 1–4, Ankara, Turkey, 2018.

[21] M. Iqbal, *An Introduction to Solar Radiation*, Academic Press, New York, NY, USA, 1983.

[22] P. I. Cooper, "The absorption of radiation in solar stills," *Solar Energy*, vol. 12, no. 3, pp. 333–346, 1969.

[23] J. A. Duffie and W. A. Beckman, *Solar Engineering of Thermal Processes*, John Wiley & Son, New York, NY, USA, 3rd edition, 2006.

[24] K. Bakirci, "General models for optimum tilt angles of solar panels: Turkey case study," *Renewable and Sustainable Energy Reviews*, vol. 16, no. 8, pp. 6149–6159, 2012.

[25] K. Chawyuyu, P. Buasri, R. Chatthawom, and A. Siritaratiwat, "Estimation of solar radiation and optimal tilt angles of solar photovoltaic for Khon Kaen University," in *International Electrical Engineering Congress (iEECON)*, pp. 1–4, Krabi, Thailand, 2018.

Hindawi
International Journal of Photoenergy
Volume 2021, Article ID 6692858, 19 pages
https://doi.org/10.1155/2021/6692858

Review Article

Current Status of Emerging PV Technologies: A Comparative Study of Dye-Sensitized, Organic, and Perovskite Solar Cells

Myrsini Giannouli

Telou Agra 18, 26442, Patras, Greece

Correspondence should be addressed to Myrsini Giannouli; myrtwg@gmail.com

Received 12 December 2020; Revised 11 April 2021; Accepted 26 April 2021; Published 17 May 2021

Academic Editor: Kumarasamy Sudhakar

Copyright © 2021 Myrsini Giannouli. This is an open access article distributed under the Creative Commons Attribution License, which permits unrestricted use, distribution, and reproduction in any medium, provided the original work is properly cited.

The imminent depletion of conventional energy sources has motivated the advancement of renewable energy technologies. Third-generation photovoltaic technologies, such as dye-sensitized solar cells (DSSCs), organic solar cells (OSCs), and perovskite solar cells (PSCs), are being developed as alternatives to silicon solar cells. In recent years, there has been considerable interest in the market development of these emerging photovoltaic technologies, especially for sustainable solar energy applications. However, these technologies have not yet reached the maturity required for large-scale commercialization. Further research is required in order to improve the efficiency and stability of these devices, while keeping their production costs to a minimum. In this study, a comparative assessment of DSSCs, OSCs, and PSCs is conducted and the current state of the art of these promising technologies is investigated. Advanced techniques and research trends are examined from the perspective of novel materials, device modelling, and innovative device structures. The comparative advantages and limitations of each of these photovoltaic technologies are assessed in terms of device efficiency, durability, ease of fabrication, and performance-price ratio. Emphasis is placed on assessing the potential of these solar cell technologies for sustainable solar energy applications. Finally, the future outlook of these technologies is featured, and avenues for progress beyond the state of the art are explored.

1. Introduction

Fossil fuel resources are rapidly being depleted due to increasing global energy demand. It is estimated that the worldwide reserves of fossil fuels could only last 40 years for oil, 60 years for natural gas, and 200 years for coal [1]. Solar energy is a promising alternative to conventional energy sources, providing a source of energy that is both sustainable and environmentally friendly. The photovoltaic market has experienced a rapid growth over the past two decades, and so far, it has been largely dominated by silicon-based solar cells [2]. The cost of Si-based photovoltaic cells however is high, and large-scale industrial production of this technology requires extensive processing [3].

Third-generation photovoltaic technologies such as dye-sensitized solar cells (DSSCs), organic solar cells (OSCs), and perovskite solar cells (PSCs) are being developed as alternatives to silicon solar cells [4]. In recent years, there has been increasing scientific interest in the development of these emerging photovoltaic technologies and their power conversion efficiencies (PCEs) have increased considerably, as shown in Figure 1.

The successful commercialization of emerging solar cell technologies however cannot be based solely on achieving high power conversion efficiencies (PCEs). These technologies need also to become cost-competitive with conventional power generation. The cost-effective deployment of photovoltaic (PV) systems is based on the following key requirements [6]:

(i) Minimum system cost

(ii) Maximum initial performance

(iii) Minimum loss of performance over time

These emerging photovoltaic technologies, although promising for sustainable solar energy applications, have not yet achieved large-scale commercialization [7]. Research

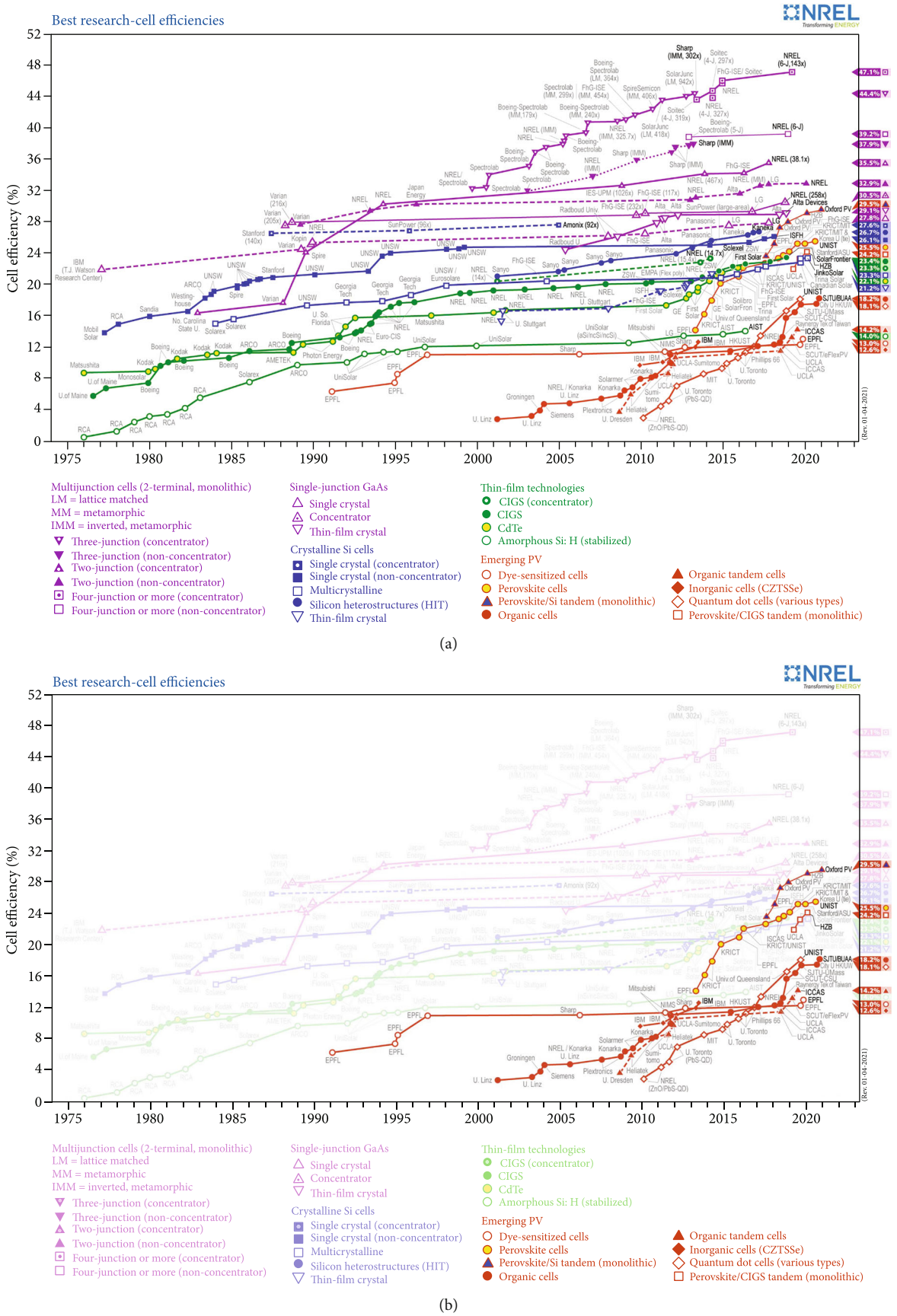

(a)

(b)

Figure 1: Best research of solar cell efficiencies: (a) all technologies and (b) emerging technologies [5].

efforts are focused on increasing the efficiency and lifetime of these devices, combined with employing low-cost materials and processes.

In this review, we present a comparative assessment of the following photovoltaic technologies: dye-sensitized solar cells, perovskite solar cells, and organic solar cells. This first section of the paper provides an introduction of the three emerging technologies and highlights the requirements that need to be met for their large-scale commercialization. Sections 2–4 give an in-depth analysis of each of these technologies in turn, starting with DSSCs, continuing with PSCs, and closing with OSCs. The main part of the review is based on the three main pillars that are used to describe and compare these emerging technologies: their current status, future outlook, and sustainable applications. In Section 2 of the review, a brief historical overview is given for each of these technologies. The main device properties and features are also presented in the second section as well as common materials and methods used for the development of each solar cell technology. The third section of the paper presents the current state-of-the-art progress for the three emerging technologies and discusses the main challenges that need to be addressed for their commercialization, as well as the focus of future research trends in terms of novel materials, device modelling, and innovative device structures. Finally, the potential of each of these technologies for sustainable solar energy applications and products is presented in Section 4. Figure 2 outlines the structure and main features of this review, including the main sources from the literature that were cited in each section of the paper.

In terms of the originality of this work, this is the first review paper that provides an in-depth comparative assessment of DSSCs, PSCs, and OSCs with emphasis on their performance, advances beyond the state of the art, and potential for commercialization. The paper highlights recent scientific progress in improving not only the efficiency but also the stability and lifetime of these devices. An additional element of originality and scientific interest is presented by discussing the issues that need to be addressed in order to achieve large-scale commercialization of each of these emerging technologies and examining future research advances that are likely to provide solutions to these problems. A comparative assessment of potential applications and products is also conducted, with the aim of ascertaining the suitability of each of these emerging technologies for various sustainable solar energy applications, ranging from wearables and small-scale devices to large-scale applications, such as vehicles and buildings.

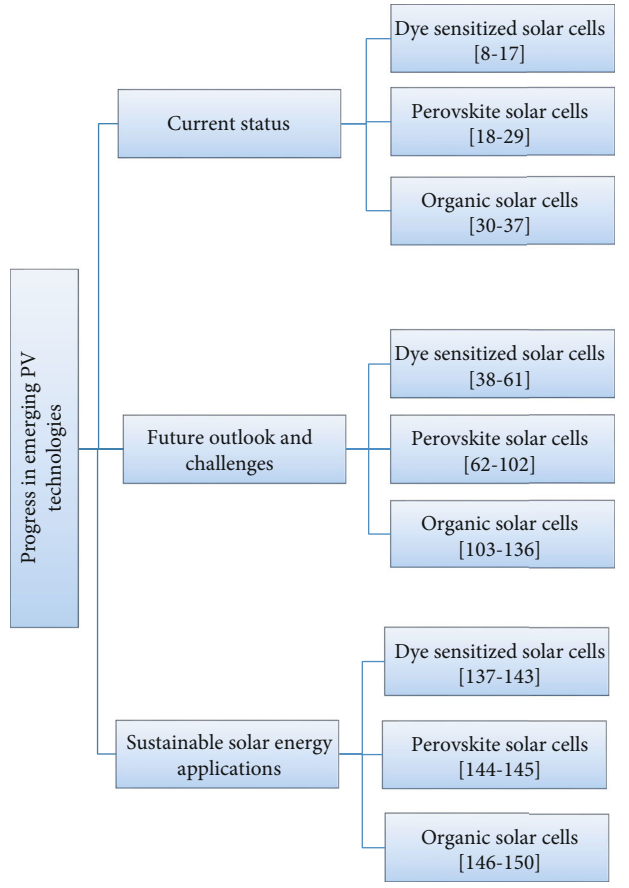

Figure 2: Outline of the main structure and literature citations of the paper.

2. Current Status

2.1. Dye-Sensitized Solar Cells. Since the pioneering work of Grätzel and O'Regan in 1991 [8], dye-sensitized solar cells (DSSCs) with the highest efficiencies approximately 13% [9, 10] have gained considerable attention for their high efficiency, their potential low cost, and simple assembly technology.

In DSSCs, the conversion of visible light to electricity is achieved through the spectral sensitization of wide bandgap semiconductors such as TiO_2, ZnO, and SnO_2 [11]. The sensitization of the semiconductors with dyes is required to improve their ability to absorb solar radiation and inject electrons into the conduction band of the semiconductor [12]. Incident light on the sensitized semiconductor surface is absorbed by dye molecules, leading to the excitation of the dye at a singlet state. Excitation of the dye molecules is then followed by Interfacial Electron Transfer (IET) into the conduction band of the semiconductor (Figure 3(a)).

In DSSCs, a platinum or platinised counter electrode is used and a liquid, gel, or solid electrolyte containing a redox couple fills the space between the two electrodes [13] (Figure 3(b)). Each part of the DSSCs considerably affects device efficiency. For that reason, research efforts have been focused on optimizing not only each part of the device individually but also the way in which the various parts of the device correlate with each other [14]. Figure 3(a) shows the sensitization process and charge transfer mechanisms in DSSCs [12], while Figure 3(b) shows the basic structure of a dye-sensitized solar cell [13].

Photoanodes have been developed using a variety of film preparation techniques, such as sol-gel, hydrothermal, electrospinning, and atomic layer deposition. A wide range of semiconductor photoanodes have been used in DSSCs, such as nanoparticle, nanorod, and nanotube [15, 16]. Various types of electrolytes have also been used in DSSCs. The main

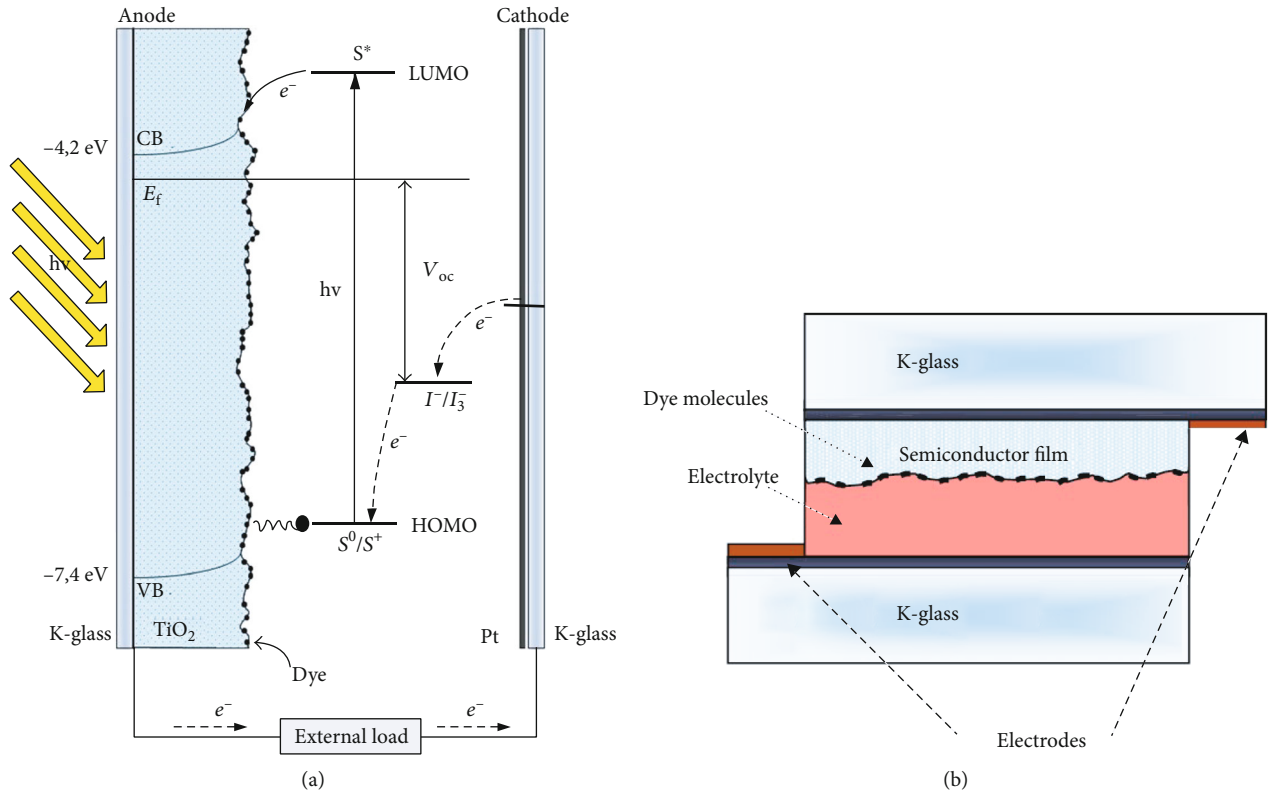

Figure 3: (a) Basic structure of a DSSC [13]. (b) Charge transfer mechanisms in DSSCs [12].

types of electrolytes used are liquid, quasi-solid, and solid electrolytes. The type of electrolyte affects device efficiency and stability considerably. Liquid electrolytes have yielded the highest efficiencies [10], but the lifetime of the resulting cells is rather limited.

The dye sensitizer used in DSSCs plays a very important role in light harvesting. Numerous dyes have been designed to broaden the absorption wavelength range of DSSCs and increase the overall efficiency of the cells. The most efficient (nonperovskite) sensitizers for wide bandgap semiconductors are metallo-organic ruthenium complexes such as N3, N719, and black dye, due to their high charge transfer efficiency to TiO_2 and light absorption in the visible spectrum [17].

2.2. Perovskite Solar Cells. Recently, organic-inorganic hybrid perovskites have gained considerable research attention due to advantages such as high electron and hole mobility (10-60 $cm^2\ V^{-1}\ s^{-1}$), bandgap tunability, long carrier diffusion length (~1 μm), and low exciton binding energy (30-50 meV) [18]. Apart from these advantages, perovskite solar cells (PSCs) can be produced using low-cost processes and materials and can even be manufactured on flexible substrates using roll-to-roll processes [9, 19]. PSCs thus have the potential to become one of the highest-efficiency and at the same time lowest-cost photovoltaic technologies on the market within the next few years and can even replace conventional Si-based solar cells. The market potential of PSCs though is as yet largely unexplored, and further research is required before this technology will become sufficiently mature for large-scale commercialization.

Organic-inorganic hybrid halide-based perovskites are a group of materials with the structure ABX_3, where A is an organic cation ($CH_3NH_3^+$ or $NH_2CH_3NH_2^+$), B is a divalent cation (Pb_2^+ or Sn_2^+), and X is a monovalent halide anion (I^-, Br^-, or Cl^-) [20].

Perovskite solar cells were originally developed from dye-sensitized solar cells. In 2009, Kojima et al. used perovskite as a sensitizer in liquid-based TiO_2 DSSCs and achieved a PCE of 3.2% and 3.8% for devices sensitized with $(CH_3NH_3)PbBr_3$ and $(CH_3NH_3)PbI_3$, respectively [21]. Two years later, Im et al. reached an efficiency of 6.5% by developing quantum dot solar cells using $(CH_3NH_3)PbI_3$ as a sensitizer [22]. However, these liquid-based solar cells presented stability issues since perovskites tend to degrade rapidly in liquid electrolytes. This issue was resolved in 2012 by Kim et al. who replaced the liquid electrolyte with the solid material spiro-MeOTAD (2,20,7,70-tetrakis(N,N-di-pmethoxyphenylamine)-9,90-spiro-bifluorene), which acted as a hole-transporting material (HTM) [23]. These solid-state devices achieved a PCE of 9.7%, and their increased stability marked a breakthrough for the PSC technology. The first PSC device architectures followed the typical structure of DSSCs in which the perovskite material played the role of the dye sensitizer. Device architectures then advanced to mesoscopic structures with the replacement of the liquid electrolyte with the aforementioned solid hole-transporting layer. Device architectures later evolved to planar structures with the perovskite material sandwiched between electron- and hole-transporting layers. Figure 4 shows various PSC device structures, including conventional n-i-p or inverted p-i-n formation [18].

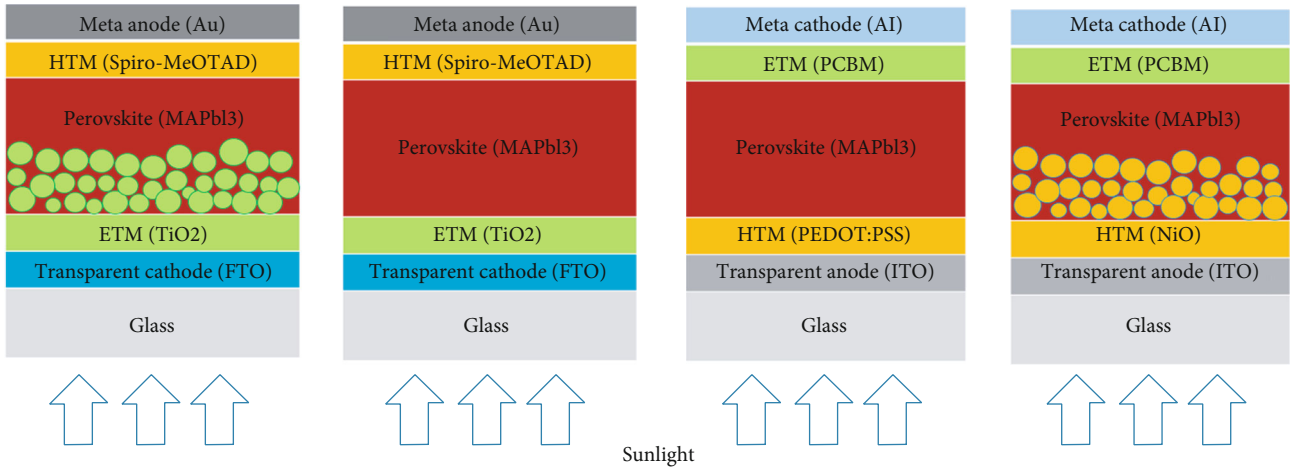

Figure 4: Perovskite solar cell architecture in the (a) n-i-p mesoscopic, (b) n-i-p planar, (c) p-i-n planar, and (d) p-i-n mesoscopic structures [18].

Femtosecond transient absorption spectroscopy studies were conducted in order to investigate electron injection dynamics in solid-state PSCs. Lee and coworkers [24] compared electron injection between devices containing a conducting (TiO_2) and a nonconducting (Al_2O_3) layer. They did not observe significant differences between the two types of cells and even achieved efficiencies of 10.9% with Al_2O_3-based devices, indicating that an electron injection layer is not required in PSCs and that electron transfer can occur in the perovskite layer.

Within the next few years, perovskite solar cells have demonstrated a remarkable progress in efficiency. In 2013, organolead halide perovskite solar cells were produced with efficiencies exceeding 15% [25, 26]. A year later, a PCE of 16.2% was achieved using a mixed solvent to optimize the perovskite layers [27]. The same year, Zhou et al. optimized perovskite layers further, by lowering the defect density of the films. They used low-temperature processing steps to control humidity while the perovskite film formed from lead chloride and methylammonium iodide and achieved a maximum cell efficiency of 19.3% [28]. More recently, Saliba and coworkers [29] incorporated inorganic cesium in the perovskite layer and produced triple-cation perovskite compositions with a stabilized power output of 21.1% and ~18% after 250 hours under operational conditions. This year, power conversion efficiencies of perovskite solar cells in excess of 25% have been reported and certified [5].

2.3. Organic Solar Cells. Organic photovoltaics represent a low-cost alternative to silicon solar cells, due to the high optical absorption coefficients of organic semiconductors, which enable the development of efficient photovoltaic devices with layers only a few nanometers thick [30]. Since polymers are usually processed in the liquid phase, simple printing and coating techniques can be utilized for their production. Organic solar cells have several promising advantages, such as their lightweight, large surface area, low production cost, and ability to be processed on flexible substrates [31]. The aforementioned advantages of OPV devices have led to increased interest in their development and, as a result, to considerable progress towards improving their performance [32]. The power conversion efficiency (PCE) of OPVs has increased from 6% in 2009 [33] to over 16% within a decade [34]. Recently, efficiencies in excess of 18% were reported and verified for organic solar cells [5].

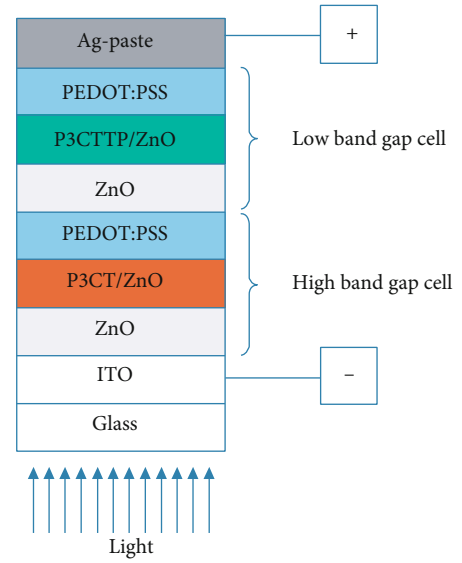

Figure 5: A schematic of an organic solar cell comprising eight layers with electrical connections [3].

In organic solar cells, the absorbing layer is based on certain organic semiconductors (OSC). The basic structure of OPVs consists of photoactive organic layers comprised of p-type and n-type semiconducting polymers (Figure 5). For organic materials to become conducting or semiconducting, a high level of conjugation is required. The highest occupied molecular orbitals (HOMOs) and lowest unoccupied molecular orbitals (LUMOs) in these materials correspond to the respective valence and conduction bands of conventional inorganic semiconductors [35, 36]. Between the highest occupied molecular orbital (HOMO) and lowest unoccupied molecular orbital (LUMO) of the OSC is an energy gap (the

Table 1: Highest recorded efficiencies and device characteristics for DSSCs, PSCs, OPVs, and tandem PSCs [5].

	Efficiency (%)	Active layer/absorber	Carrier transporting material	Innovative materials/techniques	Institution/ company
DSSC	13.0	TiO_2 dye-sensitized semiconductor	Cobalt redox couple electrolyte	Panchromatic porphyrin sensitizers	EPFL
PSC	25.2	FAPbI 3-based perovskite	Spiro-MeOTAD	Minimizing the deformation of photoactive layers by changing the type and ratio of ions	UNIST
Tandem PSC/Si	29.5	Monolithic perovskite PbI_2-based top cell/Si bottom cell	Methyl-substituted carbazole monolayer/C_{60}	Self-assembled carbazole-based monolayer with methyl group substitution	Oxford PV
Tandem PSC/CIGS	24.2	Monolithic two-terminal triple-cation PSC/CIGS	Poly [bis(4-phenyl) (2,4,6-trimethylphenyl)amine] (PTAA)/C_{60}	Rubidium-based self-assembled monolayer	HZB
OPV	18.2	PBDB-T-2F:BTP-eC9	PEDOT:PSS	Chlorinated nonfullerene acceptor	SJTU/BUAA

bandgap of the semiconductor). A high level of conjugation lowers the bandgap and allows electron excitation by visible light from HOMO to LUMO.

Electron donor materials (p-type polymers) originally used in OPVs included poly(p-phenylenevinylene) (PPV), poly(2-methoxy-5-(2-ethylhexyloxy)-1-4-phenylenevinylene) (MEH-PPV) [36], and, more recently, poly(3-hexylthiophene) (P3HT) [37]. The most common organic acceptors (n-type organic semiconductors) in OPVs were originally fullerene-based materials, such as [6,6]-phenyl-C61-butyric acid methyl ester (PCBM) [2].

In most OPV devices, poly(ethylenedioxythiophene)-poly(styrenesulfonic acid) (PEDOT:PSS) was used for the transfer of holes between the transparent electrode and the active layer for normal structures and between the metal electrode and the active layer for inverted structures. PEDOT:PSS is a hole-transporting layer (HTL) that blocks electrons while transporting holes to the transparent anode of the OSCs, thus enhancing charge collection [2].

Table 1 shows comparative efficiencies and device characteristics for cells with the highest certified efficiency to date, for DSSCs, PSCs, OPVs, and tandem PSCs [5].

3. Future Outlook and Challenges

3.1. Dye-Sensitized Solar Cells. The efficiency of DSSCs has not increased significantly over the past few years (see Figure 1). There are several reasons for this lack of progress in the area of DSSCs, such as inherent limitations imposed by the materials, interfaces, and device architectures of DSSCs [38]. There has also been a shift of scientific interest in other promising solar cell technologies, especially in perovskite cells, which are considered the successors of DSSCs, since perovskite materials were originally used as sensitizers in DSSCs. However, there are still areas of interest in the future development of DSSCs that are being explored with the aim of improving their performance.

One of the most important issues that hinder the commercialization of DSSCs is their low stability [39]. Liquid electrolytes containing a redox couple, such as iodide/triiodide, tend to evaporate easily, so a number of solid-state electrolytes have been developed in order to limit the stability issues caused by the evaporation of liquid electrolytes [40, 41]. In DSSCs, the liquid redox electrolyte can be replaced by a solid hole-transporting material in order to make solid-state DSSCs [42]. Promising results have been reported with molecular organic hole conductors such as spiro-MeO-TAD, conduction polymers such as PEDOT, and metal complexes [43]. Polymer gel electrolytes containing redox couples (such as poly(acrylonitrile), poly(vinyl chloride), and poly(vinylidene fluoride)) have been used as quasi-solid-state electrolytes to overcome the volatilization and leakage problems of liquid electrolytes [44]. Devices developed using solid electrolytes have shown relatively high stability but not as high efficiency as those filled with liquid electrolytes (13.0% PCE) [45]. Recent optimization led to a recorded efficiency of 11.7% [41]. In addition, a number of sealing techniques and sealant materials, such as Surlyn® and Bynel® foils, have been employed to limit the evaporation of liquid electrolytes and increase device lifetime [46].

In terms of the dye sensitizer used, a large number of dyes have been developed and tested for use in dye-sensitized solar cells. As mentioned above, amongst the most efficient dye sensitizers are metallo-organic ruthenium complexes. Metal-free natural dyes, such as porphyrins, or coumarins have also been used successfully for the sensitization of semiconductor films in DSSCs. These dyes do not yield efficiencies as high as those achieved using ruthenium complexes but are more environmentally friendly and tend to have lower toxicity compared to Ru-based complexes. In addition, many research efforts are focused on the synthesis of novel dyes for dye-sensitized solar cells. A number of novel dyes have been developed and tested for DSSCs, with promising results, such as carbazole, fluorine, indolin, oligothiophene, or boradiazaindacene- (BODIPY-) based dyes [46].

The ideal sensitizer for DSSCs should be panchromatic, absorbing all light below a threshold wavelength of approximately 920 nm. However, each dye individually absorbs only a small portion of the visible spectrum of solar radiation, thus limiting the light-harvesting ability of the cells. Alternatively,

cosensitization with two or more dyes, which have complementary absorption spectra, can be used to increase the range of absorption of the solar cells. This results in the conversion of photons into electrons at a wider region of the solar spectrum. Cosensitization thus increases the incident photon-to-current efficiency (IPCE) and consequently the current produced by the device [47]. Cosensitization is a successful way to improve the efficiency of DSSCs, and recording devices are usually based on cosensitized solar cells [46, 48]. Zuo and coworkers [49] developed a blend of N3 dye with a small quantity of squarylium cyanine (SQC). They reported an increase in the efficiency of TiO_2 cells sensitized with this dye blend to over 10%, due to increased dye regeneration in the dye blend. Yum and coworkers [50] also used a squaraine dye to sensitize solid-state TiO_2 cells together with the dye N877 and reported an efficiency of 1.8% for the cosensitized cells, which was over 20% higher than the efficiency of cells sensitized with each single dye. Ogura et al. [51] used a blend of two dyes with complimentary absorption spectra (D131 and black dye) to sensitize TiO_2 films and achieved efficiencies of the order of 11%, which was higher than the efficiency of cells sensitized with each one of the dyes. Similarly, Saxena et al. obtained a 4.7% efficiency for TiO_2 cells sensitized with a mixture of N3 and a rhodamine dye and reported a considerable increase in the performance of the cells compared to those sensitized with a single dye [52]. Another research group [53] developed a blend of five different dyes with complementary absorption spectra. ZnO films sensitized with this blend had an efficiency of approximately 7.9%, which was higher than the efficiency achieved with each individual dye. Porphyrin dyes have also been used successfully in cosensitization. Sharma et al. [4] synthesized a novel porphyrin dye consisting of a zinc-metallated porphyrin unit and used it to sensitize TiO_2 films, resulting in a PCE of 4.72%. When this dye was used together with a tertiary aryl-amine D, which exhibits complementary light absorption characteristics with the porphyrin dye, the solar cell efficiency was increased to 7.34%. Shibayama et al. [54] combined a black dye with an organic dye possessing a pyridine-binding group and demonstrated that the dyes adsorbed to different binding sites, thus increasing dye loading and cell performance.

Most research efforts on the cosensitization of DSSCs are focused on developing a dye cocktail with panchromatic absorption properties. Alternatively, sequential cosensitization can be used, in which the semiconductor is sensitized with one dye after another. Fan et al. reported that the order of sensitization affects the efficiency of DSSCs considerably. They achieved efficiencies of up to 8.14% by sequential cosensitization of TiO_2 films with porphyrin and organic dyes and found that cosensitization can increase device efficiency up to 61% compared with devices sensitized with a single dye [55]. Their conclusions agree with our own findings [56], in which we investigated the cosensitization of ZnO films by organic dyes, such as porphyrins and coumarins. We found that sequential sensitization with three organic dyes can yield efficiencies over 4 times greater than those of cells sensitized by any of the single dyes and almost twice as high as those of cells sensitized with a blend of these dyes. We observed that the order of sensitization and the sensitization time play a significant role in increasing device efficiency by enhancing device IPCE and dye loading. Cosensitization can thus be optimized to achieve maximum light harvesting and improve device performance.

Another approach that has been used in recent years to increase the efficiency of DSSCs is the incorporation of quantum dot (QD) nanoparticles into the cell. This process is based on the plasmonic resonance that occurs when electrons at the interface between negative and positive permittivity materials are excited by incident light. Metal nanoparticles, such as Ag or Au, are incorporated into the photoanode of the DSSCs in order to create a nanoprism that scatters light within the device. Jun et al. [57] incorporated Au nanoparticles into the commercial TiO_2 nanopowder that was used to create the photoanode and achieved an increase in efficiency by approximately 50% compared to devices that did not contain Au nanoparticles. Bakr et al. incorporated Au nanoparticles prepared by pulsed Nd:YAG laser ablation at 1064 nm in a solution of Z907 dye [58]. The addition of the synthesized gold nanoparticles to the dye resulted in an increase in device efficiency from 1.284% to 2.357%, due to increased light absorption from the gold nanoparticles. More recently, Sim et al. [59] achieved an increase in device efficiency from 6.3 to 7.2% by developing a three-dimensional transparent photoanode and a scattering layer, which was used to trap and disperse incident light within the device.

Table 2 summarizes some of the main materials, components, and techniques used for the development of novel dye-sensitized solar cells with improved device performance.

3.2. Perovskite Solar Cells. The performance of perovskite solar cells has been improving rapidly, with efficiencies in excess of 28% predicted in the near future for perovskite PSCs with ideal transport layers [60]. The performance of PSCs can be improved considerably through the optimization of the various materials and processes involved in their development [61]. Currently, many research efforts are focused on improving the morphology and stability of the perovskite layer. In terms of morphology, perovskite films should ideally be compact and free of pinholes, contain large grains, and have a high degree of crystallinity. The morphology of the perovskite layer can be controlled through a number of processes, such precursor solution processing and aging [62], perovskite film annealing [63], and incorporation of additives in the perovskite material [64]. It has also been demonstrated that optimizing the crystallinity of the perovskite absorption layer is crucial to the development of perovskite solar cells with high power conversion efficiencies [65], as improved crystallinity leads to enhanced film uniformity, thus increasing device efficiency [66].

Another area of interest is interface engineering, and several research groups report improved device efficiency and stability through interface optimization. Wu et al. introduced a thin layer of poly(ethylene oxide) as an interfacial layer in formamidinium-cesium-based PSCs, in order to modify the energy levels at the interface between the perovskite and the carbon electrode [67]. They report an increase of 2.5% in the efficiency of the PSCs that contain the interfacial level, due to improved energy alignment at the perovskite/carbon

Table 2: Novel materials and methods used for the development of DSSCs.

Photoanodes	Electrolytes containing redox couple	Sensitizers	Sensitization techniques
Wide bandgap semiconductors (TiO_2, ZnO, and SnO_2)	Liquid electrolytes (e.g., iodide/triiodide) up to 13.0% PCE	Metallo-organic ruthenium complexes (N3, N719, and black dye)	Cosensitization using dyes with complementary absorption spectra
Different photoanode layer morphologies such as nanoparticle, nanorod, and nanotube	Solid electrolytes (spiro-MeOTAD, PEDOT, and metal complexes) up to 11.7% PCE	Natural or organic dyes (porphyrins, coumarins, rhodamines, etc.)	Dye combinations: Ru complexes/squaraine dyes, N3/Rhodamine B, tertiary aryl-amine D/zinc-metallated porphyrin—11% PCE
Film deposition techniques: sol-gel, hydrothermal, electrospinning, and atomic layer deposition	Quasi-solid electrolytes (e.g., poly(acrylonitrile), poly(vinyl chloride), and poly(vinylidene fluoride))	Novel synthetic dyes (e.g., chlorin, indolin, or BODIPY-based)	Sequential cosensitization with multiple dyes (e.g., porphyrins, coumarins, and Ru complexes) up to 8.14% PCE
		Synthesized panchromatic dye sensitizers up to 13.0% PCE	Incorporation of QD nanoparticles, such as Ag or Au up to 7.2% PCE

interface. Lu et al. [68] developed cm-sized PSCs with power conversion efficiencies of up to 20% using benzenethiol molecules to modify the interface between the perovskite layer and the spiro-MeOTAD hole-transporting layer. The resulting devices showed improved efficiency and stability due to enhanced charge extraction and reduced charge recombination.

In regard to the hole-transporting layer, research trends focus on the development of inorganic p-type semiconductor materials to replace the organic hole-transporting layer that is commonly used in PSCs. Inorganic materials, such as CuI, NiO, and CuSCN, exhibit several advantages over organic materials, such as wide bandgap, high hole mobility, and simple processing. Seo et al. [69] used undoped NiO films as the hole-transporting layer in hybrid organic-inorganic PSCs and achieved power conversion efficiencies of 16.4%. Zhang et al. reported power conversion efficiencies of 18.5% for perovskite solar cells with the inorganic p-type semiconductor $CuGaO_2$ as the hole-transporting layer [70]. The resulting PSCs had also high long-term stability, retaining high efficiency after 30 days of continuous operation in ambient conditions.

Cosensitization can also be used to improve the light-harvesting ability and PCE of perovskite solar cells. The use of a dye sensitizer is not required in PSCs, since perovskite materials can simultaneously act as the absorber material and the electron injection layer. However, a dye sensitizer can be used in order to broaden the absorption wavelength range of PSCs. In PSCs, the absorption onset occurs at a wavelength of 800 nm, as measured by incident photon-to-electron conversion efficiency (IPCE) [71]. At this wavelength, the theoretical maximum photocurrent density is 27.2 mA cm^{-2} when assuming no light loss by reflection at the transparent conductive substrate. Light loss should be taken into account though practical devices, which leads to a maximum photocurrent in the range of 23.1–21.8 mA cm^{-2} [72]. Cosensitization can increase the range of absorption of perovskite solar cells, resulting in the conversion of photons into electrons at a wider region of the solar spectrum [52]. This can enhance the incident photon-to-current efficiency and consequently the current produced by the device [47]. Zhang et al. used metallophthalocyanines to sensitize $CH_3NH_3PbI_3$ solar cells and reported a PCE of almost 14%, which was increased by 28% compared to the efficiency of the devices that used only the perovskite as the absorption material [73]. They attributed the enhanced efficiency of the cosensitized devices to charge injection occurring from both sensitizers, possible energy transfer from high energy perovskite to the lower energy dye, and potential decrease in series resistance. Recently, Balachandran et al. [74] developed methyl ammonium lead bromide ($CH_3NH_3PbBr_3$) perovskites doped with the N719 dye. They reported a remarkable increase in efficiency, from 1% for the undoped cells to 4.8–6.8% for devices cosensitized with N719, demonstrating the high potential of cosensitization in improving device performance.

Perovskite materials have certain properties that make them ideal for use in tandem with other solar cell technologies: complementary solar spectral absorption, bandgap tunability, and ease of processing and process compatibility with silicon and CIGS ($Cu(In,Ga)Se_2$) technologies.

Recently, two spin-off technologies of perovskite solar cells have attracted the attention of the scientific community: perovskite/Si tandem and perovskite/CIGS tandem solar cells. From Figure 1(b), it can be observed that, although these technologies have been investigated for only a few years, the efficiencies recorded for these cells are very high and rising at an impressive rate. Currently, Oxford PV holds the highest certified efficiency recorded for perovskite/Si tandem cells and the Helmholtz-Zentrum Institute in Berlin for perovskite/CIGS cells, with 29.5% and 24.2%, respectively [5]. There are two common tandem solar cell architectures: mechanically stacked and monolithic. A mechanically stacked cell consists of two independent solar cells one on top of the other, while a monolithic cell is comprised of a two-terminal device built in series on a single substrate. The monolithic structure is the one most commonly used in industry and preferred from a technological and performance perspective.

Monolithic perovskite/Si tandem cells have attracted huge interest because they capitalize on the mature silicon solar cell industry and also have the potential to overcome the theoretical efficiency limit of single-junction silicon solar cells [75]. Perovskite/Si solar cells comprise two cells that work in tandem: a top perovskite cell and a bottom Si cell [76]. Silicon converts mostly the red part of the solar spectrum to electricity, while perovskite materials utilise the blue portions of the spectrum. A tandem solar cell made of stacked silicon and perovskite can thus achieve higher efficiency than each individual cell on its own, and solar cell efficiencies of over 30% can be achieved [77]. Photocurrent matching between the two subcells is a prerequisite to achieve high efficiency in monolithic tandem cells [78]. The efficiency of a perovskite/Si monolithic tandem cell can be enhanced by adjusting the electrical and optical properties of the electron transport layer and optimizing the bandgap and the optical density of the perovskite absorber [79].

Monolithic perovskite/CIGS tandem solar cells have a similar architecture to perovskite/Si cells, with a perovskite top cell fabricated directly on an as-grown CIGSe bottom cell [80]. Semitransparent perovskite materials have been developed using low-temperature processes and used in tandem with CIGS solar cells, reporting power conversion efficiencies in excess of 20% [81]. The combination of perovskite and CIGS materials with complementary absorption spectra can potentially lead to PCEs over 30%. To ensure optimum device efficiency, the interconnecting layer in tandem cells should have effective electrical connection as well as high optical transparency [82].

Even though rapid progress has been demonstrated in the development of highly efficient perovskite solar cells, a number of issues need to be addressed before they can become a market-competitive technology. The main drawbacks of perovskite solar cells are their poor stability and high toxicity. The low stability of PSCs, especially in conditions of high moisture, extensive illumination, and high temperatures, is one of the biggest challenges faced for the successful commercialization of this technology. Several studies are currently focused on addressing these issues by studying the degradation mechanisms in perovskite materials and other device layers. Research towards improving the stability of these cells is focused on two main strategies: (a) improving the intrinsic stability of the device and (b) protecting the device via external means. The stability of PSCs can be improved intrinsically especially by changing the component materials of the absorbing layer. The organic cations most commonly used in the absorber, especially methylammonium, are susceptible to moisture and heat degradation [83]. Devices that incorporate mixed-cation systems, such as rubidium or caesium, into the perovskite material have shown increased efficiency and stability [29]. Mixed-halide and mixed-cation systems have also exhibited high stability. Saliba et al. reported a 19% power conversion efficiency for mixed-halide and quadruple-cation PSCs that retained 95% of their efficiency for 500 hours under illumination at 85°C [84]. More recently, Matsui et al. reported efficiencies in excess of 20%, for cm-sized cells that retained 92% of their power conversion efficiencies after 1000 h in high heat/moisture conditions. They incorporated Rb in the perovskite absorber layer, which increased the thermal stability of the resulting solar cells [85].

The optimization of interfacial layers can also lead to increased stability, for example, by replacing materials that are sensitive to UV radiation, such as TiO_2, with more UV-stable interfacial layers, such as SnO_2. Zhu et al. [86] introduced ammonium chloride at the TiO_2/perovskite interface, thereby improving charge extraction and increasing device efficiency and stability. Christians et al. [87] developed a cell with optimized interfacial layers that retained 94% of its peak efficiency after 1000 hours of unencapsulated operation in ambient air conditions.

Many research efforts also concentrate on improving the stability of PSCs through external modifications, such as the encapsulation of the cell. A very effective method of encapsulation is to cover the cell with a glass film and seal it with an epoxy resin. However, this technique is not compatible with roll-to-roll processing and thus not recommended for large-scale commercial devices. Polymer sealants on the other hand have been used successfully to increase the stability of perovskite solar cells. A lifetime of 10,000 hours has been reported using polyethylene terephthalate encapsulation [88], while cells coated with a layer of luminescent photopolymer maintained 3-month lifetimes in outdoor conditions [89]. Bush et al. [90] reported a power conversion efficiency of 23.6% for a monolithic perovskite/silicon tandem cell that operated successfully for 1000 hours under a damp heat test (85°C and 85% relative humidity). In addition, self-assembled monolayers, which are ordered arrays of organic molecules, have been utilized as interfacial layers in PSCs, in order to improve their efficiency and stability [91].

Another important issue faced in the commercialization of PSCs is the presence of lead in the absorber of most perovskite solar cells. Lead is a material with widely known environmental and health impacts. Lead has high toxicity and is hazardous both for the environment and human health, which has led to its gradual elimination from most devices and components, such as batteries. A number of research groups are currently focused in discovering successful alternatives to lead in perovskite solar cells. Lead-free PSCs are being developed by substituting lead with another element that has lower toxicity. Suitable replacements for lead in PSCs need to meet a number of criteria, such as the crystal structure and the quantum mechanical properties of the materials considered. The aim is to develop environmentally friendly solar cells with similar efficiency and stability as lead-based PSCs. A number of materials, such as transition metals, alkaline-earth metals, and rare-earth ions, have been investigated, with limited success so far. Various divalent metal cations have also been tested for use in PSCs, the most successful of which have been found to be Ba^{2+}, Ca^{2+}, and Sr^{2+} [92]. Strontium in particular has an ionic radius similar to that of lead, and preliminary experiments have shown that the compound resulting from the exchange of Pb with Sr ($CH_3NH_3SrI_3$) has similar crystal structure and bonding patterns to lead-based compounds [93]. Double perovskites have also been shown to have considerable potential for developing lead-free solar cells. Compounds such as

Table 3: State-of-the-art materials, processes, and methods used for the development of PSCs.

Photoanodes	Hole-transporting layer and interfaces	Device architecture	Improved stability
Improved morphology: precursor solution aging, film annealing, and incorporation of additives	Organic hole-transporting layer (such as carbon and spiro-MeOTAD)	Single-junction perovskite solar cells	Mixed-cation systems (e.g., Rb and Cs), or mixed-halide and mixed-cation systems, retain 92% of PCE after 1000 h
Optimization of absorption layer crystallinity and film uniformity	Inorganic p-type semiconductor materials, e.g., CuI, NiO, CuSCN, and $CuGaO_2$, up to 18.5% PCE	Perovskite/CIGS tandem cells: perovskite top cell fabricated on CIGS bottom cell Up to 24.2% PCE	Interfacial layers with UV-stable materials (SnO_2, ammonium chloride) retain 94% of efficiency after 1000 h
Lead-free PSCs: transition metals, alkaline-earth metals, rare-earth ions, and divalent metal cations (Ba^{2+}, Ca^{2+}, and Sr^{2+})	Interface engineering and optimization (e.g., incorporation of benzenethiol molecules for increased charge transport)—20% PCE	Perovskite/Si tandem cells: top perovskite cell and bottom Si cell Up to 29.5% PCE	Use of self-assembled monolayers as interfacial layers
Double lead-free perovskites (Cs_2AgSbI_6, $Cs_2BiAuBr_6$, and Cs_2BiCuI_6)	Energy level modification by introducing an interfacial layer, such as poly(ethylene oxide)	Mechanically stacked and monolithic tandem device architectures	Encapsulation: glass film/epoxy resin, polymer sealants (polyethylene terephthalate), and lifetime > 10,000 h

Cs_2AgSbI_6, $Cs_2BiAuBr_6$, and Cs_2BiCuI_6 have long recombination lifetime and optimum bandgap and have been reported to exhibit adequate stability even at high temperatures [94, 95]. So far, the successful replacement of lead in PSCs has been rather limited, and future efforts are required in this area, in order to develop efficient and stable lead-free PSCs. Efforts to reduce the content of lead in PSCs rather than completely eliminating it have been more successful. Zhu et al. reported a power conversion efficiency of 15.20% for PSCs containing an alloy of Sn and Pb in the absorbing layer, developed from a solution in DMSO and DMF [96].

Table 3 summarizes some of the main materials, components, and techniques used for the development of novel single-junction perovskite and tandem perovskite cells with enhanced device performance.

3.3. Organic Solar Cells. For several years, research on OPVs was focused mainly on the design of low bandgap materials with optimum solar spectrum absorption in order to increase the PCEs of OPV cells [97, 98]. Recent progress in OPVs is dominated by the development of low bandgap nonfullerene polymer acceptors (NFAs) [99–101]. Nonfullerene acceptors tend to exhibit high tunability in terms of their absorption spectra and electron energy levels, which allows for increased optimization of the resulting solar cells. Most of the top-performing NFAs, such as IT-4F36, IEICO-4F37, and BT-CIC13, contain fluorine or chlorine atoms, and PCEs of over 16% have been obtained with chlorinated NFA-based OPV cells. Cui et al. [102] used the chlorinated nonfullerene acceptor BTP-4Cl in a blend with PBDB-TF to develop OPVs of an inverted structure with PCEs in excess of 16%. More recently, the same group synthesized new NFAs based on BTP-4Cl through side chain engineering. The new materials exhibited improved solubility, which allowed for efficient processing through blade coating techniques and exhibited efficiencies of over 15% in a blend with PBDB-TF [34]. Current research in the area of nonfullerene OPVs is focused mainly on the development and optimization of nonfullerene donor-acceptor pairs with matching properties to increase OPV performance. Examples of copolymers that have been used successfully as donors combined with nonfullerene acceptors in OPVs include PM6, P2F-EHp, D16, and PTQ10. Liu et al. recently used D16, which is based on a fused-ring thiolactone unit, as a donor in a blend with Y6 to develop OPVs with over 16% efficiency and D18 in a blend with Y6 to achieve efficiencies of over 18% [103].

The effect of blend morphology on device performance is another parameter that has been investigated extensively in recent years [104]. Vertical and lateral phase segregation between the p-type and n-type semiconducting polymers in the blend has been shown to affect charge transport within the active layer [105]. Recent studies have been aimed at improving device performance by manipulating vertical phase segregation through the introduction of various interfacial layers. The addition of interlayers, especially between the active layer of the OPVs and the hole-transporting layer, has been shown to improve energy level alignment and facilitate charge transfer throughout the device. Cao et al. [106] used PBDTTPD-COOH as an interfacial modifier between the active layer and the hole-transporting layer, in PBDTTPD-, PCDTBT-, and PTB7-based OPVs. They concluded that the improvement in OPV performance through the addition of the interlayer was due to changes in energy level alignment and vertical phase segregation, as well as in blend composition at the PBDTTPD-COOH/donor interface. Inorganic semiconductors, such as TiO_2 and ZnO, have also been used as interlayers to improve charge transfer and collection and prevent hole formation in OPVs. Liu et al. [107] used Al-doped ZnO layers to create a semiconductor-metal nanojunction in $PC_{71}BM$-based OPVs. The improved electron extraction and transport resulting from the addition of the interlayer led to an increase in efficiency from 7.89% to 9.81%. Another class of materials that can be used as interlayers in OPVs is conjugated polyelectrolytes. These are composed of side chains with ionic functional groups and conjugated backbones and have improved hole

transport and collection properties that can help boost device performance [108].

Research on small-molecule organic solar cells has also gained traction in recent years. One of the disadvantages of typical polymer-based OPVs is their relatively poor reproducibility, which hinders scalability, and is one of the main obstacles towards their commercialization. Small-molecule OPVs are a promising technology, due to their well-defined molecular structures and relatively high reproducibility compared to polymer OPVs [109]. On the other hand, small-molecule devices tend to have lower PCEs than their polymer counterparts and are usually developed through high-vacuum processes, which are not as cost-effective as solution processes that are available for polymeric materials. Recently, a number of breakthroughs in the area of small-molecule OPVs have led to a considerable increase in their efficiency, with PCEs in excess of 15% reported and certified [110]. Most research efforts in this area are directed towards synthesizing new donor and acceptor small-molecule materials with optimized properties for use in OPVs. Liu et al. introduced fluorine atoms in small-molecule donors to achieve increased high open-circuit voltage in OPVs with the polymer F-2Cl used as an acceptor [111]. Qiu et al. synthesized new donor materials and used side chain engineering of these materials to optimize active layer morphology in a blend with Y6, resulting in efficiencies of over 14% [112]. Similarly, Zhou et al. [113] synthesized a new small-molecule donor material and used a narrow bandgap small-molecule material as an acceptor, to achieve efficiencies over 14%. The increased power conversion efficiencies achieved in this study were attributed to the optimization of the hierarchical morphologies of the donor and acceptor materials. Recently, Hu et al. developed all-small-molecule OPVs with PCEs in excess of 15%. They used fullerene derivatives as additives in a BTR-Cl:Y6 active layer, which resulted in decreased electron recombination and high device fill factor [114].

Another area of increased interest in recent years is the development of ternary organic solar cells. In ternary OPVs, three organic semiconductors are used in the active layer, instead of two. The motivation behind introducing another semiconducting polymer in the device is to improve light absorption in the cell [115]. Ternary cells can be designed with complementary absorption bands to maximise the range of the solar spectrum that the cell absorbs and enhance its power conversion efficiency. In addition, the correlation between the energy levels of the three components of the ternary cells plays a crucial role in the development and optimization of these cells [116]. Good energy level alignment between the components of the ternary cells leads to increased charge transport and collection and thus improved device efficiency. Currently, research efforts are focused primarily on the synthesis and optimization of new donor and acceptor materials with synergetic properties that are suitable for ternary OPVs, in terms of their absorption, energy levels, and compatibility [117]. Ternary OPVs are ideally applicable in NFA cells, achieving efficiencies in excess of 14% [118]. Ren et al. [119] developed a strategy based on the layer-by-layer sequential deposition of a polymer donor and two non-fullerene acceptors. Using the layer-by-layer method allowed for the optimization of the polymer blend and led to the formation of a network structure with increased charge generation, transport, and collection properties. Recently, Zhan et al. [120] reported a power conversion efficiency in excess of 17% for a ternary organic solar cell based on the polymer acceptor alloy Y6:BTP-M, with PM6 as the polymer donor. Similarly, An et al. [121] achieved power conversion efficiencies of over 17% for organic solar cells based on an alloy of the polymer acceptors MF1 and Y6 with PM6 as the polymer donor.

The main challenge towards the commercialization of both fullerene and NFA OPVs is scalability [122]. OPVs can be manufactured using more scalable techniques than spin coating, such as spray coating, blade coating, and inkjet printing. Large-area OPV cells developed using printing methods however have considerably lower PCEs than those of small-area spin-coated devices [34]. Another important issue is the long-term stability of organic solar cells, especially under outdoor weather conditions [123]. A large number of research efforts are currently focused on addressing scalability and stability issues to enable future commercialization of OPVs. In recent years, there has been increased interest in understanding the degradation mechanisms of OPVs and increasing their lifetime through a number of methods varying from the development of more stable polymer materials to the use of advanced packaging techniques. There are numerous causes for the degradation of solar cells, especially under environmental conditions. The fundamental materials of these cells tend to have low resistance to oxygen, moisture, high temperatures, illumination, etc., which lead to their rapid deterioration [2]. The most important amongst these reasons is considered to be the photodegradation of the active layer polymers, through exposure to extensive illumination.

A number of strategies are investigated in order to improve the stability and overall lifetime of organic solar cells, ranging from encapsulation of the device to the development of novel materials and processes. One of the most effective methods of encapsulation is to encase the device between glass plates and seal them using an epoxy resin [124]. Peters et al. achieved an overall lifetime of 7 years under illumination, for a PCDTBT:$PC_{71}BM$ cell encased in glass containing a desiccant layer and sealed with an epoxy resin [125]. This method of encapsulation however has the obvious disadvantage of negating the flexibility of OPVs, which is one of the major advantages of this technology. For that reason, a number of flexible polymer sealants have been developed in recent years to increase the stability of OPVs. Sapkota et al. developed completely flexible devices that retained over 95% of their original efficiency, after 1000 h under a damp heat test [126].

A number of materials and device processes have also been developed in order to increase the stability and lifetime of organic solar cells. Common methods to increase device stability include synthesizing novel materials for the active and the hole-transporting layer, as well as optimising the morphology of the active blend. Notably, Lee et al. recently developed OPVs with a MoO_3 hole-transporting layer [127]. These devices exhibited excellent thermal stability at high temperatures in the range of 300–420 K, with PCEs

Table 4: Summary of materials, processes, and methods used for the development of state-of-the-art OSCs.

Nonfullerene acceptors (NFAs)	NFAs with tunable absorption spectra and electron energy levels	NFAs with fluorine or chlorine atoms (IT-4F36, IEICO-4F37, and BT-CIC13), >16% PCE	Development of donors with matching properties to NFAs (e.g., PM6, P2F-EHp, D16, and PTQ10), >18% PCE
Interfacial layers	Interfacial layers (e.g., PBDTTPD-COOH) optimize vertical phase segregation	Inorganic semiconductor interlayers, such as TiO_2 and ZnO > 9%PCE	Polyelectrolytes with side chains of ionic functional groups and conjugated backbones
Small-molecule organic solar cells	Small-molecule OPVs have well-defined molecular structures and high reproducibility	Synthesis of new donor and acceptor small-molecule materials > 15%PCE	All-small-molecule OPVs with PCEs higher than 15% have been developed
Ternary OPVs	Active layer with 3 organic semiconductors to improve light absorption	Synthesis of novel donor and acceptor materials with synergetic properties	Efficiencies of over 17% with Y6:BTP-M/PM6 and MF1:Y6/PM6 ternary OPVs
Manufacturing techniques and scalability	Spin coating for high-efficiency, small-area OPVs	Spray coating, blade coating	Inkjet printing for large-area OPVs
Stability and lifetime	Encapsulation in glass sealed with epoxy resin results in lifetime > 7 years under illumination	OPVs with polymer sealants retain >95% efficiency after 1000 h under a damp heat test	Ternary OPVs with high thermal stability retain 98% of efficiency, after 300 h of heating at 65°

dropping at a reduced rate of 0.13%/°C compared to 0.20%/°C for cells with PEDOT:PSS as the hole-extracting layer. Employing an inverted device geometry has also been used extensively to increase device lifetime, since this structure tends to have higher stability by preventing the reaction between the active layer polymer and the metal electrode [128]. Ternary solar cells also tend to be more versatile and tunable, through the introduction of a third component in the active blend [129]. A number of research efforts focus on increasing the stability of ternary OPVs through the careful selection and optimization of appropriate materials in ternary devices. Recently, Liu et al. reported an 8.5% efficiency for a ternary device based on naphthalene di-imide polymer acceptor, in a blend with the polymer donors PBDT-TAZ and PTB7-Th [130]. This device exhibited high thermal stability, retaining 98% of its efficiency, after 300 h of heating at 65°. One other promising direction towards improving the stability and overall lifetime of organic solar cells is the use of the aforementioned nonfullerene acceptors. These materials have highly tunable properties and have been shown to have increased thermal and photochemical stability, resulting in improved device lifetimes compared to fullerene-based OPVs [122].

Table 4 summarizes some of the main materials, components, and techniques used for the development of novel organic solar cells.

4. Sustainable Applications

4.1. Dye-Sensitized Solar Cells. Dye-sensitized solar cells exhibit many unique features that make this technology highly appealing for sustainable solar energy applications. These cells can be fabricated using low-cost production processes and materials and are compatible with roll-to-roll printing techniques [39]. Large-area devices can be installed on flexible substrates, such as fabric or paper, opening the way to applications in the field of wearable electronics. The resulting flexible solar cells have a variety of potential applications such as in baggage, gears, or wearables. The military has shown interest in this technology for equipping tents and fabrics with flexible, lightweight DSSCs, which could power and recharge portable electrical devices [40].

In addition, DSSCs exhibit high performance in low-light conditions, including indoor lighting, and can thus be used for interior applications, as, for example, for powering small home electronic devices. The high efficiency of DSSCs under weak-light operating conditions makes this technology promising for several marketable applications, such as indoor light-harvesting devices, portable electronics, and even the automobile industry. Small indoor electronic devices with low power requirements can be powered by their own built-in solar cells, providing systems with a high degree of autonomous function and sustainability [131]. Figure 6 shows examples of DSSC applications. Another potential application of emerging photovoltaic technologies is in various integrated electronics, such as batteries, supercapacitors, or fuel cells, with an integrated solar cell that provides electrical energy [132]. Autonomous devices, which are powered by their own flexible, lightweight solar cells, can be used in remote regions not connected to the grid or for military applications. For example, small PV units can be integrated to rechargeable batteries that store the energy produced by the solar cells, in order to provide a portable power system [133]. Several studies have demonstrated the use of Li-based batteries to successfully build a power pack with an incorporated DSSC module [134, 135]. Similarly, DSSCs have been integrated to supercapacitors, creating a fiber-like device that can achieve photoelectric conversion and energy storage at the same time and can be used in textiles and other lightweight applications [136]. Yang et al. [137] developed a

Figure 6: Examples of applications for dye-sensitized solar cells and modules [40].

stand-alone self-powered system comprised of a solid-state supercapacitor, four series-connected DSSCs, and a LED light. The system successfully lit a red LED light for over 30 minutes after being charged for only 2 minutes.

Due to their structural design and different colour dyes, DSSCs are semitransparent and can be produced in a wide array of colours. These features, combined with the aforementioned flexibility, make them compatible with a variety of architectural elements and provide unique applications in the field of building-integrated photovoltaics [41]. However, further research is required in order for this technology to become competitive for building-integrated applications. The low stability and lifetime of these devices hinder their use for large-scale architectural applications. Novel, solid-state electrolytes need to be developed in order to produce DSSCs with high stability and efficiency. In addition, the relatively low efficiency of DSSCs restricts their commercialization to niche technologies such as portable and disposable electronics. Further optimization of this technology is required to achieve efficiencies near 20% in order for DSSCs to become competitive for large-scale market commercialization.

4.2. Perovskite Solar Cells. Perovskite solar cells have become one of the most promising solar cell technologies due to their simple fabrication process and high PCEs, with recorded efficiencies of over 25% [5]. The production process of PSCs is relatively simple, and the materials used are cheap and available in large quantities. Since perovskite cells are less costly to produce than their silicon counterparts, manufacturing them translates into considerably reduced energy consumption and lower production costs, which makes them a very attractive option for sustainable solar energy applications. In addition, PSCs are lightweight and ultrathin and can be produced in different colours [45]. There is also the option of using various substrate surfaces, such as films or textiles, for the production of flexible solar cells, offering even more opportunities for specialized applications. Perovskite cells can generate energy from artificial light and are efficient even at low-scattered light, which means that they can harvest solar energy in shadowed areas or cloudy conditions and at non-vertical angles. This advantage over silicon cells, together with their lightweight, makes it possible to mount them even on vertical facade elements, thus making building integration of PSCs one of the most promising options for sustainable energy in buildings [75]. Semitransparent perovskite solar cells are especially attractive for building-integrated applications, as they offer a number of aesthetic architectural options [138]. Semitransparent PSCs can be used to cover the surface of buildings, windows, and roofs, providing an additional source of energy to the building. Their application in the windows of buildings or vehicles has been studied extensively in recent years. The absorption spectrum of PSCs can be tuned to the near-infrared or ultraviolet regions in order to increase their transparency. This offers the added benefits of protecting the building or vehicle interior from the heating effects of infrared radiation and the harmful effects of ultraviolet radiation [139].

Another promising application for PSCs would be in tandem device architectures. As discussed in Section 3.2, perovskite cell structures can be combined with another absorber material to produce high-efficiency devices. Since perovskite materials have tunable bandgaps, they can be designed to complement the absorption of other solar cells, such as Si or CIGS, thus increasing device efficiency considerably, while effectively reducing the associated cost per watt peak of the modules [132].

One issue that needs to be addressed for commercial large-scale PSC applications is the scalability of the devices. Large-scale devices need to be produced with high efficiency and reproducible processes before this technology can be used for large-area applications, such as building-integrated photovoltaics. Even though PSCs can be produced by relatively simple printing and coating techniques, large-scale devices produced to date have issues in uniformity and reproducibility, resulting in considerably lower efficiencies than small-area cells.

4.3. Organic Solar Cells. The low-cost manufacturing processing that is used for their production is a strong advantage of OPVs that is expected to make this technology competitive with conventional energy sources in certain markets. Other advantages of organic photovoltaics include their low weight and environmentally friendly degradability, which offer opportunities for new solar cell applications. Another important characteristic of OPVs is that printing and coating manufacturing techniques can be entirely conducted on flexible substrates [31], enabling the production of flexible devices that are suitable for a wider range of applications than conventional nonflexible photovoltaics.

The special properties of OPVs make them suitable for a wide range of sustainable solar energy applications, such as

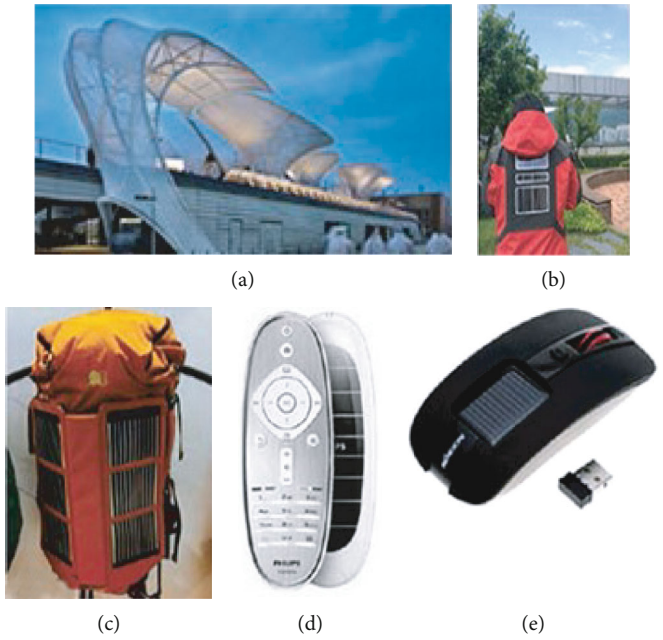

Figure 7: Examples of applications of OPVs: (a) building-integrated photovoltaics, (b) jacket with an incorporated OPV module, (c) backpack, (d) remote control, and (e) solar computer mouse [99].

Table 5: Summary of sustainable energy applications for DSSCs, PSCs, and OPVs.

DSSC	PSC	OPV
Remote regions not connected to the grid	Multicoloured, semitransparent	Flexible devices, printable solar cells
Wearable electronics: clothes, backpacks, baggage, and gears	Flexible solar cells on films or textiles	Fabrics, wearables: clothes and backpacks
Military applications: tents and fabrics that power portable electrical devices	Building-integrated solar cells: facades and roofs	Building-integrated solar cells: windows and facades
Indoor light-harvesting devices: small, indoor electronic devices with low power requirements	Semitransparent: applications in the windows of buildings or vehicles	Indoor light applications: small indoor devices
Integrated electronics: fuel cells, batteries, and supercapacitors	Tandem device architectures: combined with Si or CIGS cells	

building-integrated photovoltaics (Figure 7(a)), wearables (Figures 7(b) and 7(c)), and powering small indoor electronic devices (Figures 7(d) and 7(e)). Since OPVs are thin and flexible, they can be incorporated into a variety of substrates and building materials including standard lamination on glass [100]. In addition, OPV modules do not exhibit a drop in performance caused by typical outdoor conditions such as diffuse light and high temperatures and can be developed in different shapes and degrees of transparency making them ideal for integration in sustainable energy buildings [140]. Recently, OPVs were used to fabricate a >250 m^2 flexible power system reaching an average performance of ~5% (PCE) in a semitransparent configuration (Figure 7(a)).

The optical absorption of OPVs can be tuned to be compatible with the narrow emission spectra and lower light intensity of the commonly used indoor light sources [141]. This property, along with their lightweight, flexibility, and colouration, makes them ideal for indoor applications. Recently, Ding et al. designed all-polymer solar cells for indoor applications with high open-circuit voltage of 1.16 V and PCE of 27.4% under fluorescent lamp illumination [142]. Cui et al. developed an organic photovoltaic module for indoor applications with an area of 1 cm^2 that exhibited a power conversion efficiency of 22% under 1000 lux LED illumination [143]. More recently, Bai et al. developed a ternary OPV for indoor light applications, based on the benzotriazole donor J52-F, the chlorinated donor PM7, and the acceptor BTA3. The device yielded a power conversion efficiency in excess of 20% under 300 lux LED illumination with a temperature of 3000 K [144].

Table 5 shows a comparative summary of the main sustainable energy applications for DSSCs, PSCs, and OPVs.

5. Conclusions

Rising global demands for energy, combined with the rapid depletion of fossil fuels, has led to increased interest in renewable energy sources over the past decades. From a

purely economic standpoint however, silicon solar cells are not yet competitive with fossil fuel sources. Further reduction in the cost of solar energy is required to increase the market share of this technology. This reduction in the cost of solar energy can be achieved through the development of new solar cell materials and device concepts. A number of alternatives to silicon-based cells are being investigated, aiming at the development of photovoltaic devices with relatively high conversion efficiency at lower costs.

Third-generation photovoltaic technologies such as dye-sensitized solar cells, organic solar cells, and perovskite solar cells have emerged in recent years and have shown potential for large-scale commercialization. These promising solar cell technologies are developed using low-cost production processes, they are less sensitive to ambient temperature changes, and they have good performance in low-light conditions and can be installed on flexible substrates. Their properties make them ideal for many sustainable solar energy applications, ranging from small-scale self-powered electronic devices, such as electronic calculators, to large-scale, energetically self-sufficient buildings.

Dye-sensitized solar cells are best suited to niche applications, such as disposable electronics, due to their low cost and also to their relatively low stability. Organic solar cells can be especially used for the production of flexible solar cells using simple printing roll-to-roll processes. Perovskite solar cells are widely considered the most promising new solar cell technology. Their PCEs can rival those of silicon-based solar cells, at considerably lower cost, and they are suitable for numerous sustainable solar energy applications. They can also be used in tandem with other solar cell technologies, such as Si or CIGS, resulting in high-efficiency, cost-effective solar cell devices.

These emerging solar cell technologies however are still not commercially available in large volumes. Disadvantages such as the relatively low efficiency and stability of these cells compared to silicon-based solar cells pose a hindrance to their commercialization. Current research efforts are focused on overcoming these obstacles through the development of novel materials, processing techniques, and device architectures. The outcome of these research efforts is expected to unlock the potential of emerging solar cell technologies and lead to their future commercialization.

Data Availability

No data were used to support this study.

Conflicts of Interest

The author declares that she has no conflicts of interest.

References

[1] J. Gong, K. Sumathy, Q. Qiao, and Z. Zhou, "Review on dye-sensitized solar cells (DSSCs): Advanced techniques and research trends," *Renewable and Sustainable Energy Reviews*, vol. 68, pp. 234–246, 2017.

[2] M. Giannouli, V. M. Drakonakis, A. Savva, P. Eleftheriou, G. Florides, and S. A. Choulis, "Methods for improving the lifetime performance of organic photovoltaics with low-costing encapsulation," *ChemPhysChem*, vol. 16, no. 6, pp. 1134–1154, 2015.

[3] M. Sessolo and H. J. Bolink, "Perovskite solar cells join the major league," *Science*, vol. 350, no. 6263, p. 917, 2015.

[4] G. D. Sharma, P. A. Angaridis, S. Pipou et al., "Efficient co-sensitization of dye-sensitized solar cells by novel porphyrin/triazine dye and tertiary aryl-amine organic dye," *Organic Electronics*, vol. 25, pp. 295–307, 2015.

[5] National Renewable Energy Laboratory (NREL), Golden, CO, 2020January 2021, https://www.nrel.gov/pv/assets/pdfs/best-research-cell-efficiencies.20201228.pdf.

[6] O. Haillant, "Accelerated weathering testing principles to estimate the service life of organic PV modules," *Solar Energy Materials and Solar Cells*, vol. 95, no. 5, pp. 1284–1292, 2011.

[7] S. Prasanthkumar and L. Giribabu, "Recent advances in perovskite-based solar cells," *Current Science*, vol. 111, no. 7, pp. 1173–1181, 2016.

[8] B. O'Regan and M. Grätzel, "A low-cost, high-efficiency solar cell based on dye-sensitized colloidal TiO_2 films," *Nature*, vol. 353, no. 6346, pp. 737–740, 1991.

[9] M. A. Green, E. D. Dunlop, J. Hohl-Ebinger, M. Yoshita, N. Kopidakis, and A. W. Y. Ho-Baillie, "Solar cell efficiency tables (Version 55)," *Progress in Photovoltaics: Results and Applications*, vol. 28, no. 1, pp. 3–15, 2020.

[10] A. Yella, H.-W. Lee, H. N. Tsao et al., "Porphyrin-Sensitized Solar Cells with Cobalt (II/III)-Based Redox Electrolyte Exceed 12 Percent Efficiency," *Science*, vol. 334, no. 6056, pp. 629–634, 2011.

[11] S. Shalini, R. Balasundaraprabhu, T. S. Kumar, N. Prabavathy, S. Senthilarasu, and S. Prasanna, "Status and outlook of sensitizers/dyes used in dye sensitized solar cells (DSSC): a review," *International Journal of Energy Research*, vol. 40, no. 10, pp. 1303–1320, 2016.

[12] M. Giannouli and M. Fakis, "Interfacial electron transfer dynamics and photovoltaic performance of TiO_2 and ZnO solar cells sensitized with Coumarin 343," *Journal of Photochemistry and Photobiology A: Chemistry*, vol. 226, no. 1, pp. 42–50, 2011.

[13] M. Giannouli and F. Spiliopoulou, "Effects of the morphology of nanostructured ZnO films on the efficiency of dye-sensitized solar cells," *Renewable Energy*, vol. 41, pp. 115–122, 2012.

[14] M. Ye, X. Wen, M. Wang et al., "Recent advances in dye-sensitized solar cells: from photoanodes, sensitizers and electrolytes to counter electrodes," *Materials Today*, vol. 18, no. 3, pp. 155–162, 2015.

[15] H. Zhang, Y. Wang, D. Yang et al., "Directly Hydrothermal Growth of Single Crystal Nb3O7(OH) Nanorod Film for High Performance Dye-Sensitized Solar Cells," *Advanced Materials*, vol. 24, no. 12, pp. 1598–1603, 2012.

[16] M. Ye, X. Xin, C. Lin, and Z. Lin, "High Efficiency Dye-Sensitized Solar Cells Based on Hierarchically Structured Nanotubes," *Nanoletters*, vol. 11, no. 8, pp. 3214–3220, 2011.

[17] Q. Yu, Y. Wang, Z. Yi et al., "High-Efficiency Dye-Sensitized Solar Cells: The Influence of Lithium Ions on Exciton Dissociation, Charge Recombination, and Surface States," *ACS Nano*, vol. 4, no. 10, pp. 6032–6038, 2010.

[18] Z. Song, S. C. Watthage, A. B. Phillips, and M. J. Heben, "Pathways toward high-performance perovskite solar cells: review of recent advances in organo-metal halide perovskites for photovoltaic applications," *Journal of Photonics for Energy*, vol. 6, no. 2, article 022001, 2016.

[19] M. Grätzel, "The light and shade of perovskite solar cells," *Nature Materials*, vol. 13, no. 9, pp. 838–842, 2014.

[20] C. C. Stoumpos and M. G. Kanatzidis, "Halide Perovskites: Poor Man's High-Performance Semiconductors," *Advanced Materials*, vol. 28, no. 28, pp. 5778–5793, 2016.

[21] A. Kojima, K. Teshima, Y. Shirai, and T. Miyasaka, "Organometal Halide Perovskites as Visible-Light Sensitizers for Photovoltaic Cells," *Journal of the American Chemical Society*, vol. 131, no. 17, pp. 6050-6051, 2009.

[22] J.-H. Im, C.-R. Lee, J.-K. Lee, S.-W. Park, and N.-G. Park, "6.5% efficient perovskite quantum-dot-sensitized solar cell," *Nanoscale*, vol. 3, no. 10, pp. 4088–4093, 2011.

[23] H.-S. Kim, C.-R. Lee, J.-H. Im et al., "Lead Iodide Perovskite Sensitized All-Solid-State Submicron Thin Film Mesoscopic Solar Cell with Efficiency Exceeding 9%," *Scientific Reports*, vol. 2, no. 1, p. 591, 2012.

[24] M. M. Lee, J. Teuscher, T. Miyasaka, T. N. Murakami, and H. J. Snaith, "Efficient Hybrid Solar Cells Based on Meso-Superstructured Organometal Halide Perovskites," *Science*, vol. 338, no. 6107, pp. 643–647, 2012.

[25] J. Burschka, N. Pellet, S.-J. Moon et al., "Sequential deposition as a route to high-performance perovskite-sensitized solar cells," *Nature*, vol. 499, no. 7458, pp. 316–319, 2013.

[26] M. Liu, M. B. Johnston, and H. J. Snaith, "Efficient planar heterojunction perovskite solar cells by vapour deposition," *Nature*, vol. 501, no. 7467, pp. 395–398, 2013.

[27] N. J. Jeon, J. H. Noh, Y. C. Kim, W. S. Yang, S. Ryu, and S. I. Seok, "Solvent engineering for high-performance inorganic–organic hybrid perovskite solar cells," *Nature Materials*, vol. 13, no. 9, pp. 897–903, 2014.

[28] H. Zhou, Q. Chen, G. Li et al., "Interface engineering of highly efficient perovskite solar cells," *Science*, vol. 345, no. 6196, pp. 542–546, 2014.

[29] M. Saliba, T. Matsui, J.-Y. Seo et al., "Cesium-containing triple cation perovskite solar cells: improved stability, reproducibility and high efficiency," *Energy and Environtal Science*, vol. 9, no. 6, pp. 1989–1997, 2016.

[30] F. C. Krebs, "Fabrication and processing of polymer solar cells: A review of printing and coating techniques," *Solar Energy Materials and Solar Cells*, vol. 93, no. 4, pp. 394–412, 2009.

[31] F. C. Krebs, "All solution roll-to-roll processed polymer solar cells free from indium-tin-oxide and vacuum coating steps," *Organic Electronics*, vol. 10, no. 5, pp. 761–768, 2009.

[32] F. C. Krebs and K. Norrman, "Using light-induced thermocleavage in a roll-to-roll process for polymer solar cells," *ACS Applied Materials and Interfaces*, vol. 2, no. 3, pp. 877–887, 2010.

[33] S. H. Park, A. Roy, S. Beaupre et al., "Bulk heterojunction solar cells with internal quantum efficiency approaching 100%," *Nature Photonics*, vol. 3, no. 5, pp. 297–302, 2009.

[34] Y. Cui, H. Yao, L. Hong et al., "Organic photovoltaic cell with 17% efficiency and superior processability," *National Science Review*, vol. 7, no. 7, pp. 1239–1246, 2020.

[35] E. R. Rwenyagila, "A review of organic photovoltaic energy source and its technological designs," *International Journal of Photoenergy*, vol. 2017, Article ID 1656512, 12 pages, 2017.

[36] L. J. A. Koster, E. C. P. Smits, V. D. Mihailetchi, and P. W. Blom, "Device model for the operation of polymer/fullerene bulk heterojunction solar cells," *Physical Review B*, vol. 72, pp. 1–9, 2005.

[37] J. Yuan, J. Ouyang, V. Cimrová, M. Leclerc, A. Najari, and Y. Zou, "Development of quinoxaline-based polymers for photovoltaic applications," *Journal of Materials Chemistry C*, vol. 5, no. 8, pp. 1858–1879, 2017.

[38] G. Boschloo, "Improving the performance of dye-sensitized solar cells," *Frontiers in Chemistry*, vol. 7, p. 77, 2019.

[39] M. Giannouli, "Nanostructured ZnO, TiO2, and Composite ZnO/TiO2 Films for Application in Dye- Sensitized Solar Cells," *International Journal of Photoenergy*, vol. 2013, Article ID 612095, 8 pages, 2013.

[40] L. Calderone, *Dye Sensitized Solar Cells Is the Future of Solar*, 2020, https://www.altenergymag.com.

[41] M. Carella, F. Borbone, and R. Centore, "Research progress on photosensitizers for DSSC," *Frontiers in Chemistry*, vol. 11, 2018.

[42] S. Prasad, D. Devaraj, B. Rajender, S. Sunitha, and M. S. AlSalhi, "Fabrication, device performance, and MPPT for flexible dye-sensitized solar panel based on gel-polymer phthaloylchitosan based electrolyte and nanocluster CoS_2 counter electrode," *Materials Science for Energy Technologies*, vol. 2, no. 2, pp. 319–328, 2019.

[43] M. Freitag, F. Giordano, W. X. Yang et al., "Copper phenanthroline as a fast and high-performance redox mediator for dye-sensitized solar cells," *Journal of Physical Chemistry C*, vol. 120, no. 18, pp. 9595–9603, 2016.

[44] X. Wang, S. Kulkarni, B. Ito et al., "Nanoclay Gelation Approach toward Improved Dye-Sensitized Solar Cell Efficiencies: An Investigation of Charge Transport and Shift in the TiO_2 Conduction Band," *ACS Applied Materials and Interfaces*, vol. 5, no. 2, pp. 444–450, 2013.

[45] I. Chung, B. Lee, J. He, R. P. H. Chang, and M. G. Kanatzidis, "All-solid-state dye-sensitized solar cells with high efficiency," *Nature*, vol. 485, no. 7399, pp. 486–489, 2012.

[46] K. Sharma, V. Sharma, and S. S. Sharma, "Dye-sensitized solar cells: fundamentals and current status," *Nanoscale Research Letters*, vol. 13, no. 1, p. 381, 2018.

[47] D. Colonna, V. Capogna, A. Lembo, T. M. Brown, A. Reale, and A. Di Carlo, "Efficient Cosensitization Strategy for Dye-Sensitized Solar Cells," *Applied Physics Express*, vol. 5, no. 2, article 022303, 2012.

[48] J. Ji, H. Zhou, Y. K. Eom, C. H. Kim, and H. K. Kim, "14.2% efficiency dye-sensitized solar cells by co-sensitizing novel thieno[3,2-b] indole-based organic dyes with a promising porphyrin sensitizer," *Advanced Energy Materials*, vol. 10, no. 15, 2020.

[49] P. Zuo, C. Li, Y. S. Wu et al., "Mechanism of squarylium cyanine and $Ru(dcbpy)_2(NCS)_2$ co-sensitization of colloidal TiO_2," *Journal of Photochemistry and Photobiology A*, vol. 183, no. 1-2, pp. 138–145, 2006.

[50] J. H. Yum, B. E. Hardin, S. J. Moon et al., "Panchromatic Response in Solid-State Dye-Sensitized Solar Cells Containing Phosphorescent Energy Relay Dyes," *Molecular Solar Cells*, vol. 48, no. 49, pp. 9277–9280, 2009.

[51] R. Ogura, S. Nakane, M. Morooka, M. Orihashi, Y. Suzuki, and K. Noda, "High-performance dye-sensitized solar cell

with a multiple dye system," *Applied Physics Letters*, vol. 94, no. 7, article 073308, 2009.

[52] V. Saxena, P. Veerender, A. K. Chauhan, P. Jha, D. K. Aswal, and S. K. Gupta, "Efficiency enhancement in dye sensitized solar cells through co-sensitization of TiO_2 nanocrystalline electrodes," *Applied Physics Letters*, vol. 100, no. 13, article 133303, 2012.

[53] S. Rani, P. K. Shishodia, and R. M. Mehra, "Development of a dye with broadband absorbance in visible spectrum for an efficient dye-sensitized solar cell," *Journal of Renewable and Sustainable Energy*, vol. 2, no. 4, article 043103, 2010.

[54] N. Shibayama, H. Ozawa, M. Abe, Y. Ooyama, and H. Arakawa, "A new cosensitization method using the Lewis acid sites of a TiO_2 photoelectrode for dye-sensitized solar cells," *Chemical Communications*, vol. 50, no. 48, pp. 6398–6401, 2014.

[55] S. Fan, X. Lu, H. Sun, G. Zhou, J. Changc, and Z.-S. Wang, "Effect of the co-sensitization sequence on the performance of dye-sensitized solar cells with porphyrin and organic dyes," *Physical Chemistry Chemical Physics*, vol. 18, no. 2, pp. 932–938, 2016.

[56] M. Giannouli, G. Tziogkidou, and G. Leftheriotis, "Co-sensitization of ZnO solar cells by organic dyes," *Journal of Renewable and Sustainable Energy*, vol. 9, no. 1, article 013503, 2017.

[57] H. K. Jun, M. A. Careem, and A. K. Arof, "Plasmonic effects of quantum size gold nanoparticles on dye-sensitized solar cell," *Materials Today: Proceedings*, vol. 3, pp. S73–S79, 2016.

[58] N. A. Bakr, A. K. Ali, and S. M. Jassim, "Fabrication and efficiency enhancement of Z907 dye sensitized solar cell using gold nanoparticles," *j adv phys*, vol. 6, no. 3, pp. 370–374, 2017.

[59] Y. H. Sim, M. J. Yun, S. I. Cha, S. H. Seo, and D. Y. Lee, "Improvement in energy conversion efficiency by modification of photon distribution within the photoanode of dye-sensitized solar cells," *ACS Omega*, vol. 3, pp. 698–705, 2018.

[60] M. Stolterfoht, M. Grischek, P. Caprioglio et al., "How To Quantify the Efficiency Potential of Neat Perovskite Films: Perovskite Semiconductors with an Implied Efficiency Exceeding 28%," *Advanced Materials*, vol. 32, no. 17, article 2000080, 2020.

[61] D. Zhou, T. Zhou, Y. Tian, X. Zhu, and Y. Tu, "Perovskite-based solar cells: materials, methods, and future perspectives," *Journal of Nanomaterials*, vol. 2018, Article ID 8148072, 15 pages, 2018.

[62] P. Boonmongkolras, D. Kim, E. M. Alhabshi, I. Gereige, and B. Shin, "Understanding effects of precursor solution aging in triple cation lead perovskite," *RSC Advances*, vol. 8, no. 38, pp. 21551–21557, 2018.

[63] J. J. van Franeker, K. H. Hendriks, B. J. Bruijnaers, M. W. G. M. Verhoeven, M. M. Wienk, and R. A. J. Janssen, "Monitoring Thermal Annealing of Perovskite Solar Cells with In Situ Photoluminescence," *Advanced Energy Materials*, vol. 7, no. 7, article 1601822, 2017.

[64] D. Xin, S. Tie, X. Zheng, J. Zhu, and W.-H. Zhang, "Defect passivation through electrostatic interaction for high performance flexible perovskite solar cells," *Journal of Energy Chemistry*, vol. 46, pp. 173–177, 2020.

[65] N. Tailor, M. Abdi-Jalebi, V. Gupta et al., "Recent progress in morphology optimization in perovskite solar cell," *Journal of Materials Chemistry A*, vol. 8, no. 41, pp. 21356–21386, 2020.

[66] M. Feng, S. You, N. Cheng, and J. Du, "High quality perovskite film solar cell using methanol as additive with 19.5% power conversion efficiency," *Electrochimica Acta*, vol. 293, pp. 356–363, 2019.

[67] Z. Wu, Z. Liu, Z. Hu et al., "Highly Efficient and Stable Perovskite Solar Cells via Modification of Energy Levels at the Perovskite/Carbon Electrode Interface," *Advanced Materials*, vol. 31, no. 11, article e1804284, 2019.

[68] J. Lu, X. Lin, X. Jiao et al., "Interfacial benzenethiol modification facilitates charge transfer and improves stability of cm-sized metal halide perovskite solar cells with up to 20% efficiency," *Energy & Environmental Science*, vol. 11, no. 7, pp. 1880–1889, 2018.

[69] S. Seo, I. J. Park, M. Kim et al., "An ultra-thin, un-doped NiO hole transporting layer of highly efficient (16.4%) organic-inorganic hybrid perovskite solar cells," *Nanoscale*, vol. 8, no. 22, pp. 11403–11412, 2016.

[70] H. Zhang, H. Wang, W. Chen, and A. K.-Y. Jen, "CuGaO2: a promising inorganic hole-transporting material for highly efficient and stable perovskite solar cells," *Advanced Materials*, vol. 29, no. 8, article 1604984, 2017.

[71] F. Meillaud, A. Shah, C. Droz, E. Vallat-Sauvain, and C. Miazza, "Efficiency limits for single-junction and tandem solar cells," *Solar Energy Materials and Solar Cells*, vol. 90, no. 18-19, pp. 2952–2959, 2006.

[72] J.-W. Lee, D.-J. Seol, A.-N. Cho, and N.-G. Park, "High-Efficiency Perovskite Solar Cells Based on the Black Polymorph of HC(NH2)2PbI3," *Advanced Materials*, vol. 26, no. 29, pp. 4991–4998, 2014.

[73] F. Zhang, S. Wang, Y. Xiao, and X. Li, "Improvement in photovoltaic performance of perovskite solar cells by interface modification and co-sensitization with novel asymmetry 7-coumarinoxy-4-methyltetrasubstituted metallophthalocyanines," *Synthetic Metals*, vol. 220, pp. 187–193, 2016.

[74] N. Balachandran, T. M. Robert, D. Mathew, and J. Cyriac, "Co-sensitization of perovskite solar cells by organometallic compounds: mechanism and photovoltaic characterization," *Proceedings of the 7th International Conference on Advances in Energy Research. Springer Proceedings in Energy*, M. Bose and A. Modi, Eds., Springer, Singapore, 2021.

[75] M. Banavoth, *Perovskite Solar Cells: Properties, Application and Efficiency*, Nova Science Publishers, 2019.

[76] A. Roy, A. Ghosh, S. Bhandari, S. Sundaram, and T. K. Mallick, "Perovskite solar cells for BIPV application: a review," *Buildings*, vol. 10, no. 7, p. 129, 2020.

[77] T. Todorov, T. Gershon, O. Gunawan et al., "Monolithic perovskite-CIGS tandem solar cells via in situ band gap engineering," *Advanced Energy Materials*, vol. 5, p. 23, 2015.

[78] J. Park, J. H. Park, S. Ji, M. Park, J. Jang, and J. Kim, "A three-terminal monolithic perovskite/Si tandem solar cell characterization platform," *Joule*, vol. 3, no. 3, pp. 807–818, 2019.

[79] M. I. Hossain, W. Qarony, S. Ma, L. Zeng, D. Knipp, and Y. H. Tsang, "Perovskite/silicon tandem solar cells: from detailed balance limit calculations to photon management," *Nano-Micro Letters*, vol. 11, no. 1, p. 58, 2019.

[80] H. Shen, D. Walter, Y. Wu et al., "Monolithic perovskite/Si tandem solar cells: pathways to over 30% efficiency," *Advanced Energy Materials*, vol. 10, p. 3, 2020.

[81] F. Fu, T. Feurer, T. Jäger et al., "Low-temperature-processed efficient semi-transparent planar perovskite solar cells for

bifacial and tandem applications," *Nature Communications*, vol. 6, article 8932, 2015.

[82] Y. Hou, E. Aydin, M. De Bastiani et al., "Efficient tandem solar cells with solution-processed perovskite on textured crystalline silicon," *Science*, vol. 367, no. 6482, pp. 1135–1140, 2020.

[83] B. Conings, J. Drijkoningen, N. Gauquelin et al., "Intrinsic thermal instability of methylammonium lead trihalide perovskite," *Advanced Energy Materials*, vol. 5, no. 15, article 1500477, 2015.

[84] M. Saliba, T. Matsui, K. Domanski et al., "Incorporation of rubidium cations into perovskite solar cells improves photovoltaic performance," *Science*, vol. 354, no. 6309, pp. 206–209, 2016.

[85] T. Matsui, T. Yamamoto, T. Nishihara et al., "Compositional Engineering for Thermally Stable, Highly Efficient Perovskite Solar Cells Exceeding 20% Power Conversion Efficiency with 85 °C/85% 1000 h Stability," *Advanced Materials*, vol. 31, no. 10, article 1806823, 2019.

[86] J. Zhu, M. Tang, B. He et al., "Improved charge extraction through interface engineering for 10.12% efficiency and stable CsPbBr3perovskite solar cells," *Journal of Materials Chemistry A*, vol. 8, no. 40, pp. 20987–20997, 2020.

[87] J. A. Christians, P. Schulz, J. S. Tinkham et al., "Tailored interfaces of unencapsulated perovskite solar cells for >1,000 hour operational stability," *Nature Energy*, vol. 3, no. 1, pp. 68–74, 2018.

[88] S. A. Gevorgyan, M. V. Madsen, H. F. Dam et al., "Interlaboratory outdoor stability studies of flexible roll-to-roll coated organic photovoltaic modules: Stability over 10,000 h," *Solar Energy Materials and Solar Cells*, vol. 116, pp. 187–196, 2013.

[89] F. Bella, G. Griffini, J. Correa-Baena et al., "Improving efficiency and stability of perovskite solar cells with photocurable fluoropolymers," *Science*, vol. 354, no. 6309, pp. 203–206, 2016.

[90] K. A. Bush, A. F. Palmstrom, J. Y. Zhengshan et al., "23.6%-efficient monolithic perovskite/silicon tandem solar cells with improved stability," *Nature Energy*, vol. 2, pp. 1–7, 2017.

[91] F. Ali, C. Roldán-Carmona, M. Sohail, and M. K. Nazeeruddin, "Applications of self-assembled monolayers for perovskite solar cells interface engineering to address efficiency and stability," *Advanced Energy Materials*, vol. 10, no. 48, article 2002989, 2020.

[92] M. Pazoki, T. J. Jacobsson, A. Hagfeldt, G. Boschloo, and T. Edvinsson, "Effect of metal cation replacement on the electronic structure of metalorganic halide perovskites: replacement of lead with alkaline-earth metals," *Physical Review B: Condensed Matter and Materials Physics*, vol. 93, pp. 144105–144110, 2016.

[93] T. J. Jacobsson, M. Pazoki, A. Hagfeldt, and T. Edvinsson, "Goldschmidt's rules and strontium replacement in lead halogen perovskite solar cells: theory and preliminary experiments on CH3NH3SrI$_3$," *The Journal of Physical Chemistry C*, vol. 119, pp. 25673–25683, 2015.

[94] G. Volonakis, M. R. Filip, A. A. Haghighirad et al., "Lead-free halide double perovskites via heterovalent substitution of noble metals," *Journal of Physical Chemistry Letters*, vol. 7, pp. 1254–1259, 2016.

[95] C. Wu, Q. Zhang, Y. Liu et al., "The Dawn of Lead-Free Perovskite Solar Cell: Highly Stable Double Perovskite $Cs_2AgBiBr_6$ Film," *Advancement of Science*, vol. 5, article 1700759, 2018.

[96] H. L. Zhu, J. Xiao, J. Mao, H. Zhang, Y. Zhaoand, and W. C. H. Choy, "Controllable Crystallization of $CH_3NH_3Sn_{0.25}Pb_{0.75}I_3$ Perovskites for Hysteresis-Free Solar Cells with Efficiency Reaching 15.2%," *Advanced Functional Materials*, vol. 27, no. 11, article 1605469, 2017.

[97] Z. Qiu, Z. Xu, N. Li et al., "Monolithic perovskite/Si tandem solar cells exceeding 22% efficiency via optimizing top cell absorber," *Nano Energy*, vol. 53, pp. 798–807, 2018.

[98] M. Jost, L. Kegelmann, L. Korte, and S. Albrecht, "Monolithic perovskite tandem solar cells: a review of the present status and advanced characterization methods toward 30% efficiency," *Advanced Energy Materials*, vol. 10, no. 26, article 1904102, 2020.

[99] Q. Han, Y.-T. Hsieh, L. Meng et al., "High-performance perovskite/Cu(In,Ga)Se_2 monolithic tandem solar cells," *Science*, vol. 361, pp. 904–908, 2018.

[100] G. Morse, R. Harding, N. Blouin et al., "Organic photovoltaic applications for IoT," *Architecture, and Wearables, Material Matters*, vol. 12, no. 3, 2017.

[101] J. Zhang, H. S. Tan, X. Guo, A. Facchetti, and H. Yan, "Material insights and challenges for non-fullerene organic solar cells based on small molecular acceptors," *Nature Energy*, vol. 3, no. 9, pp. 720–731, 2018.

[102] Y. Cui, H. Yao, J. Zhang et al., "Over 16% efficiency organic photovoltaic cells enabled by a chlorinated acceptor with increased open-circuit voltages," *Nature Communications*, vol. 10, no. 1, article 2515, 2019.

[103] Q. Liu, Y. Jiang, K. Jin et al., "18% efficiency organic solar cells," *Science Bulletin*, vol. 65, no. 4, pp. 272–275, 2020.

[104] G. Chidichimo and L. Filippelli, "Organic solar cells: problems and perspectives," *International Journal of Photoenergy*, vol. 2010, Article ID 123534, 11 pages, 2010.

[105] M. Campoy-Quiles, T. Ferenczi, T. Agostinelli et al., "Morphology evolution via self-organization and lateral and vertical diffusion in polymer/fullerene solar cell blends," *Nature Materials*, vol. 7, pp. 158–164, 2008.

[106] B. Cao, X. He, C. R. Fetterly, B. C. Olsen, E. J. Luber, and J. M. Buriak, "Role of interfacial layers in organic solar cells: energy level pinning versus phase segregation," *ACS Applied Materials & Interfaces*, vol. 8, pp. 18238–18248, 2016.

[107] C. Liu, D. Zhang, Z. Li et al., "Decreased charge transport barrier and recombination of organic solar cells by constructing interfacial nanojunction with annealing-free ZnO and Al layers," *ACS Applied Materials & Interfaces*, vol. 9, pp. 22068–22075, 2017.

[108] J. W. Jo, J. W. Jung, S. Bae et al., "Development of self-doped conjugated polyelectrolytes with controlled work functions and application to hole transport layer materials for high-performance organic solar cells," *Advanced Materials Interfaces*, vol. 3, article 1500703, 2016.

[109] R. Ilmi, A. Haque, and M. S. Khan, "High efficiency small molecule-based donor materials for organic solar cells," *Organic Electronics*, vol. 58, pp. 53–62, 2018.

[110] S. Liu, J. Yuan, W. Deng et al., "High-efficiency organic solar cells with low non-radiative recombination loss and low energetic disorder," *Nature Photonics*, vol. 14, pp. 300–305, 2020.

[111] L. Chunyan, Q. Nailiang, S. Yanna et al., "All-small-molecule organic solar cells based on a fluorinated small molecule

donor with high open-circuit voltage of 1.07 V," *Frontiers in Chemistry*, vol. 8, p. 329, 2020.

[112] B. Qiu, Z. Chen, S. Qin et al., "Highly efficient all-small-molecule organic solar cells with appropriate active layer morphology by side chain engineering of donor molecules and thermal annealing," *Advanced Materials*, vol. 32, no. 21, article 1908373, 2020.

[113] R. Zhou, Z. Jiang, C. Yang et al., "All-small-molecule organic solar cells with over 14% efficiency by optimizing hierarchical morphologies," *Nature Communications*, vol. 10, article 5393, 2019.

[114] D. Hu, Q. Yang, H. Chen et al., "15.34% efficiency all-small-molecule organic solar cells with an improved fill factor enabled by a fullerene additive," *Energy & Environmental Science*, vol. 13, no. 7, pp. 2134–2141, 2020.

[115] R. Yu, H. Yao, and J. Hou, "Recent progress in ternary organic solar cells based on nonfullerene acceptors," *Advanced Energy Materials*, vol. 8, no. 28, article 1702814, 2018.

[116] V. Lami, Y. J. Hofstetter, J. F. Butscher, and Y. Vaynzof, "Energy level alignment in ternary organic solar cells," *Advanced Electronic Materials*, vol. 6, no. 8, article 2000213, 2020.

[117] M. Zhang, J. Wang, X. Ma et al., "Review on smart strategies for achieving highly efficient ternary polymer solar cells," *APL Materials*, vol. 8, article 090703, 2020.

[118] Z. Xiao, X. Jia, and L. Ding, "Ternary organic solar cells offer 14% power conversion efficiency," *Science Bulletin*, vol. 62, no. 23, pp. 1562–1564, 2017.

[119] M. Ren, G. Zhang, Z. Chen et al., "High-performance ternary organic solar cells with controllable morphology via sequential layer-by-layer deposition," *ACS Applied Materials & Interfaces*, vol. 12, no. 11, pp. 13077–13086, 2020.

[120] L. Zhan, S. Li, T. Lau et al., "Over 17% efficiency ternary organic solar cells enabled by two non-fullerene acceptors working in an alloy-like model," *Energy & Environmental Science*, vol. 13, no. 2, pp. 635–645, 2020.

[121] Q. An, J. Wang, W. Gao et al., "Alloy-like ternary polymer solar cells with over 17.2% efficiency," *Science Bulletin*, vol. 65, no. 7, pp. 538–545, 2020.

[122] C. Yan, S. Barlow, Z. Wang et al., "Non-fullerene acceptors for organic solar cells," *Nature Reviews Materials*, vol. 3, no. 3, article 18003, 2018.

[123] J. Hou, O. Inganäs, R. H. Friend, and F. Gao, "Organic solar cells based on non-fullerene acceptors," *Nature Materials*, vol. 17, no. 2, pp. 119–128, 2018.

[124] S. Schuller, P. Schilinsky, J. Hauch, and C. J. Brabec, "Determination of the degradation constant of bulk heterojunction solar cells by accelerated lifetime measurements," *Applied Physics A: Materials Science & Processing*, vol. 79, no. 1, pp. 37–40, 2004.

[125] C. H. Peters, I. T. Sachs-Quitana, J. P. Kastrop, S. Beaupre, M. Leclerc, and M. D. McGehee, "High Efficiency Polymer Solar Cells with Long Operating Lifetimes," *Advanced Energy Materials*, vol. 1, no. 4, pp. 491–494, 2011.

[126] S. B. Sapkota, A. Spies, B. Zimmermann, I. Dürr, and U. Würfel, "Promising long-term stability of encapsulated ITO-free bulk-heterojunction organic solar cells under different aging conditions," *Solar Energy Materials & Solar Cells*, vol. 130, pp. 144–150, 2014.

[127] D. Lee, J. Kim, G. Park, H. Bae, M. An, and J. Kim, "Enhanced operating temperature stability of organic solar cells with metal oxide hole extraction layer," *Polymers*, vol. 12, no. 4, p. 992, 2020.

[128] H. R. Yeom, J. Heo, G.-H. Kim et al., "Optimal top electrodes for inverted polymer solar cells," *Physical Chemistry Chemical Physics*, vol. 17, no. 3, pp. 2152–2159, 2015.

[129] Q. An, F. Zhang, J. Zhang, W. Tang, Z. Deng, and B. Hu, "Versatile ternary organic solar cells: a critical review," *Energy & Environmental Science*, vol. 9, no. 2, pp. 281–322, 2016.

[130] X. Liu, C. Zhang, S. Pang et al., "Ternary all-polymer solar cells with 8.5% power conversion efficiency and excellent thermal stability," *Frontiers in Chemistry*, vol. 8, 2020.

[131] S. Kim, M. Jahandar, J. H. Jeong, and D. C. Lim, "Recent progress in solar cell technology for low-light indoor applications," *Current Alternative Energy*, vol. 3, no. 1, pp. 3–17, 2019.

[132] S. Yun, Y. Qin, A. R. Uhl et al., "New-generation integrated devices based on dye-sensitized and perovskite solar cells," *Energy & Environmental Science*, vol. 11, no. 3, 2018.

[133] F. Bonaccorso, L. Colombo, G. Yu et al., "Graphene, related two-dimensional crystals, and hybrid systems for energy conversion and storage," *Science*, vol. 347, no. 6217, article 1246501, 2015.

[134] M. Yu, X. Ren, L. Ma, and Y. Wu, "Integrating a redox-coupled dye-sensitized photoelectrode into a lithium–oxygen battery for photoassisted charging," *Nature Communications*, vol. 5, no. 1, p. 5111, 2014.

[135] W. Guo, X. Xue, S. Wang, C. Lin, and Z. L. Wang, "An Integrated Power Pack of Dye-Sensitized Solar Cell and Li Battery Based on Double-Sided TiO2Nanotube Arrays," *Nano Letters*, vol. 12, no. 5, pp. 2520–2523, 2012.

[136] X. Chen, H. Sun, Z. Yang et al., "A novel "energy fiber" by coaxially integrating dye-sensitized solar cell and electrochemical capacitor," *Journal of Materials Chemistry A*, vol. 2, no. 6, pp. 1897–1902, 2014.

[137] P. Yang, X. Xiao, Y. Li et al., "Hydrogenated ZnO Core–Shell Nanocables for Flexible Supercapacitors and Self-Powered Systems," *ACS Nano*, vol. 7, no. 3, pp. 2617–2626, 2013.

[138] X. Qifan, R. Xia, C. J. Brabec, and H.-L. Yip, "Recent advances in semi-transparent polymer and perovskite solar cells for power generating window applications," *Energy & Environmental Science*, vol. 11, no. 7, pp. 1688–1709, 2018.

[139] Y. Zhu, L. Shu, and Z. Fan, "Recent progress on semi-transparent perovskite solar cell for building-integrated photovoltaics," *Chemical Research in Chinese Universities*, vol. 36, pp. 366–376, 2020.

[140] Z. Hu, J. Wang, X. Ma et al., "A critical review on semitransparent organic solar cells," *Nano Energy*, vol. 78, article 105376, 2020.

[141] Y. Cui, L. Hong, and J. Hou, "Organic photovoltaic cells for indoor applications: opportunities and challenges," *ACS Applied Materials & Interfaces*, vol. 12, no. 35, pp. 38815–38828, 2020.

[142] Z. Ding, R. Zhao, Y. Yua, and J. Liu, "All-polymer indoor photovoltaics with high open-circuit voltage," *Journal of Materials Chemistry A*, vol. 7, no. 46, pp. 26533–26539, 2019.

[143] Y. Cui, H. Yao, T. Zhang et al., "1 cm^2 organic photovoltaic cells for indoor application with over 20% efficiency," *Advanced Materials*, vol. 31, no. 42, 2019.

[144] Y. Bai, R. Yu, Y. Bai et al., "Ternary blend strategy in benzotriazole-based organic photovoltaics for indoor application," *Green Energy & Environment*, 2020.

Hindawi
International Journal of Photoenergy
Volume 2021, Article ID 6668079, 17 pages
https://doi.org/10.1155/2021/6668079

Research Article

Utilization of Buildings' Foundations for a Seasonal Thermal Energy Storage Medium to Meet Space and Water Heat Demands

Ammar Alkhalidi, Hamzah Al Khatba, and Mohamad K. Khawaja

Energy Engineering Department, German Jordanian University, Amman 11180, Jordan

Correspondence should be addressed to Ammar Alkhalidi; ammar.alkhalidi@gju.edu.jo

Received 5 December 2020; Revised 16 February 2021; Accepted 24 February 2021; Published 19 March 2021

Academic Editor: Kumarasamy Sudhakar

Copyright © 2021 Ammar Alkhalidi et al. This is an open access article distributed under the Creative Commons Attribution License, which permits unrestricted use, distribution, and reproduction in any medium, provided the original work is properly cited.

Seasonal thermal energy storage (STES) can be utilized to cover a portion or meet the whole space and water heat demands in residential and commercial buildings. With the scarcity of fuel resources, scientists have become aware of the importance of the utilization of thermal energy. An STES system can be charged using solar collectors to heat a storage medium when solar radiation is available. Solar irradiance is seasonal so this type of system can compensate for the shortage of energy in the winter by storing surplus solar energy in the summer. This study offers an innovative design of an STES system that takes advantage of the backfill space in a building's underground foundation to install the thermal storage medium on the excavated surface among the support pillars' base. To study the feasibility and the feasibility of such STES system, the design was simulated using the TRNSYS® tool where the STES medium was charged by a solar thermal system. The chosen building type was a four-story hotel located in three cities each with its unique climate: Potsdam (Germany), Zarqa (Jordan), and Doha (Qatar). The results showed the coverage rate of the building's annual heat demand was 56%, 82%, and 84%, and the payback periods were 3.4, 4.4, and 29 years for Potsdam, Zarqa, and Doha, respectively. Zarqa is the most efficient and feasible for STES compared to the other two cities.

1. Introduction

Buildings are one of the biggest energy consumers with 32% of the total final energy consumption in the world according to the International Energy Agency. The fossil energy systems can be replaced by solar energy systems especially for locations with high annual solar radiation, which lead to prevent large greenhouse gas emissions and reduce the negative impact on the environment as well. Solar energy, while clean and renewable, is diurnal and seasonal in nature, hence, the importance of implementing techniques to store this energy for later use when solar radiation is low or entirely unavailable. Seasonal thermal energy storage (STES) is implemented widely by using different technologies. Depending on the STES medium, surplus thermal energy from the summer can be stored and then used in the winter at various scales ranging from single-family homes, hotels, districts, towns, or regions.

Humans have been searching for means to store energy; therefore, energy storage is considered an old practice. In ancient Greece and Romans times, architects used solar energy inside their buildings to heat water. They designed their bathhouses' openings to acquire solar heating to support their existing bath fire, thus reducing the fuel needed for water heating loads [1]. Native Americans inhabited caves that best utilize solar energy in winter and summer at the Grand Canyon of Arizona. The low azimuth angle of the sun in the winter provided heat while the shading of the natural cliff blocked the summers' high azimuth angle.

Nowadays, there is a continuous increase in energy demand globally. Climate change significantly affects cooling and heating loads as well as the annual energy demands of for a building [2]. Solar thermal energy could be stored for months and seasons solar thermal systems' efficiency, sustainability, and productivity can be improved by implementing an STES criteria.

Solar thermal energy can be stored by changing the internal energy of different materials in different phases. Materials that could be utilized are sensible, latent, and thermochemical as a medium of an STES. Furthermore, materials could

be combined to achieve the required thermal properties. Due to the rising temperature of the thermal storage medium, the atoms and molecules of its materials vibrate faster and collide with each other to release the thermal energy. This allows the thermal energy to be stored as a change of the internal energy of the material in many forms. Sensible heat, latent heat, and thermochemical heat are forms of energy storage; a combination of these forms is also possible for storage [3].

The sun provides enough energy to meet global demand; however, many variables affect the accumulated energy from the sun. Therefore, some sort of energy storage system must be introduced to maximize the benefit of solar energy. Solar thermal systems use heat collectors to capture solar energy to be utilized according to the demand load. Energy can be stored for short-term and extended periods (seasonal) according to the storage system's size. Seasonal energy storage is evaluated to be 100 to 1000 times larger in capacity than short-term storage size [4].

A reference approach of STES was designed, modeled, and simulated at four buildings in different cities under various climatic zones in Europe (Stockholm, Zurich, Barcelona, and Madrid). A solar thermal system was linked with the STES to discharge the thermal energy to the buildings' heating applications. The simulation was implemented by using TRNSYS® software. The authors of the study found that a STES with 1 m^3 volume that was charged by 20 m^2 flat plate collectors and supported by 10 kW auxiliary heater can cover the buildings' annual heating demand [5].

The performance of underground fabricated sand bed STES in six different typical single-family homes' models in Richmond, Virginia, USA, was tested by using TRNSYS®, where the simulation was performed to calculate the stored thermal energy in 15 m^3 STES that gained from flat plate solar thermal collectors to cover the home's space heat demand. As a result, the overall system efficiency ranged from 50 to 70% compared with total useful solar energy. And the maximum temperature of the STES reached in the 5-year simulation was 96.1°C [6], while other researchers studied the performance of STES under the same simulation's parameters for a five-story student housing complex at Virginia Commonwealth University. The simulation was performed by using TRNSYS® on 15 thermal energy storage locations to make optimization to choose the most efficient STES system. As a result, the STES can cover more than 91% of the building's space heat demand after the fifth year of its operation [7].

Multiple authors investigated the use of solid materials as a sensible heat storage medium. A study of storing of the thermal solar energy in the soil in the summer season in Al-kreaat quarter in Baghdad used the quasi-three-dimensional model and finite line source model in their computations. The results found that 38% of the total collected energy can be stored in the soil which indicated that the amount of stored energy depends on the borehole length [8]. An investigation on covering the heat demand of four buildings within a complex by using STES placed in the ground. The capacity of STES was 5,700 m^3 that was charged by a solar thermal system with collectors' area 4,700 m^2. Several scenarios were analyzed based on the buildings' heat demand to optimize the best size of the STES, and as a result, the optimized STES could give around 53% solar fraction factor where that could decrease heat consumption by 22–100% throughout the year [9].

A TRNSYS® simulation was performed on a typical STES system for a typical 120 m^2 building in Thessaloniki, Greece. The simulation performed to calculate the covered building's space and water heat demand by 36 m^3 hot water STES. The operation of the simulated STES system was examined for two years. As a result, the hot water STES covered more than 52.3% of the building's heat demand, and the maximum temperature of the STES reached in the second year simulation was in the range 84-90°C [10].

Sand-bed thermal energy storage (TES) system experiment was conducted in a region with an extended freezing period at a two-story house located in Palmer, Alaska, using TRANSYS® simulation, and the simulated temperature of the sand-bed was compared to the measured one with a relative error of 15%. The results indicate that such types of solar thermal storage systems are viable options for very cold climates [11]. Conversely, in the United Arab Emirates (UAE), a study demonstrated that the desert sand at UAE could be used in concentrated solar power (CSP) facilities to store thermal energy up to 1000°C. The research project, Sand Stock, used sand particles as the heat collector, heat transfer, and TES media. The study concluded that desert sand can be used not only as a TES material but also as a direct solar absorber under concentrated solar flux [12].

The feasibility of STES using sensible, latent, and thermochemical heat storage technologies through a residential sector in eight cities in the United Kingdom (UK) was investigated, and a calculation modeling framework was used to estimate the critical solar collector areas and the required capacity of a TES [13].

In the case of using solid material as a medium of STES, a study examined the performance of a novel combined receiver storage system for beam down solar concentrator and tested different mixing ratios of sand and basalt to be used as the thermal storage medium. The finite element heat transfer model was used to solve the unsteady governing equations for the system. Accordingly, the achieved results showed that the utilization factor is in the range of 0.53–0.73 depending on the conductive rods configuration and the sand-basalt mixture ratio. Furthermore, the utilization factor increases by increasing the basalt percentage [14]. Others experimented with the utilization of the basalt stone as a material in sensible heat storage and found that it has a high energy density of $4.2 \times 103\ kJ\ m^{-3}\ K^{-1}$ [15].

The performance of underground water STES in a cold climatic zone in Ottawa, Canada, was tested where the storage volume was 36 m^3 and charged by 41.6 m^2 evacuated tube collectors for covering the heat demand of a single-family home. The simulation tools used were TRNSYS® and ESP-r; as a result, the covered home's heat demand was in the range of 87–98% using this system [16].

A study assessed using STES instead of using an air-source heat pump to cover the space heat demand of a 240 m^2 house in Hangzhou, China. A TRNSYS simulation was performed to develop and optimize short-term solar STES to reach the

lowest annual cost over 20 years. The electricity demand reduction was 74% by the optimized STES [17].

All researches emphasized that there is an urgent need to develop and apply smart and flexible heat systems by integrating thermal energy storage. In this case, thermal energy storage can provide high-demand response, which will need smart operating system and control techniques.

This study investigates a novel STES systems by utilizing silica sand, basalt stone, and copper mesh, in placed of the backfilled area in the foundations' layer underneath a building. Using the available spaces for the underground STES could reduce the cost of the required excavation and also providing a method for taking advantage of an otherwise underutilized area. The STES system will be simulated in three different climatic zones to assess its performance based on the variations in the climatic features of the selected locations: (i) Zarqa-Jordan, (ii) Doha-Qatar, and (iii) Potsdam-Germany. The authors chose the sensible STES type instead of latent/thermochemical because it is the safest, the most common, the simplest, and the cheapest one [1].

This research investigated the possibility and the feasibility of using such STES to meet space and water heat demands of a hotel building in the three climatic zones using TRNSYS® simulation software.

2. Methodology

The heat demand for space heating (SH) and domestic hot water (DHW) of the buildings will be calculated utilizing the degree days method. A proper solid material will be utilized in a sensible STES to cover the building's heat demand. This study investigates the thermal energy application of an STES system under a proper boundary and initial conditions that will be discussed in detail in the next sections. Investigation of the reliability of the designed STES system relied on mainly three energy pillars: energy storage, renewable production, and STES system sustainability [18]. The authors represented the three energy pillars in the results. Thermal energy transfers throughout the whole system are illustrated in Figure 1 as a simple schematic diagram. A simulation study will be performed for the STES system in the selected locations by using TRNSYS® software. An economical evaluation for capital and operation cost of the STES system compared with the heat demand electricity cost will be done in the nest sections. Finally, the simulation and the economical evaluation results will be analyzed to assess the STES performance and feasibility in the selected locations. The steps and procedures to be followed are presented in a chart shown in Figure 2.

3. Design and Simulation

Three different climatic zones were selected to test the performance of the STES and its feasibility for different weather conditions, Zarqa in Jordan, Doha in Qatar, and Potsdam in Germany. The climatic and solar properties for the three cities are shown in Table 1 according to the National Climatic Data Center [19] and Photovoltaic Geographical Information System [20], based on the different climate features, including temperature, humidity, and cloud cover. The

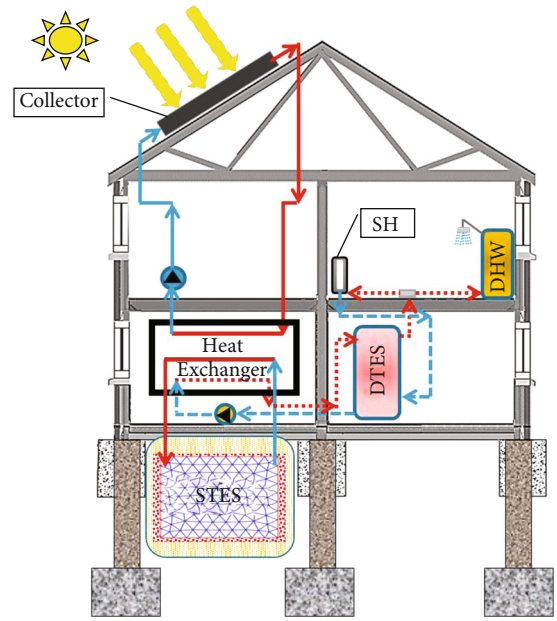

Figure 1: Seasonal thermal energy storage and solar combisystem schematic diagram in a building. *STES: seasonal thermal energy storage; DTES: diurnal thermal energy storage; SH: space heating; DHW: domestic hot water.

authors will assess the best performance of the STES that will be relevant to the best solar energy features for one of the selected locations. Jordan is characterized by having available solar energy along with more than 300 sunny days/year, where it is one of the sun-belt states and most of its area is exposed to a very high solar irradiance [21].

The annual incident solar irradiance is 2337, 2191, and 1241 kWh m^{-2} for Zarqa, Doha, and Potsdam, respectively, according to Global Solar Atlas Data [22].

3.1. Architectural Design of the Building. The four-story building, hotel with floor area 400 m^2, was chosen for this study's design and simulation. The building was designed with the same dimensions and orientation (north orientation) in the three cities but with different insulation materials due to the different weather conditions. The hotel's occupation capacity is 80 persons including the staff, while the capacity of each bedroom hosts two persons. The hotel building was drawn using SketchUp® in a three-dimensional view as shown in Figure 3(a) and a two-dimensional floorplan for the ground floor and the one above it as shown in Figure 3(b). Three different buildings' envelope constructions were designed following the codes as, listed in Table 2, to reduce the heat loss/gain due to the different levels of weather conditions. The authors used Polyurethane insulation panels between outside stone and internal concrete hollow block as a wall assembly in different thicknesses based on the climatic features of each selected location [23].

3.2. Hotel's Heat Demand

3.2.1. Hotel's Space Heating Load. The authors proposed a novel methodology for calculating hotel's space heating

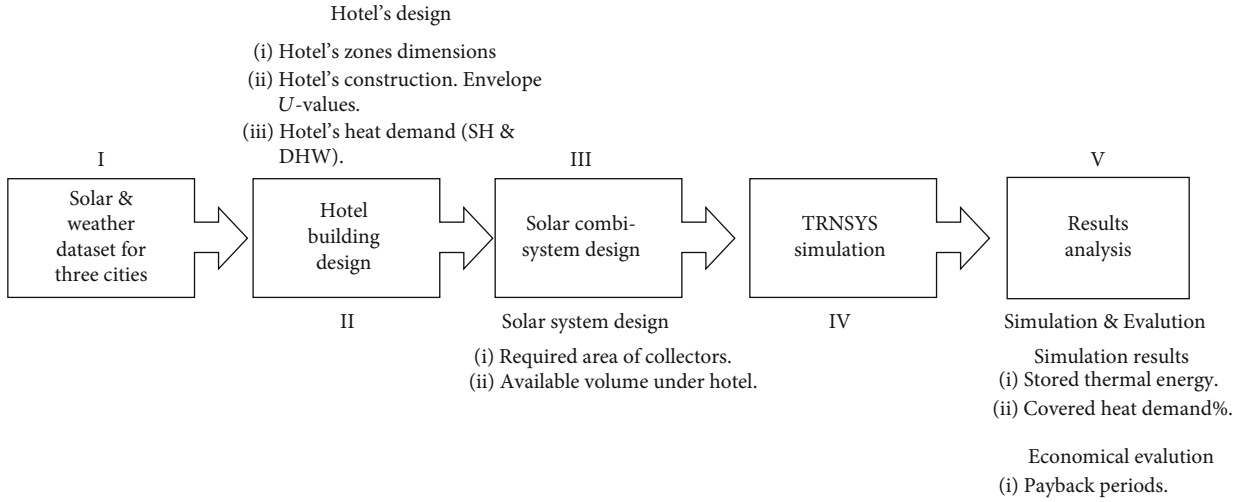

Figure 2: Block diagram of the research methodology's steps.

Table 1: Climatic properties for the three locations [19, 20].

City	Climatic zone	Lat.	Long.	Alt.	T_{avg} (°C)	T_{min} (°C)	T_{max} (°C)	I_G (kWh·m^{-2}a^{-1})	I_B (kWh m^{-2}a^{-1})	I_D (kWh m^{-2}a^{-1})	HDD (K d)
Zarqa	Semiarid	32.3	36.2	682.8	18.33	1	36	2,109	1,494.7	615.12	1,482
Doha	Desert	25.3	51.6	10.7	28.9	12	45	2,173	1,473.3	699.4	140.2
Potsdam	Humid temp.	52.4	13.1	81	10.5	-3.1	25.6	1,110	542.6	567.6	3,097.3

I_B: beam incident irradiation; I_D: diffuse incident irradiation; I_G: global (total) incident irradiation; HDD: heating degree days; T_{avg}: average air temperature; T_{min}: minimum air temperature; T_{max}: maximum air temperature.

demand. Space heating (SH) loads of the three buildings were calculated based on the degree days method [25]. The designation of heating degree days for the three different climatic zones provides a tempo-spatial map of heating demand. The knowledge of total hotel's space heating demand was used to identify the accumulated heat demand curve, appropriate for seasonal thermal energy storage system modelling.

The conduction and infiltration loads of the hotel buildings were calculated using equations ((1)–(3)) with 21°C indoor design temperature.

$$Q_T = Q_c + Q_i, \tag{1}$$

$$Q_C = \frac{24}{1000} U \times A \times \text{HDD}, \tag{2}$$

$$Q_i = \frac{24}{1000} \times \frac{\rho c_p V}{3600} \times \text{HDD}, \tag{3}$$

where Q_c is the heat gain/loss due to conduction through walls, windows, and roof (kWh); Q_i is the heat gain/loss due to infiltration (kWh); U is the overall heat transfer coefficient (W m^{-2}·K^{-1}); A is the surface area for walls, windows, or roofs (m^2); HDD is the heating degree days (K day); ρ is the density of air (1.225 kg m^{-3}); C_p is the specific heat of air (1000 J kg^{-1} K^{-1}); V is the volume changed per hour based on the Air Change Method (m^3 h^{-1}).

Two schedules of the hotel's internal load that generated by occupancy and electrical equipment were estimated by the authors to calculate the amount of heat gain.

The resulting annual space heating load is shown in Figure 4. It can be noticed that the annual space heating load for Potsdam was the highest at 101 kWh m^{-2} year^{-1}, which is comparable to the 100 kWh m^{-2} year^{-1} for the hotel sector in Germany [26]. On the other hand, the annual space heating load for Zarqa was 57 kWh m^{-2} year^{-1}; this result is a bit lower than what was previously recorded at around 95 kWh m^{-2} year^{-1} [25]. This could be attributed to the fact that this study used a building envelope's construction with U values lower by half than the one that was used in [25]. Finally, the annual space heating load for Doha city was the lowest one at 14 kWh m^{-2} year^{-1} due to its warm climate throughout the year. This result is comparable to 15 kWh m^{-2} year^{-1} previously recorded for Doha [27].

3.2.2. Hotel's Domestic Hot Water (DHW) Load. It was assumed that the percentage of the annual occupation of the hotel is 60% (around 45 residents). The daily DHW consumed per person was estimated to be equal to 30 liters person^{-1} day^{-1} at a set temperature for the hot water at 55°C according to the Standard Assessment Procedure (SAP) [28]. And the cold water temperatures were generated from NOAA website for the three cities, respectively [19]. The hotel's DHW load was calculated based on equations (4)–(5) [29].

$$Q_w = M_d \times C_{\text{water}} \times \Delta T, \tag{4}$$

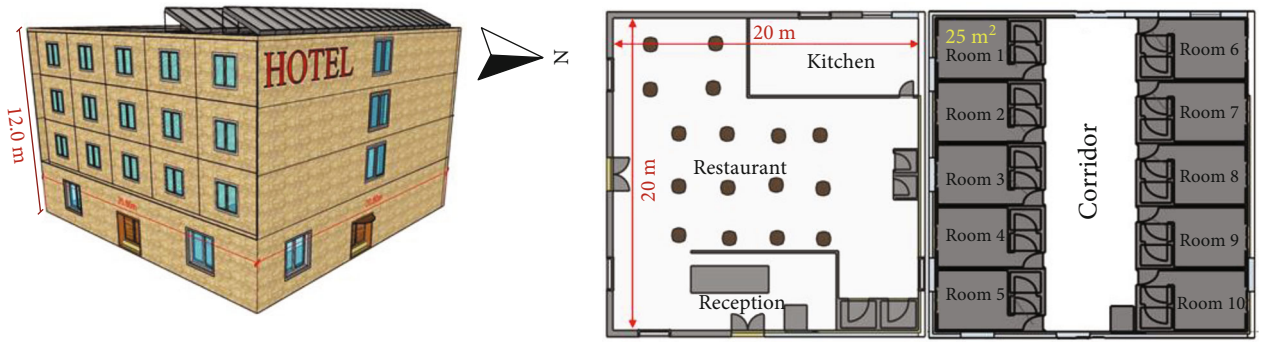

Figure 3: (a) 3D sketch of the hotel and (b) 2D cross-section for ground and first floor areas.

Table 2: Building envelope's construction specifications [23, 24].

Component	Area (m^2)	Construction thickness (m)			Construction U value (W m^{-2} K^{-1})		
		Zarqa	Doha	Potsdam	Zarqa	Doha	Potsdam
Floor	400	0.37	0.445	0.285	0.24	0.57	0.5
External wall	240x4	0.39	0.468	0.288	0.24	0.57	0.5
Roof	400	0.23	0.335	0.12	0.24	0.44	0.22
Internal walls	1,223	0.2	0.2	0.2	0.962	0.962	0.92
Doors	80	0.15	0.15	0.15	2.7	3	0.7
Windows	125	0.3	0.3	0.2	3.1	2.8	0.7

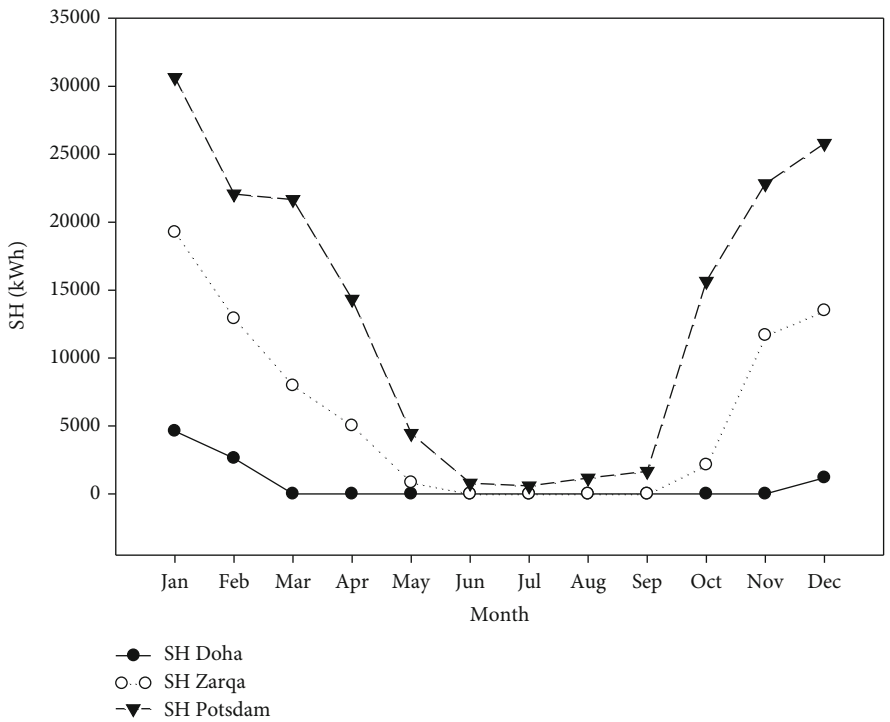

Figure 4: Monthly space heating loads for the three buildings (kWh) in the three selected cities.

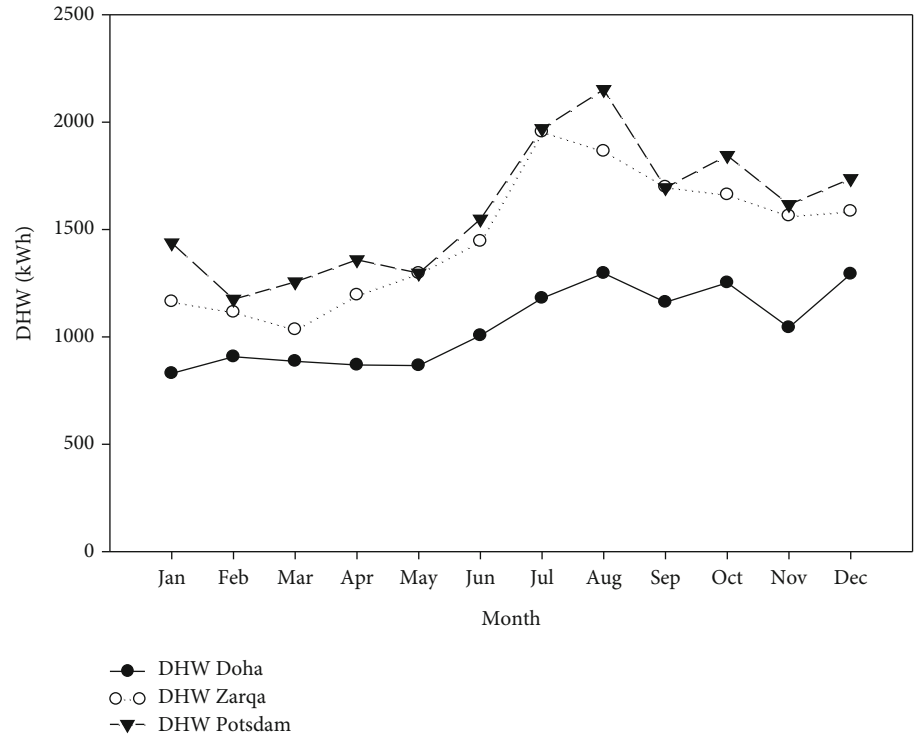

(a)

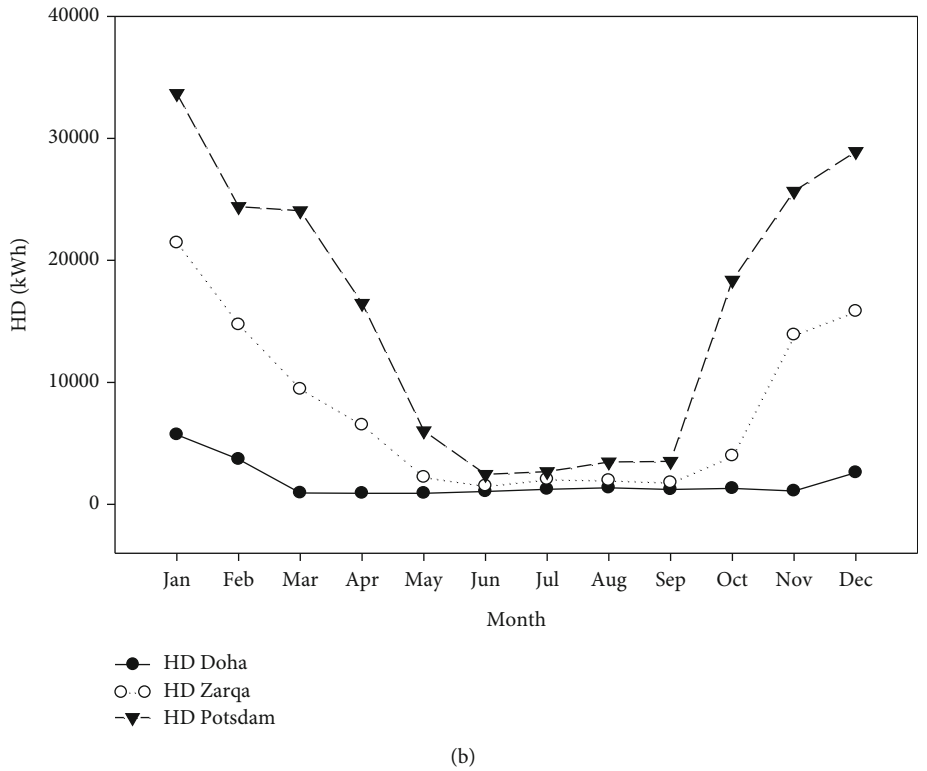

(b)

Figure 5: (a) Monthly DHW load for the three buildings (kWh) and (b) monthly total heating demand for the three buildings (kWh).

Table 3: The technical details of the used solar thermal collector (CPC 18) [33].

Type of collector	Dimensions (m)	Number of tubes	Stationary temperature (°C)	Peak output per module (W_{peak})	Conversion factor η_0	Thermal conductivity a_1 W/(m^{2}K)	Thermal conductivity a_2 W/(m^{2}K)
CPC 18	1.6 ∗ 2.1	18	249	2039	0.713	0.974	0.005

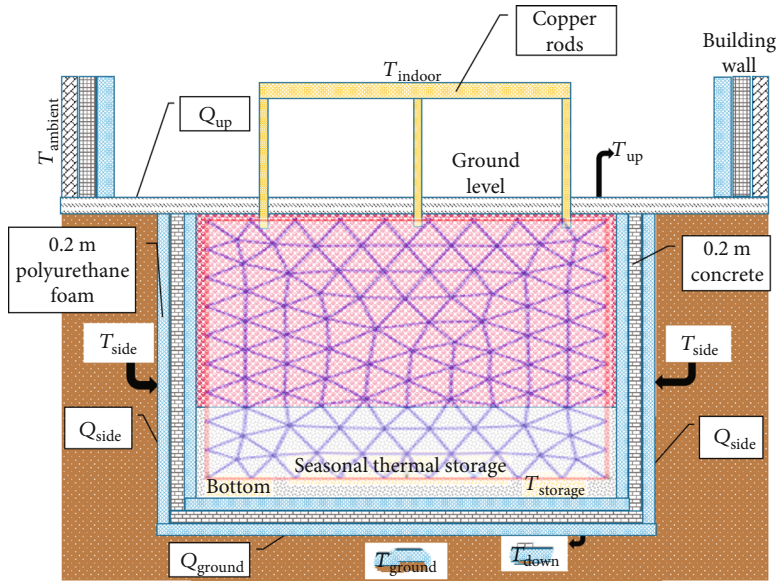

Figure 6: STES environmental variable diagram. *T_{ground}: ground temperature; T_{side}: STES surface temperature; T_{down}: STES bottom temperature; $T_{storage}$: STES temperature; T_{up}: STES upper surface temperature; T_{indoor}: hotel's indoor-air temperature. Temperature was measured by °C; all Q symbols are illustrating the heat loss according to their relevant temperatures.

$$M_d = v_d \times \rho_{water}, \quad (5)$$

where Q_w is the required energy for DHW load (kWh), M_d is the volume of daily consumed hot water (liter day^{-1}), C_{water} is the specific heat capacity of water (1.16 kWh m^{-3} K^{-1}), ΔT is the temperature difference between cold and hot water (K), and ρ_{water} is the density of water (0.988 kg m^{-3}).

The resulting annual DHW load is shown in Figure 5(a); it is observed that it varies depending on the climatic zone, whereas the annual DHW load of Zarqa was 17,583 kWh year^{-1}, the lowest annual DHW load was for Doha at 12,597 kWh year^{-1}, and the highest load was that of Potsdam at 19,095 kWh year^{-1}. All DHW loads are comparable to previously recorded results [29]. Consequently, the resulting total annual heating demand of the three cities is shown below in Figure 5(b).

3.3. Solar Thermal Combisystem

3.3.1. Solar Thermal Collector. Solar thermal collectors are the main source of the thermal energy that will supply to the building's thermal applications to cover its heat demand. The solar thermal collectors charge the STES for storing the thermal energy from the summer season to be used in the winter season. Such systems that consist of solar thermal collectors charging DHW and space heating (SH) applications is called a solar thermal combisystem.

Table 4: STES medium's material thermal specifications [15, 42, 43].

Material	Specific heat (kJ kg^{-1}K^{-1})	Density (kg m^{-3})	Thermal conductivity (W m^{-1} K^{-1})	Energy Density (kJ m^{-3} K^{-1})
Silica sand (SiO_2)	0.73	2,650	1.5	2,000-2,500
Basalt stone	0.84	2,400	3.5	4,200
Copper	0.39	8,700	400	3,500

Evacuated tube collectors are more efficient than flat plate collectors, and they have a longer life cycle with lower required maintenance [30, 31]. The used solar thermal collectors in this study were the Compound Parabolic Collector (CPC 18) due to their high efficiency and sustainability. The collectors were oriented to the south direction, and the simulation was performed with different collector tilts due to the incident solar irradiance in the three cities. The required area of collectors for three locations was calculated using equation (6) [32], where the solar fraction was estimated by authors to equal 0.8 [33]. The compound parabolic collectors (CPC) are typical collectors that are able to collect both beam and diffuse

Table 5: TRNSYS® simulation parameters.

Main	Zarqa	Doha	Potsdam
Length of simulation (years)	5	5	5
Simulation start	June	June	June
Building floor area (m^2)	400	400	400
STES			
STES volume (m^3)	300	50	300
STES insulation thickness (m)	0.4	0.4	0.4
STES C_p (kJ/kg.K)	0.77	0.77	0.77
STES initial temperature (°C)	21.5	28.9	12.73
Collector			
Working fluid	Ethylene glycol	Ethylene glycol	Ethylene glycol
Collector type	CPC 18	CPC 18	CPC 18
Collector area (m^2)	135	60	250
Tilt angle	28°	25°	32°
T_{boil} collector (°C)	155	155	155
$T_{protection}$ STES (°C)	150	150	150

*C_p: specific heat; CPC: compound parabolic collector.

radiation [34]. The technical details of the used solar thermal collector are shown in Table 3.

$$A_c = \frac{\text{No.of days} \times Q_{water} \times \text{solar fraction}}{\text{yearly solar irradince} \times \text{Avg system efficiency}}. \quad (6)$$

Two working fluid were used to be circulated in two loops that cross the heat exchanger. Ethylene glycol has far superior heat transfer properties more than propylene glycol. Accordingly, the ethylene glycol was circulated in the primary loop between the collectors and the heat exchanger because it provides effective freeze protection as long as the proper antifreeze concentration is maintained. Ethylene glycol would be changed every 3-5 years because the antifreeze fluids degrade over time [35]. The circulated hot water will pass through the second loop driven by pump power, and a part of that circulated hot water will be stored temporarily in diurnal thermal energy storage (DTES) for daily usage. The working fluid loops were illustrated as shown in Figure 1. Consequently, the volume of the DTES was calculated by using equation (7) [36].

$$V_{st} = \left[\left(\text{number of beds} \times \text{annual occupancy\%} \times HWD_p\right) + HWD_r\right] \times 1.2, \quad (7)$$

where HWD_p is the average hot water demand per person (liters) and HWD_r is the average hot water demand for the hotels' kitchens (liters) and the annual occupancy is 60% for the three cities.

3.3.2. Solar Thermal Heat Exchanger. Transferring the thermal energy from the solar collectors' circulation to the STES needs an effective heat exchanger working on a liquid to solid transferring approach as shown in Figure 1. According to the heat atlas [37], the shell and tube heat exchanger was the best choice to use in this STES system. Shell and tube heat exchanger has high effectiveness due to its large available heat transfer area. It was assumed that the effectiveness of the used heat exchanger is up to 90%.

3.4. Seasonal Thermal Energy Storage (STES). An STES system was designed to fit in the filler area above the foundations' layer underneath the building. STES medium was solid materials like silica sand and basalt stone to be utilized as sensible heat storage (SHS) combined with a copper mesh to promote the distribution and diffusion of heat throughout the STES as shown in Figure 6. The whole parameters that illustrated in Figure 6; they were inserted in the STES component's models in TRNSYS® simulation software to clarify the STES thermal variables and its boundary conditions.

Three types of solid materials were investigated in this research to be utilized in the STES for storing the produced thermal energy by the solar thermal system throughout the year. The first one is the basalt stone; basalt is a very hard and dark-colored stone that is formed by volcanic activity, and it is available in many countries [38, 39]. The second type was silica sand; it is a mineral resource that can be used for different applications due to its good thermal properties and availability in both Europe and Jordan [40]. The third type was copper; a copper mesh was used to distribute the thermal energy within the STES and then to transfer it to the building's thermal applications through the heat exchanger when it is required. Copper is characterized by its high hardness and its high transmissivity of thermal energy due to its high melting point and its high resistance to corrosion [41]. The thermal specifications of the STES medium's materials are presented in Table 4.

The required area of the buildings' foundations in the three cities is dependent on the type of land and live and dead

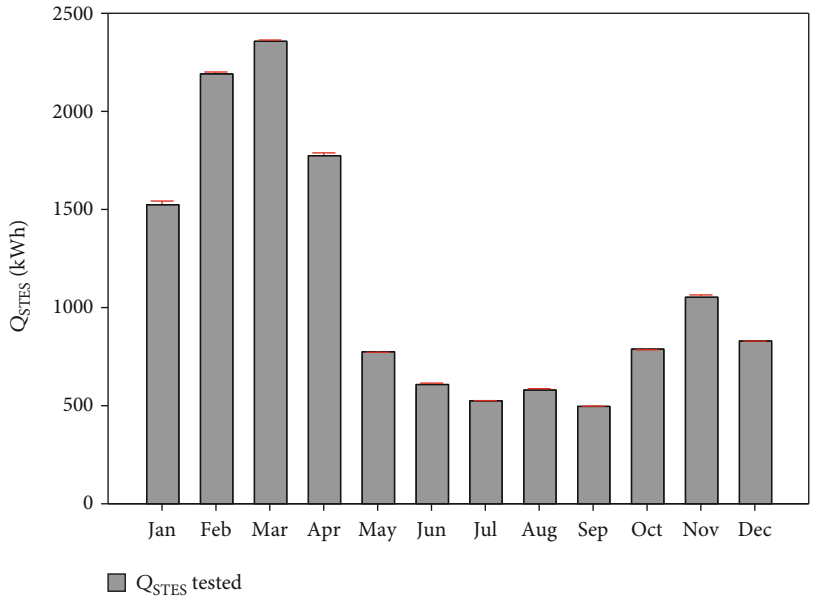

Figure 7: Comparison between Q_{STES} of [16] and tested.

loads of the buildings. Based on that, the available area of the STES can be calculated by subtracting the required area of the building foundations from the overall building area. With the high variety of that characteristic of the three cities, it was assumed that the ratio of building's foundation area is 20% of the building's floor area depending on best practice records. Therefore, the available volume under the building is 300m^3.

The overall STES-specific heat was calculated using equation (8) and in accordance with the STES materials thermal specifications listed in Table 4. The mass percentage was divided due to the highest specific heat (C_p) of the STES materials. The percentage ratios are 65% of basalt stone, 30% of silica sand, and 5% of copper mesh.

$$C_{p,STES} = \frac{m_{silica\ sand}}{m_{total}} C_{silica\ sand} + \frac{m_{basalt}}{m_{total}} C_{basalt} + \frac{m_{copper}}{m_{total}} C_{copper}, \quad (8)$$

where $m_{silica\ sand}$, m_{basalt}, and m_{copper} are the selected mass (kg) of the silica sand, basalt, and copper, respectively; m_{total} is the total mass of the STES medium (kg); $C_{silica\ sand}$, C_{basalt}, and C_{copper} are the specific heat (kJ kg^{-1} K^{-1}) of the STES materials silica sand, basalt, and copper, respectively.

The STES was insulated with 0.2 m of polyurethane foam and 0.2 m of concrete stratification to avoid the heat loss between the STES and the underground environment and to avoid the leakage from the surrounding groundwater as well [44].

3.5. Simulation Parameters. The simulation was constructed based on the deck file of the task 32 [5] by following the simulation running process steps inherent in TRNSYS®. The simulation was performed for a five-year span starting from June where the STES can operate without an auxiliary heater. The TRNSYS® simulation parameters are shown in Table 5.

Based on different heat demands of the buildings, the required collector area was calculated using equation (6) The collectors' tilt angles were fixed to a certain angle according to each city's coordinates. The authors did not use a solar tracking system according to its high cost, where it needs periodic maintenance as well [45]. The initial STES temperatures were equal to the ground temperatures for the three cities, respectively, where it is 21.5°C in Zarqa [46], 28.9°C in Doha [47], and 12.7°C in Potsdam [48].

Based on the high building's heat demand and the solid materials into the available STES volume, the temperature of the STES was set to the maximum 150°C for the three cities to avoid the heat dissipation and losses. Then, the collector boiling temperature was calibrated to 155°C [49]. The STES-specific heat was calculated using equation (8).

The rate of the covered heat demand (Q_{HD}) by the STES for each month will be calculated by using equation (9).

$$\text{Covered } Q_{HD} = \frac{Q_{Stored}}{Q_{HD}} \times 100\%. \quad (9)$$

4. Model Validation

The stored thermal energy for the long term under certain climate conditions is evaluated by the capacitance of the STES to cover the building's heat demand. Therefore, the STES capacitance is the most critical metric tool that will be taken into consideration in any STES design process. TRNSYS® simulation tool can provide an accurate illustration of the thermal performance of a STES.

In order to validate this study, another study, [16], was replicated through a TRNSYS® simulation using the same STES parameters. Accordingly, the maximum relative error for the monthly stored thermal energy between the validation and the referenced study was 1%, while the average relative error was 0.6% as shown in Figure 7.

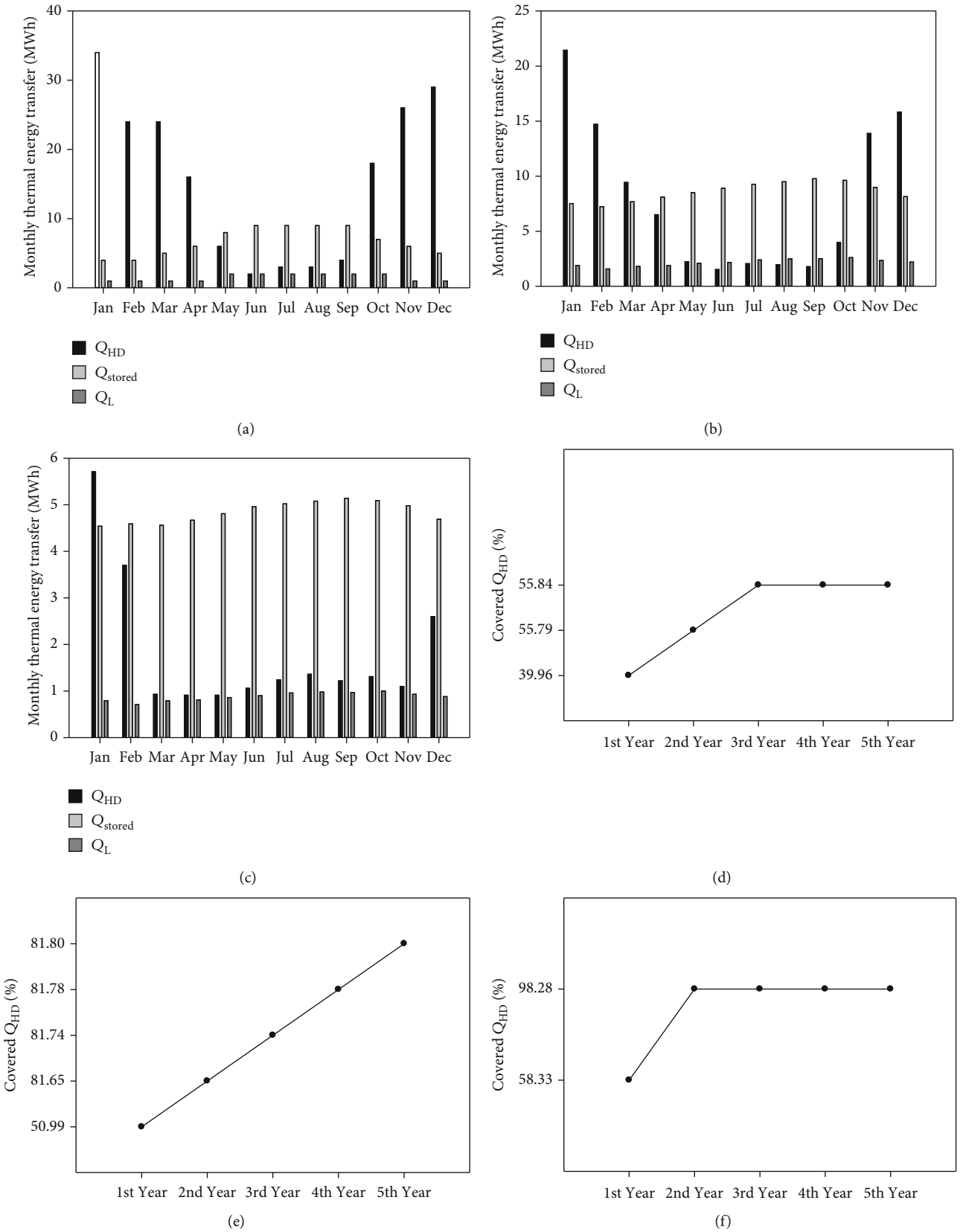

Figure 8: The TRNSYS® simulations' fifth year's STES monthly values for (a) Potsdam, (b) Zarqa, and (c) Doha. Percentage of covered heat demand (kWh) by STES during the five-year span for (d) Potsdam, (e) Zarqa, and (f) Doha.

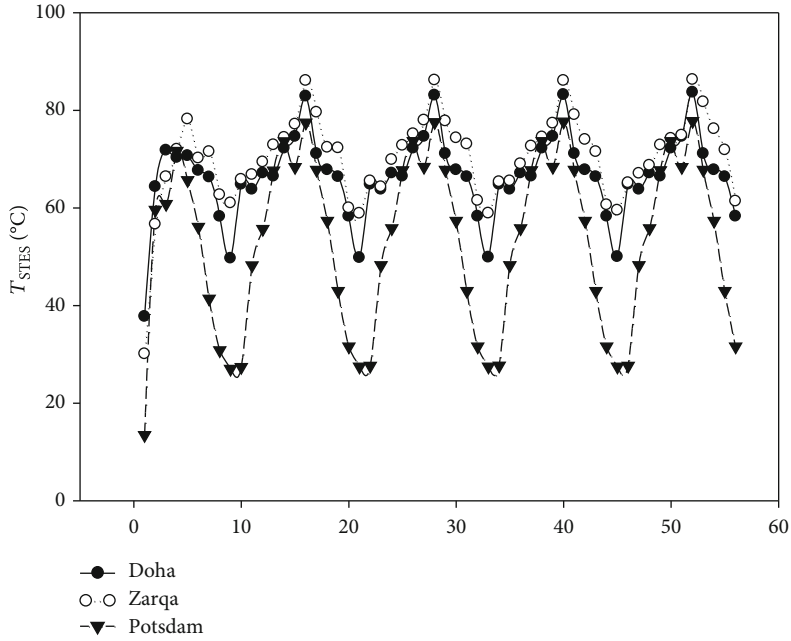

Figure 9: STES temperatures along the simulations' five-year span in the three selected cities.

5. Results

The utilization of STES allows the storage of thermal energy from the summer season to be recalled during the winter season. The design of the STES system in three different climatic zones based upon a simulation on TRNSYS® was performed, while the hotel's heat demand was calculated based on the illustrated methods and then compared with the resulted stored thermal energy from TRNSYS® simulation process. For more details about the used deck file in TRNSYS® simulation software (see Appendix (II)).

5.1. Simulation Results during the Five-Year Span for the Three Cities. The simulation results focused on the percentage of the covered hotel's heat demand where the rate of the covered heat demand (Q_{HD}) for each month along the fifth year of the STES operation was calculated by using equation (9).

5.1.1. The Thermal Energy Transfer in the STES. The values of the monthly TES in the STES and their relevant thermal losses throughout the whole system during the fifth year are shown in Figures 8(a)–8(c) for Potsdam, Zarqa, and Doha, respectively. For Potsdam, although the simulation was applied for five years to study the performance of the STES, the STES covered about 16% of building's heat demand in the winter months from December to February; the STES covered 100% of building's heat demand in the summer season, from June to August, as it was only necessary for the DHW load. For Zarqa, the stored thermal energy after five years of simulated operation of the STES system covered 45.23% of the building's heat demand in the winter, while it covered the whole heat demand in summer. For Doha, the simulation results after five years of STES covered the entire building's heat demand throughout the summer while it covered 36.11% in the winter.

5.1.2. The Fractions of the Covered Buildings' Heat Demand Supplied by STES. The fractions of the covered buildings' heat demand supplied by STES throughout the same five-year span are presented in Figures 8(d)–8(f) for Potsdam, Zarqa, and Doha, respectively. For Potsdam, despite using a large collectors' area, the STES was not able to cover the total heat demand of the building. The results show that the STES did not cover more than 55.84% in any of the five years of its operation, which could be attributed to the limited solar energy with low temperatures in the winter in Potsdam. Thus, cold temperatures cause a high heat loss between the building's construction envelope and the STES with their surrounding environment. The utilization of an STES system in Zarqa can provide about 81.8% of thermal energy annually due to the availability of incident solar radiation yearlong; the cumulative stored thermal energy with continuous charging can contribute to increasing the stored thermal energy throughout the STES operation process. High solar irradiance combined with high ambient temperatures in Doha allowed the STES system to provide 84.03% of the building's heat demand after the fifth year of its operation.

5.1.3. The STES Output Temperatures. Figure 9 shows the STES temperature variation along the five-year span for the three cities. The STES temperature did not drop below 57.2°C in the winter in Zarqa, whereas it was up to 86.1°C in the summer. On the other hand, the temperature reached 26.2°C in the winter in Potsdam, whereas it was up to 77.5°C in the summer season. The used collector area was 60 m^2, 135 m^2, 250 m^2 for Doha, Zarqa, and Potsdam, respectively. The STES volume was 50 m^3 in Doha and was the smallest

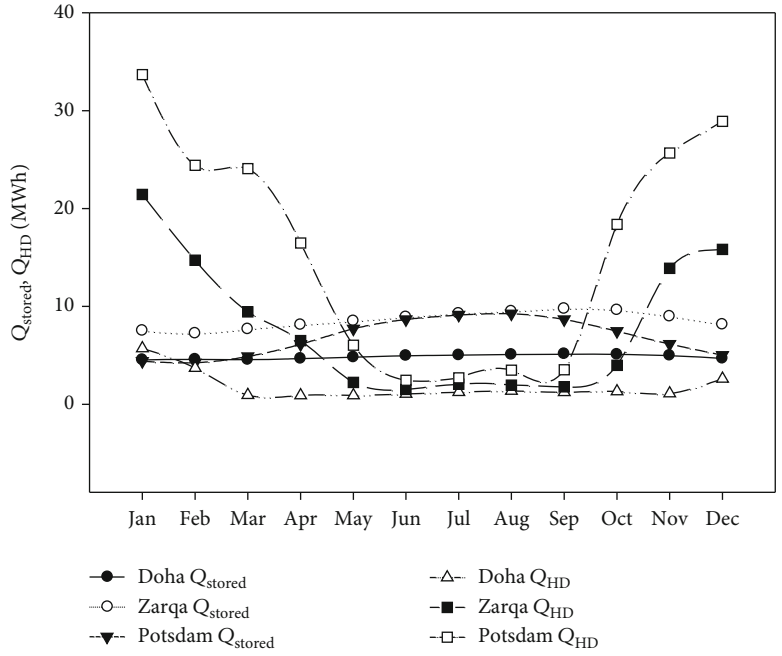

(a)

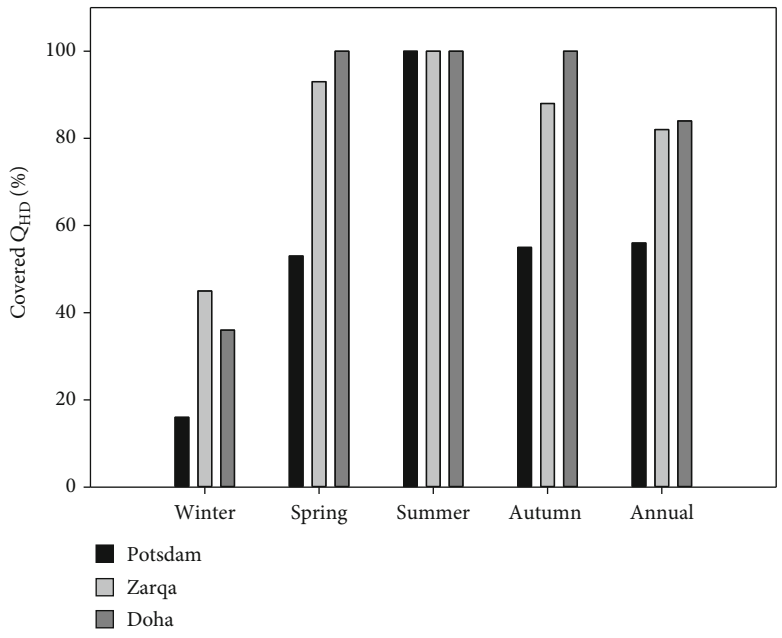

(b)

Figure 10: (a) Best results of stored solar thermal energy versus the buildings' heat demand for the three selected cities and (b) percentage of seasonal and annual covered heat demand for the same cities.

Table 6: Comparison between this study and the reference used for the simulation's validation.

	STES	STES [16]
Excavation cost ($)	Already buried between the building's foundations pillars (There is no excavation cost)	Buried underground beside the building (There is an excavation cost)
Working temperature (°C)	≈1000	≈100
Corrosion	Less corrosive	Corrosive
Freezing	Antifreezing (STES medium consists of solid materials)	It freezes below 0 °C
Maintenance	Maintenance free	Periodic maintenance
STES specific heat (kJ $kg^{-1}K^{-1}$)	Low ≈ 0.77	High = 4.19
Charge/discharge	Slow	Faster
STES annual capacity (kWh m^{-3})	(Doha: 355, Zarqa: 344, Potsdam:273)	370

Table 7: The capital cost of solar combisystem and STES [50].

Component	Initial cost ($)	Cost ($) Zarqa	Potsdam	Doha	Replacement period (years)
Solar collectors	$560 \times N_{collector} + 1146.8$	24,106	43,146	11,226	25
DTES tank	$2.746 \times V_{DTES} + 952.35$	3,066	3,066	3,066	15
Ethylene glycol	$15.53 \times N_{collector} + 148.26$	785	1,313	427.8	3
Pumps	827 (each)	1,654	1,654	1,654	10
Pipes	5 × 1 m of pipe	200	200	200	—
Silica sand	20 × volume of silica sand	1,400	1,400	400	—
Basalt stone	30 × volume of basalt stone	6,000	6,000	1,050	—
Copper mesh	10 × 1 m^2 of copper mesh	10,000	10,000	2,000	—
Insulation (polyurethane foam)	7 × 1 m^2 of polyurethane foam	9,800	9,800	1,750	—
Total		57,012	76,580	21,775	

$N_{collector}$: the solar collectors' number; V_{DTES}: the volume of the used DTES tank (770 liters, by applying equation (7)).

one due to the low heat demand, compared with 300 m^3 in Zarqa and Potsdam. Therefore, that area of collectors in Doha was able to heat 50 m^3 of STES to a maximum temperature of 84.25°C along five years of STES operation, while it dropped to 49.72°C in winter.

5.1.4. The Best Results of Stored Thermal Energy and the Covered Buildings' Heat Demand. The results of the stored thermal energy in the STES in the fifth year of simulation compared with the required building's heat demand are illustrated in Figure 10(a) along with the percentage of seasonal and annual covered heat demand simultaneously for the three cities in Figure 10(b). The stored thermal energy in Zarqa was 103,268 kWh, the highest out of three cities, due to the abundance of solar irradiance compared to Potsdam. The stored thermal energy in Potsdam at 81,800 kWh even though that the used collector area in Potsdam was twice that in Zarqa. The results for Doha were less favorable at 17,730 kWh due to the small collectors' area compared with Zarqa and Potsdam. The percentage of the buildings' annual covered heat demand was 81.8% for Zarqa, 55.84% for Potsdam, and 84.06% for Doha.

Table 8: Hotel's electricity demand cost for the three cities.

City	Annual heat demand (kWh)	Electricity cost ($ kWh^{-1})	Electricity cost reference	Annual electricity cost ($/kWh)
Potsdam	18,9737	0.21	[51]	39,845
Zarqa	94,494	0.13	[52]	15,623
Doha	22,063	0.04	[53]	883

For more details, see Appendix (I) that contains the simulation results of the thermal energy transfer in the STES for the three locations.

5.2. Comparison with Literature: STES Pros and Cons. The results of this study were compared with the results of the study used for the simulation's validation in reference [16] and are listed in Table 6.

6. Economic Evaluation

The capital cost of the solar thermal combisystem combined with STES was calculated to be compared with electricity

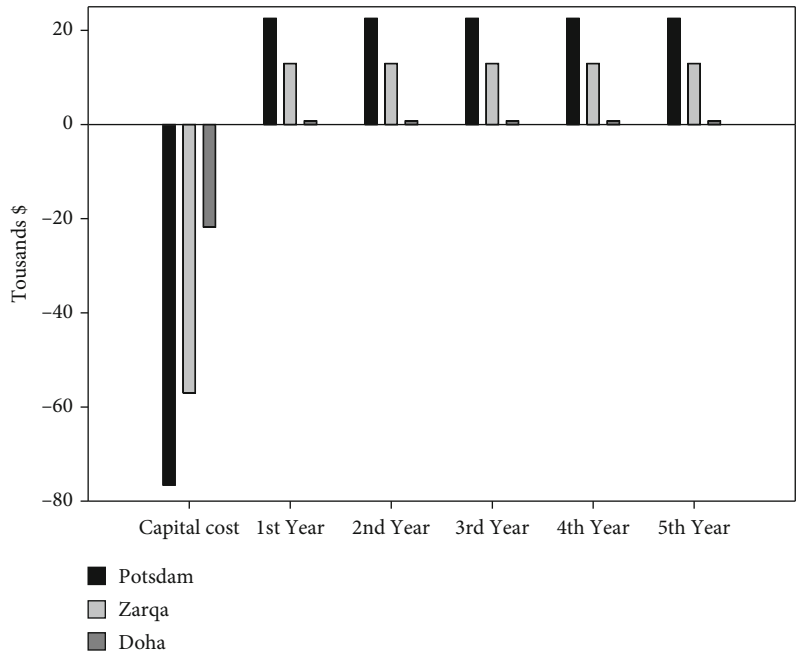

Figure 11: Cash flow diagram for the three selected locations.

consumption for covering the building's heat demand. The calculating approach of the initial cost for each component in the solar combisystem was calculated according to reference [50], while the initial cost of the STES components was calculated though best practices due to the difficulty of its pricing in the market.

6.1. The Capital Cost of the STES System for the Three Cities. The components' initial costs are listed in Table 7 for the three cities along with the replacement period of each component. The life span relevant to each component is different rendering it difficult to have a fixed life span for the whole system.

6.2. The Annual Electricity Cost and Savings for the Three Cities. The electricity consumption for covering the building's heat demand was calculated using equation (10) for the three cities in order to determine the electricity cost for each city; the results are shown in Table 8.

$$\text{Annual electricity cost}\left[\frac{\$}{\text{kWh}}\right] = \text{Annual HD}[\text{kWh}] \times \text{Electrictiy Cost}\left[\frac{\$}{\text{kWh}}\right]. \quad (10)$$

The savings from the electricity bills were calculated using equation (11) for the three cities.

$$\text{Annual Electricity Savings}\left[\frac{\$}{\text{kWh}}\right] = Q_{\text{HD}}[\text{kWh}] \times \text{Covered } Q_{\text{HD}}\% \times \text{Electricity Cost}\left[\frac{\$}{\text{kWh}}\right]. \quad (11)$$

6.3. The Cash Flow Diagram and STES System's Payback Periods for the Three Cities. Based on the calculated system's capital cost and the savings from the electricity bills for the three cities, the cash flow diagrams of the three cities were generated as shown in Figure 11.

It can be observed from Figure 11 that the net annual savings from electricity costs are around 22,533 \$ kWh^{-1}, 12,963 \$ kWh^{-1}, and 858 \$ kWh^{-1} for Potsdam, Zarqa, and Doha, respectively. When the capital cost of each city, shown in Table 7, is divided by the net annual savings from electricity cost, the yield payback periods are 3.4 years, 4.4 years, and 29.4 years for Potsdam, Zarqa, and Doha, respectively.

7. Conclusion

All buildings are built on foundation pillars that are based deep into the ground. To increase the soil consistency between these foundation's pillars, the space is backfilled with durable basaltic materials. The underground space can be utilized for an innovative solution for a seasonal energy storage system that could be buried under the building by using the same excavation for the building's foundation, replacing regular basaltic backfill materials with solid materials that have good thermal properties. This study simulated a hotel building with 400 m^2 floor area that could benefit from STES to store thermal energy during the summer and autumn seasons to take advantage of this stored energy to cover the hotel's heat demand from domestic hot water and space heating loads in the winter. The selected solid materials were silt materials that are available in the global market like silica sand and basalt stone combined with a copper mesh for heat distribution through the STES. The STES system was charged by a solar thermal combisystem for a five-year span with different collector areas in three different climate zones in Potsdam (Germany), Zarqa (Jordan), and Doha (Qatar).

Based on the economic evaluation and the simulation of the system for the three cities, the best obtained results were for Zarqa. The system's payback period was 4.4 years combined with a coverage of 81.8% of the building's annual heat demand. The STES system covered 56% of the building's annual heat demand in Potsdam due to the low incident solar radiation, where the system's payback period was 3.4 years. Finally, although the STES covered 84% of the building's annual heat demand in Doha, the system's payback period was 29 years due to the low price of the electricity in Qatar.

Accordingly, implementing this STES system in Zarqa would cover the building's heat demand in a feasible and efficient manner via this sustainable system.

Appendix

A. The best results of the stored thermal energy in the fifth year compared with the hotel's heat demand for the three cities.

Months	Potsdam			
	Q_{STES} (kWh)	Q_{HD} (kWh)	Q_L (kWh)	Covered Q_{HD} %
Jan	4,396	33,679	793	13.05%
Feb	4,252	24,406	611	17.42%
Mar	4,891	24,068	736	20.32%
Apr	6,144	16,470	1,075	37.30%
May	7,722	6,027	1,516	100%
Jun	8,680	2,454	1,963	100%
Jul	9,128	2,686	2,337	100%
Aug	9,263	3,477	2,412	100%
Sep	8,674	3,521	2,213	100%
Oct	7,470	18,371	1,971	40.66%
Nov	6,164	25,666	1,437	24.02%
Dec	5,017	28,912	1,085	17.35%
Total	81,800	189,737	18,148	—
Avg	6,817	15,811	1,512	55.84%

Months	Zarqa			
	Q_{STES} (kWh)	Q_{HD} (kWh)	Q_L (kWh)	Covered Q_{HD} %
Jan	7,523	21,436	1,898	35.10%
Feb	7,235	14,721	1,566	49.15%
Mar	7,679	9,441	1,799	81.34%
Apr	8,111	6,508	1,897	100%
May	8,504	2,231	2,092	100%
Jun	8,907	1,518	2,169	100%
Jul	9,274	2,053	2,386	100%
Aug	9,505	1,959	2,489	100%
Sep	9,774	1,783	2,495	100%
Oct	9,632	3,982	2,601	100%
Nov	8,978	13,893	2,342	64.63%
Dec	8,146	15,834	2,201	51.44%
Total	103,268	94,494	25,935	—
Avg	8,606	7,947	2,161	81.80%

Table: Continued.

Months	Doha			
	Q_{STES} (kWh)	Q_{HD} (kWh)	Q_L (kWh)	Covered Q_{HD} %
Jan	1,254	5,715	484	21.95%
Feb	1,362	3,702	468	36.78%
Mar	1,358	931	543	100%
Apr	1,431	913	591	100%
May	1,516	910	635	100%
Jun	1,592	1,057	674	100%
Jul	1,581	1,240	713	100%
Aug	1,602	1,362	721	100%
Sep	1,643	1,220	710	100%
Oct	1,592	1,315	722	100%
Nov	1,509	1,096	652	100%
Dec	1,290	2,602	580	49.59%
Total	17,730	22,063	7,492	—
Avg	1,477	1,839	624	84.03%

Data Availability

All data are included in the manuscript.

Conflicts of Interest

The authors declare that they have no conflicts of interest.

References

[1] G. Hailu, "Seasonal solar thermal energy storage," in *Thermal Energy Battery with Nano-enhanced PCM*, M. S. Kandelousi, Ed., IntechOpen, 2018.

[2] C. Spandagos and T. L. Ng, "Equivalent full-load hours for assessing climate change impact on building cooling and heating energy consumption in large Asian cities," *Applied Energy*, vol. 189, pp. 352–368, 2017.

[3] D. P. M. Meena and M. Choudhary, "Thermal energy storage in sensible materials: a review," *INTERNATIONAL JOURNAL OF ADVANCE RESEARCH, IDEAS AND INNOVATIONS IN TECHNOLOGY*, vol. 3, pp. 607–613, 2017.

[4] L. Gao, J. Zhao, and Z. Tang, "A review on borehole seasonal solar thermal energy storage," *Energy procedia*, vol. 70, pp. 209–218, 2015.

[5] R. Heimrath and M. Haller, *The Reference Heating System, the Template Solar System of task 32- Report A2 of Subtask A*, Graz, Austria, 2007.

[6] M. L. Sweet and J. T. McLeskey, "Numerical simulation of underground Seasonal Solar Thermal Energy Storage (SSTES) for a single family dwelling using TRNSYS," *Solar Energy*, vol. 86, no. 1, pp. 289–300, 2012.

[7] L. T. Terziotti, M. L. Sweet, and J. T. McLeskey Jr., "Modeling seasonal solar thermal energy storage in a large urban residential building using TRNSYS 16," *Energy and Buildings*, vol. 45, pp. 28–31, 2012.

[8] N. Al-sudany, A. Al-Sa'ady, F. Al-bahadly, and A. Al-sudany, "The seasonal storage of thermal solar energy in Iraq," *International Journal of Application or Innovation in Engineering & Management*, vol. 3, pp. 77–85, 2014.

[9] J. Milewski, M. Wołowicz, and W. Bujalski, "Seasonal thermal energy storage - a size selection," *Applied Mechanics and Materials*, vol. 467, pp. 270–276, 2014.

[10] C. N. Antoniadis and G. Martinopoulos, "Simulation of solar thermal systems with seasonal storage operation for residential scale applications," *Procedia Environmental Sciences*, vol. 38, pp. 405–412, 2017.

[11] G. Hailu, P. Hayes, and M. Masteller, "Seasonal solar thermal energy sand-bed storage in a region with extended freezing periods: Part I experimental investigation," *Energies*, vol. 10, no. 11, p. 1873, 2017.

[12] M. Diago, A. C. Iniesta, A. Soum-Glaude, and N. Calvet, "Characterization of desert sand to be used as a high-temperature thermal energy storage medium in particle solar receiver technology," *Applied Energy*, vol. 216, pp. 402–413, 2018.

[13] Z. Ma, H. Bao, and A. P. Roskilly, "Feasibility study of seasonal solar thermal energy storage in domestic dwellings in the UK," *Solar Energy*, vol. 162, pp. 489–499, 2018.

[14] S. Kiwan and Q. R. Soud, "Numerical investigation of sand-basalt heat storage system for beam-down solar concentrators," *Case Studies in Thermal Engineering*, vol. 13, article 100372, 2019.

[15] H. Gunerhan and A. Hepbasli, "Utilization of basalt stone as a sensible heat storage material," *Energy Sources*, vol. 27, no. 14, pp. 1357–1366, 2005.

[16] I. Beausoleil-Morrison, B. Kemery, A. D. Wills, and C. Meister, "Design and simulated performance of a solar-thermal system employing seasonal storage for providing the majority of space heating and domestic hot water heating needs to a single-family house in a cold climate," *Solar Energy*, vol. 191, pp. 57–69, 2019.

[17] J. Lu, G. He, and F. Mao, "Solar seasonal thermal energy storage for space heating in residential buildings: optimization and comparison with an air-source heat pump," *Policy*, vol. 15, no. 5, pp. 279–296, 2020.

[18] I. Stadler, "The three pillars for a 100 % energy supply with renewable energies," *uwf UmweltWirtschaftsForum*, vol. 22, no. 1, pp. 17–27, 2014.

[19] "National Climatic Data Center (NCDC) Search | Climate Data Online (CDO) | National Climatic Data Center (NCDC)," https://www.ncdc.noaa.gov/cdo-web/search.

[20] "Photovoltaic Geographical Information System (PVGIS) JRC Photovoltaic Geographical Information System (PVGIS) - European Commission," https://www.ncdc.noaa.govhttps//re.jrc.ec.europa.eu/pvg_tools/en/tools.html#/cdo-web/search.

[21] A. M. Baniyounes, "Renewable energy potential in Jordan," *International Journal of Applied Engineering Research*, vol. 12, pp. 8323–8331, 2017.

[22] "Global Solar Atlas (GSA) Global Solar Atlas Datavol. 3https://globalsolaratlas.info/map?c=11.523088.

[23] A. Alkhalidi, S. Kiwan, and H. Hamasha, "A comparative study between Jordanian overall heat transfer coefficient (U-value) and international building codes," in *2019 10th International Renewable Energy Congress (IREC)*, pp. 1–5, Sousse, Tunisia, 2019.

[24] D.-N. I. Daas, "National Technical Committee for Preparing and Development-Concrete Structures Requirements," 2014.

[25] I. Al-Hinti and H. Al-Sallami, "Potentials and barriers of energy saving in Jordan's residential sector through thermal insulation," *Jordan Journal of Mechanical & Industrial Engineering*, vol. 11, pp. 141–145, 2017.

[26] E. Sonderveröffentlichung and D. Hotelbau, "Hotel's energy demand in Germany," https://www.facility-manager.de/.

[27] M. Khalfan, S. Sharples, A. Alexander, C. Skelhorn, and J. A. Bryant, "The first Passivhaus in Qatar: initial monitoring and modelling energy performance," 2014.

[28] "Standard Assessment Procedure (SAP) The Government's Standard Assessment Procedure for Energy Rating of Dwellings in UK," https://www.bre.co.uk/filelibrary/SAP/2012/SAP-2012_9-92.pdf.

[29] M. Richard, *Simulating Domestic Hot Water Demand by means of a Stochastic End-Use Model*, Stellenbosch University, 2016.

[30] A. Sakhrieh and A. Al-ghandoor, "Experimental investigation of the performance of five types of solar collectors," *Energy Conversion and Management*, vol. 65, pp. 715–720, 2013.

[31] A. Maraj, A. Londo, C. Firat, and A. Gebremedhin, "Comparison of the energy performance between flat-plate and heat pipe evacuated tube collectors for solar water heating systems under Mediterranean climate conditions," *Journal of Sustainable Development of Energy, Water and Environment Systems*, vol. 7, no. 1, pp. 87–100, 2019.

[32] D.-M. Viessmann, "Technical guide - solar thermal sysetms," https://www.viessmann.be/.

[33] S. Co, "Ltd Solar Systems - Evacuated tubes & Flat plate collectors' specifications," vol. 49, 2016.

[34] J. A. Duffie and W. A. Beckman, *Solar Engineering of Thermal Processes Book*, Research supported by the University of Wisconsin, New York, 2006, Fourth Edi..

[35] J. S. LaKind, E. A. McKenna, R. P. Hubner, and R. G. Tardiff, "A review of the comparative mammalian toxicity of ethylene glycol and propylene glycol," *Critical Reviews in Toxicology*, vol. 29, no. 4, pp. 331–365, 1999.

[36] W. Weiss, "Design of solar thermal design of solar thermal systems – calculation methods," http://www.crses.sun.ac.za/files/services/events/workshops/03_Design%20ST%20Systems_Calculation%20methods.pdf.

[37] P. D.-I. P. Stephan, *VDI Heat Atlas - standard book for heat exchanger*, P. D.-I. P. Stephan and P.-I. Martin, Eds., Springer, Second Edition edition, 2010.

[38] N. Mehyar, M. Madanat, and J. Sahawneh, "Mineral status and future opportunity (Basalt)," http://www.memr.gov.jo/EchoBusV3.0/SystemAssets/PDFs/AR/MineralTR/Basalt.pdf.

[39] P.-S. A. Taqieddin, "Physical and engineering properties of some selected Jordanian basalt," http://www.ijier.net/.

[40] M. Diago, A. C. Iniesta, T. Delclos, T. Shamim, and N. Calvet, "Characterization of desert sand for its feasible use as thermal energy storage medium," *Energy Procedia*, vol. 75, pp. 2113–2118, 2015.

[41] E. C. E. Rönnebro, G. Whyatt, M. Powell, M. Westman, F. Zheng, and Z. Z. Fang, "Metal hydrides for high-temperature power generation," *Energies (Basel)*, vol. 8, no. 8, pp. 8406–8430, 2015.

[42] "AZo materials silica - silicon dioxide (SiO2)".

[43] "AZo materials copper - specifications, properties, classifications and classes".

[44] G. Hailu, P. Hayes, and M. Masteller, "Long-term monitoring of sensible thermal storage in an extremely cold region," *Energies (Basel)*, vol. 12, no. 9, p. 1821, 2019.

[45] M. Z. Jacobson and V. Jadhav, "World estimates of PV optimal tilt angles and ratios of sunlight incident upon tilted and

tracked PV panels relative to horizontal panels," *Solar Energy*, vol. 169, pp. 55–66, 2018.

[46] I. Al-Hinti, A. Al-Muhtady, and W. Al-Kouz, "Measurement and modelling of the ground temperature profile in Zarqa, Jordan for geothermal heat pump applications," *Applied Thermal Engineering*, vol. 123, pp. 131–137, 2017.

[47] L. U. Xing, *Estimations of undisturbed ground temperatures using numerical and analytical modeling (Doctoral dissertation, Oklahoma State University)*, 2014.

[48] "Potsdam Institute for Climate Impact Research (PIK) Ground temperature — PIK Research," https://www.pik-potsdam.de/services/climate-weather-potsdam/climate-diagrams/ground-temperature/index_html?set_language=en.

[49] R. Hausner and C. Fink, *Stagnation behaviour of solar thermal systems - task 26*, Gleisdorf, Feldgasse 19 Austria, 2002.

[50] J. N. C. Hin and R. Zmeureanu, "Optimization of a residential solar combi-system for minimum life cycle energy and cost," in *Proceedings of eSim 2012: The Canadian Conference on Building Simulation*, pp. 94–107, Concordia University, 2012.

[51] "Clean Energy Wire (CEW) German power cost | Journalism for the energy transition," https://www.cleanenergywire.org/factsheets/what-german-households-pay-power.

[52] "Nationl Electric Power Company (NEPCO) Nationl Electric Power Company - NEPCO," http://www.nepco.com.jo/en/electricity_tariff_en.aspx.

[53] "Qatar General Electricity & water Corporation (QGEWC) Qatar General Electricity & water Corporation," https://www.km.qa/Pages/default.aspx.

Hindawi
International Journal of Photoenergy
Volume 2021, Article ID 6618284, 10 pages
https://doi.org/10.1155/2021/6618284

Research Article

Digital Fuzzy Current Controlled Light-Emitting Diode Driver with Power Factor Correction

A. S. Veerendra,[1,2] **A. A. Shah**,[1] **M. SubbaRao**,[3] **and M. R. Mohamed**[2]

[1]*Key Laboratory of Low-Grade Energy Utilization Technologies and Systems, MOE, Chongqing University, Chongqing 400030, China*
[2]*College of Engineering, Universiti Malaysia Pahang, Gambang, 26300 Kuantan, Pahang, Malaysia*
[3]*Department of Electrical and Electronics Engineering, Vignan's Foundation for Science, Technology and Research, Vadlamudi, Andhra Pradesh, India*

Correspondence should be addressed to A. A. Shah; akeelshah@cqu.edu.cn and M. R. Mohamed; rusllim@ump.edu.my

Received 17 December 2020; Revised 1 February 2021; Accepted 4 March 2021; Published 15 March 2021

Academic Editor: Francesco Riganti Fulginei

Copyright © 2021 A. S. Veerendra et al. This is an open access article distributed under the Creative Commons Attribution License, which permits unrestricted use, distribution, and reproduction in any medium, provided the original work is properly cited.

This paper presents the design and development of a fuzzy peak current controlled (FPCC) single-stage single-phase nonisolated AC/DC high-power factor LED drive. The proposed controller includes a fuzzy logic controller (FLC) in the loop voltage and a peak current controller in the loop current for an integrated nonisolated LED driver to attain a high-power factor (PF). The proposed control avoids complexities related to nonlinearities of the converter. The control action is initially derived from a group of rules written in accordance with experience and intuitive reasoning. The proposed technique is realized using a DSP processor (TI-TMS320F2812), which is capable of executing a high number of instructions in one cycle. A 70 W, 350 mA LED driver operating with an input of 90 V-230 V, 50 Hz was designed and implemented using MATLAB/Simulink. The results of the driver are in accordance with international regulations. The steady-state and transient responses are validated experimentally.

1. Introduction

An LED is a semiconductor unit that emits visible light when a current is passed through it. Lamps have good efficiency, are mercury free, and are long lasting [1, 2]. An LED provides control over light distribution with lenses or small reflectors and affords adaptability in the design of lighting apparatuses [3]. A block diagram of driver circuit is shown in Figure 1. In the case of a sinusoidal supply voltage, the driver must draw a sinusoidal current from the mains. To achieve this, an active filter is used along with a switched-mode power supply in one of two designs, namely, two-stage [4–7] and single-stage [8–12] power factor correction (PFC) topologies.

The two-stage power factor correction approach utilizes an input current shaping converter ahead of the DC/DC converter. Both of the converters are controlled individually to accomplish PFC and fast voltage regulation. This technique is known for its superior performance, such as high-power factor and low input current harmonics, which is achieved at the cost of additional circuitry (including control circuitry). This might not be justified for low-power applications. Subsequently, a one-stage design was proposed by using the concept of integration [13, 14]. In [15], an integrated buck-boost driver with classical controllers is examined for LED applications. It consists of a single control switch operated in buck and boost modes. The main drawback of the topology is a high value of storage capacitance and a voltage ripple. To minimize the capacitance, Soares et al. discussed a slope compensation technique in [16]. However, the ripple content is still increased in the voltage and current responses.

A driver may suffer damage if the current is higher than the rated current. In order to restrict the current, a closed-loop system control is important. Severe working conditions in terms of temperature and current density certainly influence the efficiency of LEDs [17]. The LED is used not only for lighting but also for several other applications such as computer or scoreboard displays. For such applications, the LED needs a driver that can control the voltage for all of the lamps. A fast settling time is also necessary for a scoreboard, due to high lighting motion from one LED to another

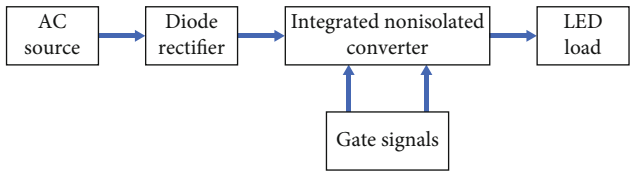

Figure 1: Block diagram of the driver.

within 5 to 100 ms. The color changing requires rapid responses in the current value and a stable voltage; therefore, proper control of the current and voltage distributions is required.

In recent years, there has been an increasing interest in control strategies to enhance the dynamic behavior of AC/DC converters. Classical (PI, sliding mode) and intelligent (fuzzy, neurofuzzy) control techniques are used in the literature to improve the performance of drivers. In [18–21], the authors considered converters possessing linear characteristics, but this strategy is not appropriate for some operating conditions. Moreover, there exists uncertainty due to source variations and load changes. Fuzzy logic control (FLC) is advantageous in this regard because it can accommodate parameter variations in the system and can therefore incorporate modeling uncertainty, neglected components, and nonlinearities [22–24]. Knowledge-based FLC attempts to code human knowledge, experience, and acumen to be able to make informed choices about the performance of the system. Knowledge-based FLC is a fuzzy rule base with suitable choices to control the activity of the plant under examination without human intervention [25–29]. In [30], the authors were able to achieve a PF of 0.98 and 13% THD using a digital fuzzy controller.

All passive components constituting the converters can be described by linear characteristics. This assumption is obviously not valid under all operational conditions, particularly since the inductance coefficients vary with the current. Moreover, there exists modeling uncertainty in the presence of input voltage fluctuations, load changes, and values of the component coefficients. Hence, in this work, we propose and develop a FLC in-the-loop voltage and fixed frequency peak current controller in the loop current for an integrated nonisolated LED driver. Unlike conventional controllers, a fuzzy peak current controller (FPCC) is used. To maintain performance under coil magnetic saturation and model uncertainty, FLC is selected because it can deal with the aforementioned uncertainty and variations, as well as neglected elements and nonlinearities. In this work, we consider source variations and load changes. The proposed controller attains a high-power factor (PF) with a low %THD, comparing favourably with conventional methods. Furthermore, the voltage loop driver feeds a regulated voltage to the LED panel. The DSP is a better option to realize the proposed FPCC due to its fast execution. Moreover, the driver is low cost, so that the controller and processor are affordable.

The objectives of this work are as follows:

(1) To design and develop an intelligent controller that can act effectively during source variations and load changes

(2) To achieve a high-power factor with a driver circuit during source and load variations in order to comply with international standards

(3) To attain a low %THD for any source and load variations in order to comply with international standards

2. Analysis of LED Driver

The integrated nonisolated LED driver is depicted in Figure 2, and the corresponding parameters are explained as follows.

2.1. Mains Current and Power. The current through L_1 during $(0 - DT_S)$ is the line current (i_s), where D is duty cycle and T_s is switching time period. The value of the mains current averaged at line frequency can be obtained using

$$(i_s) = \frac{1}{T_s}\frac{1}{2} i_{s_{\text{peak}}} DT_s = \frac{D^2 V_s}{2L_1 f_s} \sin(w_L t), \tag{1}$$

where $i_{s_{\text{peak}}}$ is the instantaneous peak current, f_s is the switching frequency, and V_s is the peak line voltage. From Equation (1), the line current is sinusoidal in shape, and subsequently, the power factor (PF) is unity by filtering electromagnetic interference (EMI) with a filter. The mean input power (P_g) is given by

$$P_g = \frac{1}{2} V_s \left(i_{s_{\text{peak}}}\right) = \frac{D^2 V_s}{4L_1 f_s}. \tag{2}$$

2.2. Load and Bus Voltages. The load voltage (V_o) for the driver can be obtained by equating the supply and load powers. The load power is given as $P_o = V_o^2/R$, where R is the static resistance of the LED, given by

$$R = \frac{V_{\text{LED}}}{I_{\text{LED}}} = \frac{V_\gamma + R_\gamma I_{\text{LED}}}{I_{\text{LED}}} = \frac{V_\gamma}{I_{\text{LED}}} + R_\gamma, \tag{3}$$

in which $R\gamma$ and $V\gamma$ are the resistance and voltage of the LED, respectively. By assuming 100% efficiency, $V_o = DV_s/2\sqrt{k}$ and $k = L_1 f_s/R$. The bus voltage can be calculated from the voltage ratio as follows:

$$V_B = \frac{1 - D}{D} V_o = \frac{(1 - D)V_g}{2\sqrt{K}}. \tag{4}$$

To ensure a high PF, the converter must be operated in discontinuous conduction mode (DCM) and the critical limit for the duty cycle (D_{lm}) can be obtained from the voltage transformation via $D_{lm} = (1 + V_s/V_B)^{-1}$.

2.3. Reactive Components. The value of L_1 can be obtained from $L_1 = D^2 V_s^2/(4P_o f_s)$ by assuming there are no losses. The bus capacitance for a known peak-to-peak voltage ripple is

$$C_1 = \frac{D^2}{8V_B \pi L_1 f_s f_L \Delta V_{B_{LF}}} V_s^2. \tag{5}$$

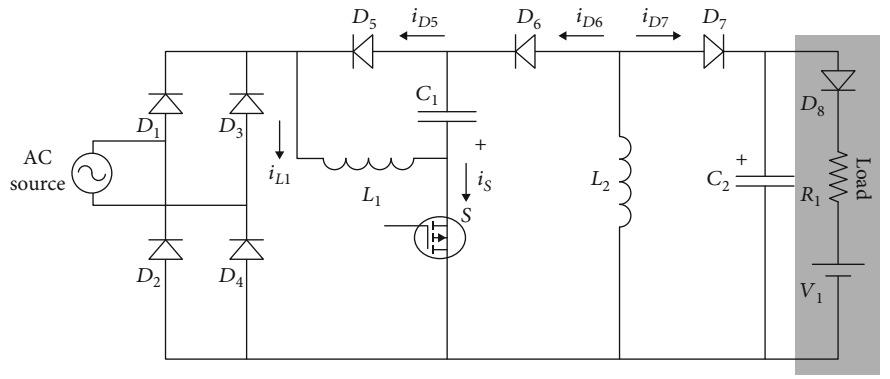

Figure 2: Circuit diagram of the integrated nonisolated LED driver.

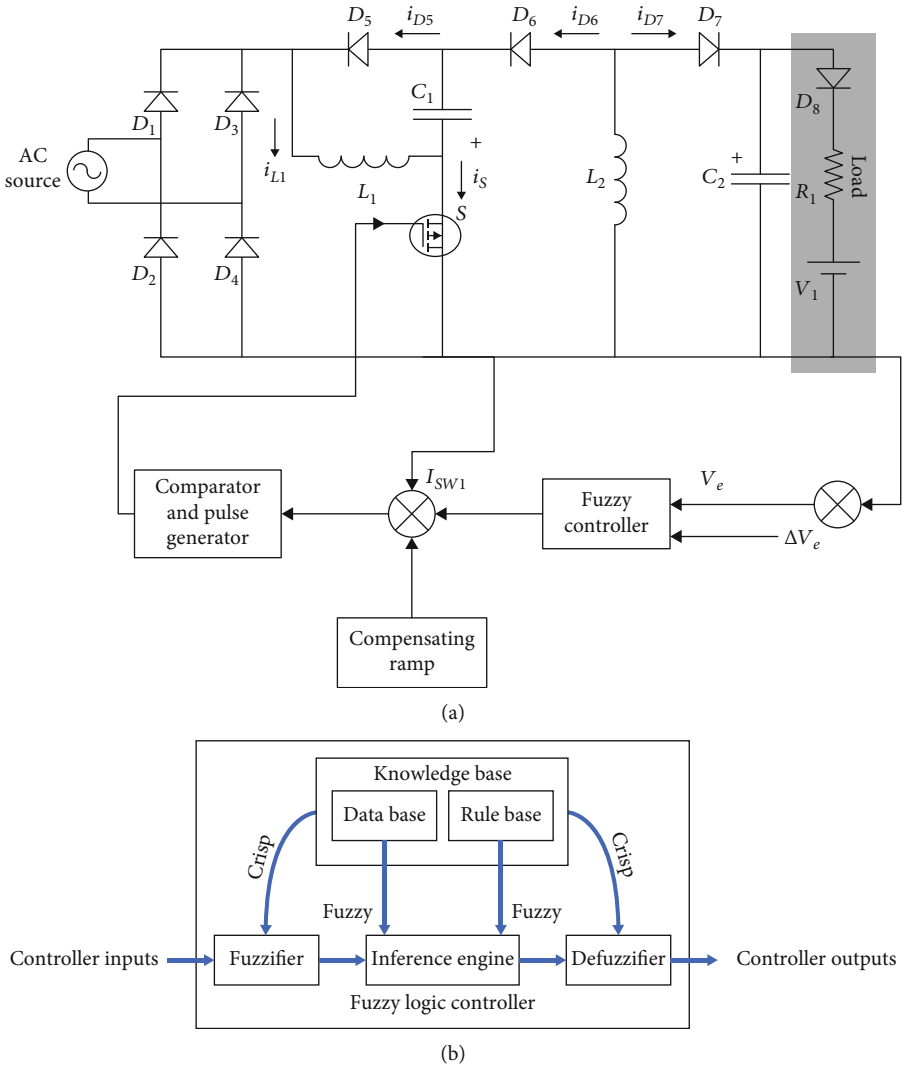

Figure 3: (a) Block diagram of the FPCC LED driver with compensating ramp; (b) FPCC components.

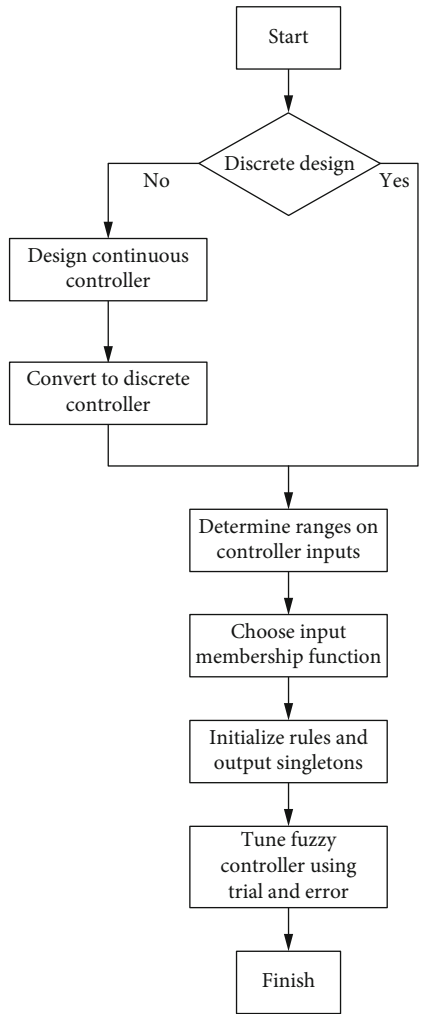

Figure 4: Process flow chart.

The inductance and capacitance L_2 and C_2 are obtained from

$$L_2 = \frac{DV_B}{0.5\Delta I_{\mathrm{LOHF}} f_s}, \qquad C_2 = \frac{DV_O}{\Delta V_{O_{\mathrm{HF}}} f_s}, \tag{6}$$

where ΔI_{LOHF} is the current ripple and $\Delta V_{O_{\mathrm{HF}}}$ is the output voltage ripple.

3. Proposed Fuzzy Controlled LED Driver

The driver is nonlinear and time varying from a control system point of view:

(1) The driver circuit possesses nonlinear characteristics owing to the voltage and power of the LEDs. At a nominal working voltage, the characteristics experience a large gradient. This means that a small change in voltage can lead to a significant change of current and therefore to a considerable change in the emitted light. Moreover, when devices are connected to nonlinear loads, there could be several nonlinear relations between the system variables

(2) The system is time varying because the parameters of the system change with the temperature and magnetic saturation

Table 1: Rule base.

E / CE	NB	NM	NS	ZE	PS	PM	PB
NB	NB	NB	NB	NB	NM	NS	ZE
NM	NB	NB	NB	NM	NS	ZE	PS
NS	NB	NB	NM	NS	ZE	PS	PM
ZE	NB	NM	NS	ZE	PS	PM	PB
PS	NM	NS	ZE	PS	PM	PB	PB
PM	NS	ZE	PS	PM	PB	PB	PB
PB	ZE	PS	PM	PB	PB	PB	PB

Table 2: Design parameters.

Component	Value
Switching frequency (f_s)	50 kHz
Inductance$_1$ (L_1)	2.5 mH
Capacitance$_1$ (C_1)	80 μF
Inductance$_2$ (L_2)	9 mH
Capacitance$_2$ (C_2)	40 μF
Load resistance (R)	570 Ω
Equivalent voltage of LED load ($V\gamma$)	170 V

A fuzzy approach offers the possibility to model a nonlinear system using knowledge of many non-well-defined relations among the variables of the system and allows for the design of a controller that adapts itself to several working conditions. Thus, fuzzy logic seems a suitable solution both to model and to control drives. The circuit diagram of the driver with a compensation ramp is shown in Figure 3(a). The driver is controlled with a fuzzy voltage loop by a Mamdani type fuzzy inference system, and the outer current loop consists of a peak current control with slope compensation.

The error between the reference voltage and converter output voltage and its variation are the inputs to the FLC (see Equations (7) and (8)). The FPCC and its components are shown in Figure 3(b). The output voltage is tracked and compared to the reference signal, and the generated error V_{e} and change in error V_{ce} are given as inputs to the FLC to obtain a suitable signal to the current controller loop. In the current controller loop, three signals are used in order to generate the pulses to the switches: the inductor signal, the FLC signal, and the compensating ramp signal. Although not considered here, parameter and model uncertainties can be incorporated directly as fuzzy numbers in the fuzzy set theory.

The FLC consists of the following components: a fuzzifier converts crisp data into fuzzy data; a knowledge base contains a data base and a fuzzy rule set; an inference engine

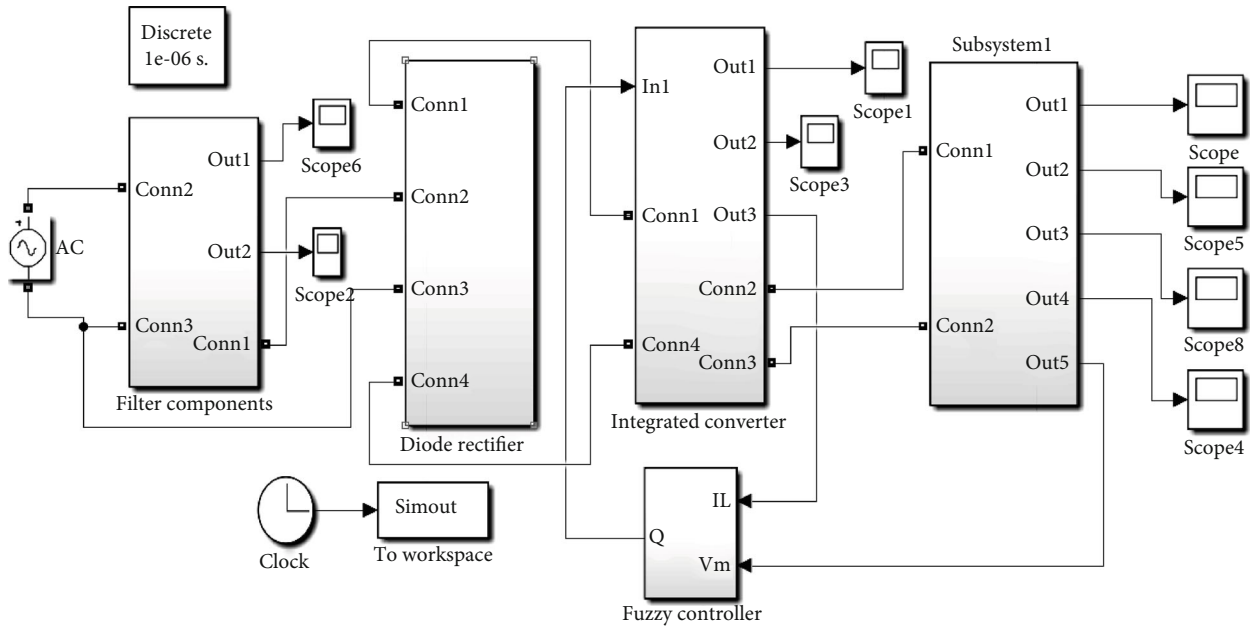

Figure 5: The Simulink model of the proposed FPCC integrated nonisolated LED driver.

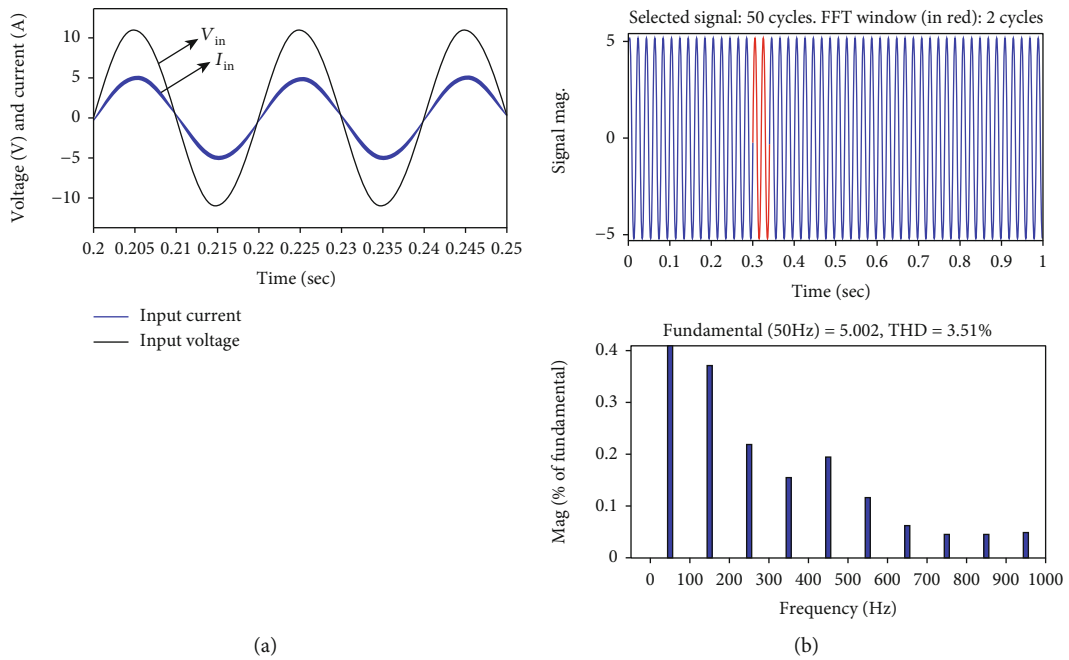

Figure 6: (a) Simulation results of input voltage and current; (b) current harmonic spectra.

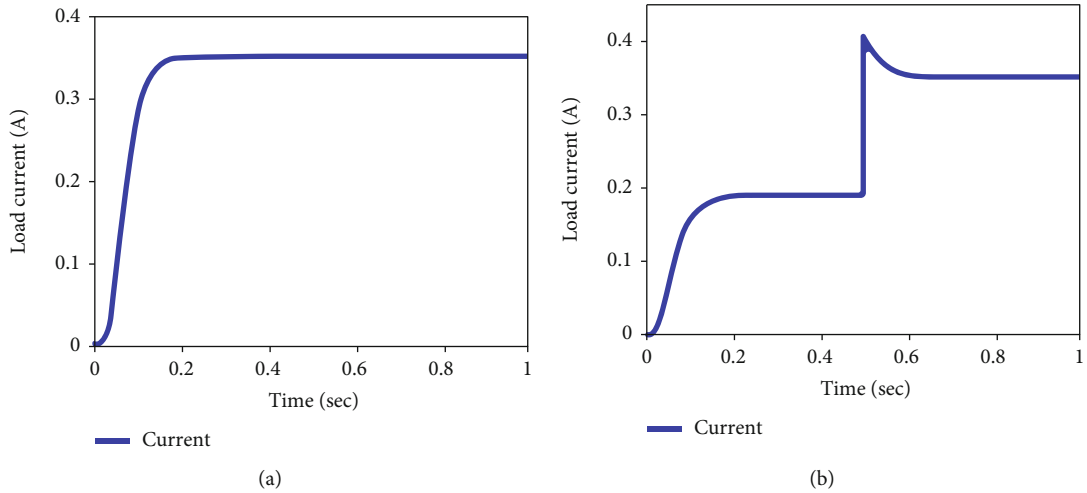

Figure 7: (a) Load current; (b) load current with dynamic change at 0.5 sec.

deduces the fuzzy control action from the knowledge base and simulates a human decision process; defuzzification yields a crisp value from the fuzzy action.

The FPCC, with the help of the knowledge and experience of an expert, improves the performance of the system. Applying intelligent control techniques for issues identified with uncertainty makes use of IF-THEN rules to define the relation between the inputs and the outputs. Simulation is carried out to check the performance of the design, and if the design is not considered satisfactory, modifications are made to tune the limits of the controller by changing the fuzzy rules and the procedure is repeated for better outcomes.

Several steps are involved in the design of fuzzy controllers as shown in Figure 4: (i) choosing the fuzzy controller inputs and outputs; (ii) choosing the preprocessing that is needed for the controller inputs, and possibly postprocessing that is needed for the outputs; and (iii) design of the four components of the fuzzy controller: the fuzzifier, the rule base, decision maker and defuzzifier.

3.1. Identification of Inputs and Outputs. The inputs of the FC are the error V_e and the variation of error V_{ce}, which are derived from

$$V_e = V_0 - V_{ref}, \tag{7}$$

$$V_{ce} = V_e(k) - V_e(k-1), \tag{8}$$

where V_0 is the extant load voltage, V_{ref} is the reference load, V_e is the voltage error, and subscript "k" denotes the value taken at the opening of the k^{th} switching cycle. The output of the FC is the duty ratio.

3.2. Fuzzifying the Inputs and Outputs. The world of the dissertation of the inputs is separated into 7 fuzzy sets of triangular shape. Outputs are also mapped into several fuzzy regions of numerous singletons.

3.3. Development of the Rule Base and Inference. The proposed system, having $7 * 7$ rules, is shown in Table 1. It has seven variables, named NB, NM, NS, Z, PB, PM, and PS. Triangular shapes are used as membership functions, and the center of gravity method is used for the defuzzification process.

Table 3: Evaluation of %THD and PF with different source voltage.

Source voltage	Current THD (%)	Power factor
90	10.82	0.962
120	8.81	0.971
150	6.73	0.978
230	3.51	0.987

Table 4: Evaluated values of power factor and %THD with different loads at rated voltage.

Load (W)	Current THD (%)	Power factor
20 W	5.74	0.949
35 W	4.63	0.965
70 W	3.51	0.987

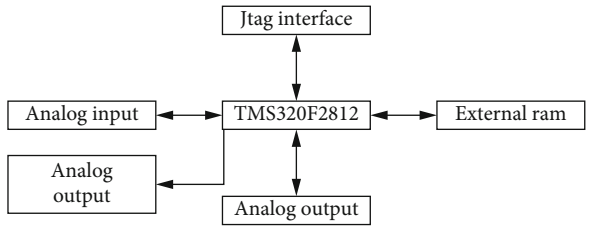

Figure 8: Hardware structure.

Table 5: Experimental component details.

Component name	Series number
Control switch (power IGBT) (SW1)	FGA15N120ANTD
Power diode (D_1, D_2, and D_3)	MUR3040PT
DSP processor	TMS320F2812

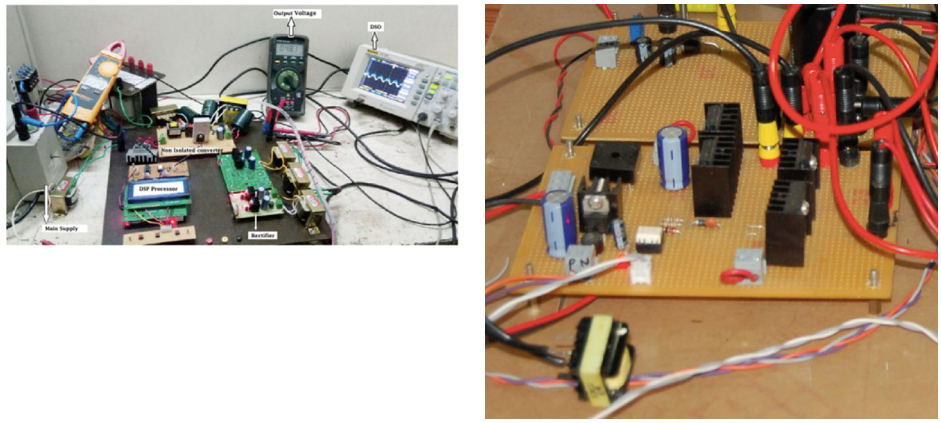

(a) (b)

Figure 9: (a) Laboratory hardware; (b) converter close up.

4. Design Parameters

The driver circuit was built in the laboratory and tested with a universal input (90 V-230 V) range. The driver was designed to provide a power of 70 W, with a rated lamp current of 350 mA. The remaining component values are shown in Table 2.

5. Results and Discussion

5.1. Simulation Results. The proposed fuzzy peak current controlled integrated nonisolated LED driver was developed in the MATLAB/Simulink software package. Figure 5 shows the simulation model, in which a diode rectifier converts the AC source into DC, which is fed to the integrated converter. The output of the integrated converter is fed to the LED panel.

In order to control the driver unit, a proposed control is presented in a feedback loop. Figure 6(a) shows the simulation results of the input voltage of a current waveform rated at a voltage of 230 V and at full load (70 W). In the simulation, the waveform voltage magnitude is scaled to 10 V by multiplying with the factor 0.0307. This result shows that the input current is in-phase with voltage and current waveform following a sinusoidal shape. The respective current harmonic spectrum is also shown in Figure 6(b), which demonstrates that the harmonic content presented in the current wave is below the international specifications (IEC-61000-3-2). The PF and percentage THD at this load are found to be 0.987 and 3.51%, respectively. Figure 7(a) is the output current of the driver, which is maintained at 350 mA. To evaluate the dynamic performance of the controller, a change of load was made at 0.5 sec as shown in Figure 7(b), with a stepwise change in load from 175 mA to 350 mA (at 0.5 sec). An improved dynamic response is observed.

From Table 3, the performance of the converter is significantly improved with the universal input (90-230 V). The THD improves from 10.82% to 3.51%. The PF of the driver in the entire range is found to be above 0.96.

It is observed from Table 4 that the power factor is higher at full load conditions and the corresponding THD is lower (0.987 and 3.51% at 70 W).

5.2. Experimental Results. An experimental setup was implemented to validate the simulation results. Microcontrollers based on FLCs for power converters were implemented, but due to the high sampling frequency, control DSPs were instead used. The proposed controller was implemented using a TMS320F2812 DSP, which is a 32-bit processor operating at 150 MHz. The digital converter contains the recompense network, fault amp, slant recompense, and PWM generator, which work in a discrete time domain. In this paper, we used a Texas Instruments TMS320F2812 DSP processor. The duty is to initially set to 100% but tripped using the cycle-by-cycle trip feature of the processor. The yield voltage of the converter is connected to a resistive "inspecting divider" arranged such that it is associated with DAC. The voltage is tested and changed over to advanced esteem. A digital reference (REF) is subtracted from the digital value, and the error value is used as an input to the digital controller. This represents the error amplifier and compensation network of the analog equivalent. The yield of the controller is increased by an additional term K, which scales the yield of the controller to computerized esteem well-suited for use with the D/A Converter (DAC). The general hardware structure is shown in Figure 8. The output of the converter is sampled by an A/D converter, which gives the digital value to the fuzzy controller. The controller processes the data to produce a PWM signal to the control switch SW1 of the converter.

The line voltage and current waveforms, load current and voltage waveforms, and current harmonic content were observed. The experimental component details are listed in Table 5. Figure 9(a) shows the experimental setup of the proposed FPCC integrated nonisolated LED driver with a controller, while Figure 9(b) is a detailed picture of the controller.

The supply current was in-phase with a supply voltage of 230 V (V_{in}: 300 V/div; I_{in}: 0.5 A/div). The corresponding measured PF is 0.973, and %THD is 5.67%. The respective harmonic spectra are shown in the left of Figure 10(a), while

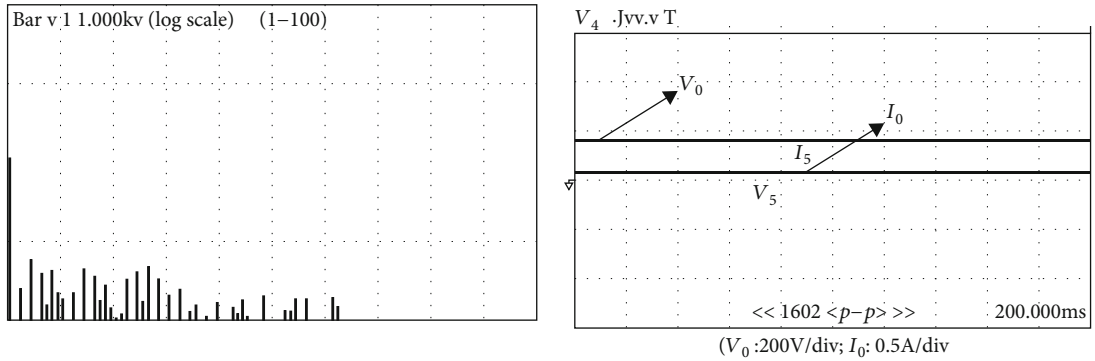

(a) (b)

Figure 10: (a) Line current harmonic spectrum; (b) load voltage (V) and load current (A).

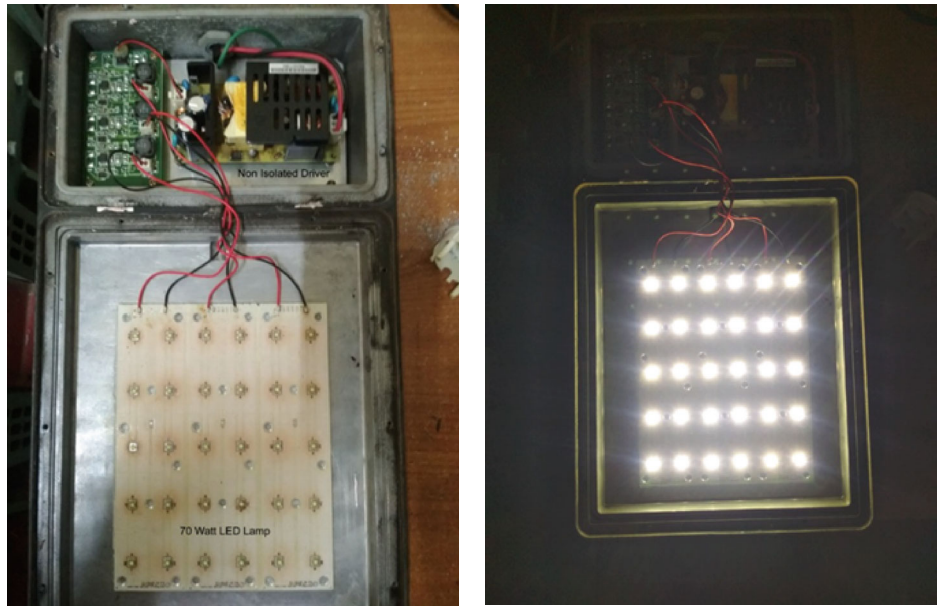

(a) (b)

Figure 11: (a) LED driver with panel; (b) system under operation.

the load current and load voltage are shown in Figure 10(b). The experimental setup of the driver with an LED lamp (component values as in Table 2) and the lamp under working conditions are shown in Figures 11(a) and 11(b), respectively.

A comparison of the simulation and experimental results is provided in Table 6, from which it can be concluded that the proposed DSP-based FPCC integrated nonisolated LED driver operating at a low voltage (90 V) gives a low PF and high %THD with respect to the current. The PF increases to 0.987 in the simulations and 0.973 in the experiments at the high voltage (230 V), and the corresponding THD is 3.51% in the simulations and 5.5% in the experiments at a full load of 70 W. From the experimental and simulation results, it is clear that the proposed FPCC integrated isolated LED driver implemented through DSP is suitable for low, medium, and high voltage operation.

Table 6: Simulation and experimental results at different source voltages at full load.

Simulation results			Experimental results		
Voltage	THD (%)	PF	Voltage	THD (%)	PF
90	10.82	0.962	90	13.2	0.94
120	8.81	0.971	110	12.4	0.956
150	6.73	0.978	150	10.71	0.961
230	3.51	0.987	230	5.67	0.973

Table 7 shows a comparison of the existing topologies with the proposed topology. The power factor is 0.987, close to unity, and the THD is 3.51%, relatively low compared to existing topologies. Furthermore, Table 8 shows a comparison of existing controllers with the proposed controller. It is observed that the proposed controller exhibits better performance.

Table 7: Comparisons between the existing single-stage LED drivers and the proposed driver.

LED driver	Specification parameter	
	Power factor (PF)	Total harmonic distortion (%THD)
Integrated buck-flyback converter [18]	0.970	27.5%
Single-stage LED driver [10]	0.99	7.9%
Single-stage LED streetlight driver with soft-switching and interleaved PFC [12]	0.97	5%
Proposed	0.987	3.51%

Table 8: Comparisons of existing controllers and the proposed controller.

Controllers	Specification parameter	
	Power factor (PF)	Total harmonic distortion (%THD)
Fixed-frequency constant-current control [18]	0.970	27.5%
QR valley-switching scheme [21]	0.93	23%
Conventional current control [15]	0.96	28%
Proposed	0.987	3.51

6. Conclusions

This paper presents a fuzzy integrated nonisolated LED driver designed to achieve a high-power factor (PF). It consists of fuzzy control in a voltage loop and peak current control in a current loop. The voltage loop regulates the output voltage, and the current loop improves the power factor. Fuzzy logic is used in a feedback path and linear programming rule to govern the magnitude of the reference current during this proposed technique in order to regulate the switch's duty cycle for shaping the input current. The proposed method avoids complexity related to nonlinearity of switching converters and is ready to react quickly to load changes, so controller processing leads to better dynamic performance. The experimental results at steady state showed that the proposed control strategy is capable of producing a power factor value of almost unity under a wide range of supply voltage and load power conditions. The experimental results show that the PF of the driver is 0.973 and the %THD is 5.67% at full load, and therefore, the efficiency of the driver is 86.5%, which meets international regulations (IEC-61000-3-2).

Abbreviations

PF: Power factor
LED: Light-emitting diode
FLC: Fuzzy logic controller
DSP: Digital signal processor
FPCC: Fuzzy peak current controlled
THD: Total harmonic distortion.

Data Availability

Data is available upon request.

Conflicts of Interest

The authors declare that they have no conflicts of interest.

Acknowledgments

This project was partially supported by the National Key Research and Development Program of China (Grant No. 2017YFB0701700). This work was supported by the National University Malaysia Pahang (UMP) (Grant No. PGRS200321), and Mr. A.S. Veerendra is working as a research scholar under UMP's Doctoral Research Scheme (DRS).

References

[1] Y. Wang, J. Alonso, and X. Ruan, "A review of LED drivers and related technologies," *IEEE Transactions on Industrial Electronics*, vol. 64, no. 7, pp. 5754–5765, 2017.

[2] W.-j. Cha, Y.-W. Cho, and J.-M. Kwon, "Single power-conversion LED backlight driving system with high power factor control," *Journal of Display Technology*, vol. 10, no. 5, pp. 407–413, 2014.

[3] T.-P. Sun and C.-H. Wang, "Specially designed driver circuits to stabilize LED light output without a photodetector," *IEEE Transactions on Power Electronics*, vol. 27, no. 9, pp. 4140–4152, 2012.

[4] Y. Wang, Y. Guan, D. Xu, and W. Wang, "A CLCL resonant DC/DC converter for two-stage LED driver system," *IEEE Transactions on Industrial Electronics*, vol. 63, pp. 2883–2891, 2015.

[5] P. Athalye, M. Harris, and G. Negley, "A two-stage LED driver for high-performance high-voltage LED fixtures," in *2012 Twenty-Seventh Annual IEEE Applied Power Electronics Conference and Exposition (APEC)*, pp. 2385–2391, Orlando, FL, USA, February 2012.

[6] X. Xie, M. Ye, Y. Cai, and J. Wu, "An opto coupler less two-stage high power factor LED driver," in *2011 Twenty-Sixth Annual IEEE Applied Power Electronics Conference and Exposition (APEC)*, pp. 2078–2083, Fort Worth, TX, USA, March 2011.

[7] W. Lin, H. Chen, and S. Ke, "Research on a single-stage flyback/boost LED driver with lower output ripple," in *2016 IEEE 2nd Annual Southern Power Electronics Conference (SPEC)*,, pp. 1–5, Auckland, New Zealand, December 2016.

[8] Y. Guo, S. Li, A. T. L. Lee, S.-C. Tan, C. K. Lee, and S. Y. R. Hui, "Single-stage AC/DC single-inductor multiple-output LED drivers," *IEEE Transactions on Power Electronics*, vol. 31, pp. 5837–5850, 2015.

[9] J. W. Fan, J. P.-W. Chow, W.-T. Chan et al., "Modeling and experimental assessment of the EMI characteristics of switching converters with power semiconductor filters," *IEEE Transactions on Power Electronics*, vol. 35, no. 3, pp. 2519–2533, 2020.

[10] S. Mangkalajan, C. Ekkaravarodome, K. Jirasereeamornkul, P. Thounthong, K. Higuchi, and M. K. Kazimierczuk, "A single-stage LED driver based on ZCDS class-E current-driven rectifier as a PFC for street-lighting applications," *IEEE Transactions on Power Electronics*, vol. 33, no. 10, pp. 8710–8727, 2018.

[11] Y. Wang, X. Deng, Y. Wang, and D. Xu, "Single-Stage bridgeless LED driver based on a CLCL resonant converter," *IEEE Transactions on Industry Applications*, vol. 54, no. 2, pp. 1832–1841, 2018.

[12] C.-A. Cheng, C.-H. Chang, H.-L. Cheng, E.-C. Chang, T.-Y. Chung, and M.-T. Chang, "A single-stage LED streetlight driver with soft-switching and interleaved PFC features," *Electronics*, vol. 8, no. 8, p. 911, 2019.

[13] G. G. Pereira, M. A. Dalla Costa, J. M. Alonso, M. F. de Melo, and C. H. Barriquello, "LED driver based on input current shaper without electrolytic capacitor," *IEEE Transactions on Industrial Electronics*, vol. 64, no. 6, pp. 4520–4529, 2017.

[14] J. M. Alonso, D. Gacio, A. J. Calleja et al., "Reducing storage capacitance in off-line LED power supplies by using integrated converters," in *2012 IEEE Industry Applications Society Annual Meeting*, pp. 1–8, Las Vegas, NV, USA, October 2012.

[15] J. Alonso, J. Vina, D. Gacio, G. Martinez, and R. O. Sanchez, "Analysis and design of the integrated double buck-boost converter as a high-power-factor driver for power-LED lamps," *IEEE Transactions on Industrial Electronics*, vol. 59, no. 4, pp. 1689–1697, 2012.

[16] G. M. Soares, P. S. Almeida, J. M. Alonso, and H. A. C. Braga, "Capacitance minimization in offline LED drivers using an active-ripple-compensation technique," *IEEE Transactions on Power Electronics*, vol. 32, no. 4, pp. 3022–3033, 2017.

[17] D. Gacio, J. M. Alonso, J. Garcia, D. Garcia-Llera, and J. Cardesin, "Optimization of a front-end DCM buck PFP for an HPF integrated single-stage LED driver," *IEEE Journal of Emerging and Selected Topics in Power Electronics*, vol. 3, no. 3, pp. 666–678, 2015.

[18] D. Gacio, J. M. Alonso, A. J. Calleja, J. Garcia, and M. Rico-Secades, "A universal-input single-stage high-power-factor power supply for HB-LEDs based on integrated buck–flyback converter," *IEEE Transactions on Industrial Electronics*, vol. 58, no. 2, pp. 589–599, 2011.

[19] T. Qian and W. Wu, "Analysis of the ramp compensation approaches to improve stability for buck converters with constant on-time control," *IET Power Electronics*, vol. 5, no. 2, pp. 196–204, 2012.

[20] M. Subbarao, C. S. Babu, and S. Satyanarayana, "Design and analysis of variable switching frequency controlled integrated switched mode power converter for class C & class D appliances," *Ain Shams Engineering Journal*, vol. 9, no. 4, pp. 2849–2858, 2018.

[21] Y.-C. Li, "A novel control scheme of quasi-resonant valley-switching for high-power-factor AC-to-DC LED drivers," *IEEE Transactions on Industrial Electronics*, vol. 62, no. 8, pp. 4787–4794, 2015.

[22] S. Sagiroglu, I. Colak, and R. Bayindir, "Power factor correction technique based on artificial neural networks," *Energy Conversion and Management*, vol. 47, no. 18-19, pp. 3204–3215, 2006.

[23] C. S. Chiu, C. T. Shen, and G. C. Hsieh, "Universal lighting control of unknown connected light emitting diode arrays via a T–S fuzzy model-based approach," *IET Power Electronics*, vol. 8, no. 2, pp. 151–164, 2015.

[24] T.-F. Wu, C.-H. Chang, and Y.-H. Chen, "A fuzzy-logic-controlled single stage converter for PV-powered lighting system applications," *IEEE Transactions on Industrial Electronics*, vol. 47, no. 2, pp. 287–296, 2000.

[25] M. He and J. Xu, "Nonlinear PID in digital controlled buck converters," in *APEC 07 - Twenty-Second Annual IEEE Applied Power Electronics Conference and Exposition*, pp. 1461–1465, Anaheim, CA, USA, March 2007.

[26] C. Buccella, C. Cecati, and H. Latafat, "Digital control of power converters — a survey," *IEEE Transactions on Industrial Informatics*, vol. 8, no. 3, pp. 437–447, 2012.

[27] C. A. Sepúlveda, J. A. Muñoz, J. R. Espinoza, M. E. Figueroa, and C. R. Baier, "FPGA v/s DSP performance comparison for a VSC-based STATCOM control application," *IEEE Transactions on Industrial Informatics*, vol. 9, no. 3, pp. 1351–1360, 2013.

[28] K.-H. Tseng and C.-L. Chen, "Design and hardware implementation for a full-bridge phase-shift PWM DC/DC converter system with FPGA-based PI gain-scheduling control," in *2011 6th IEEE Conference on Industrial Electronics and Applications*, pp. 1578–1582, Beijing, China, June 2011.

[29] L. Guo, J. Y. Hung, and R. M. Nelms, "Evaluation of DSP-based PID and fuzzy controllers for DC–DC converters," *IEEE Transactions on Industrial Electronics*, vol. 56, pp. 2237–2248, 2009.

[30] M. SubbaRao, C. S. Babu, S. Satyanarayana, and P. C. B. Naidu, "Digital fuzzy current mode controlled integrated PFC converter with external ramp compensation," *Journal of Circuits, Systems, and Computers*, vol. 27, no. 9, article 1850147, 2018.

Hindawi
International Journal of Photoenergy
Volume 2021, Article ID 6655113, 10 pages
https://doi.org/10.1155/2021/6655113

Research Article

Design and Performance of Solar PV Integrated Domestic Vapor Absorption Refrigeration System

Divya Arputham Selvaraj and Kirubakaran Victor

Centre for Rural Energy, Gandhigram Rural Institute-Deemed to be University, India

Correspondence should be addressed to Kirubakaran Victor; kirbakaran@yahoo.com

Received 3 December 2020; Revised 15 January 2021; Accepted 18 January 2021; Published 4 February 2021

Academic Editor: S. Shanmuga Priya

Copyright © 2021 Divya Arputham Selvaraj and Kirubakaran Victor. This is an open access article distributed under the Creative Commons Attribution License, which permits unrestricted use, distribution, and reproduction in any medium, provided the original work is properly cited.

The arrival of new technologies has increased the energy demand day by day and does not seem to slow down at any time soon. High energy demand is adding risk on energy depletion and cause of various environmental issues. Air conditioner, chiller, and refrigerator occupy a considerable amount of the world's total energy usage and have also proved to be a massive contributor to various environmental impacts. This technology might sound like a luxury on the surface, but they are in high demand to achieve food security. They can also help lifesaving vaccines to reach even the isolated parts of the world. Even though solar thermal refrigeration is a popular field, this paper solely concentrates on PV integrated refrigeration. In this paper, a renewable integration technology where a solar photovoltaic system is used to supply the electrical energy required to drive an absorption cycle is studied and compared with the commercial AC absorption refrigeration system. The Coefficient of Performance (COP) of the AC and DC system was 0.18 and 0.14. The simple payback of the system is 10.2 years.

1. Introduction

From the start of the day until the end of it, several types of technologies are making our life simple. Energy consumption is directly proportional to economic growth and population. In developed countries, 10-20% of total energy consumption is from HVAC [1]. In developing countries, the increase in consumption is due to economic growth, population, and urbanization [2]. Electricity has become a necessity for development, and hence, rural electrification has become a dream for many developing countries.

While discussing the advantages of energy, it has also become a necessity to discuss the disadvantages. Fossil fuels occupy a significant share in satisfying global electricity needs. As it requires millions of years for fossil fuels to form, they will be depleted sooner or later. They are also the reason for the world's biggest environmental problems. As the growth continues, energy demand would also be increasing, which in turn would increase carbon emission [3]. Even a small change in fossil fuel usage patterns would help protect energy reserves and achieve environmental sustainability [4]. Being stuck on only the impacts caused by the technologies does not add any advantage to society. The only way to move forward is by finding an alternative, which is renewable technologies that could overcome these issues.

Rural electrification is one of the solutions to remove poverty in developing countries. Villages located in rough areas like forests, deserts, and hilly regions are away from the existing grid location. To bring electricity to such places would be decentralized generation by renewable energy. This would also reduce transmission and distribution losses. Solar PV is the first choice for the Indian context among renewable technologies. A PV system was designed for a rural domestic load and proved to be a promising technology in rural development [5]. The government of India aims to achieve 175 GW of energy usage by 2022. As India is a tropical country, solar PV can provide a high yield. The lifetime of solar PV would be 25 to 30 years, making it worth investing [6].

The economic feasibility of the off-grid system for Nigeria was done and found to be an economically viable option [7]. Carbon emission per unit power production is very low compared with the coal power plant [8].

Several factors affect the performance of PV. One such factor is heating, which would affect the efficiency of the panel. This could be overcome by a heat recovery system by a continuous water cooling method. Optimizing the solar PV land utilization and growing vegetation was studied [9]. The vegetation growth would also improve panel efficiency and also reduce the payback period [10]. The author has discussed another solar PV optimization technique to enhance efficiency, and the waste heat from this process is utilized to improve the quality of drinking rural drinking water [11]. The shadowing effect and monsoon could also affect system performance [12]. A detailed design of the off-grid and the on-grid system was carried out. The economic analysis of both systems was also carried out. Though the off-grid system requires additional components, i.e., the battery, it is more economical than the on-grid system [13].

Cooling technology in the form of a hand fan or wind has been in practice even from ancient times. Even the method of ice cultivation was practiced by elites in European countries [14]. But, over a period of time, this technology has transcended from luxury to a common commodity. Cooling technology has seen a surge in growth because of its need in various fields like lifestyle, food, agriculture, processing, and pharma. Both the technology and market value of this technology is growing steadily. Being one of the most significant contributors to global energy consumption, it has a huge energy-saving potential by moving towards renewable technology. Solar energy could help achieve that dream. Even the gaps in the cold supply chain that could act as a barrier for the vaccines to reach the rural areas with no grid facility can be filled with the help of solar refrigeration [15].

Realizing the need for renewable integration, many authors have designed many solar integrated refrigeration methods. A DC-operated household refrigerator powered by solar PV was studied and found to have low exergetic efficiency due to low energy conversion efficiency [16]. A solar PV-operated stand-alone system was studied for various compression air conditioning systems [17]. A compression air conditioning system driven by solar PV was studied. The system required to operate the system includes a PV panel, charge controller, and a battery [18].

Even though absorption technology has lower COP than commercial refrigeration technology, it is more durable with a longer lifetime of 20-30 years [19]. Vapor absorption refrigeration (VAR) is proven to be an environmentally friendly replacement for commercial refrigeration. It also has better power quality in comparison with a commercial refrigerator. It can effortlessly reach 8-16°C, helping tropical agricultural product storage and achieving food security by reducing food wastage [20].

For the theoretical calculation of the COP, it is necessary to know the heat supplied and effective cooling. The experimental work was done, and it was compared with the theoretical data. The result shows that on a clear day, one pound of ice can be produced for every three to four square feet of collector area [21]. The COP of VAR can be improved from 0.39 to 0.65 by adding a heat exchanger [22].

With the high flexibility with source energy, a single-stage absorption chiller with LiBr/H_2O would make decentralized storage of fruits and vegetables in the farm itself possible by integrating renewable energy. This would be more advantageous, especially during summer, when energy is abundant, and the need for cooling was also plentiful [23]. A solar flat plate collector refrigerator with a hot water storage tank was studied. It has recorded evaporator temperature as low as 6°C [24].

The author has studied a 10-ton single-stage LiBr/H_2O system driven by an evacuated tube collector in the system. A 72 m^2 solar collector area was mounted on the rooftop of the building. In case, hot water temperature falls below 70°C, backup heating using LPG would start working. To provide continuous cooling, hot water and cold water storage tank were also included. Even though the system's cost is currently high, with steady growth, this CFC free technique could reduce price in the future. Even the VAR system's operational cost looks very attractive compared to the Vapor Compression Refrigeration (VCR) system. The system's yearly average solar fraction was 81%, and the LPG fired unit has supplied only the remaining 19% [25]. In the heat storage system, it requires an additional collector to supply the required heat energy for the storage tank [26]. This will increase the investment cost.

In a concentrated parabolic collector-driven system, the COP value was found to be 0.08, and the author has highly suggested it for no electricity areas [27]. An author has even suggested the usage of engine exhaust as the heat source to drive the system [28].

For continuous operation of the refrigeration cycle, a solar thermal integrated system would require either an auxiliary heater or a thermal storage buffer. The storage buffer can be either a heat storage tank or a cold storage tank, or both. The buffer storage tank also has thermal loss due to temperature difference with the environment. Based on the type of water heater and system design, several studies were done for a solar thermal integrated VAR system. In the case of vapor absorption technology, many studies were focused more on utilizing solar thermal energy. On the other hand, there is a lack of studies based on the solar PV integrated VAR system. So, this paper deals with solar PV-powered vapor absorption refrigeration technology.

2. System Description of Conventional and Solar-Assisted VAR

Figures 1 and 2 show the block diagram and components of the basic single-stage absorption refrigeration system, respectively. The selected system has H_2O-NH_3 as a working fluid. H_2O-NH_3 does not cause any environmental damage like other commercial refrigerants and does not have a crystallization problem below 0°C like Libr-H_2O [29]. In the generator, working fluid must be heated to be separated into refrigerant and absorbent. The heat required to achieve

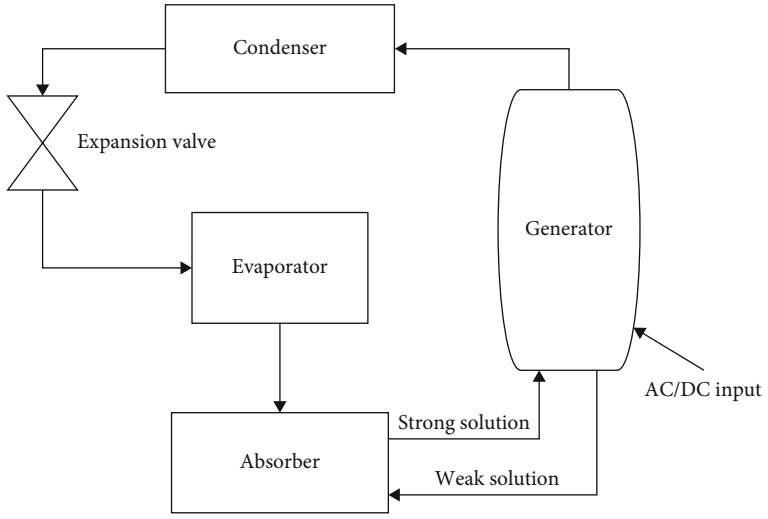

Figure 1: Block diagram of conventional VAR.

Figure 2: Components of the VAR system.

the desired temperature is supplied by a heater. The generator is the only component that requires a power supply to drive the entire system. A 220 V~240 V, 0.3 A heater was used in the AC system, and a 12 V, 5 A heater was used in the DC system. Once the refrigerant is separated from the strong solution, it will move to the condenser while the weak solution returns to the absorber. In the condenser, heat is rejected to the external environment to produce a low-temperature solution. A finned type condenser was used to increase the surface of exposure to disperse the heat quickly. After undergoing condensation and expansion, the refrigerant would be in a low-temperature low-pressure state, making it easy to absorb the heat from the selected environment, i.e., evaporator. The water in the absorber would absorb ammonia leaving the evaporator to continue the cycle.

The block diagram of the solar PV integrated DC system is shown in Figure 3. The only electrical load in the system is a heater. The heater is a resistive load that can operate in both AC and DC without any design changes. A solar PV panel would supply the electrical energy required by the system. For a country like India, solar energy is available throughout the year, so no other auxiliary energy is required. Solar energy is not available for 24 hours, but refrigeration is needed to provide continuous cooling without rest, especially for food storage. So, to run the system continuously, a battery bank is needed to drive the system even during the night time.

The circuit diagram of the PV integrated VAR system is shown in Figure 4. The charge controller acts as a control unit. Due to passing clouds, the solar intensity would vary every second. In that case, to maintain the charging and power supply, a charge controller is used. Energy generated from PV is passed through the charge controller, and a 12 V, 8 Amps regulated output can be achieved. The output from the charge controller is used to supply power to the refrigeration unit and charge the battery at the same time. During no sunshine time, the charge controller allows the power to flow from the battery to the refrigeration unit. A charge controller would also help to prevent overcharging of the battery, thus increasing the battery lifetime.

3. Objective

The main objective of this work is to integrate solar PV with the VAR system. Other objectives include calculating and comparison of the COP of conventional VAR and PV integrated VAR cycle, comparing the relationship between the generator and evaporator temperature, and calculating the payback of the system.

4. Experimental Methodology

The following conditions were considered:

(i) The specification of the AC system and a DC system taken for the study is shown in Table 1. The power

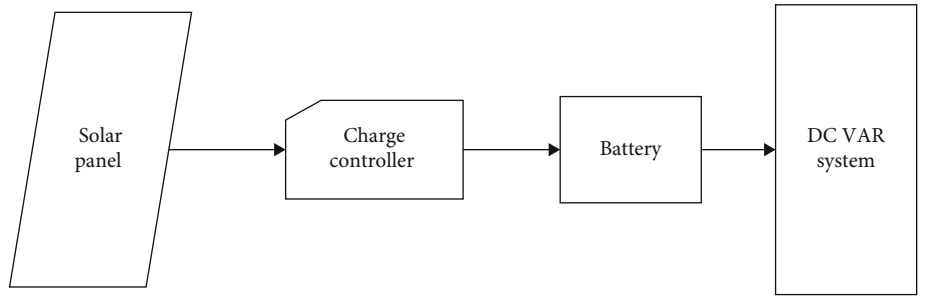

Figure 3: Block diagram of solar PV-powered system.

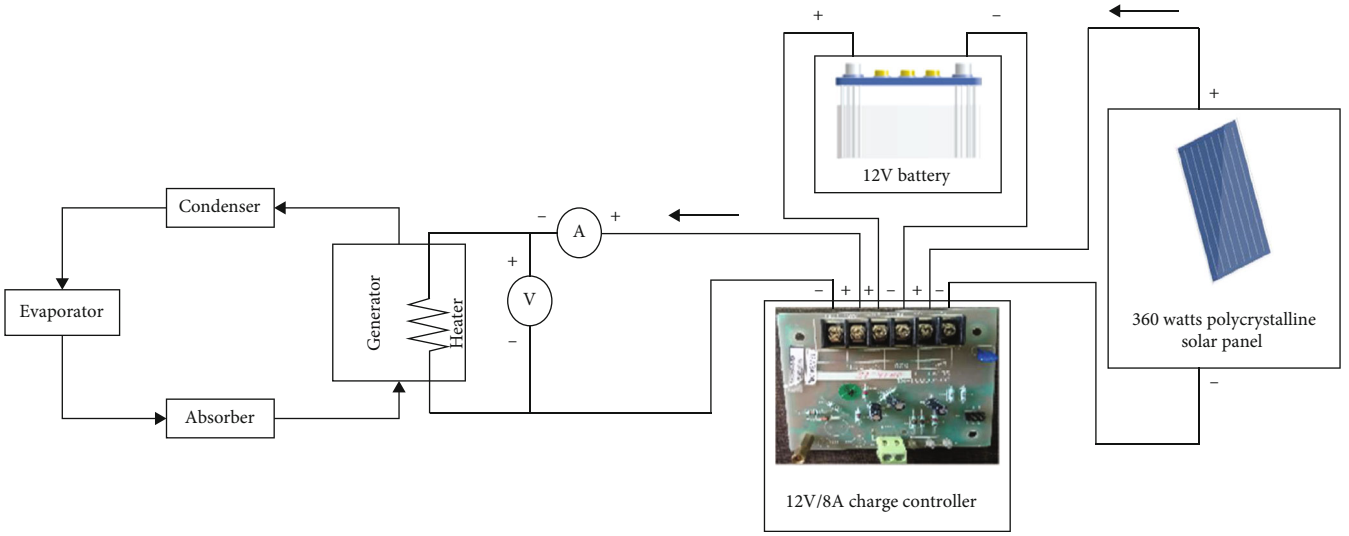

Figure 4: Circuit diagram of the proposed VAR system.

Table 1: Specification of the refrigeration system.

Name	AC VAR	DC VAR	Unit
Voltage	220–240	12	V
Current	0.3	5	A
Capacity	40	40	L
Condenser type	Finned type	Finned type	-
Dimension ($l * b * h$)	402 * 465 * 560	402 * 465 * 560	mm
Insulation	Styrofoam	Styrofoam	-
Working Fluid	H_2O-NH_3	H_2O-NH_3	-
Temperature	2-10	2-10	˚C
Gross Weight	20	22	kg

Table 2: Specification of the instruments used.

Instrument	Function	Specification
K-type thermocouple	Measure the temperature of evaporator and generator temperature	-200 to 600˚C
Fluke meter-I410	Used to measure the voltage and current	1 mV/Amp, 600 V, 400 Amp DC
Chino data logger-KR 2000	Store the measured data	1 mV/Amp, 1-400 Amp, 12 terminals, sampling -0.1 s/6 points, temperature drift - ±0.01% of full scale/˚C

plug is replaced by a crocodile clamp in the DC system for easy integration into the solar PV system

(ii) The study was conducted under a loaded condition. A two-liter of water is used as a load in both AC and solar PV integrated DC refrigeration system

(iii) Temperature, voltage, and current with respect to time were the parameter to be measured. The K-type thermocouple was used to measure the temperature. A fluke meter was used to measure the voltage and current. With the help of the chino data logger, all the measured data were monitored and recorded for every one-minute duration for higher accuracy. Specification of the instruments used is given in Table 2

(iv) System performance like COP, simple payback, energy usage, and energy conservation was calculated using the following equations:

$$\text{Annual power consumption by AC system} = \text{watts} * \text{hours of operation} * 365, \quad (1)$$

$$\text{Annual energy saving by DC system} = \text{watts} * \text{hours of operation} * 365 \quad (2)$$

Payback is calculated by the simple payback method.

$$\text{Simple payback} = \frac{\text{Cash outflow}}{\text{Cash inflow}}, \quad (3)$$

where cash outflow includes the investment cost and the cash inflow is the total amount of annual energy-saving cost after subtracting the maintenance cost.

The Coefficient of Performance (COP) is defined as the ratio of heat extracted from the evaporator to the work done.

$$\text{COP} = \frac{m * C_p * dT}{V * I}, \quad (4)$$

where m is the mass of load in kg/s, C_p is specific heat capacity in kJ/kg/°C, dT is a temperature difference between initial temperature and final temperature in °C, V is the voltage in volt, and I is the current in Amps. $V * I$ should be in kW.

5. System Design

Maximum solar radiation should be required for both driving the system and charging the battery. For the solar PV-driven system to run for 24 hours, PV requires to generate 1440 Wh a day. This energy need has to be satisfied by utilizing only five-hour peak radiation available during the day. While calculating the panel size, the efficiency of the panel must also be considered.

$$\text{Panel wattage} = \frac{\text{Total energy}}{\text{Average radiation time} * \text{pannel efficiency}} = \frac{1440}{5 * 0.8} = 360\,\text{w}. \quad (5)$$

A single 360-watt panel can be selected as there are 360 w panels available in the market. A 360-watt polycrystalline solar panel is selected from all the above considerations for driving the system and charging the battery to provide backup simultaneously. The study location is in the northern hemisphere at 10.2785°N, 77.9244°E. So, the solar panel was mounted facing south with a tilt angle of 25° with respect to the flat ground surface. Unlike other off-grid systems, it does not require any inverter because the load is a DC system. The output from the panel is passed through the 12 V, 8 A solar charge controller. This will help regulate the unpredictable energy from the solar PV to charge the battery. Charging duration and battery efficiency are required to calculate the battery size.

$$\text{Ah required} = \frac{\text{panel wattage} * \text{charging hours} * \text{battery efficiency} * 1.5}{\text{Battery voltage}} = \frac{360 * 5 * 0.8 * 1.5}{12} = 180\,\text{Ah}. \quad (6)$$

A battery does not discharge 100%, so energy extraction is increased by 1.5 times. A 12 V 180 Ah battery is used to act as a backup during no sunshine hours.

6. Experimental Setup

A 40-liter 65 W AC system is shown in Figure 5. The K-type thermocouple is positioned to measure the temperature of the cooling chamber, and the chino data logger was used to monitor and measure data.

A 40-liter 60 W DC system was taken for the study. The experimental setup is given in Figure 6. The temperature of the cooling chamber and generator was measured simultaneously. The consumption side voltage and current were measured and logged.

7. Results and Discussion

Figures 7 and 8 show the graph between temperature and power supply in the AC and DC machine, respectively. In the AC system, the temperature is dropped from 33°C to 8.9°C in five hours. The DC system's five-hour temperature drop has reached 10°C, which is enough to store tropical fruits and vegetables. When the atmospheric temperature is reduced during winter, up to 8°C can be achieved easily. In both the system, once the desired temperature is reached, not much temperature change is noticed. There is also not much difference in the operation pattern of both the systems. This allows the possibility for the AC system to be replaced by the solar PV-powered DC system. Considering the role of refrigeration technology in achieving food security, the

Figure 5: Experimental setup of AC VAR.

Figure 6: Experimental setup of solar PV-powered VAR.

solar-powered vapor absorption system is much needed in the food supply chain, especially in rural agricultural areas where electricity is still inaccessible.

The refrigerator is required to operate 365 days a year. A 65-watt system would utilize 569.4 kWh energy per year. According to CO_2 Baseline Database for the Indian Power Sector [30], the average CO_2 emission factor per kWh of energy generation is 0.82.

$$\begin{aligned} &\text{Yearly } CO_2 \text{ emission} = 569.4 * 0.82 = 466.9 \text{ kg}, \\ &CO_2 \text{ emission for 30 years} = 466.9 * 30 = 14 \text{ tons}. \end{aligned} \tag{7}$$

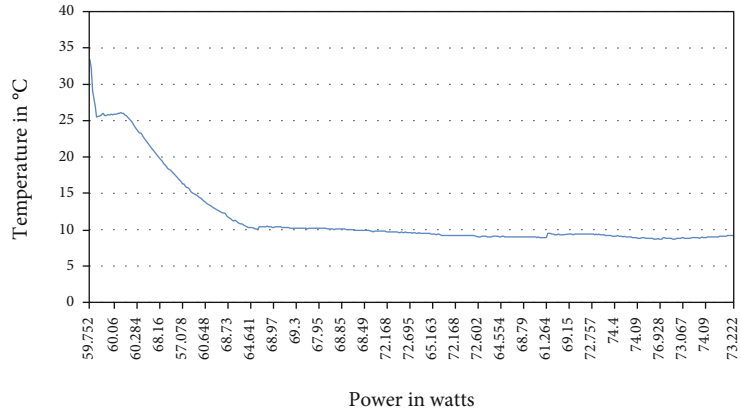

Figure 7: Performance graph of the AC system.

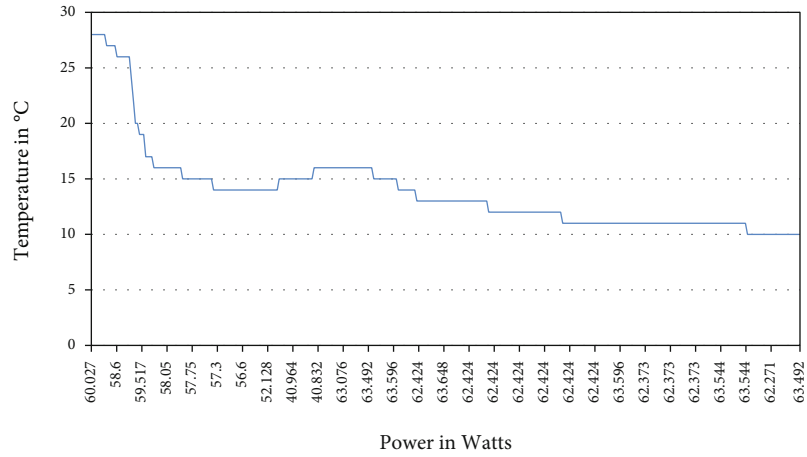

Figure 8: Performance graph of the DC system.

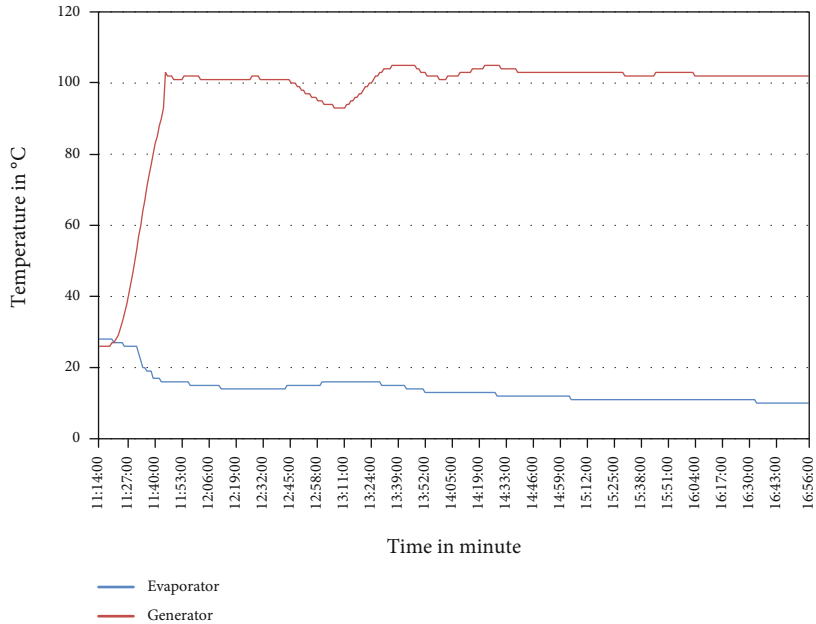

Figure 9: Comparison of generator temperature and evaporator temperature.

In a year alone, the AC system will contribute to 466.9 kg of CO_2. Throughout its entire lifetime, this system will release 14 tons of CO_2.

Figure 9 compares the evaporator temperature and generator temperature of the DC system with respect to time. Once the system is turned on, the generator temperature is slowly increasing. As the generator temperature increases, evaporator temperature reduces. When the generator temperature crosses the 60°C mark, the evaporator temperature started reducing. It took 15 minutes for the refrigerator to begin cooling. Once the generator temperature reaches an optimum temperature, the lowest evaporator temperature of 10°C is achieved and maintained continuously.

8. System Performance Calculation

Without the battery, by utilizing only the five hours of maximum sunshine radiation, in a single day, 0.3 kWh energy and ₹190 can be saved. But the refrigerator has to operate for 24 hours throughout the year.

Annual power consumption by the AC system is calculated using equation (1).

$$\begin{aligned} &= 65 * 24 * 365, \\ &= 569.4\,\text{kWh}. \end{aligned} \tag{8}$$

Annual energy saving by the DC system is calculated using equation (2).

$$\begin{aligned} &= 60 * 24 * 365, \\ &= 525.6\,\text{kWh}. \end{aligned} \tag{9}$$

Annual power consumption by the AC system is 569.4 kWh. In a PV-powered DC system, the entire power requirement is satisfied by the solar panel itself, and hence, the 525.6 kWh energy is saved by this system.

The additional components required for the solar-powered system would add to the additional investment cost. Simple payback is calculated using formula (3).

The value of each piece of equipment is given in Table 3.

A total of ₹35,500 investment cost is required for implementing the solar operated system. This system does not require any maintenance except for periodic cleaning of the solar panel. So, it does not require any maintenance cost. Solar integration has saved a total of 525.6 kWh of energy every year. For the Indian tariff rate, the yearly cost saving would amount to ₹3,469. Total cash outflow is equal to ₹35,500, and annual cash inflow is ₹3,466.

$$\text{Simple payback} = \frac{35{,}500}{3{,}466} = 10.2\,\text{years}. \tag{10}$$

The solar operated system's payback will be 10.2 years, which is not bad for a solar application.

The COP of both the systems was calculated using equation (4).

Table 3: Investment cost of the DC system.

Component	Cost in rupee (₹)
Absorption system	6000
Solar panel	11,000
Battery	17,000
Charge controller	500
Balance of system (include mounting and wire)	1,000

The COP of AC and DC systems is calculated for cooling 2 liters of water over a five-hour duration. The specific heat capacity of water is 4.186 kJ/kg/°C.

In the AC system for a five-hour duration, dT is 24.5°C, and the COP is

$$\text{COP} = \frac{(2/5 * 3600) * 4.186 * 24.5}{0.65} = 0.18. \tag{11}$$

In the DC system for a five-hour duration, dT is 10°C and the COP is

$$\text{COP} = \frac{(2/5 * 3600) * 4.186 * 10}{0.60} = 0.14. \tag{12}$$

The COP of the AC system is 0.18, while for the DC system, the COP is 0.14. There is only a small difference, so performance-wise will not affect the output.

9. Conclusion

Technology should grow and must be utilized without affecting the environment. Move towards renewable energy would not only meet energy demand but also help many satisfy their electricity dreams. In this paper, 60 w DC-operated VAR driven by a 360 w was studied, and the results have shown the possibility of reaching that dream.

(1) The annual CO_2 emission of the selected system is 466.9 kg, and this system alone contributes to 14 tons of CO_2 for its entire lifetime. The solar integrated system would help eliminate this 14 t CO_2. This is the saving from one system alone. Considering CO_2 emission control is one of the most significant issues to be tackled, the result is very encouraging to move towards the PV integrated system

(2) Refrigeration being one of the most significant contributors to power consumption in the world, solar PV integrated refrigeration would be a big stepping stone to reaching a sustainable future. A 525.6 kWh energy saving was achieved in the PV integrated DC system

(3) Even the 10.2-year payback is pretty good for a system that operates for 30 years

(4) A solar PV operated DC absorption system has a COP of 0.14. Currently, the COP of VAR is lower

than the VCR systems, which is still a disadvantage of the VAR system yet to overcome

In the future, studies related to the control system design to improve solar output can be done. The system's performance can be enhanced by giving design modification to the refrigeration system by adding additional heat exchangers or incorporating a cooling tower. An utterly renewable energy-driven absorption cycle could help this technology reach any corner of the world as far as there is enough solar energy available. This PV integrated system will allow utilizing all the technology services without compromising the environment and future energy needs.

Data Availability

The data used to support the findings of this study are available from the corresponding author upon request.

Conflicts of Interest

The authors declare that they have no competing interests.

Acknowledgments

The authors acknowledged the support received from the Ministry of New and Renewable Energy India.

References

[1] L. Pérez-Lombard, J. Ortiz, and C. Pout, "A review on buildings energy consumption information," *Energy and Buildings*, vol. 40, no. 3, pp. 394–398, 2008.

[2] P. Nejat, F. Jomehzadeh, M. M. Taheri, M. Gohari, and M. Z. Muhd, "A global review of energy consumption, CO_2 emissions and policy in the residential sector (with an overview of the top ten CO_2 emitting countries)," *Renewable and Sustainable Energy Reviews*, vol. 43, pp. 843–862, 2015.

[3] H. Khatib, "IEA world energy outlook 2011-a comment," *Energy Policy*, vol. 48, pp. 737–743, 2012.

[4] J. Goldemberg, "The promise of clean energy," *Energy Policy*, vol. 34, no. 15, pp. 2185–2190, 2006.

[5] G. D. Kamalapur and R. Y. Udaykumar, "Rural electrification in India and feasibility of photovoltaic solar home systems," *International Journal of Electrical Power & Energy Systems*, vol. 33, no. 3, pp. 594–599, 2011.

[6] G. N. L. P. Raj, V. M. Karthik, M. Mohanraj, and V. Kirubakaran, *Fast thermal degradation of biomass using scrapped solar cell with special focus on photovoltaic (PV) waste disposal*, Springer, Singapore, 2019.

[7] C. O. Okoye and B. C. Oranekwu-Okoye, "Economic feasibility of solar PV system for rural electrification in Sub- Sahara Africa," *Renewable and Sustainable Energy Reviews*, vol. 82, pp. 2537–2547, 2018.

[8] C. Marimuthu and V. Kirubakaran, "Carbon pay back period for solar and wind energy project installed in India: a critical review," *Renewable and Sustainable Energy Reviews*, vol. 23, pp. 80–90, 2013.

[9] V. Kirubakaran, P. R. G. N. Lalith, G. Prabakaran, and A. Murugaiyan, "Hybrid photovoltaic-thermal systems: innovative CHP approach," in *2018 4th International Conference on Electrical Energy Systems (ICEES)*, pp. 726–730, Chennai, India, 2018.

[10] C. Sreenath, S. S. S. Velan, C. Shankar, V. Rajakumaran, and V. Kirubakaran, "Experimental study on optimum area utilisation for maximum power output in solar photovoltaic system," *International Journal of Energy Technology and Policy*, vol. 11, no. 3, pp. 209–219, 2015.

[11] K. Kamaleswaran, M. Adammydeen, P. Harinath, M. Venkateshwaran, and V. Kirubakaran, "Reliable power and quality drinking water for rural household through integrative approach of solar PV system," *International Journal of Energy Technology and Policy*, vol. 12, no. 4, pp. 400–408, 2016.

[12] S. S. Chopade, P. R. G. N. Lalith, and G. Prabakaran, "Bench marking of grid tied solar roof top photovoltaic system: a case comparison," *International Journal of Engineering & Technology*, vol. 7, no. 3.3, 2018.

[13] C. Aarthy Vigneshwari, S. S. S. Velan, M. Venkateshwaran, M. A. Mydeen, and V. Kirubakaran, "Performance and economic study of on-grid and off-grid solar photovoltaic system," in *2016 International Conference on Energy Efficient Technologies for Sustainability (ICEETS)*, pp. 239–244, Nagercoil, India, April 2016.

[14] C. Gantz, *Refrigeration: A History*, McFarland & Co Inc, 2015.

[15] S. McCarney, J. Robertson, J. Arnaud, K. Lorenson, and J. Lloyd, "Using solar-powered refrigeration for vaccine storage where other sources of reliable electricity are inadequate or costly," *Vaccine*, vol. 31, no. 51, pp. 6050–6057, 2013.

[16] O. Ekren, A. Yilanci, E. Cetin, and H. K. Ozturk, "Experimental performance evaluation of a PV-powered refrigeration system," *Electronics and Electrical Engineering*, vol. 114, no. 8, pp. 7–10, 2011.

[17] B. J. Huang, T. F. Hou, P. C. Hsu et al., "Design of direct solar PV driven air conditioner," *Renewable Energy*, vol. 88, pp. 95–101, 2016.

[18] I. Daut, M. Adzrie, M. Irwanto, P. Ibrahim, and M. Fitra, "Solar powered air conditioning system," *Energy Procedia*, vol. 36, pp. 444–453, 2013.

[19] R. Nikbakhti, X. Wang, A. K. Hussein, and A. Iranmanesh, "Absorption cooling systems - Review of various techniques for energy performance enhancement," *Alexandria Engineering Journal*, vol. 59, no. 2, pp. 707–738, 2020.

[20] D. A. Selvaraj and K. Victor, "Vapour absorption refrigeration system for rural cold storage: a comparative study," *Environmental Science and Pollution Research*, vol. 27, 2020.

[21] J. C. V. Chinnappa, "Performance of an intermittent refrigerator operated by a flat-plate collector," *Solar Energy*, vol. 6, no. 4, pp. 143–150, 1962.

[22] M. I. Karamangil, S. Coskun, O. Kaynakli, and N. Yamankaradeniz, "A simulation study of performance evaluation of single-stage absorption refrigeration system using conventional working fluids and alternatives," *Renewable and Sustainable Energy Reviews*, vol. 14, no. 7, pp. 1969–1978, 2010.

[23] J. R. Patel, "Solar powered vapour absorption refrigeration (SPVAR) system as a rural microenterprise," in *Environmental Science*, 2016.

[24] S. Alabd Mohamed and M. Nawab Karimi, "Simulation of lithium bromide-water (LiBr-H2O) vapor absorption system (VAS) powered by solar flat plate collector (SFPC)," *IOP*

Conference Series: Materials Science and Engineering, vol. 691, no. 1, 2019.

[25] A. Pongtornkulpanich, S. Thepa, M. Amornkitbamrung, and C. Butcher, "Experience with fully operational solar-driven 10-ton LiBr/H2O single-effect absorption cooling system in Thailand," *Renewable Energy*, vol. 33, no. 5, pp. 943–949, 2008.

[26] S. A. M. Said, M. A. I. El-Shaarawi, and M. U. Siddiqui, "Alternative designs for a 24-h operating solar-powered absorption refrigeration technology," *International Journal of Refrigeration*, vol. 35, no. 7, pp. 1967–1977, 2012.

[27] W. Rivera, G. Moreno-Quintanar, C. O. Rivera, R. Best, and F. Martínez, "Evaluation of a solar intermittent refrigeration system for ice production operating with ammonia/lithium nitrate," *Solar Energy*, vol. 85, no. 1, pp. 38–45, 2011.

[28] A. A. Manzela, S. M. Hanriot, L. Cabezas-Gómez, and J. R. Sodré, "Using engine exhaust gas as energy source for an absorption refrigeration system," *Applied Energy*, vol. 87, no. 4, pp. 1141–1148, 2010.

[29] E. Kurem and I. Horuz, "A comparison between ammonia-water and water-lithium bromide solutions in absorption heat transformers," *International Communications in Heat and Mass Transfer*, vol. 28, no. 3, pp. 427–438, 2001.

[30] GOI-MOP, "CO_2 Baseline Database for the Indian Power Sector User Guide," *Report by Ministry of Power Government of India*, vol. 3, pp. 1–34, 2018, http://cea.nic.in/reports/others/thermal/tpece/cdm_co2/user_guide_ver9.pdf.

Hindawi
International Journal of Photoenergy
Volume 2021, Article ID 6651717, 19 pages
https://doi.org/10.1155/2021/6651717

Research Article

Energy Efficiency Enhancement and Climate Change Mitigations of SMEs through Grid-Interactive Solar Photovoltaic System

G. N. Lalith Pankaj Raj and V. Kirubakaran

Centre for Rural Energy, The Gandhigram Rural Institute-Deemed to be University, Gandhigram, 624 302 Tamil Nadu, India

Correspondence should be addressed to V. Kirubakaran; kirbakaran@yahoo.com

Received 26 November 2020; Revised 5 January 2021; Accepted 8 January 2021; Published 27 January 2021

Academic Editor: S. Shanmuga Priya

Copyright © 2021 G. N. Lalith Pankaj Raj and V. Kirubakaran. This is an open access article distributed under the Creative Commons Attribution License, which permits unrestricted use, distribution, and reproduction in any medium, provided the original work is properly cited.

According to the International Energy Agency's estimation, Indian primary energy demand is expected to increase by about 1250 Mtoe and 1500 Mtoe by 2030. The 3 M management concept now changed into a 4 M management concept that includes energy management. In the case of energy management, the electrical energy sector assumes critical importance. An energy cost occupies nearly 30-40% of the production cost in small and medium-size enterprises (SMEs). Bureau of Energy Efficiency (BEE) has initiated a separate energy efficiency intervention to the SME's, where the energy-efficient technologies, operational procedures, and proper awareness programs to SMEs are stated. This paper discusses the complete electrical energy audit on a small-scale Siddha and Ayurveda medicine industry. The traditional medicine manufacturing technologies make the process complex (process loads are intermittent/interlinked) during analysis. Hence, the detailed energy auditing/conservation studies on the power factor/harmonics were carried out without affecting Indian traditional medicine manufacturing technology. The postauditing design and installation of an intelligent controller by considering the intermittent/interlinked loads are carried out, and the effectiveness of the intelligent controller is ascertained with the energy conservation and the carbon emission reduction of SME. In addition, the climate change mitigation is ensured through the design and deployment of grid-interactive rooftop solar photovoltaic power plant using Solar Pro v4.5 (Photovoltaic System simulation software) with the power analysis, economic analysis and life cycle carbon emission of the proposed plant. The proposed solar photovoltaic power plant ensures energy self-sufficiency and sustainable energy utilization by carbon emission reduction on electricity utilization of SMEs.

1. Introduction

According to the Ministry of Environment and Forests (MOEF), 70% of the total industrial pollution of the whole nation (INDIA) is due to SMEs [1]. The Bureau of Energy Efficiency (BEE) has initiated the energy efficiency interventions in selected 25 SME clusters during the XI plan. During the XII plan, implementations of 100 technology demonstration real-time projects in five SME sectors envisaged facilitating large-scale replication of the successful technology. As per Energy Conservation Act, 2001, energy audit is defined as verification, monitoring, and analysis of the use of energy, including submission of technical report containing recommendations for improving energy efficiency with cost-benefit analysis and an action plan to reduce energy consumption. Energy auditing is a systematic approach for energy management and the first step in realizing the energy efficiency opportunities [2] with economic [3] consideration. The industrial energy audit is mainly focusing on the energy loss reduction [4] in the following aspects of the process, the operation modification, investment in energy-efficient technologies, load management, and conversion energy losses.

The power quality is a catchword that came into the power industry during the 1980s. According to the Institute of Electrical and Electronics Engineers (IEEE) standard IEEE 1100, power quality is "the concept of powering and grounding sensitive electronic equipment in a manner suitable for the equipment." The device may be anything; they will respond adversely towards the power quality issues. According to EDSA, power analytics ensuring business resilience, "30 to 40 % of all business downtime is closely associated with power quality problems" [5]. Businesses have many expensive investments towards the office, production equipment, and infrastructures. Power quality protection is a low-cost insurance policy against power wastage and accidents.

This paper deals with the objective of attaining the state of energy self-sufficient SME, and the quest for energy self-sufficiency commences once the conventional power grid is volatile and unreliable. The dependence on the conventional power grid will reduce the industry's overall productivity due to various constraints like peak time shutdown, off-peak time of operation, and high tariff with lower power quality. The paradigm shift from the conventional power grid to a non-conventional (renewable) power grid could address the issue and increase overall industrial productivity. Therefore, energy self-sufficiency is highly recommended for increasing productivity with less carbon emission through renewable energy resources.

This paper deals with the electrical anomalies that are pertaining to the power quality issues faced by a medium-scale Siddha and Ayurveda manufacturing enterprise in the complete electrical energy auditing perspective. The reflection of low power quality shows an increase in the electricity bill of the enterprise. This paper also deals with the postaudit proposal of grid-interactive solar photovoltaic (SPV) power plant for attaining the state of energy self-sufficiency of the SMEs using the Solar Pro simulation software, and it is a roadmap for climate change mitigation by carbon emission reduction.

2. Literature Review

The various forms of the power factor improvement in an SME unit with the underlying design calculations for power capacitors and various power quality issues in a process industry were discussed [6]. The clarity about the overall audit process of textile industry motors in turn helps us to study the old induction-type motor loads in this SME [7, 8]. The process mapping of an industrial production process is a critical area that has to be taken care of to start up with the process, which helped us create a roadmap to start with the SME audit process under investigation [9].

The various economic aspects from the point of top-level management people, to implement the various collective recommendations by the electrical service company (ESCO), Industrial Assessment Centres (IAS), helped in making suggestions and recommendations for this SME [10]. The presence of power quality issues in the food processing industry was addressed, which gave clarity in the power factor capacitor's design to act as a harmonic filter to counter-effect the harmonics generated in the industry [11]. The author focused on the practical challenges in the environmental management of the Indian SMEs and its methodologies to address the environmental issues by considering the country's need and sector-specific investigation for identifying the relationship between the small SMEs [12]. The detailed energy and economic analysis for energy conservation measures help SME's energy auditing with detailed cost economics [3, 13].

The energy audit is a consistent and useful tool for overcoming technological, information bottlenecks, and investment in energy-efficient measures [2]. The measurement [14] of data as a primary data collection is to understand the operation and event occurrence, calculate, explain, and validate the industry's energy consumption. The energy auditing tool [15] of Passive Home Planning Package (PHPP) and Transient System Simulation (TRNSYS) are used for energy estimation, and equivalent energy savings with greater accuracy and machine learning [16] algorithms are used for energy self-sufficiency. The effectiveness of energy audit diminishes with the number of employees increasing in the organizational size [17] in lighting, heating, insulation, and operations. The energy self-sufficiency [18] of SME is ensured by installing the SPV power plant with the sensitivity analysis of factors pertaining to the technical and economic consideration. The country's energy self-sufficiency and energy security is achieved by the 100% renewable energy transition based on the country's energy demand [19]. The renewable energy resource without or with negligible energy storage [20] is highly economical for attaining the state of energy self-sufficiency.

The solar PVsyst simulation software is used for designing the SPV plants in vessels [21]. The power and energy analysis of the designed SPV plant is carried out by the PVsyst software based on the vessel's route. The location-specific [22] solar potential and its performance can be analyzed using the PVsyst software. The 15 kWp grid-interactive SPV [23] is designed and simulated using the PVsyst software with the annual average performance ratio (PR) of 79.48%.

The design and performance analysis of 2 kWp SPV gives 73.5% with the PVsyst [24] simulation software in India's Odisha state. The economic analysis gives a payback period of 7.6 years. The annual average PR of 200 kWp simulated SPV plant is 81.7%. The real-time comparative analysis of performance ratio [25] ranges between 60% and 90%, and capacity utilization factor (CUF) ranges from 12% to 18% for the rooftop 20 kWp SPV power plant in the Telangana state of India. The design and performance analysis of 100 kWp Si-poly [26] SPV plant is carried out using the PVsyst simulation software. The annual average PR of 80% with a power generation of 165.38 MWh is achieved in the designed SPV plant.

The Solar Pro simulation software has a tremendous amount of metro [27] database for various global parts. Also, the interface for manual addition of the measured dataset makes the software more user-friendly and has greater accuracy. The design and performance analysis of 100 kWp SPV is carried out using the Solar Pro simulation software in the Telangana state of India. The Solar Pro simulation software is used for shadow analysis of the SPV plant. The seasonal tilt (or) inclination angle [27] for module mounting is calculated based on the field conditions using Solar Pro and

obtained 30791.64 kWh/year for building energy performance enhancement. The Solar Pro software is used for 3.15 kWp SPV plant design and its fault characteristics [28] study during the faulty condition. The design and development of circuit-based solar module performance on shadow and faulty condition and its validity is verified using the Solar Pro simulation software package. The maximum power point (MPP) error of 10.17% [29] is recorded during the effectiveness comparison of the circuit-based module and Solar Pro simulator.

From the review, SMEs have significant energy efficiency enhancement scope by enhancing the system's power quality. In addition, due to the various positive indices in the installation of SPV power plant in SMEs for attaining the state of energy self-sufficiency and climate change mitigation, the various commercial and noncommercial solar design and simulation packages are available. The Solar Pro v4.5 (Photovoltaic System simulation software) is used for obtaining an interactive 3D user interface for shading and designing panel mounting with more significant space and power optimization. It is also highly recommended for its unique features of calculation for shading and power analysis with minute-by-minute accuracy. Therefore, the proposed SPV's design and performance prediction is carried out by Solar Pro v4.5 (Photovoltaic System simulation software).

3. Methodology

The present technology practiced in Siddha and Ayurveda medicine production process is traditional cum mechanized with some modern machinery. In this enterprise, the medicine manufacturing process is undefined (i.e., intermitted in nature). The methodology of the detailed energy audit varies from industry to industry, and it is highly flexible according to the type of the industry. Here, the intermittent/interlinked traditional medicine manufacturing process is crucial to carry out the energy audit. According to the BEE guidelines, a systematic methodology for detailed energy auditing is shown in Figure 1.

The phase I: preaudit kickstarted to obtain the overall resource planning and organize the instrument for setting up a reference point for energy consumption. Here, the load curve and cost economic curves are obtained by collecting the macrolevel data from the responsible individuals and the historical dataset of the industry. The preaudit of the Siddha and Ayurvedic industry needs to be done precisely. The Indian traditional medicine manufacturing technology is unique and intermitted/noncontinuous, which cannot be altered based on the energy perspective. The lack of continuous running process machine and part loading operation is a crucial issue to address in this auditing. Therefore, planning and organizing the instruments for energy analysis and organization of resources are highly recommended.

The phase II: audit phase comprises developing the process and energy flow diagram with the active involvement of energy individuals of the industry. The survey and monitoring are carried out for all the connected loads to meet the supply and demand management of the industry. The detailed energy auditing phase is by continuous monitoring and logging of data using various energy auditing instruments like power on clamp meter for electrical energy studies, thermal imager for infrared thermography, and other various energy auditing instruments.

The process is followed by energy analysis using the obtained data and standard data. Based on the detailed energy audit, energy analysis is carried out. Therefore, the ENCON (Energy Conservation) opportunities proposed with the cost economics as a report to the top-level management.

The phase III: postenergy audit phase was initiated by the implementation of ENCON measures by the action plan recommended. The periodic reviews and follow-ups ensure the effectiveness of the implementation. Therefore, based on the detailed energy audit results, suggested ENCON recommendations were implemented accurately. The power quality analyzer analysis is a class "A" accuracy instrument used for continuous logging of electrical anomalies of the SME's power system on power quality issues like sag, swell, power factor, voltage-total harmonic distortion factor (V-THDF), and current-total harmonic distortion factor (I-THDF). The design and implementation of Intelligent Power Factor Controller (IPFC) and its effectiveness were studied in the post energy audit phase.

Also, a grid-interactive SPV power plant is designed and proposed with the power, economic, and carbon emission analysis using Solar Pro simulation software package for attaining the state of energy self-sufficiency SME. The feasibility study for the solar simulation was carried out by considering the various primary dataset of latitude, longitude, energy utilization pattern, connected load, energy demand, energy consumption details, building dimensions, type of building, and shade-free area (effective area) for solar module installation. Therefore, the proposed SPV plant is highly significant in energy self-sufficiency, and the renewable energy resource led to climate change mitigation.

The power quality analyzer (clamp-on-power meter) shown in Figure 2 is used at the vicinity of the point of common coupling (PCC) for the main power distribution panel in order to calculate the energy utilization pattern of the entire enterprise. Figure 3 shows the energy auditing carried in the enterprise. The power meter clamp is calibrated in three-phase-four-wire configuration for detailed power quality and energy analysis of the enterprise. After the energy auditing analysis, the power quality issues have arrived. The graph gave the plotted results of the analysis and interpreted the same in the analysis. The power quality graphs show the total voltage, total current, power (real (kW), reactive (KVAr), and apparent (kVA)), power factor, voltage-total harmonic distortion factor (V-THDF), current-total harmonic distortion factor (I-THDF), and frequency.

4. Results and Discussion of Preaudit Phase

Energy auditing started with the collection of load curves from enterprise historical data. The load curve gives the necessary prerequests to carry out the energy auditing in the enterprise. The primary vertical axis of Figure 4 illustrates the enterprise's annual load curve, and the secondary axis gives the month-wise energy cost of the enterprise in the overall annual load curve. This load and cost curve reveals

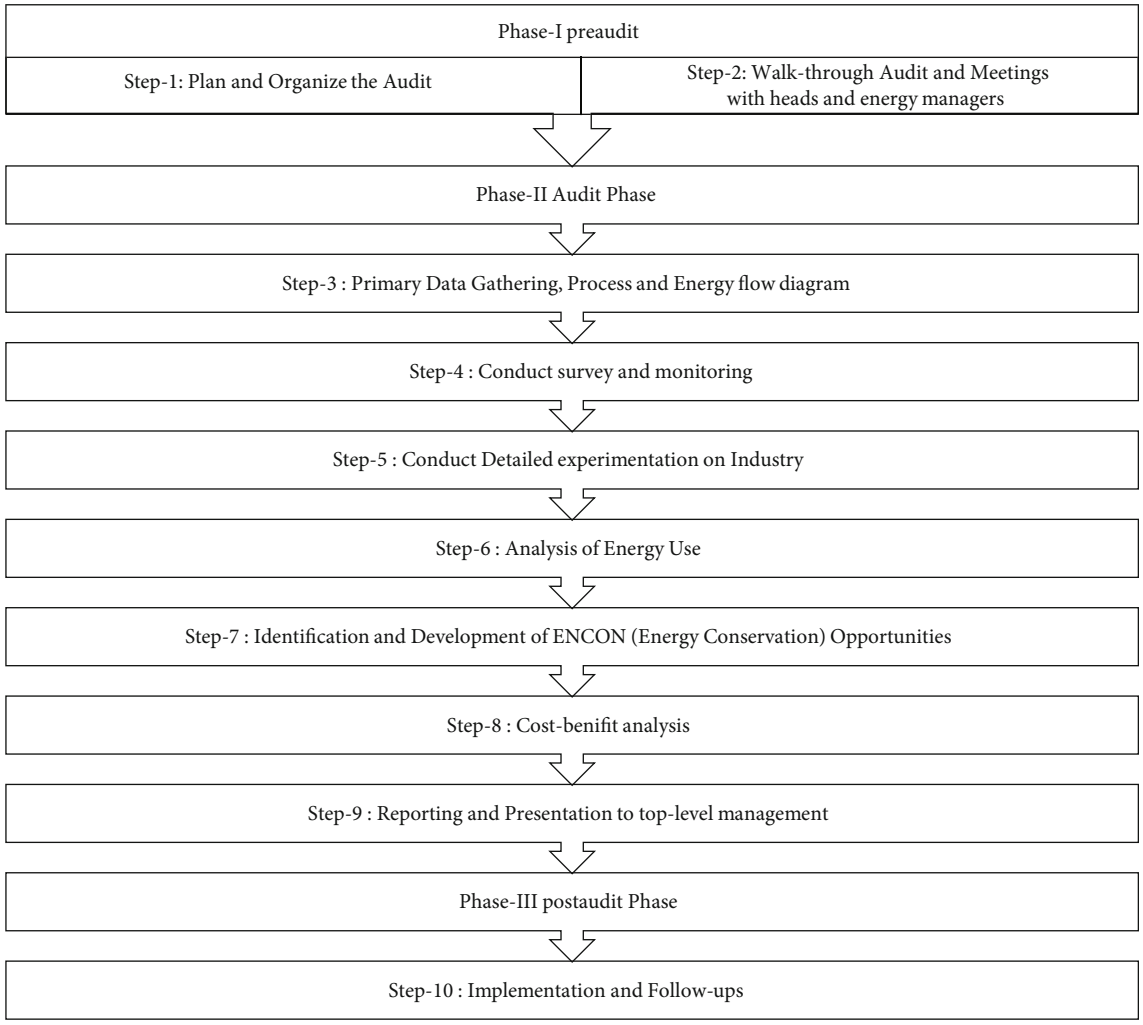

Figure 1: Systematic detailed energy auditing methodology.

Figure 2: Power on clamp meter for energy auditing.

the preaudit phase of an energy audit by revealing a power consumption pattern. The overall electrical energy consumption concerning time gives the industry's loading pattern for a particular time.

5. Results and Discussion of Audit Phase

Figure 5 shows the gives of time versus voltage performance of the enterprise. The analysis starts from the beginning of the load to the load's termination to study the starting spikes or surges in the power system by connecting the power on clamp meters on the PCC. From the voltage profile, it is inferred that the presence of voltage unbalances in the system. The 5% voltage unbalance will increase the current consumption by 1 to 6 times of rated current consumption and reduce the efficiency of the electric motor load in the power system.

Figure 6 shows the graphical representation of the time versus the current profile of the enterprise. The phase-wise current consumption is R-phase (A), Y-phase (A), B-phase (A), and neutral (N), respectively. Here, nearly 30 A of neutral current is present in the unit, and the total current is about 35 A during the recording period. The presence of unbalance in the current consumption profile clearly defines the poor load sharing between each phase. The unbalanced loads and the presence of current harmonics lead to a high neutral current in the system.

Figure 3: Energy auditing at point of common coupling.

Figure 7 shows the time versus real (W), reactive (VAr), and apparent power (VA). The presence of apparent power is more in the unit. The significance of reactive power injection in the SME is a minimum value, which concludes the consequence of the enormous consumption of the real power since there is a prevalence of lagging power factor in the enterprise. The need for compensation is essential to equate the power consumption without a considerable amount of wastage.

Figure 8 shows the graphical representation of time versus % voltage-total harmonic distortion factor (V-THDF) from the graphical representation; the Y-phase voltage THDF is higher than other phases. At the PCC, the maximum allowable V-THDF is of 5% as per the IEEE 519-2014 and IEC 61000 standards. This voltage harmonic distortion in the enterprise is under the Central Electricity Authority (CEA) regulations. The presence of poor V-THDF directly reflects the temperature rise of the electric motor load in the enterprise. As the temperature increases, the efficiency of the motor drastically decreases.

Figure 9 shows the time versus current-total harmonic distortion factor (I-THDF). At the PCC, the maximum allowable I-THDF if of 8% as per the IEEE 519-2014 and IEC 61000 standards. The presence of harmonics in the Y-phase has higher value compared that with the other phase harmonics. The overall harmonic level of the enterprise is exceeding the central electricity authority rules and regulations.

Figure 10 gives a graphical representation of the time versus the power factor of the enterprise. The range of power factor varies from 0.65 to 0.8 without any compensation technologies. The inefficient, ancient, and rewinding induction electric motor loads are the primary sources for producing low power factor. Figure 11 gives the graphical representation of the time versus frequency of the enterprise. There is no significant variation of frequency. Therefore, skin effect is minimum in the SME.

The enterprise has low power quality indices like lagging power factor, voltage, and current harmonic distortion, which unbalance from the detailed energy audit analysis. Therefore, the harmonic mitigating filter circuit is highly recommended, and proper load balancing between the phases is essential for better power quality. Also, the power factor improvement capacitors will address the above-mentioned power quality issues by the compensation technique.

From the detailed energy auditing, it is perceived that there is an unbalance exists in phases [30]. The loads are not evenly distributed in the system, and several loads are critical, which generates positive, negative, and zero sequence errors. Frequency variations are high due to nonlinear loading examples like Hammer Machine, Ball Mill. The power factor for the motors is about 0.65. Total harmonic distortion factor (THDF) is higher in the Y-phase, which recorded as 14%, which is above IEEE standard limits of V-THDF of 5% and I-THDF [31] of 8% at point of common coupling (PCC) as per the norms of Central Electricity Authority (CEA).

There are steps to study the sequence of operation of a particular medicine manufacturing process to get rid of the harmonic prone environment. The electrical operation is scheduled accordingly to the phase balancing with careful consideration of critical and nonlinear loads without affecting their traditional operations during the production process. This will reduce the neutral current and enhance the overall power quality of the enterprise.

5.1. Condenser Calculation of Intelligent Power Factor Controller (IPFC). The required leading KVAr compensation by P.F. correction equipment [32]

$$\text{KVAr} = \text{kW}(\tan\varnothing 1 - \tan\varnothing 2). \quad (1)$$

The sum of the machine's horse power rating is the active power for the power factor improvement calculation from 0.65 to 0.99.

$$\text{Total active power} = (\text{sum of all connected HP}) * 746, \quad (2)$$

$$\text{Total active power} = (94 * 0.746) = 70.124\,\text{kW}, \quad (3)$$

$$\text{KVAr} = 70.124\,(\tan 49.46 - \tan 8.11). \quad (4)$$

The leading reactive power (KVAr) was supplied by power factor correction equipment = 72,052.41 KVAr.

The KVAr compensator rating of 72,052.41 is sufficient to enhance the power factor.

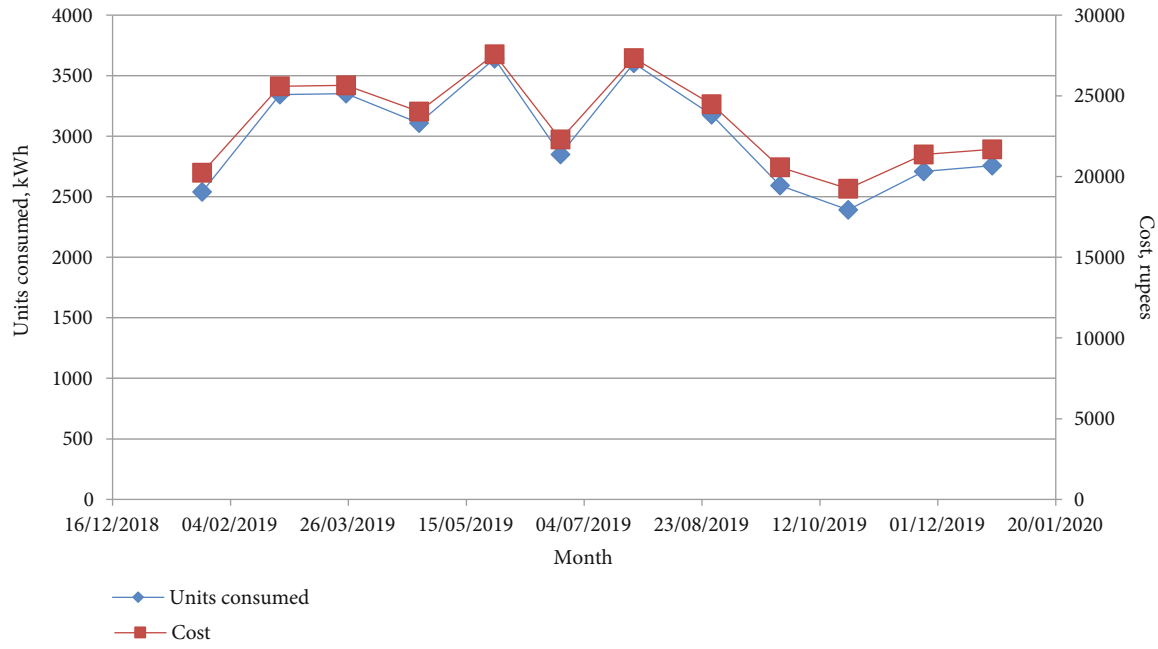

Figure 4: Load and cost economics curve of SME (phase I—preaudit).

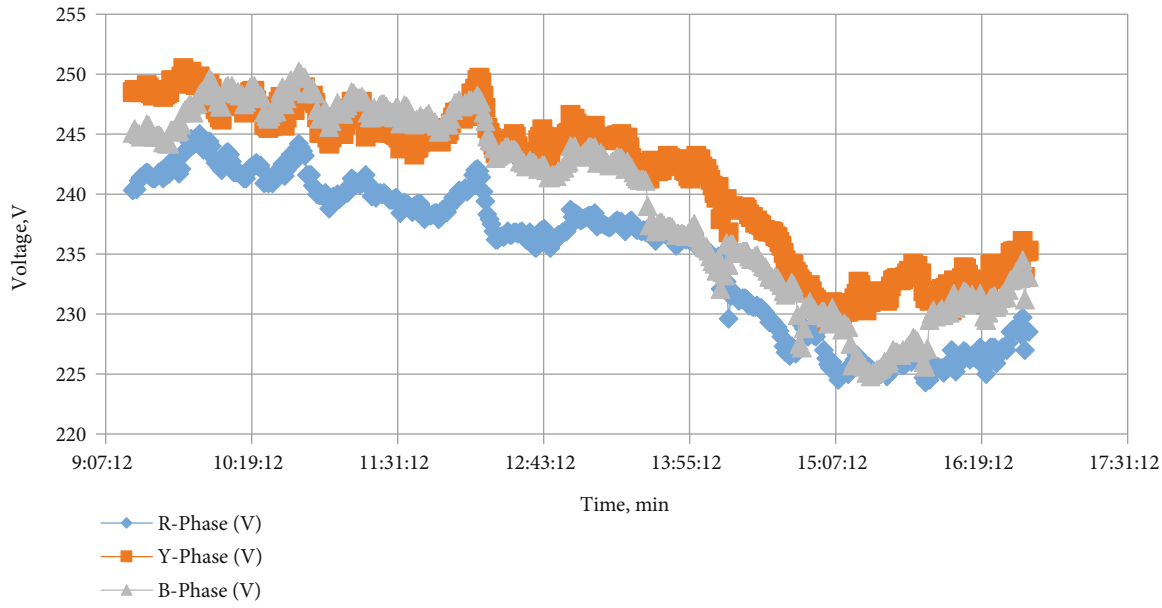

Figure 5: Time vs. voltage (phase II—audit phase).

5.2. Intelligent Controller. Figure 12 shows the Intelligent Power Factor Controller (IPFC), a smart, simple, accurate [33], and robust reactive power compensator. It is versatile in power factor mitigation [34] by its smart features of load sensing and storage of historical datasets. The IPFC is powered by various combinations of power capacitors for reactive power compensation [32]. The AT89S52 [35] is low power consuming, high-performance 8-bit Microcontroller with 8 k bit in-system programmable flash memory. It provides the following standard features: 32 input-output lines, 256 bytes of RAM, watchdog times, two data pointers, fully duplex serial port, clock circuit, and memory storage facility. The voltage and current transformers are used to sense and measure the system's input voltage and current. The zero-crossing filter is used to obtain the instantaneous voltage and current point at which there is no voltage and current, respectively. The IPFC is equipped with the data storage facility for logging of present load and historical

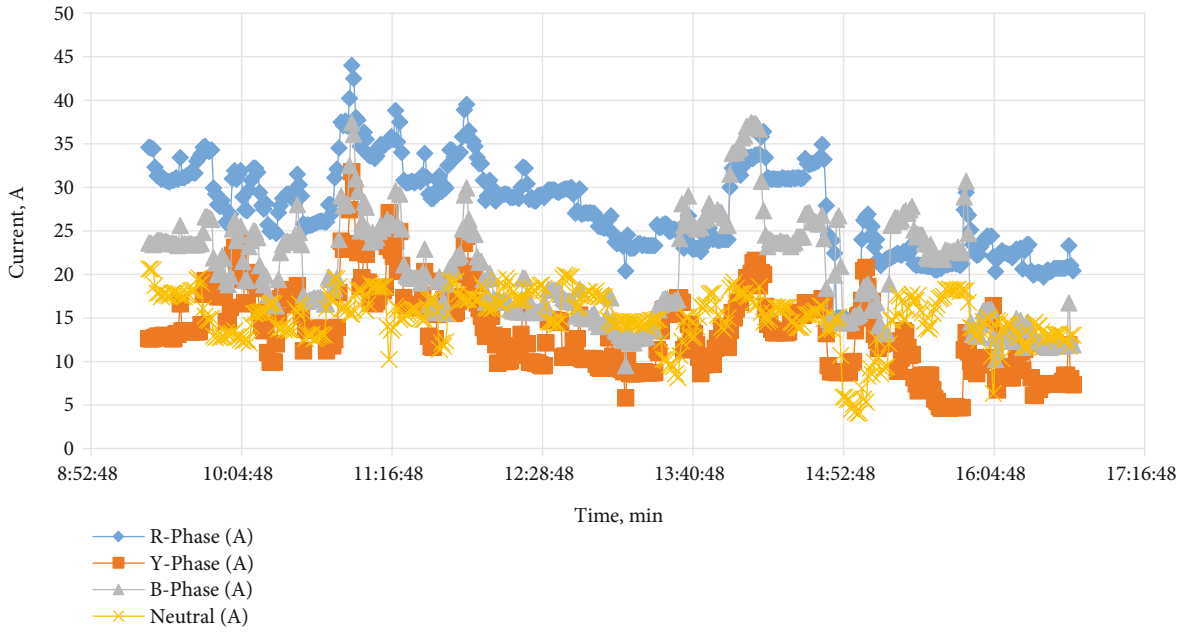

Figure 6: Time vs. current (phase II—audit phase).

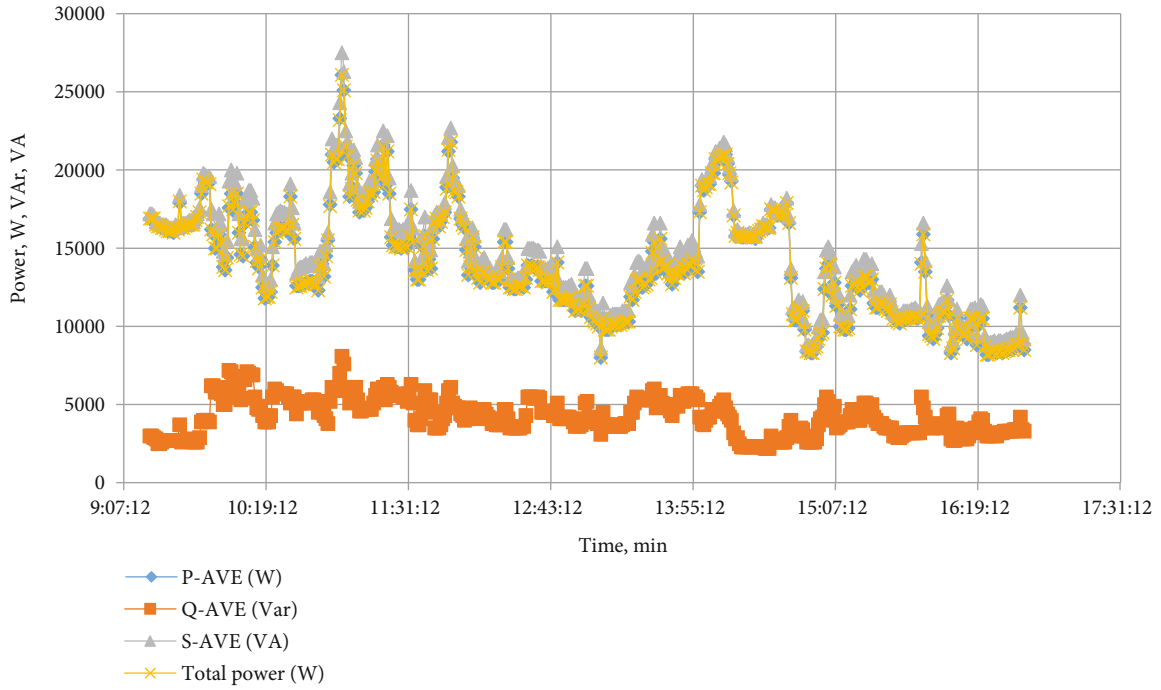

Figure 7: Time vs. power (phase II—audit phase).

datasets for better reliable and faster compensation. The relay circuit is to electrically make (turn on) and break (turn off) the shunt capacitors [36] from the system. Based on the controller's load-sensing signal, the switching on and off of shunt capacitors is carried out. The relay drive is powered by the embedded system [37] to reduce the overall system cost to have robust, accurate control, and cost-effective.

6. Results and Discussion of Postaudit Phase

The postaudit phase is carried out to calculate the effectiveness of the installed IPFC unit. Figure 13 gives the graphical representation of the time versus voltage profile of SME after improvement using IPFC installation. The IPFC unit's installation achieves a 5% increase in the voltage profile. Figure 14

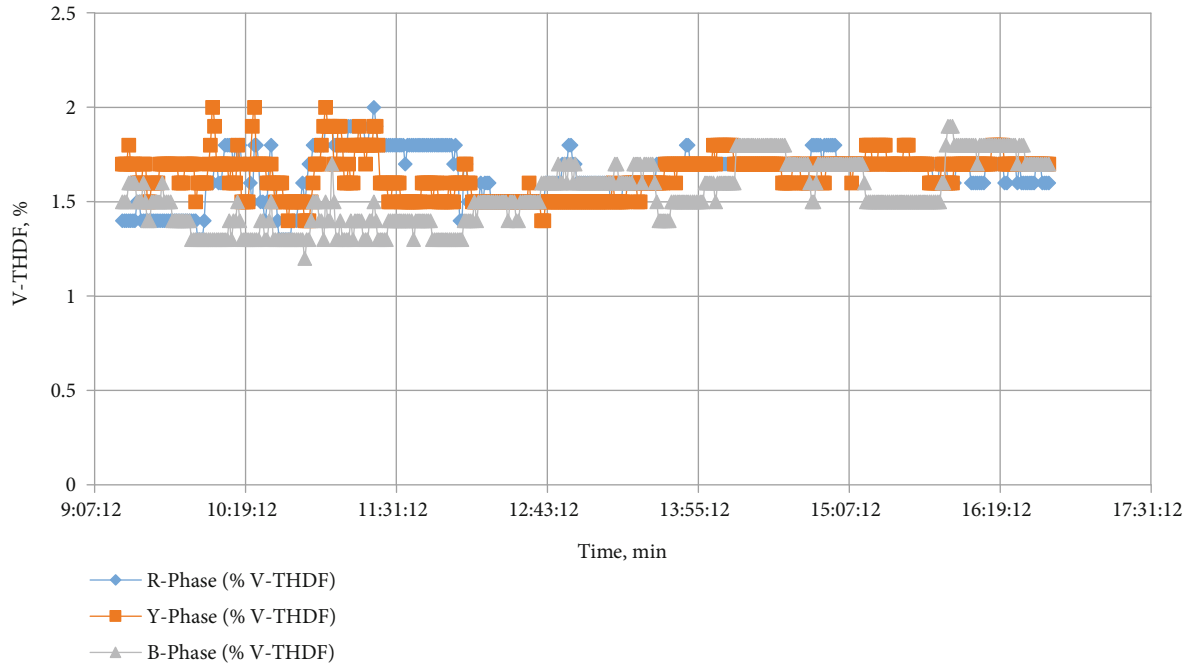

Figure 8: Time vs. V-THDF (phase II—audit phase).

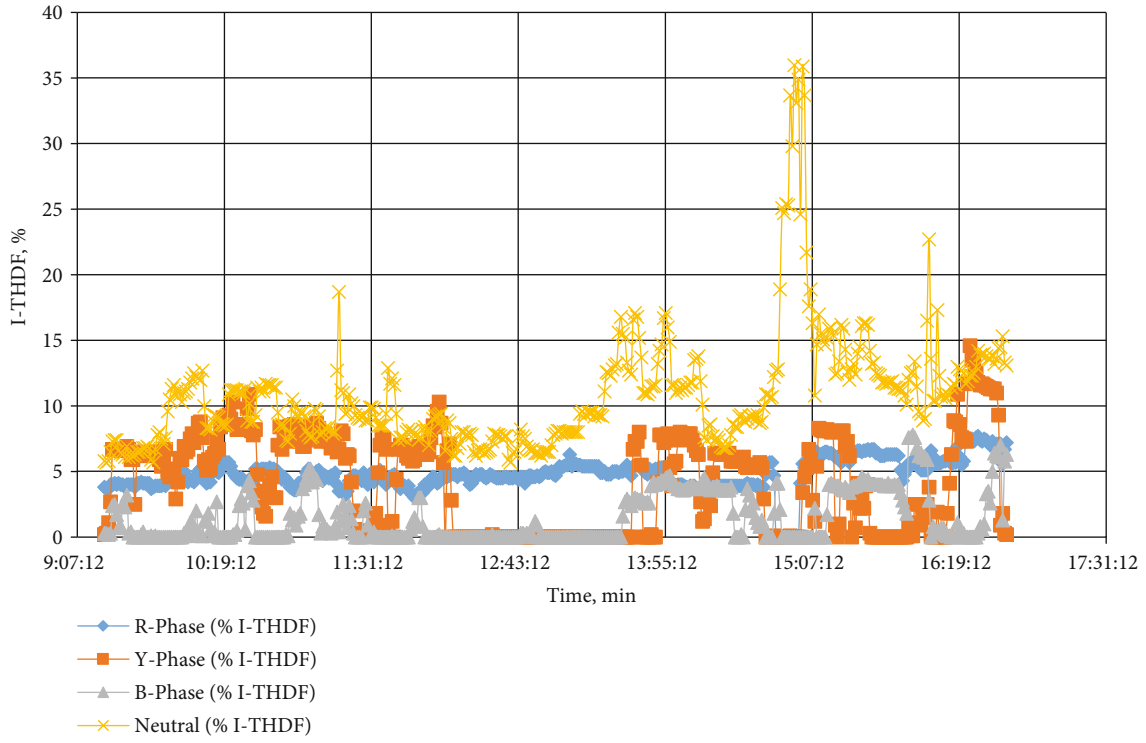

Figure 9: Time vs. I-THDF (phase II—audit phase).

illustrates the postaudit time versus the current profile of the SME. The installation of the IPFC unit achieves a 33.33% reduction in the current consumption profile.

Figure 15 illustrates the graphical representation of time versus power includes active (or) real, reactive, apparent, and total SME power profile. The 28.88% reduction of total

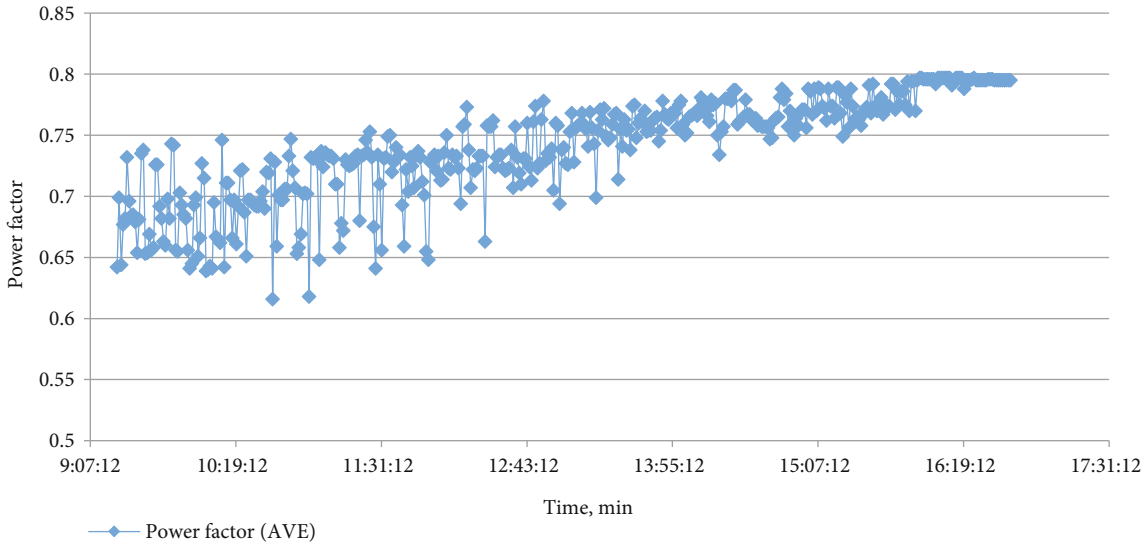

Figure 10: Time vs. power factor (phase II—audit phase).

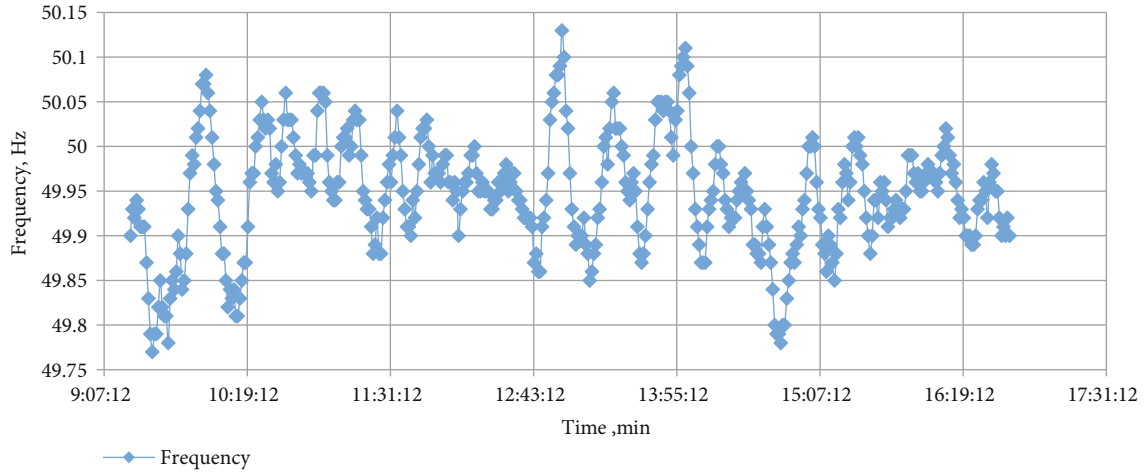

Figure 11: Time vs. frequency (phase II—audit phase).

power is achieved by installing the IPFC unit in the SME. Figure 16 gives the graphical representation of time versus the overall power factor of the SME at the point of common coupling after the installation of the IPFC unit. The 65% increase in the overall power factor is achieved after installing the IPFC unit in the SME. Figure 17 gives the time versus total voltage harmonic distortion factor after the installation of the IPFC unit. The V-THDF of 1.6% is within the IEEE 519 standards and limits under central electricity authority guidelines. Figure 18 gives the time versus total current harmonic distortion factor after the installation of the IPFC unit. The I-THDF of 4.8% is within the IEEE 519 standards and limits under central electricity authority guidelines. Also, the 27.27% reduction is achieved in the neutral I-THDF after installing the IPFC unit. Figure 19 gives the graphical representation of the time versus frequency profile that ensures the less amount of skin effect after installing the IPFC unit.

Figure 20 gives the graphical representation of the exact comparison of power factor before and after installing power factor improvement capacitors (Intelligent Power Factor Controller). The average increase of lagging power factor from 0.6 to 0.99, with the IPFC controller's installation, is ascertained and shown in Figure 20. The 65% increase in the lagging power factor is achieved after the installation of the IPFC.

6.1. Climate Change Mitigations through Power Factor Improvement. According to the Energy Information Administration (EIA), the USA, the electricity utilization holds 37% of carbon emission in the overall greenhouse gas emission. As per the CEA of India [38], 1 kWh of electricity emits 2 kg of CO_2. From the detailed energy audit, we came to know the amount of CO_2 emitted from the enterprise operation.

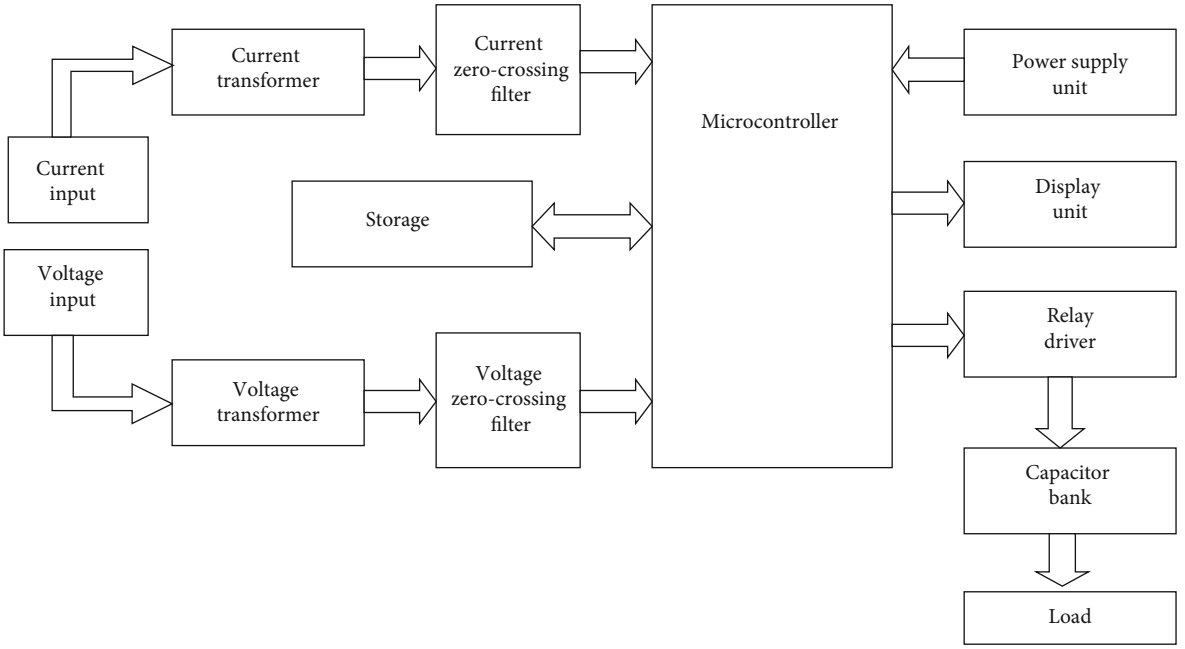

Figure 12: Block diagram of the designed intelligent controller.

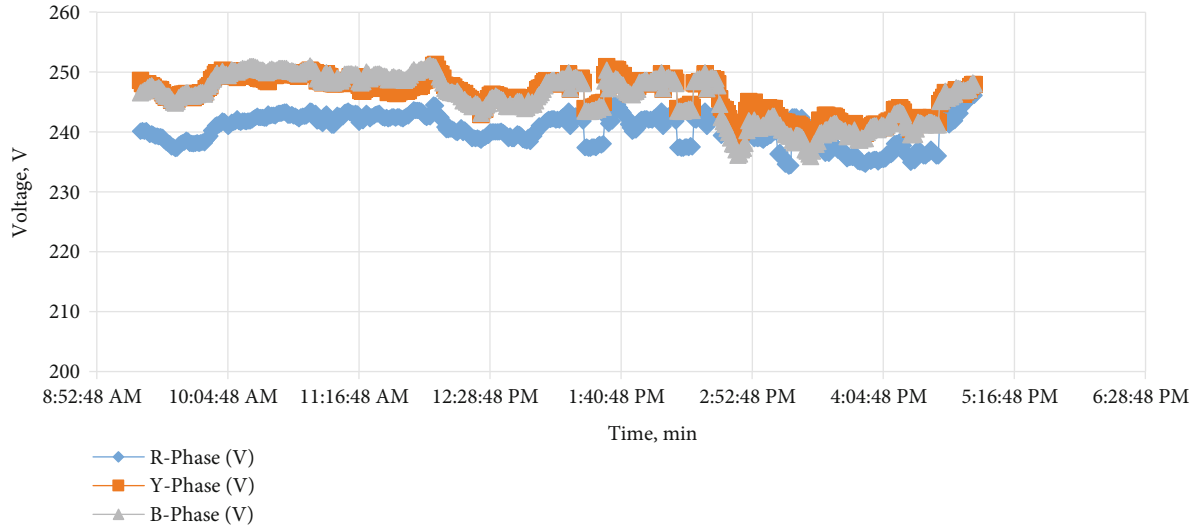

Figure 13: Time vs. voltage (phase III—postaudit).

6.1.1. Before Power Factor Improvement.

$$\text{CO2 emission} = (\text{power in kWh/day}) * 2\,\text{kg of } CO_2. \quad (5)$$

The per-day power consumption is of 208 kWh before improvement; therefore, the following carbon dioxide emissions are calculated as follows:

$$\text{CO2 emission} = 416\,\text{kg of CO2 per day} \quad (6)$$

6.1.2. CO_2 Reduction after Power Factor Improvement.

$$\text{CO2 emission} = (\text{power in kWh/day}) * 2\,\text{kg of } CO_2 \quad (7)$$

The per-day power consumption is of 205.92 kWh before improvement; therefore, the following carbon dioxide emissions are calculated as follows:

$$\text{CO2 emission} = 411.5\,\text{kg of } CO_2 \text{ per day} \quad (8)$$

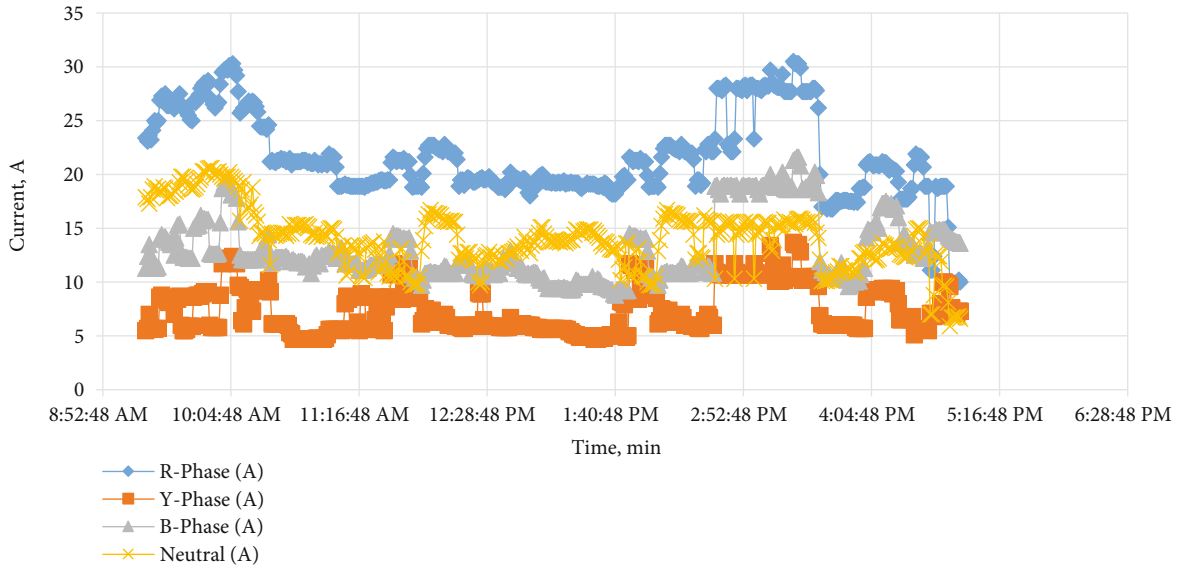

Figure 14: Time vs. current (phase III—postaudit).

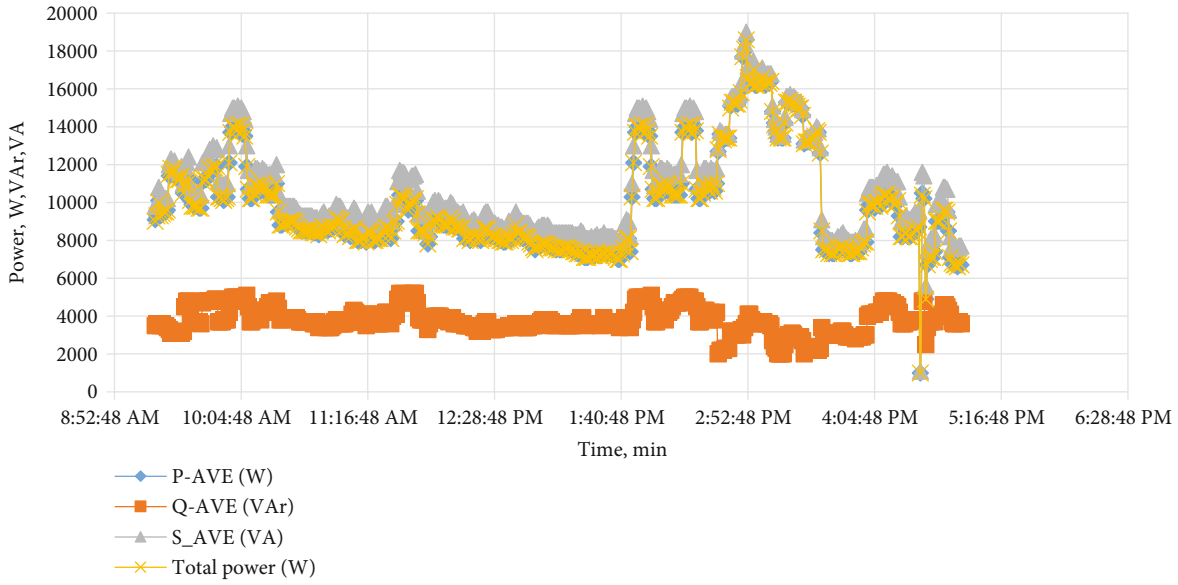

Figure 15: Time vs. power (phase III—postaudit).

Therefore, per day saving is 4.5 kg of CO_2.

$$\text{Per year saving of } CO_2 = 1296 \text{ kg of } CO_2. \quad (9)$$

7. Design of Proposed Grid-Interactive Solar Photovoltaic System

Based on the detailed energy audit of the SME, the grid-interactive photovoltaic system is proposed for climate change mitigation and designed by the Solar Pro v4.5 (Photovoltaic System simulation software). As per norms of Central Electricity Authority (CEA) and Tamil Nadu Electricity Regulatory Commission (TNERC), 100% of the sanctioned demand [39] can be taken as the capacity of a grid-connected solar photovoltaic rooftop system. Also, the overall energy self-sufficiency is ensured via SPV installation sustainably.

Figure 21 gives the overall single line diagram of the proposed 100 kWp solar photovoltaic power plant created using the PVsyst software. The general construction of the plant is divided into three prominent cases as PV array side (includes PV array and diodes), system side (includes inverter and its energy out), and load side (includes load, energy used, energy over, and energy back-up) for ease of operation and maintenance purposes. A 360 Wp polycrystalline module powers the 100 kWp SPV plant with a compactable string inverter for better grid interaction.

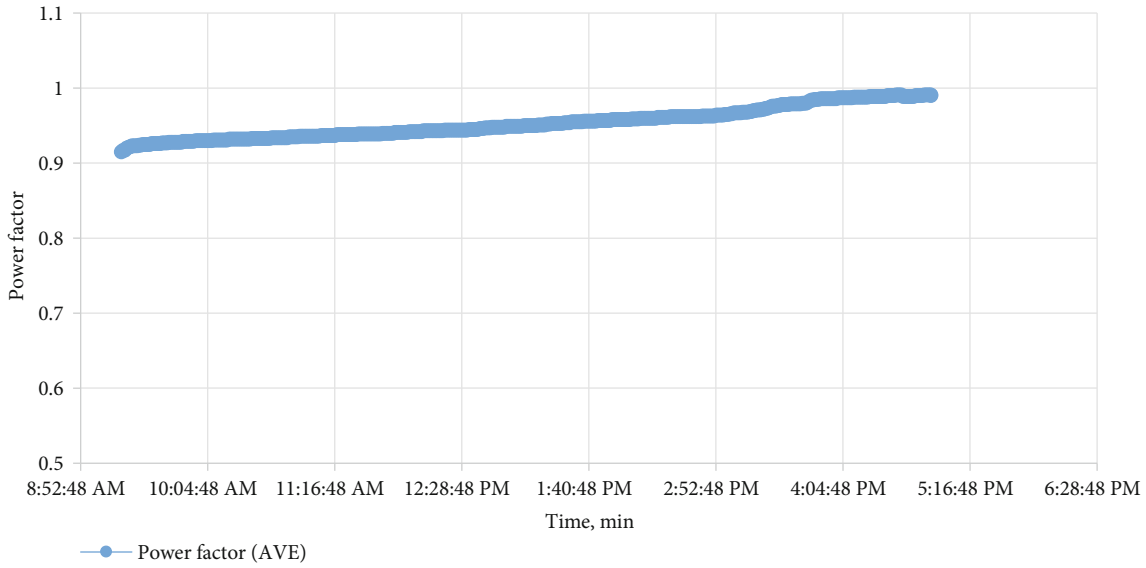

Figure 16: Time vs. power factor (phase III—postaudit).

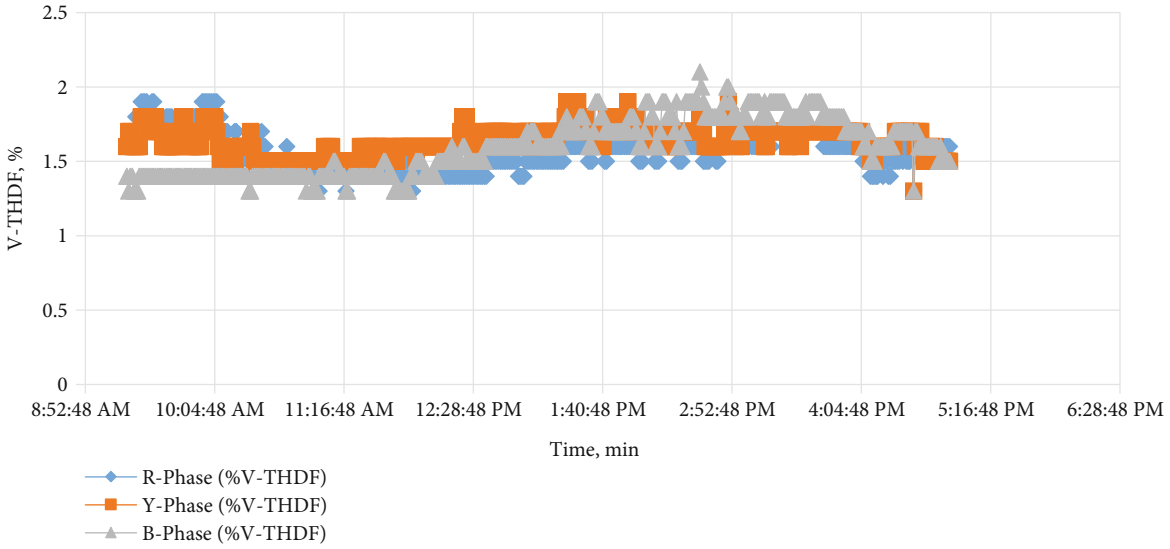

Figure 17: Time vs. V-THDF (phase III—postaudit).

Figure 22 gives the 3D CAD simulation of the proposed 100 kWp SPV plant. The interactive 3D CAD of Solar Pro software aids in developing the virtual design of 100 kWp SPV plant in the SME enterprise, which creates better performance optimization like shading and space distribution of SPV module installation in the premises of the enterprise.

The space optimization of the SPV plant is carried out by 3D CAD simulation of the proposed plant. The module-level dimension specifications are given as input, and optimal string and array combinations arrive by considering the inverter specification's capacity. The real-time two primary criteria are weight distribution for load-bearing capacity of the building and space availability for demand and installed capacity match. The ample space is available in the SME for the installation of the SPV plant. Therefore, space optimization is carried out by choosing the weight distribution for load-bearing capacity in the building. According to the guidelines, space and weight distribution are precisely taken as 30 kg/m^2 to 60 kg/m^2 of weight distribution throughout the SPV plant's installation, including module and module mounting structure.

Figure 23 illustrates the solar irradiation details like total, horizontal, and direct irradiation of the enterprise generated by Solar Pro design software. The metrological data of Solar Pro simulation software is developed with the accurate metrological dataset from the NADO (New Energy and Industrial Technology Development Organization), a Japanese weather association. The collection of 1600 location dataset is equipped with the Solar Pro software. Here, the month of March is significantly having the maximum recorded irradiation of 220 kWh/m^2 with the maximum generation potential.

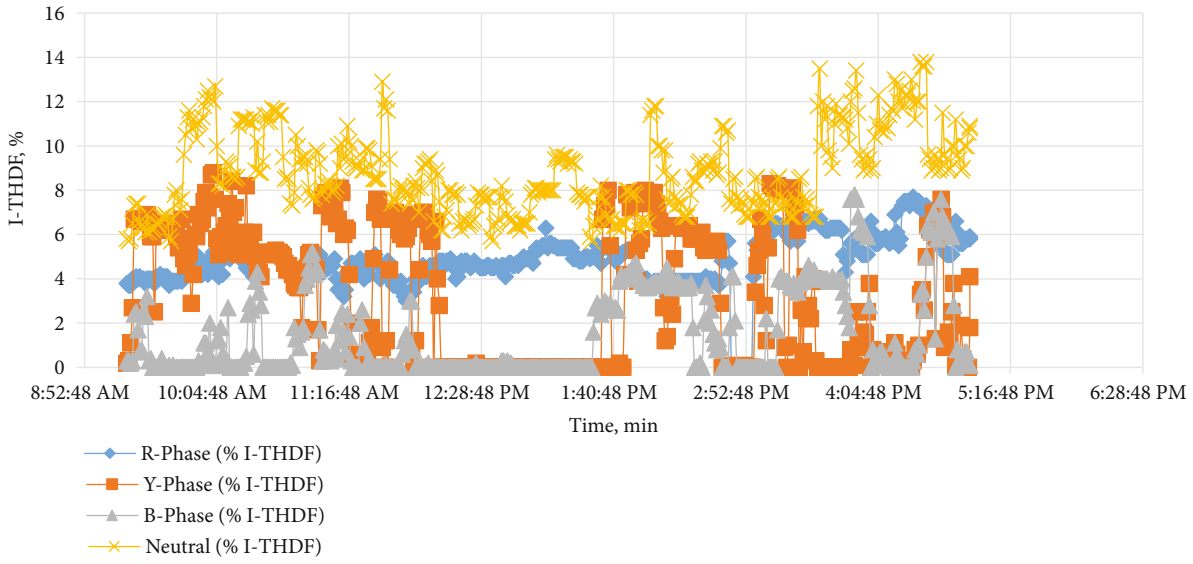

Figure 18: Time vs. I-THDF (phase III—postaudit).

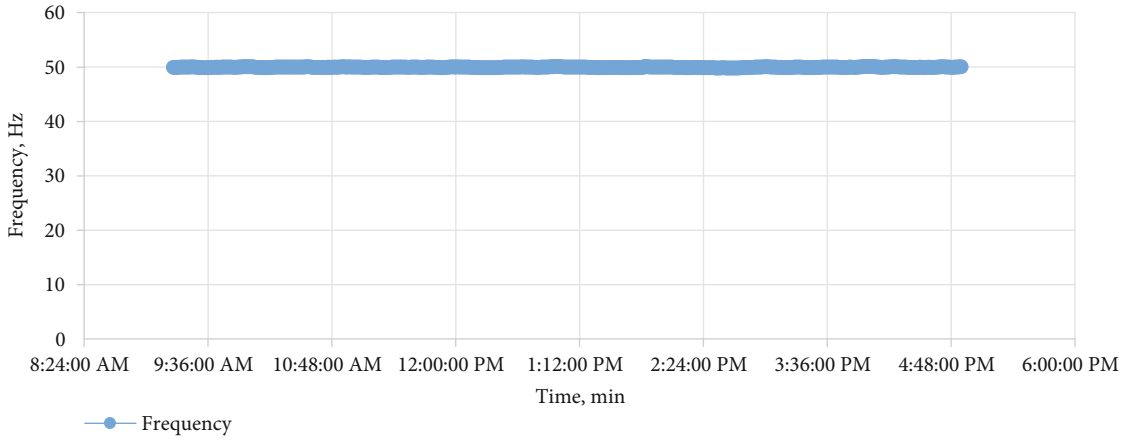

Figure 19: Time vs. frequency (phase III—postaudit).

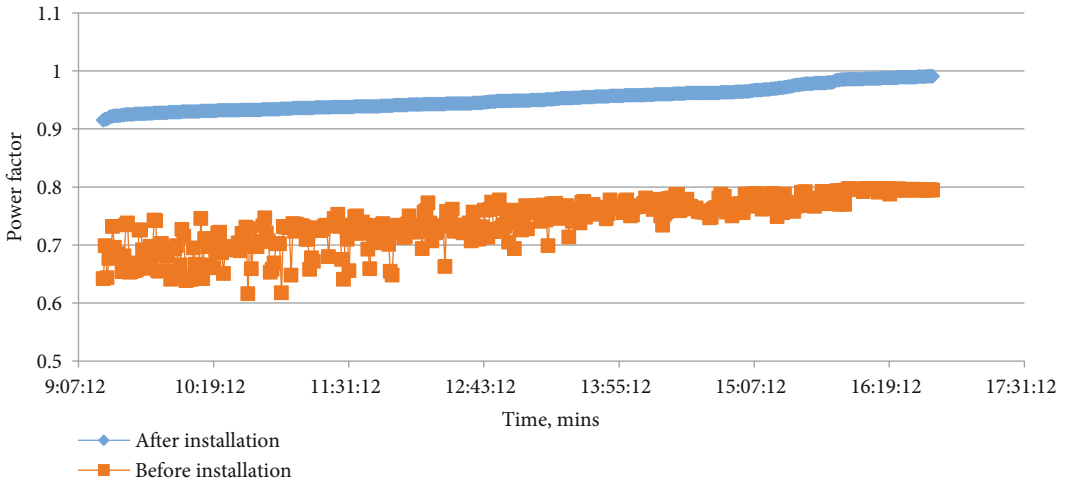

Figure 20: Effect of IPFC installation on overall power factor (phase III—postaudit).

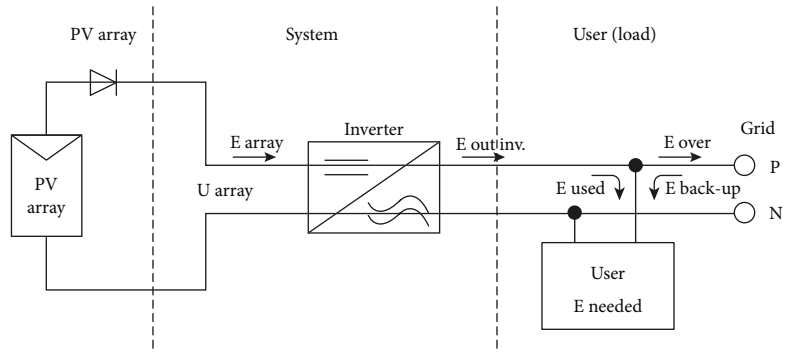

Figure 21: Layout of proposed solar photovoltaic plant (Source: PVsyst simulation software).

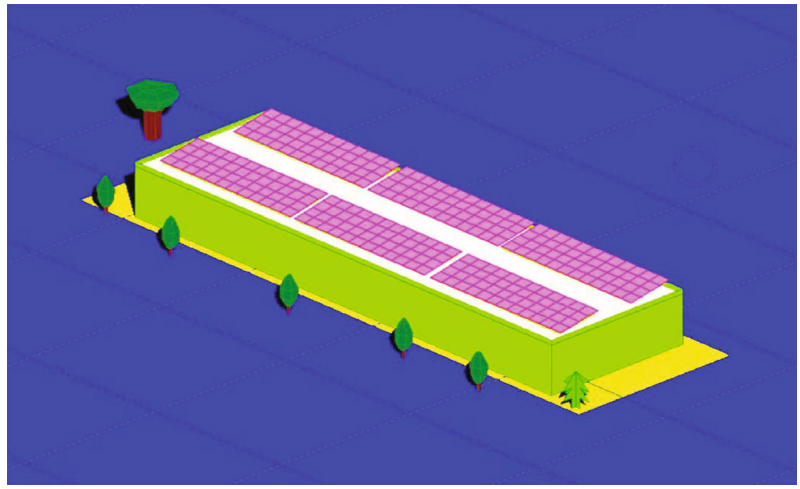

Figure 22: Solar Pro 3D CAD modelling of proposed 100 kWp SPV plant.

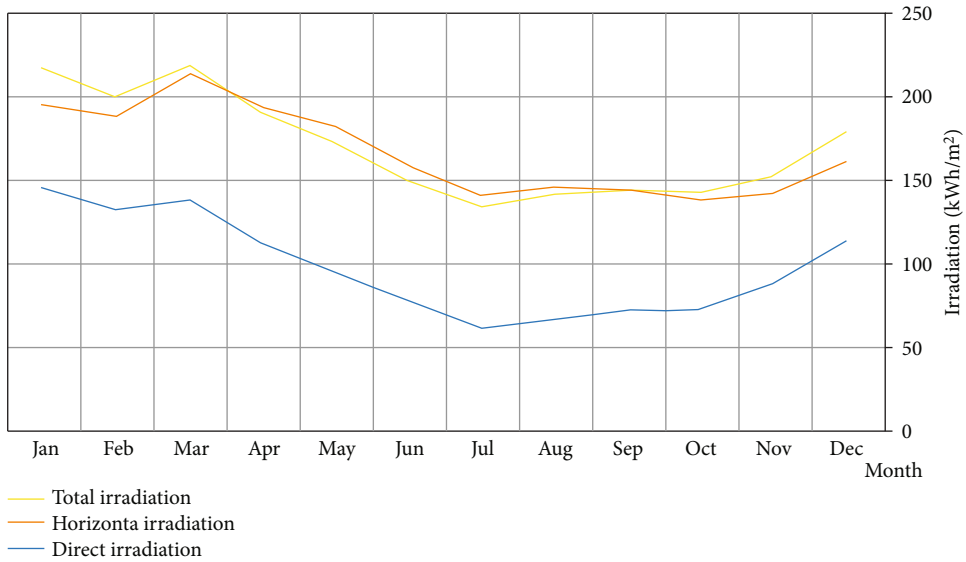

Figure 23: Month-wise solar irradiation of the proposed SPV plant.

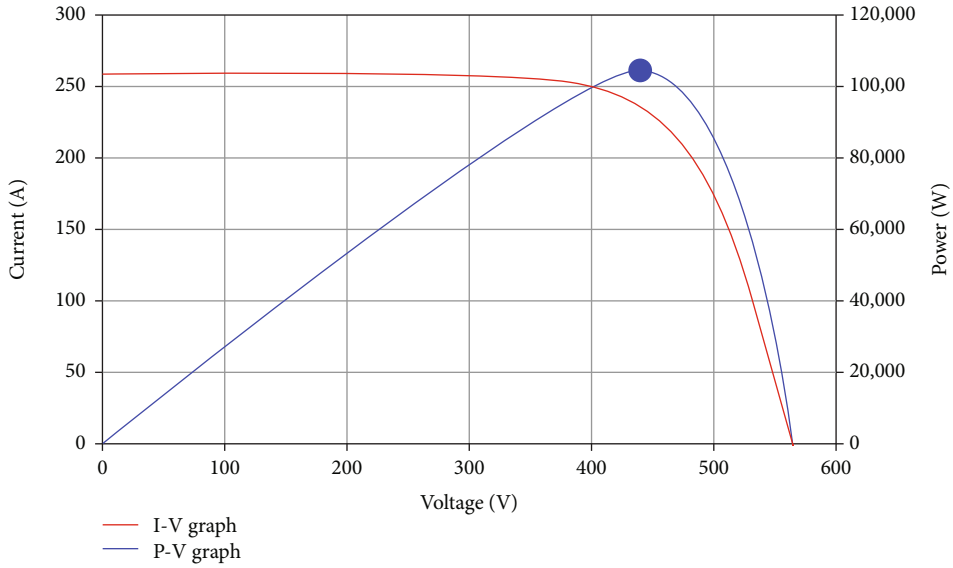

Figure 24: Voltage vs. current and power characteristic curve of the proposed SPV plant.

8. Results and Discussion of the Proposed Solar Photovoltaic Power Plant

8.1. Power Analysis of the Proposed SPV Plant. Figure 24 illustrates the voltage versus current characteristics of the overall SPV power plant in the primary vertical axis. The manufacturer datasheet provides the following parameters of the module: rated power of 360 Wp solar PV module is powered by the open-circuit voltage of 187.50 (V_{OC}) and short-circuit current of (I_{SC}) 2.7 A. The voltage versus power characteristics are shown in the secondary vertical axis of Figure 24. The maximum power point (MPP) is the maximum point at which maximum (or) optimum power generation is ascertained. The maximum voltage and maximum current of 146.2 V and 2.46 A are achieved during the Solar Pro simulation software calculation mode.

The effect of the average increase in the ambient temperature is directly proportional to the temperature rise of the SPV module. As per the Standard Test Conditions (STC), the SPV modules perform more effectively at 25 degrees Celsius. The negative temperature coefficient of voltage and power is about -0.35%/°C and -0.45%/°C, respectively [40]. Therefore, the temperature rise directly affects the power output and efficiency [40] of the SPV plants.

Figure 25 illustrates the month-wise solar PV and AC energy generation (power analysis) of the proposed solar photovoltaic power plant. The maximum peak generation of 12,000 kWh is achieved during the month of March with the maximum total irradiation. The power analysis is carried out based on the solar generation and the historical power consumption pattern of the SME under investigation. Therefore, the average generation of 8000 kWh is maintained throughout the year as a positive indicator to move forward into the proposed SPV plant.

8.2. Economic Analysis of the Proposed SPV Plant. The economic analysis of SPV is carried out using the Solar Pro simulation software with the month-wise historical data of SME power consumption. Figure 26 gives the month-wise selling, buying, and bill reduction price of the proposed SPV plant. As per the guidelines and regulations of state and central nodal agencies, the selling price of the SPV power plant is fixed. The higher average annual bill reduction is achieved based on the economic and power analysis due to the maximum SPV power generation, excess power evacuation (power export), and optimized energy utilization of SMEs.

Figure 27 gives the month-wise load energy (i.e., load consumption and AC energy generated by the proposed SPV power plant of SME in the primary vertical axis). The secondary vertical axis gives month-wise cost economics of energy consumption and its bill reduction due to SPV power penetration and power export to the grid. The period from March to May is having the highest SPV generation and bill reduction. The average energy bill reduction (savings) is significantly maintained throughout the year. Figure 28 gives the economic payback period of 7 years on the proposed SPV plant, which is a positive indicator for the proposed SPV power plant.

8.3. Life Cycle Carbon Emission of the Proposed SPV Plant. The life cycle carbon [41] emission of the proposed solar power plant is calculated in detail with the SPV modules, supports (includes the balance of system and other auxiliaries), and inverters. The amount of carbon emission generated from the proposed SPV plant's installation and operation is about 188.61 tCO_2 for the 30 years lifetime of the SPV plant. Therefore, the replacement carbon emission is based on SPV power generation as per the Central Electricity Authority (CEA) guidelines and regulations.

The carbon emission of grid-interactive SPV is taken, and the replacement emission is calculated as 4694.8 tCO_2 with the annual SPV power production of 167.17 MWh. The following International Energy Agency (IEA) considerations like the SPV power plant lifespan of 30 years, the 1% annual degradation, and the grid lifecycle emission of 936 gCO_2/kWh are

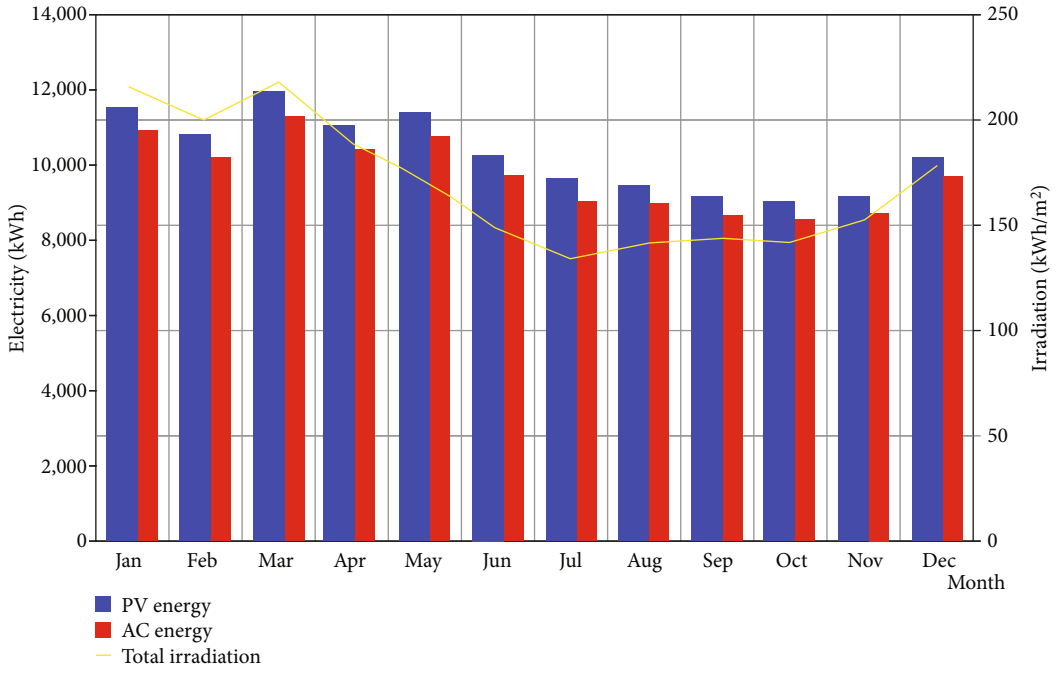

Figure 25: Month vs. power analysis of the proposed SPV plant.

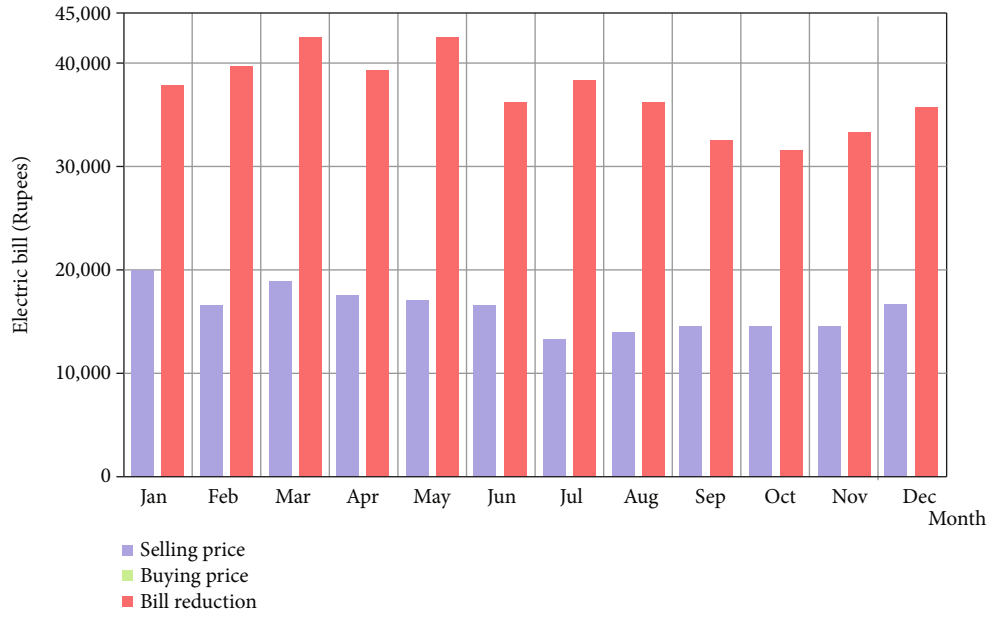

Figure 26: Month-wise economic analysis of the proposed SPV plant.

considered for the calculation of CO_2 emission balance analysis. Therefore, the resultant CO_2 emission balance of 4506.2 tCO_2 is achieved from the proposed SPV power plant.

9. Conclusion

Complete electrical energy auditing was carried out. Based on the detailed analysis, the following suggestions and recommendations are prepared. The design and installation of 73 KVAr compensator capacitors will enhance the enterprise's power factor to improve the SME's overall energy efficiency. The effectiveness of IPFC is ensured by 33.33% current reduction, 28.88% total power consumption reduction, 27.22% neutral I-THDF reduction, and a 65% increase in the overall power factor. Therefore, the effectiveness of installed Intelligent Power Factor Correction (IPFC) panel is highly significant, and it could enable the cost-effective, accurate, and high-performance reactive power compensation by installing the IPFC unit in the point of common coupling (PCC) instead of going with the load side reactive

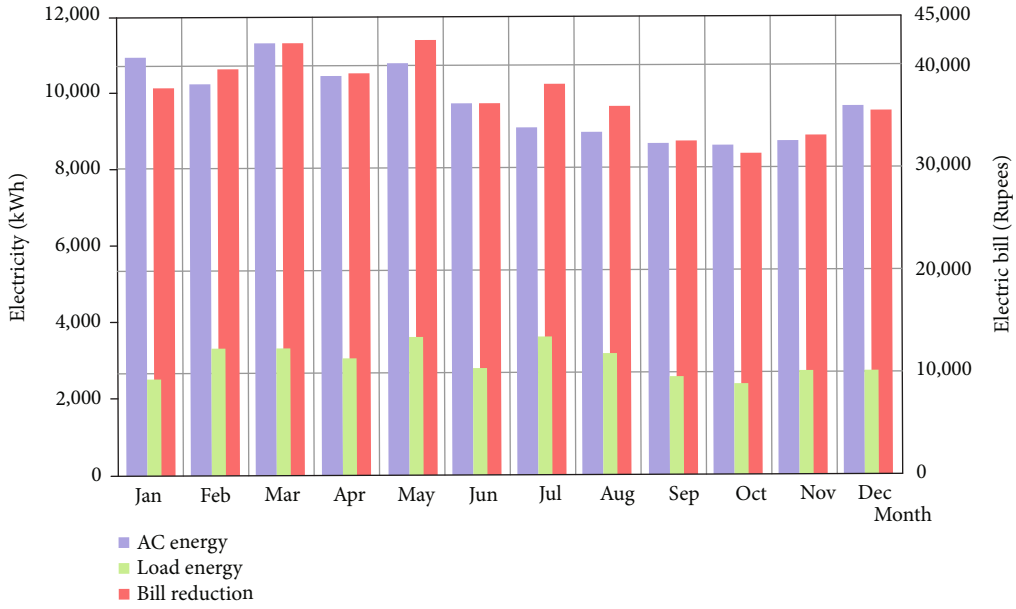

Figure 27: Month-wise economic saving of the proposed SPV plant.

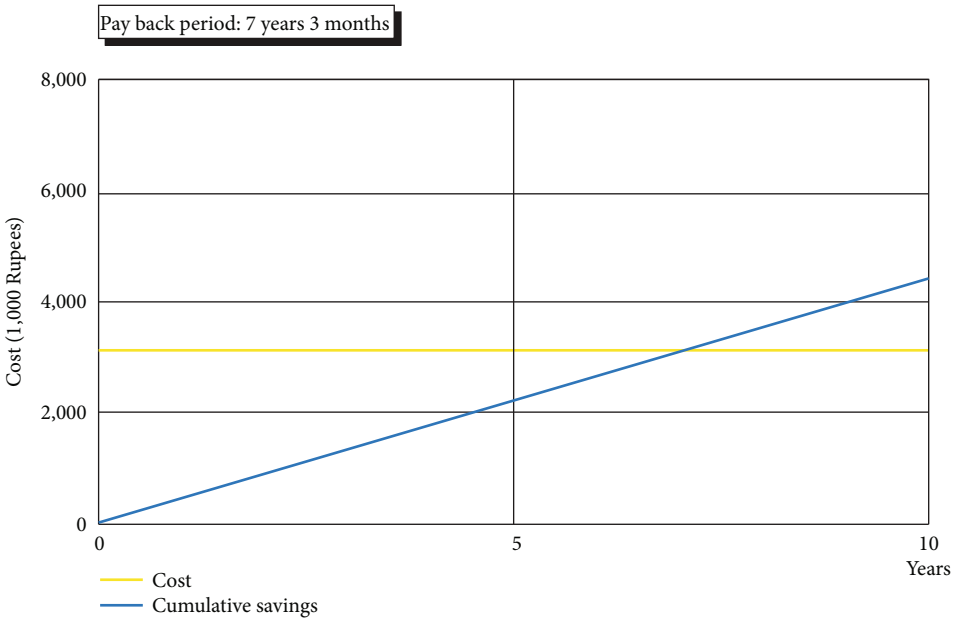

Figure 28: Economic payback analysis of the proposed SPV plant.

power compensation to get the desirable compensation. There is a significant reduction in the enterprise's power consumption by installing the IPFC compensator, paving a roadmap to achieve climate change mitigation by reducing carbon dioxide emission by reducing 1296 kg of CO_2 from the electrical power consumption.

From the design of the SPV power plant, the availability of SPV potential, energy, and cost economic performance is highly feasible for SMEs to deploy the SPV power plant. The SPV energy generation and utilization lead to energy bill reduction of SME and additional revenue by exporting the excess power to the grid. The replacement carbon emission of 4694.8 tCO_2 is possible by the installation of the proposed SPV plant. Therefore, the proposed solar photovoltaic power plant is highly feasible to deploy in the SME for its energy and economic savings with the more significant environmental sustainability for climate change mitigation. Therefore, the energy self-sufficient of SME is highly feasible by the proposed SPV plant in a sustainable manner.

Data Availability

The data used to support the findings of this study are available from the corresponding author upon request.

Conflicts of Interest

The authors declare that there are no conflicts of interest regarding the publication of this paper.

Acknowledgments

The authors gratefully acknowledge the Department of Science and Technology (DST), India, for financial support under the DST-INSPIRE Fellowship (ID No: IF180435) and the secretary of Lakshmi Seva Sangam, Gandhigram, for providing permission to carry out the analysis.

References

[1] R. Saidur, "A review on electrical motors energy use and energy savings," *Renewable and Sustainable Energy Reviews*, vol. 14, no. 3, pp. 877–898, 2010.

[2] F. Kalantzis and D. Revoltella, "Do energy audits help SMEs to realize energy-efficiency opportunities?," *Energy Economics*, vol. 83, pp. 229–239, 2019.

[3] A. Kubule, K. Ločmelis, and D. Blumberga, "Analysis of the results of national energy audit program in Latvia," *Energy*, vol. 202, p. 117679, 2020.

[4] P. Thollander, M. Karlsson, P. Rohdin, J. Wollin, and J. Rosenqvist, "Energy auditing[1]," *Introduction to Industrial Energy Efficiency*, vol. 50, pp. 61–87, 2020.

[5] J. R. Neumann, *Ensuring Business Resilience. EDSA Micro Corporation n.d.:1–5*, 2020, http://www.poweranalytics.com/pa_articles/pdf/EnsuringBusinessResilience.pdf.

[6] C. Sreenath, S. Prabhakaran, V. Rajakumaran, C. Shankar, S. S. S. Velan, and V. Kirubakaran, "Energy auditing of payment tiles making small scale industry: suggestions and recommendations for energy conservation," in *2015 International Conference on Circuits, Power and Computing Technologies ICCPCT-2015*, pp. 1–4, March 2015.

[7] S. K. Rajput and O. Singh, "Energy audit in textile industry: a study with ring frame motor," in *2016 International Conference on Control, Computing, Communication and Materials (ICCCCM)*, pp. 1–4, October 2016.

[8] A. L. Divya, C. A. Vigneshwari, M. Damini, M. A. Sabeena, V. Kolambikai, and V. Kirubakaran, "Energy auditing for a farm house10.1109/ICCPCT.2015.7159446," in *2015 International Conference on Circuits, Power and Computing Technologies ICCPCT-2015*, pp. 1–6, March 2015.

[9] I. Palcic, M. Pons, A. Bikfalvi, J. Llach, and B. Buchmeister, "Analysing energy and material saving technologies' adoption and adopters/Analiza uporabe in uporabnikov okolju prijaznih tehnologij v proizvodnih podjetjih," *Strojniski Vestnik - Journal of Mechanical Engineering*, vol. 59, 2013.

[10] V. Blass, C. J. Corbett, M. A. Delmas, and S. Muthulingam, "Top management and the adoption of energy efficiency practices: evidence from small and medium-sized manufacturing firms in the US," *Energy*, vol. 65, pp. 560–571, 2014.

[11] R. Shinde, A. Pathak, and B. Chaughule, "Harmonic analysis and power factor correction for food processing industry," *International Journal of Computational Engineering Research*, vol. 3, no. 6, pp. 53–58, 2013.

[12] M. Singh, "Environment management systems in Indian small and medium-sized enterprises," *Academy of Taiwan Business Management Review*, vol. 8, no. 2, pp. 45–55, 2010.

[13] S. S. S. Velan and V. Kirubakaran, "Implementation of energy conservation and management activities and its economics in GRI boy's hostel - a case study," in *2016 Biennial International Conference on Power and Energy Systems: Towards Sustainable Energy (PESTSE)*, pp. 1–10, January 2016.

[14] P. Thollander, M. Karlsson, P. Rohdin, J. Wollin, and J. Rosenqvist, *Energy auditing and measurements in practice. Introduction to Industrial Energy Efficiency*, Elsevier, 2020.

[15] G. Dermentzis, F. Ochs, M. Gustafsson et al., "A comprehensive evaluation of a monthly-based energy auditing tool through dynamic simulations, and monitoring in a renovation case study," *Energy and Buildings*, vol. 183, pp. 713–726, 2019.

[16] Z. De Grève, J. Bottieau, D. Vangulick et al., "Machine learning techniques for improving self-consumption in renewable energy communities," *Energies*, vol. 13, no. 18, p. 4892, 2020.

[17] J. Schleich and T. Fleiter, "Effectiveness of energy audits in small business organizations," *Resource and Energy Economics*, vol. 56, pp. 59–70, 2019.

[18] R. Scozzari and M. Santarelli, "Techno-economic analysis of a small size short range EES (electric energy storage) system for a PV (photovoltaic) plant serving a SME (small and medium enterprise) in a given regulatory context," *Energy*, vol. 71, pp. 180–193, 2014.

[19] A. Khoodaruth, V. Oree, M. K. Elahee, and W. W. Clark, "Exploring options for a 100% renewable energy system in Mauritius by 2050," *Utilities Policy*, vol. 44, pp. 38–49, 2017.

[20] A. Pechmann and M. Zarte, "Economic analysis of decentralized, electrical- and thermal renewable energy supply for small and medium-sized enterprises," *Procedia CIRP*, vol. 61, pp. 422–427, 2017.

[21] Ç. Karatuğ and Y. Durmuşoğlu, "Design of a solar photovoltaic system for a Ro-Ro ship and estimation of performance analysis: a case study," *Solar Energy*, vol. 207, pp. 1259–1268, 2020.

[22] M. Satish, S. Santhosh, and A. Yadav, "Simulation of a Dubai based 200 KW power plant using PVsyst Software," in *2020 7th International Conference on Signal Processing and Integrated Networks (SPIN)*, pp. 824–847, Febuary 2020.

[23] A. Chauhan, M. Sharma, and S. Baghel, "Designing and performance analysis of 15KWP grid connection photovoltaic system using Pvsyst software," in *2020 Second International Conference on Inventive Research in Computing Applications (ICIRCA)*, pp. 1003–1008, July 2020.

[24] K. C. Rout and P. Kulkarni, "Design and performance evaluation of proposed 2 kW solar PV rooftop on grid system in Odisha using PVsyst," in *2020 IEEE International Students' Conference on Electrical,Electronics and Computer Science (SCEECS)*, pp. 1–6, Febuary 2020.

[25] S. S. Chopade, L. P. Raj, and G. N. Prabakaran, "Bench marking of grid tied solar roof top photovoltaic system: a case comparison," *International Journal of Engineering & Technology*, vol. 7, 2018.

[26] N. M. Kumar, M. R. Kumar, P. R. Rejoice, and M. Mathew, "Performance analysis of 100 kWp grid connected Si-poly photovoltaic system using PVsyst simulation tool," *Energy Procedia*, vol. 117, pp. 180–189, 2017.

[27] L. G. Popa and M. Brumaru, "Optimizing buildings energy performance through photovoltaic panel integration within a mobile shading system," *Procedia Manufacturing*, vol. 22, pp. 765–772, 2018.

[28] K. H. Chao and C. T. Chen, "A remote supervision fault diagnosis meter for photovoltaic power generation systems," *Measurement: Journal of the International Measurement Confederation*, vol. 104, pp. 93–104, 2017.

[29] K.-H. Chao, Y.-W. Chao, and J.-P. Chen, "A circuit-based photovoltaic module simulator with shadow and fault settings," *International Journal of Electronics*, vol. 103, pp. 424–438, 2015.

[30] K. Kamaleswaran, M. Venkateshwaran, P. Harinath, M. A. Mydeen, and V. Kirubakaran, "Energy conservation potential in rural industry: a case study on coir industry," in *IEEE International Conference on Circuit, Power and Computing Technologies, ICCPCT 2015*, March 2015.

[31] T. Mariprasath and V. Kirubakaran, "Real time harmonic analysis on rural industries," *Indian Journal of Science and Technology*, vol. 9, no. 2, 2016.

[32] N. R. Kulkami, H. Vijay Murthy, and A. P. Raju, "PLC based intelligent power factor correctors for industrial power systems-a case study," in *Proceedings of the 2015 IEEE International Conference on Power and Advanced Control Engineering, ICPACE 2015*, pp. 75–79, August 2015.

[33] R. Bayindir, S. Sagiroglu, and I. Colak, "An intelligent power factor corrector for power system using artificial neural networks," *Electric Power Systems Research*, vol. 79, no. 1, pp. 152–160, 2009.

[34] K. Kamaleswaran, S. Prabhakaran, P. Harinath, M. Damini, and V. Kirubakaran, "Capacity building on energy conservation in rural industries: a case study," in *2016 3rd International Conference on Electrical Energy Systems (ICEES)*, pp. 306–311, March 2016.

[35] *Atmel. AT89S52 - Datasheet Microcontroller with 8K Bytes Programmable Flash. Atmel 2001*, pp. 1–30, 2020, http://www.atmel.com/images/doc1919.pdf.

[36] P. Harinath, K. Kamaleswaran, M. Venkateshwaran, C. Sreenath, S. Prabhakaran, and V. Kirubakaran, "A critical analysis of power quality issues in data center," in *2016 Biennial International Conference on Power and Energy Systems: Towards Sustainable Energy (PESTSE)*, pp. 1–6, January 2016.

[37] M. Ravindran and V. Kirubakaran, "Electrical energy conservation in automatic power factor correction by embedded system," *Energy and Power*, vol. 2, no. 4, pp. 51–54, 2012.

[38] GOI-MOP, *CO2 baseline database for the Indian power sector user guide*, vol. 3, Report by Ministry of Power Govt of India 2014, 2020, http://www.indiaenvironmentportal.org.in/files/file/CO2%20Baseline%20Database%20for%20the%20Indian%20Power%20Sector.pdf.

[39] T. N. E. REGULATORY, C. Solar, and On RG, *Tamil Nadu Electricity Regulatory Commission*, Tamil Nadu State Press 2013, 2020, http://www.tnerc.gov.in/.

[40] P. R. G. N. P. R. G. N. Lalith, G. Prabakaran, A. Murugaiyan, and V. Kirubakaran, "Hybrid photovoltaic-thermal systems: innovative CHP approach," in *Proceedings of the 4th International Conference on Electrical Energy Systems, ICEES 2018*, pp. 726–730, Febuary 2018.

[41] C. Marimuthu and V. Kirubakaran, "Carbon pay back period for solar and wind energy project installed in India: a critical review," *Renewable and Sustainable Energy Reviews*, vol. 23, pp. 80–90, 2013.

Hindawi
International Journal of Photoenergy
Volume 2020, Article ID 6698904, 24 pages
https://doi.org/10.1155/2020/6698904

Research Article

Experimental Investigation of a Direct Evaporative Cooling System for Year-Round Thermal Management with Solar-Assisted Dryer

Sujatha Abaranji,[1] **Karthik Panchabikesan**,[2] **and Velraj Ramalingam**[3]

[1]*Department of Mechanical Engineering, Thanthai Periyar Government Institute of Technology, Vellore, 632002 Tamil Nadu, India*
[2]*Department of Building, Civil and Environmental Engineering, Concordia University, Montreal, Canada*
[3]*Department of Mechanical Engineering, Institute of Energy Studies, Anna University, Chennai, 600025 Tamil Nadu, India*

Correspondence should be addressed to Sujatha Abaranji; asujatha.06@gmail.com

Received 14 October 2020; Revised 14 November 2020; Accepted 21 November 2020; Published 19 December 2020

Academic Editor: Kumarasamy Sudhakar

Copyright © 2020 Sujatha Abaranji et al. This is an open access article distributed under the Creative Commons Attribution License, which permits unrestricted use, distribution, and reproduction in any medium, provided the original work is properly cited.

Building cooling is achieved by the extensive use of air conditioners. These mechanically driven devices provide thermal comfort by deteriorating the environment with increased energy consumption. To alleviate environmental degradation, the need for energy-efficient and eco-friendly systems for building cooling becomes essential. Evaporative cooling, a typical passive cooling technique, could meet the energy demand and global climatic issues. In conventional direct evaporative cooling, the sensible cooling of air is achieved by continuous water circulation over the cooling pad. Despite its simple operation, the problem of the pad material and water stagnation in the sump limits its usage. Moreover, the continuous pump operation increases the electrical energy consumption. In the present work, a porous material is used as the water storage medium eliminating the pump and sump. An experimental investigation is performed on the developed setup, and experiments are conducted for three different RH conditions (low, medium, and high) to assess the porous material's ability as a cooling medium. Cooling capacity, effectiveness, and water evaporation rate are determined to evaluate the direct evaporative cooling system's performance. The material that replaces the pump and sump is vermicompost due to its excellent water retention characteristics. There is no necessity to change material each time. However, the vermicompost is regenerated at the end of the experiment using a solar dryer. The passing of hot air over the vermicompost also avoids mould spores' transmission, if any, present through the air. The results show that vermicompost produces an average temperature drop of 9.5°C during low RH conditions. Besides, vermicompost helps with the energy savings of 21.7% by eliminating the pump. Hence, vermicompost could be an alternate energy-efficient material to replace the pad-pump-sump of the conventional evaporative cooling system. Further, if this direct evaporative cooling system is integrated with solar-assisted drying of vermicompost, it is possible to provide a clean and sustainable indoor environment. This system could pave the way for year-round thermal management of building cooling applications with environmental safety.

1. Introduction

The rapid population growth has attributed to the drastic rise in energy consumption. The critical factor driving energy consumption is the weather effect, which leads to an increase in cooling and heating requirements to provide thermal comfort. Air conditioners play a vital role in providing thermal comfort to the occupants of the building. The continuous operation of these devices increased greenhouse gas emissions. The rise in emissions directly related to energy demand poses a severe threat to the environment. In the current scenario, sustainable and energy-efficient technologies would be convincing to provide a clean and safe ecosystem. Since ancient times, passive cooling techniques have provided comfortable living space without any emissions. Moreover, the use of renewable energy sources could reduce energy

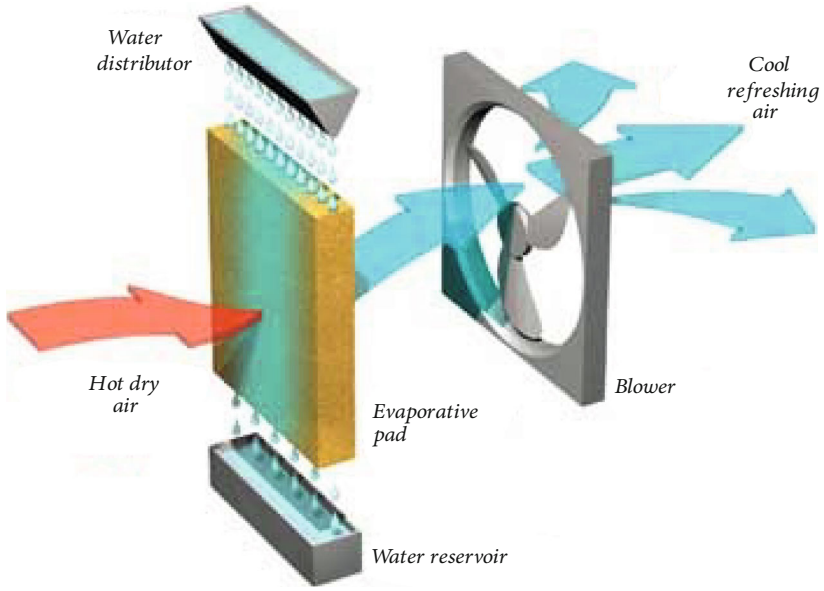

Figure 1: Conventional pad pump system [1].

Table 1: Research work carried out for different climates.

Authors	System type	Building type	Region	Climate	Key findings
Costelloe and Finn [11]	Indirect contact evaporative cooling system	Office buildings	Dublin and Milan	Temperate	As a consequence of 16°C cooling water from October to May, the office buildings in Dublin can be cooled throughout the year without the use of conventional cooling. In Milan, a similar performance can be achieved from November to March
Heidarinejad et al. [12]	Two-stage indirect–direct evaporative cooling system	Public buildings	Tehran	Multi	Two-stage indirect–direct evaporative cooling system can be preferred to mechanical vapour compression systems in regions with higher wet-bulb temperatures to minimise energy consumption. However, water consumption of the two-stage system is 55% greater than that of traditional DEC
Ibrahim et al. [13]	Direct evaporative cooling system equipped with porous ceramic evaporators	Residential buildings	Nottingham	Multi	Direct evaporative cooling system supported with porous ceramic evaporators can provide 6–8°C in dry-bulb temperature with a 30% rise in relative humidity. The maximum cooling achieved from the system is 224 W/m^2
Hajidavalloo [14]	Indirect contact evaporative cooling system	Residential buildings	Khoozestan, Iran	Very hot	Through this system, power consumption can be decreased by about 16% in very hot climates, and the COP can be enhanced by 55% compared to conventional air conditioners
He and Hoyano [15]	Passive evaporative cooling wall (PECW)	Residential courtyards	Japan	Hot and dry	PECW constructed as ceramic pipes absorb water using capillary action. It can reduce the surface temperature of the pipe by 3–5°C than the ambient, and the ambient air temperature is dropped to 3–4°C
Katsuki et al. [16]	Porous ceramic plates	—	Korea	Hot and dry	The study reports that porous properties and relative humidity of air are the key factors influencing the self-cooling effect of porous ceramic plates

demand. Hence, passive cooling integrated with renewable energy sources could be the best alternative to meet conventional mechanically driven equipment's challenges.

Evaporative cooling, a passive cooling method, had been in use since 2500 B.C. An evaporative cooler makes use of water to cool the hot and dry air. The water takes up the air's

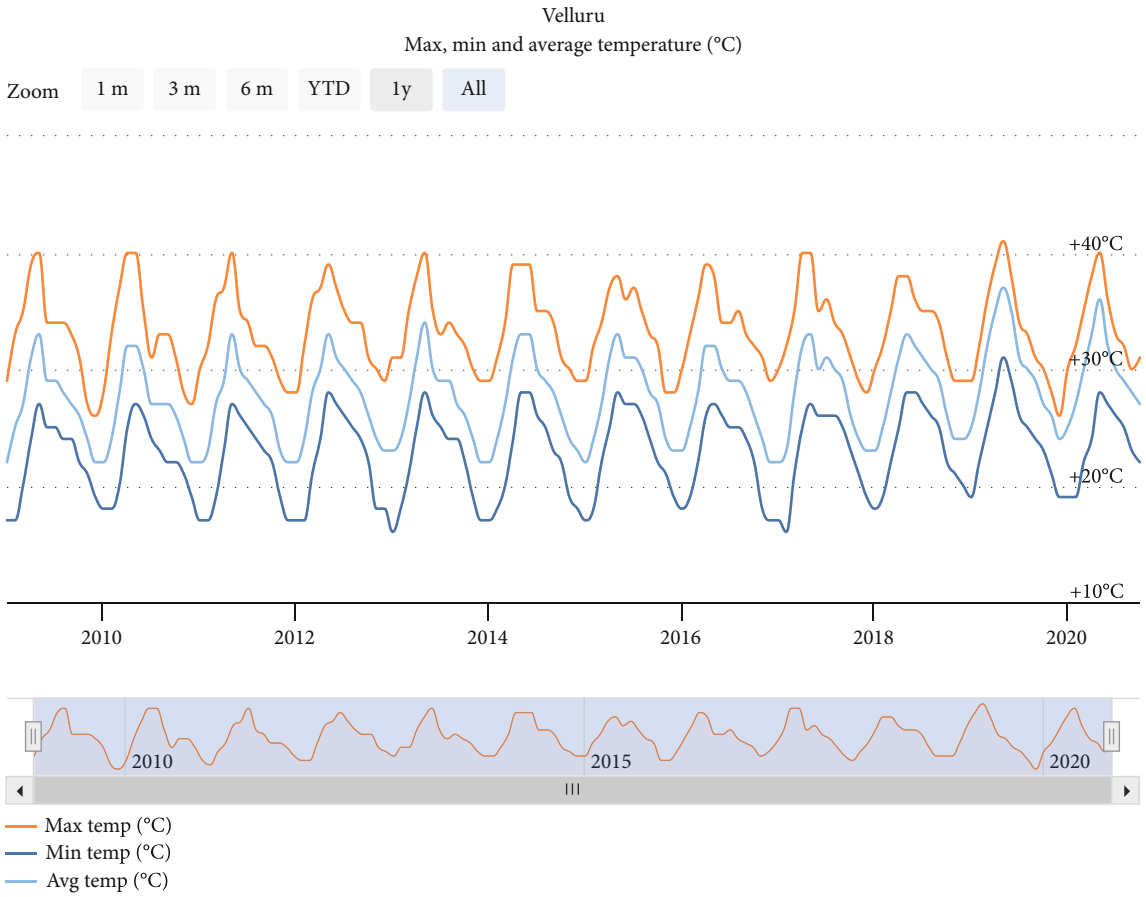

Figure 2: Yearly temperature average of Vellore from 2009 to 2019 [19].

sensible heat and gets evaporated to produce cold and humid air. It takes shape in several forms, and the modern evaporative coolers consist of a pad-pump system with a reservoir to recirculate the water. The working principle of a direct evaporative cooling system is shown in Figure 1.

Evaporative cooling pads are generally made of cellulose materials. These materials are used in desert air coolers due to their excellent cooling performance with high durability. However, its high cost limits its utility to higher-end coolers. Cellulose impregnated cooling pads were employed for different studies. Rong et al. [2] studied the dynamic performance of a cross-fluted cellulose pad by controlling the pump's on and off time (control time cycle), water flow rate, etc. A relationship between cooling efficiency and the water-air ratio was one of the useful parameters for the controller. This prediction model for transient conditions provides the solution for poultry houses' control systems in a hot-arid climate. Xu et al. [3] developed an evaporative cooling setup with corrugated cellulose pads to provide thermal comfort for greenhouses in a humid subtropical climate. Evaporative coolers made of cellulose pads were combined with air conditioners and tested by Harby and Al-Amri [4] and Dhamneya et al. [5] to study their performance in achieving energy savings of a split air conditioner and window air conditioner, respectively. Aspen cooling pads were preferred in some air coolers due to their lower cost and effectiveness. Bishoyi and Sudhakar [6] compared the performance of aspen and honeycomb cooling pads. The results had shown that the honeycomb cooling pad achieved the highest effectiveness compared with the aspen cooling pad.

Many natural and synthetic fibres and other materials were also tested for their suitability to be used as a cooling pad material. Al-Sulaiman [7] proposed an experimental setup to evaluate the cooling pads' performance made from the fibres of date palm (stem), luffa, and jute. The results were compared with a commercially available cooling pad. The results showed that the highest effectiveness of 62.1% was obtained for jute material, while the conventional cooling pad material gave 49.9% effectiveness. Doğramacı et al. [8] used eucalyptus fibres as cooling pad material and showed that these fibres perform better in cooling efficiency at lower velocities. Jain and Hindoliya [9] tested the effectiveness of a cooling pad with coconut and palash fibres and compared them with a conventional pad made of aspen and khus fibres. The palash fibres offered a low pressure drop than the aspen pad, and its effectiveness was comparatively higher.

Many researchers tested different evaporative cooling systems for their local climatic conditions. Cuce and Riffat [10] presented the types of evaporative cooling systems, thermodynamic analyses, thermal performance assessment, and their applications in buildings. The different types of direct and indirect evaporative cooling are employed in the cooling

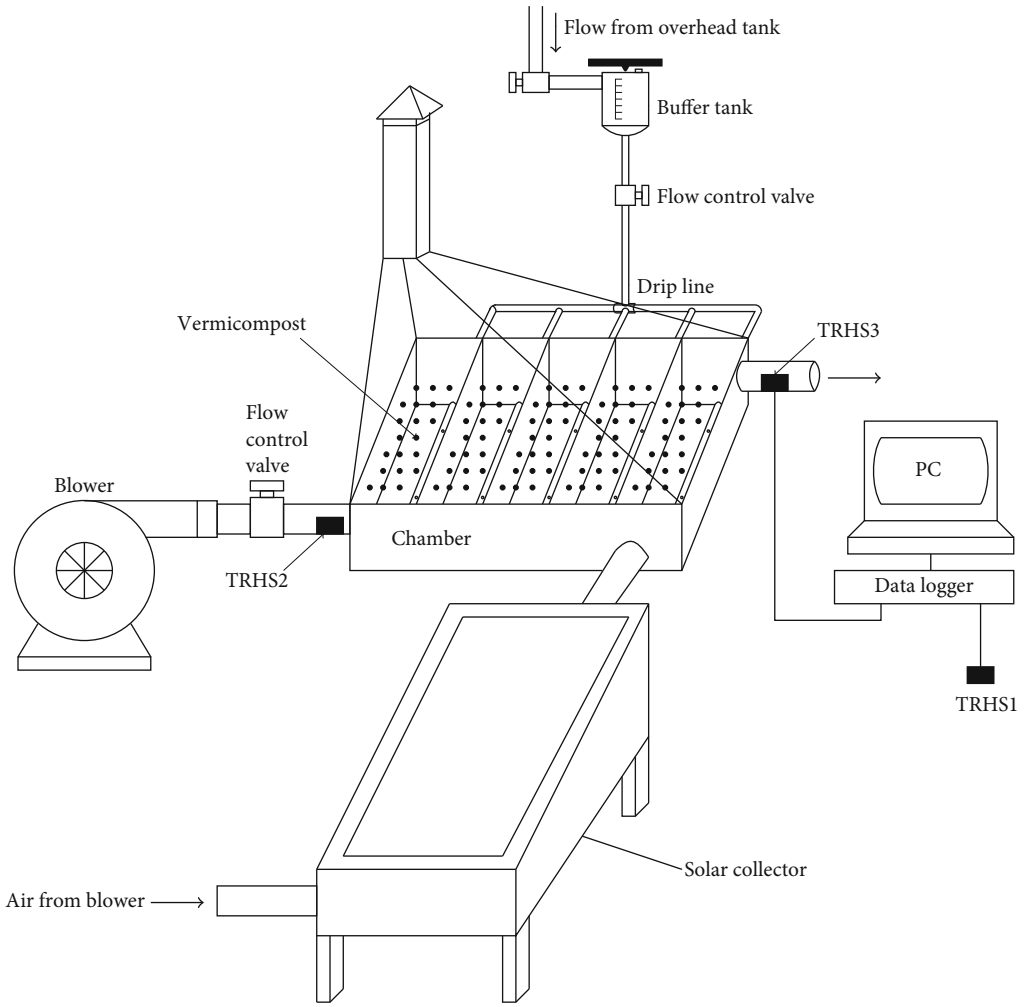

Figure 3: Schematic of the experimental setup. TRHS: temperature and relative humidity sensor.

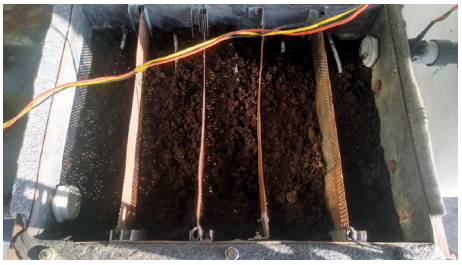

Figure 4: Photographic view of the cooling chamber loaded with vermicompost.

Figure 5: Photographic view of the solar collector.

system based on humidity conditions. Based on the building's cooling load requirement, novel evaporative cooling systems were tested for different climatic conditions and are presented in Table 1.

From the extensive literature, it is understood that evaporative cooling, which is quite simple and inexpensive, is suitable for hot and dry climates. However, the pad material is subjected to problems like sagging, clogging, and scaling. Watt [17] had addressed these problems, which led to the deterioration of pad material and reduced its life. The continuous operation of the pump increases the electrical energy consumption. The reservoir, which stores the water for recirculation, provides a favourable environment for breeding disease-spreading insects. In the present work, a porous material—vermicompost is used to replace the pad, pump, and reservoir. Vermicompost is highly porous with high water storing capability [18]. The specific objective of the system is to study the performance of vermicompost based

Table 2: Specifications of the measuring instruments.

Instrument	Parameter	Device	Range	Accuracy
Load cell	Mass of vermicompost	Load cell module ITB-04CE	0-5 kg	1.5% of full-scale division
Digital vane anemometer	Velocity of air	Lutron AM4201	0.4 ms^{-1} to 30 ms^{-1}	±2%
Digital hygro thermometer	Temperature and RH of air	DHT 22	Temp: -40°C to 80°C RH: 0% to 100%	Temp: ±0.5°C RH: ±2%

direct evaporative cooling system with three different velocities (0.9 ms^{-1}, 1.8 ms^{-1}, and 2.7 ms^{-1}) under different relative humidity conditions of ambient air (high, medium, and low). The water retention ability of vermicompost is evaluated in terms of evaporative cooling capacity, effectiveness, and water evaporation rate. Thus, vermicompost's cooling potential for use in direct evaporative cooling to provide a sustainable and clean indoor environment for year-round thermal management is explored in this work.

2. Materials and Methodology

2.1. Vermicompost: An Alternative Material for Direct Evaporative Cooling. Vermicompost, a porous material with high water storage capacity, is extensively used in agriculture to promote plant growth during water stress conditions. Many scientists had studied the performance of evaporative cooling systems with porous materials. However, vermicompost, which possesses high porosity and high water retaining ability, is not explored yet, as a cooling medium in the evaporative cooling system. The problems of continuous pump operation and water stagnation in the sump are to be eliminated using vermicompost as a water storage medium. Vermicompost loaded in the system can be used again, and there is no necessity to change material each time. However, the vermicompost should be regenerated at the end of each cycle to sterilize the material from the mould growth. Vermicompost drying is achieved using an indirect solar dryer. The hot air from the solar collector dries the vermicompost.

2.2. Site Selection. The outstanding performance of evaporative coolers in arid regions facilitated to test the vermicompost as a cooling medium in a direct evaporative cooling system at Vellore, an Indian city with hot and dry weather. The yearly average temperature history of Vellore from 2009 to 2019 is shown in Figure 2. The average temperature throughout the year is 30°C ± 5°C. The maximum temperature of 42°C and minimum temperature of 19°C are almost reached every year. This temperature history indicates that Vellore weather conditions have great potential for evaporative cooling throughout the year.

2.3. Experimental Investigation. This section describes the experimental setup and the operational procedures adopted to evaluate the performance of the vermicompost.

2.3.1. Experimental Setup Description. Figure 3 shows a vermicompost-based evaporative cooling system integrated with an indirect solar dryer. The experimental setup consists of a cooling chamber tray with a baffle arrangement, air blower, buffer tank of 0.5-liter capacity to supply water, the monitoring sensors, and instruments with a data acquisition system. The cooling chamber tray is made of a rectangular box of 400 × 300 × 100 mm for charging the vermicompost. The tray consists of five baffle plates with perforations at the end to create turbulence in the flowing air. The photographic view of the cooling chamber loaded with vermicompost is shown in Figure 4. A centrifugal blower of 180 W capacity forces the air into the cooling chamber through a galvanized iron pipe of 25.4 mm diameter. A flow control valve is provided after the blower for varying the velocity of air. Water is supplied to the vermicompost through small tubes of 4 mm diameter. An insulation material (polyurethane foam) of 5 mm thickness is provided over the entire setup to avoid heat entry from the ambient to the cooling system. The vermicompost in the cooling chamber is dried with a solar dryer. The solar dryer consists of a solar collector to receive the radiation. It has an aluminium absorber plate, glass cover, plywood, and insulation material. Figure 5 shows the photographic view of the solar collector. Asbestos is used as the insulation material at the bottom of the absorber. The absorber plate is coated with black paint to enhance solar absorption. The absorber area is 0.4 m^2. A chimney of 300 mm height is used for discharging the air after drying the vermicompost in the chamber. Temperature and relative humidity sensors (DHT 22) are placed at three locations of the setup. DHT 22 uses a capacitive-type sensor for humidity measurement and a thermistor for temperature measurement. The sensor (TRHS1) used for measuring the ambient conditions is kept exposed to the atmosphere on the outer surface of the setup. TRHS2 placed at 30 mm before the entry of the chamber and TRHS3 located 30 mm after the exit of the chamber measure the temperature and RH of air entering and leaving the chamber, respectively. The measurements are made continuously at a scanning rate of 1 minute using a data acquisition system (Agilent Keysight, Model no. 34972A). The details of the instruments used for measurement are presented in Table 2.

Table 3: Uncertainties in measured parameters and evaluated parameters.

Measured parameters	
Temperature	1.51%
Relative humidity	4.83%
Air velocity	2.22%
Evaluated parameters	
Effectiveness	0.88%
Evaporative cooling capacity	2.28%

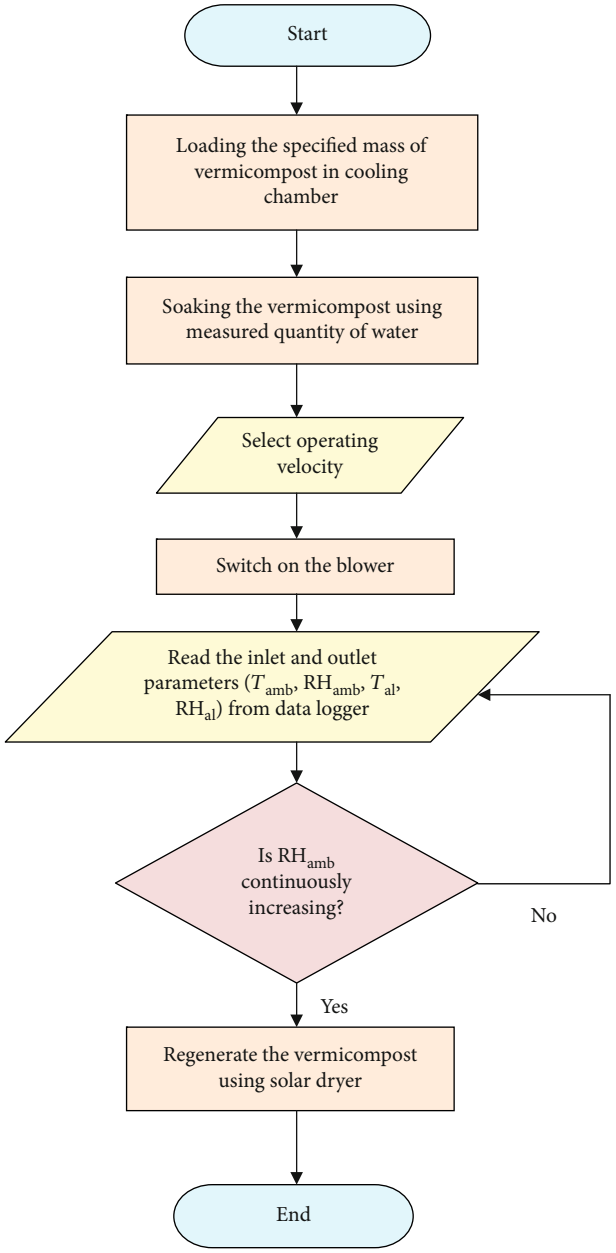

Figure 6: Flowchart of the methodology of the experimental analysis.

The parameters measured directly using the instruments are used to obtain the derived parameters of interest. Table 3 presents the uncertainties of the parameters which were measured directly using instruments and the evaluated parameters using the rules of error propagation suggested by Taylor [20].

2.3.2. Experimental Procedure. Cattle manure-based vermicompost was dried before its use in the cooling system. A known quantity of vermicompost (1000 grams) was measured using the load cell. The material was loaded in the cooling chamber. Initially, trial experiments were conducted for various water quantities to find the vermicompost's maximum water holding capacity. It was found that with the vermicompost : water mass ratio of 100 : 75, the material attained fully saturated condition. Then, water was supplied to the vermicompost in the above ratio until its saturation. No additional water was provided during the operation of the system. The blower was switched on to allow the air to pass over the vermicompost, and the flow control valve was adjusted to set the desired velocity of 0.9 ms^{-1}. Usually, direct evaporative coolers are not operated with air velocity exceeding 3 ms^{-1} to avoid aerosols' formation [21]. The temperature and relative humidity were measured by the sensors placed at different locations and were recorded continuously. The same procedure was repeated for other velocities of 1.8 ms^{-1} and 2.7 ms^{-1}. The same material can be used again, and there is no necessity to change material each time. However, the vermicompost is regenerated at the end of the experiment using a solar dryer. The passing of hot air over the vermicompost also avoids mould spores' transmission, if any, present through the air. The experiments were conducted during October 2019, February 2020, and May 2020 for high RH, medium RH, and low RH conditions. Direct evaporative coolers are employed in places with hot and dry weather to provide cooling during peak sunshine hours (11 a.m. to 3 p.m.). In Vellore, where the experiments were conducted, three distinct seasons could be observed in a year (peak summer, winter, and monsoon season). Hence, three months were selected that represent the above three seasons. Accordingly, it is found that in September, the RH value is high in the range of 60% to 75%; in February, the RH is in the midrange of 45% to 60%; and in May, the RH value is low in the range of 30% to 45%. The duration of the experiments was 180 minutes, 360 minutes, and 480 minutes for high, medium, and low RH conditions, respectively. Though all the experiments were started at 10 a.m., the experiments were terminated when there was an appreciable change in ambient RH during certain months. However, it was continued till 6 p.m. in May (peak summer month) when the low ambient RH existed till late evening. Since the end of the experiment varied in different months, the experiments' duration also varied.

Figure 6 shows the detailed methodology of the experimental analysis in a flowchart form.

3. Data Analysis

This section explains the formulae used for calculating the following derived parameters: evaporative cooling capacity, effectiveness, and evaporation rate of water.

3.1. Evaporative Cooling Capacity. The evaporative cooling capacity is calculated using the following equation:

$$Q_{ec} = \dot{m}\, c_p (T_{amb} - T_{al}). \quad (1)$$

3.2. Effectiveness. Effectiveness is one of the key factors in evaluating the evaporative cooler performance. The ratio of temperature difference of inlet air and outlet air to the temperature difference of inlet air and its wet-bulb temperature is called effectiveness.

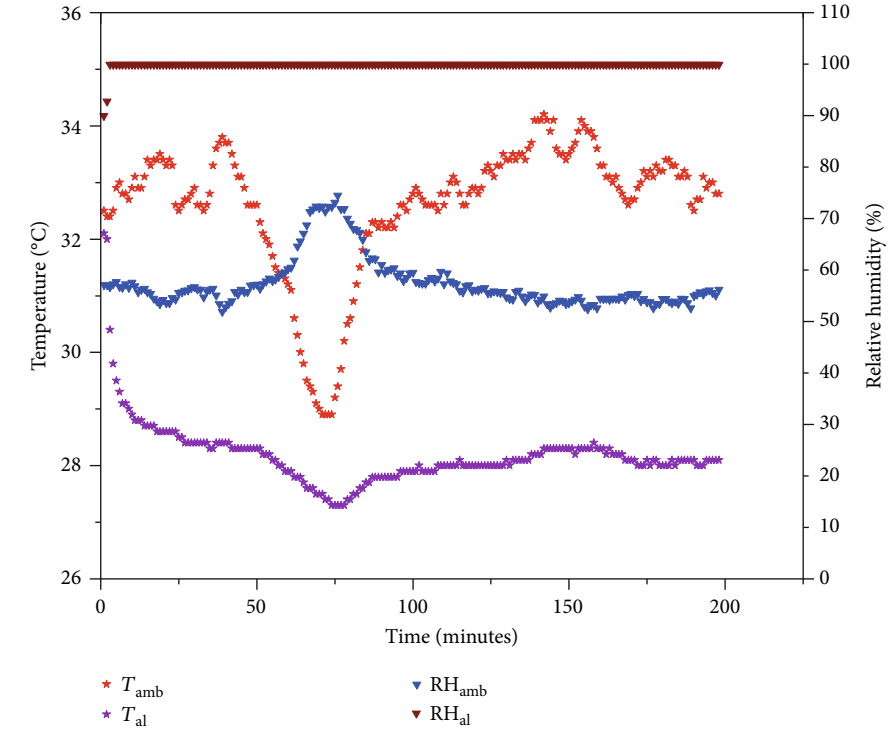

(a) 0.9 ms^{-1}

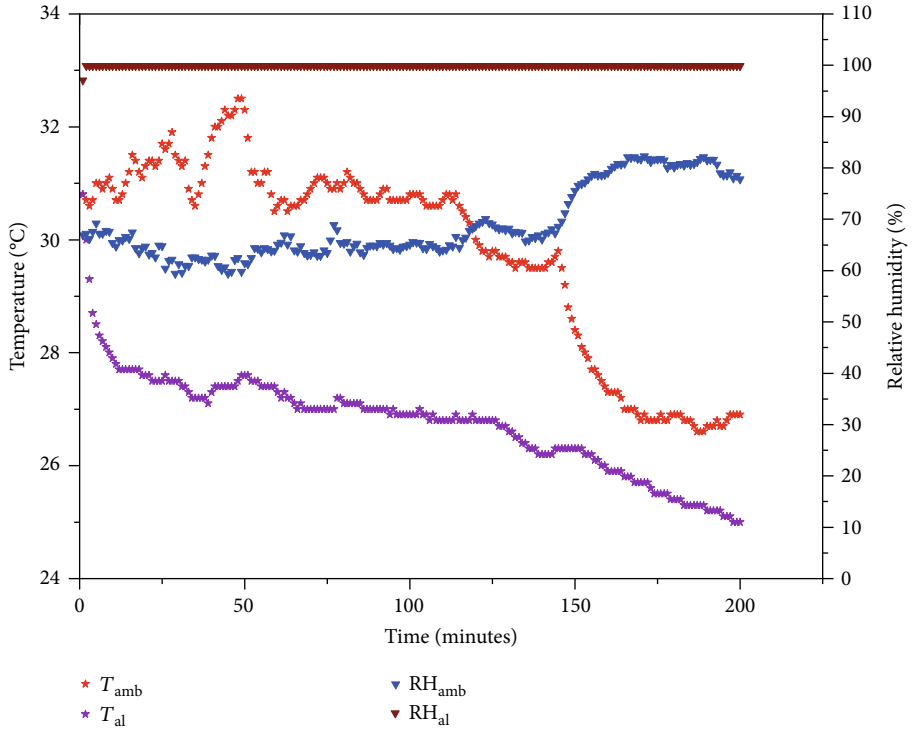

(b) 1.8 ms^{-1}

Figure 7: Continued.

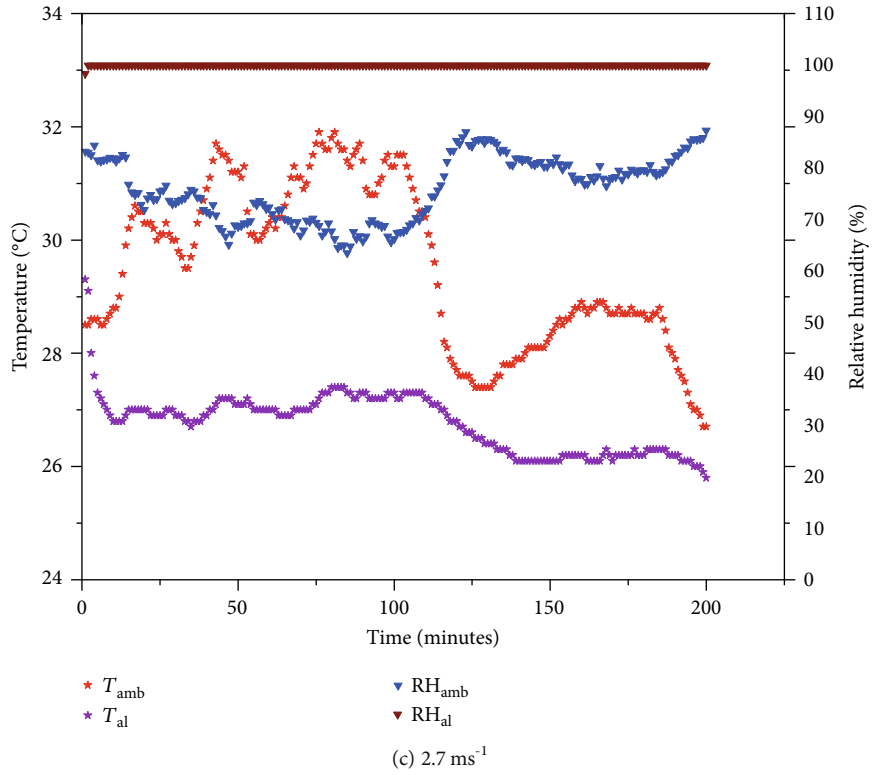

FIGURE 7: Temperature and RH variations of the air from the air cooler at three different velocities under high RH condition.

It is given by

$$\varepsilon = \frac{T_{amb} - T_{al}}{T_{amb} - T_{wbt}}. \quad (2)$$

3.3. Evaporation Rate of Water. The amount of water required to produce the cooling effect is calculated using the formula given by

$$\dot{m}_w = \dot{m}_a(\omega_2 - \omega_1). \quad (3)$$

4. Results and Discussion

In this section, the variations of temperature and relative humidity of air are initially presented, followed by the discussion of derived parameters such as evaporative cooling capacity, effectiveness, and evaporation rate of water. Subsequently, the temperature drop and effectiveness of the previous studies are compared with the present system.

4.1. Variations in Temperature and Relative Humidity of the Air. Figure 7 shows the temperature and relative humidity of ambient air and outlet air from the cooling chamber when the air was supplied at three different velocities for high RH conditions.

It is seen from the figures that the ambient conditions play a significant role in deciding the performance of the cooling system. In Figure 7(a), the fluctuations of the temperature and relative humidity of ambient air were quite small except for a short duration. A sudden change in ambient conditions was observed after 150 minutes, as shown in Figure 7(b), and 100 minutes, as shown in Figure 7(c). However, the average drop in temperature was 4°C to 5°C for all velocities up to 150 minutes. The outlet relative humidity is 99%, as the ambient relative humidity varied from 60% to 75%. It is also found from the figures that when the system is operated at lower velocities, maximum temperature drop was achieved with slight fluctuations. Moreover, the time taken to attain this condition is large. When the system was operated at higher velocities, the maximum temperature drop was achieved within a few minutes, and the same drop was sustained for a more extended period.

Figure 8 shows the temperature and relative humidity of ambient air and outlet air from the cooling chamber when the air was supplied at three different air velocities for medium RH conditions. It is seen in Figure 8(a) that the system produced an average temperature drop of 5°C for 60 minutes for a velocity of 0.9 ms^{-1}. After this, there was a continuous decrease in the temperature drop until the end of the experiment. For the operational velocity of 1.8 ms^{-1}, it is observed in Figure 8(b) that an average temperature drop of 7°C was produced until 150 minutes, followed by a gradual decrease in the temperature drop. Figure 8(c) shows that an average temperature drop of 8°C was produced by the system for 300 minutes when the system was operated at a velocity of 2.7 ms^{-1}. The outlet relative humidity produced by the system is 99% for all velocities.

It is inferred from the above results that an average temperature drop of 5°C to 8°Cand a relative humidity of 99%

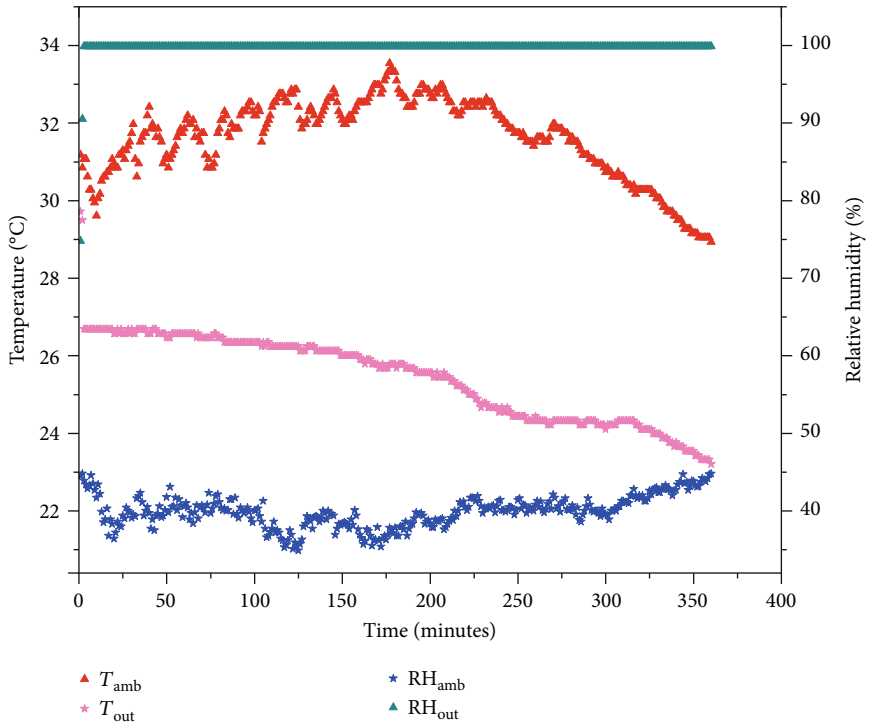

(a) 0.9 ms^{-1}

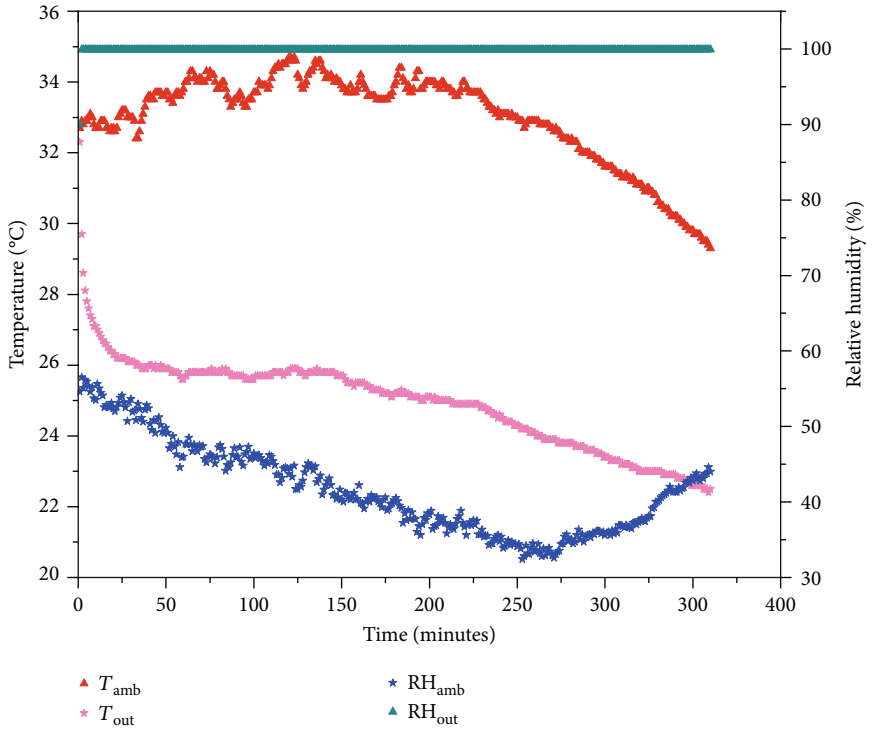

(b) 1.8 ms^{-1}

Figure 8: Continued.

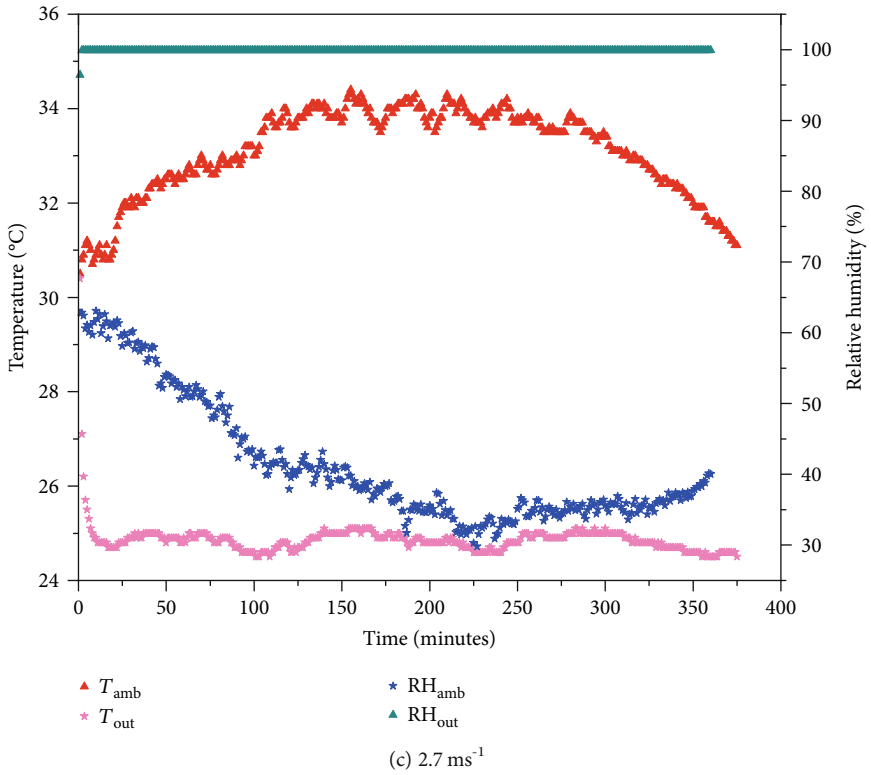

Figure 8: Temperature and RH variations of the air from the air cooler at three different velocities under medium RH condition.

could be achieved with this system based on the operating velocity if the ambient air has a temperature of 30°C to 34°C and relative humidity of 45% to 60%.

Figure 9 shows the temperature and relative humidity of ambient air and outlet air from the cooling chamber when the air was supplied at three different air velocities for low RH conditions. It is illustrated from the figures that the temperature drop produced by the vermicompost is maintained for a longer duration at all velocities during low RH conditions compared to other RH conditions. An average temperature drop of 6.5°C, 9.4°C, and 8.8°C was produced by the system up to 400 minutes when the system was operated at velocities of 0.9 ms^{-1}, 1.8 ms^{-1}, and 2.7 ms^{-1}, respectively. The relative humidity of air leaving the system is 99% for all velocities. It is inferred from the above results that an average temperature drop of 6.5°C to 9.5°C and relative humidity of 99% could be achieved with this system based on the operating velocity. The ambient air has a temperature of 38°C to 42°C and relative humidity of 30% to 45%.

Figure 10 shows the average temperature drop produced by the cooling system operated at three different velocities during three different RH conditions.

The above results elucidate that the vermicompost-based evaporative cooling system performs better at velocities of 1.8 ms^{-1} and 2.7 ms^{-1} during low and medium RH conditions. However, for high RH conditions, though the temperature drop produced by vermicompost at 0.9 ms^{-1} velocity is high, the time taken to achieve a higher reduction is more. At the same time, the system operated at higher velocities produces a maximum drop within a few minutes. Hence, it is clear that ambient relative humidity and operating velocity are the key factors that influence the performance of a vermicompost-based evaporative cooling system.

4.2. Instantaneous Cooling Capacity. Figure 11 shows the instantaneous cooling capacity calculated using Equation (1) for three different velocities under three different RH conditions.

It is clear from the figures that the duration of sustained cooling effect varies based on the temperature drop for all velocities during different RH conditions. The period of sustainability is 120 minutes for high RH conditions, 300 minutes for medium RH conditions, and 400 minutes for low RH conditions.

Figure 12 shows the average instantaneous cooling capacity produced by the cooling system at three different velocities under three different RH conditions. It is seen from the figure that the system produces a higher cooling capacity for a velocity of 2.7 ms^{-1} during all RH conditions. It is also observed that there is a dependency between the mass flow rate and evaporative cooling capacity. The higher cooling rate could be achieved by increasing the airflow velocity and area of flow. Since the maximum velocity should be limited to 3 ms^{-1} to avoid health issues, the area of flow can be increased, and hence, mass flow rate can be increased. However, 1000 grams of vermicompost with the same mass flow rate is capable of producing a higher cooling effect during low RH conditions. This increases the amount of water to be evaporated for providing the required cooling effect. Hence, a large sump is needed for

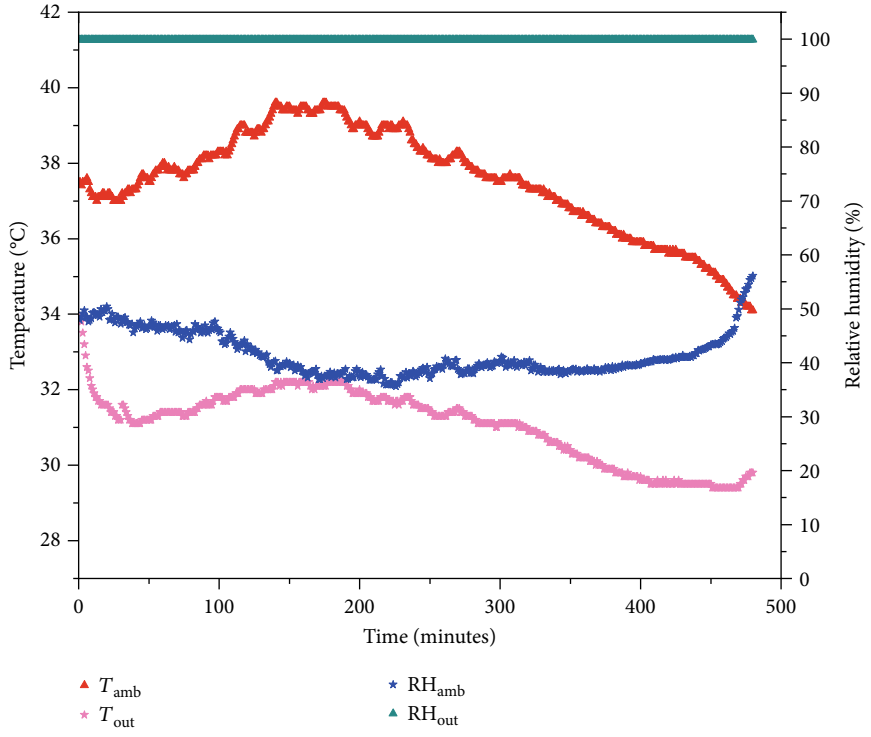

(a) 0.9 ms^{-1}

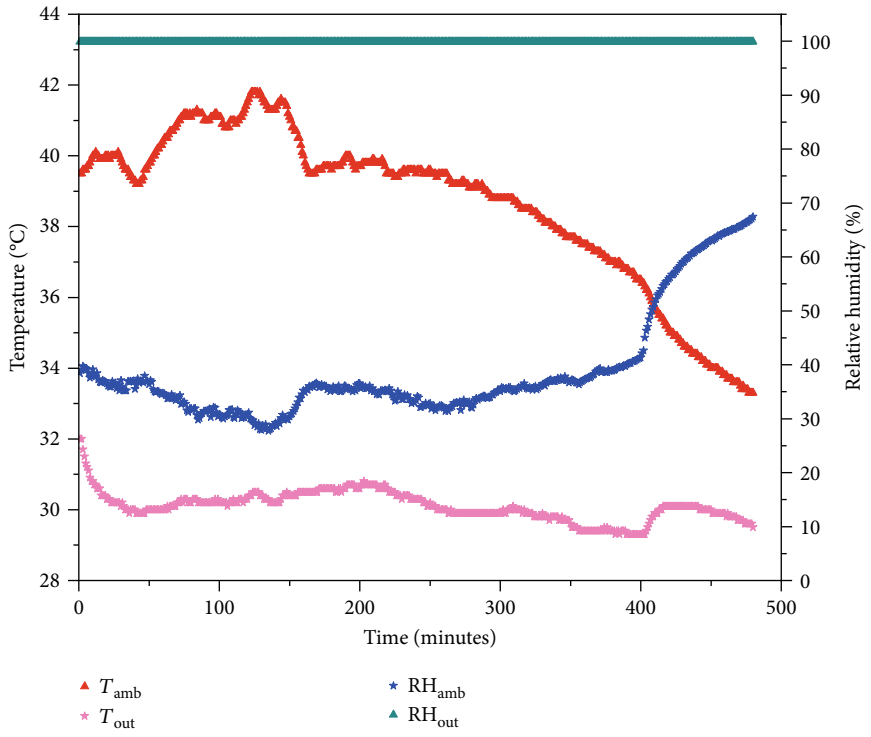

(b) 1.8 ms^{-1}

Figure 9: Continued.

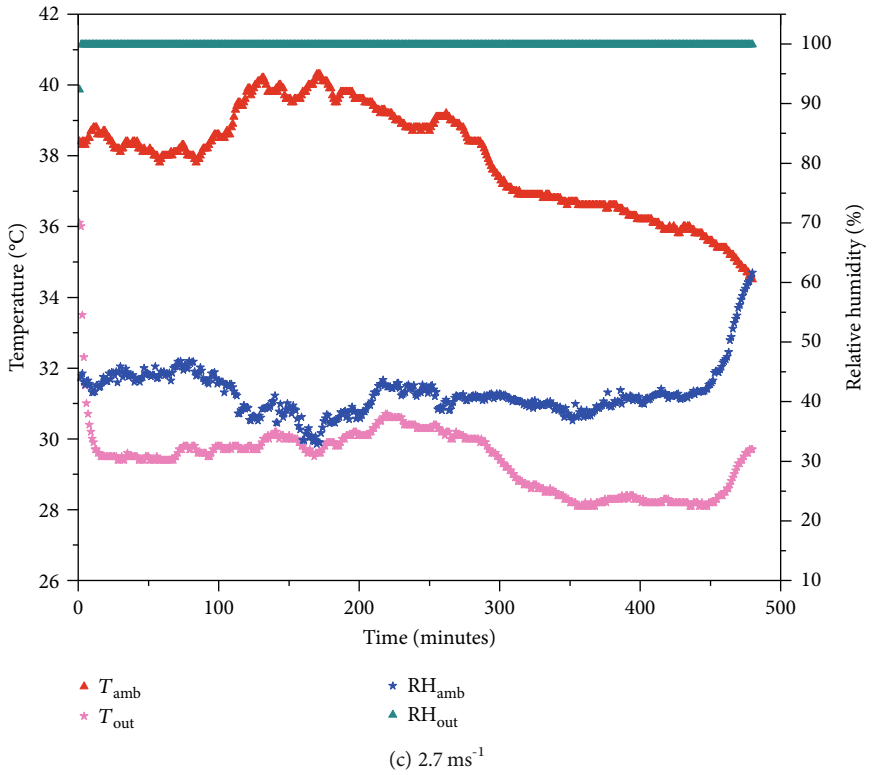

Figure 9: Temperature and RH variations of the air from the air cooler at three different velocities under low RH condition.

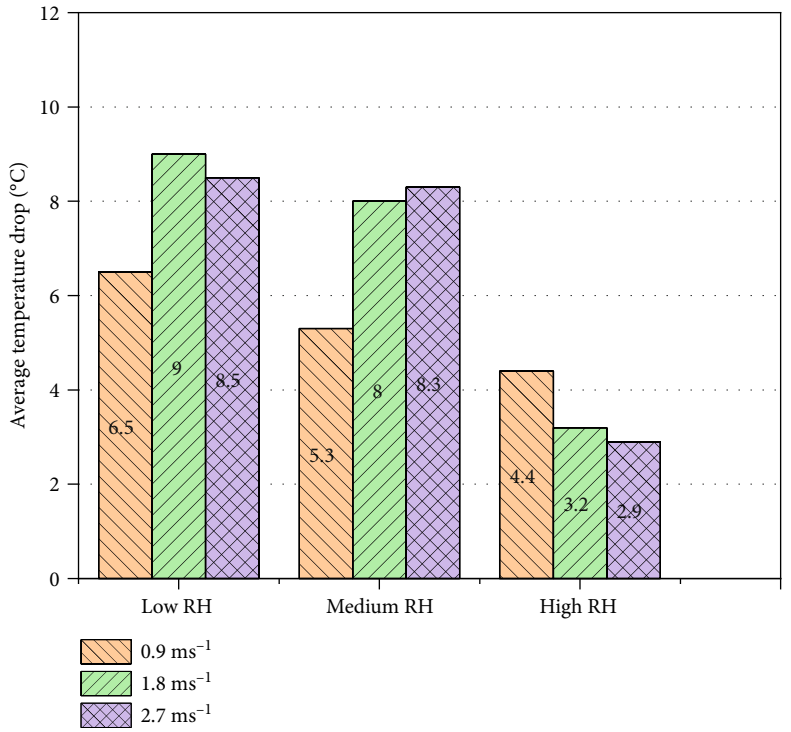

Figure 10: Average temperature drop of the air from the air cooler at three different velocities under three different RH conditions.

water storage. This vermicompost-based cooling system is producing the cooling effect by utilizing only the initial water supply and thus eliminating the water sump system and related health issues. Hence, the vermicompost-based cooling system can produce sustained cooling at higher velocities during all RH conditions.

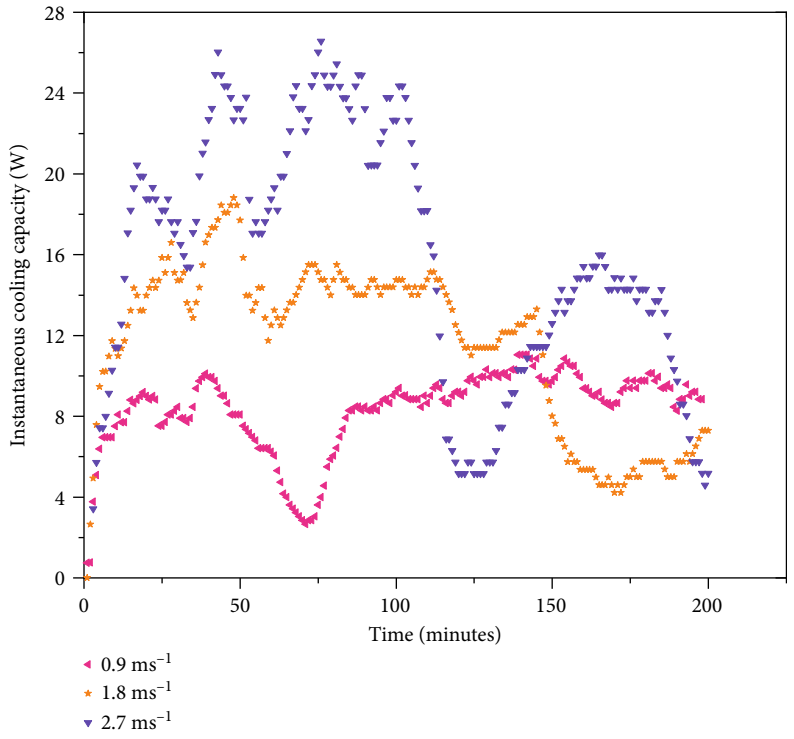

(a) High RH

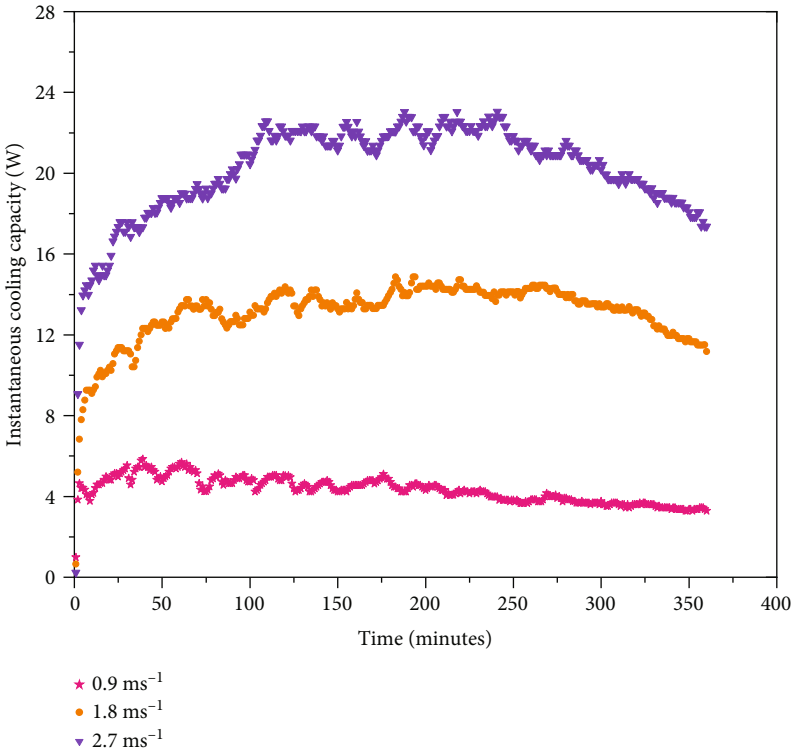

(b) Medium RH

Figure 11: Continued.

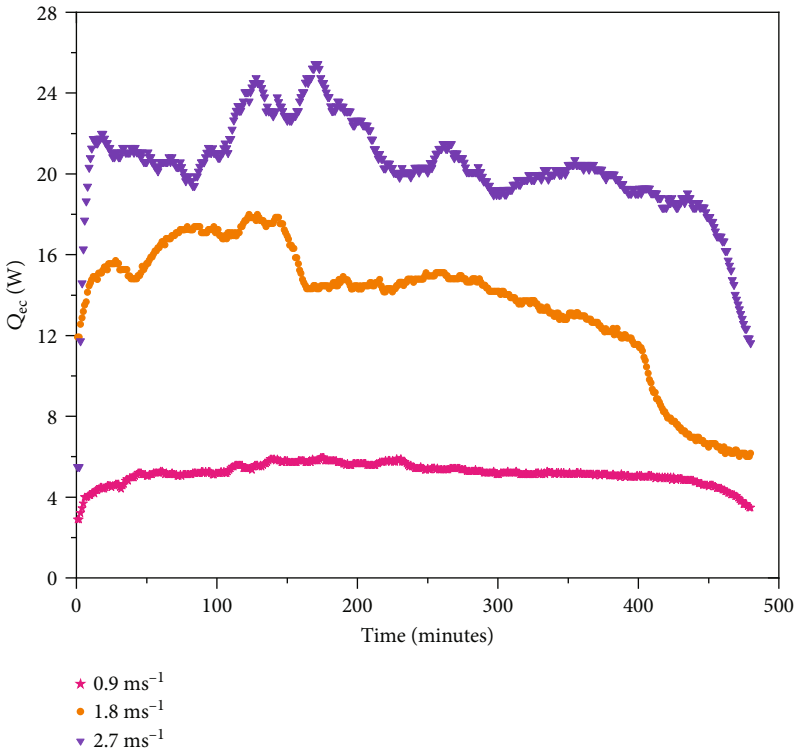

(c) Low RH

Figure 11: Instantaneous cooling capacity of the air cooler at three different velocities under three different RH conditions.

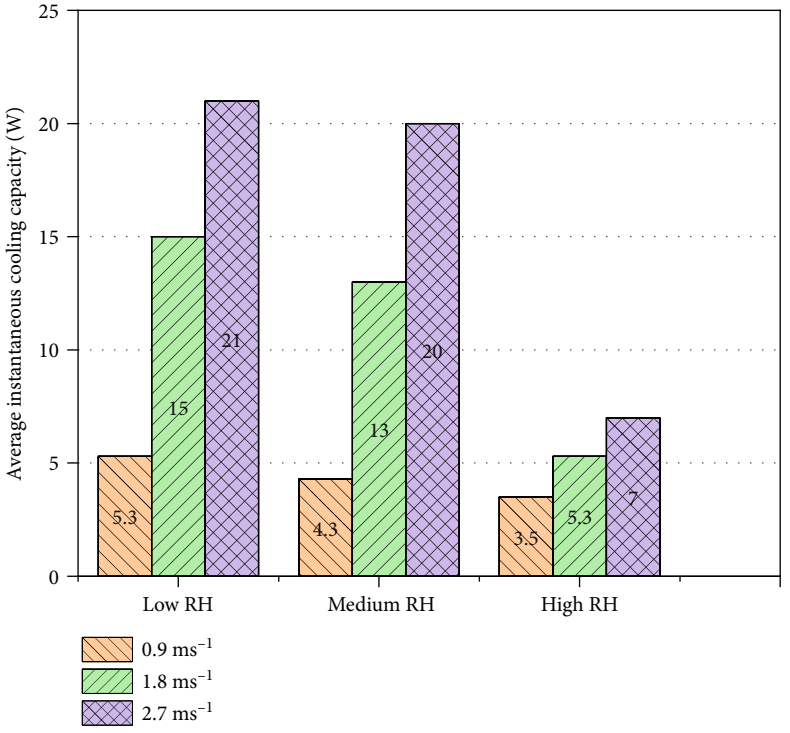

Figure 12: Average instantaneous cooling capacity of the air cooler at three different velocities under three different RH conditions.

4.3. Effectiveness. Figure 13 shows the effectiveness calculated using Equation (2) for three different velocities under three different RH conditions. It is noticed from Figure 8(a) that for all velocities, the system is very effective for 60 minutes. After that, there are fluctuations which are mainly due to the change in ambient conditions. In Figures 8(b) and 8(c), it is

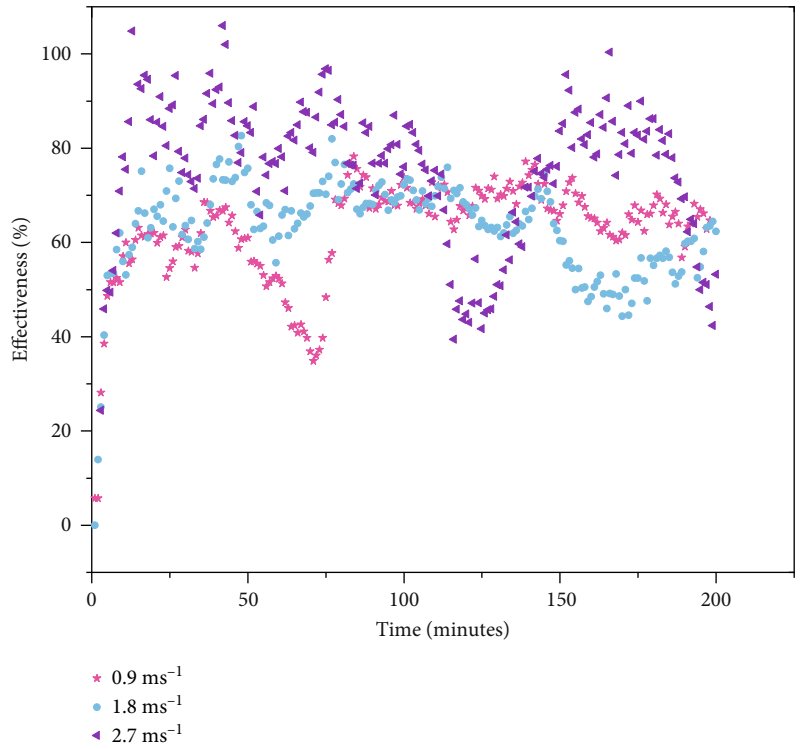

(a) High RH

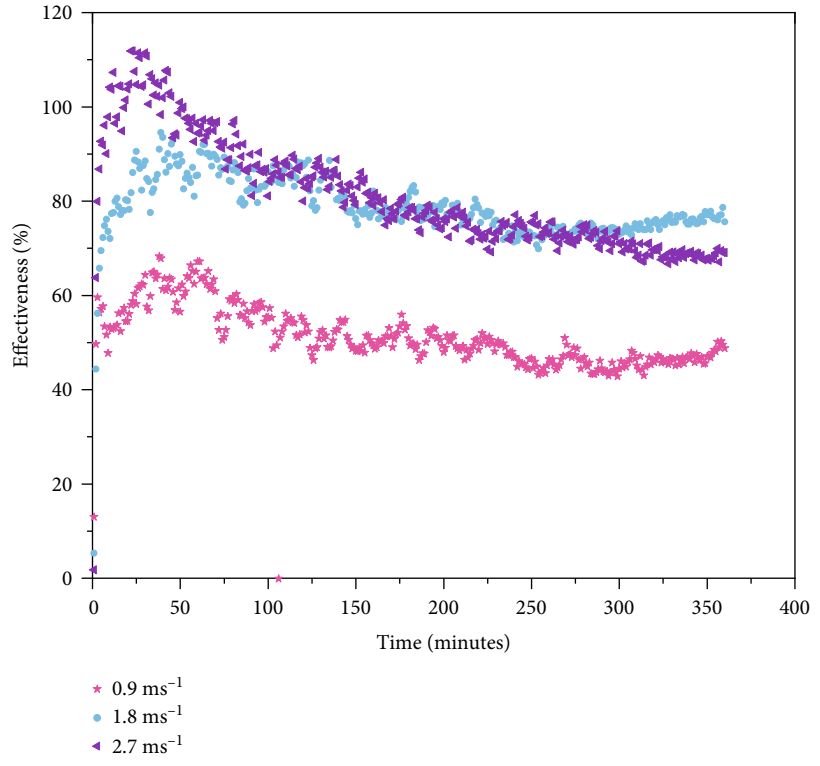

(b) Medium RH

Figure 13: Continued.

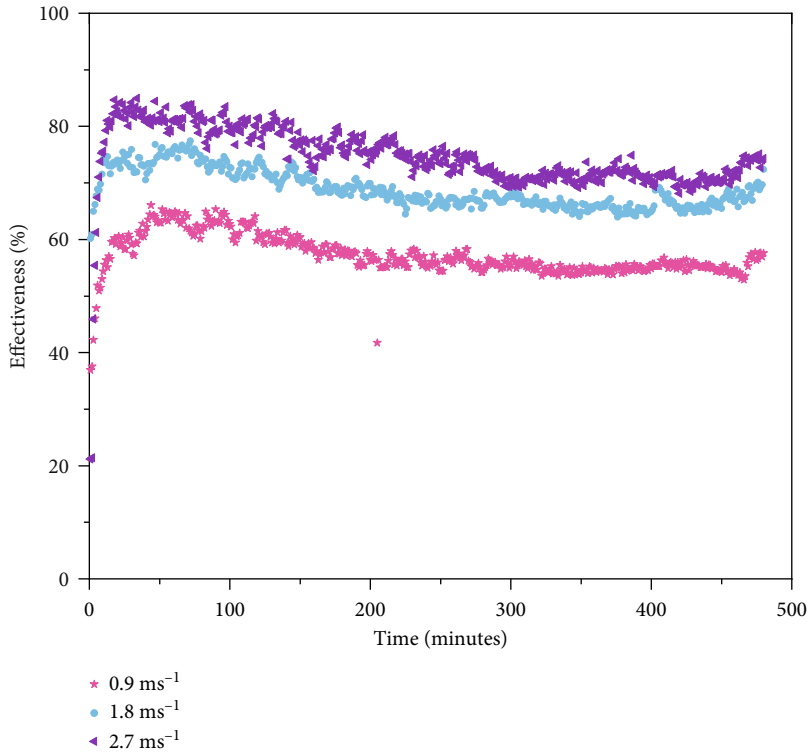

(c) Low RH

Figure 13: Effectiveness of the air cooler at three different velocities under three different RH conditions.

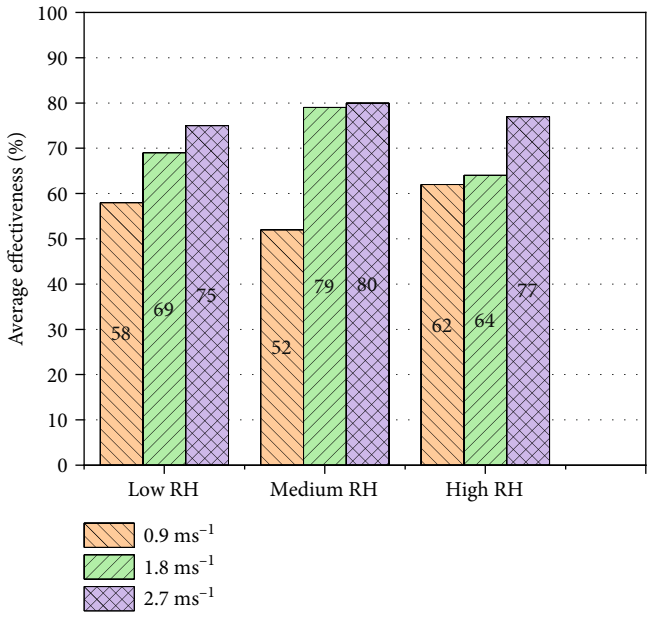

Figure 14: Average effectiveness of the air cooler at three different velocities under three different RH conditions.

found that higher average effectiveness was achieved when the velocities of air were 2.7 ms^{-1} and 1.8 ms^{-1}. The system's effectiveness was less at 0.9 ms^{-1} compared to other velocities. It is further observed that the effectiveness was maintained until the end of the experiment, which is mainly due to the water stored in the vermicompost to attain sustainable cooling.

Figure 14 shows the average effectiveness of the vermicompost-based evaporative cooling system tested during three different RH conditions operated at three different velocities. It is clear from the figure that effectiveness is above 75% when the system is operated at high velocity during all RH conditions. It is also understood that the ambient temperature and relative humidity influences the effectiveness of the vermicompost-based cooling system.

4.4. Water Evaporation Rate. Figure 15 shows the instantaneous evaporation rate calculated using Equation (3), cumulative evaporation rate, and ambient relative humidity for three different velocities under high RH condition.

It is observed from the figures that due to the relative humidity, which varies from 60% to 90%, the instantaneous evaporation rate is in the range of 0.2 g min^{-1} to 0.7 g min^{-1} at all velocities. However, the average instantaneous evaporation rate is more at 1.8 ms^{-1} velocity compared to other velocities. The average cumulative evaporation rate is in the range of 60 grams to 80 grams.

It is clear from Figure 16 that the instantaneous evaporation rate increases with velocity, and the average instantaneous evaporation rate is highest for 2.7 ms^{-1}. Its value is in the range of 0.5 g min^{-1} to 1.0 g min^{-1}. The average cumulative evaporation rate is increased from 200 grams to 400 grams for medium RH conditions.

It is seen from Figure 17 that the instantaneous evaporation rate is more when the air enters dry, i.e., with low relative humidity in the range of 30% to 45%. The cumulative

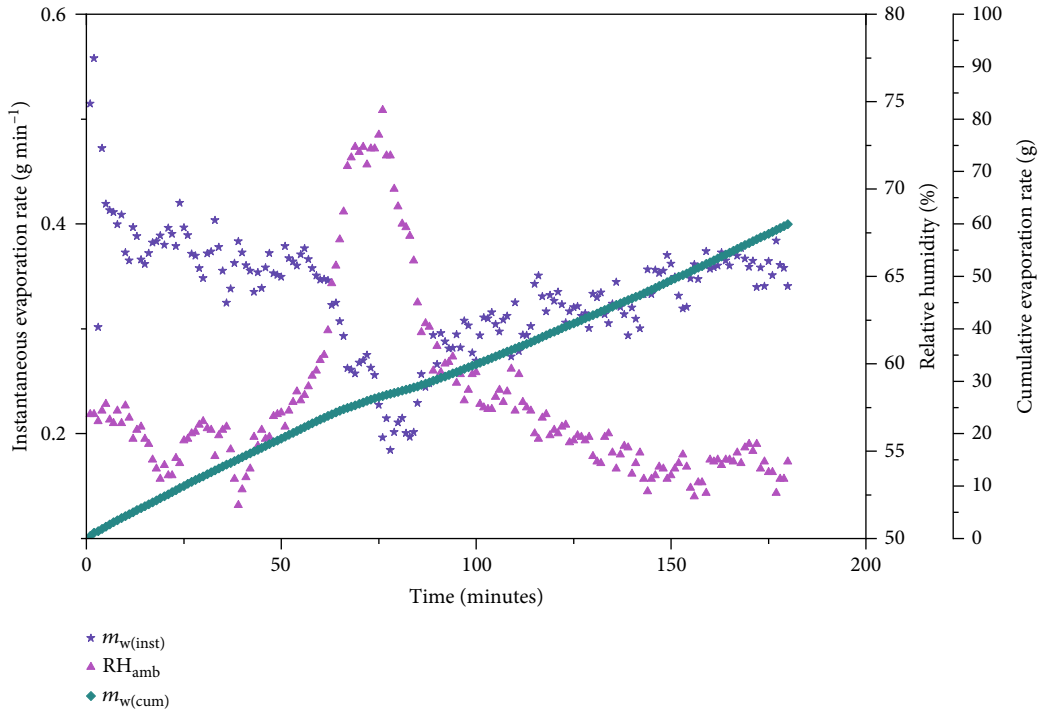

(a) 0.9 ms^{-1}

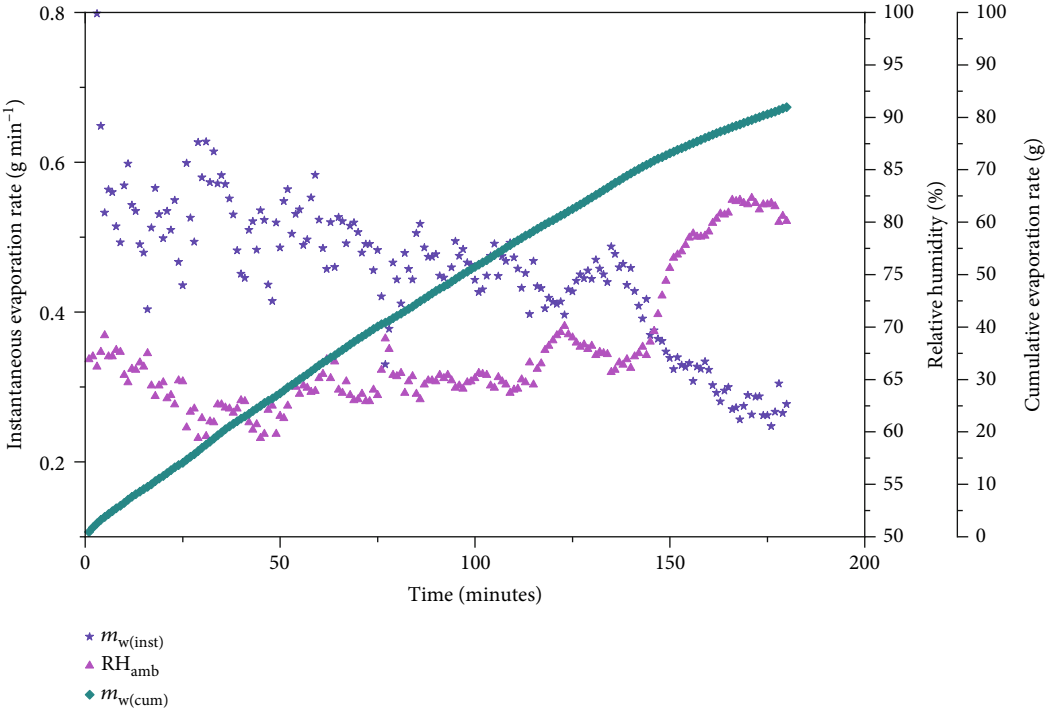

(b) 1.8 ms^{-1}

Figure 15: Continued.

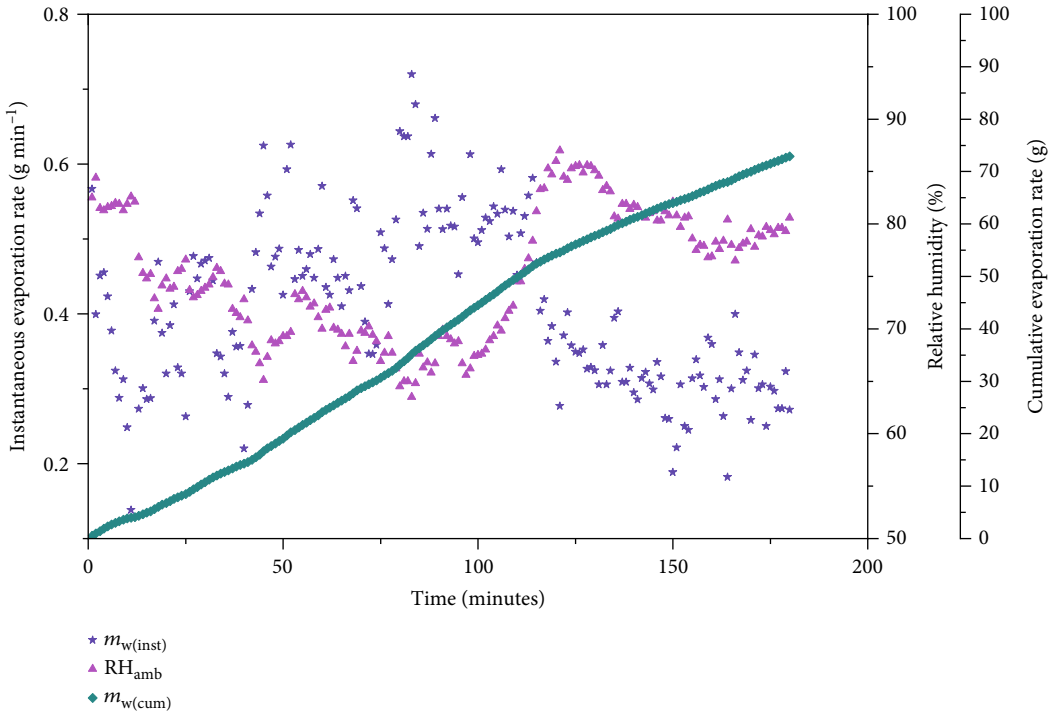

(c) 2.7 ms^{-1}

Figure 15: Ambient RH and instantaneous and cumulative evaporation rates of the air cooler at three different velocities under high RH condition.

evaporation rate is also increased, and it is in the range of 250 grams to 550 grams.

Figures 18 and 19 show the average values of instantaneous and cumulative evaporation rates at all velocities for three different RH conditions. It is construed from the figures that instantaneous evaporation and cumulative evaporation rates are inversely proportional to ambient relative humidity and directly proportional to velocity. The highest values are obtained by 1000 grams of vermicompost for low RH condition operated at 2.7 ms^{-1}.

4.5. Economic Analysis. If a pump had been used for supplying the water at the rate of 1 liter per hour, a 0.05 kW pump would have been employed for producing the same cooling effect. The energy consumption for the pump is calculated as follows:

(i) Power consumption of blower = 0.18 kW

(ii) Power consumption of blower and pump for conventional evaporative cooling system = 0.23 kW

(iii) Energy consumed by blower for 8 hours = 1.44 kW – hr

(iv) Energy consumed by both blower and pump for 8 hours = 1.84 kW – hr

(v) Energy savings due to the elimination of the pump = 21.7%

Assume a floral shop to be supplied with washed air from a direct evaporative cooler. The flowers are to be kept fresh from 5 a.m. to 8 p.m. The applicable monthly tariff for the shop using a conventional evaporative cooler and the present system is given below.

4.5.1. Conventional Evaporative Cooler

(i) Energy consumed by the conventional cooler operating for 15 hrs = 3.45 kW – hr

(ii) Monthly energy consumption = 106.95 kW – hr

(iii) Energy consumption charge for nondomestic consumers (0 to 100 units) = Rs.5.10/kWh

(iv) Energy consumption charge for nondomestic consumers (101 to 500 units) = Rs.6.10/kWh

(v) Fixed charges = Rs.75 per kW per month

(vi) Total monthly electricity charges for conventional cooler = (Rs.5.10 ∗ 100) + (Rs.6.10 ∗ 6.95) + (Rs.75 ∗ 0.23) = Rs.569.64

4.5.2. Present System

(i) Energy consumed by the present system operating for 15 hrs = 2.7 kW – hr

(ii) Monthly energy consumption = 83.7 kW – hr

(iii) Energy consumption charge for nondomestic consumers (0 to 100 units) = Rs.5.10/kWh

(iv) Fixed charges = Rs.75 per kW per month

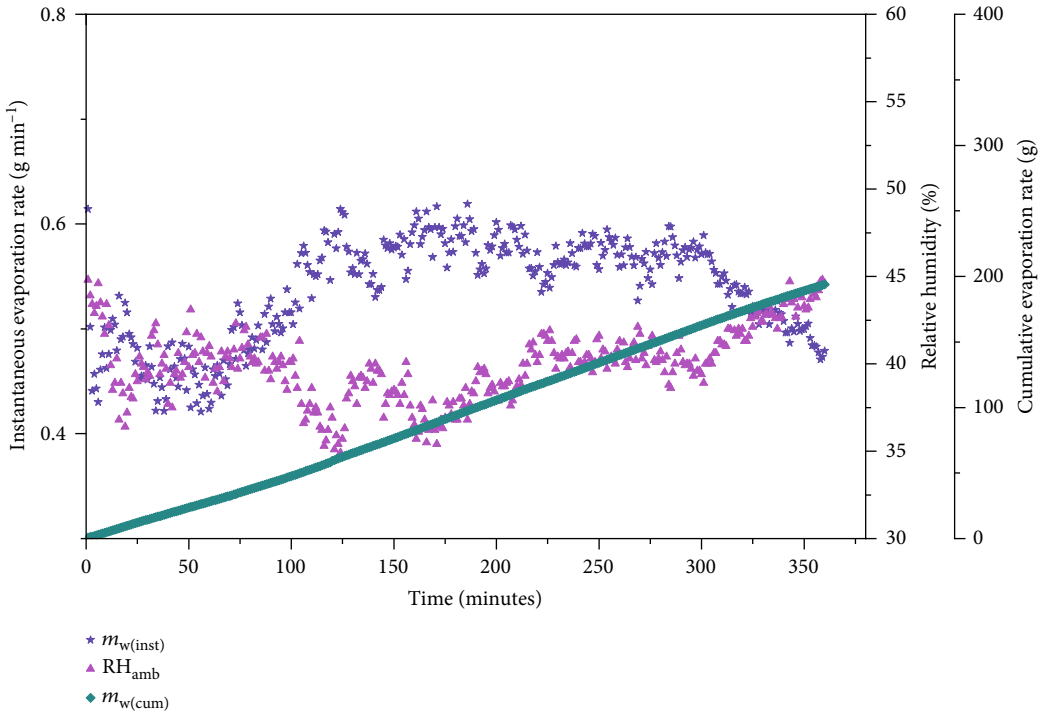

(a) 0.9 ms^{-1}

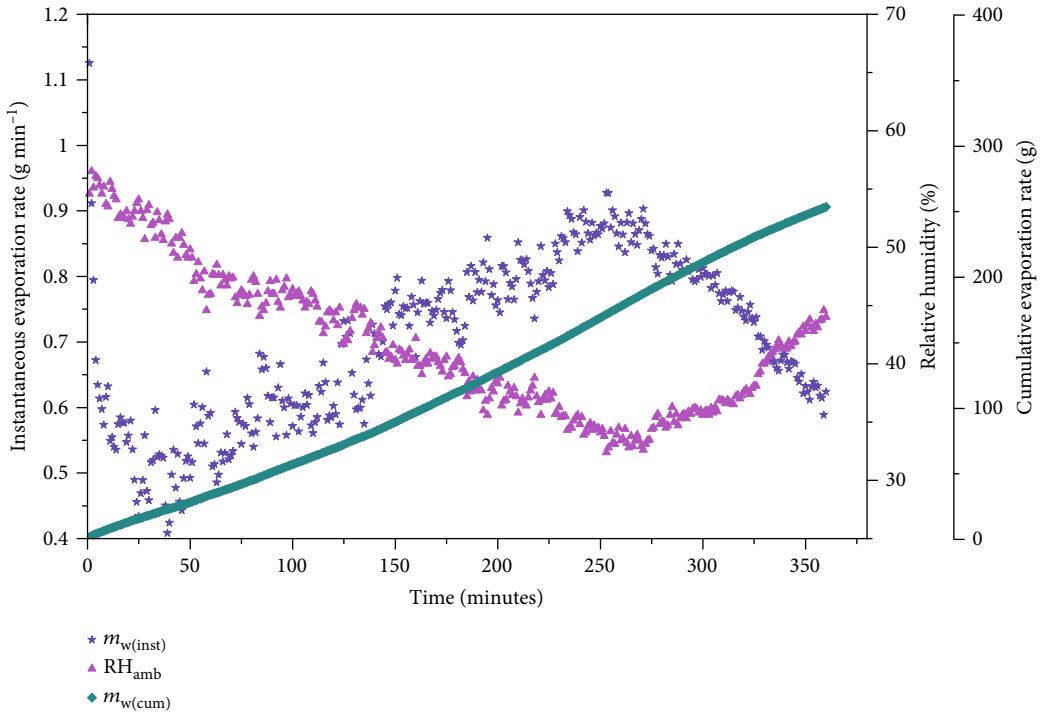

(b) 1.8 ms^{-1}

Figure 16: Continued.

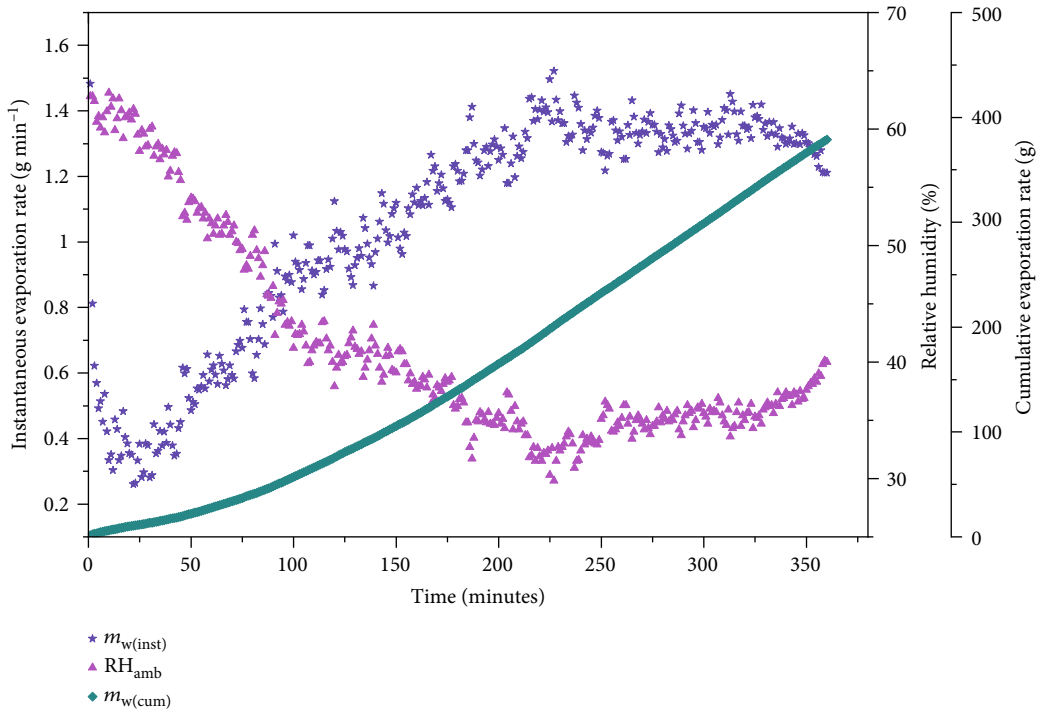

(c) 2.7 ms^{-1}

Figure 16: Ambient RH and instantaneous and cumulative evaporation rates of the air cooler at three different velocities under medium RH condition.

(v) Total monthly electricity charges for present system = (Rs.5.10 ∗ 83.7) + (Rs.75 ∗ 0.18) = Rs. 440.37

(vi) Net monthly savings in electricity charges = Rs. 129.27

(vii) Annual savings in electricity charges = Rs.1551.24

It is understood from the analysis that vermicompost as an energy-efficient material provides thermal comfort by eliminating the pump and issues related to water storage in the sump with energy savings of 21.7% and an annual electricity cost savings of Rs. 1551.24.

4.6. Comparison with Previous Studies. Many researchers had done extensive work in evaporative cooling systems with different pad materials. The results of their investigations are given in Table 4.

It is observed from the table that the conventional pad-pump system using various pad materials had been used for a hot and dry climate. The effectiveness of the systems varies from 60% to 80%. The highest temperature drop produced by eucalyptus fibre has an effectiveness of 71%. The present vermicompost-based evaporative cooling system produces an average temperature drop of 9.5°C with an average effectiveness of 80% for low RH conditions. Moreover, this system could produce an average temperature drop of 5°C, even during high RH conditions. It is construed that vermicompost has the potential to replace the pad-pump system of the conventional direct evaporative cooling system. Hence, this system could be used for cooling applications throughout the year.

5. Conclusion

The following conclusions are arrived from the present investigation performed on a vermicompost-based evaporative cooling system.

(i) The vermicompost-based cooling system could produce an average temperature drop of 4°C to 5°C for all velocities up to 150 minutes, as the ambient relative humidity varied from 60% to 75% during high RH condition

(ii) For medium RH condition, an average temperature drop of 5°C to 8°C and relative humidity of 99% could be achieved with this system based on the operating velocity if the ambient air has a temperature of 30°C to 34°C and relative humidity of 45% to 60%

(iii) An average temperature drop of 6.5°C to 9.5°C and relative humidity of 99% could be achieved with this system based on the operating velocity when the ambient air has a temperature of 38°C to 42°C and RH of 30% to 45% for low RH condition

(iv) The vermicompost-based evaporative cooling system performs better at velocities of 1.8 ms^{-1} and 2.7 ms^{-1} during low and medium RH conditions

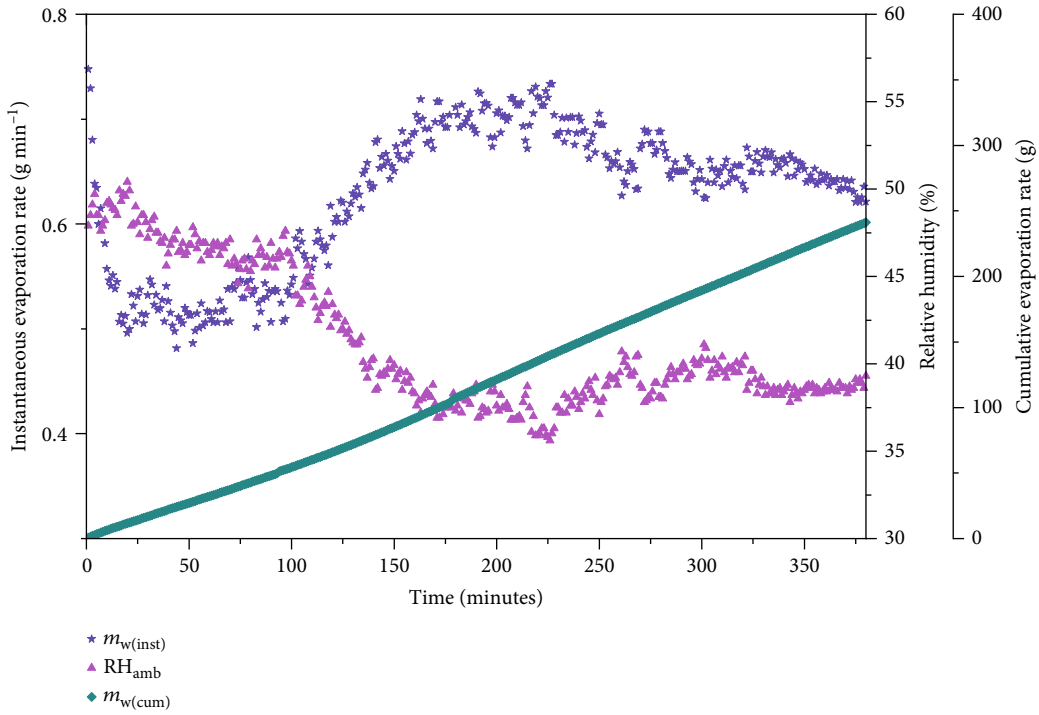

(a) 0.9 ms^{-1}

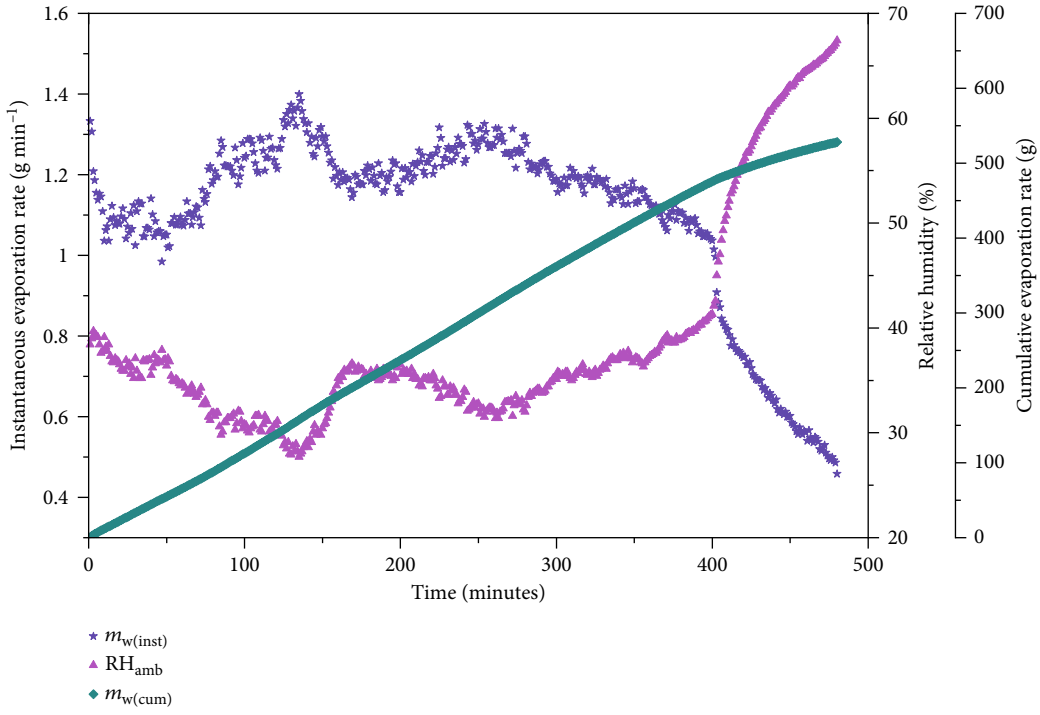

(b) 1.8 ms^{-1}

Figure 17: Continued.

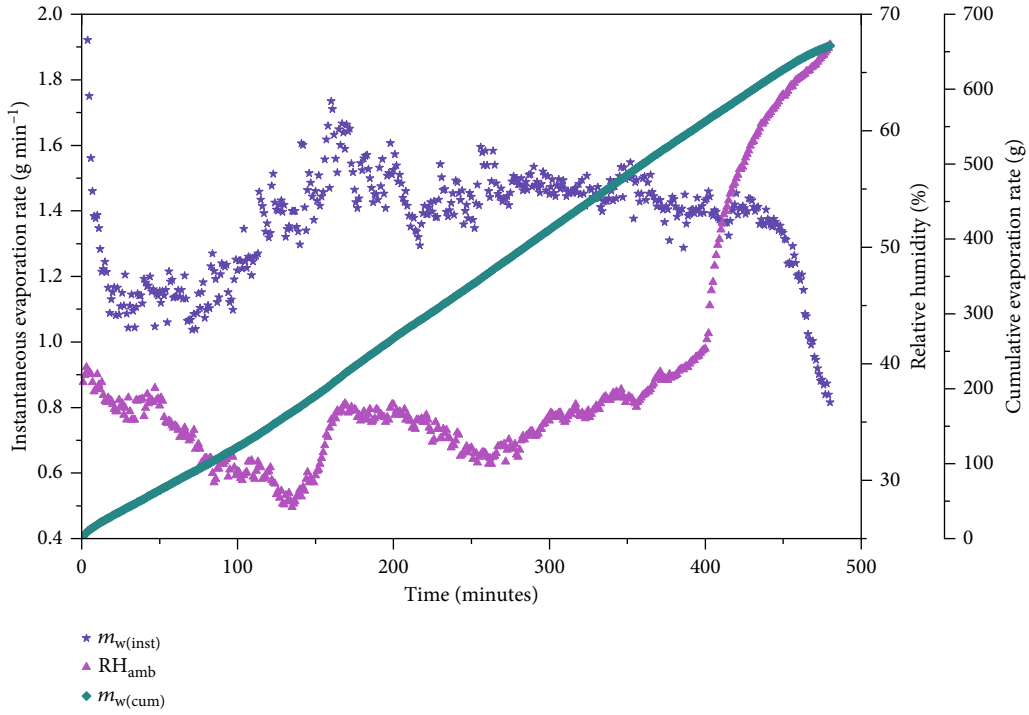

(c) 2.7 ms^{-1}

Figure 17: Ambient RH and instantaneous and cumulative evaporation rates of the air cooler at three different velocities under low RH condition.

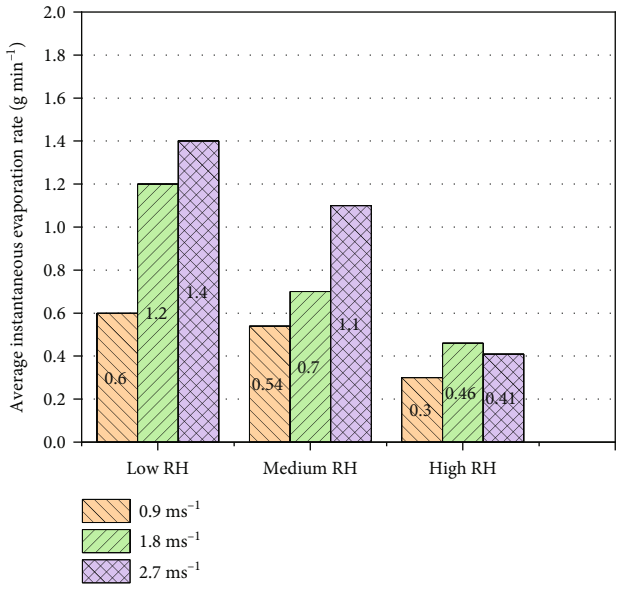

Figure 18: Average instantaneous evaporation rate of the air cooler at three different velocities under three different RH conditions.

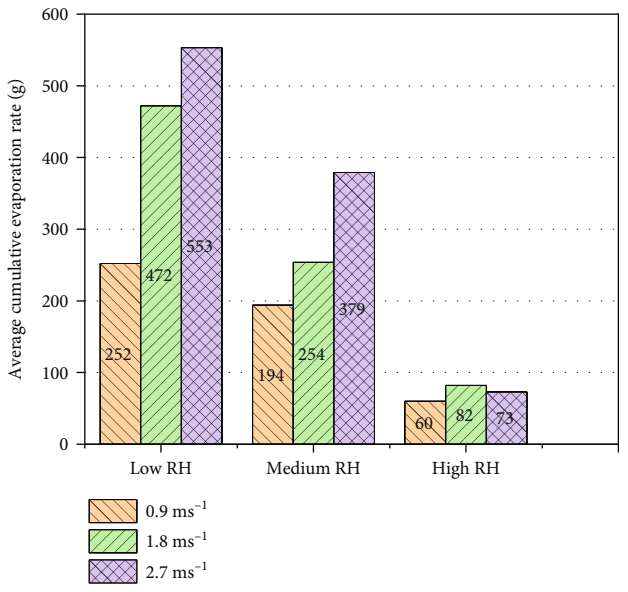

Figure 19: Average cumulative evaporation rate of the air cooler at three different velocities under three different RH conditions.

(v) Ambient relative humidity and operating velocity are the key factors that influence a vermicompost-based evaporative cooling system's performance

(vi) This system produces the cooling effect by utilizing only the initial water supply and eliminating the water sump system and related health issues. Hence, the vermicompost-based cooling system can produce higher cooling rates and sustained cooling at higher velocities and low RH conditions

(vii) Effectiveness is above 75% when the system is operated at high velocity during all RH conditions

Table 4: Research outcomes of different pad materials in evaporative cooling.

Authors	Material	Country	Temperature drop (°C)	Effectiveness (%)	Velocity (ms^{-1})
Bishoyi et al. [6]	Honeycomb	India	8	75-80	1.5
Al-Sulaiman [7]	Jute	Saudi Arabia	—	62.1	3-4
Doğramacı et al. [8]	Eucalyptus fibre	United Kingdom	11.3	71	0.1-1.2
He and Hoyano [15]	Ceramics	Japan	3-4	50-70	1-2
Katsuki et al. [16]	Ceramics with Onggi clay and bamboo charcoal	Korea	3.6	—	0.4
Soponpongpipat and Kositchaimongkol [22]	Rice husk	Thailand	3.3	60	1
Present work	Vermicompost	India	9.5	80	0.9-2.7

(viii) Instantaneous evaporation and cumulative evaporation rates are inversely proportional to relative humidity and directly proportional to velocity. The highest values are obtained by 1000 grams of vermicompost for low RH condition operated at 2.7 ms^{-1}

(ix) It could be used under all operating conditions; however, excellent performance characteristics are observed when the system is operated under low RH conditions. Hence, the vermicompost-based evaporative cooling system could be used in places with hot and dry weather conditions

(x) The use of a solar dryer for regenerating the vermicompost ensures the prevention of mould growth in the cooling chamber

This energy-efficient cooling technology has the potential to provide a clean and sustainable indoor environment throughout the year in places with hot-dry weather conditions. This system acts as a water storage medium and thus eradicates the problems of water stagnation. The elimination of the pump increases the energy savings of the system by 21.7% and an annual electricity cost savings of Rs. 1551.24. This system could pave the way for year-round thermal management of building cooling applications in an environmentally friendly manner. The present setup technically demonstrates the lab-scale feasibility of a vermicompost-based evaporative cooling system. When it is proposed to make it a user-friendly commercial setup, new limitations and challenges may arise. The future scope of the work is to test the life cycle of the vermicompost in the repeated charging and discharging cycles for long-term utilization.

Abbreviations

DEC: Direct evaporative cooling
DHT: Digital hygro thermometer
TRHS: Temperature relative humidity sensor
RH: Relative humidity.

Symbols

T_{amb}: Ambient temperature (°C)
T_{al}: Temperature of air leaving the cooling chamber (°C)
T_{wbt}: Thermodynamic wet-bulb temperature of entering air (°C)
RH_{amb}: Ambient relative humidity (%)
RH_{al}: Relative humidity of air leaving the cooling chamber (%)
$\dot{m}_a$: Mass flow rate of air (kgs^{-1})
c_p: Specific heat capacity of moist air ($J\,kg^{-1}\,K^{-1}$)
Q_{ec}: Evaporative cooling capacity (W)
$\dot{m}_{wi}$: Instantaneous evaporation rate of water ($g\,min^{-1}$)
$\dot{m}_{wc}$: Cumulative evaporation rate of water (g).

Greek Symbols

ε: Effectiveness (%)
ω_1: Humidity ratio of inlet air ($kg_w{\cdot}kg_{dryair}^{-1}$)
ω_2: Humidity ratio of leaving air ($kg_w{\cdot}kg_{dryair}^{-1}$).

Data Availability

The data used to support the findings of this study are included within the article.

Conflicts of Interest

The authors declare that there is no conflict of interest regarding the publication of this article.

References

[1] "How evaporative cooling works," 2020, https://www.pinterest.com/pin/328692472785595064/.

[2] L. Rong, P. Pedersen, T. L. Jensen, S. Morsing, and G. Zhang, "Dynamic performance of an evaporative cooling pad investigated in a wind tunnel for application in hot and arid climate," *Biosystems Engineering*, vol. 156, pp. 173–182, 2017.

[3] J. Xu, Y. Li, R. Z. Wang, W. Liu, and P. Zhou, "Experimental performance of evaporative cooling pad systems in greenhouses in humid subtropical climates," *Applied Energy*, vol. 138, pp. 291–301, 2015.

[4] K. Harby and F. Al-Amri, "An investigation on energy savings of a split air-conditioning using different commercial cooling pad thicknesses and climatic conditions," *Energy*, vol. 182, pp. 321–336, 2019.

[5] A. K. Dhamneya, S. P. S. Rajput, and A. Singh, "Theoretical performance analysis of window air conditioner combined with evaporative cooling for better indoor thermal comfort

and energy saving," *Journal of Building Engineering*, vol. 17, pp. 52–64, 2018.

[6] D. Bishoyi and K. Sudhakar, "Experimental performance of a direct evaporative cooler in composite climate of India," *Energy and Buildings*, vol. 153, pp. 190–200, 2017.

[7] F. Al-Sulaiman, "Evaluation of the performance of local fibers in evaporative cooling," *Energy Conversion and Management*, vol. 43, no. 16, pp. 2267–2273, 2002.

[8] P. Abohorlu Doğramacı, S. Riffat, G. Gan, and D. Aydın, "Experimental study of the potential of eucalyptus fibres for evaporative cooling," *Renewable Energy*, vol. 131, pp. 250–260, 2019.

[9] J. K. Jain and D. A. Hindoliya, "Experimental performance of new evaporative cooling pad materials," *Sustainable Cities and Society*, vol. 1, no. 4, pp. 252–256, 2011.

[10] P. M. Cuce and S. Riffat, "A state of the art review of evaporative cooling systems for building applications," *Renewable and Sustainable Energy Reviews*, vol. 54, pp. 1240–1249, 2016.

[11] B. Costelloe and D. Finn, "Indirect evaporative cooling potential in air-water systems in temperate climates," *Energy and Buildings*, vol. 35, no. 6, pp. 573–591, 2003.

[12] G. Heidarinejad, M. Bozorgmehr, S. Delfani, and J. Esmaeelian, "Experimental investigation of two-stage indirect/direct evaporative cooling system in various climatic conditions," *Building and Environment*, vol. 44, no. 10, pp. 2073–2079, 2009.

[13] E. Ibrahim, L. Shao, and S. B. Riffat, "Performance of porous ceramic evaporators for building cooling application," *Energy and Buildings*, vol. 35, no. 9, pp. 941–949, 2003.

[14] E. Hajidavalloo, "Application of evaporative cooling on the condenser of window-air-conditioner," *Applied Thermal Engineering*, vol. 27, no. 11–12, pp. 1937–1943, 2007.

[15] J. He and A. Hoyano, "Experimental study of cooling effects of a passive evaporative cooling wall constructed of porous ceramics with high water soaking-up ability," *Building and Environment*, vol. 45, no. 2, pp. 461–472, 2010.

[16] H. Katsuki, E. K. Choi, W. J. Lee, U. S. Kim, K. T. Hwang, and W. S. Cho, "Eco-friendly self-cooling system of porous onggi ceramic plate by evaporation of absorbed water," *Journal of the Korean Ceramic Society*, vol. 55, no. 2, pp. 153–159, 2018.

[17] J. R. Watt, *Evaporative Air Conditioning Handbook*, Chapman and Hall, New York, 1986.

[18] C. A. Edwards and I. Burrows, "The potential of earthworms composts as plant growth media," in *Earthworms in Waste and Environmental Management. Hague 2132*, C. A. Edward and E. F. Neuhauser, Eds., SPB Academic Publishing, 1988.

[19] "Velluru historical weather," 2020, https://www.worldweatheronline.com/velluru-weather-history/tamil-nadu/in.aspx.

[20] J. R. Taylor, *An Introduction to Error Analysis*, University Science Books, California, 1982.

[21] S. K. Wang, *Hand Book of Air Conditioning and Refrigeration*, McGraw-Hill, Second, 2001.

[22] N. Soponpongpipat and S. Kositchaimongkol, "Recycled high-density polyethylene and rice husk as a wetted pad in evaporative cooling system," *American Journal of Applied Sciences*, vol. 8, no. 2, pp. 186–191, 2011.

Hindawi
International Journal of Photoenergy
Volume 2020, Article ID 8855477, 14 pages
https://doi.org/10.1155/2020/8855477

Research Article

Comparative Analysis of Reliable, Feasible, and Low-Cost Photovoltaic Microgrid for a Residential Load in Rwanda

Cyprien Nsengimana, Xin Tong Han, and Ling-ling Li

State Key Laboratory of Reliability and Intelligence of Electrical Equipment, School of Electrical Engineering, Hebei University of Technology, Tianjin 300130, China

Correspondence should be addressed to Cyprien Nsengimana; cyprienn98@gmail.com

Received 9 September 2020; Revised 23 October 2020; Accepted 30 October 2020; Published 21 November 2020

Academic Editor: Kumarasamy Sudhakar

Copyright © 2020 Cyprien Nsengimana et al. This is an open access article distributed under the Creative Commons Attribution License, which permits unrestricted use, distribution, and reproduction in any medium, provided the original work is properly cited.

Photovoltaic microgrids provide free renewable energy solutions for Rwandans. Although solar technology keeps on its advancement, hydropower remains the principal power source in Rwanda. Other renewable power sources include wind and geothermal energies that are not yet fully exploited. Nonrenewable sources in Rwanda including methane, peat, thermal, and fuels are also used for providing energy solutions for the citizens. Rwanda Energy Group (REG) sets the energy strategic plan since 2015 for achieving the minimum of 512 MW of energy production in 2024/2025 to meet the total energy demand. The plan predicted 52% for grid-connected and 48% for off-grid (standalone) connections. The literature survey and data analysis collected on site were used to evaluate and determine the best cheaper microgrid model from the three comparison case studies for the household in Rwanda. The study focused on the economic power generation model mainly based on solar resources to minimize the electricity cost and provide income for the excess energy produced. Moreover, the study resulted in a low-cost (four times cheaper), reliable, and affordable grid-connected PV and battery microgrid model for a residential home with a minimum daily load of 5.467 kWh. The simulation results based on economic comparison analysis found the levelized cost of energy (LCOE) and net present cost (NPC) for each power-generated model by using Hybrid Optimization Model for Electric Renewable (Homer) pro software. The results show that the LCOE for electricity production by each of the Grid connected-PV-Battery system, Diesel GenSet-PV-Batteries, and PV-Batteries systems was 0.0645 US$/1 kWh, 1.38 US$/1 kWh and 1.82 US$/1 kWh, respectively, compared with 0.2621 US$/1 kWh, the current residential electricity price (2020) for Rwanda.

1. Introduction

Photovoltaic technology has been an important topic for researchers from the last decade up to date. PV systems are placed into a microgrid as a local electricity distribution system that is operated in a controlled way and include both energy users and renewable energy generation. Other sources of renewable energy are wind, fuel cells, biogas, tidal, and geothermal that can be produced to generate electricity locally [1]. PV microgrid distribution across the globe has been grown while taking advantage of free solar insolation during the day period. However, its variability and uncontrollability are greatly depending on weather conditions. In Rwanda, the minimum global horizontal irradiation is varying from 4.2 up to 5.8 kWh/m^2 [2]. To avoid the effect of instant varying solar insolation, a backup energy storage system has been provided by so many authors. For grid-connected systems, the backup will take effect only during the off-peak load hours or during power cut or blackout or any power failure. To evaluate more opportunities, diesel generator has been simulated with photovoltaic system as the other source of energy generating system to find its efficacy. The global studies confirm the continuous increase of the world's total installed photovoltaic capacity up-to-date [3]. In Rwanda, a lot of effort is currently made to sensitize private investors on the implementation of solar energy projects to remove the big gap between electricity demand and power generation capacity [4]. Recently, electrical loads in Rwanda are power supported by diesel generators during heavy peak hours which may rise the fuel electricity cost,

equivalent to 0.2621 US$/1 kWh for residential homes consuming above 50 kW per month [5]. The authors in [6] highlight the drawbacks from diesel generator usage relied on their fuel cost and environment pollution. Three case scenarios were simulated with HOMER software where one is grid-connected and the other two are off-grid systems with and without a diesel generator. The resulting conclusion comes up with a recommended model suitable for enough power production, electrical load capacity, financial costs, and society benefits such as power reliability and affordability and ability to reduce $C0_2$ emissions. The levelized cost of electricity from PV microgrid supply scheme, LCOE, for each model type has been compared to recent electricity purchase in Rwanda, and the best economic model was chosen. This paper starts by Introduction, Literature Survey, Methodology, Optimization Results and Analysis with Homer Pro Software, Comparison of Different State-of-the-Art Results with the Proposed Study, and finally Conclusion.

2. Literature Survey

Nowadays, some literatures are available for the optimization of renewable energy systems by operating different distribution energy sources [7]. Across the continent, the development of new power sources for fossil fuel replacement, such as renewable energy sources, has given high priority for both economic and environmental advantages. Studies [8, 9] used HOMER to simulate, analyze, and optimize renewable power sources which can substitute conventional energy sources, and the authors confirmed a feasibility solution of a reliable standalone electric power system for people living far from the national grid. For power back-up, different authors use storage systems including battery or inline diesel generator support. [10] used HOMER appliances in the village and show the result of adding renewable generation to the current supply scheme. Sharmin et al. proved that Off-Grid Biogas Power Generation Model for a rural area is feasible by using Homer software tool and confirmed the feasibility of the representation. The authors [11] evaluated both off-grid and grid-connected for a variety of applications and made a cost-benefit study using Homer Pro software tool. However, the study elaborates the analysis of data based on a particular residential home with specific detailed load in Rwanda by using three different alternative PV microgrid models such as a grid-connected system and two standalone systems. The selection choice is based on which model would be reliable, feasible, and affordable for the home with 5.47 kWh load.

3. Methodology

The methodology of the research is based on the economic analysis of three PV microgrid systems based on two principal economic indicators such as total NPC and LCOE for each model design. The first one is a grid-connected photovoltaic system with lithium ion battery. The other two systems are off-grid systems with PV, generator, and battery and are then compared with the purely renewable system with PV and battery only using Homer Pro to find the least

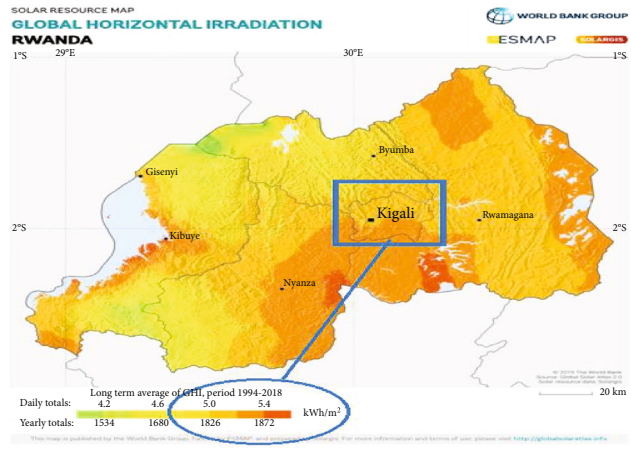

Figure 1: Kigali horizontal radiation [2].

LCOE values and minimum net present cost for respective models. Homer Pro software was selected due to its merit to simulate different energy systems, shows system configurations optimized by cost, and finally provides sensitivity analyses on which the authors conclude based on the study purposes.

3.1. Site Profile. The site location is a home located in the city of Kigali, the central capital of, Rwanda, with the geographical coordinates (1°56.6′S, 30°3.7′E) in Kigali city, Africa. Its coordinated universal time (UTC) zone is UTC plus two hours, i.e., [UTC+02]. This is the home location where the data has been taken for model design. Figure 1 indicates the map for the site location with long-term average global horizontal irradiation.

3.2. Load Description. The items and their power rating have been detailed in Table 1. The total load can be split into three different consumption parts. The first part starts from 4:00 AM to 8:00 AM, where both parents and children are staying at home and therefore use some power to prepare morning work. It is their time to use lights, microwave, and iron for preparing the starting of their daily journey. The second part starts from 9:00 AM to 14:00 AM where the load is consumed by watching TV, using a shaver and fridge. The last part comes from 5:00 PM to 21:00 PM where both parents and children come back home from their jobs and they can use high electrical loads such as lights, watching TV, charging phones, and using high-consumption electrical loads like fridge and microwaves as distributed in Figure 2. In this paper, the load profile is considered the energy consumption of the residential home in Kigali city and it is about 5.467 kWh/day as illustrated in Table 1.

The daily distribution of the load is hereby shown in Figure 2. It is clear that a high-power consumption in the morning rises around 7:00 AM and around 13:00 PM and the peak load is observed from 19:00-20:00 PM. The reason of this peak load is justified by the time where the whole family get back home and use much power for their daily needs. It is highly noted that during the peak power period, the sun

Table 1: Electrical consumption of equipment and daily energy usage for a home in Kigali city.

Serial number	Item name	Quantity required	Power rating (W)	Hour of use per day	Daily energy usage (Wh)
1	Home lights	8	20	12	1920
2	Computers usage	2	25	6	300
3	TV	1	125	5	625
4	Iron	1	1000	0.5	500
5	Shaver	4	15	0.2	12
6	Mobile phones	4	2.5	5	50
7	Refrigerator	1	150	12	1800
8	Microwave	1	1300	0.2	260
Total daily load profile (watt-hour/day)					5,467

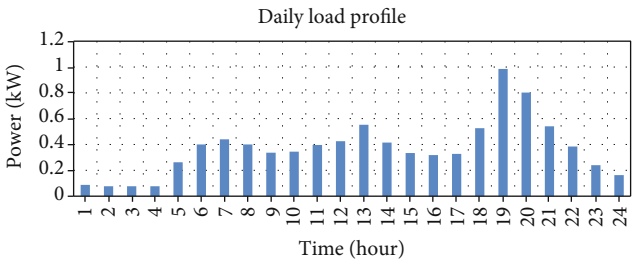

Figure 2: Daily electric load distribution for a residential home in Kigali city.

has already been set, which explains the necessity of storage energy resources.

3.3. PV Radiation. The annual average data of the global horizontal radiation (GHI) and clearness index from a residential home obtained with the help of the National Aeronautics and Space Administration (NASA) Surface meteorology database based on the geographical location of KN 4Ave, Kigali, Rwanda, with longitude and altitude herewith shown (1°56.6′S, 30°3.7′E). At this location, the annual average solar radiation is 5.5 kWh/m^2 and the annual average clearness index is 0.55. As it is shown in Figure 3, the three months with higher solar radiation are February, March, and September with their respective insolation of 5.84, 5.81, and 5.85 kWh/m^2/day (2020). During this period, the majority of the sun interchanges with little rain at normal temperature around 25°C. A measurement of atmospheric clearness noted as clearness index is averaged to 0.55 from to its highest possible value of 1.0, which means the study site is mostly clear and sunny.

3.4. Selection of PV System. The following PV specifications were chosen based on its design performance. The295-Watt CS6K-295MS features efficient Passivated Emitter and Rear Contact (PERC) solar cells to significantly improve the performance of its power in morning, evening, and other low light conditions at a low price per watt. The important parameters of the selected PV panel are available in the datasheet of the manufacturer's website, and it is summarized in Table 2.

3.4.1. On-Grid PV Microgrid System Design. The grid-connected microgrid topology is given by the Monocrystalline solar PV with 295 Wp (Watts peak), CS6K-295MS with 1 kWh string of lithium-ion, ASM battery model with bidirectional converter, and Leonics model supplying the daily minimum load demand of 5.467 kWh. Furthermore, the respective design models were analyzed economically with Homer Pro based on their respective LCOE and NPC values. As stated in different literatures like Dekker, et al. [12], NPC values should be kept minimum as much as possible. The following schematic diagrams are showing different simulation strategies to be evaluated to find a reliable, feasible, and optimum model for Kigali city citizens. Figure 4 illustrates the on-grid microgrid with PV, battery, and converter to feed the AC load demand.

3.4.2. Off-Grid PV Microgrid System Design. The off-grid PV systems, also called standalone PV systems, are relying on solar power as the main power production unit. The following PV microgrid systems consist of a standalone solar system with (Figure 5) or without diesel (Figure 6) to meet the daily load demand of 5,467 Wh of a residential house in Kigali city, the capital of Rwanda. All those system models use batteries for energy storage during periods of poor weather. The charge controllers are also included here—with the solar PV to control the state of charging and discharging of batteries [13]. When batteries are fully charged, they are disconnected from the PV modules and may also be disconnected from the load to protect the batteries from over-discharging. Figures 5 and 6 are the design layout models of, respectively, the off-grid topology with solar PV, generator, and battery systems to feed the AC load demand through a bidirectional converter, while the last model is done with PV and battery system to supply the same AC load demand through the two-way converter. These three cases give an intuition view of the system operation, and the simulations have been done using Homer Pro software.

3.5. Battery. The three model systems designed for the comparison study require all energy storage elements, which is in this manuscript the lithium-ion battery. The battery belongs to the advanced kinetic storage model (ASM) that includes

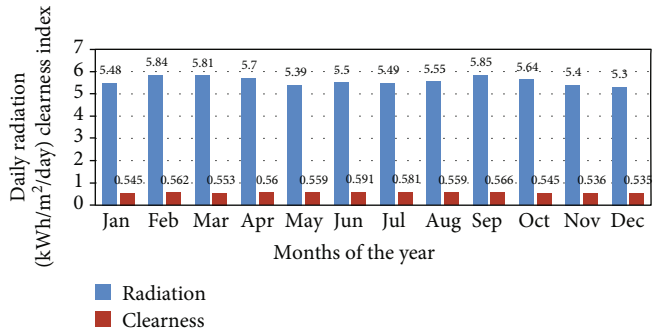

Figure 3: Global solar radiation with the corresponding clearness index at Kigali city, Rwanda (data gathered by NASA, Surface Solar Energy database, 2020).

Table 2: Parameters of CS6K-295MS PV Module at Standard Test Conditions (STC) and temperature = 25°C and insolation = 1000 W/m^2.

Solar model	CS6K-295MS
STC rating	295 W
Efficiency	18.02%
Open circuit voltage (V_{oc})	39.5 V
Short circuit current (I_{sc})	9.75A
Optimum operating voltage (V_{mp})	32.3 V
Optimum operating current (I_{mp})	9.14 V

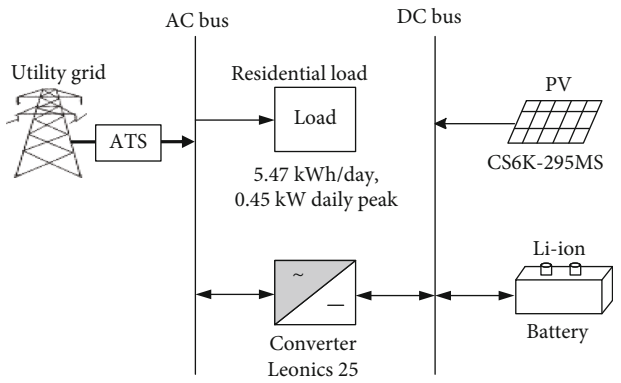

Figure 4: Layout diagram for on-grid power system with PV, battery and converter.

rate-dependent losses, temperature dependence on capacity, cycle lifetime estimation using rain flow counting, and temperature effects on calendar life. In the model design, the capacity and configuration of the battery must be evaluated so that it can work with respect to the system requirements. The sizing of the battery for two days of autonomy is herein calculated by using the nominal voltage of 12 V/100 Ah that is mostly used in solar panels. Table 3 indicates the worst scenario of battery and solar sizing in the zone without grid utility for a home load of 5,467 Wh.

3.6. Utility Grid. The national utility for major power production is from hydropower plants (53%), and the current power is 224.6 MW distributed to an estimate of 51% (37% on-grid and 14% off-grid) of the total of 12.5 million of the population [4]. Rwanda has a plan to increase electricity access in 2024 to a total of 556 MW that will be able to supply power to 100% of inhabitants. Among them, 52% are targeting on-grid while 48% will be off-grid [14].

The cost of electrical energy to be purchased from the national utility grid is annually revised, and it is currently US$ 0.2621 per each 1 kWh purchased and US$ 0.15 per each kWh of solar sold back to the grid.

3.7. Economic Cost Optimization of the System. In this paper, the grid-connected system with PV and battery system gives the most promising results for Kigali city inhabitants. The selection of the best model is done based on the economic analysis of the system with the lowest levelized cost of energy (LCOE) and the total net present cost (NPC). The NPC of a component is also called life-cycle cost as it was explained in Homer Pro user manual (2020), which includes the costs of installing and operating the component over the project lifetime, subtracting the present value of all revenues earned over the project lifetime. The system costs here include the capital cost, replacement cost, operation and maintenance costs, fuel costs, emissions penalties, and the cost for power purchase from the grid while the salvage and grids sales are revenues [15]. Despite the low values of LCOE and NPC which are one of the indicators of feasibility study, the availability of natural resources at the investigated location is also considered while deciding on the reliability and feasibility of the power system. There are places which are rich in wind, fuels, and gas energy but which may be poor in solar energy or are having potential in both wind and solar. The decision of the best power system model is therefore done on case basis depending on which energy resource is dominating in the study location. In Homer optimization results, the lower is the LCOE, the lower is the electricity tariff. Similarly, the lower is the NPC imply, the lower is the initial investment required to initiate the energy infrastructure. The NPC is mathematically derived, while the levelized cost of energy (LCOE) value to a certain extent is arbitrary making the NPC more reliable [16, 17].

3.8. Mathematical Analysis Relied on the Power System Cost Minimization System. The optimization of each power system is done using HOMER software for finding the feasibility

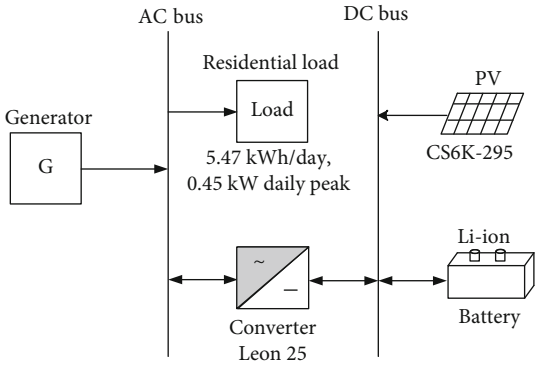

Figure 5: Layout diagram for off-grid power system with generator, PV, battery and converter.

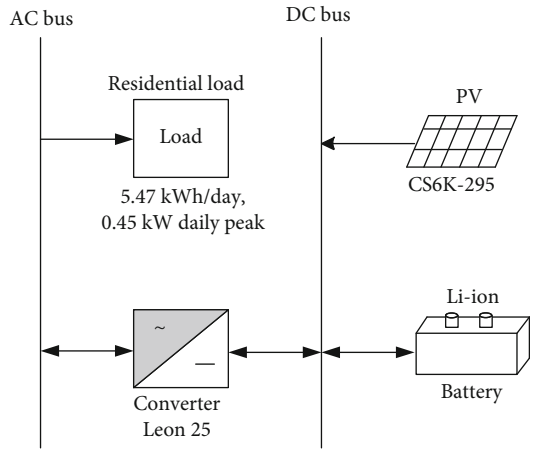

Figure 6: Layout diagram for off-grid power system with PV, battery and converter.

cost by referring to the following cost minimization procedure. Each schematic model among the three categories will undergo the minimization steps using the below formula. The following is an example of a photovoltaic grid-connected system with a battery to supply the AC load demand.

Let the function (f) be expressed in the cost of each installed component (x).

$$f(x) = \text{Cc} + \text{Rc} + \text{Mc} + \text{ChBc}, \tag{1}$$

where Cc is the capital cost, Rc is the replacement cost, Mc is the maintenance cost, and ChBc is the charging battery cost.

Equation (1) can be detailed as follows:

(i) Capital cost (Cc): capital cost symbolizes the total installed cost of each component (PV panels, battery, charge controller, power converter, and cabling) at the beginning of the project.

$$\text{ChBc} = E_{\text{Grid–Bat}} * c_h. \tag{2}$$

Equation (2) represents the amount of money to be spent in order to charge the battery from the main energy source during its availability and $E_{\text{Grid–Bat}}$ is the amount of energy extracted from the grid for the charging process, while c_h defines the cost of kWh imposed by the utility power providers.

It is required to find the value of the annuity based on the interest rate (i_L) and the period ($h \le n$) of the payment using the term known as capital recovery factor (CRF).

$$\text{CRF}(i_L, h) = \frac{i_L(i_L + 1)^h}{(i_L + 1)^h - 1}. \tag{3}$$

The total capital cost (TCc) is the sum ($\sum$.) of each component as it was derived from [16].

$$\text{TCc} = \sum_{\text{co}} \text{Cc}_{\text{co}} * \text{CRF} * h, \tag{4}$$

where "co" is the installation components and "Cc_{co}" is the capital cost of a specific component which depends on the number of installed components.

(ii) Replacement cost (Rc): the cost related to component changes in the worst scenario. An example may be a battery that may be replaced more than once during the lifetime of the project (R_{Bat}).

$$R_c = n_{\text{Bat}} * R_{\text{Bat}} * \text{SFF} * n, \tag{5}$$

where n is the project lifetime (Yr.) and it is estimated to be 25 years for PV systems; n_{Bat} is the number of installed batteries; R_{Bat} is battery replacement during the lifetime of the project; and SFF are the sinking fund factors. It allows the computation of the real amount of money that can be spent while considering the interest rate of the saving account. It is mostly used when the future payment is forecast.

$$\text{SFF} = \frac{i_L}{(1 + i_L)^n - 1}, \tag{6}$$

where i_L is the interest rate offered by a bank for a saving account. It is also called real discount rate (%).

(iii) Maintenance cost (Mc): the total maintenance cost (TMc) of each component of the system is generally set to a value of 1% of its capital cost. It depends on the inflation rate (i_r) and the final value of the payment (FVA) over the project's lifetime (n) after adding the inflation rate.

$$\text{FVA} = \frac{(1 + i_r)^n}{i_r + 1}$$
$$\text{TMc} = \sum_{\text{co}} \text{Mc}_{\text{co}} * \text{FVA}. \tag{7}$$

Table 3: The sizing of PV, battery, and converter to supply power to AC load. This case can well fit in regions far from the national utility.

Load demand: 5467 Wh	Battery needed Li-ion (ASM) 12 V/100 Ah with DoD 100%	Solar panels needed for off-grid systems with 5.5k Wh/m^2 yearly radiation
Load by considering two days of autonomy: 10934 Wh	1200 Wh need to charge this load for one day with 10934/1200 = 9.1 or 10 strings which makes battery size of 10 ∗ 1200 Wh = 12,000 Wh	We consider solar irradiance of 1000 W/m^2 with 5.5 hours of solar availability
The site where data was collected manifests clearness index of 0.55 (Figure 3) which is a good indicator for clear and sunny region, so two days of autonomy is a good approximation to minimize the battery cost in this design	The 10 strings of batteries will be connected in parallel to make a battery bank be able to accumulate maximum solar charges. It is noted that the battery is the only component that is mostly expensive, and they need a replacement before the lifetime of solar photovoltaics	Solar panel capacity: 12,000 Wh/5.5 h = 2181.8 W. Using this CS6K-295MS solar, we get minimum of 2182/295 = 7.4 or simply 8 solar panels to meet the daily load demand

The optimization problem is constrained by the technical constraints in Homer Pro optimization tool and by the maintenance of a permanent power supply of the residential house load and thus maintaining a nil loss of power supply probability (LPSP). It can be important to compute the loss of power supply (LPS_h) when the energy produced by the PV panels and the energy stored in batteries are not sufficient to meet the load demand. The PV output is served as input to battery and the battery output to DC/AC inverter which feeds the load through AC bus. Its formula is given by the following expression:

$$\mathrm{LPS}_h = E_{\mathrm{Load},h} - \left(E_{\mathrm{PV},h} + E_{\mathrm{Bat},h-1} - E_{\mathrm{Bat,min}}\right) * \eta_{\mathrm{inv}}, \quad (8)$$

where η_{inv} is the inverter efficiency; $E_{\mathrm{Load},h}$ is the amount of energy consumed by the load at step period h; $E_{\mathrm{PV},h}$ is the amount of energy produced by the PV panels at step period h; $E_{\mathrm{Bat},h-1}$ is the amount of stored energy in battery bank at the previous period $h-1$; and $E_{\mathrm{Bat,min}}$ is the minimum amount of battery energy to maintain its depth of discharge.

$$\mathrm{LPSP} = \frac{\sum_h \mathrm{LPS}_h}{\sum_h \mathrm{E}_{\mathrm{Load},h}}. \quad (9)$$

The optimization problem from of the PV-battery backup system is then summarized as follows:

$$\begin{cases} \text{minimize } f(x) = \mathrm{Cc} + \mathrm{Mc} + \mathrm{Rc} + \mathrm{ChBc} \\ x \text{ is subjected to LPSP} = 0 \\ P_{\mathrm{Load},h} \le P_{\mathrm{max;for\,all}\,h}, \end{cases} \quad (10)$$

where $P_{\mathrm{Load},h}$ is the amount of power consumed by the load at step period h and P_{max} is the contracted power limit of the utility grid and it is a fixed preset threshold.To maximize the output of PV microgrid and protect the state of charge of battery within the prescribed limits of charging and discharging, a PV charge controller is used. In Homer software, the charge controller cost is not separated from the PV panels. The efficiency of charge controller n_{chco} can be computed as follows:

$$n_{\mathrm{chco}} = \frac{P_{\mathrm{mpp}} * n_{\mathrm{PV}}}{i_{\mathrm{chco}} * V_{\mathrm{sys}}}, \quad (11)$$

where i_{chco} is the rated current of the charge controller, P_{mpp} is the maximum power of PV panels, n_{PV} is the number of PV panels to make PV array, and V_{sys} is the system bus voltage.In Homer software, the charge controller is not separated from the PV panels.

4. Optimization Results and Analysis with Homer Pro Software

With Homer Pro software, three case studies are analyzed for a residential home of 5,467 kWh/day in Kigali city with the following components: The national utility grid price per unit (0.2621 US$/kWh) [5], Canadian solar superpower CS6K-295MS, Generic 1 kWh Li-ion Battery of ASM model, and the System converter with the model Leonics, MTP-413F.

The following are the detailed cost summary results obtained from simulations with Homer Pro for the three respective schematic models.

4.1. Case I: Grid (999,999 kW)-CS6K-295MS (18 kW)-Li-ion (1kWh) and Leonics-MTP-413F (25 kW). In this case, the proposed microgrid was optimized in Homer Pro with components such as solar Canadian model CS6K-295MS (18 kW) for a cost of 37,800 US$, i.e., 2.1US$/1 watt, battery model Li-ion (1 kWh) for a cost of 700 US$, and utility grid that is highly depending on monthly bills. Through the converter model, Leonics MTP-413F (25 kW) at a cost of 15,000 US$, a residential load demand of 5.467 kW, was supplied. The total system requires investments of 53,500 US$. The simulation results are NPC of 22,155 US$ and LCOE of 0.0645 US$/kWh. Operating and replacement cost is evaluated to 43,041 US$, and 13,549 US$, respectively. The system salvage results in 1,853 US$ from the converter contribution of 1,797 US$, and battery's salvage is 55.9 US$. Figure 7 gives the

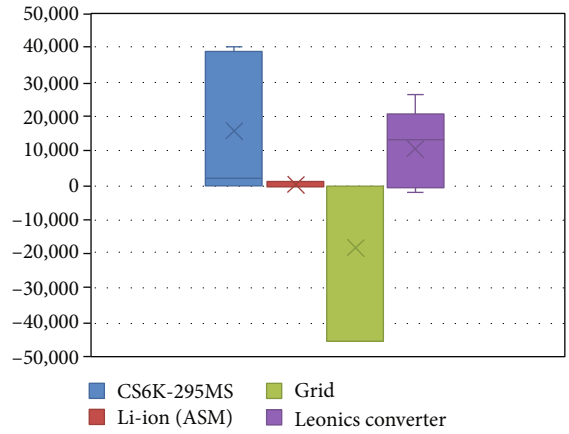

Figure 7: Cost summary (US$) results for PV (CS6K-295MS), battery (Li-ion), grid, and converter system.

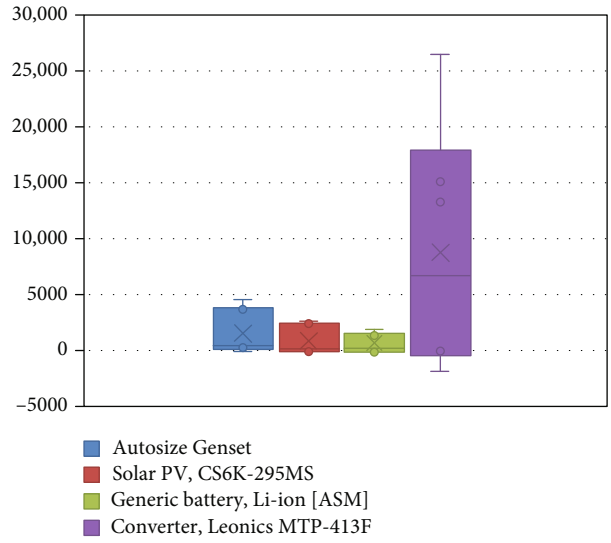

Figure 8: Cost summary (US$) from Homer Pro simulation results for PV, generator, battery, and converter.

details of the cost contribution in US$ for each component in the system. The roles of PV and converter are mentioned with big contribution in supplying load demand. The outputs of PV and Battery are all DC power which are converted into AC power through the converter model (Leonics MTP-413F, 25 kW) to both feed the AC load and producing the excess power to sell back to the grid. The Homer Pro optimization software minimized the low usage of batteries which may be only needed during power back up or peak hour period. The PV and converter manifest high cost contribution in the system. The system is designed to minimize the grid cost and therefore put much focus to renewable energies usages by regulating the automatic transfer switch (ATS). The battery contribution is low in order to minimize the system cost. Figure 7 illustrates the cost summary (US$) of PV (CS6K-295 MS), battery (Li-ion), grid connected, and converter system.

The installed capacity that is explored in Case I resulted in electrical energy production of 27,647 kWh/year of which

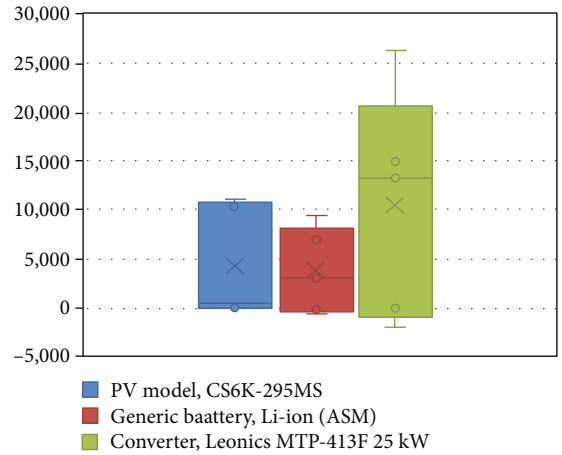

Figure 9: Cost summary (US$) from Homer Pro simulation results for PV, battery, and converter.

the solar PV (CS6K-295MS) produce 26,973 kWh/year, i.e., 97.6% with Grid purchases equivalent to 673 kWh/year, i.e., 2. 43%. Among the total energy produced, only 1,995 kWh/year, i.e., 7.51% is dedicated to AC load demand while the remaining 24,815 kWh/year, i.e., 92.6% has been sold to the grid. This justify why the solar PV for the grid connected PV system is highly rated (up to 18 kW) with its corresponding converter (25 kW) while in the case of the other two off-grid systems, their power ratings are exactly matching the load requirement. The energy purchased from the grid is much lower than the energy sold to the Grid. This motivate the PV microgrid owner to stack on solar PV energy production in the country where the energy sells and buy policy is well structured.

4.2. Case II: Generator (1.3 kW)-CS6K-295MS (1.69 kW)-Li-ion Battery (5 kWh)-Leonics-MTP-413F (25 kW). Case II proposes PV microgrid with their components such as diesel generator (0.5 kW) for the cost of 4,650 US$, solar PV model CS6K-295MS (1.16 kW) for a cost of 2,597 US$, battery model Li-ion (2 kWh) for a cost of 1,903 US$, and the converter model, Leonics MTP-413F (25 kW) for a cost of 26,455 US$ which are all designed to supply the residential load demand of 5.467 kW/day. The total system requires investments of NPC of 35,605 US$ to raise the LCOE of 1.38 US$/kWh. To meet the AC load demand while minimizing the high fuel cost of generator, the converter contribution is more enormous than other components due to its high task to invert the DC power output from both PV and battery into their equivalent AC power. Although the initial capital is relatively small with 19,096 US$, there is an additional great cost mainly related to generator component, battery, and converter replacement equivalent to 361.97 US$, 603.82 US$, and 13,252 US$, respectively. The operation, salvage, and resources are, respectively, given by 577.78 US$, 1,917 US$, and 3,631 US$ for an estimated lifetime of more than 25 years. It is noted that the salvage is the value remaining in a component of power system at the end of the project lifetime. Figure 8 shows the cost contribution for each component.

Table 4: Comparison of different state-of-the-art results based on economic analysis and the proposed approach.

Reference	Study location & irradiation (kWh/m^2/d)	Model architecture with power ratings	Principal economic indicators (cost units)				Electrical production and/or power consumption.
			Initial capital cost	Operating cost ($/Yr.)	NPC	LCOE	
[18]	Baru Sahib in India & [7.57]	PV: 6 kW DG: 3 kW Converter: 1 kW	11,530$	5,067	76,307$	1.211$/kWh	Consumption (kWh/Yr.) AC load demand: 13kWh/day with 2.5 kWp
[19]	Residential load of Sunderbans in India & [4.978]	Case A: hybrid (PV-FC) PV: 2 kW FC: 0.1 kW Electrolyzer: 0.5 kW BT: 8 Converter: 1 kW	18,375$	353$	21,141$	2.473$/kWh	Production (kWh/Yr.) PV: 2416, i.e., 98% FC: 52, i.e., 2% Consumption (kWh/Yr.) AC load: 1095, i.e., 57% Electrolyzer load: 822, i.e., 43%
		Case B: Hybrid (WT-FC) WT: 10 kW FC: 0.1 kW Electrolyzer: 1.5 kW BT: 24 Converter: 0.5 kW	31,450$	1,512$	50,785$	3.628$/kWh	Production (kWh/Yr.) WT: 5,111, i.e., 98% FC: 92, i.e., 2% Consumption (kWh/Yr.) AC load: 1,095 i.e.43% Electrolyzer load: 1,442, i.e., 57%.
		Case C Hybrid (PV-WT-FC) PV: 0.5 kW WT: 10 kW FC: 0.1 kW Electrolyser:1 kW BT: 8 Converter: 0.5 kW	29,475$	931$	41,373$	2.956$/kWh	Production (kWh/Yr.) PV: 604, i.e., 10% WT: 5,111 i.e.88% FC: 106, i.e., 2% Consumption (kWh/Yr.) AC load: 1,090, i.e., 39% Electrolyzer load: 1,714, i.e., 61%
[20]	Technical (Matlab) and economic (Homer Pro) Papua in Indonesia & [4.74]	Pure PV BT: 12 V/100 Ah	C_{BT}: 186.19$	—	203,271$	0.64$/kWh	Load consumption (kWh/day) AC load: 45,6
		Pure DG	0.54$/1 L	—	320,661$	1.17 $/kWh (1$ =14,877.22Rp)	
[21]	Off-grid rural electrification in Rwanda & [5.4]	Hyd: 10 kW WT: 100 kW PV: 10 kW Hyd (1Turbine): 10 kW PV: 1.09 kW Converter: 10 kW	C_{WT}: 80,000$ C_{Hyd}: 20,000$ C_{PV}: 16,000$ C_{BT} (1 kWh each): 2,400$; $C_{Converter}$: 30,000$	1,495.49$	41,210.80$	0.0560$/kWh	Production (kWh/Yr.) Hyd: 122,716, i.e., 98.7% PV: 1,620, i.e., 1.3% Consumption (kWh/day) AC load: 158.1 Peak:18 kW
		Hyd: 10 kW WT: 100 kW WT:100 kW PV: 10 kW					

Table 4: Continued.

Reference	Study location & irradiation ($kWh/m^2/d$)	Model architecture with power ratings	Principal economic indicators (cost units)				Electrical production and/or power consumption.
			Initial capital cost	Operating cost ($/Yr.)	NPC	LCOE	
[22]	Rural area in the southern city of Bangladesh	Hybrid (Grid-PV-WT) Grid: 999,999 kW PV: 150 kW WT (3 WGs) Converter: 180 kW Off-grid (WT-PV)	600,000$	-4,977$	535,661$	0.0995$/kWh	Production (kWh/Yr.) WT: 124,625, i.e., 28.57% PV: 198,814, i.e., 45.58% Grid purchases: 112,747, i.e., 25.85% Consumption (kWh/Yr.) AC load: 238,976, i.e., 57.4% Grid sales:177328, i.e., 42.6%
[23]	The hybrid (PV-FC) power system residential community in Sharjah (150houses)	PV: 517 kW FC: 750 kW H_2 tank: 900 kg Inverter: 738 kW	—	—	3.07 million$	145$/MWh	Production (MWh/Yr.) PV: 1052.68, i.e., 52% FC: 980.32, i.e., 48% Consumption (MWh/Yr.) AC load: 238,976, i.e., 80.7% Electrolyzer load: 286.37, i.e., 14.08% Excess power: 37.53, i.e., 1.8% Losses in power conversion: 68.37, i.e., 3.3%
[12]	HPSs for typical residential loads for the rural community in South Africa.	PV: 5 kW BT (30): 720 Ah Regulator: 12/24 V,5A DG: 5.5 kW, 50 Hz @ 3,000 rpm Converter: 6 kW	C_{PV}: 4,250$ C_{BT}: 269$ C_{Fuel1}: 15,398$ (0.7$/L) C_{Fuel2}: 32,990$ (0.9$/L) C_{DG}: 313$ $C_{Converter}$: 3,731$	—	62,402$ for (0.7$/L) 65,833$ for (0.9$/L)	—	Upington city results RF: 0.75 Lowest diesel used: 1,267 [L/year] at (0.7$/1 L) & 1,275 [L/year] at (0.9$/1 L) Lowest emission of CO_2 3.336 [tons/year] for diesel 1 price (0.7$/1 L) 3.359 [tons/year] for diesel 2 price (0.9$/1 L)
[16]		First site location: Pulau Banggi in Malaysia					
	Solar radiation averaging [4.8–6.1]	Optimized Hybrid 1PV/(G1-G5) Diesels/Battery system (42.38% RE)	—	536,081$	9,345,510$	0.302$/kWh	Existing LCOE: 0.5352$/kWh The improvement: 0.2332$/kWh Load consumption: 6,632.86 kWh/day with 476.23 kWp
		Second site location: Tanjung Labian in Malaysia					
	Solar radiation averaging [4.8 –6.1]	Optimized Hybrid 1PV/(G1-G3) Diesels/Battery system (39.89% RE)	—	302,203$	5,571,168$	0.312$/kWh	The improvement: 0.2234$/kWh Load consumption: 3,830.07 kWh/day with 417.55 kWp

Table 4: Continued.

Reference	Study location & irradiation ($kWh/m^2/d$)	Model architecture with power ratings	Principal economic indicators (cost units)				Electrical production and/or power consumption.
			Initial capital cost	Operating cost ($/Yr.)	NPC	LCOE	
[24]	Khorramabad in Iran (data of 2012) Solar radiation averaging [5.15]	C_{PV}: 6,900$ C_{FC}: 2,500$ C_{H2Tank}: 1,200$ $C_{Electrolyzer}$: 1,500$-3,000$ C_{WT} (1.24 kW): 3,900$	215,500$	3,910$	234,843$	7.367$/kWh	Scheme A is not economical due to low efficiency of fuel cells Residential load consumption: 19 kWh/day with 2.6 kWp
		PV: 6,900$ WT(1.24 kW): 3,900$ DG (0.25$/L): 3,500$ Bat:6 V/1.156 ah: 1,200$; converter (efficiency:90%): 800$	24,600$	713$	28,128$	0.871 $/kWh	Scheme B: Economical and recommended by the authors. Residential load consumption 19 kWh/day with 2.6 kWp
[25]	Off-grid with PV, WT, DG	Optimal design: Puerto Estrella PV: 160 kW WT: 10 kW DG: 25 kW BT: 250 Converter: 80 kW	521,078$	24,652	836,210$	0.473$/kWh	Energy production (kWh/Yr.) PV: 180,475 DG: 2,789 WT: 2,988 CO_2 emission: 3,169 kg/Yr. RF: 0.99 Electricity consumption: 379 kWh/day with 88 kWp
	Off-grid with PV, DG	Optimal design for Unguia PV: 100 kW DG: 25 kW BT: 100 Converter: 30 kW	227,350$	11,373	372,736$	0.444$/kWh	Energy production (kWh/Yr.) PV: 180,475 DG: 4,553 CO_2 emission: 5,120 kg/Yr. RF: 0.98 Electricity consumption: 180 kWh/day with 38 kWp
	Off-grid with PV, DG.	Optimal design: Jerico PV: 150 kW DG: 25 kW BT: 100 Converter: 40 kW	268,100$	12,855	445,207$	0.488 $/kWh	Energy production (kWh/Yr.) PV: 267,345 DG: 5,250 CO_2 emission:5923 kg/Yr. RF:0.98 Electricity consumption 213 kWh/day with 41 kWp
[26]	Taleghan in Iran	PV: 0.8 kW WT (×2): 0.4 kW each Inverter: 2.5 kW BT (12 V/200 Ah): 8	22,998$	218	24,623$	1.655$/kWh	Energy production (kWh/Yr.) PV: 1,234 (41%) WT: 1,794 (59%) Energy consumption (kWh/Yr.) AC primary load: 1992, i.e., 100%

Table 4: Continued.

Reference	Study location & irradiation ($kWh/m^2/d$)	Model architecture with power ratings	Principal economic indicators (cost units)				Electrical production and/or power consumption.
			Initial capital cost	Operating cost ($/Yr.)	NPC	LCOE	
	Irradiation: [4.8]		Off-grid connection hybrid system				
	Case A	DG: 10 kW BG: 15 kW PV: 5 kW BT: 20 kW Converter:15 kW	C_{BG}: 1,600$/1 kW C_{PV}: 2,800$/1 kW C_{DG}: 370$/1 kWh C_{BT}: 1,295$ $C_{Converter}$: 1,000$/1 kWh		123,668$	0.145-0.119$/kWh	RF: 0.93 Load consumption: 117-186 kWh/day with 19 kWp
	Case B	DG: 10 kW BG: 15 kW			172,003$	0.129$/kWh	RF: 1, i.e., 100% Load consumption: 152-242 kWh/day with 25 kWp
	Case C	DG: 10 kW PV: 5 kW BT: 20 kW Converter:10 kW BG: 35 kW			217,551$	0.12$/kWh	RF: 1, i.e., 100% Load consumption: 248-392 kWh/day with 41 kWp
[27]			Grid-connected hybrid system				
	Case A	Grid: 100 kW BG: 15 kW	—	—	82,822$	0.064$/kWh	Energy production Grid purchase: 9% Grid sales: 23% RF: 0.91 Load consumption: 178 kWh/day with 19 kWp
	Case B	Grid: 100 kW BG: 15 kW			79,538$	0.064$/kWh	Energy production Grid purchase: 10% Grid sales: 28% RF: 0.90 Load consumption: 182 kWh/day with 25 kWp
	Case C	Grid: 100 kW BG: 30 kW			134,270$	0.064$/kWh	Energy production Grid purchase: 11% Grid sales: 5% RF: 0.89 Load consumption: 86 kWh/day with 41 kWp
[28]	Agricultural village in Pakistan & Irradiation: [5.18-6.95]	PV: 10 kW BT: 32 × 1 kWh Converter: 12 kW BG: 08 kW	16,057.31$, i.e., 2.64 M (Rs) 1$ = 164.41 Rs (2020)	864.32, i.e., 142,103 (Rs)	27,248.77$, i.e., 4.48 M (Rs)	0.034$/kWh or 5.51 Rs/kWh	Electricity production (kWh/Yr.) PV: 16,872, i.e., 24.6% BG: 57,721, i.e., 75.4% Consumption (kWh/Yr.) AC primary load: 65,372, i.e., 100%

Table 4: Continued.

Reference	Study location & irradiation (kWh/m^2/d)	Model architecture with power ratings	Principal economic indicators (cost units)				Electrical production and/or power consumption.
			Initial capital cost	Operating cost ($/Yr.)	NPC	LCOE	
			Case I: on-grid PV microgrid system design				
The proposed study	Residential home in Rwanda & Irradiation: [5.5]	Case I PV: 18 kW BT: 1 × 1 kWh Converter: 25 kW Grid: 999,999 kW	53,500$	-2,397*	22,155$	0.0645$/kWh	Electricity production (kWh/Yr.) PV: 26,973, i.e., 97.6% Grid purchase: 673, i.e., 2.4% EIRR: 2.47% Payback period: 18.1 Yrs. Consumption (kWh/Yr.) AC primary load: 1,995, i.e., 7.5% Grid sales: 24,572, i.e., 92.5%
			Case II and Case III: off-grid PV microgrid system design				
		Case II DG: 0.5 kW PV: 1.16 kW BT (1 kWh): 2 Converter Leonics model: 25 kW	19,096$	1,277	35,605$	1.38$/kWh	Electricity production (kWh/Yr.) Excess electricity:537 PV: 1,746, i.e., 65.8% & DG: 906, i.e., 34.2% Consumption (kWh/Yr.) AC primary load: 1,995, i.e., 100% Fuel used: 275 L/0.3 L/kWh.
		Case III PV: 5 kW BT (1kWh): 10 Converter Leonics model: 25 kW	32,500$	1,123	7,012$	1.82$/kWh	Electricity production (kWh/Yr.) Excess electricity: 5,349 PV: 7,493, i.e., 100% Unmet electric load: 1.33 Consumption (kWh/Yr.) AC primary load: 1,994, i.e., 100%

PV: photovoltaic array; Hyd: hydropower; WT/G: wind turbine/generator; FC: fuel cell; DG: diesel generator; BG: biomass generator; BT: battery; RF: renewable fraction; Mgt: management; C_{op}: operational cost (*i.e., $C_{op} = C_{Annual,total} - C_{Annual,capital}$); EIRR: economic internal rate of return. Annual costs are less than revenues.

The electrical and production summary from the Case II analysis are herewith explained in details:

The excess electricity produced was 537 kWh/year. There was no capacity shortage or unmet electric load. The solar PV (CS6K-295MS) produces 1,746 kWh/year, i.e., 65.8%, while the generator produces 906 kWh/year, i.e., 34.2%. The total annual power production of 2,652 kWh has been able to meet the load requirement by 100%. No energy excess or overproduction was observed. However, for a land locked country, like Rwanda, this system is not advisable since its NPC and LCOE are higher than Case I.

4.3. Case III: PV Power CS6K-295MS (5 kW)-Li-ion (1 kWh) for 10 Strings and Leonics MTP-413F (25 kW). The last case is the PV microgrid with all parts are renewable. The system has been optimized in Homer Pro with components such as Solar Canadian model CS6K-295MS (5 kW) for a cost of 11,146 US$, Battery model Li-ion (1 kWh) for a cost of 10 strings equivalent to 9,411 US$, and the converter model, Leonics-MTP-413F (25 kW) for a cost of 26,455 US$ and thus supplies the residential AC load demand of 5.467 kWh/day. The total system requires investments of NPC of 47,012 US$ to get LCOE of 1.82 US$/kWh. The converter cost contribution is similarly high as in Case II, which is followed by the solar PV array cost of 5 kW and 1 kWh battery for 10 string cost.

The operating and replacement costs are 646.38 US$ and 16,221 US$ of which 82% are due to converter and 18% are dedicated to battery cost replacements. The salvage was equal to 2,356 US$ with no resources. Figure 9 gives the result details.

The electrical and production summary from the Case III analysis is herewith detailed below:

The system produced the excess electricity of 5,349 kWh/year with 1.33 kWh/year of capacity shortage and 1.95 kWh/year of unmet electric load. The solar PV (CS6K-295MS) produces 7,493 kWh/year, i.e., 100% to meet the yearly load consumption of 1994. Although this is 100% renewable energy system, the economic indicators obtained do not permit it to be advisable in the proposed study when compared to Case I. The manual calculation in Table 3 met the simulation results on the required number of batteries needed for the model design for the total off-grid systems.

5. Comparison of Different State-of-the-Art Results with the Proposed Study

Table 4 shows the state of art of different studies using the various renewable energy resources and their results have been compared with the proposed study while focusing on two principal economic indicators. Two fundamental economic parameters such as net present cost (NPC) and levelized cost of energy (LCOE) have been set as the economic indicator for deciding the feasibility studies of the respective models' design. Other important parameters such as initial capital cost and operating cost have been reviewed. Those concluding parameters should be optimally minimized as much as possible in order to lower the cost of energy while providing reliable and feasible energy solutions to the citizens.

6. Conclusion

This study demonstrated the comparison analysis of three designed schematic models. One model is the grid-connected system with PV and battery (Figure 4) and the other two models are the off-grid system with PV-battery-diesel (Figure 5) and PV-battery only (Figure 6). With Homer Pro optimization results, it was possible to decide which layout is reliable, feasible, and benefiting the residential home in the city of Kigali based on the lowest fundamental and economic indicators. The results show the grid connected system in Figure 4 is able to meet the load demand on the lowest LCOE of 0.0645 US$/kWh and the NPC of 22,155 US$. The electricity price is four times cheaper than the current national electricity tariff. The system model provides more benefits such as the excess of PV microgrid energy produced at rate of 97.6% and the grid sales equivalent to 92.5%. This system has very low energy purchase of 2.4% from the grid, and it is meeting the load requirement of 7.5%. The more additional benefit from Figure 4 model is its excellent impact on the environmental weather due to the high rate of PV microgrid usage to supply the load demand. It has better economic impact due to its possibility to sell the excess power produced during the sunny period and the low peak hours. Therefore, it is highly recommended for this study. The other results from Figures 5 and 6 are, respectively, the LCOE of 1.38 US$/kWh and NPC of 35,605 US$ and LCOE of 1.82 US$/kWh with NPC of 32,500 US$. The contribution results of Figure 5 are 65.8% and 34.2% of solar PV and Diesel Generator's electrical energy production to supply the daily load demand of 5.47 kWh. The model produces 537 kWh/year of the excess electricity, but due to the geographical location of Rwanda which make it a land locked country with the unavailability of fuel to maintain the normal operation of diesel generator, it is not the best choice. The remaining contribution results are from the Figure 6 model where the system is 100% solar PV usage with a string of ten batteries for energy backup during the period of solar power failure to meet the designed load. The Figure 6 model has an annual of 1.33 kWh of unmet electric load with 5,349 kWh of the excess of electricity production. Although the model is excellently renewable, it may not be easy for a low or a middle-income population to handle its higher electricity tariff. Therefore, it is not recommended in this study.

Data Availability

The data used to support the study was given in supplementary files as Case 1, Case 2 and Case 3.

Conflicts of Interest

The authors declare that they have no conflicts of interest.

Acknowledgments

This work was supported by the key project of Tianjin Natural Science Foundation (Project No. 19JCZDJC32100) and the Natural Science Foundation of Hebei Province of China (Project No. E2018202282).

References

[1] B. Safari, "A review of energy in Rwanda," *Renewable and Sustainable Energy Reviews*, vol. 14, no. 1, pp. 524–529, 2010.

[2] Solargis, "The World Bank," 2019, https://solargis.com/maps-and-gis-data/download/rwanda.

[3] J. Dong, M. M. Olama, T. Kuruganti et al., "Novel stochastic methods to predict short-term solar radiation and photovoltaic power," *Renewable Energy*, vol. 145, pp. 333–346, 2020.

[4] J. D. Dieu Niyonteze, F. Zou, G. N. Osarumwense Asemota, and S. Bimenyimana, "Solar-powered mini-grids and smart metering systems, the solution to Rwanda energy crisis," *Journal of Physics: Conference Series*, vol. 1311, no. 1, article 012002, 2019.

[5] Rura, "Electricity tariffs in Rwanda," January 2020, https://rura.rw/fileadmin/publication/Press_release_for_Electricity_Tariffs.pdf.

[6] K. Kusakana and H. J. Vermaak, "Hybrid renewable power systems for mobile telephony base stations in developing countries," *Renewable Energy*, vol. 51, pp. 419–425, 2013.

[7] M. Fadaee and M. A. M. Radzi, "Multi-objective optimization of a stand-alone hybrid renewable energy system by using evolutionary algorithms: a review," *Renewable and Sustainable Energy Reviews*, vol. 16, no. 5, pp. 3364–3369, 2012.

[8] A. R. Gautam, K. Gourav, J. M. Guerrero, and D. M. Fulwani, "Ripple mitigation with improved line-load transients response in a two-stage DC-DC-AC converter: adaptive SMC approach," *IEEE Transactions on Industrial Electronics*, vol. 65, no. 4, pp. 3125–3135, 2018.

[9] D. K. Lal, B. B. Dash, and A. K. Akella, "Optimization of PV/wind/micro-hydro/diesel hybrid power system in HOMER for the study area," *International Journal on Electrical Engineering and Informatics*, vol. 3, no. 3, pp. 307–325, 2011.

[10] V. B. Mary, I. W. Christopher, and G. Themozhi, "RHES-economic analysis and power management for a technical institution using homer," in *5th International Conference on Electrical Energy Systems, ICEES*, Chennai, India, 2019.

[11] K. Ajao, O. Oladosu, and O. Popoola, "Summary for Policy-makers," *International Journal of Research and Reviews in Applied Sciences*, vol. 7, no. 1, pp. 96–102, 2014.

[12] J. Dekker, M. Nthontho, S. Chowdhury, and S. P. Chowdhury, "Economic analysis of PV/diesel hybrid power systems in different climatic zones of South Africa," *International Journal of Electrical Power & Energy Systems*, vol. 40, no. 1, pp. 104–112, 2012.

[13] Y. Li, M. Vilathgamuwa, S. S. Choi et al., "Design of minimum cost degradation-conscious lithium-ion battery energy storage system to achieve renewable power dispatchability," *Applied Energy*, vol. 260, article 114282, 2020.

[14] USAID/Power Africa/Rwanda2020. https://www.usaid.gov/powerafrica/rwanda.

[15] Homer Pro, "Homer Pro 3.14 user manual," 2020, https://www.homerenergy.com/products/pro/docs/latest/index.html.

[16] L. M. Halabi and S. Mekhilef, "Flexible hybrid renewable energy system design for a typical remote village located in tropical climate," *Journal of Cleaner Production*, vol. 177, pp. 908–924, 2018.

[17] N. Pawar and P. Nema, "Techno-economic performance analysis of grid connected PV solar power generation system using HOMER software," in *2018 IEEE International Conference on Computational Intelligence and Computing Research, ICCIC*, Madurai, India, 2018.

[18] H. Singh, D. Kaur, and P. S. Cheema, "Optimal design of photovoltaic power system for a residential load," in *Proceedings of the International Conference on Inventive Systems and Control, ICISC*, pp. 9–12, Coimbatore, India, 2017.

[19] S. Dey, R. Dash, and S. C. Swain, "Optimal design and feasibility study of renewable hybrid energy systems," in *1st International Conference on Emerging Trends in Engineering, Technology and Science, ICETETS*, Pudukkottai, India, 2016.

[20] A. I. Malakani, D. Handoko Arthanto, B. G. Dwi Wicaksono, and A. Purwadi, "Study and design of off-grid PV power system in Pirien, Asmat Regency, Papua Province using MATLAB/SIMULINK," *Proceedings of the 2nd International Conference on High Voltage Engineering and Power Systems: Towards Sustainable and Reliable Power Delivery, ICHVEPS*, 2019, pp. 339–343, Denpasar, Bali, Indonesia, 2019.

[21] J. D. D. Niyonteze, F. Zou, G. Norense Osarumwense Asemota, S. Bimenyimana, and G. Shyirambere, "Key technology development needs and applicability analysis of renewable energy hybrid technologies in off-grid areas for the Rwanda power sector," *Heliyon*, vol. 6, no. 1, article e03300, 2020.

[22] M. Nurunnabi and N. K. Roy, "Grid connected hybrid power system design using HOMER," in *Proceedings of 2015 3rd International Conference on Advances in Electrical Engineering, ICAEE*, pp. 18–21, Dhaka, Bangladesh, 2015.

[23] C. Ghenai, T. Salameh, and A. Merabet, "Technico-economic analysis of off grid solar PV/fuel cell energy system for residential community in desert region," *International Journal of Hydrogen Energy*, vol. 45, no. 20, pp. 11460–11470, 2020.

[24] M. Jahangiri, O. Nematollahi, A. Sedaghat, and M. Saghafian, "Techno-economical assessment of renewable energies integrated with fuel cell for off grid electrification: a case study for developing countries," *Journal of Renewable and Sustainable Energy*, vol. 7, no. 2, 2015.

[25] A. Haghighat Mamaghani, S. A. Avella Escandon, B. Najafi, A. Shirazi, and F. Rinaldi, "Techno-economic feasibility of photovoltaic, wind, diesel and hybrid electrification systems for off-grid rural electrification in Colombia," *Renewable Energy*, vol. 97, pp. 293–305, 2016.

[26] A. Shiroudi, R. Rashidi, G. B. Gharehpetian, S. A. Mousavifar, and A. Akbari Foroud, "Case study: simulation and optimization of photovoltaic-wind-battery hybrid energy system in Taleghan-Iran usinghomersoftware," *Journal of Renewable and Sustainable Energy*, vol. 4, no. 5, 2012.

[27] R. Rajbongshi, D. Borgohain, and S. Mahapatra, "Optimization of PV-biomass-diesel and grid base hybrid energy systems for rural electrification by using HOMER," *Energy*, vol. 126, pp. 461–474, 2017.

[28] M. K. Shahzad, A. Zahid, T. ur Rashid, M. A. Rehan, M. Ali, and M. Ahmad, "Techno-economic feasibility analysis of a solar-biomass off grid system for the electrification of remote rural areas in Pakistan using HOMER software," *Renewable Energy*, vol. 106, pp. 264–273, 2017.